



HAL
open science

Biogeochemistry at the dawn of Carbonate deposition on Earth: elemental and isotopic chemostratigraphy of the Mesoarchean Red Lake carbonate platform, Canada

Munira Afroz

► **To cite this version:**

Munira Afroz. Biogeochemistry at the dawn of Carbonate deposition on Earth: elemental and isotopic chemostratigraphy of the Mesoarchean Red Lake carbonate platform, Canada. *Geochemistry. Université de Bretagne occidentale - Brest*, 2023. English. NNT: 2023BRES0031 . tel-04247867

HAL Id: tel-04247867

<https://theses.hal.science/tel-04247867>

Submitted on 18 Oct 2023

HAL is a multi-disciplinary open access archive for the deposit and dissemination of scientific research documents, whether they are published or not. The documents may come from teaching and research institutions in France or abroad, or from public or private research centers.

L'archive ouverte pluridisciplinaire **HAL**, est destinée au dépôt et à la diffusion de documents scientifiques de niveau recherche, publiés ou non, émanant des établissements d'enseignement et de recherche français ou étrangers, des laboratoires publics ou privés.

THESE DE DOCTORAT DE

L'UNIVERSITE DE BRETAGNE OCCIDENTALE

ECOLE DOCTORALE N° 598
Sciences de la Mer et du Littoral
Spécialité : *Géosciences marines*

Par

Munira AFROZ

Biogeochemistry at the Dawn of Carbonate Deposition on Earth: Elemental and Isotopic Chemostratigraphy of the Mesoarchean Red Lake Carbonate Platform, Canada

Thèse présentée et soutenue à Plouzané, le 22 juin 2023
Unité de recherche : UMR 6538 GEO-OCEAN

Rapporteurs avant soutenance :

Paul MASON Professor, Utrecht university
Stefan SCHRÖDER Senior Lecturer, University of Manchester

Composition du Jury :

Président:	Marina RABINEAU	Research Director, CNRS, Université de Bretagne Occidentale
Examineurs:	Paul MASON Stefan SCHRÖDER	Professor, Utrecht university Senior Lecturer, University of Manchester
Directeur de thèse:	Stefan LALONDE	Research Fellow, CNRS, Université de Bretagne Occidentale

**Biogeochemistry at the Dawn of
Carbonate Deposition on Earth:
Elemental and Isotopic
Chemostratigraphy of the
Mesoarchean Red Lake Carbonate
Platform, Canada**

Munira Afroz

Summary

The Mesoarchean (2.87 Ga) Ball Assemblage of the Red Lake Greenstone Belt (Superior Craton, NW Ontario, Canada) preserves Earth's oldest known thick carbonate platform. Here, a diverse 290 m-thick carbonate assemblage of stromatolitic dolostones and massive limestone, along with associated chemical and siliciclastic rocks, make up the 490 m-thick Red Lake carbonate platform, which provides a unique opportunity to understand Mesoarchean marine biogeochemistry at the inception of Earth's carbonate factory. This doctoral thesis presents sedimentological, elemental, and isotopic (stable carbon, oxygen, and multiple sulfur isotopes) analyses of five cored drill holes capturing a variety of sediments deposited in shallow-water, platform slope, and deep-water settings, which were examined and analyzed to establish a multi-parameter chemostratigraphy spanning the entire succession. Major element data clearly demonstrate the sedimentological and geochemical responses to changes in sea level and associated water column chemistry of the carbonate-producing Mesoarchean margin. The rare earth element systematics of the diverse lithofacies reveal modern-like seawater signatures but with several additional characteristics specific to Archean seawater. A general lack of Ce anomalies testifies to prevailing anoxic conditions while important Eu anomalies reveal the influence of high-temperature hydrothermal inputs to the basin. The occasional presence of oxygen in the water column is inferred from rare Ce anomalies, both positive and negative, and along with associated Mn and Cr enrichments in some iron formation and limestone samples, suggest periodic oxygenation of the water column, at least locally. The mild but significant authigenic enrichment of certain redox-sensitive trace elements (i.e., Mo, V, U, and Cr) in carbonates and iron formations further suggest redox cycling under mildly oxic water column conditions. The carbon and oxygen stable isotope compositions of the carbonates are mineralogically and water-depth-controlled; stromatolitic dolostone shows evidence of meteoric water interaction during dolomitization, while the deeper water limestone appears to have captured the isotopic signature of the open ocean DIC pool. The carbon stable isotope data are examined in a global mass balance model that reveals that the Mesoarchean carbon cycle must have been dramatically different than today. Multiple sulfur isotope data indicate that the sulfide-rich shales preserved at Red Lake possess typical Mesoarchean isotopic compositions, with contributions from juvenile sulfur along with atmospherically processed elemental sulfur and sulfate. Overall, this work provides important new context for Mesoarchean ocean chemistry, carbon and metal cycling, and the occasional presence of oxygen during the earliest history of significant carbonate sedimentation on Earth.

Sommaire

L'assemblage mésoarchéen (2,87 Ga) de Ball de la ceinture de roches vertes de Red Lake (craton Supérieur, nord-ouest de l'Ontario, Canada) préserve la plus ancienne plate-forme carbonatée épaisse connue de la Terre. Ici, un assemblage carbonaté diversifié de 290 m d'épaisseur, composé de dolomies stromatolitiques et de calcaires massifs, ainsi que de roches chimiques et siliciclastiques associées, constitue la plate-forme carbonatée de Red Lake, qui offre une occasion unique de comprendre la biogéochimie marine du Mésoarchéen au début de l'usine carbonatée de la Terre. Cette thèse de doctorat présente des analyses sédimentologiques, élémentaires et isotopiques de cinq forages carottés capturant une variété de sédiments déposés dans des eaux peu profondes, sur la pente de la plate-forme et en eaux profondes. Les données sur les éléments majeurs démontrent clairement les réponses sédimentologiques et géochimiques aux changements du niveau de la mer et à la chimie de la colonne d'eau. La systématique des éléments des terres rares des divers lithofaciès révèle des signatures d'eau de mer de type moderne, mais avec des caractéristiques supplémentaires propres à l'eau de mer archéenne. L'absence générale d'anomalies en Ce témoigne des conditions anoxiques qui prévalent, tandis que des anomalies en Eu révèlent l'influence des apports hydrothermaux à haute température dans le bassin. La présence occasionnelle d'oxygène dans la colonne d'eau est déduite de rares anomalies de Ce, tant positives que négatives, et, avec les enrichissements en Mn et Cr associés, suggère une oxygénation périodique de la colonne d'eau, au moins localement. L'enrichissement authigène de certains oligo-éléments sensibles à l'oxydoréduction (Mo, V, U et Cr) suggère également des conditions de colonne d'eau légèrement oxique. Les compositions en isotopes stables du carbone et de l'oxygène des carbonates sont contrôlées par la minéralogie et la profondeur de l'eau ; la dolomie montre des signes d'interaction avec l'eau météorique pendant la dolomitisation, tandis que le calcaire des eaux plus profondes semble avoir capturé la signature isotopique l'océan ouvert. Les données sont examinées dans le cadre d'un modèle de bilan de masse global qui révèle que le cycle du carbone au Mésoarchéen devait être radicalement différent de celui d'aujourd'hui. Les données isotopiques multiples du soufre indiquent que les schistes riches en sulfures préservés à Red Lake possèdent des compositions isotopiques typiques du Mésoarchéen, avec des contributions de soufre juvénile ainsi que de soufre élémentaire et de sulfate transformés par l'atmosphère. Dans l'ensemble, ces travaux fournissent un nouveau contexte important pour la chimie océanique du Mésoarchéen, les cycles du carbone et des métaux, et la présence occasionnelle d'oxygène au cours de la première histoire de sédimentation carbonatée significative sur Terre.

Acknowledgments

I would like to express my gratitude to my supervisor, Dr. Stefan Lalonde, for his outstanding guidance, motivation, and unwavering support throughout my PhD. I am deeply thankful to Dr. Lalonde for all he has done to make my life in France easier. I am also indebted to Dr. Philip Fralick for introducing me to the fascinating field of Archean geology during my MSc and for providing valuable advice and encouragement throughout my PhD research.

I extend my gratitude to the members of the CSI committee - Dr. Magali Ader, Dr. Germain Bayon, Dr. Philippe Nonnotte, and Dr. Pierre Bonnand - for their suggestions and support during the past few years. I am also thankful to Dr. Johanna Marin Carbonne for her assistance in working in SwissSIMS at the University of Lausanne.

I would like to thank the dedicated staff and technicians at IUEM for their consistent support over the years. This research was made possible through the generous funding support of CNRS and ERC.

I am grateful to the EARTHBLoom team for their exceptional assistance in the fieldwork and core logging. Special thanks to Sophie Kurucz, Brittany Ramsay, and Dylan Wilmeth, whose intellectual support and companionship made every fieldwork enjoyable and memorable. I would also like to thank Laureline Patry and Amandine Migeon for being cordial lab mates and always available to help me translate from French to English.

Lastly, I want to acknowledge my family for their continuous support and inspiration throughout this journey. With that, I dedicate this dissertation to my late father.

Table of Contents

Title Page	3
Summary	5
Sommaire	6
Acknowledgments	7
Table of Contents	8
List of Figures	13
List of Tables	17
Résumé	287
Abstract	287

Chapter 1: Introduction	19
1.1 The earliest history of Earth: the Hadean and Archean Eons	20
1.2 Archean carbonates around the globe	21
1.2.1 Eoarchean carbonates (4.0-3.6 Ga)	23
1.2.2 Paleoarchean carbonates (3.6-3.2 Ga)	24
1.2.3 Mesoarchean carbonates (3.2 - 2.8 Ga)	28
1.2.4 Neoproterozoic carbonates (2.8-2.5 Ga)	30
1.3 Shallow to deep water carbonates in Archean rock records	35
1.4 Previous studies of the Red Lake carbonate platform	36
1.5 Research objectives and overview of the dissertation	38
1.6 References	41

Chapter 2: Geological setting.....	51
2.1 Geology of the Red Lake greenstone belt.....	52
2.2 Geology of the Red Lake carbonate platform.....	55
2.3 Chemical sedimentary rocks in the Red Lake carbonate platform	57
2.3.1 Carbonates	58

2.3.1.1	Stromatolitic carbonate.....	58
2.3.1.2	Carbonate-magnetite.....	60
2.3.1.3	Slumped carbonate	61
2.3.2	Oxide iron formation.....	63
2.3.3	Chert.....	63
2.4	Siliciclastic rocks in the Red Lake carbonate platform	63
2.4.1	Conglomerate and sandstone.....	63
2.4.2	Siltstone.....	64
2.4.3	Black shale	64
2.4.4	Sulfidic shale	65
2.5	Reference	66
Chapter 3: Methodology.....		69
3.1	Fieldwork	70
3.2	Core logging and location of the cored drill holes.....	70
3.3	Sample preparation	71
3.4	Whole-rock major element analysis.....	72
3.5	Whole-rock trace element and REE analysis.....	73
3.5.1	Total digestion	73
3.5.2	Leach digestion	74
3.6	XRF core scanning.....	74
3.7	μ XRF scanning	75
3.8	Carbonate carbon and oxygen stable isotope analysis.....	75
3.9	In-situ multiple sulfur isotope analysis	76
3.10	Loss on ignition analysis.....	77
3.11	X-ray diffraction (XRD)	77
3.12	Petrographic analysis	78
3.13	References.....	79
Chapter 4: Chemostratigraphy of the Mesoarchean (2.87 Ga) Red Lake carbonate platform, Northwest Ontario, Canada.....		81
	Abstract.....	82
4.1	Introduction.....	84
4.2	Geological setting	87
4.2.1	Drill hole locations.....	88

4.3	Methodology	88
4.4	Results	91
4.4.1	Stratigraphy of the Red Lake carbonate platform	91
4.4.2	Chemostratigraphy of redox-sensitive trace and rare earth elements	93
4.4.2.1	Chemostratigraphy of the PB12-35 drill hole	93
4.4.2.1.1	Redox-sensitive trace element compositions of PB12-35	93
4.4.2.1.2	Rare earth element compositions of PB12-35	95
4.4.2.2	Chemostratigraphy of the PB12-32 drill hole	95
4.4.2.2.1	Redox-sensitive trace element compositions of PB12-32	95
4.4.2.2.2	Rare earth element compositions of PB12-32	97
4.4.2.3	Chemostratigraphy of the PB12-33 drill hole	97
4.4.2.3.1	Redox-sensitive trace element compositions of PB12-33	97
4.4.2.3.2	Rare earth element compositions of PB12-33	99
4.4.2.4	Chemostratigraphy of the EBL10-28 drill hole	99
4.4.2.4.1	Redox-sensitive trace element compositions of EBL10-28	99
4.4.2.4.2	Rare earth element compositions of EBL10-28	99
4.4.2.5	Chemostratigraphy of the NGI10-31 drill hole	101
4.4.2.5.1	Redox-sensitive trace element compositions of NGI10-31	101
4.4.2.5.2	Rare earth element compositions of NGI10-31	101
4.5	Discussion	103
4.5.1	High-resolution chemostratigraphy of Archean sediments by XRF core scanning	103
4.5.2	Weathering and provenance analysis of siliciclastic rocks	104
4.5.3	Redox proxies in the Mesoarchean ocean	106
4.5.4	Rare earth element insights into Mesoarchean ocean chemistry	113
4.5.5	Red Lake carbonate platform architecture	122
4.6	Conclusions	125
4.7	Reference	127

Chapter 5: Carbon and Oxygen Isotope Chemostratigraphy of the Mesoarchean Carbonate Platform at Red Lake, Canada.....143

Abstract	144
5.1 Introduction	146
5.2 Geological Background and Sampled Material	149
5.3 Methods	150
5.4 Results	151
5.5 Discussion	156
5.5.1 Lithological, diagenetic, and metamorphic controls on carbon and oxygen stable isotope compositions	157

5.5.2	Potential paleoenvironmental signals preserved at Red Lake carbonate platform.....	165
5.5.3	Isotope mass balance in the Mesoarchean carbon cycle: the carbon level model revisited.....	170
5.6	Conclusions.....	175
5.7	References.....	177
Chapter 6: In-situ multiple sulfur isotope analyses of shale-hosted sulfides of the Red Lake carbonate platform.....		185
	Abstract.....	186
6.1	Introduction.....	187
6.2	Samples and Methods	190
6.3	Results.....	191
6.4	Discussion.....	192
6.4.1	Sources of sulfur in sedimentary sulfides at Red Lake.....	194
6.5	Conclusion	201
6.6	References.....	202
Chapter 7: Conclusion and Perspectives		211
7.1.	Summary of the principal findings	212
7.2.	Implications for trace element cycling and paleo-redox reconstruction at the dawn of oxygenic photosynthesis	217
7.3.	Perspectives for global carbon cycling at the dawn of carbonate precipitation on Earth	220
7.4.	A multiple isotope perspective on the deposition of one of Earth's most ancient sulfidic black shales	222
7.5.	Concluding remarks.....	223
7.6	References.....	225
Appendices		
Appendix A.....		227
A.1.	Whole rock major element concentrations (wt.%) for the Red Lake samples.....	228

A.2. Whole rock minor and trace element concentrations (ppm) for the Red Lake samples....	234
A.3. Whole rock REE concentrations (ppm) for the Red Lake samples.....	241
A.4. Carbonate leach minor and trace element concentrations (ppm) for the Red Lake samples	248
A.5. Carbonate leach REE concentrations (ppm) for the Red Lake samples.....	254
A.6. Supplementary figures.....	260
Supplementary Figure 4.1. Major elements profile with superimposed calibrated XRF data for PB12-35 and PB12-32 drill holes.....	260
Supplementary Figure 4.2. Major elements profile with superimposed calibrated XRF data for PB12-33 and EBL10-28 drill holes.....	261
Supplementary Figure 4.3. Major elements profile with superimposed calibrated XRF data for NGI10-31 hole.....	262
Supplementary Figure 4.4. Al-normalized redox-sensitive trace elements versus Eu/Eu* anomalies plot.....	263
Supplementary Figure 4.5. Al-normalized redox-sensitive element profiles and PAAS- normalized REE profiles for the 17-GA1 drill hole.....	264
Appendix B.....	265
Appendix B.1. $\delta^{13}\text{C}$ and $\delta^{18}\text{O}$ isotope data for the Red Lake carbonate samples.....	266
Appendix C.....	275
Appendix C.1. Multiple sulfur ($\delta^{34}\text{S}$, $\Delta^{33}\text{S}$, and $\Delta^{36}\text{S}$) isotope data for the Red Lake sulfidic shale samples.....	276

List of Figures

Chapter 1: Introduction

1.1. Global occurrence of Archean sedimentary carbonates.....	21
1.2. Thickness of Archean sedimentary carbonate units.....	23
1.3. Drawings and field photographs of stromatolites in the Strelley Pool Chert.....	26
1.4. Columnar stromatolites and conical stromatolites of the Chobeni Formation.....	27
1.5. Columnar and laterally linked stromatolites of the Woman Lake carbonate platform.....	29
1.6. Giant domes, crystal fans, stratifiers, and columnar stromatolites of the Steep Rock carbonate platform.....	30
1.7. Small domal, columnar, and giant domal stromatolites of the Campbellrand-Malmani carbonate platform.....	34

Chapter 2: Geological Setting

2.1. Map of the Canadian Shield and subprovince of the Superior Province in the Superior Craton, Canada, and stratigraphy of the Ball assemblage containing the Red Lake carbonate platform.....	53
2.2. Geological map of the Ball Assemblage containing the Red Lake carbonate platform along with the locations of the cored drill holes analyzed in this study.....	55
2.3. Stratigraphic correlation of the nine cored industry drill holes.....	57
2.4. Domal stromatolites, laterally linked low domes, crinkly stromatolites, and large dome in the Red Lake carbonate platform.....	59
2.5. Carbonate-magnetite in the Red Lake carbonate platform.....	60
2.6. Slumped carbonate in the Red Lake carbonate platform.....	62
2.7. Oxide iron formation in the Red Lake carbonate platform.....	62
2.8. Sulfidic shale in the Red Lake carbonate platform.....	64

Chapter 4: Chemostratigraphy of the Mesoarchean (2.87 Ga) Red Lake carbonate platform, Northwest Ontario, Canada

4.1. Geological map of the Red Lake carbonate platform and stratigraphic correlations from the nine cored drill holes.....	86
4.2. Al-normalized redox-sensitive element profiles and PAAS-normalized rare earth element profiles of the PB12-35 hole.....	94
4.3. Al-normalized redox-sensitive element profiles and PAAS-normalized rare earth element profiles of the PB12-32 hole.....	96
4.4. Al-normalized redox-sensitive element profiles and PAAS-normalized rare earth element profiles of the PB12-33 hole.....	98
4.5. Al-normalized redox-sensitive element profiles and PAAS-normalized rare earth element profiles of the EBL10-28 hole.....	100
4.6. Al-normalized redox-sensitive element profiles and PAAS-normalized rare earth element profiles of the NGI10-31 hole.....	102
4.7. Chemical index of alteration (CIA) box and whisker plot and Co-Th versus La-Sc plot of siliciclastic rocks in the Red Lake carbonate platform.....	104
4.8. Ti-normalized redox-sensitive trace elements versus Al ₂ O ₃ plot for different chemical and siliciclastic sedimentary rocks.....	107
4.9. Y/Ho versus Al ₂ O ₃ , and La/La* versus Al ₂ O ₃ plots for different lithofacies.....	113
4.10. PAAS-normalized Ce/Ce* anomaly versus Pr/Pr* anomaly plot for whole rock data from different lithofacies and weak leach digests data.....	117
4.11. PAAS-normalized REE systematics of different chemical sedimentary and siliciclastic rocks of the Red Lake carbonate platform.....	120
4.12. Pr/Yb versus La/La*, Y/Ho, and Al ₂ O ₃ for different lithofacies.....	121

Chapter 5: Carbon and Oxygen Isotope Chemostratigraphy of the Mesoarchean Carbonate Platform at Red Lake, Canada

5.1. Geological map of the Red Lake carbonate platform and stratigraphic correlations from nine cored drill holes.....	148
5.2. Chemostratigraphic profiles of oxygen isotopes, carbon isotopes, and TOC contents of the PB12-35 and PB12-32 holes.....	152
5.3. Chemostratigraphic profiles of oxygen isotopes, carbon isotopes, and TOC contents of the PB12-33 and EBL10-28 holes.....	154
5.4. Chemostratigraphic profiles of oxygen isotopes, carbon isotopes, and TOC contents of the NGI10-31 and 17-GA1 holes.....	155
5.5. Histograms of $\delta^{13}\text{C}$ and $\delta^{18}\text{O}$ for limestone and dolostone samples of the Red Lake carbonate platform.....	158
5.6. Plots of $\delta^{13}\text{C}$ and $\delta^{18}\text{O}$ versus Y/Ho ratio and La anomalies for whole rock and weak leach digest data for Red Lake carbonate.....	159
5.7. TOC versus $\delta^{13}\text{C}$ and TOC versus $\delta^{18}\text{O}$ for limestone and dolostone samples.....	160
5.8. $\delta^{13}\text{C}$ versus $\delta^{18}\text{O}$, and both versus geologic age, for Red Lake carbonates and for a global carbonate dataset.....	163
5.9. $\delta^{13}\text{C}$ versus $\delta^{18}\text{O}$ plot for Archean carbonates from different localities.....	166
5.10. $\delta^{18}\text{O}_{\text{calcite}}$ and $\delta^{18}\text{O}_{\text{dolomite}}$ values against temperature.....	169
5.11. Seafloor carbonitization model.....	174

Chapter 6: In-situ multiple sulfur isotope analyses of shale-hosted sulfides of the Red Lake carbonate platform

6.1. SEM-BSE images of sulfide samples containing pyrite and pyrrhotite.....	193
--	-----

6.2. $\delta^{34}\text{S}$ versus $\Delta^{33}\text{S}$ plot and $\Delta^{33}\text{S}$ versus $\Delta^{36}\text{S}$ plot for Red Lake sulfidic shale samples...	195
6.3. $\delta^{34}\text{S}$ versus $\Delta^{33}\text{S}$ plot and $\Delta^{33}\text{S}$ versus $\Delta^{36}\text{S}$ plot for nodular and disseminated pyrite sample.....	196
6.4. $\delta^{34}\text{S}$ versus $\Delta^{33}\text{S}$ plot and $\Delta^{33}\text{S}$ versus $\Delta^{36}\text{S}$ plot for Red Lake samples compared with other Mesoarchean samples.....	200

Chapter 7: Conclusion and Perspectives

7.1. A synthetic diagram of the Red Lake carbonate platform.....	212
--	-----

List of Tables

Chapter 3: Methodology

- 3.1. Summary of the studied Red Lake drill hole locations, orientations, and depths.....71
- 3.2. Summary of sample types and the number of analyses made by ICP-AES, HR-ICP-MS (whole-rock and carbonate leach), IRMS, and SIMS.....72

Chapter 1

Introduction

1.1 The earliest history of Earth: the Hadean and Archean Eons

In the beginning, the conditions at Earth's surface were very different than today, and it has experienced multiple dramatic chemical and biological evolutionary events that led to its modern form. The geological history of Earth is divided into two supereons: the Precambrian and the Phanerozoic. The Precambrian Eon covers the time from the beginning of Earth's formation 4.6 Ga to 500 Ma. It includes three eons, i.e., the Hadean (~4.6 - 4.0 Ga), the Archean (~4.0 - 2.5 Ga), and the Proterozoic (~2.0 - 0.5 Ga) eons, while the Phanerozoic eon covers the Earth's past 500 Ma to present. Throughout the Archean, the focus of this thesis, numerous dramatic changes occurred on Earth that constituted essential steps towards establishing its current surface conditions habitable for complex animal life.

The Hadean commenced from the accretion of the Earth approximately 4.56 Ga ago and is characterized by the stabilization of Earth's lithosphere and the formation of the hydrosphere and atmosphere (Harrison, 2020). Much of our knowledge of this timespan is derived from the analysis of meteorites due to the absence of rock records on Earth. About 4.56 Ga ago, the formation of Earth started from the solar nebula, and it is assumed that the Hadean Earth passed through a magma ocean stage. A transitory proto-crust and the presence of water are indicated for the Hadean Eon from the analysis of sedimentary zircons of 4.4 to 4.0 Ga in age (Bibikova, 2010; Caro et al., 2005; Mojzsis et al., 2001). Oxygen isotope analysis of ~4.3 Ga old zircons from western Australia suggests that at that time, zircon-forming magma of Earth's early crust likely interacted with the hydrosphere (Mojzsis et al., 2001). The Earth's Hadean crust, oceans, and atmosphere are thought to have been far removed compositionally from those observed in modern settings, although this is an area of ongoing research that is complicated by a lack of available geological records recording Earth's surface conditions.

Chapter 1: Introduction

The Archean Eon spans from 4.0 Ga to 2.5 Ga and includes four Eras: the Eoarchean (4.0 to 3.6 Ga), the Paleoarchean (3.6 to 3.2 Ga), the Mesoarchean (3.2 to 2.8 Ga), and the Neoarchean (2.8 to 2.5 Ga). The Archean is characterized by significant steps towards a planet resembling the modern Earth, including the onset of plate tectonics, the formation and emergence of the first continents, and the evolution of life, and the expansion of microbial metabolisms, including the production of free oxygenation by photosynthesis. Stromatolites are preserved in most of the Archean carbonate rock record and represent a clear signature of environments favorable for photosynthetic activity, by unknown phototrophs at first, and eventually by cyanobacteria.

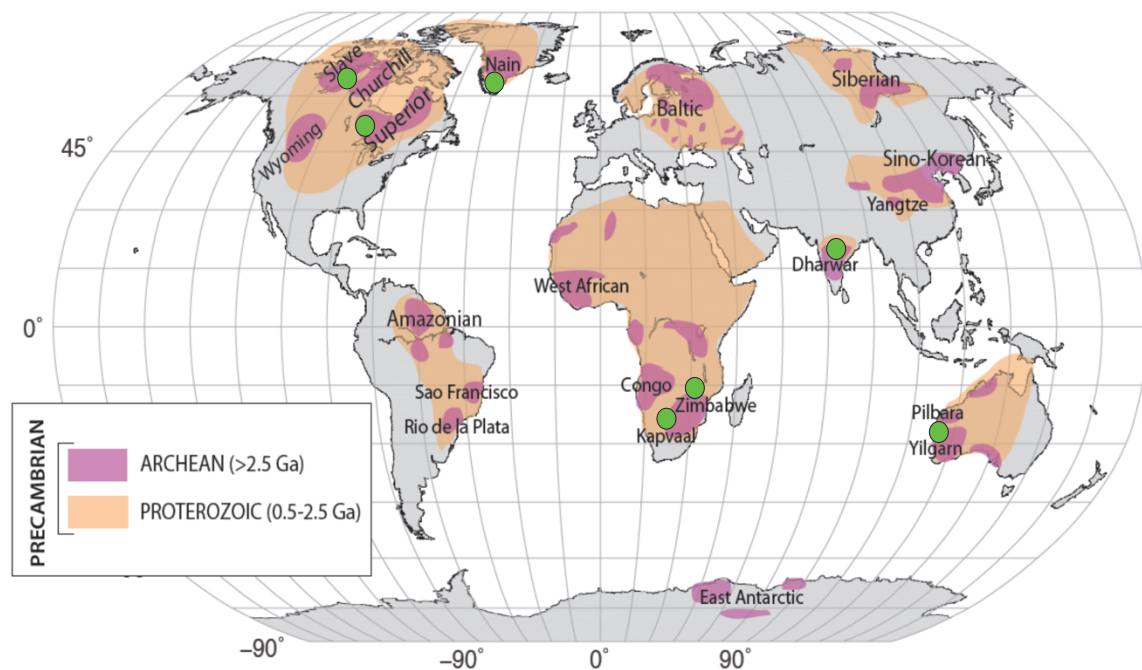


Figure 1.1: Global occurrence of Archean sedimentary carbonates (green dots; modified after Petrescu, 2017).

1.2 Archean carbonates around the globe

Carbonate platforms are large tabular bodies composed of limestone (CaCO_3) and dolostone ($\text{CaMg}(\text{CO}_3)_2$) that gradually build up as the result of chemical sedimentation, often

Chapter 1: Introduction

under the influence of photosynthetic organisms. Carbonate platforms are a feature of the geological record that spans billions of years, beginning in the Mesoarchean. Carbonate rocks are particularly important for the long-term sequestration of CO₂ from Earth's surface, which is important in maintaining Earth's equable climate (Holland, 1978; Walker et al., 1981). Carbonate rocks are widely used as a proxy to infer the composition of ancient seawater and represent a repository of mineralogical, textural, chemical, and isotopic information related to ancient microbial life, paleoenvironmental conditions, and past biogeochemical cycling (Kamber et al., 2014, 2004; Kamber and Webb, 2001; Nothdurft et al., 2004; Webb and Kamber, 2000). Remnants of Archean carbonate platforms are rarely well-preserved, and their abundance is scarce in geological rock records (Figure 1.1). Studies of preserved Archean carbonate platforms over the past few decades have yielded important insights into the beginning of carbonate platform formation on Earth and their gradual development from small, thin occurrences in the most ancient rock records into the multi-km-thick deposits that characterize the Earth today. The earliest undisputed sedimentary carbonate, a 1m-thick ferroan calcite horizon, is preserved in the Coonterunah Group (3.52 Ga) in the Pilbara Craton, Western Australia (Green, 2001; Harnmeijer, 2010). The 3.45 Ga Strelley Pool Chert (Allwood et al., 2007; Van Kranendonk, 2006) is comprised of encrusting domical, coniform, and wavy laminite stromatolites in 8 to 30 m thick units, and constitute among the oldest undisputed evidence of life on Earth. Carbonate rocks dating to the Paleoproterozoic to Mesoproterozoic time are generally less well-preserved compared to their Neoproterozoic counterparts, and there remain important knowledge gaps remaining regarding carbonate platform formation in the Mesoproterozoic. Carbonate platforms gradually started to appear in greater abundance and thickness in geologic rock records during the transition from Mesoproterozoic to Neoproterozoic (Figure 1.2). The evolution of Archean carbonate deposition around the globe through time is described below.

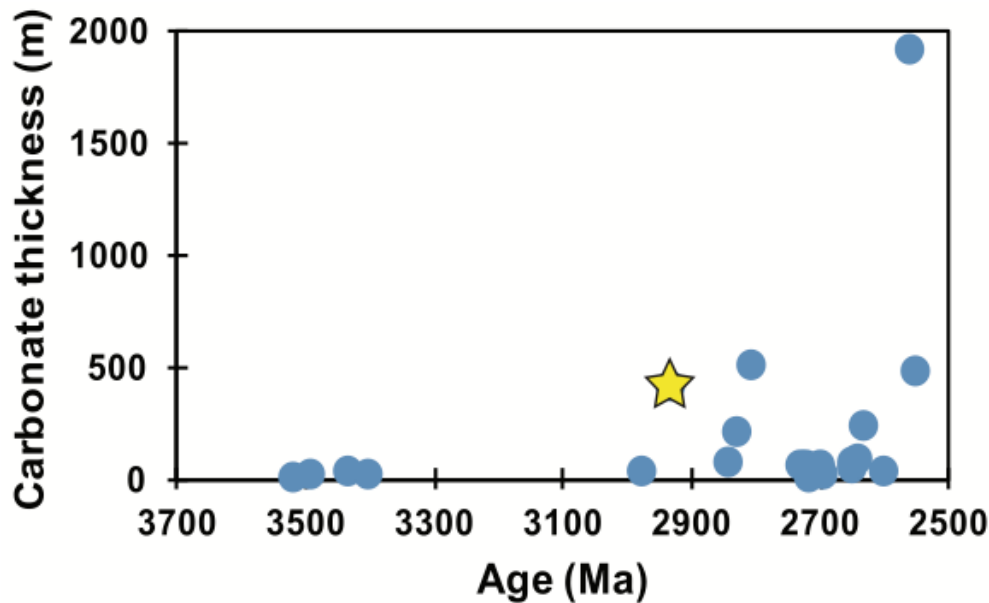


Figure 1.2: Thickness of Archean sedimentary carbonate units. The study site of this thesis, the Red Lake carbonate platform, is marked by a yellow star. Adapted from Riding et al. (2014).

1.2.1 Eoarchean carbonates (4.0-3.6 Ga)

Eoarchean rocks occur in several cratons as metamorphosed gneiss complexes, including the Itsaq Gneiss Complex of southwest Greenland, the Nuvvuagittuq greenstone belt of the northeastern Superior Province, the Acasta Gneiss in Slave Province, the Uivak Gneisses of Labrador, the Napier Complex in Antarctica, the Narryer Gneiss Complex of Western Australia, and the Gneiss Complex in northwestern Swaziland (Harley and Kelly, 2007; Kinny and Nutman, 1996; Nutman et al., 2016, 1996; Schiøtte et al., 1989). Carbonate rocks of Eoarchean age are either rare or not well-preserved in these cratons. There is a sparse carbonate rock record for the Eoarchean, and the only evidence for their possible occurrence is present in the Isua greenstone belt within the Itsaq Gneiss Complex. The Isua greenstone belt comprises deformed and metamorphosed basaltic pillow lavas, pillow lava breccia, layered mafic-ultramafic intrusive sheets, ultramafic volcanic rocks, and a small quantity of chemical and clastic sedimentary rocks including dolomite, dolomitic marble, chert, banded iron formation,

meta-conglomerate, and turbidite rocks (Fedó, 2000; Komiya et al., 1999; Myers and Crowley, 2000; Nutman et al., 2016). A shallow subtidal environment is suggested for the deposition of the marble (Dimroth, 1982). However, based on their composition and observations of their occurrence in outcrop, the metacarbonate rocks in this greenstone belt have also been argued to represent the product of metasomatism, formed by carbonation and de-silicification of various country rocks in the deep crust by metamorphic fluids (Rose et al., 1996; Rosing et al., 1996). Several 1 to 4 cm-thick stromatolitic dolomite beds of shallow-marine origin have been recently reported in a new outcrop of the Isua Supracrustal belt (Nutman et al., 2016), although their sedimentary origin and stromatolitic nature remain debated (Allwood et al., 2018).

1.2.2 Paleoproterozoic carbonates (3.6-3.2 Ga)

Carbonate rocks are sporadically preserved in the Paleoproterozoic sedimentary record, with limited occurrences preserved in the ~3.5 to 3.2 Ga old Barberton greenstone belt of the Kaapvaal Craton, South Africa (Kröner et al., 1996; Lowe and Byerly, 2007) and in ~3.5 – 3.4 Ga sediments of the Pilbara Craton in Western Australia (Allwood et al., 2010, 2006; Becker and Clayton, 1972; Kaufman et al., 1990; Van Kranendonk, 2006; Van Kranendonk et al., 2003; Veizer et al., 1990). Highly silicified carbonate successions typically < 20 m thickness are present in these greenstone belts and are mainly associated with metamorphosed volcano-sedimentary rocks, i.e., komatiite, tholeiite, felsic volcanic to volcanoclastic rocks along with siliciclastic and deep-water chemical sedimentary rocks such as banded iron formation and chert (Allwood et al., 2010; John P. Grotzinger, 1989; Hickman, 2012; Lowe and Byerly, 2007; Van Kranendonk et al., 2003).

The ~ 3.55 - 3.26 Ga Onverwacht Group (Kröner et al., 1996) and the ~ 3.26 - 3.23 Ga Fig Tree Group (Byerly et al., 1996) of the Swaziland Supergroup of Barberton greenstone belt, and the ~ 3.4 Ga Nondweni Group (Xie et al., 2012) of the Nondweni greenstone belt of

Chapter 1: Introduction

Kaapvaal Craton, South Africa, preserves variably silicified carbonate rocks intercalated with metavolcanic and metasedimentary rocks. The Onverwacht Group consists mainly of mafic to ultramafic volcanic rocks, minor felsic tuff and lavas, and different types of chemical and siliciclastic sedimentary rocks. Chert present in this group is interpreted as a replacement of fine-grained carbonate or other chemical sediments (Lowe and Byerly, 1999a; Lowe and Knauth, 1977; Viljoen and Viljoen, 1969). The Fig Tree Group includes volcanic and volcanoclastic rocks interlayered with terrigenous rocks (Lowe and Byerly, 2007, 1999b). The Mapepe Formation of this Group predominantly consists of terrigenous clastic rocks, felsic pyroclastic rocks, and minor chemical precipitates such as limestone, dolomite, banded ferruginous chert, barite, and calcareous chert (Lowe and Byerly, 2007, 1999b; Lowe and Knauth, 1977; Lowe and Nocita, 1999). There are low relief, nearly stratiform, laterally linked domes, and rare pseudocolumnar and crinkly stratiform stromatolites present in the thin chert layers within the Fig Tree Group that grew on an altered komatiitic lava substrate (Byerly et al., 1986).

The ca. 3.4 Ga Nondweni Group of the Nondweni greenstone belt, also in South Africa, is mainly composed of volcanic rocks. The uppermost Witkop Formation of the Nondweni Group consists of basalts, komatiites, and komatiitic basalts intercalated with chert layers and is overlain by a clastic sedimentary succession and a 5 to 8 m thick silicified carbonate unit containing domal stromatolites which are in turn overlain by barite and layered lapilli tuffs (Wilson and Versfeld, 1994). A shallow water or subaerial depositional environment has been suggested for the stromatolites, evaporites, and coarse clastic sediments (Wilson and Versfeld, 1994).

The ~3.5 - 3.4 Ga Warrawoona Group of the Pilbara Supergroup in Western Australia is comprised of felsic to mafic volcanic rocks, pyroclastic deposits, bedded chert, sandstone,

and carbonate (Bolhar and Van Kranendonk, 2007; Kranendonk et al., 2002; Van Kranendonk, 2006). The lowest unit of the Warrawoona Group is Dresser Formation (~3.49 Ga), which

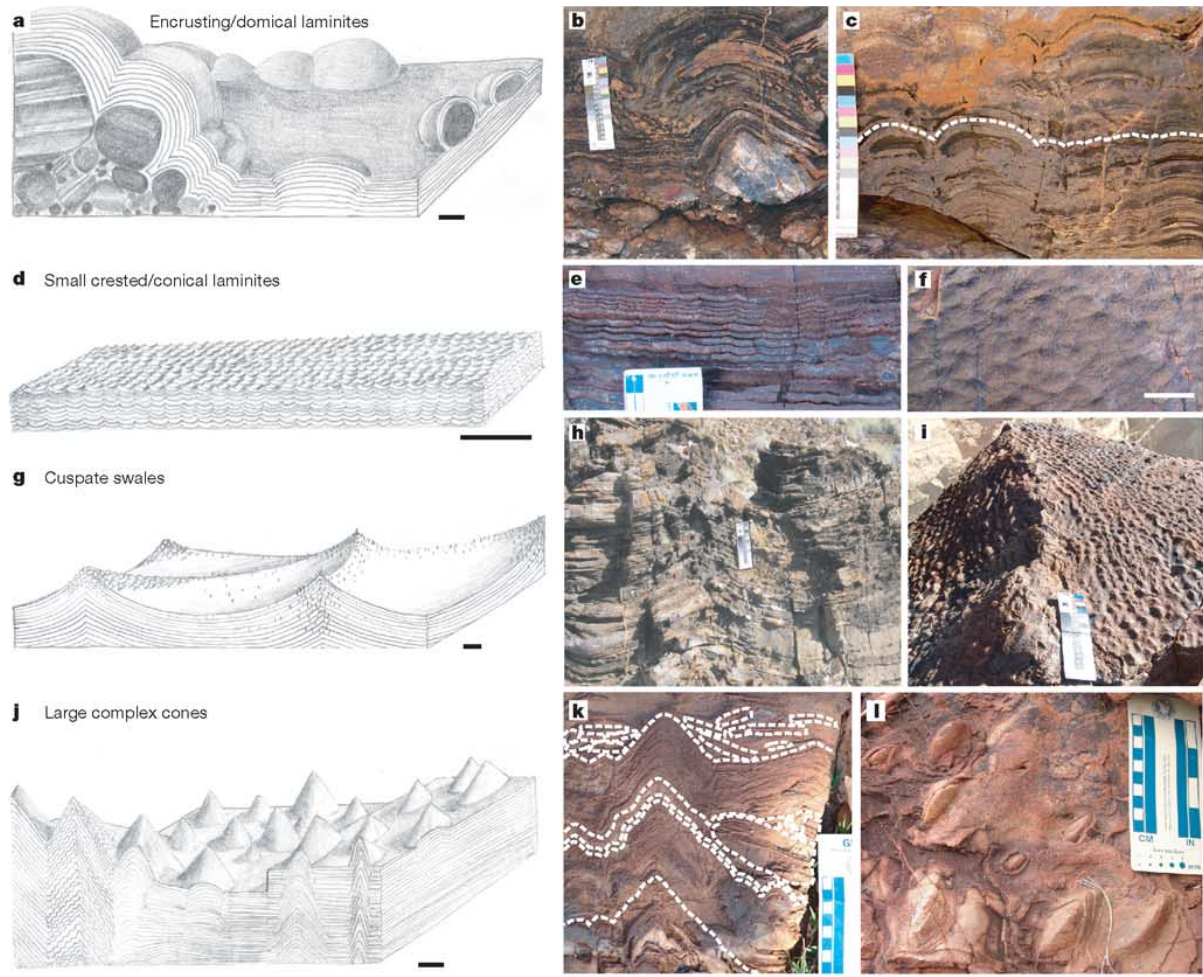


Figure 1.3: Drawings and field photographs of the diverse stromatolite preserved in the 2.43 Ga Strelley Pool Chert, Pilbara Craton, Western Australia. Figure from Allwood et al. (2006).

contains interbedded chert and barite units and pillow basalt. The chert-barite unit consists of bedded chert, crystalline barite, stromatolitic dolomite (up to 8 m thick) with varied stromatolite morphologies, and siliciclastic rocks (Buick and Dunlop, 1990; Van Kranendonk, 2006). The 3.42 - 3.35 Ga Strelley Pool Chert of the Kelly Group consists of a 30 - 1000 m thick cherty sedimentary unit in which the middle unit includes variably silicified stromatolites of diverse morphologies, while the upper unit consists of conglomerate and sandstone, and the

Chapter 1: Introduction

lower unit is comprised of quartzite with conglomeratic and volcanoclastic rocks (Buick and Dunlop, 1990; Hofmann et al., 1999; Lowe, 1980; Van Kranendonk, 2006; Van Kranendonk et al., 2003). The silicified stromatolitic carbonate is characterized by conical to columnar stromatolites, stratiform, radiating aragonitic or gypsum crystal fans replaced by dolomite, and these features are believed to represent a low energy depositional setting in a partially restricted peritidal marine environment or hypersaline lake (Buick and Dunlop, 1990; Hofmann et al., 1999; Lowe, 1980; Van Kranendonk, 2006; Van Kranendonk et al., 2003) (Figure 1.3).



Figure 1.4: Laterally linked domal stromatolites (A), columnar stromatolites (B, D), and conical stromatolites (D) of the 2.96 Ga Chobeni Formation, Pongola Supergroup, South Africa. Adapted from Siah et al. (2016).

1.2.3 Mesoarchean carbonates (3.2 - 2.8 Ga)

Mesoarchean well-preserved carbonate rocks occur in the Pongola Supergroup, South Africa, and several greenstone belts of the Superior Province of Canadian Shield (Beukes and Lowe, 1989; Fralick and Riding, 2015; Hofmann et al., 1985; Siahi et al., 2016).

The oldest Mesoarchean carbonate rock is present in the Nsuze Group (3.0 - 2.9 Ga) of the Pongola Supergroup in the Kaapvaal Craton, South Africa. The 2.96 Ga Chobeni Formation of the Nsuze Group comprises several 20 to 50 m thick stromatolitic carbonate layers and are characterized by 5 to 60 cm-thick stromatolitic bioherms together with ooids, peloids, and oncoids (Beukes and Lowe, 1989; Dixon, 2004; Siahi et al., 2016) (Figure 1.4). This stromatolitic carbonate was deposited in a tide-dominated clastic-carbonate shallow marine environment (Beukes and Lowe, 1989; Mason and Von Brunn, 1977; Siahi et al., 2016).

Mesoarchean carbonate rocks in the Superior Province of the Canadian Shield are exposed in different localities including the Red Lake greenstone belt, Wallace Lake greenstone belt, Uchi-Confederation Lakes greenstone belt, and the Finlayson Lake and Lumby Lake greenstone belts. The 3.0 - 2.9 Ga Conley formation of Wallace Lake assemblage comprises sandstone and conglomerate capped by dolostone, iron formation, and argillites (Fralick et al., 2008; Sasseville et al., 2006). The 50 m-thick dolomitic carbonate is characterized by stratiform and domal stromatolites that formed in a shallow marine environment.

The 2.87 Ga Red Lake greenstone belt (Afroz et al., 2023; Corfu and Wallace, 1986; Patry et al., in review) contains a > 200 m thick carbonate package composed of stromatolitic dolostones and limestones associated with various deep-water chemical and siliciclastic sedimentary rocks which are overlain and underlain by mafic to ultramafic volcanic rocks

(Afroz et al., 2023; Hofmann et al., 1985; Hollings et al., 1999; Pirie, 1981; Sanborn-Barrie et al., 2001, 2000). The Red Lake carbonate platform, the subject of this thesis, is the most ancient thick (>100m) occurrence of carbonate on Earth and its geological context is described in detail in Chapter 2.

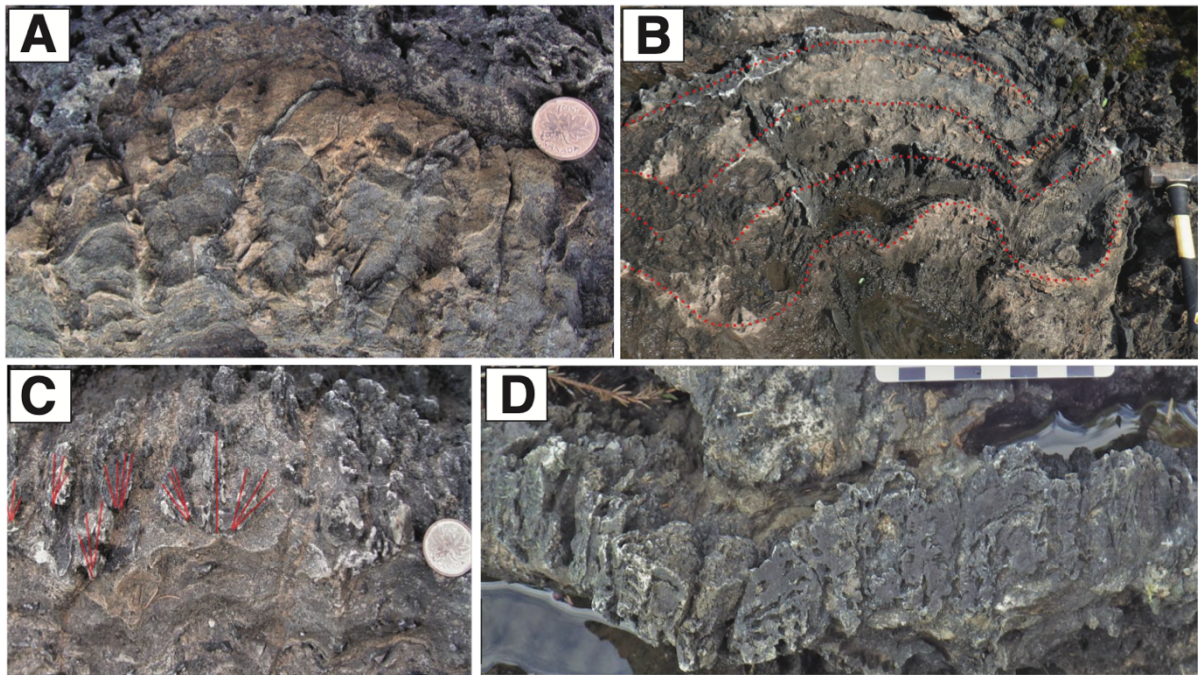


Figure 1.5: Columnar stromatolites (A), laterally linked domal stromatolites (B), domal stromatolite with radiating silicified features (C), and stubby columnar stromatolites (D) of the 2.87 Ga Woman Lake carbonate. Images from Ramsay (2020).

The 2.85 Ga Woman Lake assemblage of the Birch-Uchi-Confederation greenstone belt consists of chert, felsic to mafic volcanic rocks, and a 90 m thick succession of carbonates lying above felsic subaerial tuff (Ayers et al., 1971; Nunes and Thurston, 1980). The carbonate succession consists of stratiform stromatolites interbedded with thin beds of massive carbonate grainstone, laterally linked low domal stromatolites, larger domes, pseudocolumnar stromatolites, and a shallow marine peritidal setting has been interpreted for its depositional environment (Ramsay, 2020) (Figure 1.5).

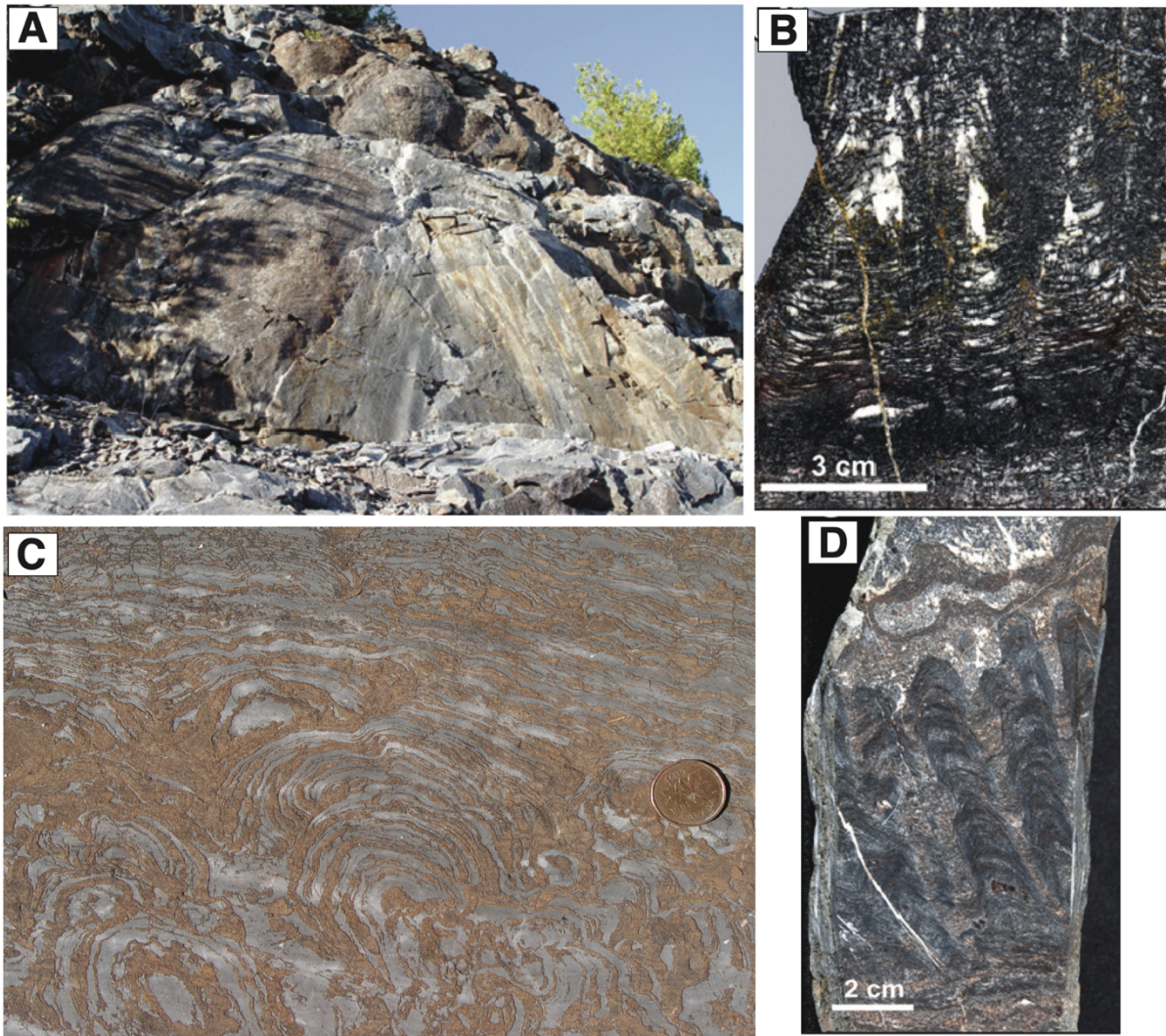


Figure 1.6: Giant domes (A), crystal fans (B), stratified stromatolites (C), and columnar stromatolites (D) from the 2.80 Ga Steep Rock Lake carbonate platform. Images from Fralick and Riding (2015).

1.2.4 Neoproterozoic carbonates (2.8-2.5 Ga)

Carbonate rocks become significantly more prevalent in the rock record of the Neoproterozoic. The emergence of large cratons and subsequent weathering of continental crust, including the Kaapvaal, Pilbara, and Superior cratons during the Paleoproterozoic to Mesoproterozoic, and the stabilization of late Archean cratons, such as the Yilgarn, Slave, and Zimbabwe cratons, created stable surfaces that were periodically flooded by shallow seas, leading to the accumulation of carbonates from seawater that was at times carbonate-saturated. Thick

Chapter 1: Introduction

carbonate successions appear in many places during the Neoproterozoic, including the Steep Rock Group and the Yellowknife Supergroup in Canada, the Hamersley and Fortescue Groups of Western Australia, the Ventersdorp and Transvaal Supergroups in South Africa, the Ngezi Group of Zimbabwe, and different greenstone belts of the Dharwar Craton, India. These carbonates formed in a variety of depositional settings, including both continental margin platforms and foredeep basins (John P. Grotzinger, 1989).

The Steep Rock Group belongs to the Lumby Lake greenstone belt of Superior Province in Canada. The 2.80 - 2.78 Ga Steep Rock Group hosts one of the thickest Archean carbonate platforms on Earth (Fralick & Riding, 2015). The 500 m thick Mosher carbonate consists of stromatolitic carbonates (ankerite, calcite, and dolomite) with diverse morphologies including domal, conical, columnar, tabular, and large stromatolite mounds with crystal fans, herringbone calcite, and gypsum molds (Fralick & Riding, 2015; Kusky & Hudleston, 1999; Wilks & Nisbet, 1988) (Figure 1.6). These carbonates were precipitated in a shallow marine environment with short-lived anaerobic and hypersaline conditions, as inferred from the presence of gypsum molds and herringbone calcite (Fralick & Riding, 2015; Kusky & Hudleston, 1999).

The ~2.7 Ga Yellowknife Supergroup of Slave Province in Canada contains ~ 40 m-thick discontinuous stromatolitic carbonates intercalated with felsic to mafic volcanic rocks, clastic turbidites, and sporadic conglomerate (Breemen et al., 1992; Henderson, 1975a). The carbonates likely formed as short-lived reefs which were capped by a felsic volcanic unit (Grotzinger, 1986; John P Grotzinger, 1989; Henderson, 1975b; Lambert, 1998).

The 2.7 - 2.6 Ga Fortescue Group, Mount Bruce Supergroup, Pilbara Craton exhibits carbonate successions in association with flood basalt along with volcanoclastic and siliciclastic rocks (Blake et al., 2004; Thorne and Trendall, 2001; Van Kranendonk, 2006). The

Chapter 1: Introduction

Tumbiana Formation of this group consists of limestone, rare dolostone, siliciclastic rocks, tuffs, and mafic volcanic rocks, and is overlain and underlain by amygdaloidal basalt (Awramik and Buchheim, 2009; Buick, 1992; Thorne and Trendall, 2001). The Meentheena Member consist of 30 to 50 m-thick stromatolitic limestones and siliciclastic rocks while the Mingah Member consists of several cm-thick stromatolitic limestones, minor mudstone, volcanoclastic sandstone, and basalt (Buick, 1992; Thorne and Trendall, 2001). The depositional environment of this carbonate is debated, and both shallow-marine settings (Sakurai et al., 2005) and lacustrine settings (Awramik and Buchheim, 2009; Bolhar and Van Kranendonk, 2007; Buick, 1992) have been proposed.

The Hamersley Group, Western Australia, hosts two well-preserved and extensive carbonate exposures, namely the Carawine Dolomite and Paraburdoo Member of the Wittenoom Formation (Simonson et al., 1993). The ~2.6 Ga Carawine Dolomite reaches > 500 m in thickness and consists predominantly of stromatolitic dolomites, although it is intercalated with argillite and chert in some places. These carbonates were precipitated directly on or beneath the seafloor as inorganic precipitates, e.g., acicular or prismatic crystals, zebraic dolomite cement, stubby vertically aligned crystals, and hollow-faced cubes in a restricted area subject to evaporative concentration (Simonson et al., 1993). The ~2.56 Ga Wittenoom Formation is classified into three members: the West Angelas Shale member, the Paraburdoo Member, and the Bee Gorge member, and all of them contain carbonates of variable thickness that are associated with argillite, banded iron formation, chert, and volcanoclastic rocks (Blockley et al., 1993; Simonson, 1992; Simonson et al., 1993). The large stromatolitic domes and laminites with roll-up structures in these carbonates suggest that deposition occurred in a deeper-water depositional environment than many other Neoproterozoic stromatolite occurrences (Simonson, 1992; Simonson et al., 1993).

Chapter 1: Introduction

The 2.7 Ga Ventersdrop Supergroup of the Kaapvaal Craton in South Africa is divided into several groups which are mainly composed of mafic volcanic rocks as well as terrigenous and chemical sedimentary rocks. The Platberg Group of this Supergroup contains stratiform to small-scale domal stromatolitic dolomites with cherty laminae, together with giant ooids, shale, sandstone, and conglomerate thought to be deposited in a lacustrine environment. The Omdraaiivlei Formation of Sodium Group also contains carbonates that consist of 10 - 90 cm-thick stromatolitic cherty limestone with diverse stromatolite morphologies intercalated with tuffaceous shale along with tuff, mafic to intermediate lava flows, and pillow lavas intercalated with arkose sandstone (Altermann and Lenhardt, 2012; Grobler et al., 1989; Van der Westhuizen et al., 2006, 1991).

The ~2.6 - 2.0 Ga Transvaal Supergroup of the Kaapvaal Craton exhibits well-preserved thick carbonate units (Altermann and Nelson, 1998; Walraven et al., 1990). The Schmidtsdrif Subgroup of Ghaap Group, Transvaal Supergroup, contains over 200 m of subtidal to tidal flat deposits consisting of wavy laminated stromatolitic and oolitic dolomites, calcarenite, and dolarenites, along with sediments with important siliciclastic influence, including, shale, calcareous shale, and quartzite (Altermann and Siegfried, 1997; Altermann and Wotherspoon, 1995; Beukes, 1987, 1983). The ~2.56 Ga Campbellrand Subgroup of the Ghaap Group consists of eight carbonate formations up to 2500 m in thickness, and its correlative in the Griqualand West basin, the Malmani Subgroup, comprises a ~1700 m thick carbonate succession (Barton et al., 1994). The stromatolitic carbonate successions alternate with chert and shale layers, thin tuff beds, mafic lava, and minor siliciclastic rocks, and their deposition occurred in a shallow marine tide-dominated, peritidal depositional setting (Altermann and Siegfried, 1997; Altermann and Wotherspoon, 1995; Beukes, 1987) (Figure 1.7).

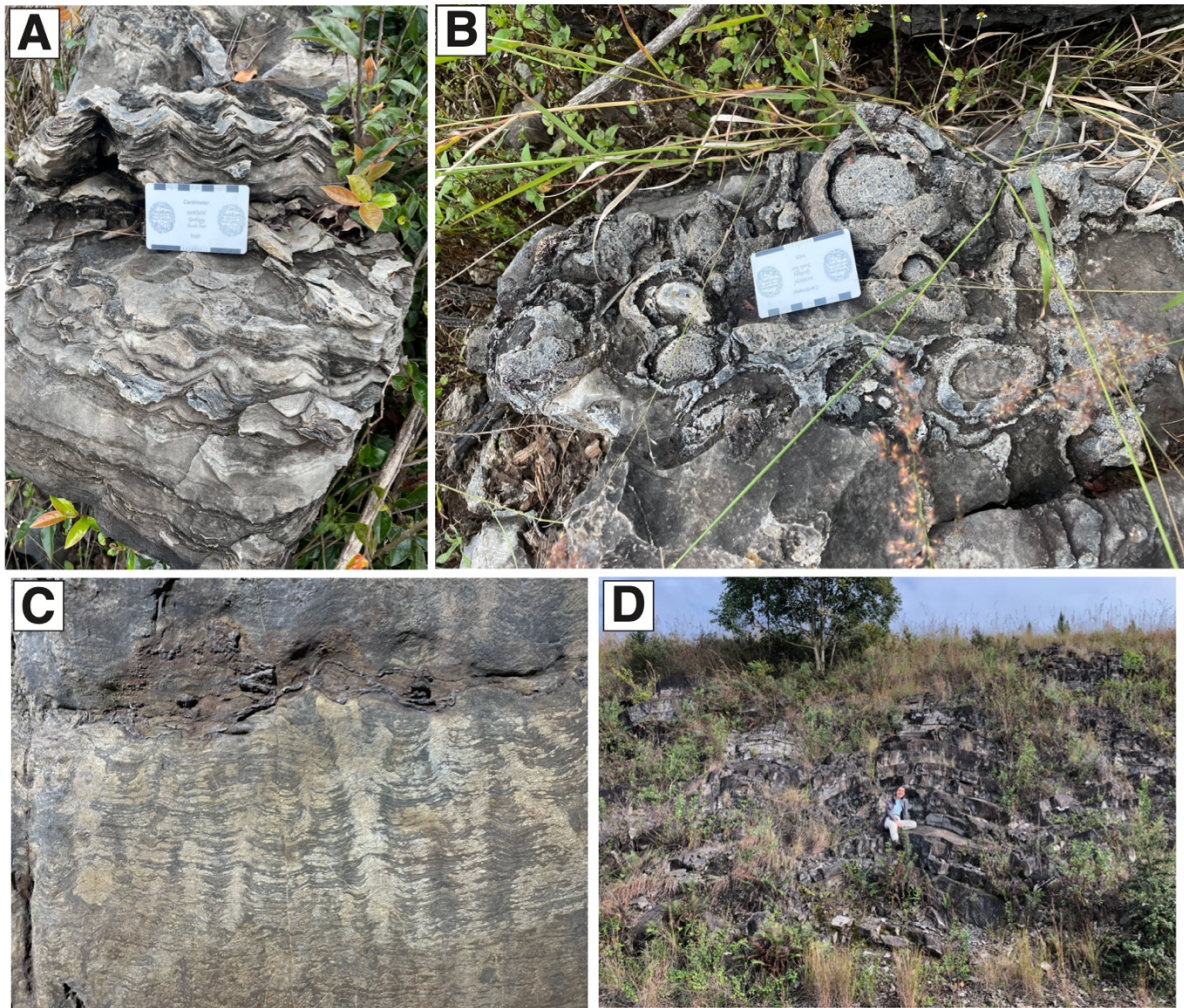


Figure 1.7: Small domal (A, B), Columnar (C), and Giant domal (D) stromatolites from the 2.55 Ga Campbellrand-Malmani carbonate platform, Kaapvaal Craton, South Africa. Photos courtesy of S. Lalonde.

The Ngezi Group belongs to the Belingwe greenstone belt of the Zimbabwe Craton and consists of four formations (Martin et al., 2020). The ~2.7 Ga Manjeri formation contains 50 - 100 m thick fluvial and shallow-water deposits composed of conglomerate, sandstone, shale, stromatolitic carbonates, and ironstone (Bickle et al., 2020, 1975; Hunter et al., 1998). The carbonates were probably formed under intertidal conditions (Bickle et al., 1975; Martin et al., 2020, 1980). The ~2.6 Ga Cheshire Formation is comprised of limestone interbedded with fine-grained terrigenous sedimentary rocks and with minor dolomite in a ~350 m thick succession (Abell et al., 1985; Bolhar et al., 2002; Hofmann et al., 2001; Hofmann and Kusky, 2004;

Martin et al., 1980). The suggested depositional environment of this carbonate is shallow-marine to protected lagoon (Abell et al., 1985; Martin et al., 2020, 1980), as well as wave- and storm-dominated shallow-marine open environment (Hofmann et al., 2001).

The ~2.9 - 2.6 Ga Dharwar Supergroup of the Dharwar craton in southwestern India hosts two groups: the Bababudan and Chitradurga Groups (Ramakrishnan and Nath, 1981; Russell et al., 1996). The lower portion of the ~2.7 Ga Chitradurga Group is composed mainly of greywacke, banded ferruginous chert interlayered with calcitic and dolomitic layers and lenses of shallow-marine origin (Jayananda et al., 1995; Trendall et al., 1997). Columnar and pseudo-columnar stromatolites are present in the cherty dolomite sections of this group (Chadwick et al., 1985, 1989; Srinivasan et al., 1989). The ~2.7 Ga Sandur Schist Belt of the eastern side of the Dharwar Craton consists of stromatolitic carbonates, turbidites, and mafic-ultramafic volcanic rocks (Baral, 1986; Manikyamba and Naqvi, 1998, 1997; Nutman et al., 1996). A shallow-marine depositional environment is inferred for these carbonates and siliciclastics (Chadwick et al., 1989, 2000; Chadwick et al., 1997).

1.3 Shallow to deep water carbonates in Archean rock records

Archean carbonate deposition occurred mostly in shallow marine to restricted evaporitic shallow water settings. Most of the earliest Archean (Paleoarchean to Mesoarchean) carbonate platforms preserve only shallow-water marine strata, and for the most part, carbonate strata spanning shallow-to-deep-water settings only began to become important in the geological record in the Neoproterozoic. The 2.56 Ga Campbellrand-Malmani carbonate platform of South Africa and the ~2.7 Ga Manjeri formation of the Belingwe greenstone belt of Zimbabwe Craton preserve carbonates that span shallow-to-deep-water depositional settings. The 2.87 Ga Red Lake carbonate platform of the Superior Craton is unique in this sense as it is the oldest known place on Earth where siliciclastic and chemical sedimentary successions spanning shallow-to-

deep-water settings are well preserved. At this site, the lateral transition from shallow water stromatolitic carbonates to offshore deeper water lithofacies is clear in both outcrop and drill core. The details of the geological settings and different lithofacies associated with the Red Lake carbonate platform are described in Chapter 2.

1.4 Previous studies of the Red Lake carbonate platform

Hofmann et al. (1985) first described the stromatolites and pseudofossil termed 'Atikokania' from a carbonate section of the Red Lake carbonate platform. No detailed stratigraphic and geochemical work was reported in this study. Three types of stromatolites, namely mounded (*Colleniella*), stratiform (*Stratifera*), pseudocolumnar (*Collumnaefacta*) were documented, along with the pseudofossil *Atikokania* (see Chapter 2). The *Colleniella* structures are partly silicified, isolated, bulbous mounds, rare in outcrop, and are preserved in a single outcrop on the west shore of Bridget Lake. They occur in close association with planar, stratiform stromatolites, small channel fills, and flat-pebble breccia likely derived from the stratiform mats and deposited under intertidal to shallow subtidal settings. *Stratifera* is the most common type of stromatolite in the Red Lake area and occurs in several outcrops. These are laterally linked biostromes up to several meters thick, obtuse, and composed of corrugate laminae that are contiguous to closely spaced. Based on the size, extent, and absence of shallow water features in *Stratifera*, a much deeper water environment than for the *Colleniella* mounds was inferred for the depositional setting of *Stratifera*. The pseudocolumnar or *Collumnaefacta* stromatolites are defined by closely spaced biostromes 1 - 10 cm wide with ragged stubby columns and pseudocolumns and are several decimeters thick. These structures are present only in the Hahn Lake area and are found stratigraphically slightly below the *Stratifera* stromatolites. A subaqueous deeper water environment is postulated for this type of stromatolite. The pseudofossil *Atikokania* is characterized by pseudomorphic crystals (possibly once gypsum) with a cm-to dm-wide prominent radial fabric of chert and carbonate.

Chapter 1: Introduction

A stromatolitic origin is not inferred for this structure, which represents instead predominantly abiotic chemical precipitation at large scales, although microbial influence cannot be excluded at the micro-scale. Bundles of diverging acicular aggregates grew on top of basal layers which are composed of finely laminated dark grey carbonate. A shallow-water peritidal setting with high salinity conditions is inferred for the radial acicular growths comprising the *Atikokania*.

McIntyre and Fralick (2017) re-examined the peritidal stromatolites at Red Lake and also described the rock types that are closely associated with the stromatolites, including laminated carbonate, ribbon rock, intraclastic carbonate lithoclasts and marl lithofacies, and carbonate-associated oxide facies iron formation through outcrop investigation. They reported detailed descriptions and depositional environments for the stromatolitic carbonates and other sedimentary rocks present in this carbonate platform based on outcrop studies combined with geochemical data that included major elements, trace elements including REE, and C, O, and Sr isotopic compositions from a small sample suite of samples (n=30). The sedimentological study of McIntyre and Fralick (2017) was focused mainly on outcrops representative of shallow water carbonates, with few hints from the limited outcrops of the deeper water rocks that were captured in the industrial drill cores studied in this thesis. Dolomitic carbonates with peritidal depositional features were reported to dominate the carbonate platform top, while calcitic carbonates dominate the deep subtidal to upper slope lithofacies and crystal fan mounds that were likely deposited as aragonite (McIntyre and Fralick, 2017).

In my MSc work at Lakehead University, I first described the deeper water lithofacies at Red Lake, including the carbonate-magnetite, slumped carbonate, oxide iron formation, chert, black shale, and sulfidic shale preserved in the Red Lake carbonate platform (Afroz et al., 2023). A detailed stratigraphic correlation panel transecting the carbonate platform was constructed using cored drill hole data and outcrop studies. In addition, the depositional

environment of the deeper water lithofacies, and redox conditions were interpreted using major, trace, and rare earth element geochemical data. In this doctoral thesis, I aimed to significantly expand the stratigraphic, elemental, and isotopic characterization of the carbonate platform at Red Lake through the integrated study of the ensemble of industry drill cores as well as additional field observations of the unique Mesoarchean sediments occurring at this understudied locality.

1.5 Research objectives and overview of the dissertation

There exist important knowledge gaps relating to the chemical composition and architecture of the Red Lake carbonate platform, and more generally, of Mesoarchean carbonate platform formation, of ocean chemistry and redox during the Mesoarchean, and the biogeochemical cycling of carbon and sulfur in Mesoarchean paleo depositional environments. This doctoral dissertation aims to address these gaps by addressing the following specific research objectives:

1. Constrain the major element, trace element, and REE geochemical composition of the Red Lake sediments captured in multiple cored industry drill holes that span the diverse lithofacies present at Red Lake, in order to establish a chemostratigraphic framework for Earth's earliest thick carbonate platform.
2. Shed new light onto the operation of the carbon cycle during the Mesoarchean, as well as the origin of unusually light oxygen isotope signatures in Archean chemical sediments, through the stable isotope analysis of carbon and oxygen in Red Lake carbonates.
3. To better understand sulfur cycling in the Mesoarchean ocean by a preliminary study of the in-situ multiple sulfur isotope composition of unusually sulfide-rich fine grained sediments associated with the Red Lake carbonate platform.

Chapter 1: Introduction

Each of these objectives are presented as individual chapters, formatted as research articles, that form the scientific heart of this dissertation. These are accompanied by chapters containing introductory and supporting material, including geological context, methods, and conclusions and perspectives.

Specifically, this thesis is structured into seven chapters:

Chapter 1 presents an overview of the early Earth and the global occurrence of Archean carbonate platforms. It is followed by a brief synthesis of previous studies of the sediments preserved at Red Lake and a brief description of the research objectives and thesis structure.

Chapter 2 describes the geological setting of the study area. This chapter includes a detailed description of the Red Lake greenstone belt and the surrounding area, the Red Lake carbonate platform, and lithofacies descriptions of the diverse lithologies present in the Red Lake carbonate platform.

Chapter 3 describes the fieldwork, core logging, sample preparation, and details concerning the various methods used to obtain the elemental and isotopic data presented in this thesis.

Chapters 4, 5, and 6 present the individual objectives of this thesis in the form of articles formatted for scientific journals. In Chapter 4, an elemental chemostratigraphy of the cored drill holes is established using major element data, redox-sensitive trace element data, and REE data representing the diverse lithofacies of the Red Lake carbonate platform in order to understand the composition of seawater, weathering processes on land and solute fluxes into the basin, and redox conditions prevailing at the time of deposition of the Red Lake carbonate platform.

Chapter 1: Introduction

Chapter 5 presents a carbon and oxygen stable isotope chemostratigraphy of the stromatolite-rich dolomitic carbonate and massive calcic carbonate rocks preserved in multiple drill holes. This chapter addresses the lithological, diagenetic, and metamorphic controls, as well as paleoenvironmental signals, preserved in the stable carbon and oxygen isotopic composition of carbonates of the Red Lake carbonate platform.

Chapter 6 presents a preliminary study of the in-situ multiple sulfur isotope composition of sulfidic shale samples found in the Red Lake carbonate platform. Sources of sulfur to the Mesoarchean ocean as well as microbial and metamorphic processes affecting these sources are discussed in this chapter.

Chapter 7 concludes the thesis with a summary of the main findings as well as the perspectives for future research opened by this study.

1.6 References

- Abell, P.I., McClory, J., Martin, A., Nisbet, E.G., 1985. Archaean stromatolites from the Ngesi Group, Belingwe greenstone belt, Zimbabwe; preservation and stable isotopes—preliminary results. *Precambrian Res.* 27, 357–383.
- Afroz, M., Fralick, P.W., Lalonde, S. V, 2023. Sedimentology and geochemistry of basinal lithofacies in the Mesoarchean (2.93 Ga) Red Lake carbonate platform, northwest Ontario, Canada. *Precambrian Res.* 388, 106996.
<https://doi.org/https://doi.org/10.1016/j.precamres.2023.106996>
- Allwood, A.C., Kamber, B.S., Walter, M.R., Burch, I.W., Kanik, I., 2010. Trace elements record depositional history of an Early Archean stromatolitic carbonate platform. *Chem. Geol.* 270, 148–163. <https://doi.org/10.1016/j.chemgeo.2009.11.013>
- Allwood, A.C., Rosing, M.T., Flannery, D.T., Hurowitz, J.A., Heirweh, C.M., 2018. Reassessing evidence of life in 3,700-million-year-old rocks of Greenland. *Nature* 563, 241–244.
- Allwood, A.C., Walter, M.R., Burch, I.W., Kamber, B.S., 2007. 3.43 billion-year-old stromatolite reef from the Pilbara Craton of Western Australia: ecosystem-scale insights to early life on Earth. *Precambrian Res.* 158, 198–227.
- Allwood, A.C., Walter, M.R., Kamber, B.S., Marshall, C.P., Burch, I.W., 2006. Stromatolite reef from the Early Archaean era of Australia. *Nature* 441, 714–718.
<https://doi.org/10.1038/nature04764>
- Altermann, W., Lenhardt, N., 2012. The volcano-sedimentary succession of the Archean Sodium Group, Ventersdorp Supergroup, South Africa: volcanology, sedimentology and geochemistry. *Precambrian Res.* 214, 60–81.
- Altermann, W., Nelson, D.R., 1998. Sedimentation rates, basin analysis and regional correlations of three Neoarchean and Palaeoproterozoic sub-basins of the Kaapvaal craton as inferred from precise U–Pb zircon ages from volcanoclastic sediments. *Sediment. Geol.* 120, 225–256.
- Altermann, W., Siegfried, H.P., 1997. Sedimentology and facies development of an Archaean shelf: carbonate platform transition in the Kaapvaal Craton, as deduced from a deep borehole at Kathu, South Africa. *J. African Earth Sci.* 24, 391–IN4.
- Altermann, W., Wotherspoon, J.M., 1995. The carbonates of the Transvaal and Griqualand West Sequences of the Kaapvaal craton, with special reference to the Lime Acres limestone deposit. *Miner. Depos.* 30, 124–134.
- Awramik, S.M., Buchheim, H.P., 2009. A giant, late archean lake system: the meentheena member (tumbiana formation; fortescue group), Western Australia. *Precambrian Res.* 174, 215–240.
- Ayers, L.D., Lumbers, S.B., Milne, V.G., Robertson, D.W., 1971. Ontario geological map, southern sheet. Ontario Dep. Mines.

Chapter 1: Introduction

- Baral, M.C., 1986. Archaean stromatolites from Dodguni belt of Karnataka craton, India. *Geol. Soc. India* 28, 328–333.
- Barton, E.S., Altermann, W., Williams, I.S., Smith, C.B., 1994. U-Pb zircon age for a tuff in the Campbell Group, Griqualand West Sequence, South Africa: Implications for Early Proterozoic rock accumulation rates. *Geology* 22, 343–346.
- Becker, R.H., Clayton, R.N., 1972. Carbon isotopic evidence for the origin of a banded iron-formation in Western Australia. *Geochim. Cosmochim. Acta* 36, 577–595.
[https://doi.org/https://doi.org/10.1016/0016-7037\(72\)90077-4](https://doi.org/https://doi.org/10.1016/0016-7037(72)90077-4)
- Beukes, N.J., 1987. Facies relations, depositional environments and diagenesis in a major early Proterozoic stromatolitic carbonate platform to basinal sequence, Campbellrand Subgroup, Transvaal Supergroup, Southern Africa. *Sediment. Geol.* 54, 1–46.
- Beukes, N.J., 1983. Palaeoenvironmental setting of iron-formations in the depositional basin of the Transvaal Supergroup, South Africa, in: *Developments in Precambrian Geology*. Elsevier, pp. 131–198.
- Beukes, N.J., Lowe, D.R., 1989. Environmental control on diverse stromatolite morphologies in the 3000 Myr Pongola Supergroup, South Africa. *Sedimentology* 36, 383–397.
- Bibikova, E. V., 2010. Isotope-geochemical constraints on the formation of the early Earth' crust. *Petrology* 18, 482–488. <https://doi.org/10.1134/S0869591110050036>
- Bickle, M.J., Martin, A., Nisbet, E.G., 1975. Basaltic and peridotitic komatiites and stromatolites above a basal unconformity in the Belingwe greenstone belt, Rhodesia. *Earth Planet. Sci. Lett.* 27, 155–162.
- Bickle, M.J., Martin, A., Nisbet, E.G., Orpen, J.L., 2020. *The Geology of the Belingwe Greenstone Belt, Zimbabwe: A Study of Archaean Continental Crust*. CRC Press.
- Blake, T.S., Buick, R., Brown, S.J.A., Barley, M.E., 2004. Geochronology of a Late Archaean flood basalt province in the Pilbara Craton, Australia: constraints on basin evolution, volcanic and sedimentary accumulation, and continental drift rates. *Precambrian Res.* 133, 143–173.
- Blockley, J.G., Tehnas, I.J., Mandyczewsky, A., Morris, R.C., 1993. Proposed stratigraphic subdivisions of the Marra Mamba Iron Formation and the lower Wittenoom Dolomite, Hamersley Group, Western Australia. *Geol. Surv. West. Aust. Rep.* 34, 47–63.
- Bolhar, R., Hofmann, A., Woodhead, J., Hergt, J., Dirks, P., 2002. Pb-and Nd-isotope systematics of stromatolitic limestones from the 2.7 Ga Ngezi Group of the Belingwe Greenstone Belt: constraints on timing of deposition and provenance. *Precambrian Res.* 114, 277–294.
- Bolhar, R., Van Kranendonk, M.J., 2007. A non-marine depositional setting for the northern Fortescue Group, Pilbara Craton, inferred from trace element geochemistry of stromatolitic carbonates. *Precambrian Res.* 155, 229–250.
<https://doi.org/10.1016/j.precamres.2007.02.002>
- Breemen, O. van, Davis, W.J., King, J.E., 1992. Temporal distribution of granitoid plutonic

Chapter 1: Introduction

- rocks in the Archean Slave Province, northwest Canadian Shield. *Can. J. Earth Sci.* 29, 2186–2199.
- Buick, R., 1992. The Antiquity of Oxygenic Photosynthesis : Evidence from Stromatolites in Sulphate- Deficient Archean Lakes 255, 74–77.
- Buick, R., Dunlop, J.S.R., 1990. Evaporitic sediments of early Archean age from the Warrawoona Group, North Pole, Western Australia. *Sedimentology* 37, 247–277.
- Byerly, G.R., Kröner, A., Lowe, D.R., Todt, W., Walsh, M.M., 1996. Prolonged magmatism and time constraints for sediment deposition in the early Archean Barberton greenstone belt: evidence from the Upper Onverwacht and Fig Tree groups. *Precambrian Res.* 78, 125–138.
- Byerly, G.R., Lower, D.R., Walsh, M.M., 1986. Stromatolites from the 3,300–3,500-Myr Swaziland Supergroup, Barberton Mountain Land, South Africa. *Nature* 319, 489–491.
- Caro, G., Bourdon, B., Wood, B.J., Corgne, A., 2005. Trace-element fractionation in Hadean mantle generated by melt segregation from a magma ocean. *Nature* 436, 246–249.
- Chadwick, B., Ramakrishnan, M., Vasudev, V.N., Viswanatha, M.N., 1989. Facies distributions and structure of a Dharwar volcanosedimentary basin: evidence for late Archean transpression in southern India? *J. Geol. Soc. London.* 146, 825–834.
- Chadwick, B., Ramakrishnan, M., Viswanatha, M.N., 1985. A comparative study of tectonic fabrics and deformation mechanisms in Dharwar grits and phyllites and Sargur quartzites on the west of the Chitradurga supracrustal belt, Karnataka. *J. Geol. Soc. India* 26, 526–546.
- Chadwick, B., Vasudev, V.N., Hegde, G. V, 2000. The Dharwar craton, southern India, interpreted as the result of Late Archean oblique convergence. *Precambrian Res.* 99, 91–111.
- Chadwick, B., Vasudev, V.N., Hegde, G. V, 1997. The Dharwar craton, southern India, and its Late Archean plate tectonic setting: current interpretations and controversies. *Proc. Indian Acad. Sci. Planet. Sci.* 106, 249–258.
- Corfu, F., Wallace, H., 1986. U–Pb zircon ages for magmatism in the Red Lake greenstone belt, northwestern Ontario. *Can. J. Earth Sci.* 23, 27–42. <https://doi.org/10.1139/e86-004>
- Dimroth, E., 1982. The oldest rocks on Earth: stratigraphy and sedimentology of the 3.8 billion years old Isua supracrustal sequence. *Sediment. Geol. highly Metamorph. Precambrian complexes* 16–27.
- Dixon, J.G.P., 2004. Archean Geology of Buffalo River Gorge, KwaZulu-Natal.
- Fedo, C.M., 2000. Setting and origin for problematic rocks from the >3.7 Ga Isua Greenstone Belt, southern west Greenland: Earth’s oldest coarse clastic sediments. *Precambrian Res.* 101, 69–78. [https://doi.org/https://doi.org/10.1016/S0301-9268\(99\)00100-X](https://doi.org/https://doi.org/10.1016/S0301-9268(99)00100-X)
- Fralick, P., Riding, R., 2015. Steep Rock Lake: Sedimentology and geochemistry of an Archean carbonate platform. *Earth-Science Rev.* 151, 132–175.

<https://doi.org/10.1016/j.earscirev.2015.10.006>

- Fralick, P.W., Hollings, P., King, D., 2008. Stratigraphy, geochemistry and depositional environments of Mesoarchean sedimentary units in Western Superior Province: implications for generation of early crust. When did plate tectonics begin planet Earth 77–96.
- Green, M.G., 2001. Early Archaean crustal evolution: evidence from ~ 3.5 million year old greenstone successions in the Pilgangoora Belt, Pilbara Craton, Australia. Doctoral Dissertation. University of Sydney. Geosciences.
- Grobler, N.J., Van der Westhuizen, W.A., Tordiffe, E.A.W., 1989. The Sodium Group, South Africa: reference section for late Archaean-early Proterozoic cratonic cover sequences. *J. Geol. Soc. Aust.* 36, 41–64.
- Grotzinger, John P., 1989. Facies and evolution of Precambrian carbonate depositional systems: emergence of the modern platform archetype. *Control. carbonate Platf. basin Dev.* 71–106. <https://doi.org/10.2110/pec.89.44.0079>
- Grotzinger, John P., 1989. Facies and evolution of Precambrian carbonate depositional systems: emergence of the modern platform archetype.
- Grotzinger, J.P., 1986. Cyclicity and paleoenvironmental dynamics, Rocknest platform, northwest Canada. *Geol. Soc. Am. Bull.* 97, 1208–1231.
- Harley, S.L., Kelly, N.M., 2007. Ancient Antarctica: the Archaean of the east Antarctic shield. *Dev. Precambrian Geol.* 15, 149–186.
- Harnmeijer, J., 2010. *Squeezing Blood from A Stone: Inferences into the life and depositional environments of the early Archaean.* University of Washington.
- Harrison, T.M., 2020. Morpho- and Chemo-Fossil Evidence of Early Life BT - Hadean Earth, in: Harrison, T.M. (Ed.), . Springer International Publishing, Cham, pp. 249–272. https://doi.org/10.1007/978-3-030-46687-9_11
- Henderson, J.B., 1975a. Archean stromatolites in the northern slave province, Northwest Territories, Canada. *Can. J. Earth Sci.* 12, 1619–1630.
- Henderson, J.B., 1975b. SEDIMENTOLOGY OF THE ARCHEAN YELLOWKNIFE SUPERGROUP AT YELLOWKNIFE, DISTRICT OF MACKENZIE.
- Hickman, A., 2012. Review of the Pilbara Craton and Fortescue Basin, Western Australia: crustal evolution providing environments for early life. *Isl. Arc* 21, 1–31.
- Hofmann, A., Dirks, P.H.G.M., Jelsma, H.A., 2001. Late Archaean foreland basin deposits, Belingwe greenstone belt, Zimbabwe. *Sediment. Geol.* 141, 131–168.
- Hofmann, A., Kusky, T., 2004. The Belingwe greenstone belt: ensialic or oceanic? *Dev. Precambrian Geol.* 13, 487–538.
- Hofmann, H.J., Grey, K., Hickman, A.H., Thorpe, R.I., 1999. Origin of 3.45 Ga coniform stromatolites in Warrawoona group, Western Australia. *Geol. Soc. Am. Bull.* 111,

1256–1262.

- Hofmann, H.J., Thurston, P.C., Wallace, H., 1985. Archean stromatolites from Uchi greenstone belt, northwestern Ontario, in: *Evolution of Archean Supracrustal Sequences*. Geol. Assoc. Can. Spec. Pap., pp. 125–132.
- Holland, H.D., 1978. *The chemistry of the atmosphere and oceans*.
- Hollings, P., Wyman, D., Kerrich, R., 1999. Komatiite–basalt–rhyolite volcanic associations in Northern Superior Province greenstone belts: significance of plume-arc interaction in the generation of the proto continental Superior Province. *Lithos* 46, 137–161.
[https://doi.org/10.1016/S0024-4937\(98\)00058-9](https://doi.org/10.1016/S0024-4937(98)00058-9)
- Hunter, M.A., Bickle, M.J., Nisbet, E.G., Martin, A., Chapman, H.J., 1998. Continental extensional setting for the Archean Belingwe greenstone belt, Zimbabwe. *Geology* 26, 883–886.
- Jayananda, M., Martin, H., Peucat, J.-J., Mahabaleswar, B., 1995. Late Archaean crust-mantle interactions: geochemistry of LREE-enriched mantle derived magmas. Example of the Closepet batholith, southern India. *Contrib. to Mineral. Petrol.* 119, 314–329.
- Kamber, B.S., Bolhar, R., Webb, G.E., 2004. Geochemistry of late Archaean stromatolites from Zimbabwe: evidence for microbial life in restricted epicontinental seas. *Precambrian Res.* 132, 379–399.
<https://doi.org/https://doi.org/10.1016/j.precamres.2004.03.006>
- Kamber, B.S., Webb, G.E., 2001. The geochemistry of late Archaean microbial carbonate: Implications for ocean chemistry and continental erosion history. *Geochim. Cosmochim. Acta* 65, 2509–2525. [https://doi.org/10.1016/S0016-7037\(01\)00613-5](https://doi.org/10.1016/S0016-7037(01)00613-5)
- Kamber, B.S., Webb, G.E., Gallagher, M., 2014. The rare earth element signal in Archaean microbial carbonate: information on ocean redox and biogenicity. *J. Geol. Soc. London.* 171, 745–763.
- Kaufman, A.J., Hayes, J.M., Klein, C., 1990. Primary and diagenetic controls of isotopic compositions of iron-formation carbonates. *Geochim. Cosmochim. Acta* 54, 3461–3473.
[https://doi.org/https://doi.org/10.1016/0016-7037\(90\)90298-Y](https://doi.org/https://doi.org/10.1016/0016-7037(90)90298-Y)
- Kinny, P.D., Nutman, A.P., 1996. Zirconology of the Meeberrie gneiss, Yilgarn Craton, Western Australia: an early Archaean migmatite. *Precambrian Res.* 78, 165–178.
- Komiya, T., Maruyama, S., Masuda, T., Nohda, S., Hayashi, M., Okamoto, K., 1999. Plate tectonics at 3.8–3.7 Ga: Field evidence from the Isua accretionary complex, southern West Greenland. *J. Geol.* 107, 515–554.
- Kranendonk, M.J. Van, Hickman, A.H., Smithies, R.H., Nelson, D.R., Pike, G., 2002. Geology and tectonic evolution of the archaean North Pilbara terrain, Pilbara Craton, Western Australia. *Econ. Geol.* 97, 695–732.
- Kröner, A., Hegner, E., Wendt, J.I., Byerly, G.R., 1996. The oldest part of the Barberton granitoid-greenstone terrain, South Africa: evidence for crust formation between 3.5 and 3.7 Ga. *Precambrian Res.* 78, 105–124.

Chapter 1: Introduction

- Kusky, T.M., Hudleston, P.J., 1999. Growth and demise of an Archean carbonate platform, Steep Rock Lake, Ontario, Canada. *Can. J. Earth Sci.* 36, 565–584.
- Lambert, M.B., 1998. Stromatolites of the late Archean back River stratovolcano, Slave structural province, Northwest Territories, Canada. *Can. J. Earth Sci.* 35, 290–301.
- Lowe, D.R., 1980. Stromatolites 3,400-myr old from the Archean of Western Australia. *Nature* 284, 441–443.
- Lowe, D.R., Byerly, G.R., 2007. Chapter 5.3 An Overview of the Geology of the Barberton Greenstone Belt and Vicinity: Implications for Early Crustal Development, in: van Kranendonk, M.J., Smithies, R.H., Bennett, V.C.B.T.-D. in P.G. (Eds.), *Earth's Oldest Rocks*. Elsevier, pp. 481–526. [https://doi.org/https://doi.org/10.1016/S0166-2635\(07\)15053-2](https://doi.org/https://doi.org/10.1016/S0166-2635(07)15053-2)
- Lowe, D.R., Byerly, G.R., 1999a. Stratigraphy of the west-central part of the Barberton Greenstone Belt, South Africa. *Geol. Soc. Am. Spec. Pap.* 329, 1–36.
- Lowe, D.R., Byerly, G.R., 1999b. Geologic evolution of the Barberton greenstone belt, South Africa. Geological Society of America.
- Lowe, D.R., Knauth, L.P., 1977. Sedimentology of the Onverwacht Group (3.4 billion years), Transvaal, South Africa, and its bearing on the characteristics and evolution of the early earth. *J. Geol.* 85, 699–723.
- Lowe, D.R., Nocita, B.W., 1999. Foreland basin sedimentation in the Mapepe Formation, southern-facies Fig Tree Group. *Spec. Pap. Soc. Am.* 233–258.
- Manikyamba, C., Naqvi, S.M., 1998. Type and processes of greenstone belt formation. *Indian Precambrian. Sci. Publ. Jodhpur* 18–32.
- Manikyamba, C., Naqvi, S.M., 1997. Mineralogy and geochemistry of Archaean greenstone belt-hosted Mn formations and deposits of the Dharwar Craton: redox potential of proto-oceans. *Geol. Soc. London, Spec. Publ.* 119, 91–103.
- Martin, A., Nisbet, E.G., Bickle, M.J., 1980. Archaean stromatolites of the Belingwe greenstone belt, Zimbabwe (Rhodesia). *Precambrian Res.* 13, 337–362.
- Martin, A., Nisbet, E.G., Bickle, M.J., Orpen, J.L., 2020. Rock units and stratigraphy of the Belingwe Greenstone Belt: the complexity of the tectonic setting, in: *The Geology of the Belingwe Greenstone Belt, Zimbabwe*. CRC Press, pp. 13–37.
- McIntyre, T., Fralick, P., 2017. Sedimentology and Geochemistry of the 2930 Ma Red Lake-Wallace Lake Carbonate Platform, Western Superior Province, Canada. *Depos. Rec.* 3, 258–287. <https://doi.org/10.1002/dep2.36>
- Mojzsis, S.J., Harrison, T.M., Pidgeon, R.T., 2001. Oxygen-isotope evidence from ancient zircons for liquid water at the Earth's surface 4,300 Myr ago. *Nature* 409, 178–181.
- Myers, J.S., Crowley, J.L., 2000. Vestiges of life in the oldest Greenland rocks? A review of early Archean geology in the Godthåbsfjord region, and reappraisal of field evidence for >3850 Ma life on Akilia. *Precambrian Res.* 103, 101–124.

[https://doi.org/https://doi.org/10.1016/S0301-9268\(00\)00089-9](https://doi.org/https://doi.org/10.1016/S0301-9268(00)00089-9)

- Nothdurft, L.D., Webb, G.E., Kamber, B.S., 2004. Rare earth element geochemistry of Late Devonian reefal carbonates, Canning Basin, Western Australia: confirmation of a seawater REE proxy in ancient limestones. *Geochim. Cosmochim. Acta* 68, 263–283.
- Nunes, P.D., Thurston, P.C., 1980. Two hundred and twenty million years of Archean evolution: a zircon U–Pb age stratigraphic study of the Uchi–Confederation Lakes greenstone belt, northwestern Ontario. *Can. J. Earth Sci.* 17, 710–721.
- Nutman, A.P., Bennett, V.C., Friend, C.R.L., Van Kranendonk, M.J., Chivas, A.R., 2016. Rapid emergence of life shown by discovery of 3,700-million-year-old microbial structures. *Nature* 537, 535–538. <https://doi.org/10.1038/nature19355>
- Nutman, A.P., Chadwick, B., Rao, B.K., Vasudev, V.N., 1996. SHRIMP U/Pb zircon ages of acid volcanic rocks in the Chitradurga and Sandur groups, and granites adjacent to the Sandur schist belt, Karnataka. *Geol. Soc. India* 47, 153–164.
- Patry, L. A., Bonnard, P., Boyet, M., Afroz, M., Wilmeth, D. T., Ramsay, B., Nonnotte, P., Homann, M., Sansjofre, P., Fralick, P. W., & Lalonde, S. V. Archean origins of oxygenic photosynthesis confirmed by La-Ce geochronology. *Nature*, in review (Submission 2023-04-05860)
- Pirie, J., 1981. Regional setting of gold deposits in the Red Lake area, northwestern Ontario; in *Genesis of Archean volcanic-hosted gold deposits*; Ontario Geological Survey, Miscellaneous Paper 97, 71–93.
- Ramakrishnan, M., Nath, J.S., 1981. Early Precambrian supracrustals of southern Karnataka. Geological Survey of India.
- Ramsay, B., 2020. Environmental control of seawater geochemistry in a Mesoarchean Peritidal System, Woman Lake, Superior Province. MSc Thesis. Lakehead University, Canada.
- Rose, N.M., Rosing, M.T., Bridgwater, D., 1996. The origin of metacarbonate rocks in the Archaean Isua supracrustal belt, West Greenland. *Am. J. Sci.* 296, 1004–1044.
- Rosing, M.T., Rose, N.M., Bridgwater, D., Thomsen, H.S., 1996. Earliest part of Earth's stratigraphic record: A reappraisal of the > 3.7 Ga Isua (Greenland) supracrustal sequence. *Geology* 24, 43–46.
- Russell, J., Chadwick, B., Rao, B.K., Vasudev, V.N., 1996. Whole-rock PbPb isotopic ages of Late Archaean limestones, Karnataka, India. *Precambrian Res.* 78, 261–272.
- Sakurai, R., Ito, M., Ueno, Y., Kitajima, K., Maruyama, S., 2005. Facies architecture and sequence-stratigraphic features of the Tumbiana Formation in the Pilbara Craton, northwestern Australia: implications for depositional environments of oxygenic stromatolites during the Late Archean. *Precambrian Res.* 138, 255–273.
- Sanborn-Barrie, M., Skulski, T., Parker, J., Dubé, B., 2000. Integrated regional analysis of the Red Lake greenstone belt and its mineral deposits, western Superior Province, Ontario. *Geol. Surv. Canada Current Re.* 14.

Chapter 1: Introduction

- Sanborn-Barrie, M., Skulski, T., Parker, J.R., 2001. Three hundred million years of tectonic history recorded by the Red Lake greenstone belt, Ontario. *Geol. Surv. Canada Current Re.* 14. <https://doi.org/10.4095/212109>
- Sasseville, C., Tomlinson, K.Y., Hynes, A., McNicoll, V., 2006. Stratigraphy, structure, and geochronology of the 3.0–2.7 Ga Wallace Lake greenstone belt, western Superior Province, southeast Manitoba, Canada. *Can. J. Earth Sci.* 43, 929–945.
- Schiøtte, L., Compston, W., Bridgwater, D., 1989. U–Pb single-zircon age for the Tinissaq gneiss of southern West Greenland: A controversy resolved. *Chem. Geol. Isot. Geosci. Sect.* 79, 21–30.
- Siahi, M., Hofmann, A., Hegner, E., Master, S., 2016. Sedimentology and facies analysis of Mesoarchaeon stromatolitic carbonate rocks of the Pongola Supergroup, South Africa. *Precambrian Res.* 278, 244–264. <https://doi.org/https://doi.org/10.1016/j.precamres.2016.03.004>
- Simonson, B.M., 1992. Geological evidence for a strewn field of impact spherules in the early Precambrian Hamersley Basin of Western Australia. *Geol. Soc. Am. Bull.* 104, 829–839.
- Simonson, B.M., Schubel, K.A., Hassler, S.W., 1993. Carbonate sedimentology of the early Precambrian Hamersley Group of western Australia. *Precambrian Res.* 60, 287–335.
- Srinivasan, R., Shukla, M., Naqvi, S.M., Yadav, V.K., Venkatachala, B.S., Raj, B.U., Rao, D.V.S., 1989. Archaean stromatolites from the Chitradurga schist belt, Dharwar craton, South India. *Precambrian Res.* 43, 239–250.
- Thorne, A.M., Trendall, A.F., 2001. Geology of the Fortescue Group, Pilbara Craton, Western Australia. Geological Survey of Western Australia, Department of Minerals and Energy.
- Trendall, A.F., De Laeter, J.R., Nelson, D.R., Bhaskar, R., 1997. Further zircon U-Pb age data for the Daginkatte formation, Dharwar Supergroup, Karnataka craton. *J. Geol. Soc. India* 50, 25–30.
- Van der Westhuizen, W.A., De Bruijn, H., Meintjes, P.G., 2006. The Ventersdorp Supergroup. *Geol. South Africa* 1.
- Van der Westhuizen, W.A., De Bruijn, H., Meintjes, P.G., 1991. The Ventersdorp supergroup: an overview. *J. African Earth Sci. (and Middle East)* 13, 83–105.
- Van Kranendonk, M.J., 2006. Volcanic degassing, hydrothermal circulation and the flourishing of early life on Earth: A review of the evidence from c. 3490–3240 Ma rocks of the Pilbara Supergroup, Pilbara Craton, Western Australia. *Earth-Science Rev.* 74, 197–240. <https://doi.org/https://doi.org/10.1016/j.earscirev.2005.09.005>
- Van Kranendonk, M.J., Webb, G.E., Kamber, B.S., 2003. Geological and trace element evidence for a marine sedimentary environment of deposition and biogenicity of 3.45 Ga stromatolitic carbonates in the Pilbara Craton, and support for a reducing Archaean ocean. *Geobiology* 1, 91–108.

Chapter 1: Introduction

- Veizer, J., Clayton, R.N., Hinton, R.W., Von Brunn, V., Mason, T.R., Buck, S.G., Hoefs, J., 1990. Geochemistry of Precambrian carbonates: 3-shelf seas and non-marine environments of the Archean. *Geochim. Cosmochim. Acta* 54, 2717–2729.
[https://doi.org/https://doi.org/10.1016/0016-7037\(90\)90007-8](https://doi.org/https://doi.org/10.1016/0016-7037(90)90007-8)
- Viljoen, M.J., Viljoen, R., 1969. The geology and geochemistry of the lower ultramafic unit of the Onverwacht Group and a proposed new class of igneous rocks. *Geol. Soc. South Africa Spec. Publ.* 2, 55–86.
- Walker, J.C.G., Hays, P.B., Kasting, J.F., 1981. A negative feedback mechanism for the long-term stabilization of Earth's surface temperature. *J. Geophys. Res. Ocean.* 86, 9776–9782.
- Walraven, F., Armstrong, R.A., Kruger, F.J., 1990. A chronostratigraphic framework for the north-central Kaapvaal craton, the Bushveld Complex and the Vredefort structure. *Tectonophysics* 171, 23–48.
- Webb, G.E., Kamber, B.S., 2000. Rare earth elements in Holocene reefal microbialites: A new shallow seawater proxy. *Geochim. Cosmochim. Acta* 64, 1557–1565.
[https://doi.org/10.1016/S0016-7037\(99\)00400-7](https://doi.org/10.1016/S0016-7037(99)00400-7)
- Wilks, M.E., Nisbet, E.G., 1988. Stratigraphy of the Steep Rock Group, northwest Ontario: a major Archaean unconformity and Archaean stromatolites. *Can. J. Earth Sci.* 25, 370–391.
- Wilson, A.H., Versfeld, J.A., 1994. The early Archaean Nondweni greenstone belt, southern Kaapvaal Craton, South Africa, part II. Characteristics of the volcanic rocks and constraints on magma genesis. *Precambrian Res.* 67, 277–320.
- Xie, H., Hofmann, A., Hegner, E., Wilson, A., Wan, Y., Liu, D., 2012. Zircon SHRIMP dating confirms a Palaeoarchaean supracrustal terrain in the southeastern Kaapvaal Craton, Southern Africa. *Gondwana Res.* 21, 818–828.

Chapter 1: Introduction

Chapter 2

Geological Setting

2.1 Geology of the Red Lake greenstone belt

The Superior Province, located in Canada, comprises about 23% of the exposed Archean crust of the Earth, and consists of mainly Meso- to Neo-archean age rocks (Thurston et al., 1991). The Superior Province is divided into nine subprovinces: Sachigo subprovince, Berens River subprovince, Uchi subprovince, English River subprovince, Winnipeg River subprovince, Wabigoon subprovince, Quetico subprovince, Abitibi subprovince, and Wawa subprovince (Card and Ciesielski, 1986) (Figure 2.1). The Uchi subprovince is an east-west trending, semi-continuous ribbon-like region of metavolcanic and metasedimentary rocks interlinked between granitic bodies (Stott et al., 1991). The Uchi Subprovince is bordered to the north by a plutonic belt, the Berens River Subprovince, and to the south by a high-grade metasedimentary-plutonic belt, the English River Subprovince (Stott et al., 1991). A series of Neoproterozoic to Mesoproterozoic rocks spanning 3000-2700 Ma occur in this subprovince (Corfu and Wallace, 1986). Most parts of the Uchi subprovince were subjected to greenschist to lower amphibolite facies metamorphism, while higher-grade metamorphosed rocks occur mostly at the major pluton boundaries and in areas with high degrees of strain (Corfu and Wallace, 1986; Thurston and Breaks, 1978). The Uchi subprovince consists of seven supracrustal assemblages of Mesoproterozoic to Neoproterozoic age, all of which have undergone subsequent metamorphism and hydrothermal alteration. Supracrustal assemblages that formed the Uchi subprovince include mafic tholeiitic-komatiitic sequences to calc-alkalic and tholeiitic volcanic arc sequences, and chemical and clastic sedimentary rocks (Card, 1990; Card & Ciesielski, 1986; Hollings et al., 1999). The Uchi Subprovince contains several greenstone belts, including the Red Lake greenstone belt (RLGB). The RLGB is characterized by 300 Ma of episodic magmatism, volcanism, deposition of diverse sedimentary rocks, emplacement of granitoid batholiths, multi-phase deformation, and metamorphism (Corfu and Andrews, 1987; Sanborn-Barrie et al., 2001, 2000).

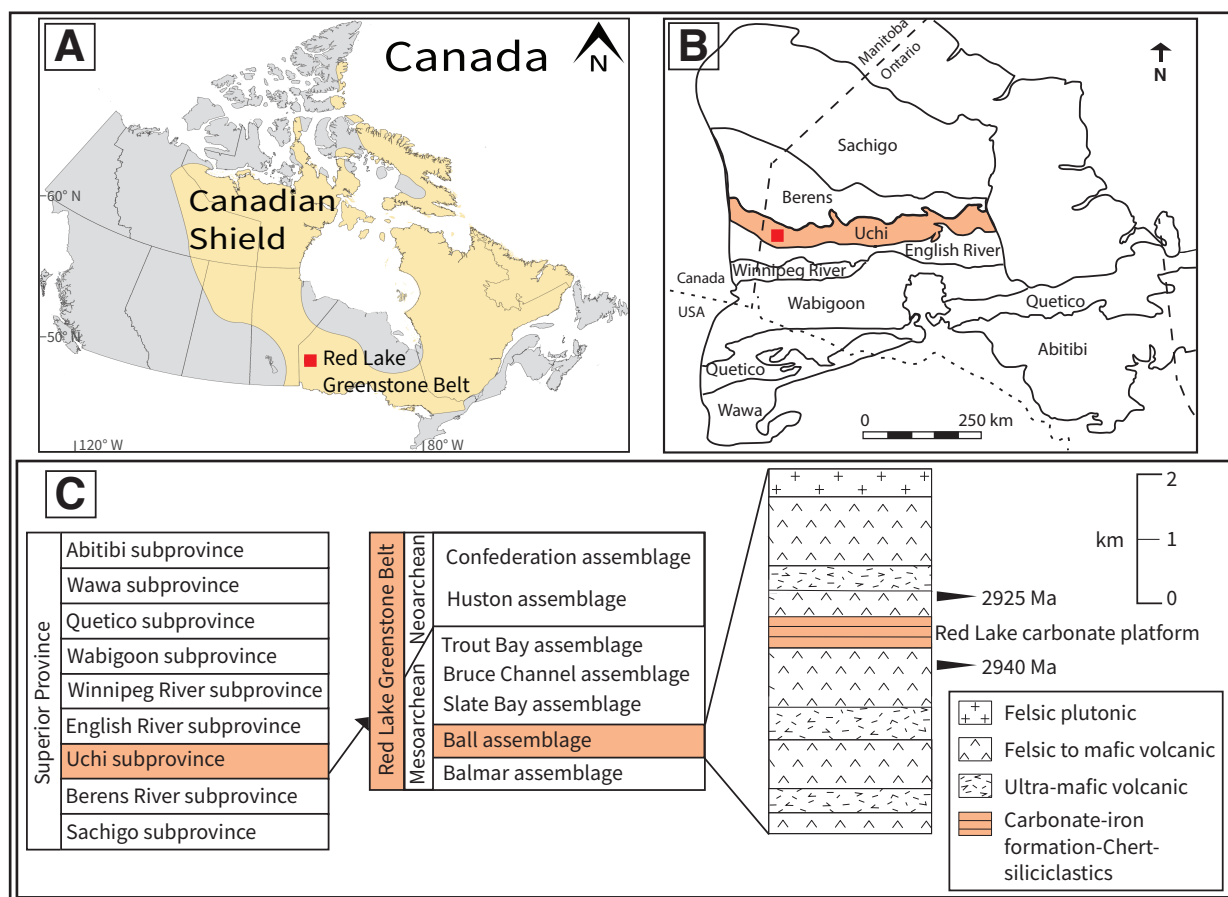


Figure 2.1: (A) Map of the Canadian Shield, (B) subprovince map of the Superior Province (studied area marked in red square) in the Superior Craton, central Canada, and (C) Stratigraphy of the Ball assemblage containing the Red Lake carbonate platform (modified after Afroz et al., 2023).

The RLGB is mainly formed of Mesoarchean assemblages, which include three volcanic assemblages and one clastic assemblage: the Balmer, Ball, and Bruce Channel assemblages, and the Slate Bay assemblage, respectively. The Balmer assemblage (2.99 - 2.96 Ga) constitutes about half of the RLGB, and occurred at an island arc with mantle plume activity (Hollings, 1999; Sanborn-Barrie et al., 2001; Tomlinson et al., 1998). It is composed of submarine tholeiitic basalt, komatiite, komatiitic basalt with minor felsic metavolcanic rocks, mafic to ultramafic intrusive rocks, clastic metasedimentary rocks, and chert-magnetite iron formation (Hollings et al., 1999; Sanborn-Barrie et al., 2001; Tomlinson et al., 1998). The Ball assemblage, originally dated to 2.94 - 2.92 Ga (but new zircon U-Pb data from the

Chapter 2: Geological Setting

EARTHBLOOM project indicate it may be as young as 2.87 Ga; see below), hosts stratigraphy comprised of diverse volcanic rocks, including komatiitic to tholeiitic basalt, andesite, dacite, and rhyolite intercalated with minor komatiite and komatiitic basalt flows, which are interlayered with chemical and siliciclastic metasedimentary rocks. Chemical metasedimentary rocks include chert-magnetite iron formation, dolomitic marble-chert, and siliciclastic metasedimentary rocks including conglomerate and quartzite. The Slate Bay assemblage (<2.92 Ga) comprises clastic and conglomerate units containing Balmer- and Ball-age zircons (Corfu et al., 1998), indicating an erosional event affecting the Ball assemblage. After the deposition of the clastic-dominated Slate Bay assemblage, the Bruce Channel assemblage (<2.89 Ga) represents explosive, arc-like volcanism with later subsidence and deposition of clastic sediments. The Trout Bay assemblage (<2.85 Ga) consists of volcano-sedimentary sequences and represents a back-arc or oceanic plateau setting (Sanborn-Barrie et al., 2001). This assemblage consists of clastic rocks underlain by basalt, intermediate tuff, chert-magnetite iron formation, and intrusive gabbro and ultramafic rocks. Later, a regional angular unconformity comprising polymictic conglomerate separated the Mesoarchean rocks (Balmer and Bruce Channel assemblages) from the Neoproterozoic rocks (Confederation assemblage). The Neoproterozoic Huston assemblage (2.71 Ga) is comprised of argillite, turbiditic wacke, and a thin layer of tuff. The Confederation assemblage (2.73 Ga) consists of three temporally and spatially distinct volcanic packages (Sanborn-Barrie et al., 2001). The RLGB was affected by three distinct metamorphic events, and the peak metamorphic event produced lower greenschist to upper amphibolite facies (Easton, 2000; Thompson, 2003). Peak metamorphism was caused by plutonism and/or orogenic events in the RLGB (Dubé et al., 2004; Easton, 2000; Stott et al., 1991).

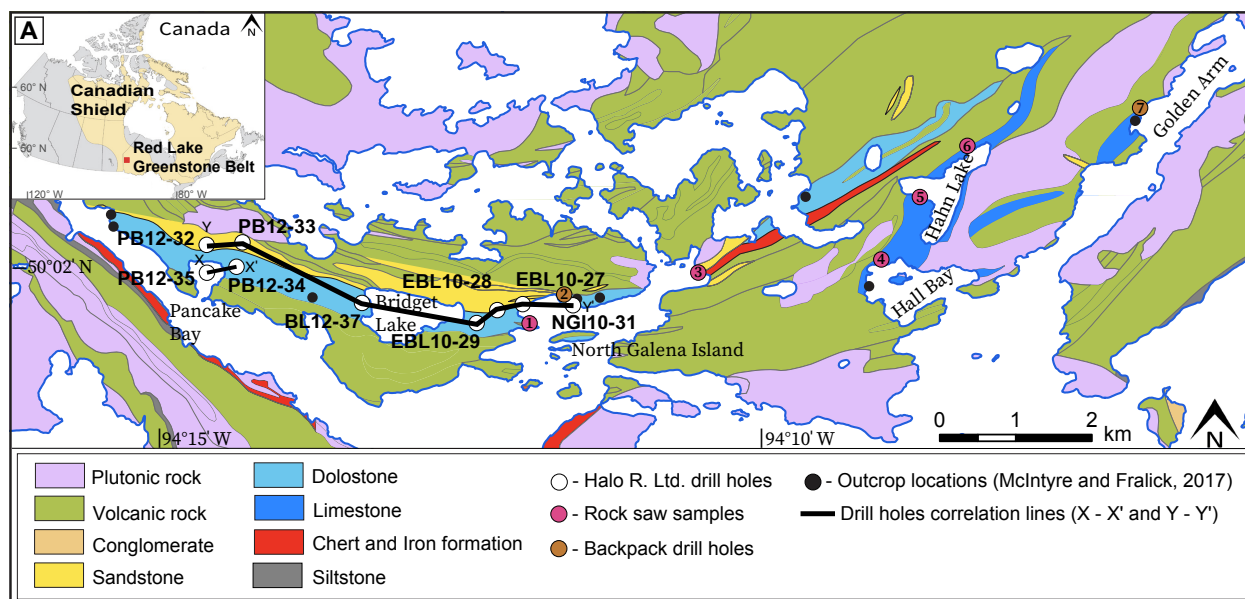


Figure 2.2: Geological map of the Ball Assemblage containing the Red Lake carbonate platform along with the locations of the cored drill holes analyzed in this study (modified after Sanborn-Barrie et al., 2004).

2.2 Geology of the Red Lake carbonate platform

The Red Lake carbonate platform (RLCP) is the oldest known thick Mesoproterozoic carbonate platform on Earth, located within the Red Lake greenstone belt (RLGB) of the Uchi Subprovince, Superior Province Canada (Figure 2.1). The carbonate platform lies between the North Caribou Terrane and the English River subprovince (McIntyre and Fralick, 2017; Sanborn-Barrie et al., 2001, 2000). Corfu and Wallace (1986) constrained the age of this carbonate platform by U-Pb dating of zircons isolated from the underlying rhyolitic lapilli tuff (2940 ± 2 Ma) and overlying rhyolitic flow (2925 ± 3 Ma). However, approximately two months before completion of this thesis, new LA-ICP-MS U-Pb ages from zircons isolated from a tuffaceous interval in the carbonate platform itself constrain deposition to ca. 2.87 Ga (Patry et al., in review). This indicates that the zircons dated by Corfu and Wallace may have been detrital in origin; accordingly, the new 2.87 Ga age is adopted for the platform throughout this thesis, although it is underlined that this may be subject to later re-interpretation by the EARTHBLoom team.

Chapter 2: Geological Setting

The carbonate platform is comprised of a complex succession of metavolcanic-metasedimentary rocks of the Ball assemblage (Figure 2.2). The metasedimentary assemblage is overlaid and underlaid by mafic to felsic metavolcanic rocks. The Ball assemblage in the RLCP mainly consists of tholeiitic basalt flows, felsic calc-alkalic flows, pyroclastic rocks, chemical sediments, e.g. dolomite-chert, magnetite-chert, sulfides, and metasedimentary siliciclastic rocks (Corfu and Wallace, 1986; Hofmann et al., 1985; Hollings et al., 1999; Pirie, 1981; Sanborn-Barrie et al., 2001, 2000). The stromatolite-bearing carbonate is trending east to west and dipping to the south (McIntyre and Fralick, 2017). The 490 m thick metasedimentary package contains 290 m of carbonates, and the rest is composed of various types of chemical sedimentary and siliciclastic rocks. The stratigraphy of the Red Lake transecting through the carbonate platform was constructed using the stratigraphic logs from the nine cored industry drill holes donated by Goldcorp Inc. for the EARTHBLoom project (see Methods in Chapter 3 as well as Afroz et al., 2023).

2.3.1 Carbonates

2.3.1.1 Stromatolitic carbonate

Laterally linked domal stromatolites (McIntyre and Fralick, 2017) aka *Stratifera* (Hofmann et al., 1985), isolated domal stromatolites (McIntyre and Fralick, 2017) aka *Colleniella* (Hofmann et al., 1985), and large low-relief domes (McIntyre and Fralick, 2017) are preserved in the Red Lake carbonate platform. The stromatolites are highly silicified and composed of coarse to fine laminoid fenestral fabric. Isolated domal stromatolites have laminoid fenestral fabric, bird-eye vugs, and reticulate stromatactis-like structures and similar dimensions to the laterally linked domal type (McIntyre and Fralick, 2017). This stromatolite type is overlain by herring-bone cross bedding composed of intraformational mud chips. Laterally linked domal stromatolites are the most common stromatolitic facies in the Red Lake carbonate platform and are mostly associated with wavy laminae, laminated carbonate stromatolites, and pseudomorph fans (Figure 2.4A) (McIntyre and Fralick, 2017). The large low-relief dome-type stromatolites show regular and smooth layering and are similar to the other stromatolites (Figure 2.4B). They form mounds with topographic relief of 1 m and a diameter of 2 m.

Crystal fans of variable sizes and lithofacies associations are preserved in the Red Lake carbonate platform. These are actually crystal pseudomorphs with acicular radiating crystals present in otherwise fine-grained ferroan dolomite or calcite matrix and are preferentially silicified. Atikokania consists of larger, stacked, densely packed fans ranging from 5 to 30 cm in height (McIntyre and Fralick, 2017). The stacked fan beds of about 2 m in diameter and 1.5 m in height have a dome-like structure (Figure 2.4D).

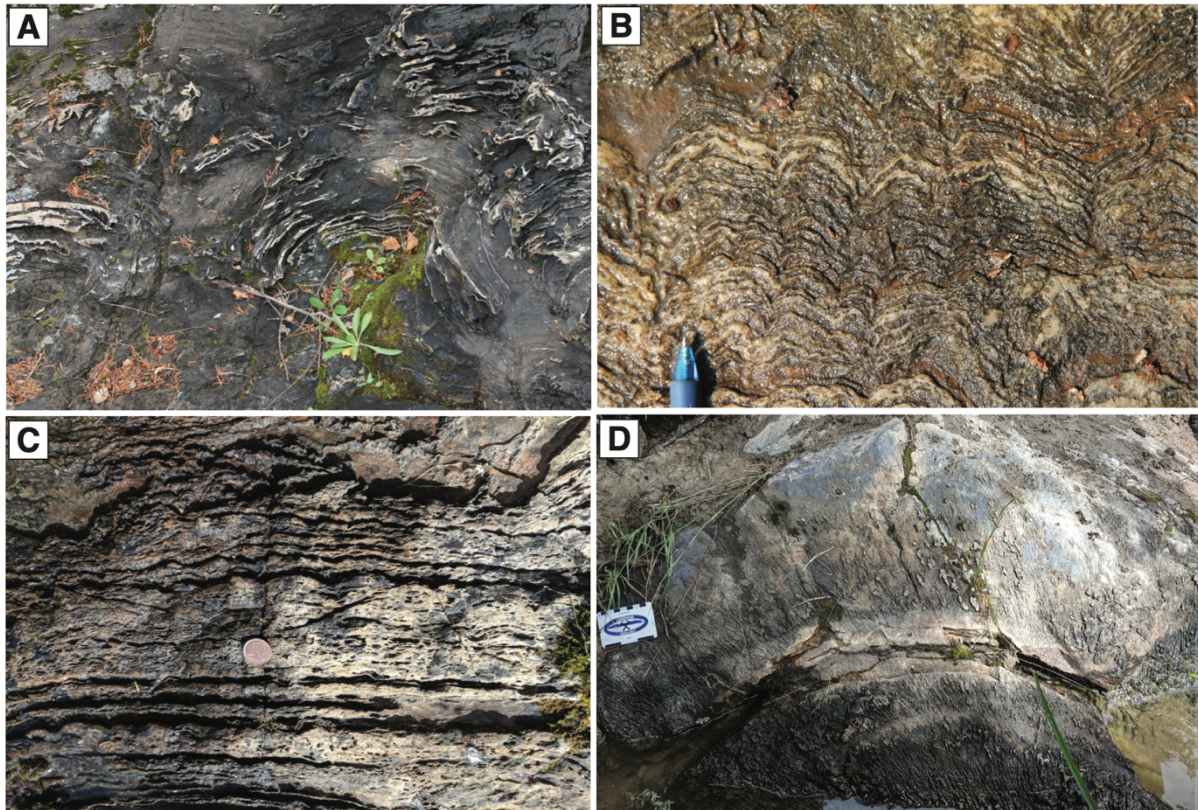


Figure 2.4: (A) Dolomitic domal stromatolites (B) Wavy stromatolitic laminae associated with laterally linked low domes (C) Crinkly stromatolites, and (D) Large dome containing crystal fans and massive carbonates composed of calcite in the Red Lake carbonate platform.

A variety of carbonate sediments with less obvious microbially-influenced features are also present in the RLCP. Laminated carbonate consists of light-colored chert and dark grey mm-scale limestone bands. This type of carbonate occurs in association with large low-relief domes and crystal fans. The wavy laminae lithofacies consist of flat, wavy, and crinkly laminae of massive carbonate separated by mm-scale chert laminae (McIntyre and Fralick, 2017) (Figure 2.4C). Also present is Herring-bone calcite, a type of cement, characterized by 1 to 3 cm thick laterally continuous irregular banding and composed of serrated, sub-mm-scale fibrous calcite or dolomite cement with elongated crystals that are perpendicular to banding (McIntyre and Fralick, 2017). Different types of features such as sheet cracks, stromatactis-like cavities, roll-ups, crinkly laminae, irregular folding, teepee structures, apparent desiccation

cracks, small mm-scale fibrous colloform cement crusts, pseudomorphs after gypsum and colleniella occur locally (McIntyre and Fralick, 2017).

2.3.1.2 Carbonate-magnetite

Carbonate-magnetite facies consist of white, ~1cm thick calcite layers alternating with mm-scale magnetite laminae (Afroz et al., 2023). The calcite bands are straight while the magnetite laminae are straight to wavy (Figure 2.5). Calcite and magnetite layers show sharp contacts, but

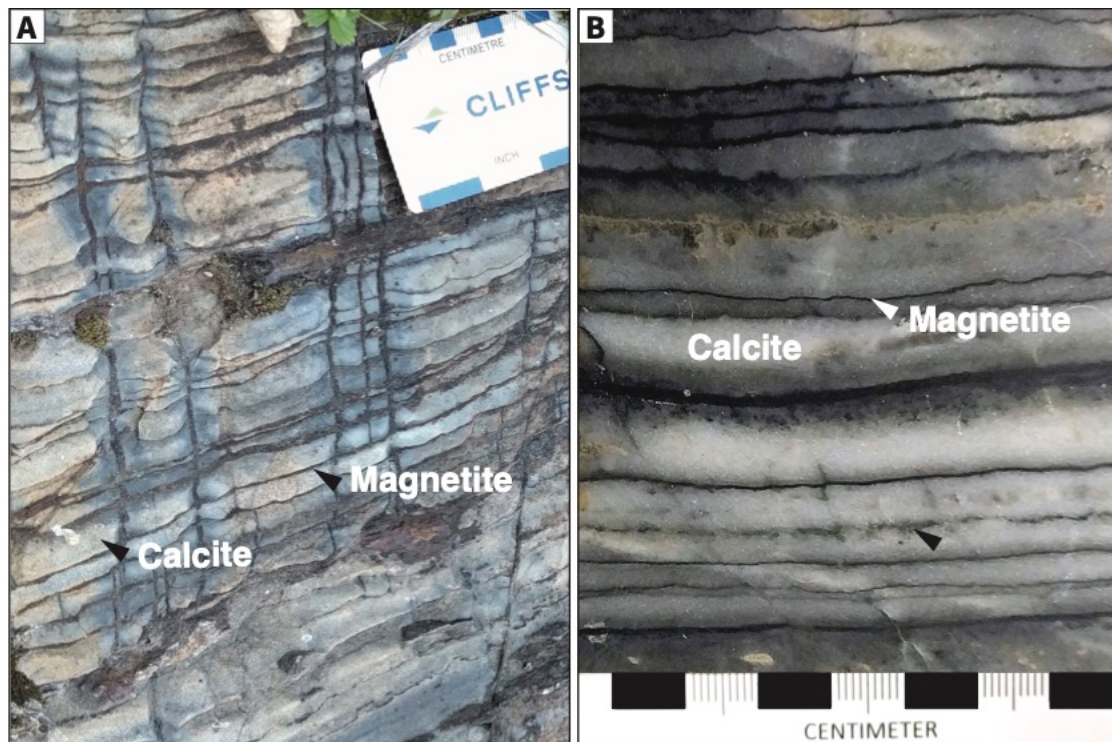


Figure 2.5: (A) Carbonate-magnetite in outcrop (B) polished section of carbonate-magnetite shows alternating calcite and magnetite bands.

sometimes diffusive magnetite is present in the carbonate layers. Primary structures and textures of calcite and magnetite bands have been obliterated due to recrystallization. In thin sections, inequigranular, fine to coarse crystalline calcite grains shows xenotopic fabric. These facies are absent in drill holes and shows limited occurrence in outcrops in the Red Lake area and are best exposed next to the stromatolitic carbonate unit on the NW shoreline of the Hall

Bay area and on the shoreline immediately south of the oxide facies iron formations from the WNW of Galena Island. These facies are considered transitional facies between shallow- to deep-water facies as they are underlying by shallow-water stromatolitic carbonate and overlying by slumped carbonate.

2.3.1.3 Slumped carbonate

Slumped carbonates occur in association with iron formations and/or siliciclastic sediments (Afroz et al., 2023). They consist of mass-flows of contorted calcite clasts and/or broken layers of different sizes and shapes (Figure 2.6). Fine-grained dark gray to black siliciclastic mudstone, magnetite-rich iron formation, or an assemblage of both hosts the calcite clasts/fragmented layers. The siliciclastic matrix is sometimes calcite-rich, indicating slumping likely to occur before lithification. These lithofacies occur next to the carbonate-magnetite facies on the shoreline of the Hall Bay area and are not present in the cored drill holes. Slumping of carbonate is not likely due to tectonic brecciation as the broken carbonate layers/clasts are irregularly oriented and the facies overlying and underlying the slumped units show no sign of tectonic brecciation but rather are parallel-laminated. This mass flow of carbonates was likely formed by soft-sediment deformation in the outer carbonate-dominated area of the platform due to slope instability, leading to the mixing and deposition of dislocated carbonates with other non-lithified sediments in the down-slope areas.

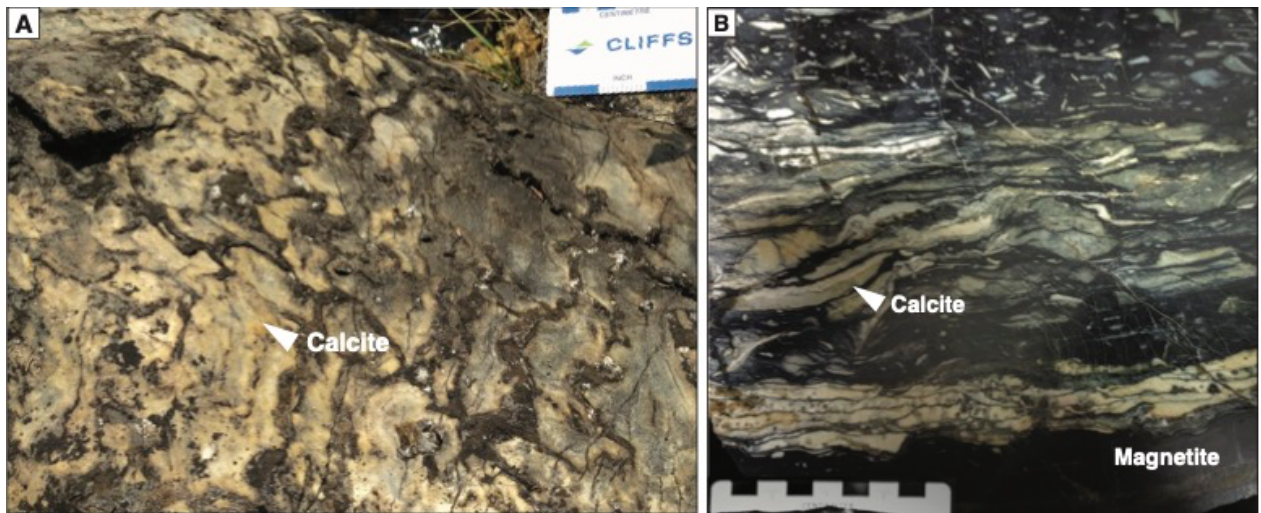


Figure 2.6: (A) Slumped carbonate in outcrop, (B) polished section shows broken, contorted clasts and/or broken layers of calcite hosted in siliciclastic mudstone, magnetite-rich iron formation, or an assemblage of both. Oxide iron formation

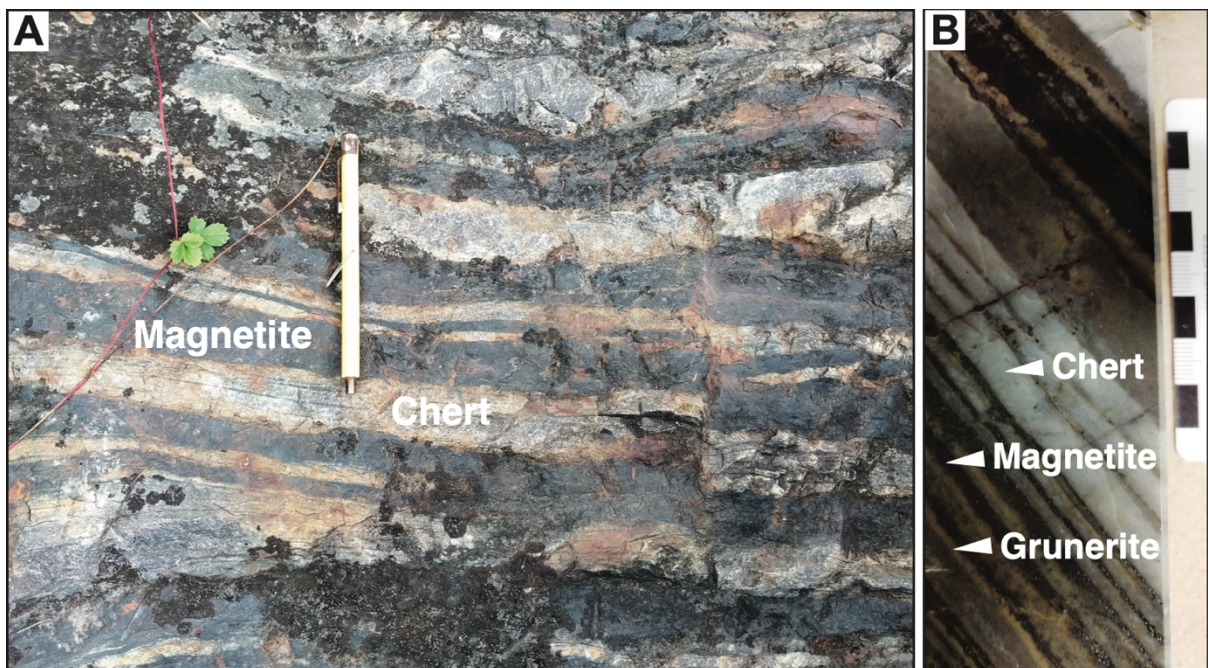


Figure 2.7: (A) Oxide iron formation composed of magnetite alternating with chert in outcrop, and (B) polished core sample showing magnetite interlayered with chert. Grunerite is often found at the contact between magnetite and chert, an indicator mineral of regional metamorphism.

2.3.2 Oxide iron formation

The oxide facies iron formation consists of a 1-5 cm thick magnetite band interbedded with chert of similar thickness (Afroz et al., 2023). Magnetite bands typically show sharp contact with the chert bands and layering is parallel, straight to slightly wavy, and laterally continuous (Figure 2.7). Oxide facies iron formation is well-preserved in outcrops in the Red Lake area and several drill holes captured this lithofacies.

2.3.3 Chert

Chert mainly occurs as massive chert and as chert interbedded with magnetite in the Red Lake area (Afroz et al., 2023). Massive chert bed thicknesses vary from 10 to 30 cm in outcrop. They are often interbedded with 0.5 to 4 cm thick magnetite bands, and in some places associated with sulfidic shale layers (Figure 2.8). White to grey, straight to slightly wavy chert bands of 1 to 5 cm thickness also alternate with magnetite in outcrop and core samples (Figure 2.7). Grunerite is sometimes present along the contacts between magnetite and chert. A fractured appearance is apparent in some cored drill holes.

2.4 Siliciclastic rocks in the Red Lake carbonate platform

Siliciclastic sedimentary rocks such as conglomerate, sandstone, siltstone, and black shale-sulfidic shale (technically slate) are preserved in the RLCP. These coarse-grained clastic rocks are well-preserved in outcrops while the fine-grained clastic rocks are uncommon in outcrops. However, all these rocks are well-captured in many of the cored drill holes.

2.4.1 Conglomerate and sandstone

Fine to coarse-grained massive sandstone beds up to 35 m thick are preserved in the Red Lake Stratigraphy. No primary depositional features are preserved in this rock. Conglomerate beds of 0.2 to 1.2 m thick are present in PB12-32, PB12-33, and EBL10-28 drill holes.

Polymictic, subrounded to flattened quartz clasts and yellowish-brown silt clasts of 0.5 to 2 cm size are present in the conglomerate beds.

2.4.2 Siltstone

Siltstone beds of variable thickness are common in Red Lake successions. Siltstones are massive and grey-colored, and no primary depositional features are apparent. They occur in outcrops and in most of the cored drill holes.

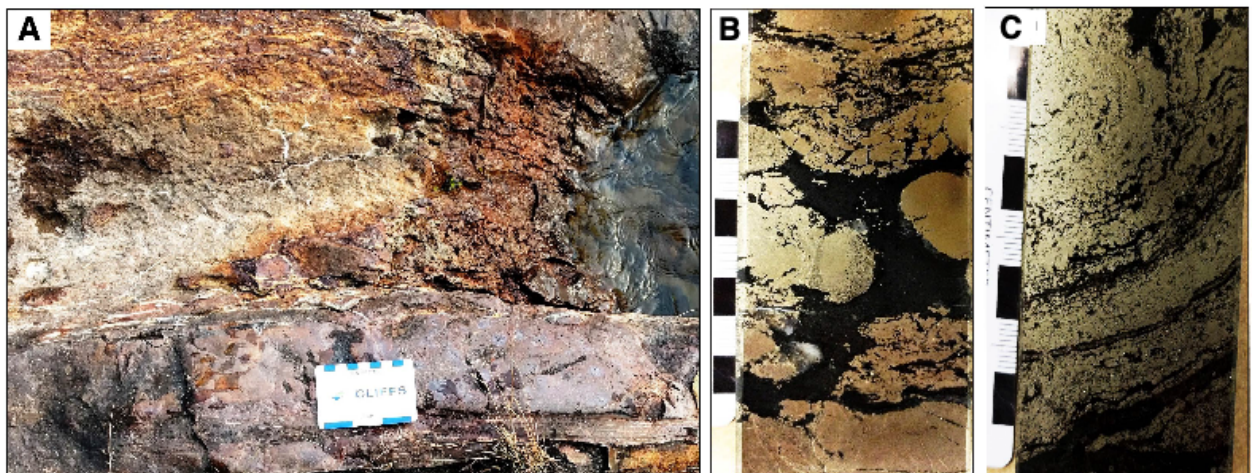


Figure 2.8: (A) Sulfidic shale in association with massive chert and a thin magnetite layer in outcrop, (B) polished core sample showing pyrite nodules scattered in a black shale matrix; (D) mm-scale crenulated pyrite lamination embedded in black shale.

2.4.3 Black shale

Organic carbon-rich (TOC up to 5 %) metamorphosed carbonaceous black shale (technically slate) are preserved in the Red Lake successions (Afroz et al., 2023). Black shale occurrences are mostly massive, with no preserved sedimentary structure inside the layers. They are rare in outcrop due to weathering but are well-preserved in the numerous cored drill holes, where their thicknesses vary from a few meters to 40 m. They are mainly composed of quartz, feldspar, and muscovite, but are also sometimes pyrite rich. Black shales are mostly associated with sulfidic shale and siltstone, but in some places, they are underlain and underlain

by dolomitic carbonate. These black shales are clearly metamorphic product of black shale which accumulated with varying amounts of organic matter when sedimentation of chemical or other clastic sediments was absent.

2.4.4 Sulfidic shale

Sulfide slate, the metamorphic product of sulfidic black shale, is composed of either pyrite or pyrrhotite or both and is associated with black shale (Figure 2.8). They are usually highly weathered in outcrops but are better preserved in drill hole cores. Sub-rounded to rounded pyrite nodules of > 1 cm in diameter show fractured and/or coalescent appearance in cored drill hole samples. Generally, mm to cm-scale pyrite layers are interlayered with black shale or disseminated as cubes. In some places, crenulated, mm-scale, coalesced pyrite laminations alternate with black shale. The thickness of sulfidic shale ranges from 5 to 25 m and is interlayered with oxide iron formation and overlain and underlain by dolomitic carbonate.

2.5 Reference

- Afroz, M., Fralick, P.W., Lalonde, S. V, 2023. Sedimentology and geochemistry of basinal lithofacies in the Mesoarchean (2.93 Ga) Red Lake carbonate platform, northwest Ontario, Canada. *Precambrian Res.* 388, 106996.
<https://doi.org/https://doi.org/10.1016/j.precamres.2023.106996>
- Card, K.D., 1990. A review of the Superior Province of the Canadian Shield, a product of Archean accretion. *Precambrian Res.* 48, 99–156.
[https://doi.org/https://doi.org/10.1016/0301-9268\(90\)90059-Y](https://doi.org/https://doi.org/10.1016/0301-9268(90)90059-Y)
- Card, K.D., Ciesielski, A., 1986. Subdivisions of the Superior Province of the Canadian Shield. *Geosci. Canada* 13, 5–13.
- Corfu, F., Andrews, A.J., 1987. Geochronological constraints on the timing of magmatism, deformation, and gold mineralization in the Red Lake greenstone belt, northwestern Ontario. *Can. J. Earth Sci.* 24, 1302–1320.
- Corfu, F., Davis, D.W., Stone, D., Moore, M.L., 1998. Chronostratigraphic constraints on the genesis of Archean greenstone belts, northwestern Superior Province, Ontario, Canada. *Precambrian Res.* 92, 277–295.
- Corfu, F., Wallace, H., 1986. U–Pb zircon ages for magmatism in the Red Lake greenstone belt, northwestern Ontario. *Can. J. Earth Sci.* 23, 27–42. <https://doi.org/10.1139/e86-004>
- Dubé, B., Williamson, K., McNicoll, V., Malo, M., Skulski, T., Twomey, T., Sanborn-Barrie, M., 2004. Timing of gold mineralization at Red Lake, northwestern Ontario, Canada: New constraints from U-Pb geochronology at the Goldcorp high-grade zone, Red Lake mine, and the Madsen mine. *Econ. Geol.* 99, 1611–1641.

Chapter 2: Geological Setting

- Easton, R.M., 2000. Metamorphism of the Canadian Shield, Ontario, Canada. I. The Superior Province. *Can. Mineral.* 38, 287–317.
- Hofmann, H.J., Thurston, P.C., Wallace, H., 1985. Archean stromatolites from Uchi greenstone belt, northwestern Ontario, in: *Evolution of Archean Supracrustal Sequences*. Geol. Assoc. Can. Spec. Pap., pp. 125–132.
- Hollings, P., Wyman, D., Kerrich, R., 1999. Komatiite–basalt–rhyolite volcanic associations in Northern Superior Province greenstone belts: significance of plume-arc interaction in the generation of the proto continental Superior Province. *Lithos* 46, 137–161.
[https://doi.org/10.1016/S0024-4937\(98\)00058-9](https://doi.org/10.1016/S0024-4937(98)00058-9)
- Hollings, P.N., 1999. Geochemistry in the Uchi subprovince, northern Superior Province: an evaluation of the geodynamic evolution of the northern margin of the Superior Province ocean basin.
- McIntyre, T., Fralick, P., 2017. Sedimentology and Geochemistry of the 2930 Ma Red Lake-Wallace Lake Carbonate Platform, Western Superior Province, Canada. *Depos. Rec.* 3, 258–287. <https://doi.org/10.1002/dep2.36>
- Patry, L. A., Bonnard, P., Boyet, M., Afroz, M., Wilmeth, D. T., Ramsay, B., Nonnotte, P., Homann, M., Sansjofre, P., Fralick, P. W., & Lalonde, S. V. Archean origins of oxygenic photosynthesis confirmed by La-Ce geochronology. *Nature*, in review (Submission 2023-04-05860)
- Pirie, J., 1981. Regional setting of gold deposits in the Red Lake area, northwestern Ontario; in *Genesis of Archean volcanic-hosted gold deposits*; Ontario Geological Survey, Miscellaneous Paper 97, 71–93.

Chapter 2: Geological Setting

- Sanborn-Barrie, M., Skulski, T., Parker, J., Dubé, B., 2000. Integrated regional analysis of the Red Lake greenstone belt and its mineral deposits , western Superior Province , Ontario. Geol. Surv. Canada Current Re, 14.
- Sanborn-Barrie, M., Skulski, T., Parker, J.R., 2001. Three hundred million years of tectonic history recorded by the Red Lake greenstone belt, Ontario. Geol. Surv. Canada Current Re, 14. <https://doi.org/10.4095/212109>
- Stott, G.M., Corfu, F., Thurston, P.C., Williams, H.R., Sutcliffe, R.H., 1991. Uchi subprovince. Geol. Ontario. Ed. by PC Thurston, HR Williams, RH Sutcliffe, GM Stott. Ontario Geol. Surv. Spec. 4, 145–238.
- Thompson, P.H., 2003. Toward a new metamorphic framework for gold exploration in the Red Lake greenstone belt. Ontario Geological Survey.
- Thurston, P.C., Breaks, F.W., 1978. Metamorphic and tectonic evolution of the Uchi-English River Subprovince, in: *Metamorphism in the Canadian Shield*. pp. 49–62.
- Thurston, P.C., Osmani, I.A., Stone, D., Williams, H.R., Sutcliffe, R.H., Stott, G.M., 1991. Northwestern Superior Province: review and terrane analysis. Geol. Ontario. Ed. by PC Thurston, HR Williams, RH Sutcliffe, GM Stott. Ontario Geol. Surv. Spec. 4, 81–144.
- Tomlinson, K.Y., Stevenson, R.K., Hughes, D.J., Hall, R.P., Thurston, P.C., Henry, P., 1998. The Red Lake greenstone belt, Superior Province: evidence of plume-related magmatism at 3 Ga and evidence of an older enriched source. *Precambrian Res.* 89, 59–76.

Chapter 3 Methodology

3.1 Fieldwork

Fieldwork in the Red Lake area was conducted for several weeks in three separate field seasons during the summers of 2017, 2019, and 2021. Outcrop sections along the shorelines of the Pancake Bay, Bridget Lake, Trout Bay, Sadler Bay, Hall Bay, and Hahn Lake areas were logged and layer-by-layer stratigraphic measurements of various lithofacies with any discernable primary sedimentary structures were documented. Outcrop samples were carefully collected from different lithofacies to avoid neomorphosed zones and zones of alteration. In addition, two < 4 m drill cores (NQ-sized) were drilled using a Shaw Backpack drill in the field season of 2017 in the Golden Arm area (17-GA1 and 17-GA2). Collected outcrop and short drill core samples were utilized for petrographic and geochemical analysis, slabbing, polishing, and for μ XRF scanning.

3.2 Core logging and location of the cored drill holes

Several exploration drill holes were drilled by Goldcorp Inc. and Halo Resources Ltd. between 2010 and 2012 in the Red Lake area. Nine cored drill holes were donated by Goldcorp Inc. for this study and approximately 3000 m of PQ-sized core were logged in detail in the summer of 2017. Detailed section-by-section logging was performed to establish the stratigraphy and identify diverse lithofacies captured in these cored drill holes. I examined the deep-water facies during my Masters work, which resulted in the publication of an MSc thesis (Afroz, 2019) as well as an article in *Precambrian Research* (Afroz et al., 2023). For this doctoral thesis, sampling was extended to cover the entire stratigraphy of the Ball assemblage as captured in the Goldcorp Inc. exploration holes. Samples were usually taken at 1 to 2 m intervals from different lithofacies for petrographic and geochemical analysis as well as for XRF scanning.

Three drill holes are located to the east of Bridget Lake (EBL10-27, EBL10-28, and EBL10-29), one (NGI10-31) is directly across from Galena Island, four of the drill holes are

in the Pancake Bay area (PB12-32, PB12-22, PB12-34, and PB12-35), and one (BL12-37) is in the Bridget Lake area (see Figure 2.2). A summary of the location, orientation, and depths of the nine available cored drill holes is provided in Table 3.1.

Table 3.1 Summary of the studied Red Lake drill hole locations, orientations, and depths

Hole	Easting	Northing	Azimuth	Dip	Drilling depth (m)	True vertical depth (m)
PB12-32	412950	5654540	210°	42°	301	272
PB12-33	413225	5654560	216°	43°	250	138
PB12-34	413128	5654391	210°	44°	250	123
PB12-35	412845	5654352	214°	40°	286	236
BL12-37	414405	5653996	120°	45°	330	206
EBL10-27	415838	5653986	216°	48°	396	174
EBL10-28	415727	5653936	230°	48°	453	204
EBL10-29	415473	5653970	215°	47°	180	61
NGI10-31	416319	5653970	180°	51°	372	142

3.3 Sample preparation

Samples from different lithofacies such as carbonates, oxide iron formations, chert, black shale, sulfidic black shale, siltstone, and sandstone were taken from five cored drill holes (PB12-35, PB12-32, PB12-33, EBL10-28, and NGI10-31), selected to cover the entire 490 m of Ball assemblage stratigraphy captured by the cores, and representing approximately 800 m of total stratigraphy sampled, with significant sampling overlap between some cores. Geochemical analyses included whole-rock major, trace, and REE analysis, partial digestion of carbonate samples, stable carbon-oxygen isotope analysis, and in-situ multiple sulfur isotopes analysis. Drill core and outcrop samples were cut and outer surfaces were trimmed with a water-cooled diamond rock saw to obtain fresh samples without weathering surfaces. In addition, any rock saw traces or surfaces in contact with the drill bit were removed with coarse sandpaper, and samples were rinsed with distilled water and air-dried. The dried samples were coarsely crushed using a pure tungsten carbide hammer-operated piston and cylinder, and then

powdered in an agate ring mill to <200 mesh. Samples were stored in standard air-tight plastic vials. Samples that are used for the different analyses are listed in Table 3.2.

Whole-rock major, minor, and trace element analyses were executed using inductively coupled plasma atomic emission spectroscopy (ICP-AES) and high-resolution inductively coupled plasma mass spectrometry (HR-ICP-MS) at the Pôle Spectrométrie Océan (PSO) facilities at the European Institute of Marine Studies (IUEM), France. Carbonate carbon and oxygen stable isotope analyses were performed at the PSO's IRMS stable isotope laboratory, while SIMS analyses were performed at the SwissSIMS facility at the University of Lausanne.

Table 3.2 Summary of sample types and number of analyses made by ICP-AES, HR-ICP-MS (whole-rock and carbonate leach), IRMS, and SIMS analyses.

Sample type	Number of samples analyzed for			
	Whole-rock major, trace, and REE analysis (ICP-AES and HR-ICP-MS)	Carbonate leach trace and REE analysis (HR-ICP-MS)	Carbonate carbon and oxygen stable isotope analysis by IRMS	In-situ multiple sulfur isotope analysis by SIMS
Dolostone	130	130	122	
Limestone	47	46	65	
Oxide iron formation	30			
Chert	13			
Sulfidic shale	15			9
Black shale	43			
Siltstone	12			
Sandstone	11			

3.4 Whole-rock major element analysis

For major element analyses, approximately 250 mg of powdered samples were weighed into PFA vials. Three ml of concentrated HCl (32%) and HF (40%), together with 1 ml of concentrated HNO₃ (65%), all reagent-grade, were added to dissolve the samples overnight closed on a hot plate at 90°C. The next day, hot plate temperature were raised to 110° and samples were left for one hour, then removed to cool. After cooling, liquid samples were

transferred into 100 ml PFA bottles. To neutralize the excess HF and to retain Si from volatilizing as SiF₄, 93 ml of saturated boric acid (H₃BO₃) solution was added as per Cotton et al. (1995), and samples were stored for up to a week before the analysis. Analysis was performed by ICP-AES using the HORIBA Ultima2 instrument of the PSO at IUEM based on the analytical procedure of Cotton et al. (1995). Three international geo-standards, i.e., ACE, JB2, and WSE, were prepared under identical conditions and used to calibrate the instrument. Precision expressed as relative standard deviation (RSD) for the analytical sessions was $\leq 1\%$ for SiO₂ and $\leq 2\%$ for the major elements.

3.5 Whole-rock trace element and REE analysis

3.5.1 Total digestion

Approximately 70 mg of powdered samples were weighed into PFA vials and digested using 2 ml of PFA-distilled concentrated HNO₃ and 2 ml of trace-metal grade concentrated hydrofluoric acid (HF) in a class 1000 clean laboratory of the PSO. Closed vials were left overnight on hot plates at 80°C to digest and then uncapped to evaporate at the same temperature. Subsequently, 3 ml of HCl and 1 ml of HNO₃ (aqua regia) were added to the samples, and the samples placed on hot plates to evaporate at 80°C. After complete evaporation, 4 ml of 6N HCl was added, and closed vials were left to digest overnight at 80°C. For trace element and REE analyses, 100 μ l was extracted from the digest solution and added to 4.9 ml of 2% HNO₃ that was pre-spiked with 2 ppb Indium in 5 ml tubes for trace and REE analysis at low, medium, and high resolution using the ThermoFisher Scientific ElementXR HR-ICP-MS of the PSO. Instrument calibration was performed using commercial multi-element solutions and the international geo-standards BHVO-2 and IF-G were used included in all runs to verify accuracy. Analytical precision estimated from repeat analyses of a 5 ppb multi-element standard throughout the runs was $\sim 1\%$ RSD for most elements and $\sim 2\%$ RSD for REE.

3.5.2 Leach digestion

A weak leach digestion method was used to isolate trace elements in the carbonate fraction of carbonate samples. This method allows complete digestion of diverse carbonates (including dolomite) while minimizing the digestion of clays, oxides, and crystalline silicates present in carbonate samples, as per Rongemaille et al. (2011). Powdered carbonate samples (~100 mg) were digested using 2 ml of 5% trace-metal grade acetic acid in PFA vials left overnight at room temperature. The next day, dissolved samples were transferred into pre-cleaned (overnight in 10% HCl) 15 ml centrifuge tubes and centrifuged at ~2000G for 5 min to separate the liquid phase from solid residues. 100 µl from the liquid phase was extracted and 4.9 ml of 2% HNO₃ + 2 ppb Indium was added in 5 ml tubes for the REE measurement using the PSO's ThermoFisher Scientific ElementXR HR-ICP-MS operating in low, medium, and high resolution. Calibration was performed using commercial multi-element standards and the international geostandard CAL-S was included in each run.

3.6 XRF core scanning

To obtain continuous records of select major and trace element abundances throughout the diverse lithofacies, drill hole cores were scanned using a high-resolution X-Ray Fluorescence (XRF) core scanner (Avaatech) at IFREMER (Brest, France). The entire lengths of the PB12-35 and PB12-32 drill cores, and approximately 90 m sections of the PB12-33, EBL 10-28, and NGI10-31 drill cores, were scanned. XRF core scanning provides semi-quantitative elemental composition data at cm to mm scales, which were inter-calibrated in this study with whole-rock ICP-AES and -MS data to obtain high-resolution quantitative profiles of elemental composition. Core sections not exceeding 1.5m in total length were covered with x-ray transparent ultralene film and fixed in custom-made PVC supports using putty. Helium was flushed at the interface between the sample and the moving detector head to increase sensitivity and X-ray transmission. A dual-scan approach at different energy levels was

employed: first, a 10 keV scan for the analysis of lighter elements (Al, Si, K, Ti, Ca, Mg, P, S, Cr, Mn, and Fe), followed by a pass at 30 keV to analyze heavier elements (Ni, Sr, Rb, Zn, and Zr). The instrument was programmed for 10 sec acquisitions per step, with variable step sizes adjusted according to lithology, ranging from 2 cm to 10 cm. The XRF data obtained from the different lithofacies were calibrated against the whole-rock major and trace element data obtained from acid digestion using the AvaXelerate program (Weltje and Tjallingii, 2008), which generates quantitative XRF concentration datasets using a log-ratio calibration model. This involves a computer-optimized sub-sampling of available calibration points by the software, with optimal calibration points algorithmically selected from the high-precision whole-rock ICP-AES and HR-ICP-MS datasets.

3.7 μ XRF scanning

A Bruker M4 Tornado μ XRF spectrometer was used to scan small pieces of core and slabbed samples, up to $\sim 15 \times 25$ cm in surface area, to obtain maps of the spatial distribution of elements in the samples. This technique enables the rapid visualization of the spatial distribution of many major and trace elements, depending on natural abundances in the sample and the X-Ray fluorescence responses of the different elements. Spot sizes of 30 μm and dwell times of 4 ms per pixel were employed for high spatial resolution across large samples, generating element maps of up to 2000 x 3000 pixels over a maximum scanning time of about 6 hours. X-ray tube excitation energies of 50 kV and 600 μA were employed for rapid signal acquisition and the chamber was pumped to a vacuum of 20 mbar to enhance the detection of light elements. All data reduction was performed in the Bruker M4 Tornado software package.

3.8 Carbonate carbon and oxygen stable isotope analysis

A total of 187 dolostones and limestone samples were analyzed for their carbon and oxygen stable isotope composition. Powdered carbonate samples (200 to 250 μg) were weighed using a precision microbalance and placed into small glass vials. Inside the Kiel IV carbonate

device, the glass vials were placed in a carousel along with similarly prepared standards. Four drops of 100% phosphoric acid (H_3PO_4) were added and the reaction was performed at 72°C . The released CO_2 and H_2O gases were cryogenically trapped using liquid nitrogen (-192°C) and the residual products were emptied by vacuum pumping at the end of the reaction. The cryogenically trapped gases were warmed to -90°C to release CO_2 in gaseous form and again transferred to liquid nitrogen to be concentrated. To analyze the stable isotope composition of carbon and oxygen, the viscous purified CO_2 then flowed via capillary into a dual-inlet ThermoFisher MAT 253 gas source mass spectrometer at the PSO's IRMS stable isotope laboratory at the European Institute of Marine Studies (IUEM).

The international standards NBS-18, NBS-19, and the internal standard CAMIL-21 were used to calibrate the $\delta^{13}\text{C}$ and $\delta^{18}\text{O}$ isotope compositions. The isotopic ratios, expressed in delta notation (δ), were calculated by the following equation, and results are reported in per mille units (‰) relative to the VPDB standard (Vienna Pee Dee Belemnite), according to:

$$\delta = [(R_s/R_{std}) - 1] \times 1000 \text{ ‰}$$

where $R = {}^{13}\text{C}/{}^{12}\text{C}$ or ${}^{18}\text{O}/{}^{16}\text{O}$; R_s = Measured ratio in the sample, and R_{std} = Ratio of the standard.

3.9 In-situ multiple sulfur isotope analysis

A 10 m sulfidic shale horizon containing abundant pyrite and pyrrhotite in the NG110-31 hole was selected for multiple sulfur isotope analysis. Nine samples placed in five epoxy-mounted 25 mm disks were analyzed by secondary ion mass spectrometry (SIMS) at the SWISSIMS facility at the Institut des Sciences de la Terre, Université de Lausanne. To characterize multiple sulfur isotope compositions of the samples, 150 spot analyses were obtained using the SwissSIMS Cameca IMS1280HR of the SWISSims facility by simultaneous measurements of ${}^{32}\text{S}$, ${}^{33}\text{S}$, ${}^{34}\text{S}$, and ${}^{36}\text{S}$ in multi-collection mode with three Faraday cups. Six pyrite standards (Maine, Balmat, Ruttan, Son, Pyr, and Spain; Muller et al., 2017) and the

pyrrhotite standard Anderson were used to constrain instrumental mass fractionation. The internal precision was $\pm 0.05\text{‰}$ for $\delta^{34}\text{S}$ (2σ) and $\pm 0.03\text{‰}$ for $\delta^{33}\text{S}$ (2σ). The external precision was $\pm 0.40\text{‰}$ (2σ) for $\delta^{34}\text{S}$ and $\pm 0.1\text{‰}$ (2σ) for $\Delta^{33}\text{S}$.

The isotopic compositions $\delta^{34}\text{S}$, $\Delta^{33}\text{S}$, and $\Delta^{36}\text{S}$ were calculated using the following equations:

$$\delta^{34}\text{S} = \left[\left(\frac{{}^{34}\text{S}/{}^{32}\text{S}}{\text{sample}} / \left(\frac{{}^{34}\text{S}/{}^{32}\text{S}}{\text{VCDT}} \right) - 1 \right) * 1000$$

$$\Delta^{33}\text{S} = \delta^{33}\text{S} - \left[\left(1 + \delta^{34}\text{S}/1000 \right)^{0.515} - 1 \right] * 1000$$

$$\Delta^{36}\text{S} = \delta^{36}\text{S} - \left[\left(1 + \delta^{34}\text{S}/1000 \right)^{1.9} - 1 \right] * 1000$$

3.10 Loss on ignition analysis

Loss on ignition of samples was obtained using 600 to 800 mg of powdered samples weighed before and after heating to 550°C to remove organic carbon and 1050°C to volatilize the inorganic carbonate fraction of the samples. This analysis was done using a microbalance and the CARBOLITE GERO (30-3000°C) furnace at the European Institute of Marine Studies (IUEM), France.

3.11 X-ray diffraction (XRD)

X-ray diffraction analyses were performed for mineral identification and to determine the types and proportions of carbonate minerals present in selected samples. Powdered samples were dried at 110°C and analyzed in a Bruker D8 Advance X-ray diffractometer with Bragg-Brentano geometry at the Géosciences Marine Unit, IFREMER (Brest, France). The instrument is equipped with a Cu X-ray tube and a VANTEC-1 position-sensitive detector. Analytical conditions consisted of a scan from 5° to 70° in 0.01° steps with 1 second acquisition times per step. Voltage and amperage were 40 kV and 30 mA, respectively, and a nickel filter was employed. Qualitative analyses of the diffraction patterns were carried out using the identification phase procedure of Bruker's EVA software, and quantitative analyses were performed according to the Rietveld refinement method as implemented by Bruker's TOPAS software.

3.12 Petrographic analysis

Thin sections were made from selected lithofacies samples at the Geo-Ocean Laboratory's thin section laboratory. Thin sections were examined under reflected and transmitted light and digital photographs were taken under plane-polarized light (PPL) and cross-polarized light (XPL) using an Olympus DP-70 petrographic microscope.

3.13 References

- Afroz, M., 2019. Sedimentology and geochemistry of the 2.93 Ga Basinal Facies of the Red Lake carbonate platform. MSc Thesis. Lakehead University, Canada.
- Afroz, M., Fralick, P.W., Lalonde, S. V, 2023. Sedimentology and geochemistry of basinal lithofacies in the Mesoarchean (2.93 Ga) Red Lake carbonate platform, northwest Ontario, Canada. *Precambrian Res.* 388, 106996.
<https://doi.org/https://doi.org/10.1016/j.precamres.2023.106996>
- Cotten, J., Le Dez, A., Bau, M., Caroff, M., Maury, R.C., Dulski, P., Fourcade, S., Bohn, M., Brousse, R., 1995. Origin of anomalous rare-earth element and yttrium enrichments in subaerially exposed basalts: evidence from French Polynesia. *Chem. Geol.* 119, 115–138.
- Muller, É., Philippot, P., Rollion-Bard, C., Cartigny, P., Assayag, N., Marin-Carbonne, J., Mohan, M.R., Sarma, D.S., 2017. Primary sulfur isotope signatures preserved in high-grade Archean barite deposits of the Sargur Group, Dharwar Craton, India. *Precambrian Res.* 295, 38–47.
- Rongemaille, E., Bayon, G., Pierre, C., Bollinger, C., Chu, N.C., Fouquet, Y., Riboulot, V., Voisset, M., 2011. Rare earth elements in cold seep carbonates from the Niger delta. *Chem. Geol.* 286, 196–206.
- Weltje, G.J., Tjallingii, R., 2008. Calibration of XRF core scanners for quantitative geochemical logging of sediment cores: Theory and application. *Earth Planet. Sci. Lett.* 274, 423–438. <https://doi.org/10.1016/J.EPSL.2008.07.054>

Chapter 3: Methodology

Chapter 4

Chemostratigraphy of the Mesoarchean (2.87 Ga) Red Lake carbonate platform, Northwest Ontario, Canada

ABSTRACT

The 2.87 Ga carbonate platform of the Ball Assemblage in the Red Lake Greenstone Belt (Red Lake, Ontario, Canada) preserves the Earth's oldest known large accumulation of carbonates (>200 m) associated with various chemical and siliciclastic sedimentary rocks. Its study presents a unique opportunity to fill important knowledge gaps regarding carbonate platform sedimentation and ocean chemistry on the early Earth. We present here whole rock geochemical analyses including major, trace, and rare earth element (REE) compositions of diverse lithofacies from five cored drill holes that provide a high-resolution chemostratigraphy of this important deposit, spanning shallow water carbonates to offshore fine-grained siliciclastic and chemical sedimentary rocks. The geochemical data of siliciclastic lithologies show moderate degrees of chemical weathering and siliciclastic supply derived from both felsic and mafic rocks. Enrichment in redox-sensitive trace elements (i.e., Mo, V, U, and Cr) is significant in both carbonates and iron formations. The source of these elements is interpreted to be predominantly the weathering of crustal material and marine hydrothermal inputs that were in some cases subject to redox cycling under mildly oxic water column conditions. Post-Archean Australian Shale (PAAS)-normalized REE systematics of the Red Lake carbonate rocks and iron formations exhibit signatures typically attributed to anoxic and hydrothermally influenced Archean ocean conditions, including a general lack of pronounced Ce anomalies and strong positive Eu anomalies, but otherwise show several characteristics of modern seawater, including supra-chondritic Y/Ho ratios, positive La anomalies, positive Gd anomalies, and heavy REE enrichment relative to light REE. While the observed trace metal enrichments have multiple possible interpretations, the occasional presence of oxygen in the depositional environment is strongly implied by the positive Ce anomalies associated with Mn enrichment in several horizons, as well as less abundant samples of deep water limestone showing mild negative Ce anomalies. Positioned at a critical time in the Mesoarchean when

Chapter 4: Chemostratigraphy of the Red Lake Carbonate Platform

thick carbonate platforms make their first appearance in the rock record, this study reveals a sedimentary environment characterized by variable sediment sources with localized significant weathering, fluctuating sea level, and dynamic ocean chemistry, including mild oxygenation recorded in both carbonate and iron formation.

4.1 Introduction

Carbonate platforms are excellent archives of information about the early Earth, providing valuable clues about ancient paleoenvironments, biogeochemical cycling, diagenetic processes, and the chemical and isotopic composition of contemporaneous fluids (Kamber and Webb, 2001; Webb and Kamber, 2000). However, carbonate platforms are largely absent in the sedimentary record before 2.96 Ga and gradually occurred in greater abundance and thickness in the late Mesoarchean and throughout the Neoarchean. For example, the Mesoarchean 2.96 Ga Chobeni Formation of the Pongola Supergroup in South Africa preserves a 50 m thick carbonate succession (Beukes and Lowe, 1989; Siah et al., 2016) while the ca. 2.58-2.52 Ga Neoarchean Campbellrand-Malmani carbonate platform of South Africa reaches up to 2 km of thickness (Beukes, 1987; Kamber and Webb, 2001; Knoll and Beukes, 2009; Sumner, 1996; Sumner and Grotzinger, 1996). The Campbellrand-Malmani carbonate platform is one of the most well-studied Archean carbonate platforms and has provided multi-faceted insight into sedimentary processes, ancient microbial life, biogeochemistry, and water chemistry (Beukes, 1987; Eroglu et al., 2017; Fischer et al., 2009; Kamber and Webb, 2001; Knoll and Beukes, 2009; Sumner, 1996; Sumner and Grotzinger, 2004, 1996). Between 2.96 Ga and 2.58 Ga, several carbonate platforms were preserved in progressively greater thickness in the rock record, including the 2.86 Ga Woman Lake carbonate platform (~90 m-thick) in Ontario, Canada (Hofmann, 1981; Ramsay, 2020; Thurston, 1980; Walter, 1983) and the 2.80 Ga Mosher Carbonate (500 m-thick) of the Steep Rock Group in northwestern Ontario, Canada (Fralick and Riding, 2015; Riding et al., 2014). However, the oldest known Mesoarchean platform is preserved in the Ball Assemblage of the Red Lake Greenstone Belt, northwestern Ontario, Canada (Figure 4.1). While this deposit was originally thought to have been deposited between 2.925 and 2.940 Ga based on TIMS U-Pb ages from zircons isolated from the volcanic units immediately above and below the sedimentary package at Red Lake (Corfu and Wallace,

1986), a new LA-ICP-MS U-Pb age of ca. 2.87 Ga was recently obtained from zircons isolated from a tuffaceous interval interlayered within the itself carbonate (Patry et al., in review). This new data necessitates a downward revision of the age of the Ball Assemblage, the carbonates preserved here nonetheless still represent the oldest known occurrence of a thick (>100 m) carbonate platform on Earth.

The >200 m thick Red Lake carbonate platform is predominantly composed of stromatolitic dolostone with some massive limestone. This thick carbonate platform is capped by volcanic rocks and interlayered with assemblages of chert-iron formation, black shale-sulfidic shale, and siltstone-sandstone spanning an additional thickness of 250 m. The various assemblages of shallow- to deep-water lithofacies have made the Red Lake platform the only known occurrence in the Mesoarchean where juxtaposed shallow and deep water chemical strata are preserved together. Hofmann et al. (1985) first documented the presence of stromatolites and crystal fans (“atikokania”) at the Red Lake carbonate platform. From outcrop studies, McIntyre and Fralick (2017) described stromatolites deposited in the shallow water environment and their geochemistry (major-trace-REE, and C, O, and Sr isotopic compositions) while the lithofacies and geochemistry (major-trace-REE) of deep water environment were studied by (Afroz et al., 2023) from both outcrop and core data. However, geochemical data in stratigraphic context remains limited despite the important place of this unique deposit in the history of carbonate platform sedimentation on Earth.

The aim of this study was to establish a continuous record of geochemical profiles including major elements, redox-sensitive trace elements, and rare earth elements of diverse lithofacies from five cored industry drill holes transecting the carbonate platform (Figure 4.1) to capture temporal and spatial marine chemical dynamics as well as the provenance of siliciclastic materials deposited in the Red Lake basin. Our analyses significantly augment

previously published geochemical datasets (Afroz et al., 2023; McIntyre and Fralick, 2017) and are now placed a stratigraphic correlation framework constructed from nine drill hole cores which recorded repeated transitions from shallow water carbonates to offshore deeper water platform lithofacies that span a remarkable diversity of sedimentary environments. The top-to-bottom chemostratigraphic study of this unique sedimentary package was thus undertaken to provide new insight into coeval ocean chemistry in a variety of Mesoarchean marine environments at the dawn of extensive carbonate sedimentation on Earth.

4.2 Geological setting

The Red Lake Greenstone Belt (RLGB) is located in Superior Province, the largest known Archean craton in the world, representing about 23% of the exposed Archean crust of the Earth (Thurston et al., 1991). The Superior Province is divided into several subprovinces, including the Uchi subprovince which comprises a series of Mesoarchean to Neoarchean (3000-2700 Ma) rocks (Corfu and Wallace, 1986; Fralick and Burton, 2008). The Red Lake carbonate platform occurs within the Ball assemblage of the Uchi subprovince (Sanborn-Barrie et al., 2001, 2000), which has undergone greenschist to lower amphibolite facies (300°-550° C) metamorphism (Corfu and Wallace, 1986; Thurston and Breaks, 1978). Supracrustal rocks of the Uchi subprovince include Mesoarchean mafic tholeiitic-komatiitic-carbonate oceanic platform sequences to Neoarchean basaltic-andesitic-rhyolitic calc-alkalic and tholeiitic volcanic arc sequences and with associated chemical and clastic sedimentary rocks (Card, 1990; Card and Ciesielski, 1986; Corfu and Wallace, 1986; Hofmann et al., 1985; Hollings et al., 1999; Pirie, 1981; Sanborn-Barrie et al., 2001, 2000). The Mesoarchean carbonate platform in the Red Lake area, in addition to dolomitic carbonate with stromatolitic and domal features and deeper water calcitic carbonate, is also comprised of chert, magnetite-rich iron formation, black shale, siltstone, sandstone, and conglomerate (McIntyre and Fralick, 2017). The carbonates are predominantly composed of stromatolitic dolostone, with massive limestone

occurring at the easternmost (Hahn Lake, Golden Arm) and westernmost (Pancake Bay) exposures. Volcanic rocks overlie and underlie the 450 m thick assemblage of sedimentary rocks. The age of the platform is constrained by U-Pb dating of zircons from the enclosing volcanics, specifically an overlying rhyolitic flow and underlying rhyolitic lapilli tuff that is dated to 2940 ± 2 Ma and 2925 ± 3 Ma ago, respectively (Corfu and Wallace, 1986). However, a recent LA-ICP-MS U-Pb ages from zircons isolated from a tuffaceous interval interlayered with the carbonate constrain deposition to ca. 2.87 Ga (Patry et al., in review).

4.2.1 Drill hole locations

Cores were examined from five PQ-sized exploration drill holes completed between 2010 and 2012 by Goldcorp Inc. and Halo Resources in the Red Lake area, with their collar locations shown in Figure 4.1. Furthermore, two NQ-sized short drill cores (<4 m) were drilled in the field in 2017 in the Golden Arm area (17-GA1 and 17-GA2) using a Shaw Backpack drill. Detailed information on all drill holes (coordinates, inclinations, azimuths, dips, drilling depth, and true stratigraphic depth) is provided in Table 3.1 in Chapter 3. All depths are reported as true stratigraphic depth.

4.3 Methodology

Approximately 3000 m of core from nine drill holes was logged in detail. Among the nine drill holes, five drill holes were selected to obtain chemostratigraphic profiles throughout the platform. A total of 520 samples from approximately 800 m of cores from PB12-35, PB12-32, PB12-33, EBL10-2, and NGI10-31 drill holes were taken for geochemical analysis. Generally, samples were taken at 1 to 2 m intervals from different lithofacies including carbonates, oxide facies iron formations, chert, black shale, sulfidic black shale, siltstone, and sandstone. These samples were analyzed for whole rock major, minor, and trace elements using inductively coupled plasma atomic emission spectroscopy (ICP-AES) and high-resolution

Chapter 4: Chemostratigraphy of the Red Lake Carbonate Platform

inductively coupled plasma mass spectrometry (HR-ICP-MS) at the Pôle Spectrométrie Océan (PSO) facilities at the European Institute of Marine Studies (IUEM), France. Drill core samples were cut and surfaces in contact with the drill bit were removed with a water-cooled diamond rock saw, and any rock saw traces were then removed with coarse silicon carbide abrasive paper. Samples were rinsed with distilled water, crushed using a pure tungsten carbide hammer-operated piston and cylinder, and then powdered in an agate ring mill.

For major elements, powdered samples (250 mg) were weighed into PFA vials and 1 ml of reagent-grade concentrated HNO_3 (65%), 3 ml of concentrated HCl (32%), and 3 ml of concentrated HF (40%) were added. Samples were left sealed on hot plates to dissolve at 90°C for a day and then at 110° for an hour. Liquid samples were rapidly transferred into 100 ml PFA bottles and 93 ml of a saturated boric acid solution (H_3BO_3) was added to neutralize the excess HF and retain SiO_2 from volatilizing. Bottled samples were set aside for a week to ensure the complete neutralization of the HF before the analysis. Three international geo-standards, ACE, JB2, and WSE were used to calibrate the data. The relative standard deviation was $\leq 2\%$ for the major elements and $\leq 1\%$ for SiO_2 . Analyses were performed by inductively coupled plasma-atomic emission spectrometry (ICP-AES) using the HORIBA Ultima2 instrument of the PSO at IUEM based on the analytical procedure of Cotten et al. (1995).

All preparations for HR-ICP-MS were performed in class 1000 clean labs of the PSO. Approximately 70 mg of powdered samples were weighed into PFA vials and 2 ml of PFA-distilled concentrated HNO_3 and 2 ml of trace-metal grade concentrated hydrofluoric acid (HF) were added. Vials were left sealed overnight on hot plates at 80°C to digest, followed by evaporation at 80°C . 3 ml of HCl and 1 ml of HNO_3 (aqua regia) were added and the samples were left overnight on hot plates to evaporate at 80°C . After evaporation to dryness, 4 ml of 6N HCl was added, and the samples were left closed overnight with heating at 80°C . Finally, 100 μl was extracted from the liquid phase and added to 4.9 ml of 2% HNO_3 pre-spiked with 2

Chapter 4: Chemostratigraphy of the Red Lake Carbonate Platform

ppm Indium in 5 ml tubes for analysis at low, medium, and high resolution using the ThermoFisher Scientific ElementXR HR-ICP-MS at the PSO. Instrumental drift at each resolution was corrected by normalizing to the average indium value of the session, detection limits were determined by the average values of the 2% HNO₃ rinses that were passed and analyzed between each sample, and concentrations were established using a range of multi-element standards measured at the beginning and end of the sessions. The 5 ppb multi-element standard was further analyzed for every ~8-10 sample to constrain precision, and the international geo-standards BHVO-2 and IF-G were systematically included in the sample series as unknowns, which constrained precision and accuracy to better than 5% (1 relative standard deviation, RSD) for most elements and better than 2% RSD for REE. The geochemical data for whole rock major, trace, and REE is tabulated in Appendix A.1, A.2, and A.3, respectively.

Weak leach digestions were used to isolate trace elements in the carbonate fraction from the carbonate samples. The method we employed has been shown to fully digest diverse carbonates (including dolomite) while minimizing the digestion of clays, oxides, and crystalline silicates present in carbonate samples (Rongemaille et al., 2011). After weighing the powdered samples (~ 100 mg) in PFA vials, 2 ml of 5% trace-metal grade acetic acid was added to the samples and left overnight at room temperature. The next day, the dissolved samples were transferred into 15 ml centrifuge tubes and centrifuged at ~2000G for 5 min to separate the solid and liquid phases. From the liquid phase, 100 µl samples were extracted and diluted into 4.9 ml of 2% HNO₃ + Indium in 5 ml tubes for HR-ICP-MS analysis as described above for Total Digestion analyses. The geochemical data of weak leach digested samples is presented in Appendix A.4 and A.5.

The entire drill core lengths of PB12-35 and PB12-32, an approximately 85 m section of PB12-33, a 90 m section of EBL 10-28, and a 95 m section of NGI10-31 were scanned using

a high-resolution X-ray Fluorescence (XRF) core scanner (Avaatech) at IFREMER (Brest, France) to obtain more continuous records of major and trace element abundances throughout the different lithologies. This provided semi-quantitative elemental compositions that were then calibrated against whole-rock ICP-AES and -MS data. First, fragmented core sections were wrapped with x-ray transparent ultralene film and fixed in custom-made PVC supports using putty. For better x-ray transmission and increased sensitivity, helium was flushed at the interface between the sample and the moving detector head. The instrument was configured for step sizes ranging from 2 cm to 10 cm, with 10-sec acquisitions per step. Two sets of scans with different energy levels were completed: a 10 keV scan was used for the analysis of lighter elements (Al, Si, K, Ti, Ca, Mg, P, S, Cr, Mn, and Fe) while a 30 keV scan was used for heavier elements (Ni, Sr, Rb, Zn, and Zr). Based on a set of pre-selected elements, the raw XRF data were baseline-corrected and all the XRF peaks were fitted iteratively for their areas using WinAxil. The XRF data of the different lithofacies were then calibrated against the major and trace element data obtained from the bulk rock acid digestion using the log-ratio calibration model of the Avaaxelerate program (Weltje and Tjallingii, 2008) to produce quantitative datasets that were directly comparable to the higher precision whole-rock measurements.

4.4 Results

4.4.1 Stratigraphy of the Red Lake carbonate platform

The surface expression of the Red Lake carbonate platform is approximately 14 km wide from east to west. While the stratigraphy of the platform is best constrained by the drill holes (Figure 4.1B), lithofacies examination and validation on outcrops were also performed. The drill holes are located in four different areas on the west end of Red Lake (Figure 4.1A). The carbonate lithofacies were described by McIntyre and Fralick (2017), and the deeper subtidal chemical and siliciclastic sedimentary rocks were described by Afroz et al. (2023).

Chapter 4: Chemostratigraphy of the Red Lake Carbonate Platform

The >200 m thick carbonate package has a predominance of stromatolitic dolostones in every drill hole, corresponding to its abundance in outcrop, whereas subordinate occurrences of limestone are captured only in the PB12-35 and PB12-34 holes and at the easternmost (Hahn Lake, Golden Arm) and westernmost (Pancake Bay) outcrop exposures. The stromatolitic dolostones show biogenic features in both outcrop and drill core and are variably silicified (see McIntyre and Fralick, 2017, for detailed stromatolite descriptions), whereas the limestones show no visible macroscopic biogenic features, are diffusively banded, are highly recrystallized with a massive appearance, and are rarely silicified. Previous studies indicate that the dolostones have a shallow water origin, whereas the limestones have deeper water origins. This is especially evident from the latter's close associations with carbonaceous shale (Afroz et al., 2023; McIntyre and Fralick, 2017). In addition to the dominant dolostone and limestone units, minor beds of carbonate-associated magnetite and slumped carbonate are preserved in outcrops along the shoreline of Hall Bay, which are interpreted as transitional facies between the shallow water carbonate facies and deeper-water oxide facies iron formation and shale (Afroz et al., 2023). Oxide facies iron formation and chert are preserved in both outcrops and drill holes, primarily in the NGI10-31 and EBL10-27 holes, and to a lesser extent in the EBL10-29, BL12-37, and PB12-32 holes. Chert also occurs in the other drill holes without association with magnetite, and massive chert up to 30 cm thick appears in outcrops (Afroz et al., 2023). Sulfidic shale is common in the NGI10-31, EBL10-27, and PB12-32 holes in association with black shale. Except for EBL10-28, EBL10-29, and BL12-37 holes, all drill holes contain black shales which are occasionally pyrite-rich, though due to its fissile nature black shale is uncommon in outcrop. The deeper water assemblages (oxide facies iron formation, chert, sulfidic shale-black shale) overlying and underlying the shallow water stromatolitic dolostones in drill holes suggest that important fluctuations in relative sea level occurred over the depositional history.

The drill hole correlations (Figure 4.1B) reveal the overarching stratigraphy of the Red Lake carbonate platform and a record of diverse and cyclic sedimentation. The sandstones forming the base of the sedimentary succession are transitional upward into stromatolitic dolostones whose deposition is interrupted by a package of fine-grained siliciclastics at approximately 60 m above the highest sandstone. This is overlain by stromatolitic dolostone, which thickens to the west, and then a package dominated by chert and oxide facies iron formation, which thickens to the east. The middle area of the platform consists of interlayered packages of siliciclastics, which are thickest in the west, and stromatolitic dolostone. The upper portion has similar interlayering, but with significant limestone, and stromatolites become far less common.

4.4.2 Chemostratigraphy of redox-sensitive trace and rare earth elements

4.4.2.1 Chemostratigraphy of the PB12-35 drill hole

4.4.2.1.1 Redox-sensitive trace element compositions of PB12-35

Redox-sensitive element (RSE) compositions normalized with chemically immobile elements (i.e., Al, Ti) provide important insights into the enrichment of RSE in different lithofacies. The Al-normalized RSE profiles are displayed in Figure 4.2A where the dashed black line represents the Al-normalized average shale values of Red Lake. Variable enrichment of Cr in the carbonates is observed in this hole, with the lower 80 m and uppermost sections displaying significant enrichments. Limestones have higher Cr enrichments than dolostones. The V enrichment trends in the carbonates are somewhat similar to Cr enrichments, except dolostone systematically shows higher enrichment than limestone. Mo enrichment is more subdued in the lower 80 m of the drill hole compared to Cr, V, and U. However, it is more pronounced in the uppermost portion of the carbonate platform. U enrichment is higher in limestone than dolostone throughout the profile. Where it attains higher values in the lower 80 m, directly

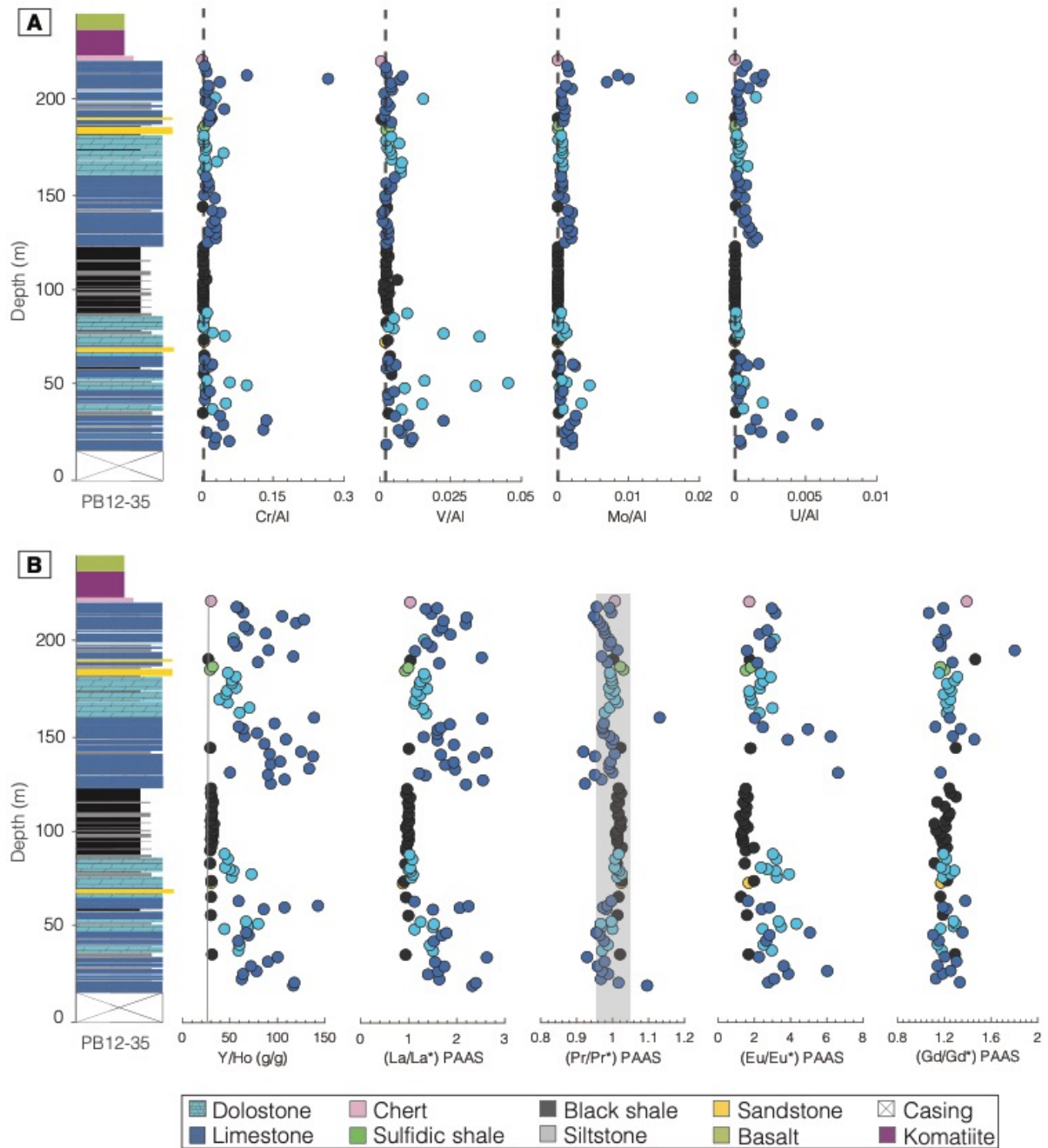


Figure 4.2: (A) Al-normalized redox-sensitive element profiles of the PB12-35 hole. The dashed black line represents the Al-normalized average shale values of Red Lake. Division by Al allows separation of samples from the general trend that contain larger amounts of a redox-sensitive element than expected to be present in its siliciclastic component. All redox-sensitive elements have higher than average concentrations near the bottom and near the top of the hole. (B) PAAS-normalized rare earth element profiles of core from the PB12-35 hole. Limestones have higher Y/Ho and La/La* values than dolostones. Two limestone samples show negative Ce (Pr/Pr*) anomalies while a few limestone samples display mild positive Ce (Pr/Pr*) anomalies. All lithofacies exhibit Eu/Eu* and Gd/Gd* anomalies.

above the thick carbonaceous shale unit, as well as in the uppermost portion of the hole, U shows similar behavior to the other RSE investigated.

4.4.2.1.2 Rare earth element compositions of PB12-35

Post-Archean Australian Shale (PAAS)-normalized REE profiles from the PB12-35 hole are displayed in Figure 4.2B (PAAS source data and the equations used for the various REE proxy indicators La/La^* , Ce/Ce^* , Pr/Pr^* , Eu/Eu^* , Gd/Gd^* , and Y/Ho , are detailed in section 5.4). Y/Ho ratios vary widely throughout this hole. Limestones have higher Y/Ho ratios and more pronounced La anomalies than dolostones. The Y/Ho ratios for limestones and dolostones range from 50 to 142 and 39 to 80, respectively. La anomalies are also elevated in limestone (1.12 to 2.62) compared to dolostone (1.00 to 1.53) and black shale (0.91 to 1.04). Two of the limestone samples exhibit true negative Ce anomalies, at 20 m ($Pr/Pr^*=1.09$) and 158 m ($Pr/Pr^*=1.13$) depth, while one sample at 35 m and a cluster of samples above the thick shale interval display true mild positive Ce anomalies. Limestones contain positive Eu anomalies that vary from 1.59 to 6.62. Dolostones and black shales have smaller positive Eu anomalies ranging from 1.71 to 4.32 and 1.21 to 1.97, respectively. Positive Gd anomalies are present in all lithofacies, ranging from 1.07 to 1.80.

4.4.2.2 Chemostratigraphy of the PB12-32 drill hole

4.4.2.2.1 Redox-sensitive trace element compositions of PB12-32

Figure 4.3A shows the Al-normalized RSEs with a dashed black line representing the Al-normalized average shale values of Red Lake. The Al-normalized redox-sensitive element profile shows a significant Cr enrichment in dolomite and chert associated with the iron formation intervals. Slight enrichment of V is present at stratigraphic intervals similar to those at which Cr enrichment occurs. Uranium enrichment is similar to Mo, occurring near the base of the hole.

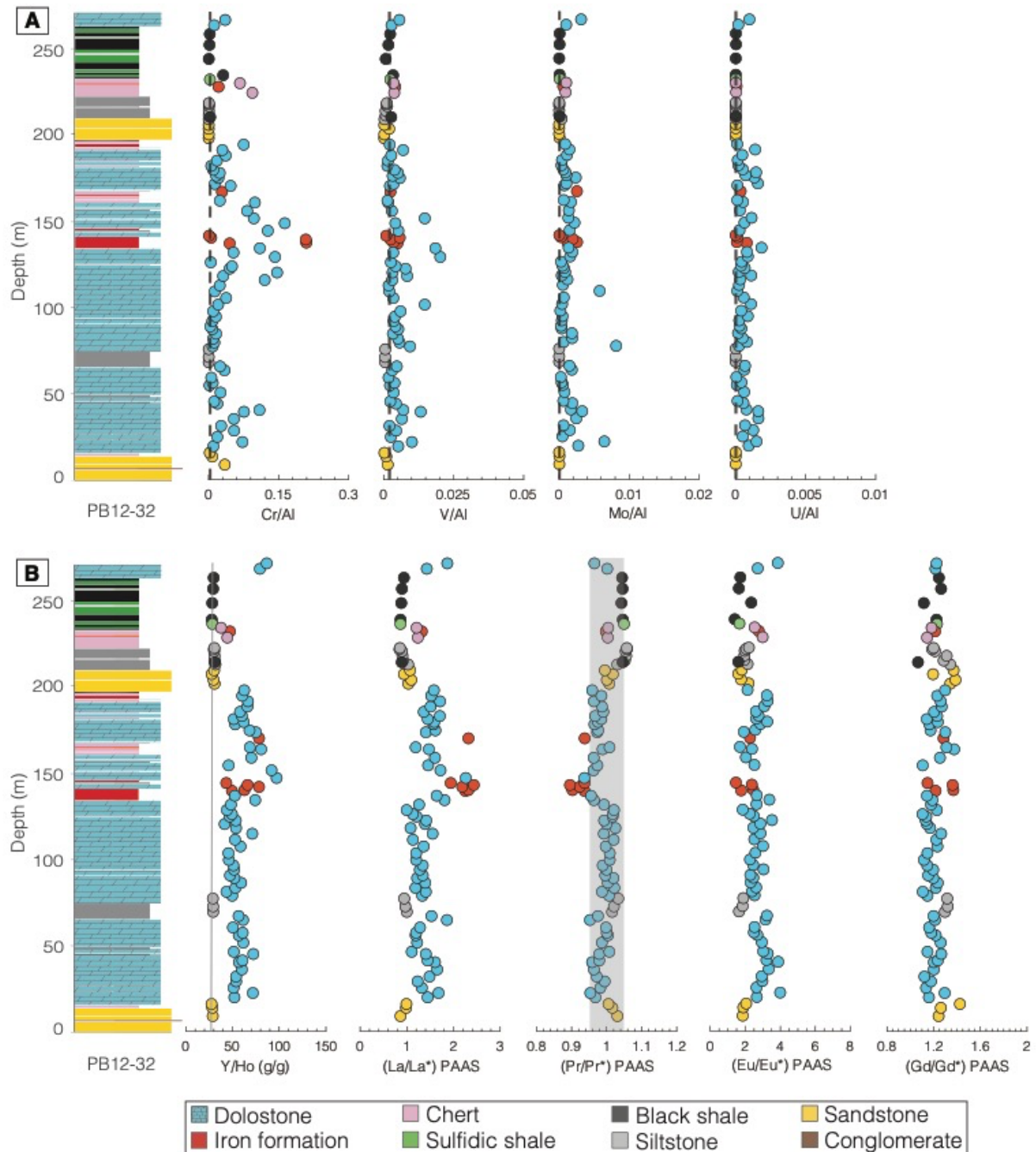


Figure 4.3: (A) Al-normalized redox-sensitive element profiles of the PB12-32 hole. The dashed black line represents the Al-normalized average shale values of Red Lake. Enrichment in Cr and V, and to a lesser degree Mo and U, occur near the base of the carbonate succession above the thick succession of sandstone. More prominent enrichments in Cr and V are associated with the iron formations. (B) PAAS-normalized rare earth element profiles of core from the PB12-32 drill hole. Elevated Y/Ho and La/La* values in addition to positive Ce anomalies are associated with the iron formation horizons. Eu/Eu* and Gd/Gd* anomalies are common for all lithofacies.

4.4.2.2 Rare earth element compositions of PB12-32

Depth profiles of PAAS-normalized REE proxies for the PB12-32 hole are shown in Figure 4.3B. In this hole, dolostone and oxide facies iron formation have higher Y/Ho than other lithofacies and reach their greatest values in association with one another. The ranges of Y/Ho ratios for the lithofacies are dolostone (41 to 97), oxide facies iron formation (43 to 78), chert (37 to 44), black shale (27 to 30), siltstone (28 to 31), and sandstone (27 to 30). Strong positive La anomalies are present in oxide facies iron formation (mean 2.11, maximum 2.43) and associated dolostone (mean 1.43, maximum 2.26), mimicking the elevated Y/Ho anomalies. La anomalies are markedly lower in other lithofacies: chert (1.21 to 1.24), black shale (0.86 to 0.94), siltstone (0.84 to 1.03), and sandstone (0.86 to 1.09). Importantly there is greater scatter in the Y/Ho and La/La* values of the limestones in hole PB12-35 than dolomites in hole PB12-32. Only the oxide facies iron formations display positive Ce anomalies, while the rest of the lithofacies have no appreciable Ce anomalies. All lithofacies have positive Eu anomalies, with higher ones in dolostone and chert, 1.69 to 3.99 and 2.53 to 2.99 respectively, while the other lithofacies have Eu anomalies ranging from oxide iron formation = 1.46 to 2.76, black shale = 1.39 to 2.34, siltstone = 1.64 to 2.20, and sandstone = 1.60 to 2.19. All lithofacies show Gd anomalies ranging between 1.07 and 1.43. Eu/Eu* and Gd/Gd* have somewhat less scatter in the carbonate samples from hole PB12-32 than those from hole PB12-35.

4.4.2.3 Chemostratigraphy of the PB12-33 drill hole

4.4.2.3.1 Redox-sensitive trace element compositions of PB12-33

The Al-normalized RSE profiles are displayed in Figure 4.4A where the dashed black line represents the Al-normalized average shale values of Red Lake. Very little Al-normalized redox-sensitive element data is available in this hole since Al₂O₃ concentrations were below the detection limit. However, a few dolostone samples show notable enrichments in Cr, V, Mo, and U at 85 m and 130 m depths, respectively.

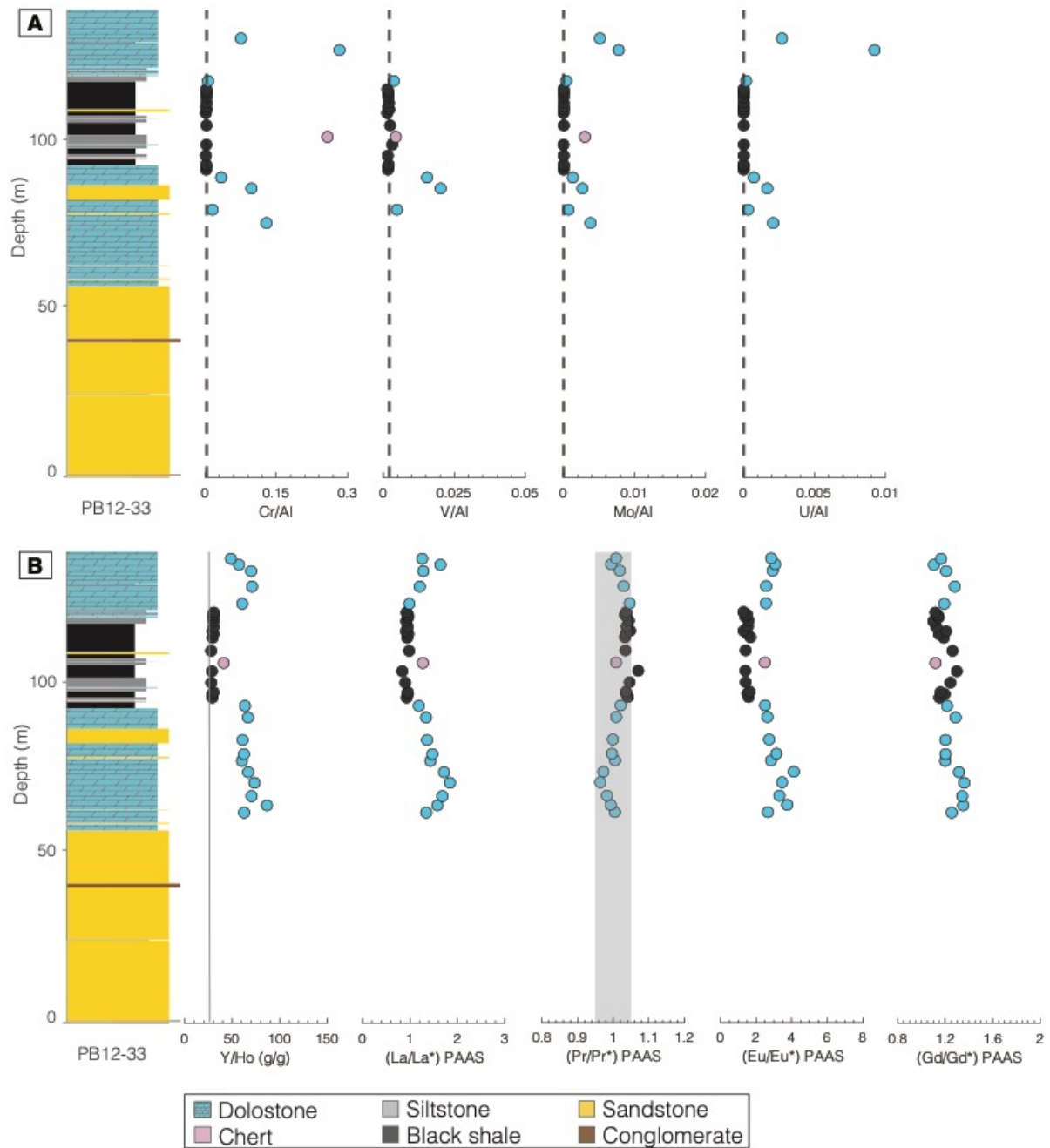


Figure 4.4: (A) Al-normalized redox-sensitive element profiles of the PB12-33 hole. The dashed black line represents the Al-normalized average shale values of Red Lake. Very little Al-normalized redox-sensitive element data is available in this hole because of Al_2O_3 concentrations that were often below the detection limit. A few dolostone samples display enrichments in Cr, V, Mo, and U. (B) PAAS-normalized rare earth element profiles of PB12-33 hole show more elevated Y/Ho ratios and La/La* anomalies in dolostones than the rest of the lithofacies. No Pr/Pr* anomalies are preserved and all lithofacies show important Eu/Eu* and Gd/Gd* anomalies.

4.4.2.3.2 Rare earth element compositions of PB12-33

Figure 4.4B displays the Post-Archean Australian Shale (PAAS)-normalized REE profiles of the PB12-33 hole. The average Y/Ho ratios for dolostones and black shales are 55 and 28, respectively. Anomalies of La and Eu in dolostones vary from 0.98 to 1.84 and 2.51 to 4.12, respectively, while in black shales they vary from 0.84 to 0.98 and 1.30 to 1.68, respectively. No Ce anomalies are preserved in both lithofacies. The average value of Gd anomalies in dolostone is 1.25 while in black shale it is 1.18.

4.4.2.4 Chemostratigraphy of the EBL10-28 drill hole

4.4.2.4.1 Redox-sensitive trace element compositions of EBL10-28

The Al-normalized RSE profile (Figure 4.5A) shows that normalization of the redox-sensitive elements with Al for most of the samples was not possible because of Al_2O_3 concentrations that were generally below the detection limit. It is thus difficult to examine possible enrichments in RSE with such a small dataset.

4.4.2.4.2 Rare earth element compositions of EBL10-28

PAAS-normalized REE profiles for EBL10-28 are displayed in Figure 4.5B. Dolostones show high Y/Ho values, ranging from 43 to 92, while chert and siliciclastic intervals have Y/Ho ratios varying from 33 to 46 and 28 to 34, respectively. Dolostone and chert have pronounced positive La anomalies (1.32 to 2.16) compared to siliciclastics (0.96 to 1.09). Ce anomalies are absent in this hole, and Ce/Ce* ranges from 0.96 to 1.02 and 1.01 to 1.04 for dolostone-chert and clastic lithologies, respectively. Eu anomalies in dolostone, chert, and siliciclastic successions range from 2.43 to 5.53, 1.48 to 2.39, and 1.48 to 2.72, respectively. Siliciclastic samples and dolostones have Gd anomalies ranging from 1.19 to 1.42 and 0.99 to 1.30, respectively. A few chert samples show an absence of Gd anomalies at 130 m depth.

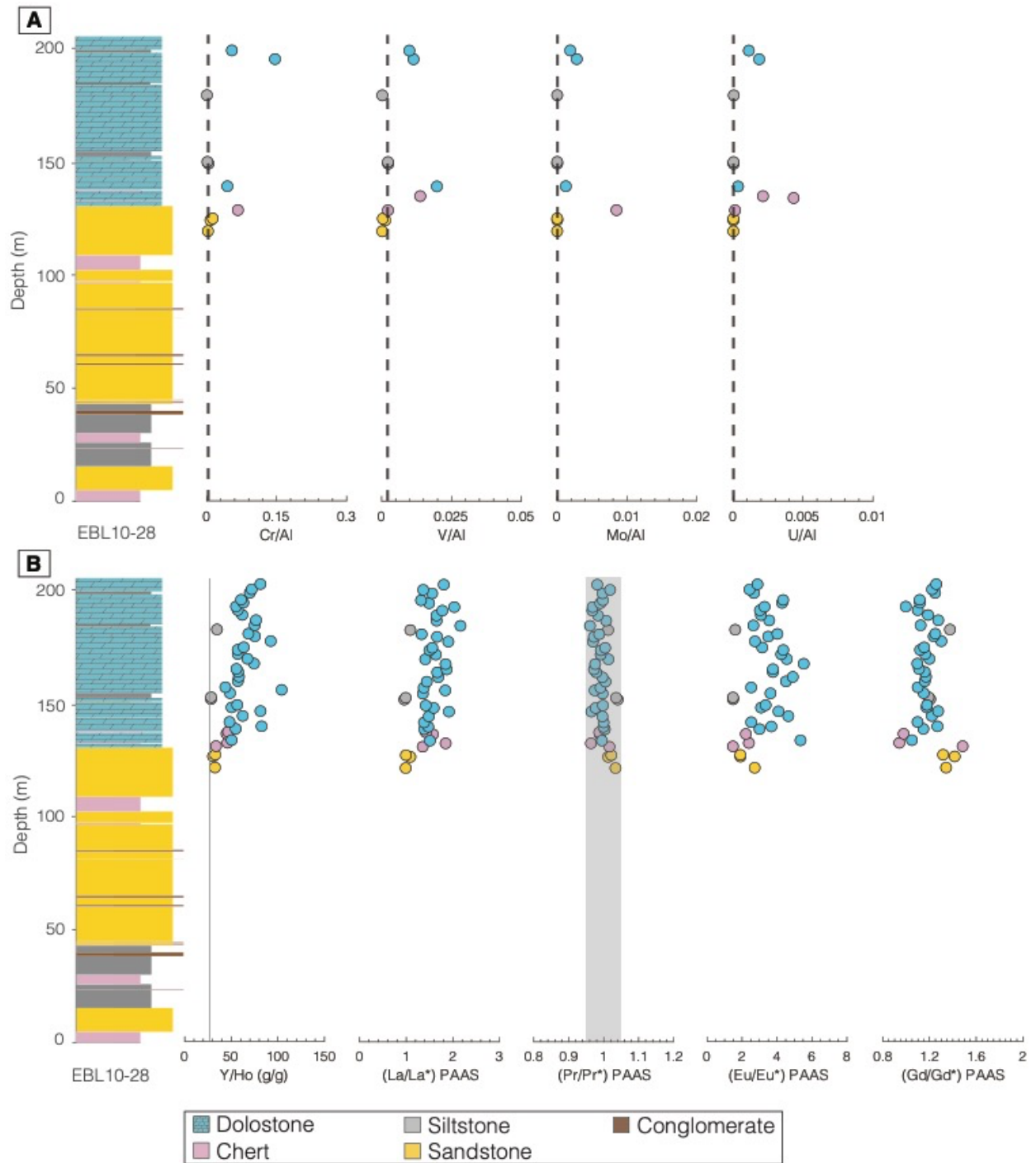


Figure 4.5: (A) Al-normalized redox-sensitive element profiles of the EBL10-28 hole. The dashed black line represents the Al-normalized average shale values of Red Lake. Data are insufficient to assess possible enrichment of RSE because Al_2O_3 concentrations were often below detection. (B) PAAS-normalized rare earth element profiles from the EBL10-28 hole. Dolostone samples exhibit elevated Y/Ho ratios and La/La* anomalies. All lithofacies lack Pr/Pr* anomalies but show important Eu/Eu* and Gd/Gd* anomalies.

4.4.2.5 Chemostratigraphy of the NGI10-31 drill hole

4.4.2.5.1 Redox-sensitive trace element compositions of NGI10-31

The Al-normalized RSE profiles are displayed in Figure 4.6A where the dashed black line represents the Al-normalized average shale values of Red Lake. The bottom part of the dolostone unit shows Cr enrichment, and slight Cr enrichment is also evident near the top of this unit. Iron formation displays enrichment in Cr near the lowest occurrence. There is no noticeable enrichment in V except for one dolostone sample at 13 m depth which shows an anomalously high V content. The bottom 20 m section of the dolostone unit shows a slight increase in Mo content while the uppermost section is below the detection limit for Mo. There is no important U enrichment in this hole.

4.4.2.5.2 Rare earth element compositions of NGI10-31

PAAS-normalized depth profiles of REE proxies are presented in Figure 4.6B. The Y/Ho ratios vary from 40 to 100 in dolostone, and the siliciclastic intervals have Y/Ho ratios between 27 to 37. In oxide iron formation, Y/Ho ratios range from 30 to 43. The La/La* values in dolostone, oxide iron formation, and siliciclastic samples range from 1.11 to 2.08, 1.00 to 1.56, and 0.93 to 1.16, respectively. True negative Ce anomalies are not present in any of the lithofacies but some dolostone samples around 75 m depth show slight positive Ce anomalies. The Ce/Ce* values range from 0.93 to 1.02 in dolostone, 0.99 to 1.01 in oxide iron formation, and 0.98 to 1.04 in siliciclastics. Positive Eu anomalies in dolostone, oxide iron formation, and siliciclastics vary from 2.09 to 5.66, 2.26 to 3.70, and 1.15 to 2.56 respectively. All lithofacies have a similar range in Gd/Gd*, varying from 1.07 to 1.44.

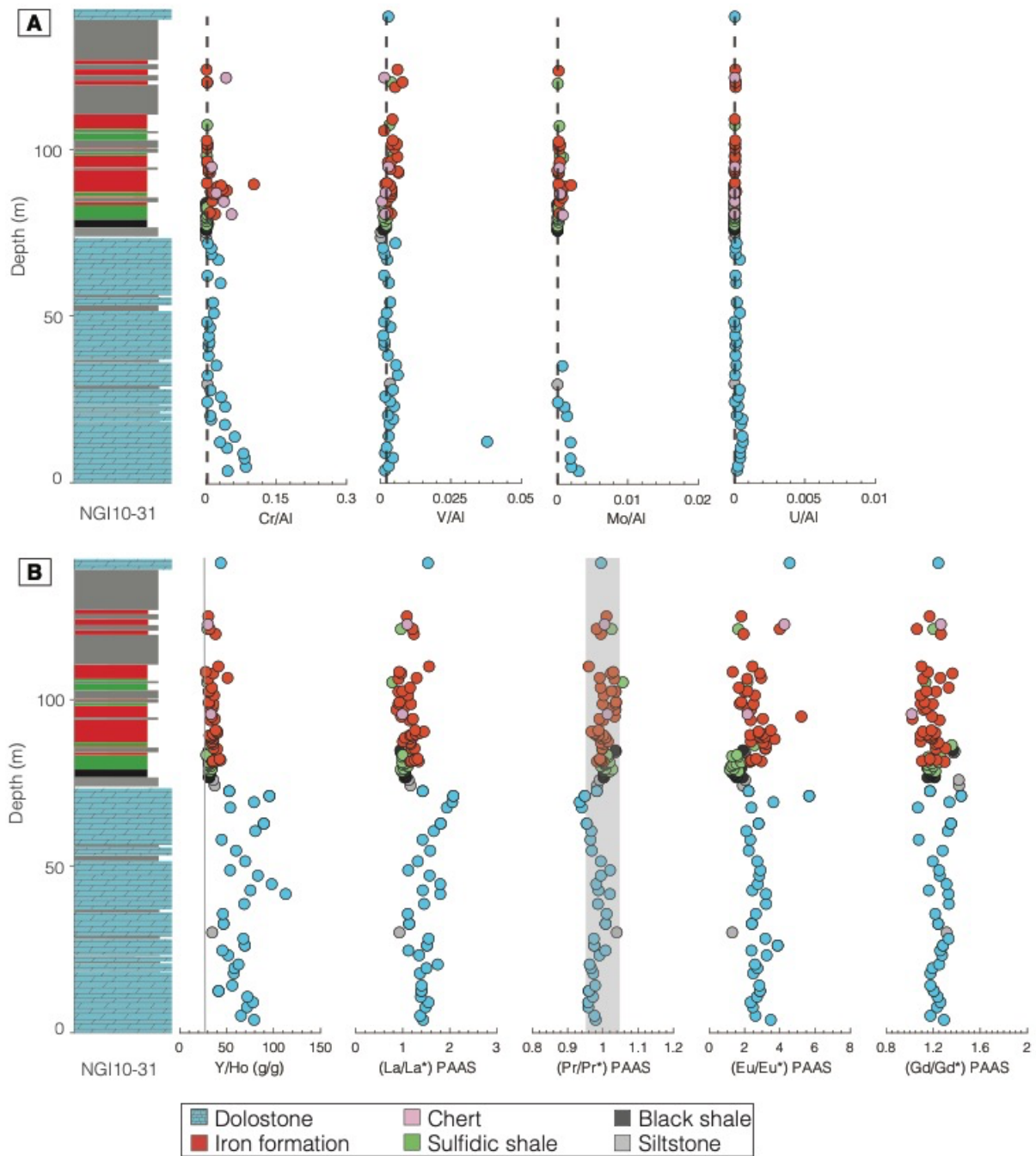


Figure 4.6: (A) Al-normalized redox-sensitive element profiles of the NGI10-31 hole. The dashed black line represents the Al-normalized average shale values of Red Lake. The dolostone samples near the base of the hole and the iron formation samples above the black shale-sulfidic shale show Cr enrichment. There is no noticeable enrichment of V and U in this hole and slight enrichment of Mo is present near the bottom of the hole. (B) PAAS-normalized rare earth element profiles from the NGI10-31 hole displayed higher Y/Ho ratios and La/La* anomalies in dolostones than the other lithofacies. All lithofacies lack Pr/Pr* anomalies but show important Eu/Eu* and Gd/Gd* anomalies.

4.5 Discussion

4.5.1 High-resolution chemostratigraphy of Archean sediments by XRF core scanning

Although it is a common practice for modern sediments, the high-resolution XRF core scanning of the Red Lake cores provides, to our knowledge, the first large (multi-hundred-meter scale) ICP-AES intercalibrated core scan XRF dataset for Archean metasediments. XRF scanning of cores yields a near-comprehensive, high-resolution (cm-scale) picture of elemental composition throughout the stratigraphy, capturing subtle changes in lithofacies and guiding sample selection for subsequent geochemical analysis.

High-resolution XRF core scans revealed cm-scale changes in sedimentology and chemistry that were otherwise not observed in meter-scale whole rock analyses. Core scanning detected numerous cm-scale siliciclastic layers within nominally “continuous” carbonate beds and other chemical sedimentary units, revealing short-term hiatuses in chemical sediment deposition (Supplementary figures 1, 2, and 3 in Appendix A.6). Small, cm-scale intervals rich in manganese and sulfur are also observed in the XRF core scan dataset that are less obvious within the coarser sampling resolution of the whole rock geochemical datasets, revealing several thin intervals of S enrichment in the Red Lake cores outside the conspicuous sulfidic horizons. Thin S-rich layers in cores PB12- 35, PB12-32, and the NGI10-31 may be related to pore water sulfate reduction below the sediment-water interface in a sulfate-limited environment (Afroz et al., 2022), while thin Mn-rich intervals may indicate the temporary presence of oxygen in ocean basins surrounding the carbonate platform. The high-resolution chemostratigraphy distinctly differentiates the composition of carbonates (calcite and dolomite) and reveals several sulfide-rich zones, manganese enrichments, and siliciclastic intervals, suggesting important temporal or spatial variations in water chemistry and redox conditions on the margin of carbonate platform (Supplementary figures 1, 2, and 3 in Appendix A.6). The chemostratigraphic profile also reveals in fine detail the geochemical transition from

one facies to another as well as siliciclastic interference during the precipitation of carbonate and iron formation facies. This dataset unveils several periods of carbonate deposition disrupted by deeper water facies and siliciclastic sedimentation. Sulfur enrichment in the sulfidic black shale-black shale intervals implies that sulfidic conditions might have prevailed in the deeper part of the basin or simply the occurrence of particularly S-rich, high-TOC sediment, while manganese enrichment points to fluctuating basinal redox conditions (Supplementary figures 1 and 2 in Appendix A.6).

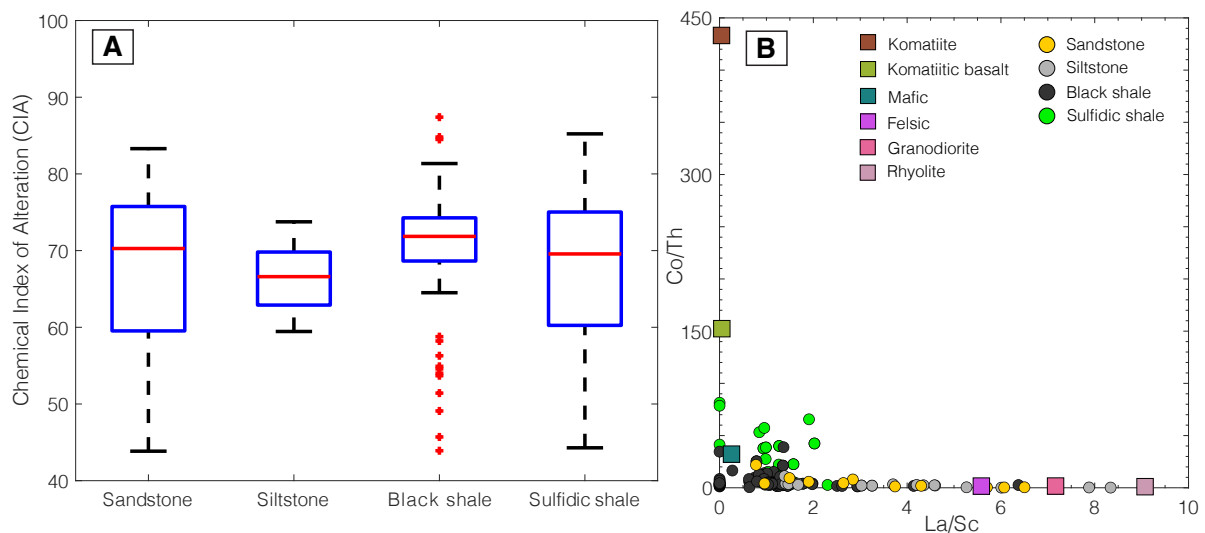


Figure 4.7: (A) Chemical index of alteration (CIA) box and whisker plot of siliciclastic rocks associated with the Red Lake carbonate platform. The bottom and top of each box indicate the 25th and 75th percentiles, respectively, with the 50th percentile (i.e., median) value marked by the central red bar. Error bars are showing the maximum and minimum values of data and the red crosses represent the outliers. (B) Co-Th vs La-Sc plot shows that several sandstone and siltstone samples are plotted along the felsic-dominated axis (high La/Sc) while some of the sandstone, siltstone, and most of the black shale, and sulfidic shale plot along the mafic-dominated axis (high Co/Th).

4.5.2 Weathering and provenance analysis of siliciclastic rocks

The abundant and diverse siliciclastic rocks captured in the Red Lake drill cores provide an opportunity to evaluate different detrital sediment sources feeding the Ball Assemblage and the intensity of the weathering that they experienced. The influence of weathering on

Chapter 4: Chemostratigraphy of the Red Lake Carbonate Platform

sedimentary rocks can be evaluated by the chemical index of alteration (CIA) using the formula: $CIA = [Al_2O_3 / (Al_2O_3 + CaO^* + Na_2O + K_2O)] \times 100$ (Nesbitt and Young, 1982). This formula is used as a basic measure of the weathering intensity in the source terrain and indicates the proportion of weathered materials present in the sample (Sawyer, 1986). However, diagenesis and metamorphism-related changes experienced by such ancient and altered sediments are not considered in this index. The CIA has been broadly used to indicate the intensity of silicate weathering, whereby higher values of the CIA reflect the increasing influence of chemical weathering and a greater degree of leaching of Ca-, Na-, and K-rich minerals from source rocks. Fedo et al. (1995) defined various degrees of chemical weathering based on the CIA: CIA values between 50 and 60 indicate low chemical weathering, values between 60 and 80 suggest moderate chemical weathering, and values > 80 indicate an extreme degree of chemical weathering. Sometimes the chemical index of weathering (CIW) is used instead to quantify the intensity of chemical weathering (Condie, 1993; Condie et al., 1992; Maynard, 1992; Sreenivas and Srinivasan, 1994) but this calculation can be misleading because this approach accounts for the total aluminum without correcting Al in K-feldspar, which leads to very high CIW values even for chemically unweathered K-feldspar-rich rocks (Fedo et al., 1995).

Red Lake siliciclastic rocks show variable CIA values, specifically for sandstone (43-83), siltstone (55-74), black shale (44-87), and sulfidic shale (56-86), suggesting variable degrees of weathering. (Figure 4.7A). The shale and sulfidic shale provide reliable results as the CIA index was developed for fine-grained sediment (Nesbitt and Young, 1982). These originally clay-rich rocks both have average CIA values of 70, placing them firmly in the moderately weathered category. There is no evidence for K metasomatism in these siliciclastic rocks, hence the CIW is not plotted.

A diagram of Co/Th vs La/Sc can discriminate between different potential sediment sources weathering to form siliciclastic rocks (McLennan et al., 1983). The Red Lake siliciclastic samples were plotted along with the values of felsic, mafic, and ultramafic rocks of the Red Lake greenstone belt from Hollings et al. (1999) (Figure 4.7B). It appears that sandstone and siltstone samples were mostly derived from felsic sources while black shale and sulfidic shale were apparently derived from mafic rocks. However, older rocks in the region, which would have served as the source area are mostly mafic and ultramafic extrusives and tonalite intrusives. Under moderate weathering, most of the silt- and sand-sized material would have come from the tonalities and most of the clay would have come from the mafic rocks in the source area. Thus, the different compositions of the clay-rich and clay-poor sediment do not necessitate separate source areas for each. In fact, as the shale, siltstones, and sandstones are interlayered in areas of the core, it is very unlikely that their sediment came from differing areas, but rather reflect sediment sorting under different energy regimes.

4.5.3 Redox proxies in the Mesoarchean ocean

The enrichment of redox-sensitive elements such as chromium (Cr), vanadium (V), molybdenum (Mo), and uranium (U) in fine-grained and chemical sediments serve as powerful proxies for redox conditions at the time of erosion and, to a lesser degree, of deposition. These elements are sensitive to redox conditions and can change their valence state and solubility depending on the quantity of oxygen present (Calvert and Pedersen, 1993; Russell and Morford, 2001; Voegelin et al., 2010; Wille et al., 2013). The enrichment of such redox-sensitive elements preserved in ancient marine sedimentary rocks has been commonly used to constrain the timing of oxygenation on Earth (Anbar et al., 2007; Wille et al., 2007). For this study, redox-sensitive trace elements were normalized to the chemically immobile element Ti and plotted against Al_2O_3 to show variable enrichment of these elements in different lithofacies (Figure 4.8). The black dashed line in Figure 4.8 represents the Ti-normalized average shale

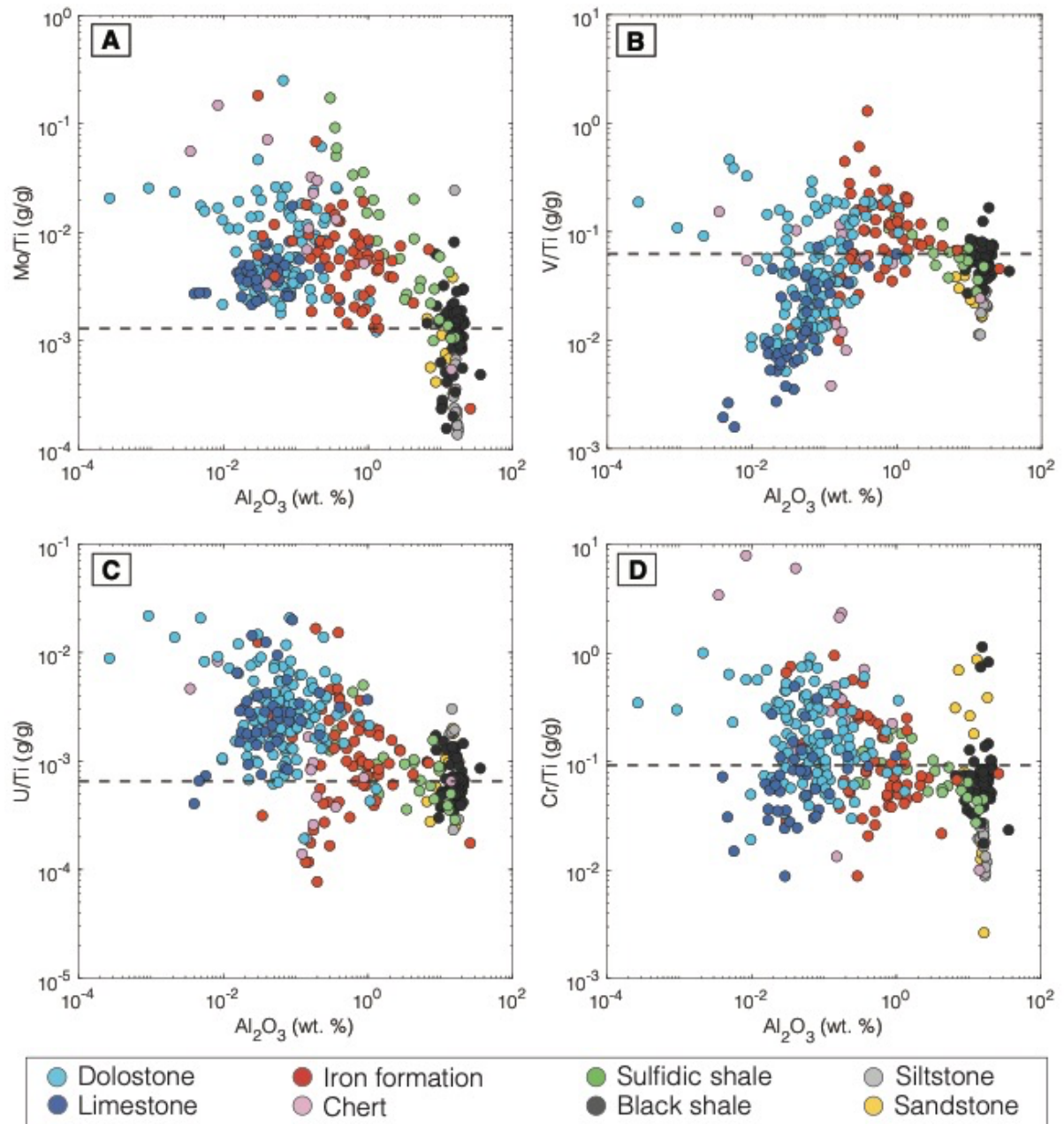


Figure 4.8: Ti-normalized redox-sensitive trace elements plotted against Al_2O_3 show variable enrichment of these elements in different lithofacies. The dashed black line represents the Ti-normalized average shale values of Red Lake. (A) All chemical sedimentary rocks and the sulfidic shale samples are markedly enriched in Mo. (B) Most of the limestone and several dolostone and iron formation samples are depleted in V while a number of iron formation, chert, and dolostone samples show enrichment in V. (C) All chemical sedimentary rocks display variable degrees of U enrichment except some chert and iron formation samples. (D) Most of the dolostone, chert, some iron formation, and a few limestone samples have notable Cr enrichments compared to the average shale values of Red Lake. Most of the limestone and several iron formation samples fall below the average shale values of Red Lake.

value of Red Lake. Most of the chemical sediments show a higher Ti-normalized degree of enrichment of these elements compared to their siliciclastic counterparts, reflecting substantial authigenic enrichments except for several carbonates, iron formation, and chert in the V/Ti diagram; chert and iron formation in the U/Ti diagram, and carbonates and iron formation in the Cr/Ti diagram.

Chemical weathering of crustal rocks and transport via river runoff is the main source of dissolved Mo in the ocean today (McManus et al., 2002; Voegelin et al., 2010). Mo resides in oxic seawater as molybdate (MoO_4^{2-}), but in the presence of dissolved sulfide, it may undergo thiolation to more reactive forms, promoting sedimentary enrichment (Helz et al., 2011, 1996; Vorlicek et al., 2004). Organic matter also acts as an additional agent for facilitating the transfer of Mo into sediments (Piper and Perkins, 2004). Mo is also removed from the water column via adsorption onto iron and manganese oxyhydroxides under oxic water column conditions (Morford and Emerson, 1999). Generally, when abundant in the water column, Mo shows the greatest enrichments in reducing sediments, especially in the presence of free H_2S (Algeo and Maynard, 2004; Crusius et al., 1996). The Red Lake black shale-sulfidic shale samples with high sulfide and TOC are considerably enriched in Mo, suggesting water column scavenging of Mo under reducing and sulfidic conditions. Authigenic Mo can be found either in the organic-rich fraction or in the carbonate fraction, although little is known about Mo incorporation into carbonate minerals (Smrzka et al., 2019). Based on Mo enrichments alone, it is difficult to ascertain whether Mo enrichment was driven by local redox-related processes (e.g., Fe or Mn-oxide shuttling, enhanced scavenging under euxinic conditions), or it simply reflects partial uptake to organic-rich sediments of small but non-negligible dissolved Mo reservoir. In this regard, Mo stable isotope compositions can help identify specific scavenging pathways due to their different associated Mo isotope fractionation processes (e.g., Arnold et al., 2004). Thoby et al. (2019) reported $\delta^{98/95}\text{Mo}$ isotopic compositions that varied

Chapter 4: Chemostratigraphy of the Red Lake Carbonate Platform

from -1.79‰ to 0.78‰ in stromatolitic dolostone samples from Red Lake outcrops, which are isotopically fractionated relative to crustal and riverine sources. It was proposed that oxic (Mn-oxide-related) sinks were operational at that time and drove the isotopic composition of the seawater Mo reservoir towards heavier values, as is the case in modern oxic seawater. The minor degree of enrichment of Mo in the Red Lake samples reported here suggests a small dissolved Mo reservoir fed by incipient continental weathering (under oxic or anoxic conditions) that enabled mild sedimentary enrichments into suitable lithologies.

Weathering of crustal rocks delivers V to the ocean by river runoff. Vanadium exists in various oxidation states which depend on pH and redox conditions (Wanty and Goldhaber, 1992). In oxic waters, V is present as vanadate oxyanions (HVO_4^{2-} and H_2VO_4^-) with the valency state V(V), but under mildly reducing conditions, it is reduced to V(IV) and forms insoluble $\text{VO}(\text{OH})_2$. Under euxinic conditions, V(IV) will be further reduced to V(III) and form solid V_2O_3 oxide or $\text{V}(\text{OH})_3$ hydroxide that leads to V enrichment in marine sedimentary rocks (Breit and Wanty, 1991; Wanty and Goldhaber, 1992). There is little information available regarding V incorporation into carbonates under anoxic conditions. During organic matter remineralization, V can be released into solution, and its sedimentary accumulation under slightly suboxic conditions may hint at some potential for constraining paleo redox conditions (Smrzka et al., 2019; Tribovillard et al., 2006). Sahoo et al. (2012) described V enrichment in euxinic black shales throughout geological time, and V contents correlate well with organic matter (Breit and Wanty, 1991), which is also observed in TOC-rich Red Lake carbonate samples. Several high-TOC dolostone samples show V enrichment relative to low-TOC dolostone samples, indicating a role in scavenging of V by organic matter. Sorption and particle scavenging are the most effective delivery mechanisms of V to marine sediments from oxygenated waters (Brumsack, 1986; Prange and Kremling, 1985; Trefry and Metz, 1989). Vanadium is typically associated with both Fe and Mn oxide precipitates, and V, Fe, and Mn

usually correlate in various marine environments (e.g., Auger et al., 1999; Rudnicki and Elderfield, 1993). The iron formation samples of Red Lake show higher enrichments of V than carbonates, suggesting preferential incorporation of V during iron oxyhydroxide precipitation under suboxic to oxic environmental conditions.

Riverine runoff is the principal source of dissolved U in seawater today as the result of oxidative continental weathering and the transformation of rock-hosted U(IV) to soluble U(VI). Uranium-rich minerals are predominantly derived from felsic igneous rocks, such as granites or pegmatites (Grandstaff, 1976), and accessory minerals, e.g. zircon, apatite, allanite, and monazite, are also important sources of U (Partin et al., 2013). U is mobile in aqueous solution in the oxidized U(VI) form and immobile in the reduced U(IV) form. Uranium (IV) fits easily into the calcite lattice due to its small size, often leading to elevated U contents in carbonates (Sturchio et al., 1998). Iron formations can scavenge seawater U(VI) through sorption to the surface ligands of iron oxyhydroxides. Coprecipitation or adsorption of U(VI) onto ferrihydrite can be reduced during the alteration of the iron oxyhydroxide to goethite, which incorporates reduced U(IV) into its mineral structure (Boland et al., 2011), although reduction of U(VI) requires a particle catalyst (Boland et al., 2011; Duff et al., 2002; Hsi and Langmuir, 1985; Liger et al., 1999; Waite et al., 1994). The Red Lake sample set is remarkable for the slight but non-negligible U enrichments observed in various lithofacies, similar to the case for Mo. Low U concentrations (<6.6 ppm; mean = 0.99 ppm) is typical for iron formations accumulated worldwide during the 3.50 Ga to 2.47 Ga interval (Partin et al., 2013). Red Lake iron formation samples fit within this established range, with U concentrations generally < 2.0 ppm and with an average value of 0.2 ppm. Such low concentrations of U in Red Lake iron formation indicate that the seawater U reservoir was small, most likely due to the limited mobilization of U from the continents to the ocean during weathering in an oxygen-poor environment.

Chapter 4: Chemostratigraphy of the Red Lake Carbonate Platform

Chromium in sediments is largely sourced from terrigenous detrital input. Cr contents in igneous rocks widely vary from 3000 ppm to <10 ppm for ultramafic and felsic rocks, respectively (Shiraki, 1997). Cr exists as Cr(VI) and Cr(III) in oxic aqueous solutions (Brumsack, 1989; Pettine et al., 1998b; Tribovillard et al., 2006), but can be reduced efficiently in aqueous solution by organic matter, dissolved Fe, and other reductants, especially at higher pH (Buerge and Hug, 1997; Pettine et al., 1998a; Schlautman and Han, 2001). Cr(III) is immobile at neutral to alkaline pH but is mobile under these conditions when oxidized to Cr(VI). The Red Lake depositional basin was likely Cr-rich due to the weathering of ultramafic-mafic rocks, Cr(III) from hydrothermal inputs, or a combination of both. During the Archean, iron formations show low Cr concentrations, and iron formations from different Archean localities such as Fig Tree Group (3.25 Ga), Pongola Supergroup (2.96 Ga), and Beardmore-Geraldton Greenstone Belt (2.71 Ga) show minimal enrichment of Cr, suggesting limited continental supply of authigenic Cr (Konhauser et al., 2011). Red Lake iron formation samples show only mild enrichment of Cr, similar to these iron formations, similarly suggesting limited oxidative weathering. Cr does not co-precipitate with iron sulfides due to its very slow reaction with dissolved sulfide (Morse and Luther Iii, 1999). A few Red Lake sulfidic shale samples with notable Cr enrichment may instead reflect enhanced sequestration due to Cr adsorption onto organic matter from localized waters of the platform that have relatively large amounts of Cr(III) from the weathering of the ultramafics. Some sandstone samples are Cr-rich, which is related to their high concentrations of chrome mica (Fuchsite). A recent Cr isotope study of a Mesoarchean (2.95 Ga) paleosol in the Pongola Supergroup in South Africa revealed unfractionated isotopic compositions of Cr, which supports the idea that anoxic continental or seafloor hydrothermal weathering dominated Mesoarchean Cr inputs (Heard et al., 2021) and that oxidative continental weathering of Cr-rich minerals was generally unimportant at that time. Stable isotope analysis of Cr in Red Lake samples might provide

additional information regarding the sources and redox cycling of Cr in the 2.87 Ga Red Lake basin (Frei et al., 2009).

The geochemistry of the redox-sensitive elements in the Red Lake chemical sedimentary rocks is best explained by the hypothesis that they were predominantly sourced from crustal weathering and scavenged from seawater through various processes into the chemical sediments. The question regarding what type of weathering (oxidative vs. anoxic weathering) brought these elements into the ocean remains controversial. Some of the Mo, V, U, and Cr enrichments in the iron formation, chert, and carbonate samples correlate with the magnitude of Eu anomalies in the same samples, indicating that hydrothermal input was an additional source of these elements to seawater (Supplementary Figure 4 in Appendix A.6). The relatively mild enrichments in Mo, V, U, and Cr alone may not distinctly imply oxidative weathering and mobilization of these elements, as at such low abundances, small riverine inputs and mild water column accumulation under highly anoxic conditions, as well as hydrothermal inputs, could also conceivably drive enrichment. The low concentration of redox-sensitive elements in Red Lake samples renders more work necessary to determine the weathering conditions and variables in Mesoarchean paleoenvironments that would have led to the mobilization of these elements into the water column. The mild but significant enrichments of Mo, V, U, and Cr in Red Lake chemical sediments may constitute an interesting case whereby small standing seawater reservoirs of these classic redox indicators might have occurred during the Archean in the absence of effective oxidative cycling, generating mild enrichments in suitable lithologies, without necessarily indicating an important role for the presence of free O₂.

4.5.4 Rare earth element insights into Mesoarchean ocean chemistry

Geochemical investigations of marine sedimentary rocks including banded iron formation, chert, and carbonates provide critical information on seawater chemistry where sediments precipitated directly from marine waters (Bau and Möller, 1993; Derry and Jacobsen, 1990; Kamber et al., 2004). Concentrations and enrichment patterns of REE in chemical precipitates are useful tools for reconstructing depositional environments, such as freshwater vs. marine settings (e.g., Bolhar and Van Kranendonk, 2007), redox conditions (De Baar et al., 1988; Elderfield, 1988; Kato et al., 2002), and importance of hydrothermal inputs (e.g., Allwood et al., 2010; Derry and Jacobsen, 1990). Post-depositional alteration and metamorphism can change the original mineralogy and elemental concentrations, but REE enrichment patterns remain largely unaffected by diagenesis (Webb et al., 2009). Therefore, REE is widely used as proxies in geochemical studies of chemical sedimentary rocks to decipher ancient ocean chemistry due to their clear signatures, immobile nature, and resistance to post-depositional alteration (Kamber et al., 2014; McConchie, 1987). Where applicable, we present data normalized to PAAS using the values provided by Taylor and McLennan (1985).

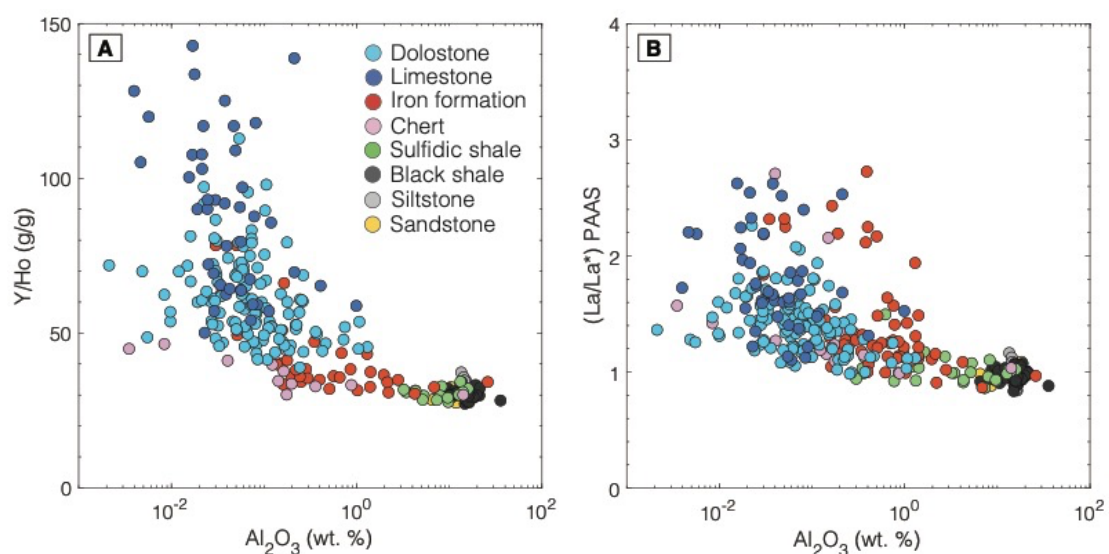


Figure 4.9: (A) Al_2O_3 vs Y/Ho and La/La* plots. (A) The higher the Al concentration, the lower the Y/Ho ratio, and (B) the lower the La/La* value, suggesting crustal contamination.

Chapter 4: Chemostratigraphy of the Red Lake Carbonate Platform

Samples with Y/Ho ratios above crustal values are generally accepted to reflect precipitation from seawater, which is characterized by elevated Y/Ho (up to 105) (Nozaki et al., 1997). A lower Y/Ho ratio (e.g., close to the chondritic mass ratio of 26-28) suggests deposition in a shallower marine environment with a substantial influx of freshwater and/or terrestrial inputs (Johannesson et al., 2006; Webb and Kamber, 2000; Zhao et al., 2009). Yttrium and holmium display different complexation properties in aqueous solutions (Bau and Dulski, 1996, 1995); Ho is scavenged on particulate matter at approximately twice the rate of Y, resulting in a super-chondritic Y/Ho ratio in seawater, expressed as prominent positive Y anomalies in shale normalized REE+Y distribution patterns (Bau and Dulski, 1999, 1996, 1995; Nozaki et al., 1997) of between 44 and 120 in modern and Archean seawater (Kamber and Webb, 2001; Nozaki et al., 1997). Elevated Y/Ho ratios are prevalent throughout the limestones and dolostone of the Red Lake area, confirming their marine origin. However, between limestone and dolostone, the higher Y/Ho ratios of limestone (max: 142; min: 50; mean: 89) relative to dolostone (max: 90; min: 42, mean: 62) would appear related to water depth control. The geochemical data of this study matches previous sedimentological interpretations that limestones precipitated offshore while dolostones accumulated in nearshore environments (McIntyre and Fralick, 2017). Hence, the open ocean seawater Y/Ho composition is best captured by limestone. Iron formation (mean: 60) and chert (mean: 48) also show high Y/Ho ratios but lower than the limestones. Siliciclastics and/or volcanic ash addition can suppress Y/Ho ratios in chemical sediments, and indeed, both carbonate lithologies (limestone and dolostone) are characterized by a lower degree of detrital contamination, as reflected in their lower Ti and Al contents. Iron formation samples commonly have lower ratios of Y/Ho than the carbonate samples due to crustal contamination (Figure 4.9A). Red Lake clastic rocks have near chondritic Y/Ho ratios averaging 30.

Chapter 4: Chemostratigraphy of the Red Lake Carbonate Platform

A positive La_{PAAS} anomaly is an additional REE indicator of marine deposition (e.g., Bau and Dulski, 1996) and is widely present in the Red Lake chemical sedimentary rocks. Positive La_{PAAS} anomalies are the result of the higher stability of La in seawater and its longer residence time in the ocean compared to its light and middle REE neighbors (Alibo and Nozaki, 1999). The Y/Ho and La/La^* vs. Al_2O_3 plot (Figures 4.9A and 4.9B) shows that the Y/Ho ratio and La/La^* anomalies of carbonates vary for any given wt.% of Al_2O_3 , and this variability in the carbonates suggests a primary environmental influence (e.g., different water sources) in addition to detrital contamination. Red Lake samples with the highest La_{PAAS} anomalies correlate with the highest Y/Ho ratios and are interpreted as the signature of open Mesoarchean seawater, while those with less pronounced La_{PAAS} anomalies and Y/Ho ratios would appear to reflect contamination by clastic or volcanoclastic detritus, or alternatively, record deposition during estuarine mixing with open seawater (Kamber et al., 2014; Zhao et al., 2009).

Gd anomalies were calculated using $\text{Gd}/\text{Gd}^*_{\text{PAAS}} = \text{Gd}/([\text{0.33}]\text{Sm} + [\text{0.67}]\text{Tb})$, and almost all Red Lake samples possess positive Gd_{PAAS} anomalies. Positive Gd anomalies are a common feature of modern seawater, stemming from the higher stability of Gd in seawater relative to neighboring REEs during scavenging (e.g., (Alibo and Nozaki, 1999; Bau et al., 1997; De Baar et al., 1985).

A negative Ce anomaly is common in modern oxic seawater (Elderfield and Greaves, 1982; Goldberg et al., 1963). However, anomalous abundances of La can mask the presence of Ce anomalies in seawater or generate false negative Ce anomalies in some calculation schemes. In the presence of oxygen in the weathering environment, the aqueous transport system and/or seawater, Ce^{3+} is oxidized to Ce^{4+} and subsequently removed from the water column by adsorption to mineral surfaces. This results in Ce-depleted seawater, and carbonates precipitated from that seawater will inherit negative Ce anomalies (Webb and Kamber, 2000).

Chapter 4: Chemostratigraphy of the Red Lake Carbonate Platform

One way to distinguish true negative Ce anomalies from those arising solely due to the presence of La anomalies is to calculate Pr/Pr^* as equal to $Pr/(0.5Ce + 0.5Nd)$, whereby the calculation $Ce/Ce^* = Ce/(0.5La + 0.5Pr)$ (Bau and Dulski, 1996) reflects a combination of Ce and La anomalies (Figure 4.10A and 4.10B). The Ce/Ce^* vs. Pr/Pr^* plots for whole rock analyses show that in the industry drill hole samples, only two limestone samples from the PB12-35 hole contain substantial true negative Ce anomalies, while most of the limestone, dolostone, oxide facies iron formation, and chert samples contain no significant negative Ce anomalies. The short backpack drill hole 17-GA1, drilled in the Golden Arm area where prior negative Ce anomalies have been reported (McIntyre and Fralick, 2017), shows a greater number of samples bearing negative Ce anomalies, reaching down to 1.1 Pr/Pr^* (Figure 4.10B; and Supplementary Figure 5 in Appendix A.6). In contrast, several limestones, dolostone, chert, and oxide facies iron formation samples show mild but clearly resolved positive Ce anomalies. Almost all siliciclastics samples show no La and Ce anomalies. Data for partial digestion of carbonate samples is similar to the bulk analysis.

The presence of negative Ce anomalies in the offshore limestones is difficult to explain as oxygen levels in shallow marine settings are not thought to have reached substantial levels by 2.87 Ga. However, several hypotheses can be formulated to explain the Ce anomalies in the offshore limestone facies of the Red Lake carbonate platform. First, most carbonate samples, and all shallow water carbonates, show little to no appreciable Ce anomalies. Negative Ce anomalies are observed only in the offshore limestone facies at Golden Arm and in rare samples of the PB12-35 drill hole. The observation of negative Ce anomalies, surprisingly restricted only to the limestone facies, maybe a common feature of Archean carbonate platforms (Fralick and Riding, 2015; Riding et al., 2014). Residence time of REE under different conditions is likely a crucial factor controlling the development of Ce anomalies. Particulate scavenging leads to rapid Ce(III) removal in shallow marine environments, and in high particulate

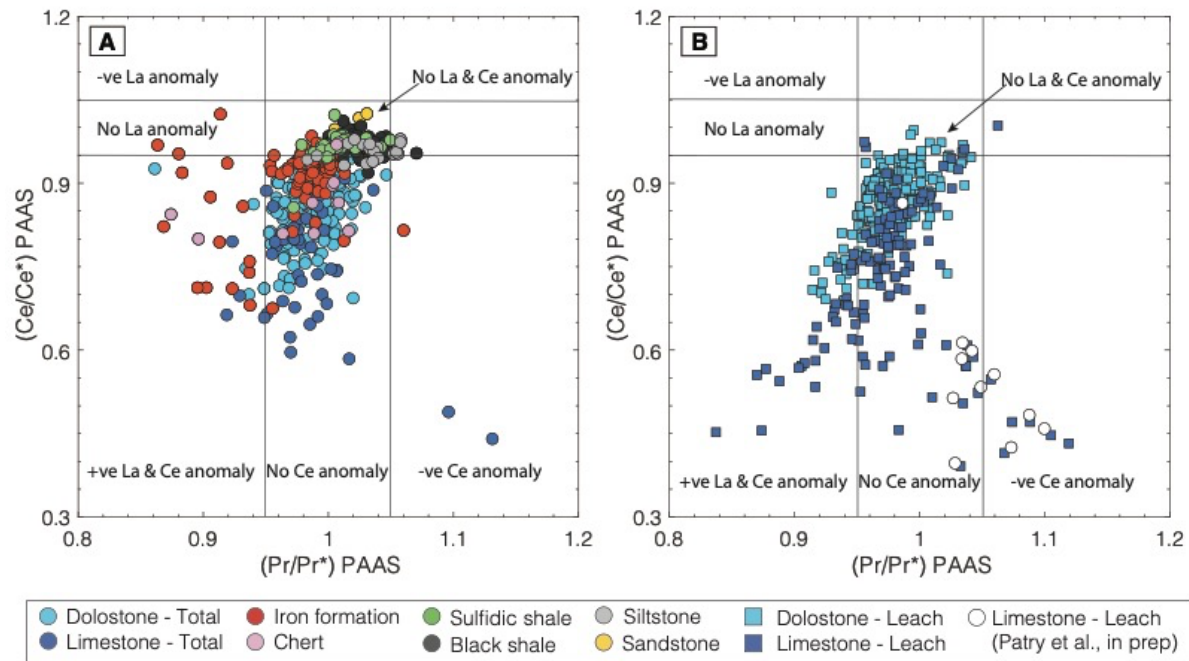


Figure 4.10: (A) PAAS-normalized Ce/Ce^* anomaly (reflecting a combination of true La and Ce anomalies) versus Pr/Pr^* anomaly plot (reflecting only the Ce anomaly; formulas from Bau and Dulski, 1996). Whole rock data from the different lithofacies reveal that only three limestone samples and one oxide iron formation sample possess true negative Ce anomalies, whereas 24 limestones, dolostone, chert, and oxide facies iron formation samples have positive Ce anomalies. Almost all siliciclastics samples show no La or Ce anomalies. (B) Data from weak leach digests of carbonate samples are identical to the bulk rock analysis. Some outcrop samples from the Golden Arm area to the northeast of Red Lake exhibit negative Ce anomalies. A significant number of limestone samples show both positive La and Ce anomalies.

environments such as lagoons and estuaries, the oxidation rate of $Ce(III)$ (and thus generation of $Ce(IV)$) is slow compared to particulate scavenging rates (Moffett, 1990). Under these conditions, appreciable Ce anomalies cannot develop in the water column even if $Ce(III)$ oxidation is occurring. In deeper waters where particulate flocculation is minor, the rate of particulate scavenging of $Ce(III)$ becomes slower than the $Ce(III)$ oxidation rate, permitting the water column expression of Ce oxidation. Such a relationship between water depth and the magnitude of Ce anomalies also appears to be evident in the Steep Rock Lake carbonate platform (Fralick and Riding, 2015). The second possibility that might explain the absence of

negative Ce anomalies in all but the deepest-water carbonates is the reductive dissolution of Ce-sequestering particles, which would result in the remobilization and remixing of water column Ce(III) and Ce(IV) bearing particles under suboxic and anoxic water column conditions (c.f., Planavsky et al., 2009). Early diagenesis of sediments under reducing conditions can preferentially release Ce (Byrne and Sholkovitz, 1996; Haley et al., 2004), and indeed, the lack of significant negative Ce anomalies in suboxic and anoxic waters may thus reflect the near-complete reductive dissolution of settling Mn–Fe-rich particles (Byrne and Sholkovitz, 1996; German et al., 1991) along a water-column depth gradient (Kamber and Webb, 2001), rather than a complete absence of Ce oxidation. The fact that positive Ce anomalies are preserved in several iron formation and carbonate samples support this suggestion and indicates that oxidation of Ce³⁺ and precipitation of Ce⁴⁺ was at times associated with reductive dissolution of iron oxyhydroxide producing positive Ce anomalies in the water column.

The third possibility that might have spatially limited the development of Ce anomalies is that elevated concentrations of reduced Fe and Mn (>50 nM) can buffer the Eh of water to low redox potentials and inhibit the development of negative Ce anomalies in seawater even if free O₂ was being produced (Seto and Akagi, 2008). It could be that Fe and Mn must be first drawn down in the shallow-marine environment to concentrations around a few μM before Ce is oxidized in important quantities in the presence of oxygen. The Fe and Mn concentrations of Red Lake dolostone samples are significantly higher than the limestone samples, which may be linked to the absence of detectable Ce anomalies in the shallow water dolostone facies. All of the above mechanisms likely contributed to the clear pattern of muted Ce anomalies, a predominance of positive Ce anomalies, and the occurrence of significant negative Ce anomalies only in the most distal lithofacies of the carbonate platform.

Chapter 4: Chemostratigraphy of the Red Lake Carbonate Platform

Iron formation samples in the 137 to 141 m interval and at 167 m depth in the PB12-32 hole show positive Ce anomalies, while the overlying and underlying dolostone units display no Ce anomalies. The positioning of this iron formation and the relatively low Fe content (18 %) in this interval compared to the iron formation of the NGI10-31 hole (up to 70 %) suggests precipitation occurred in proximity to shore. If there was a persistent free oxygen supply, then both iron formation and carbonates might be expected to show positive Ce anomalies. Instead, it would appear that oxygen was being brought into the depositional sites where Ce(III) oxidation occurred in the presence of oxygen, and co-precipitated preferentially with iron oxyhydroxide, leading to a positive Ce anomaly. These positive Ce anomalies correlate with increasing Mn content (>1.5 wt. %) as well as enrichment in Cr, suggesting in these horizons a shuttle of oxygen either by storm events or by transient photosynthetic blooming. Similarly, in the PB12-35 hole, limestone samples at 35 m depth and in the 125 to 130 m interval display positive Ce anomalies with accompanying enrichments in Cr, Mo, and U, supporting the occasional presence of oxygen in the depositional environment.

Near-ubiquitous positive Eu_{PAAS} anomalies ($Eu_{PAAS} > 1$) in Archean metasediments imply an overall larger proportion of marine REE+Y input stemming from high-temperature (> 250° C) hydrothermal fluids into Archean seawater (Bau and Dulski, 1996; Derry and Jacobsen, 1990, 1988). The combined REE+Y patterns for different chemical and siliciclastic sedimentary rocks are presented in Figure 4.11. PAAS-normalized Eu anomalies (Eu/Eu^*_{PAAS}) were calculated using $Eu/Eu^*_{PAAS} = Eu / ([0.67]Sm + [0.33]Tb)$ (Bau and Dulski, 1996). Positive Eu anomalies are prevalent in all marine sedimentary rocks from Red Lake, and siliciclastic rocks also exhibit this anomaly throughout the drill hole core (Figure 4.11). The ubiquitous presence of positive Eu anomalies in the sedimentary rocks of Red Lake, higher in the chemical sediments than their siliciclastic counterparts, implies that high-temperature hydrothermally derived positive Eu anomalies were pervasive in the Mesoarchean

Chapter 4: Chemostratigraphy of the Red Lake Carbonate Platform

ocean, and these rocks inherited the seawater composition of the Mesoproterozoic ocean (McIntyre and Fralick, 2017).

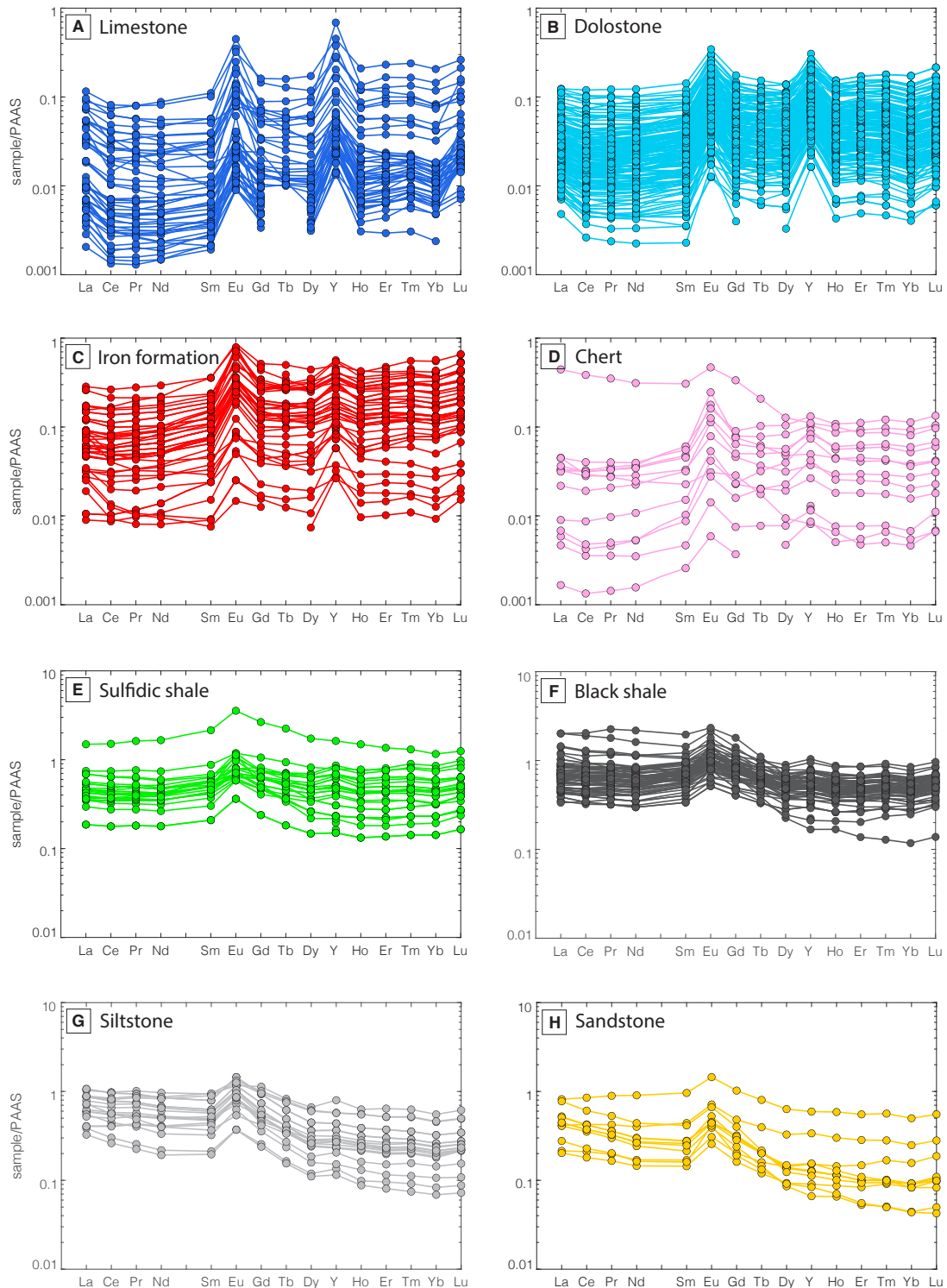


Figure 4.11: PAAS-normalized REE systematics of different chemical sedimentary and siliciclastic rocks of the Red Lake carbonate platform. Positive Eu anomalies are common in marine chemical sedimentary rocks, and the siliciclastic rocks also contain mild Eu anomalies.

Chapter 4: Chemostratigraphy of the Red Lake Carbonate Platform

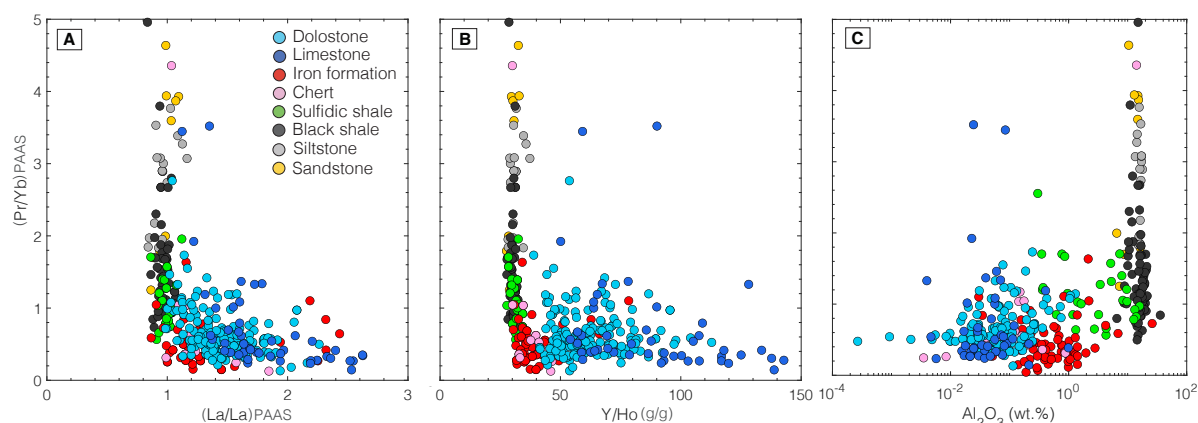


Figure 4.12: PAAS-normalized slope of Pr/Yb plotted against (A) La/La*, (B) Y/Ho, and (C) Al₂O₃. Samples with a slope value of >1 indicate enrichment of LREE while a slope value <1 shows enrichment of HREE.

Hypothetically, relative enrichment of HREE is related to the seawater abundance of CO₃²⁻ and in turn seawater alkalinity, pH, and ultimately, atmospheric pCO₂. In the modern ocean, complexation with ligands, mainly CO₃²⁻, stabilizes HREEs preferentially and retains them in solution, whereas LREEs forming weaker complexes are lost more rapidly through scavenging, which leads to the characteristic positive slope of REEs in seawater. A plot of light to heavy REE (Pr/Yb) slope versus Y/Ho ratio and La anomalies (Figure 4.12) differentiates between the enrichment or depletion of LREEs or HREEs as a function of open seawater influence. Pr/Yb ratios >1 represent samples that are HREE-depleted and/or LREE-enriched, while Pr/Yb ratios <1 indicate the reverse. Archean chemical precipitates derived from seawater are typically HREE enriched, and the same is true for the Red Lake sample suite, which shows obvious HREE-enriched patterns in the oxide iron formation and carbonate samples, suggesting that the ancient ocean had similar LREE and HREE fractionation trends and slope as the modern ocean (Kamber and Webb, 2001).

In brief, the PAAS-normalized REE distribution patterns of the Mesoarchean Red Lake carbonate rocks and iron formation exhibit several attributes similar to modern open seawater, including supra-chondritic Y/Ho ratios, positive La_{PAAS} anomalies, positive Gd_{PAAS}, and HREE

enrichment relative to LREE (Alibo and Nozaki, 1999; Bau et al., 1997; De Baar et al., 1988, 1983; Elderfield, 1988; German and Elderfield, 1989; Kamber et al., 2014) as well as signatures attributed to anoxic and hydrothermally influenced Archean ocean conditions. These include a general lack of pronounced negative C_{EPAAAS} anomalies and strong positive E_{UPAAAS} anomalies. That said, significant anomalies in Ce, both positive and negative, reveal the likely imprint of oxygenic photosynthesis generating free O_2 , at least ephemerally, on this 2.87 Ga carbonate platform.

4.5.5 Red Lake carbonate platform architecture

During the deposition of the >200 m thick Red Lake carbonate platform, the composition of seawater in the basin clearly varied significantly spatially and temporally to produce the various assemblages of chemical sedimentary rocks preserved in this platform. The Red Lake carbonate platform records a protracted period of Mesoarchean platform building punctuated by sea level fluctuations that sometimes lead to platform flooding. Lithofacies assemblages from onshore to offshore depositional settings include (1) Peritidal dolomitic carbonates that dominate the platform top, consisting of abundant *Stratifera* and *Colleniella* stromatolites, coliform crusts, thin layers of crystal fans, and grainstones (McIntyre and Fralick, 2017). (2) Subtidal calcic carbonate zones composed of *Stratifera* and ~ 1m “atikokania” crystal fan mounds and larger crystal fan mounds further offshore (McIntyre and Fralick, 2017). (3) Irregularly developed slope areas comprised of carbonate-magnetite laminae and carbonate slump deposits mixing with carbonaceous mud and iron formation (Afroz et al., 2023). (4) Offshore areas extend from the base of the slope and/or areas adjacent to carbonate where the slope is poorly defined and were dominated by the accumulation of black shale, sulfidic black shale, oxide iron formation, and chert (Afroz et al., 2023).

Chapter 4: Chemostratigraphy of the Red Lake Carbonate Platform

It is likely that transgressive flooding initiated a steady platform environment where carbonate sedimentation in productive shallow waters kept pace with increasing relative sea level, allowing stromatolites to grow in the warm waters of the photic zone. Stromatolite abundance lessens with water depth due to decreasing light penetration in the water column and gave way to crystal fan mounds that developed in carbonate-saturated environments further offshore. Carbonates precipitated in both shallow and deeper waters of the platform generally contain a low amount of siliciclastic material (<1 wt.% Al, <0.5 wt. % Ti), suggesting non-episodic siliciclastic supply was slow relative to carbonate sedimentation. Deposition of massive and channelized sand occurred at times in the shallower areas of the platform and these areas may even have been exposed subaerially during sea level fall. This was ultimately outpaced by carbonate deposition on multiple occasions, either due to repositioning of channels or platform flooding. The non-correlating sandstone horizons and thin (cm to m scale) siltstone layers that punctuated carbonate deposition might be related to shifts in river channels supplying detrital materials, or alternatively storm events that carried sand and silt, with rapid siliciclastic deposition temporarily outpacing carbonate precipitation. A major flooding event is marked by the accumulation of chert-iron formation along with sulfidic shale-black shale assemblages on the eastern side of the platform while the accumulation of chert-iron formation becomes thinner on the central and western side of the platform and there is a general absence of sulfidic shale -black shale assemblages on this side (Figure 4.1). However, the black shale and siltstone successions in the PB12-32 and PB 12-33 holes may not represent a flooding surface, rather they may indicate greater delivery of mud and silt to the carbonate shelf, overwhelming carbonate precipitation. Similarly, the correlated siliciclastic successions between the PB12-32 and BL12-37 holes represent increased clastic supply, and the correlated black shale -siltstone successions between the PB12-35 and PB12-34 holes represent hiatus in carbonate precipitation due to increased delivery of siliciclastics.

Chapter 4: Chemostratigraphy of the Red Lake Carbonate Platform

The distribution of lithofacies on the Red Lake carbonate platform provides important constraints on the nature of the various carbonate depositional environments and the overall architectural organization of the platform. There is no clear evidence of high-energy platform margin conditions; based on the lateral and vertical variations of lithotypes and stromatolites, McIntyre and Fralick (2017) reported an extensive shallow-water platform in a low-energy environment. This overall picture is further supported by the present work. The ensemble of observations suggests that the Red Lake carbonate platform might best be described in a non-rimmed margin framework. This is in contrast to later Archean carbonate platforms; for example, the ca. 2.6 Ga Campbellrand-Malmani carbonate platform which shows evidence of a ramp to rimmed margin architecture (Sumner and Beukes, 2006), the ca. 2.80 Ga Steep Rock carbonate platform contains evidence of an important margin rimmed by giant domes (Fralick and Riding, 2015; Riding et al., 2014), and the ca. 2.86 Ga Woman Lake carbonate platform also provides evidence for an important ramp margin (Ramsay, 2020). The lithofacies associations of the Red Lake carbonate platform, capturing shallow to deeper water depositional environments in both lateral and vertical directions, suggest that carbonate buildup here occurred in a non-rimmed platform setting. Non-rimmed platforms provide substantial shallow water environments where a productive carbonate factory ensures upward growth that matches or temporarily succeeds subsidence. Due to the absence of features forming a barrier reef or rim and the rarity of large domal structures, e.g., the abundant giant domes preserved at Steep Rock Lake (Fralick and Riding, 2015), it is likely that the Red Lake platform was not rimmed by domes, or it had only a minor rim component, as only one clear large domal feature has been identified (at Golden Arm), with possibly another on the north-western margin of Hahn Lake, although poor exposure renders this occurrence ambiguous. For comparison, the Campbellrand-Malmani carbonate platform was initiated with deposition of a mixed siliciclastic-carbonate ramp that steepened upward and gave way to a more shallow setting with

supratidal to intertidal flat deposits (Sumner and Beukes, 2006). This shallow water environment then evolved into a broad lagoon with a clear rimmed margin that separated the lagoonal deposits from deeper water sediments deposited on the open ocean e.g., deep water iron formation (Sumner and Beukes, 2006). The terminal drowning of the Campbellrand-Malmani carbonate platform is indicated by the deposition of banded iron formation across the Kaapvaal Craton (Sumner and Beukes, 2006). Similarly, the Red Lake platform contains deposits of iron formation of variable thickness across the Red Lake platform induced by platform flooding, although carbonate sedimentation continued after the most widely recorded flooding event.

Together, these observations provide important context to the establishment of Earth's first large carbonate platforms. The association of carbonate, other chemical sedimentary rocks, and finer and coarser siliciclastic rock reflect transgression-regression events driven by a combination of absolute sea level change, varying subsidence rate, and/or fluctuating accumulation rate.

4.6 Conclusions

We draw five general conclusions from our chemostratigraphic study of the 2.87 Ga Ball assemblage and associated carbonate platform at Red Lake:

1. The high-resolution chemostratigraphy of five cored drill holes spanning shallow water carbonates to offshore fine-grained siliciclastic and chemical sedimentary rocks and their repetitive transitions indicate dynamic ocean chemistry in a depositional paleoenvironment that experienced important marine transgressions and regressions.
2. The siliciclastic rocks of the Red Lake carbonate platform were mainly derived from felsic to mafic rocks, with the original clay minerals dominantly from the moderate

Chapter 4: Chemostratigraphy of the Red Lake Carbonate Platform

weathering of mafic igneous rocks, whereas the silts and sands were principally sourced from the felsic igneous units in the area.

3. Enrichments in redox-sensitive elements (i.e., Mo, V, U, and Cr) suggest that these elements were present in local seawater, supplied by hydrothermal delivery and possibly by limited oxidative weathering.
4. The occasional presence of oxygen in the depositional environment is inferred from the occurrence of Ce anomalies (both positive and negative) and associated Mn and Cr enrichments evident in iron formation of the PB12-32 hole and some limestone samples from the PB12-35 hole. The presence of non-negligible true negative Ce anomalies indicates periodic oxygenation of the water column, at least locally.
5. The REE composition of Red Lake chemical sediments reveals multiple seawater signatures (i.e., supra-chondritic Y/Ho ratios, positive La and Gd anomalies, and HREE enrichment relative to LREE), but differs from modern seawater with a general absence of negative Ce anomalies and pronounced Eu anomalies due to more important hydrothermal fluxes to the Mesoarchean ocean relative to today.

4.7 Reference

- Afroz, M., Fralick, P.W., Lalonde, S. V, 2023. Sedimentology and geochemistry of basinal lithofacies in the Mesoarchean (2.93 Ga) Red Lake carbonate platform, northwest Ontario, Canada. *Precambrian Res.* 388, 106996.
<https://doi.org/https://doi.org/10.1016/j.precamres.2023.106996>
- Afroz, M., Marin-Carbonne, J., Fralick, P.W., Patry, L., Lalonde, S. V, 2022. In situ Multiple Sulfur Isotope Analyses of a Mesoarchean (2.93 Ga) Sulfidic Shale, Red Lake, Canada. Conference abstract in Goldschmidt.
<https://doi.org/https://doi.org/10.46427/gold2022.11993>
- Algeo, T.J., Maynard, J.B., 2004. Trace-element behavior and redox facies in core shales of Upper Pennsylvanian Kansas-type cyclothems. *Chem. Geol.* 206, 289–318.
- Alibo, D.S., Nozaki, Y., 1999. Rare earth elements in seawater: particle association, shale-normalization, and Ce oxidation. *Geochim. Cosmochim. Acta* 63, 363–372.
- Allwood, A.C., Kamber, B.S., Walter, M.R., Burch, I.W., Kanik, I., 2010. Trace elements record depositional history of an Early Archean stromatolitic carbonate platform. *Chem. Geol.* 270, 148–163. <https://doi.org/10.1016/j.chemgeo.2009.11.013>
- Anbar, A.D., Duan, Y., Lyons, T.W., Arnold, G.L., Kendall, B., Creaser, R.A., Kaufman, A.J., Gordon, G.W., Scott, C., Garvin, J., 2007. A whiff of oxygen before the great oxidation event? *Science* (80-.). 317, 1903–1906.
- Arnold, G.L., Anbar, A.D., Barling, J., Lyons, T.W., 2004. Molybdenum isotope evidence for widespread anoxia in mid-Proterozoic oceans. *Science* (80-.). 304, 87–90.
- Auger, Y., Bodineau, L., Leclercq, S., Wartel, M., 1999. Some aspects of vanadium and

chromium chemistry in the English Channel. *Cont. Shelf Res.* 19, 2003–2018.

Bau, M., Dulski, P., 1999. Comparing yttrium and rare earths in hydrothermal fluids from the Mid-Atlantic Ridge: Implications for Y and REE behaviour during near-vent mixing and for the Y/Ho ratio of proterozoic seawater. *Chem. Geol.* 155, 77–90.

[https://doi.org/10.1016/S0009-2541\(98\)00142-9](https://doi.org/10.1016/S0009-2541(98)00142-9)

Bau, M., Dulski, P., 1996. Distribution of yttrium and rare-earth elements in the Penge and Kuruman iron-formations, Transvaal Supergroup, South Africa. *Precambrian Res.* 79, 37–55. [https://doi.org/https://doi.org/10.1016/0301-9268\(95\)00087-9](https://doi.org/https://doi.org/10.1016/0301-9268(95)00087-9)

Bau, M., Dulski, P., 1995. Comparative study of yttrium and rare-earth element behaviours in fluorine-rich hydrothermal fluids. *Contrib. to Mineral. Petrol.* 119, 213–223.

<https://doi.org/10.1007/BF00307282>

Bau, M., Möller, P., 1993. Rare earth element systematics of the chemically precipitated component in early precambrian iron formations and the evolution of the terrestrial atmosphere-hydrosphere-lithosphere system. *Geochim. Cosmochim. Acta* 57, 2239–2249. [https://doi.org/https://doi.org/10.1016/0016-7037\(93\)90566-F](https://doi.org/https://doi.org/10.1016/0016-7037(93)90566-F)

Bau, M., Möller, P., Dulski, P., 1997. Yttrium and lanthanides in eastern Mediterranean seawater and their fractionation during redox-cycling. *Mar. Chem.* 56, 123–131.

Beukes, N.J., 1987. Facies relations, depositional environments and diagenesis in a major early Proterozoic stromatolitic carbonate platform to basinal sequence, Campbellrand Subgroup, Transvaal Supergroup, Southern Africa. *Sediment. Geol.* 54, 1–46.

Beukes, N.J., Lowe, D.R., 1989. Environmental control on diverse stromatolite morphologies in the 3000 Myr Pongola Supergroup, South Africa. *Sedimentology* 36, 383–397.

Chapter 4: Chemostratigraphy of the Red Lake Carbonate Platform

- Boland, D.D., Collins, R.N., Payne, T.E., Waite, T.D., 2011. Effect of amorphous Fe (III) oxide transformation on the Fe (II)-mediated reduction of U (VI). *Environ. Sci. Technol.* 45, 1327–1333.
- Bolhar, R., Van Kranendonk, M.J., 2007. A non-marine depositional setting for the northern Fortescue Group, Pilbara Craton, inferred from trace element geochemistry of stromatolitic carbonates. *Precambrian Res.* 155, 229–250.
<https://doi.org/10.1016/j.precamres.2007.02.002>
- Breit, G.N., Wanty, R.B., 1991. Vanadium accumulation in carbonaceous rocks: a review of geochemical controls during deposition and diagenesis. *Chem. Geol.* 91, 83–97.
- Brumsack, H.-J., 1989. Geochemistry of recent TOC-rich sediments from the Gulf of California and the Black Sea. *Geol. Rundschau* 78, 851–882.
- Brumsack, H.-J., 1986. Trace metal accumulation in black shales from the Cenomanian/Turonian boundary event, in: *Global Bio-Events*. Springer, pp. 337–343.
- Buerge, I.J., Hug, S.J., 1997. Kinetics and pH dependence of chromium (VI) reduction by iron (II). *Environ. Sci. Technol.* 31, 1426–1432.
- Byrne, R.H., Sholkovitz, E.R., 1996. Marine chemistry and geochemistry of the lanthanides. *Handb. Phys. Chem. rare earths* 23, 497–593.
- Calvert, S.E., Pedersen, T.F., 1993. Geochemistry of Recent oxic and anoxic marine sediments: Implications for the geological record. *Mar. Geol.* 113, 67–88.
[https://doi.org/https://doi.org/10.1016/0025-3227\(93\)90150-T](https://doi.org/https://doi.org/10.1016/0025-3227(93)90150-T)
- Card, K.D., 1990. A review of the Superior Province of the Canadian Shield, a product of Archean accretion. *Precambrian Res.* 48, 99–156.

Chapter 4: Chemostratigraphy of the Red Lake Carbonate Platform

[https://doi.org/https://doi.org/10.1016/0301-9268\(90\)90059-Y](https://doi.org/https://doi.org/10.1016/0301-9268(90)90059-Y)

Card, K.D., Ciesielski, A., 1986. Subdivisions of the Superior Province of the Canadian Shield. *Geosci. Canada* 13, 5–13.

Condie, K.C., 1993. Chemical composition and evolution of the upper continental crust: contrasting results from surface samples and shales. *Chem. Geol.* 104, 1–37.

Condie, K.C., Boryta, M.D., Liu, J., Qian, X., 1992. The origin of khondalites: geochemical evidence from the Archean to early Proterozoic granulite belt in the North China craton. *Precambrian Res.* 59, 207–223.

Corfu, F., Wallace, H., 1986. U–Pb zircon ages for magmatism in the Red Lake greenstone belt, northwestern Ontario. *Can. J. Earth Sci.* 23, 27–42. <https://doi.org/10.1139/e86-004>

Cotten, J., Le Dez, A., Bau, M., Caroff, M., Maury, R.C., Dulski, P., Fourcade, S., Bohn, M., Brousse, R., 1995. Origin of anomalous rare-earth element and yttrium enrichments in subaerially exposed basalts: evidence from French Polynesia. *Chem. Geol.* 119, 115–138.

Crusius, J., Calvert, S., Pedersen, T., Sage, D., 1996. Rhenium and molybdenum enrichments in sediments as indicators of oxic, suboxic and sulfidic conditions of deposition. *Earth Planet. Sci. Lett.* 145, 65–78.

De Baar, H.J.W., Bacon, M.P., Brewer, P.G., 1983. Rare-earth distributions with a positive Ce anomaly in the Western North Atlantic Ocean. *Nature* 301, 324–327.

De Baar, H.J.W., Brewer, P.G., Bacon, M.P., 1985. Anomalies in rare earth distributions in seawater: Gd and Tb. *Geochim. Cosmochim. Acta* 49, 1961–1969.

Chapter 4: Chemostratigraphy of the Red Lake Carbonate Platform

- De Baar, H.J.W., German, C.R., Elderfield, H., Van Gaans, P., 1988. Rare earth element distributions in anoxic waters of the Cariaco Trench. *Geochim. Cosmochim. Acta* 52, 1203–1219. [https://doi.org/10.1016/0016-7037\(88\)90275-X](https://doi.org/10.1016/0016-7037(88)90275-X)
- Derry, L.A., Jacobsen, S.B., 1990. The chemical evolution of Precambrian seawater: Evidence from REEs in banded iron formations. *Geochim. Cosmochim. Acta* 54, 2965–2977. [https://doi.org/10.1016/0016-7037\(90\)90114-Z](https://doi.org/10.1016/0016-7037(90)90114-Z)
- Derry, L.A., Jacobsen, S.B., 1988. The Nd and Sr isotopic evolution of Proterozoic seawater. *Geophys. Res. Lett.* 15, 397–400.
- Duff, M.C., Coughlin, J.U., Hunter, D.B., 2002. Uranium co-precipitation with iron oxide minerals. *Geochim. Cosmochim. Acta* 66, 3533–3547.
- Elderfield, H., 1988. The oceanic chemistry of the rare-earth elements. *Philos. Trans. R. Soc. London. Ser. A, Math. Phys. Sci.* 325, 105–126.
- Elderfield, H., Greaves, M.J., 1982. The rare earth elements in seawater. *Nature* 296, 214–219. <https://doi.org/10.1038/296214a0>
- Eroglu, S., van Zuilen, M.A., Taubald, H., Drost, K., Wille, M., Swanner, E.D., Beukes, N.J., Schoenberg, R., 2017. Depth-dependent $\delta^{13}\text{C}$ trends in platform and slope settings of the Campbellrand-Malmani carbonate platform and possible implications for Early Earth oxygenation. *Precambrian Res.* 302, 122–139.
- Fedo, C.M., Wayne Nesbitt, H., Young, G.M., 1995. Unraveling the effects of potassium metasomatism in sedimentary rocks and paleosols, with implications for paleoweathering conditions and provenance. *Geology* 23, 921–924.
- Fischer, W.W., Schroeder, S., Lacassie, J.P., Beukes, N.J., Goldberg, T., Strauss, H.,

Chapter 4: Chemostratigraphy of the Red Lake Carbonate Platform

- Horstmann, U.E., Schrag, D.P., Knoll, A.H., 2009. Isotopic constraints on the Late Archean carbon cycle from the Transvaal Supergroup along the western margin of the Kaapvaal Craton, South Africa. *Precambrian Res.* 169, 15–27.
- Fralick, P., Burton, J., 2008. Geochemistry of Paleoproterozoic Gunflint Formation carbonate: implications for early hydrosphere-atmosphere evolution. *Geochim. Cosmochim. Acta* 72, A280. <https://doi.org/10.1016/j.precamres.2016.12.014>
- Fralick, P., Riding, R., 2015. Steep Rock Lake: Sedimentology and geochemistry of an Archean carbonate platform. *Earth-Science Rev.* 151, 132–175. <https://doi.org/10.1016/j.earscirev.2015.10.006>
- Frei, R., Gaucher, C., Poulton, S.W., Canfield, D.E., 2009. Fluctuations in Precambrian atmospheric oxygenation recorded by chromium isotopes. *Nature* 461, 250–253. <https://doi.org/10.1038/nature08266>
- German, C.R., Elderfield, H., 1989. Rare earth elements in Saanich Inlet, British Columbia, a seasonally anoxic basin. *Geochim. Cosmochim. Acta* 53, 2561–2571.
- German, C.R., Holliday, B.P., Elderfield, H., 1991. Redox cycling of rare earth elements in the suboxic zone of the Black Sea. *Geochim. Cosmochim. Acta* 55, 3553–3558.
- Goldberg, E.D., Koide, M., Schmitt, R.A., Smith, R.H., 1963. Rare-Earth distributions in the marine environment. *J. Geophys. Res.* 68, 4209–4217. <https://doi.org/10.1029/JZ068i014p04209>
- Grandstaff, D.E., 1976. A kinetic study of the dissolution of uraninite. *Econ. Geol.* 71, 1493–1506.
- Haley, B.A., Klinkhammer, G.P., McManus, J., 2004. Rare earth elements in pore waters of

Chapter 4: Chemostratigraphy of the Red Lake Carbonate Platform

- marine sediments. *Geochim. Cosmochim. Acta* 68, 1265–1279.
- Heard, A.W., Aarons, S.M., Hofmann, A., He, X., Ireland, T., Bekker, A., Qin, L., Dauphas, N., 2021. Anoxic continental surface weathering recorded by the 2.95 Ga Denny Dalton Paleosol (Pongola Supergroup, South Africa). *Geochim. Cosmochim. Acta* 295, 1–23.
- Helz, G.R., Bura-Nakić, E., Mikac, N., Ciglencčki, I., 2011. New model for molybdenum behavior in euxinic waters. *Chem. Geol.* 284, 323–332.
- Helz, G.R., Miller, C. V, Charnock, J.M., Mosselmans, J.F.W., Patrick, R.A.D., Garner, C.D., Vaughan, D.J., 1996. Mechanism of molybdenum removal from the sea and its concentration in black shales: EXAFS evidence. *Geochim. Cosmochim. Acta* 60, 3631–3642.
- Hofmann, H.J., 1981. Precambrian fossils in Canada-the 1970s in retrospect, in: *Proterozoic Basins of Canada*. Geological Survey of Canada, pp. 419–443.
- Hofmann, H.J., Thurston, P.C., Wallace, H., 1985. Archean stromatolites from Uchi greenstone belt, northwestern Ontario, in: *Evolution of Archean Supracrustal Sequences*. Geol. Assoc. Can. Spec. Pap., pp. 125–132.
- Hollings, P., Wyman, D., Kerrich, R., 1999. Komatiite–basalt–rhyolite volcanic associations in Northern Superior Province greenstone belts: significance of plume-arc interaction in the generation of the proto continental Superior Province. *Lithos* 46, 137–161.
[https://doi.org/10.1016/S0024-4937\(98\)00058-9](https://doi.org/10.1016/S0024-4937(98)00058-9)
- Hsi, C.D., Langmuir, D., 1985. Adsorption of uranyl onto ferric oxyhydroxides: application of the surface complexation site-binding model. *Geochim. Cosmochim. Acta* 49, 1931–1941.

Chapter 4: Chemostratigraphy of the Red Lake Carbonate Platform

- Johannesson, K.H., Hawkins, D.L., Cortés, A., 2006. Do Archean chemical sediments record ancient seawater rare earth element patterns? *Geochim. Cosmochim. Acta* 70, 871–890. <https://doi.org/10.1016/j.gca.2005.10.013>
- Kamber, B.S., Bolhar, R., Webb, G.E., 2004. Geochemistry of late Archaean stromatolites from Zimbabwe: evidence for microbial life in restricted epicontinental seas. *Precambrian Res.* 132, 379–399. <https://doi.org/https://doi.org/10.1016/j.precamres.2004.03.006>
- Kamber, B.S., Webb, G.E., 2001. The geochemistry of late Archaean microbial carbonate: Implications for ocean chemistry and continental erosion history. *Geochim. Cosmochim. Acta* 65, 2509–2525. [https://doi.org/10.1016/S0016-7037\(01\)00613-5](https://doi.org/10.1016/S0016-7037(01)00613-5)
- Kamber, B.S., Webb, G.E., Gallagher, M., 2014. The rare earth element signal in Archaean microbial carbonate: information on ocean redox and biogenicity. *J. Geol. Soc. London.* 171, 745–763.
- Kato, Y., Kano, T., Kunugiza, K., 2002. Negative Ce Anomaly in the Indian Banded Iron Formations: Evidence for the Emergence of Oxygenated Deep-Sea at 2.9-2.7 Ga. *Resour. Geol.* 52, 101–110.
- Knoll, A.H., Beukes, N.J., 2009. Introduction: Initial investigations of a Neoproterozoic shelf margin-basin transition (Transvaal Supergroup, South Africa). *Precambrian Res.* 169, 1–14. <https://doi.org/https://doi.org/10.1016/j.precamres.2008.10.009>
- Konhauser, K.O., Lalonde, S. V, Planavsky, N.J., Pecoits, E., Lyons, T.W., Mojzsis, S.J., Rouxel, O.J., Barley, M.E., Rosiere, C., Fralick, P.W., 2011. Aerobic bacterial pyrite oxidation and acid rock drainage during the Great Oxidation Event. *Nature* 478, 369–373.

Chapter 4: Chemostratigraphy of the Red Lake Carbonate Platform

- Liger, E., Charlet, L., Van Cappellen, P., 1999. Surface catalysis of uranium (VI) reduction by iron (II). *Geochim. Cosmochim. Acta* 63, 2939–2955.
- Maynard, J.B., 1992. Chemistry of modern soils as a guide to interpreting Precambrian paleosols. *J. Geol.* 100, 279–289.
- McConchie, D.M., 1987. The geology and geochemistry of the Joffre and Whaleback shale members of the Brockman Iron Formation, Western Australia. University of Western Australia.
- McIntyre, T., Fralick, P., 2017. Sedimentology and Geochemistry of the 2930 Ma Red Lake-Wallace Lake Carbonate Platform, Western Superior Province, Canada. *Depos. Rec.* 3, 258–287. <https://doi.org/10.1002/dep2.36>
- McLennan, S.M., Taylor, S.R., Eriksson, K.A., 1983. Geochemistry of Archean shales from the Pilbara Supergroup, western Australia. *Geochim. Cosmochim. Acta* 47, 1211–1222.
- McManus, J., Nägler, T.F., Siebert, C., Wheat, C.G., Hammond, D.E., 2002. Oceanic molybdenum isotope fractionation: Diagenesis and hydrothermal ridge-flank alteration. *Geochemistry, Geophys. Geosystems* 3, 1–9. <https://doi.org/10.1029/2002GC000356>
- Moffett, J.W., 1990. Microbially mediated cerium oxidation in sea water. *Nature* 345, 421–423.
- Morford, J.L., Emerson, S., 1999. The geochemistry of redox sensitive trace metals in sediments. *Geochim. Cosmochim. Acta* 63, 1735–1750.
- Morse, J.W., Luther Iii, G.W., 1999. Chemical influences on trace metal-sulfide interactions in anoxic sediments. *Geochim. Cosmochim. Acta* 63, 3373–3378.

Chapter 4: Chemostratigraphy of the Red Lake Carbonate Platform

- Nesbitt, Hw., Young, G.M., 1982. Early Proterozoic climates and plate motions inferred from major element chemistry of lutites. *Nature* 299, 715–717.
- Nozaki, Y., Zhang, J., Amakawa, H., 1997. The fractionation between Y and Ho in the marine environment. *Earth Planet. Sci. Lett.* 148, 329–340.
[https://doi.org/10.1016/S0012-821X\(97\)00034-4](https://doi.org/10.1016/S0012-821X(97)00034-4)
- Partin, C.A., Lalonde, S. V, Planavsky, N.J., Bekker, A., Rouxel, O.J., Lyons, T.W., Konhauser, K.O., 2013. Uranium in iron formations and the rise of atmospheric oxygen. *Chem. Geol.* 362, 82–90.
- Patry, L. A., Bonnand, P., Boyet, M., Afroz, M., Wilmeth, D. T., Ramsay, B., Nonnotte, P., Homann, M., Sansjofre, P., Fralick, P. W., & Lalonde, S. V. Archean origins of oxygenic photosynthesis confirmed by La-Ce geochronology. *Nature*, in review (Submission 2023-04-05860)
- Pettine, M., Barra, I., Campanella, L., Millero, F.J., 1998a. Effect of metals on the reduction of chromium (VI) with hydrogen sulfide. *Water Res.* 32, 2807–2813.
- Pettine, M., D’ottone, L., Campanella, L., Millero, F.J., Passino, R., 1998b. The reduction of chromium (VI) by iron (II) in aqueous solutions. *Geochim. Cosmochim. Acta* 62, 1509–1519.
- Piper, D.Z., Perkins, R.B., 2004. A modern vs. Permian black shale—the hydrography, primary productivity, and water-column chemistry of deposition. *Chem. Geol.* 206, 177–197.
- Pirie, J., 1981. Regional setting of gold deposits in the Red Lake area, northwestern Ontario; in *Genesis of Archean volcanic-hosted gold deposits*; Ontario Geological Survey,

Chapter 4: Chemostratigraphy of the Red Lake Carbonate Platform

Miscellaneous Paper 97, 71–93.

Planavsky, N., Rouxel, O., Bekker, A., Shapiro, R., Fralick, P., Knudsen, A., 2009. Iron-oxidizing microbial ecosystems thrived in late Paleoproterozoic redox-stratified oceans. *Earth Planet. Sci. Lett.* 286, 230–242.

Prange, A., Kremling, K., 1985. Distribution of dissolved molybdenum, uranium and vanadium in Baltic Sea waters. *Mar. Chem.* 16, 259–274.

Ramsay, B., 2020. Environmental control of seawater geochemistry in a Mesoarchean Peritidal System, Woman Lake, Superior Province. MSc Thesis. Lakehead University, Canada.

Riding, R., Fralick, P., Liang, L., 2014. Identification of an Archean marine oxygen oasis. *Precambrian Res.* 251, 232–237. <https://doi.org/10.1016/j.precamres.2014.06.017>

Rongemaille, E., Bayon, G., Pierre, C., Bollinger, C., Chu, N.C., Fouquet, Y., Riboulot, V., Voisset, M., 2011. Rare earth elements in cold seep carbonates from the Niger delta. *Chem. Geol.* 286, 196–206.

Rudnicki, M.D., Elderfield, H., 1993. A chemical model of the buoyant and neutrally buoyant plume above the TAG vent field, 26 degrees N, Mid-Atlantic Ridge. *Geochim. Cosmochim. Acta* 57, 2939–2957.

Russell, A.D., Morford, J.L., 2001. The behavior of redox-sensitive metals across a laminated–massive–laminated transition in Saanich Inlet, British Columbia. *Mar. Geol.* 174, 341–354. [https://doi.org/https://doi.org/10.1016/S0025-3227\(00\)00159-6](https://doi.org/10.1016/S0025-3227(00)00159-6)

Sahoo, S.K., Planavsky, N.J., Kendall, B., Wang, X., Shi, X., Scott, C., Anbar, A.D., Lyons, T.W., Jiang, G., 2012. Ocean oxygenation in the wake of the Marinoan glaciation.

Chapter 4: Chemostratigraphy of the Red Lake Carbonate Platform

Nature 489, 546–549.

Sanborn-Barrie, M., Skulski, T., Parker, J., Dubé, B., 2000. Integrated regional analysis of the Red Lake greenstone belt and its mineral deposits , western Superior Province , Ontario. Geol. Surv. Canada Current Re, 14.

Sanborn-Barrie, M., Skulski, T., Parker, J.R., 2004. Geology, Red Lake greenstone belt, western Superior province, Ontario: Geological Survey of Canada Open File 4594, 1:50,000 scale color map. <https://doi.org/10.4095/215464>

Sanborn-Barrie, M., Skulski, T., Parker, J.R., 2001. Three hundred million years of tectonic history recorded by the Red Lake greenstone belt, Ontario. Geol. Surv. Canada Current Re, 14. <https://doi.org/10.4095/212109>

Sawyer, E.W., 1986. The influence of source rock type, chemical weathering and sorting on the geochemistry of clastic sediments from the Quetico metasedimentary belt, Superior Province, Canada. Chem. Geol. 55, 77–95.

Schlautman, M.A., Han, I., 2001. Effects of pH and dissolved oxygen on the reduction of hexavalent chromium by dissolved ferrous iron in poorly buffered aqueous systems. Water Res. 35, 1534–1546.

Seto, M., Akagi, T., 2008. Chemical condition for the appearance of a negative Ce anomaly in stream waters and groundwaters. Geochem. J. 42, 371–380.

Shiraki, K., 1997. Geochemical behavior of chromium. Shigen-Chishitsu 47, 319–330.

Siahi, M., Hofmann, A., Hegner, E., Master, S., 2016. Sedimentology and facies analysis of Mesoarchaeon stromatolitic carbonate rocks of the Pongola Supergroup, South Africa. Precambrian Res. 278, 244–264.

Chapter 4: Chemostratigraphy of the Red Lake Carbonate Platform

<https://doi.org/https://doi.org/10.1016/j.precamres.2016.03.004>

Smrzka, D., Zwicker, J., Bach, W., Feng, D., Himmler, T., Chen, D., Peckmann, J., 2019.

The behavior of trace elements in seawater, sedimentary pore water, and their incorporation into carbonate minerals: A review. *Facies* 65, 1–47.

Sreenivas, B., Srinivasan, R., 1994. Identification of paleosols in the Precambrian metapelitic assemblages of peninsular India—A major element geochemical approach. *Curr. Sci.* 89–94.

Sturchio, N.C., Antonio, M.R., Soderholm, L., Sutton, S.R., Brannon, J.C., 1998. Tetravalent uranium in calcite. *Science* (80-.). 281, 971–973.

Sumner, D.Y., 1996. Evidence for low late Archean atmospheric oxygen from oceanic depth gradients in iron concentration. *Geol. Soc. Am. Bull.* 28, 218.

Sumner, D.Y., Beukes, N.J., 2006. Sequence stratigraphic development of the Neoproterozoic Transvaal carbonate platform, Kaapvaal Craton, South Africa. *South African J. Geol.* 109, 11–22.

Sumner, D.Y., Grotzinger, J.P., 2004. Implications for Neoproterozoic ocean chemistry from primary carbonate mineralogy of the Campbellrand-Malmani Platform, South Africa. *Sedimentology* 51, 1273–1299. <https://doi.org/10.1111/j.1365-3091.2004.00670.x>

Sumner, D.Y., Grotzinger, J.P., 1996. Were kinetics of Archean calcium carbonate precipitation related to oxygen concentration? *Geology* 24, 119–122.
[https://doi.org/10.1130/0091-7613\(1996\)024<0119:WKOACC>2.3.CO;2](https://doi.org/10.1130/0091-7613(1996)024<0119:WKOACC>2.3.CO;2)

Taylor, S.R., McLennan, S.M., 1985. *The continental crust: its composition and evolution.* Blackwell Scientific Pub., Palo Alto, CA.

Chapter 4: Chemostratigraphy of the Red Lake Carbonate Platform

- Thoby, M., Konhauser, K.O., Fralick, P.W., Altermann, W., Visscher, P.T., Lalonde, S. V, 2019. Global importance of oxic molybdenum sinks prior to 2.6 Ga revealed by the Mo isotope composition of Precambrian carbonates. *Geology* 47, 559–562.
- Thurston, P.C., 1980. Subaerial volcanism in the Archean Uchi-Confederation volcanic belt. *Precambrian Res.* 12, 79–98.
- Thurston, P.C., Breaks, F.W., 1978. Metamorphic and tectonic evolution of the Uchi-English River Subprovince, in: *Metamorphism in the Canadian Shield*. pp. 49–62.
- Thurston, P.C., Osmani, I.A., Stone, D., Williams, H.R., Sutcliffe, R.H., Stott, G.M., 1991. Northwestern Superior Province: review and terrane analysis. *Geol. Ontario*. Ed. by PC Thurston, HR Williams, RH Sutcliffe, GM Stott. *Ontario Geol. Surv. Spec.* 4, 81–144.
- Trefry, J.H., Metz, S., 1989. Role of hydrothermal precipitates in the geochemical cycling of vanadium. *Nature* 342, 531–533.
- Tribouillard, N., Algeo, T.J., Lyons, T., Riboulleau, A., 2006. Trace metals as paleoredox and paleoproductivity proxies: an update. *Chem. Geol.* 232, 12–32.
- Voegelin, A.R., Nägler, T.F., Beukes, N.J., Lacassie, J.P., 2010. Molybdenum isotopes in late Archean carbonate rocks: Implications for early Earth oxygenation. *Precambrian Res.* 182, 70–82. <https://doi.org/https://doi.org/10.1016/j.precamres.2010.07.001>
- Vorlicek, T.P., Kahn, M.D., Kasuya, Y., Helz, G.R., 2004. Capture of molybdenum in pyrite-forming sediments: role of ligand-induced reduction by polysulfides. *Geochim. Cosmochim. Acta* 68, 547–556.
- Waite, T.D., Davis, J.A., Payne, T.E., Waychunas, G.A., Xu, N., 1994. Uranium (VI) adsorption to ferrihydrite: Application of a surface complexation model. *Geochim.*

Chapter 4: Chemostratigraphy of the Red Lake Carbonate Platform

Cosmochim. Acta 58, 5465–5478.

Walter, M.R., 1983. Archean stromatolites: evidence of the Earth's earliest benthos. *Earth's Earliest Biosph.* 187–213.

Wanty, R.B., Goldhaber, M.B., 1992. Thermodynamics and kinetics of reactions involving vanadium in natural systems: Accumulation of vanadium in sedimentary rocks. *Geochim. Cosmochim. Acta* 56, 1471–1483.

Webb, G.E., Kamber, B.S., 2000. Rare earth elements in Holocene reefal microbialites: A new shallow seawater proxy. *Geochim. Cosmochim. Acta* 64, 1557–1565.
[https://doi.org/10.1016/S0016-7037\(99\)00400-7](https://doi.org/10.1016/S0016-7037(99)00400-7)

Webb, G.E., Nothdurft, L.D., Kamber, B.S., Kloprogge, J.T., ZHAO, J., 2009. Rare earth element geochemistry of scleractinian coral skeleton during meteoric diagenesis: a sequence through neomorphism of aragonite to calcite. *Sedimentology* 56, 1433–1463.

Weltje, G.J., Tjallingii, R., 2008. Calibration of XRF core scanners for quantitative geochemical logging of sediment cores: Theory and application. *Earth Planet. Sci. Lett.* 274, 423–438. <https://doi.org/10.1016/J.EPSL.2008.07.054>

Wille, M., Kramers, J.D., Nägler, T.F., Beukes, N.J., Schröder, S., Meisel, T., Lacassie, J.P., Voegelin, A.R., 2007. Evidence for a gradual rise of oxygen between 2.6 and 2.5 Ga from Mo isotopes and Re-PGE signatures in shales. *Geochim. Cosmochim. Acta* 71, 2417–2435.

Wille, M., Nebel, O., Van Kranendonk, M.J., Schoenberg, R., Kleinhans, I.C., Ellwood, M.J., 2013. Mo-Cr isotope evidence for a reducing Archean atmosphere in 3.46-2.76Ga black shales from the Pilbara, Western Australia. *Chem. Geol.* 340, 68–76.

Chapter 4: Chemostratigraphy of the Red Lake Carbonate Platform

<https://doi.org/10.1016/j.chemgeo.2012.12.018>

Zhao, H., Gao, F., Li, X., Zhang, C., Zhao, Y., 2009. Electrical properties of yttrium doped strontium titanate with A-site deficiency as potential anode materials for solid oxide fuel cells. *Solid State Ionics* 180, 193–197.

Chapter 5

Carbon and Oxygen Isotope Chemostratigraphy of the Mesoarchean Carbonate Platform at Red Lake, Canada

Abstract

The Mesoarchean Red Lake carbonate platform presents a unique opportunity to examine the carbon and oxygen isotopic chemostratigraphy through Earth's earliest known thick carbonate platform. This carbonate platform was deposited ca. 2.87 Ga ago and is preserved in the Ball Assemblage of the Red Lake Greenstone Belt in northwestern Ontario, Canada. The >200 m thick carbonate package is predominantly composed of stromatolitic dolostones of shallow water origin, with lesser occurrences of deeper water limestone in the easternmost (Hahn Lake, Golden Arm) and westernmost (Pancake Bay) exposures. The stromatolitic dolostones show variable degrees of silicification and biogenic features in both outcrop and drill core, whereas the limestones are generally massive with diffusive banding and no noticeable macroscopic biogenic features in drill cores, but in outcrops, exposures show the presence of wrinkly laminar microbialites, crystal fans, and rare m-scale domes. Dolostone and limestone samples from five cored industry drill holes spanning the entire thickness of the platform were analyzed using a Kiel IV carbonate device coupled to a dual-inlet ThermoFisher MAT 253 mass spectrometer. The $\delta^{13}\text{C}$ values of dolostone and limestone range from -4.89 to 1.04 ‰ and -3.27 to 1.33 ‰, respectively, while $\delta^{18}\text{O}$ values range from -17.75 to -12.21 ‰ and -15.12 to -8.62 ‰, respectively (all values relative to VPDB). The data reveal a strong mineralogical control on stable isotopic compositions of the limestone and dolostone facies, which are likely related to periodic sea-level fluctuation. The relatively heavier $\delta^{13}\text{C}$ (> 0.5 ‰) and $\delta^{18}\text{O}$ (> -10 ‰) isotopic compositions of limestone, combined with rare earth element indicators for fully marine depositional settings, suggest that they captured the open ocean DIC pool. Rare $\delta^{13}\text{C}$ values lighter than -2 ‰ observed in certain limestone and dolostone samples likely represent contributions from remineralized organic matter and may be related in some cases to higher total organic carbon (TOC) contents, but not systematically. The consistently lighter isotopic compositions of $\delta^{18}\text{O}$ in dolostones are considered to reflect the influence of

Chapter 5: Carbon and Oxygen Isotope Chemostratigraphy

meteoric water during dolomitization, providing a significant and isotopically light freshwater component. While these carbonates were subjected to meteoric and late-stage burial diagenesis, a metamorphic origin of the remarkably lighter $\delta^{18}\text{O}$ isotope composition of these carbonates can be ruled out based on correlation with rare earth element signatures of primary sedimentary origin. Finally, a simple isotope mass balance model is presented to better understand the Mesoarchean carbon cycle. While the $\delta^{13}\text{C}$ values of the carbonates analyzed here are typical for those observed over most of the geological time, carbon isotope mass balance requires a carbon cycle that was significantly different than today, with an important yet previously unrecognized sink of near mantle $\delta^{13}\text{C}$ composition, most likely seafloor carbonation. This study significantly expands the available stable $\delta^{13}\text{C}$ and $\delta^{18}\text{O}$ isotope data for Mesoarchean carbonates and provides new insights into the deposition of the Red Lake carbonate platform via a chemostratigraphic approach.

5.1 Introduction

The geological carbon cycle is fundamental to our understanding of the evolving Earth and the functioning of biogeochemical cycles at its surface. The isotopic signature of carbon preserved in the sedimentary record is the result of the interaction of a variety of geochemical and biogeochemical processes. Ultimately, carbon is derived from outgassing of CO₂ from the solid Earth through metamorphism and volcanism, delivered to the ocean-atmosphere system, and eventually buried and subducted. Over long geological timescales, this cycle is effectively balanced, with the large majority of sequestration of CO₂ from Earth's atmospheric and oceans occurring into carbonate sediments (Holland, 1978). The precipitation of sedimentary carbonates is thus important for maintaining Earth's equable climate (Walker et al., 1981).

Carbon and oxygen stable isotope analyses have proven themselves important tools for exploring paleoenvironmental conditions, carbon cycling, aqueous geochemistry, and diagenesis in carbonate-producing sedimentary environments of the primitive Earth. Carbonates can record the isotopic composition of dissolved inorganic carbon (DIC) in a well-mixed ocean in equilibrium with the atmosphere, as well as deviation from it due to biogeochemical processes (Kump and Arthur, 1999). The absence of biostratigraphic index fossils makes carbon isotope chemostratigraphy particularly useful in the study Precambrian sediments (Knoll et al., 1986). In addition, the stable isotope geochemistry of ancient sedimentary carbonates is of special interest for deducing the behavior of carbon in the ocean-atmosphere system (Berner, 2006) and perturbations and changes to the geological carbon cycle as recorded by carbon stable isotope ratios (Broecker, 1970; Knoll et al., 1986; Schidlowski et al., 1975). Prior work on Archean carbonate platforms has provided multiple lines of evidence for exploring these aspects. For example, Siah et al. (2018) reported an approximate composition of DIC of 2.5 ‰ in coeval seawater based on the $\delta^{13}\text{C}$ isotope values of least altered carbonate samples of 2.96 Ga Chobeni Formation (Pongola Supergroup, South

Africa), which are similar to the previously published data (Perry and Tan, 1972; Schidlowski et al., 1983; Veizer et al., 1990). In contrast, carbonate $\delta^{18}\text{O}$ values may record source-water contributions and/or diagenesis- and metamorphism-related overprints (Siahi et al., 2018). The 2.80 Ga Steep Rock carbonate $\delta^{13}\text{C}$ and $\delta^{18}\text{O}$ values (Fralick and Riding, 2015) are somewhat similar to the $\delta^{13}\text{C}$ and $\delta^{18}\text{O}$ values of the Neoarchean (2.62-2.55 Ga) Campbellrand-Malmani carbonate platform (Fischer et al., 2009; Eroglu et al., 2017) as well as the Neoarchean Cheshire (Abell et al., 1985a), Neoarchean Mushandike (Abell et al., 1985b), and Paleoproterozoic Carwine (Veizer et al., 1990) carbonate platforms. However, there exist significantly less carbonate stable isotope data for the earliest carbonate platforms on Earth, which are Mesoarchean in age.

The Red Lake greenstone belt hosts Earth's first substantially thick (>200 m) accumulation of sedimentary carbonate, the 2.87 Ga Red Lake carbonate platform (RLCP) in northwest Ontario, Canada. Amongst Mesoarchean sedimentary carbonates, the Red Lake carbonate platform is particularly interesting as it preserves both shallow-water (stromatolitic carbonate) and deep-water (abiotic carbonate) carbonate lithofacies, providing an exceptional opportunity to examine Mesoarchean carbonate deposits in shallow-to-deep transect and fill critical gaps regarding the isotopic composition of inorganic carbon and oxygen in the Mesoarchean sedimentary carbonate record (Afroz et al., 2023). McIntyre and Fralick (2017) reported the isotopic composition of carbon and oxygen of dolomite-rich stromatolites and a few calcite-rich *Atikokania* samples from Red Lake outcrops, but little stratigraphic context is available between the different studied outcrops. This chapter presents a detailed stable carbon-oxygen isotope chemostratigraphy of five cored drill holes transecting shallow- to deep-water carbonates in the RLCP, with the goal of better understanding their origin, post-depositional modification, and operation of the Mesoarchean carbon cycle more generally.

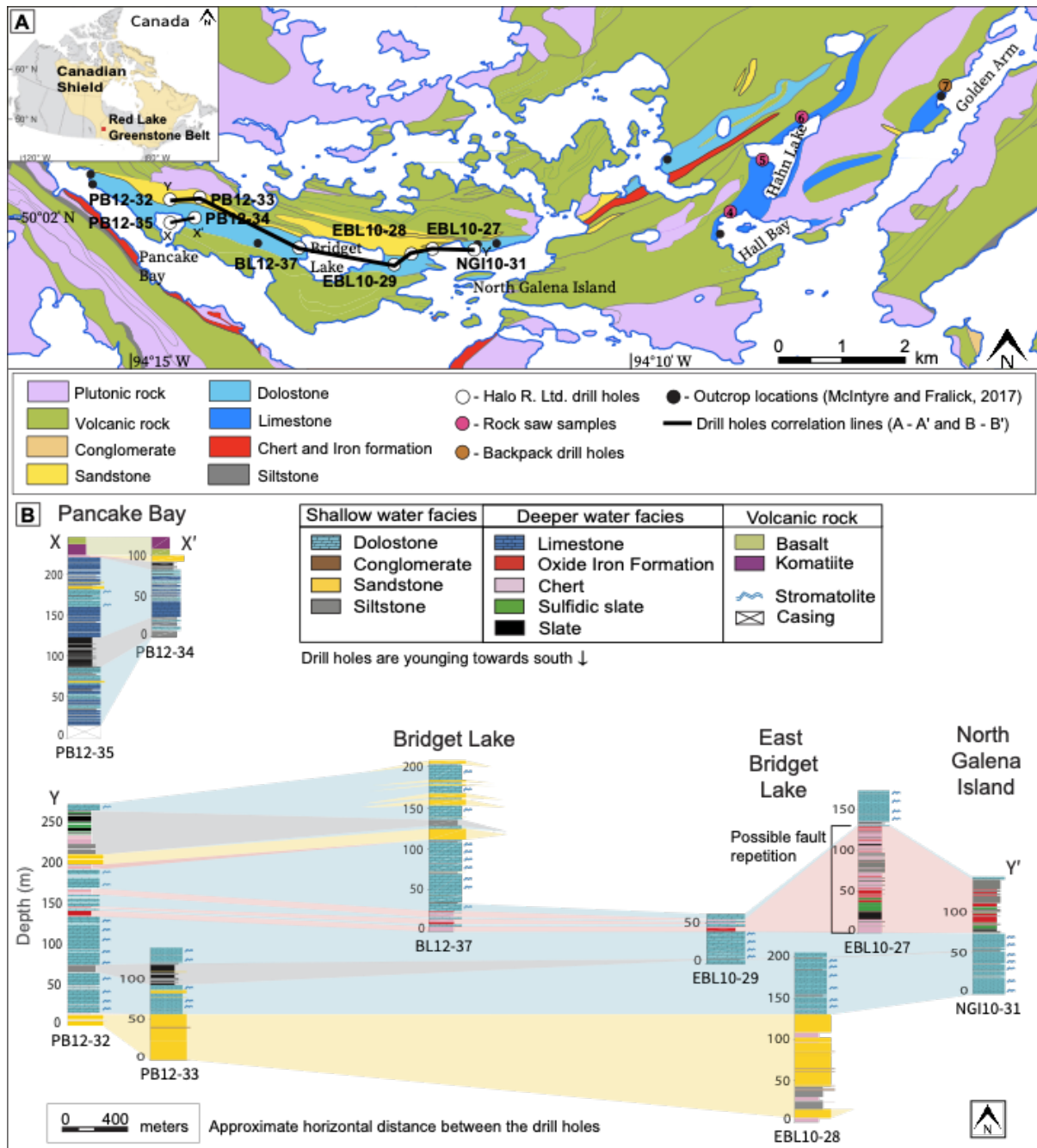


Figure 5.1. (A) Geological map of the Red Lake carbonate platform with an inset showing location of the Red Lake Greenstone Belt (red square) in the Canadian Shield. Dips are sub-vertical with regional younging to the south. Modified after Sanborn-Barrie et al., 2004. (B) Stratigraphic profiles and correlations were prepared from nine cored drill holes. Chemical sedimentary rocks alternate with siliciclastic rocks, with shallow water stromatolitic carbonate overlying and underlying other lithologies deposited in deeper water. The X to X' and Y to Y' lines show the correlation lines between the PB12-35 and the PB12-34 holes and the PB12-32 and the NGI10-31 holes, respectively. The horizontal distance of the stratigraphic columns in the figure represents the approximate drill collar positions from west to east (modified after Afroz et al., 2023).

5.2 Geological background and sampled material

The Red Lake carbonate platform belongs to the Red Lake Greenstone Belt, located in the Ball assemblage of Uchi Subprovince of the Superior Province, northwestern Ontario, Canada (Corfu and Wallace, 1986, Sanborn-Barrie et al., 2001, 2000). Originally thought to be deposited 2940 ± 2 to 2925 ± 3 Ma ago (Corfu and Wallace, 1986) its age was recently revised ca. 2.87 Ga (Patry et al., in review). Most parts of the Uchi subprovince were subjected to greenschist to lower amphibolite facies metamorphism (Corfu and Wallace, 1986; Thurston and Breaks, 1978). The Mesoarchean Red Lake carbonate platform comprises various chemical sedimentary rocks and siliciclastic sedimentary rocks, and the entire sedimentary assemblage is overlain and underlain by mafic to felsic volcanic rocks (Corfu and Wallace, 1986; Sanborn-Barrie et al., 2001, 2000). This platform is 290 m thick, and its modern known exposure is approximately 14 km wide from east to west (Figure 5.1). It consists predominantly of stromatolitic dolostone and a lesser occurrence of massive limestone with the occasional presence of crystal fans (Hofmann et al., 1985; McIntyre and Fralick, 2017). Various other chemical sedimentary rocks, such as chert, oxide iron formation, and siliciclastic sedimentary rocks, such as black shale, sulfidic black shale, siltstone, and sandstone are also preserved in this carbonate platform and overlaid, underlaid, and interlaid by carbonates (Afroz et al., 2023).

The depositional settings of the carbonate platform have been reconstructed using sedimentological and geochemical data from outcrops and nine-cored drill holes (Afroz et al., 2023; Hofmann et al., 1985; McIntyre and Fralick, 2017). The stromatolitic dolostones are highly silicified, showing peritidal depositional features and suggesting shallow water depositional environments, whereas the massive limestones are devoid of biogenic features and recrystallized, representing deep subtidal to upper slope depositional environment (Afroz et al., 2023; McIntyre and Fralick, 2017). The dolostone facies is well preserved in outcrops, dominating the platform top, and captured in multiple industry drill holes cores, whereas the

limestone facies are preserved in the eastern and western margins of the carbonate platform and captured only in the PB12-35 and PB12-34 holes (Afroz et al., 2023; McIntyre and Fralick, 2017). Carbonate samples for stable carbon and oxygen isotope analysis were taken from five cored drill holes i.e., PB12-35, PB12-32, PB12-33, EBL10-28, and NGI10-31. Among these drill holes, the PB12-35 hole contains dolostone and limestone facies; the rest contain only dolostone facies (Afroz et al., 2023). Two short drill cores, 17-GA1 (2.1 m in length) and 17-NG (1.8 m in length) were obtained in the field from outcrops in the Golden Arm area and the shoreline north of Galena island, near the collar location of the industry drill hole NGI10-31 (Figure 5.1). These sampled a m-scale dome consisting of alternating layers of crystal fans and massive calcite that outcrops on the western shore of Golden Arm, and a package of stromatolitic bioherms composed of partially silicified dolostone with abundant microbialite features that is typical of the shoreline north of Galena island.

5.3 Methods

A total of 187 samples of dolostone and limestone were analyzed for their carbon and oxygen stable isotope composition. A pure tungsten carbide hammer-operated piston and cylinder were used to crush samples, and then an agate ring mill was used to powder samples to below 200 mesh. Approximately 200 to 250 μg of powdered carbonate samples were weighed on a precision microbalance and put into small glass vials. The glass vials were placed in a carousel along with similarly prepared standards inside a Kiel IV carbonate device. Samples were reacted with four drops of 100% phosphoric acid (H_3PO_4) at 72°C , releasing CO_2 and H_2O . These gases were cryogenically trapped using liquid nitrogen (-192°C) while the residual products were emptied by vacuum pumping at the end of the reaction. The trap is then warmed to -90°C , releasing CO_2 in gaseous form which was again transferred to liquid nitrogen to be concentrated. Finally, to analyze the stable isotope composition of carbon and oxygen, the viscous purified CO_2 flowed was in a capillary connected to a dual-inlet ThermoFisher

MAT 253 gas source mass spectrometer at the PSO's IRMS stable isotope laboratory at the European Institute of Marine Studies (IUEM), France.

The results are presented in the conventional delta (δ) notation, defined by the following equation, and reported in per mille (‰) units relative to the VPDB-standard (Vienna Pee Dee Belemnite):

$$\delta = [(R_s/R_{std}) - 1] \times 1000 \text{ ‰}$$

where $R = {}^{13}\text{C}/{}^{12}\text{C}$ or ${}^{18}\text{O}/{}^{16}\text{O}$; R_s = Measured ratio in the sample, and R_{std} = Ratio of the standard.

The international standards NBS-18, NBS-19, and the internal standard CAMIL-21 were used to calibrate the $\delta^{13}\text{C}$ and $\delta^{18}\text{O}$ isotope compositions and the precision for $\delta^{13}\text{C}$ and $\delta^{18}\text{O}$ was 0.1 ‰ (2σ) and 0.2 ‰ (2σ), respectively.

5.4 Results

The $\delta^{13}\text{C}$ and $\delta^{18}\text{O}$ values of the analyzed Red Lake carbonate samples from different drill hole cores and outcrops are tabulated in Appendix B. The $\delta^{13}\text{C}$ values of limestone samples from the PB12-35 hole range from -1.18 to 1.33 ‰ and $\delta^{18}\text{O}$ values range from -15.90 to -8.62 ‰ (Figure 5.2A). The dolostone samples from this hole ranged from -3.0 to 0.13 ‰ and -16.29 to -12.31 ‰ for $\delta^{13}\text{C}$ and $\delta^{18}\text{O}$, respectively. Most of the limestone samples show heavier isotopic compositions while the dolostone samples have a lighter isotopic composition, for both $\delta^{13}\text{C}$ and $\delta^{18}\text{O}$ isotopes. Throughout the stratigraphic profile, the $\delta^{13}\text{C}$ isotopic composition of limestone samples is >0 ‰ except for a few samples between 45 m to 63 m, 150 m to 160 m, and 185 m to 200 m intervals where several samples show the isotopic composition of greater than 0 ‰. Conversely, most of the dolostone samples possess $\delta^{13}\text{C}$ isotopic compositions below 0 ‰, except for two samples at 162m and 180 m depth. The $\delta^{18}\text{O}$ values in limestone samples spanning from 20 m to 35 m, 130 m to 145 m, and 210 m to 215

m intervals are $> -10\text{‰}$, whereas the rest of the limestone samples have values between -15.21 and -10‰ . The majority of the dolostone samples have $\delta^{18}\text{O}$ values between -16.29 and

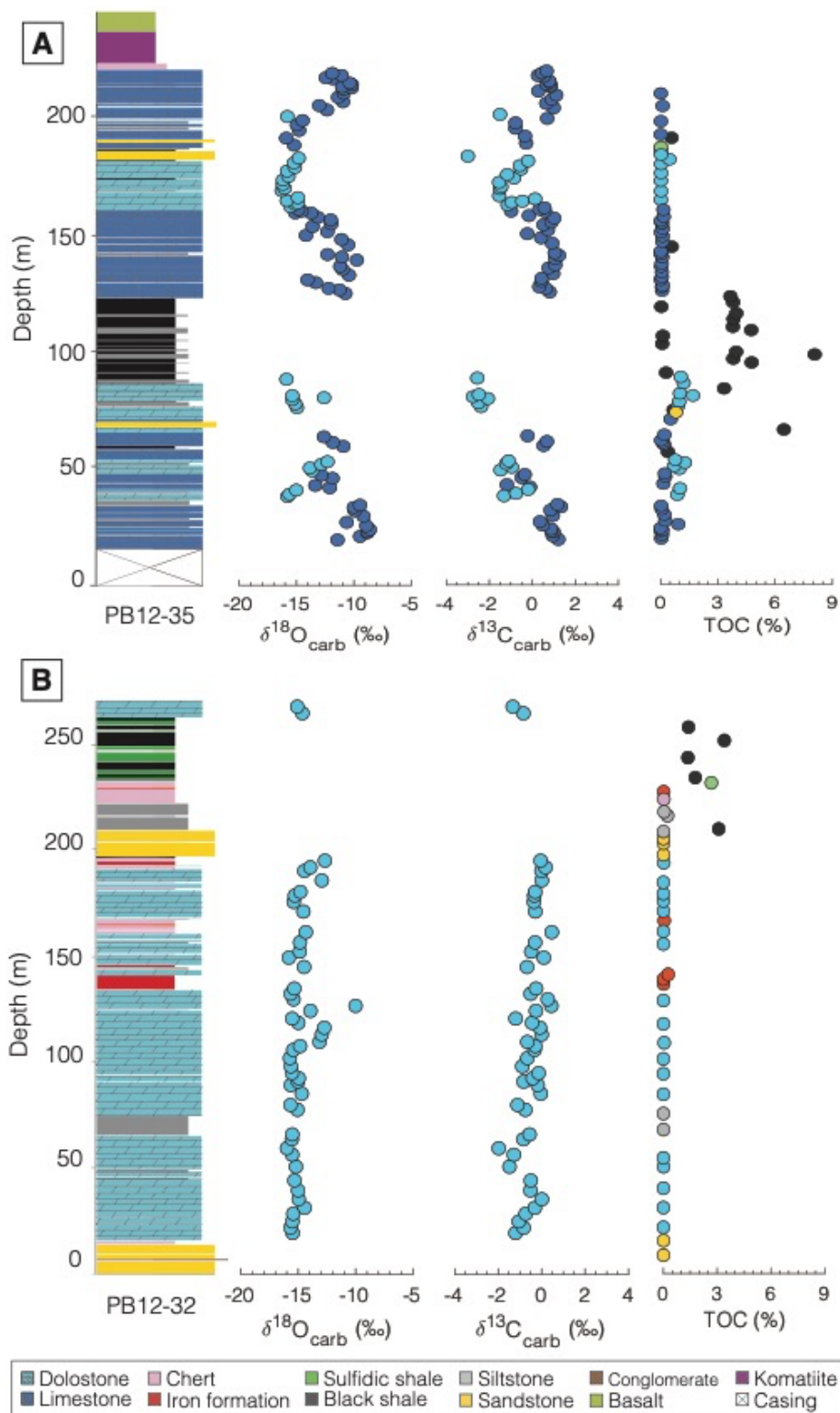


Figure 5.2. (A) Chemostratigraphic profiles of oxygen isotopes, carbon isotopes, and TOC contents of the PB12-35 hole. (B) Chemostratigraphic profiles of oxygen isotopes, carbon isotopes, and TOC contents of the PB12-32 hole.

-14.82 ‰, while a few samples in the 48 to 52 m interval have $\delta^{18}\text{O}$ values between -13.8 and -12.3 ‰.

Dolostones of the PB12-32 core yield $\delta^{13}\text{C}$ values between -4.89 and 0.47 ‰ and $\delta^{18}\text{O}$ values between -17.26 and -8.75 ‰ (Figure 5.2B). Samples mostly possess $\delta^{13}\text{C}$ values greater than 0 ‰, there exist a few exceptions. Most of the dolostone samples have light isotopic values of $\delta^{18}\text{O}$, but slightly heavier isotopic values are observed from the 110 m to 125 m and 185 m to 195 m depth intervals.

Samples of dolostone from the PB12-33 core show $\delta^{13}\text{C}$ values of -1.10 to 0.84 ‰ and $\delta^{18}\text{O}$ values of -15.75 to -13.69 ‰, respectively (Figure 5.3A). In this hole, $\delta^{13}\text{C}$ values are predominantly near -0.3 ‰ for most of the dolostone samples, while the $\delta^{18}\text{O}$ isotopic signature is relatively static around -15 ‰, except a few samples at 89.8 m and 118.8 m depths that show values around -13.69 and 13.90 ‰, respectively.

The isotopic composition of dolostone samples of the EBL10-28 hole varies from -0.19 to 0.75 ‰ for $\delta^{13}\text{C}$ and -15.51 to -13.07 ‰ for $\delta^{18}\text{O}$ (Figure 5.3B). The $\delta^{13}\text{C}$ values are consistently positive throughout the profile, with only two samples at 143 m (-0.19 ‰) and 164 m (-0.04 ‰) depth showing $\delta^{13}\text{C}$ values below zero. The $\delta^{18}\text{O}$ isotopic compositions are also consistently around -14 ‰ with no remarkable deviations.

The $\delta^{13}\text{C}$ and $\delta^{18}\text{O}$ values of dolostone samples in the NGI10-31 core range from -2.85 to 1.04 ‰ and -16.65 to -12.21 ‰, respectively (Figure 5.4A). Again, most of the dolostone samples have >0 ‰ isotopic composition of $\delta^{13}\text{C}$ and the rest of the samples have lighter (<0 ‰) isotopic values. The $\delta^{18}\text{O}$ isotopic composition of dolostone samples is relatively stable around the value of -14 ‰ but some samples near the bottom of the hole have slightly heavier values.

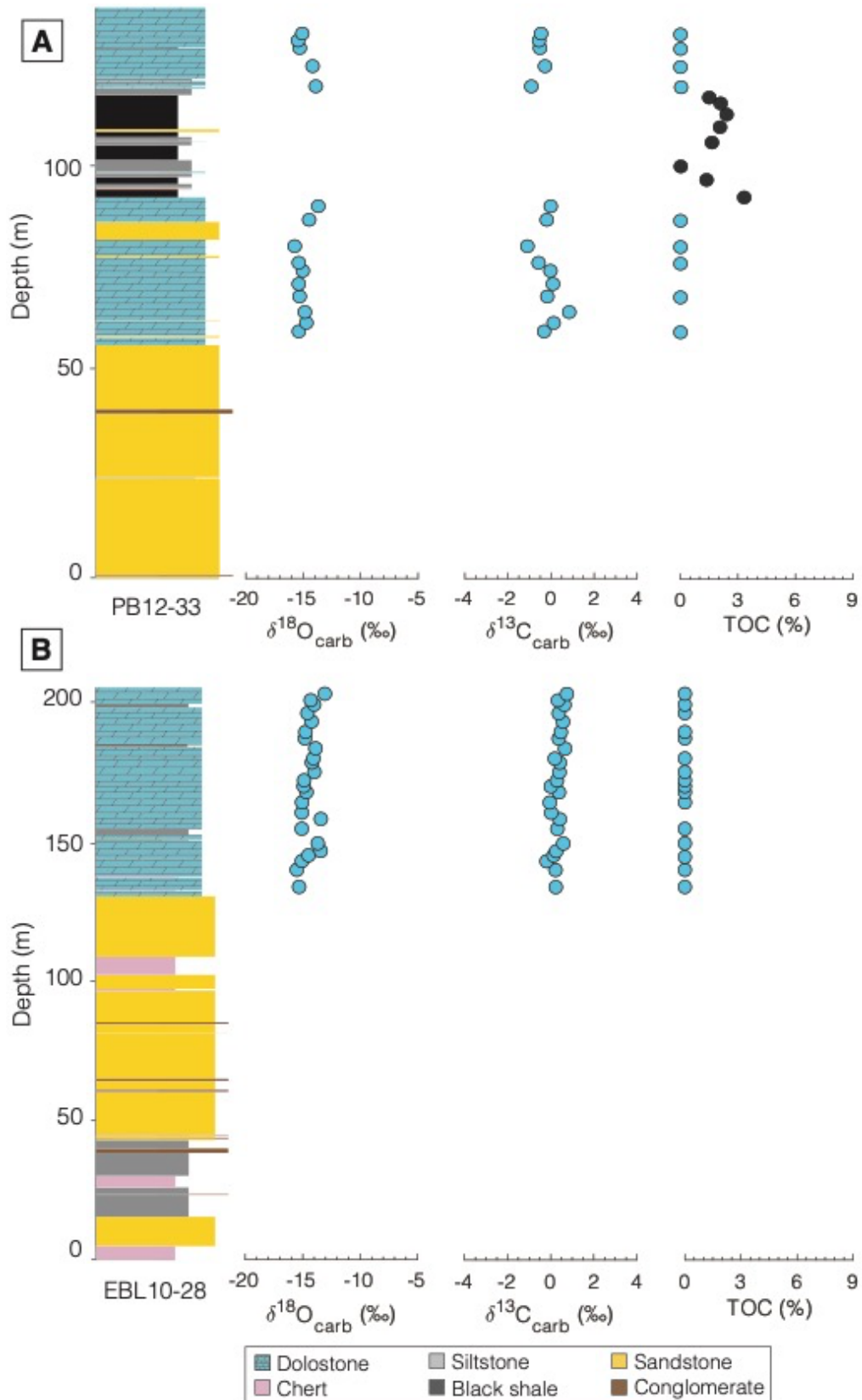


Figure 5.3. (A) Chemostratigraphic profiles of oxygen isotopes, carbon isotopes, and TOC contents of the PB12-33 hole. (B) Chemostratigraphic profiles of oxygen isotopes, carbon isotopes, and TOC contents of the EBL10-28 hole.

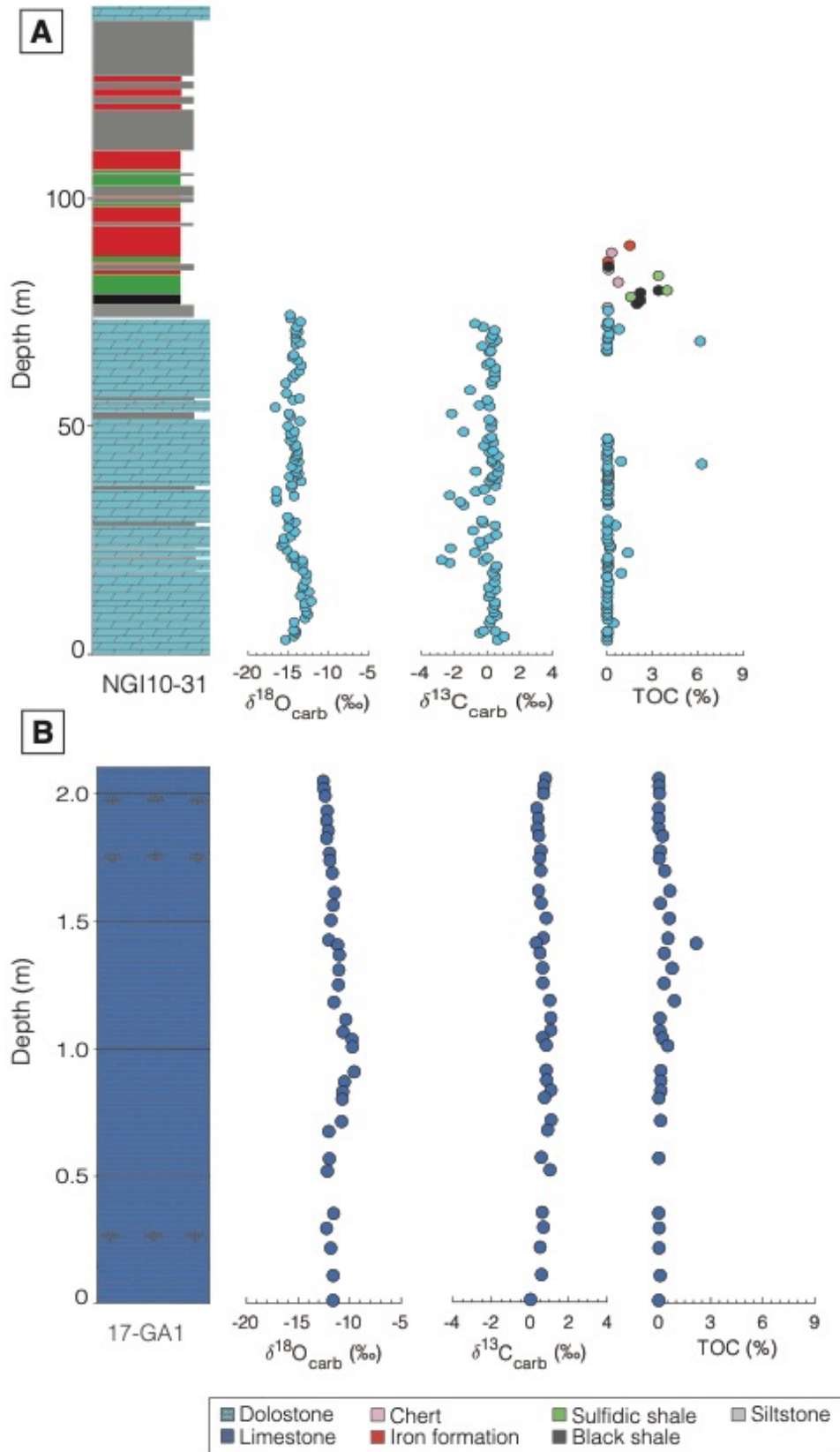


Figure 5.4. (A) Chemostratigraphic profiles of oxygen isotopes, carbon isotopes, and TOC contents of the NGI10-31 hole. (B) Chemostratigraphic profiles of oxygen isotopes, carbon isotopes, and TOC contents of the 17-GA1 hole.

Limestone samples from the short drill core obtained in the field from outcrop at Golden Arm (17-GA1) show $\delta^{13}\text{C}$ values varying from -0.72 to 1.52 ‰ and $\delta^{18}\text{O}$ values varying from -12.74 to -8.52 ‰. Dolostone samples from the short backpack core 17-NG yield 0.34 to 0.87 ‰ for $\delta^{13}\text{C}$ and -14.49 to -11.89 ‰ for $\delta^{18}\text{O}$; while not plotted here in stratigraphic section as this interval was spanned by the NGI10-31 hole collared nearby, these data are tabulated in Appendix B and included in all figures.

5.5 Discussion

The bulk Precambrian marine sedimentary carbonates have $\delta^{13}\text{C}$ values around 0 ‰, similar to the values of the Phanerozoic marine carbonates (Schidlowski et al., 1983). The isotopic composition of marine carbonates can reveal important information about both local and global paleoenvironments, but caution is warranted as primary isotopic signatures are often secondarily modified by later interaction with hydrothermal fluids and/or freshwater. The $\delta^{18}\text{O}_{\text{VPDB}}$ value of Archean carbonates varies from -15 to -9 ‰ (Beukes et al., 1990; Fischer et al., 2009; Heimann et al., 2010; Kaufman et al., 1990), which is significantly lower than Phanerozoic marine carbonates. Diagenetic processes such as meteoric diagenesis or metamorphism tend to reduce both the $\delta^{13}\text{C}$ and $\delta^{18}\text{O}$ composition of carbonate rocks, and dolomitization also generally acts to lower the $\delta^{18}\text{O}$ value (Bristow and Kennedy, 2008; Fairchild and Kennedy, 2007; Kaufman and Knoll, 1995; Melezhik et al., 2003; Quinn and Matthews, 1990; Singh et al., 1998). Meteoric waters are depleted in $\delta^{18}\text{O}$ relative to seawater, so $\delta^{18}\text{O}$ tends to decrease with an increased influx of meteoric water. Depending on the water/rock (W/R) ratio of metamorphic fluids during recrystallization, the isotopic composition of carbonate rocks also can be re-equilibrated with high-temperature fluids of diverse isotopic composition (Choquette and James, 1987; Reinhold, 1998). High-temperature metamorphic fluids are characterized by high oxygen and low carbon contents, and therefore, the $\delta^{18}\text{O}$ isotope compositions of carbonate rocks tend to shift towards lower values while $\delta^{13}\text{C}$ shows little

change (Banner and Hanson, 1990; Masters and Benestad, 2013; Melezhik et al., 2003) after exchange with metamorphic fluids. Thus, while events occurring during early lithification or later metamorphism may generate lighter secondary $\delta^{18}\text{O}$ isotopic values in ancient carbonates, the correlation between $\delta^{13}\text{C}$ and $\delta^{18}\text{O}$ can be useful for distinguishing meteoric and burial lithification from marine excursions (Knauth and Kennedy, 2009). When primary isotopic compositions are preserved in carbonates, the isotopic compositions of seawater and/or seawater temperature during carbonate precipitation can be reconstructed by the oxygen isotope composition of carbonates (Epstein et al., 1951)

5.5.1 Lithological, diagenetic, and metamorphic controls on carbon and oxygen stable isotope compositions

Across all studied samples, the limestone samples have relatively heavier isotopic compositions in $\delta^{13}\text{C}$ and $\delta^{18}\text{O}$ than the dolostone samples. Among the Red Lake carbonate samples, most of the limestone samples have $\delta^{13}\text{C}$ values >0 ‰ while only a few of the samples have lower values down to -1.25 ‰, whereas most of the dolostone samples have $\delta^{13}\text{C}$ values between -1 to 0.7 ‰ and the remainder have slightly more negative values (up to -3.2 ‰). The $\delta^{18}\text{O}$ values also show an important contrast between carbonate mineralogies, with values from -8.62 ‰ to -15.21 ‰ and -12.21 ‰ to -16.66 ‰ for the limestone and dolostone samples, respectively. Some of the limestone samples have a heavier $\delta^{18}\text{O}$ isotopic composition while others have lighter isotopic compositions, similar to the dolostone samples (Figure 5.5).

The Red Lake carbonate dataset thus shows an important mineralogical control on the $\delta^{13}\text{C}$ and $\delta^{18}\text{O}$ isotope compositions between the limestone and dolostone facies. The limestones were precipitated offshore while the peritidal stromatolitic dolostones were formed in a near-shore environment (McIntyre and Fralick, 2017). Thus, water depth possibly controlled the variations in carbonate stable isotope compositions observed in the chemostratigraphic profiles, with heavier $\delta^{13}\text{C}$ and $\delta^{18}\text{O}$ isotopic compositions in limestone

being driven by sea level fluctuations. Sea level rise drowns siliciclastic sources, restrains meteoric water invasion, promotes extension of a carbonate platform, and results in continental runoff with low $\delta^{13}\text{C}$ and $\delta^{18}\text{O}$ values. Inversely, pervasive invasion of meteoric waters into carbonate platforms occurs during sea-level fall when the shallow marine segment of the carbonate platform may be exposed subaerially, allowing freshwater to penetrate into pore fluids and result in the lighter isotopic composition in carbonates (Knauth and Kennedy, 2009).

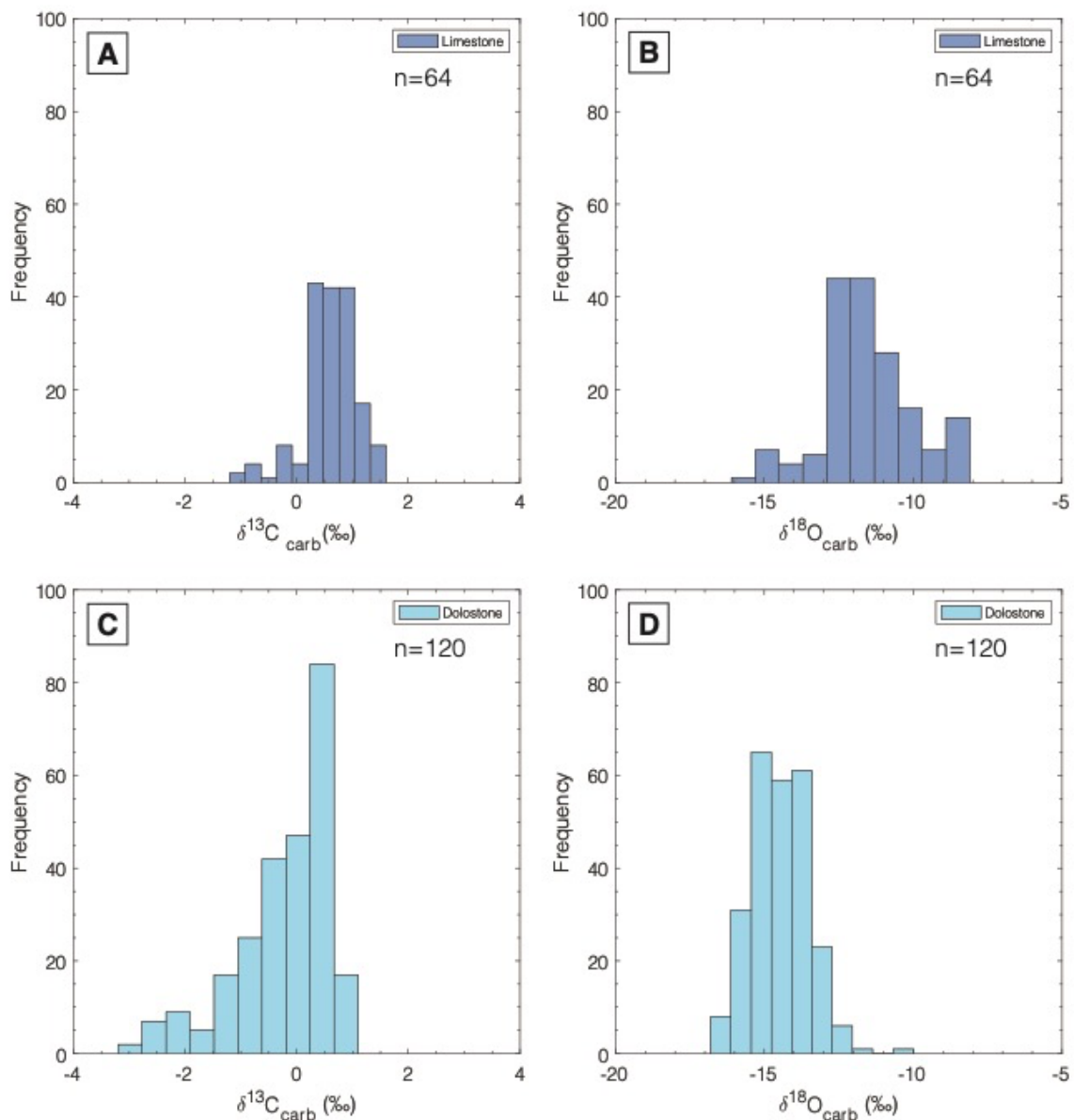


Figure 5.5. Histograms of $\delta^{13}\text{C}$ and $\delta^{18}\text{O}$ for limestone and dolostone samples of the Red Lake carbonate platform.

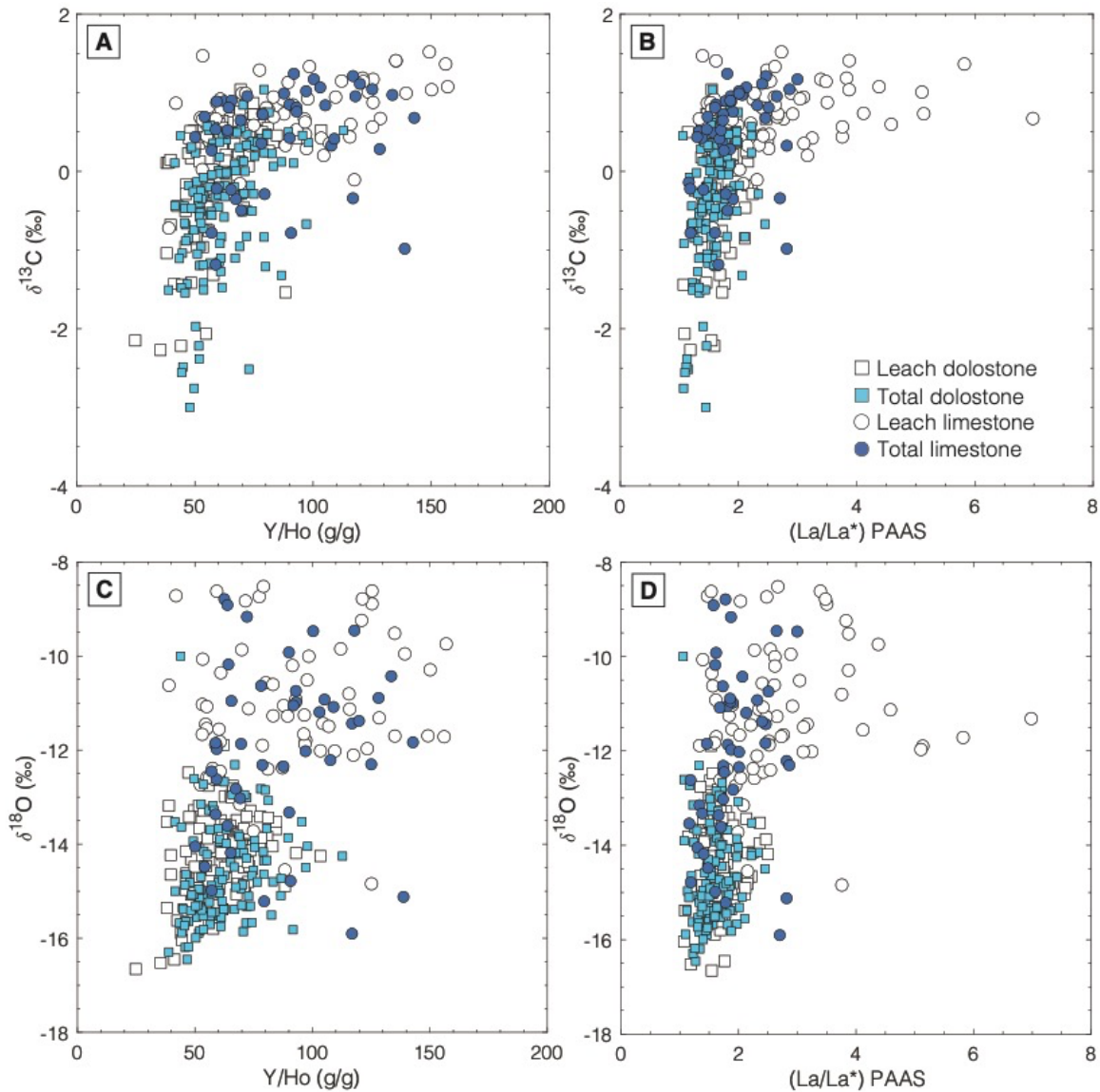


Figure 5.6. Plots of $\delta^{13}\text{C}$ and $\delta^{18}\text{O}$ versus Y/Ho ratio and La anomalies for whole rock and weak leach digest data for Red Lake carbonate.

If primary signatures are preserved, in a well-mixed ocean that is in equilibrium with the atmosphere (Kump and Arthur, 1999), then the chemostratigraphy of $\delta^{13}\text{C}_{\text{carb}}$ would reflect the $\delta^{13}\text{C}$ of dissolved inorganic carbon (DIC) values of contemporaneous seawater ($\delta^{13}\text{C}_{\text{DIC}}$). Interestingly, the heavier isotopic compositions for both $\delta^{13}\text{C}$ and $\delta^{18}\text{O}$ in offshore Red Lake limestones is correlated with evidence from REE indicators, specifically high Y/Ho ratio and La/La* anomalies, indicative of more fully open marine conditions (Figure 5.6). This signature is difficult to explain by metamorphic processes as they are unlikely to affect the REE

systematics of the samples. Rather, the correlation between C and O isotope compositions (potentially modifiable) and REE indicators (unlikely to be modified) indicates that carbonate C and O isotope compositions were controlled by the loci of carbonate precipitation on the paleoshelf and not by late-stage metamorphic processes. Dolomitization is a special case that is discussed below; in any case, regarding the limestones, the most positive values for both $\delta^{13}\text{C}$ and $\delta^{18}\text{O}$, corresponding to those samples showing the largest Y/Ho ratios and La/La* anomalies, may point towards the open ocean DIC signature. The $\delta^{18}\text{O}$ values of >-10 ‰ for limestone samples would thus be the result of precipitation in the offshore environment, whereas the lighter isotopic compositions in dolostones are associated with a more shallow-water environment where occasional fluvial influx may have been present.

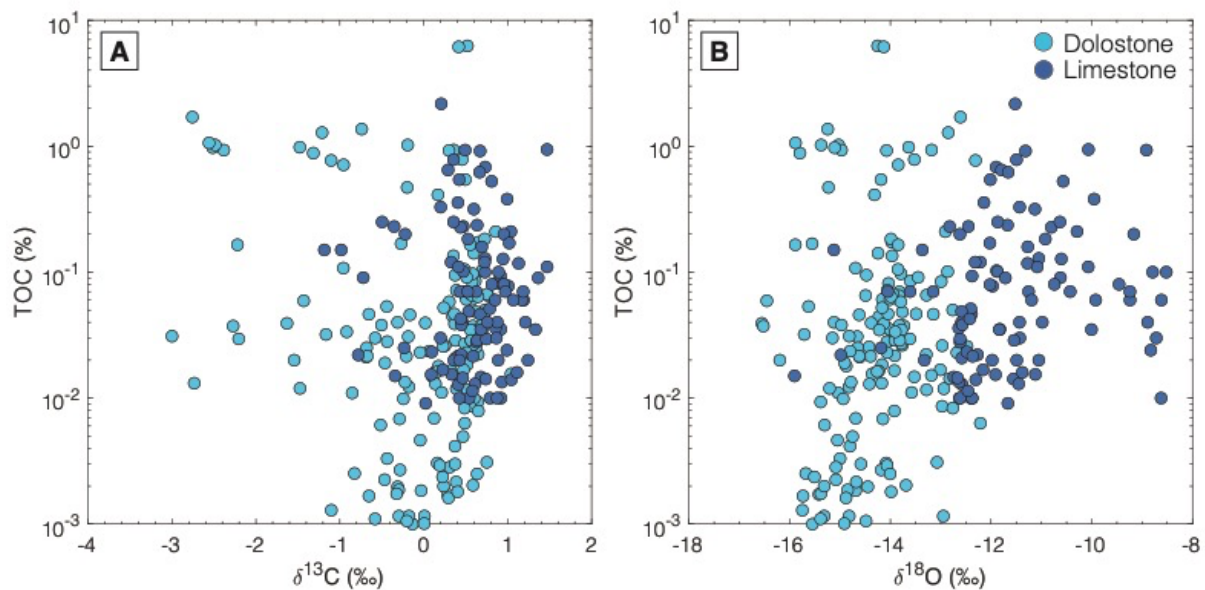


Figure 5.7. (A) TOC vs. $\delta^{13}\text{C}$ plot for limestone and dolostone samples. (B) TOC vs. $\delta^{18}\text{O}$ for limestone and dolostone samples.

The high TOC carbonate samples from transitional facies such as carbonate-magnetite and slumped carbonates of the RLCP correlate with lighter $\delta^{13}\text{C}$ isotopic signatures in carbonate (Afroz et al., 2023). However, lighter $\delta^{13}\text{C}$ values for the Red Lake carbonate samples analyzed here are sometimes, but not systematically, related to high TOC contents. Depleted

$\delta^{13}\text{C}$ values have been reported for deeper water carbonates in Archean carbonate platforms from different localities such as the Hamersley Group (Becker and Clayton, 1972; Kaufman et al., 1990), Transvaal Supergroup (Beukes et al., 1990; Fischer et al., 2009; Schneiderhan et al., 2006) and Steep Rock Lake (Fralick and Riding, 2015). In aqueous environment, photosynthesis occurs in surface waters, but the oxidation of organic matter continues throughout the water column. This process can lead to a decreasing gradient of $\delta^{13}\text{C}$ values in dissolved inorganic carbon (DIC) with depth, and marine carbonates precipitated along this gradient may reflect these variations (Broecker and Peng, 1982). Red Lake limestone and dolostone samples show variable $\delta^{13}\text{C}$ isotopic compositions though they have similar TOC content, therefore, it remains ambiguous as to whether lighter $\delta^{13}\text{C}$ isotopic compositions are dependent on TOC (Figure 5.7). The TOC contents of Red Lake dolostone samples are similar to the limestone samples, but they achieve lighter isotopic compositions at times, which we interpret to reflect the oxidation of organic matter influencing the DIC pool of the shallow marine environment. Thus, lighter $\delta^{13}\text{C}$ values in Red Lake carbonates could reflect organic matter recycling during diagenesis and/or enhanced inputs from organic-matter-derived DIC in productive shallow waters, while less productive deep waters forming limestone from the open ocean DIC pool would expect to be less susceptible to water column shifts in $\delta^{13}\text{C}_{\text{DIC}}$.

Dolomitization warrants special consideration and can occur in many ways in nature. The intimate co-occurrence of calcite and dolomite in the Red Lake carbonate platform means that they experienced the same metamorphic history, indicating against selective resetting of oxygen isotope compositions in dolomite during metamorphism. In modern environments, dolomite is commonly formed in restricted evaporative settings with hypersaline seawater (Friedman, 1980) imparting an isotopically heavier composition in $\delta^{18}\text{O}$. Lighter isotopic compositions of $\delta^{18}\text{O}$ in dolomites are typically interpreted to reflect the presence of isotopically light waters during dolomitization (Wright and Tucker, 1990). The consistently

lighter $\delta^{18}\text{O}$ isotopic composition of Red Lake dolomite suggests diagenetic alteration of the composition of $\delta^{18}\text{O}$ in dolomite. Under the microscope, both dolomite and calcite samples show twinning, and calcite grains commonly have thick twins which is an indication of deformation above 200°C (Ferrill et al., 2004). Raman analysis of Red Lake samples also confirms that the metamorphic temperature reached up to 550°C (M. Van Zuilen, personnel communication). Because of the high-grade metamorphism, no primary mineralogical features are preserved in the limestone and dolostone samples, and the recrystallization of carbonate grains makes it difficult to assess diagenetic fingerprints using petrography.

Sediment-buffered diagenesis tends to retain the original isotopic composition of sediments if the diagenetic fluid carries a low abundance of major elements contained in the sediments. Sediment-buffered diagenesis typically occurs on the seafloor where diffusion-driven fluid flow rates are low (Fantle et al., 2010), or in a setting with low concentrations of carbon-rich fluid. In contrast, fluid-buffered diagenesis can reset the isotopic composition of the primary carbonate sediments as the fluid-to-rock ratio for carbon becomes cumulatively higher due to high fluid flow rates. Fluid-buffered diagenesis commonly occurs in shallow water and peri-platform settings where buoyancy and geothermal convection-driven high fluid flow prevail (Henderson et al., 1999; Kohout, 1965). The Sr/Ca ratio tends to be comparatively high for sediment-buffered calcium carbonate rocks, and low for fluid-buffered diagenetic dolomite (Higgins et al., 2018), and the Red Lake limestone and dolostone samples show such a distribution in Sr/Ca ratios, with calcite samples possessing high Sr/Ca ratios and dolomites low Sr/Ca ratios (data not shown). Based on $\delta^{13}\text{C}$ data from the 0.77 to 0.59 Ga Otavi/Swakop platform (Kunene Region, Namibia), Hoffman and Lamothe (2019), reported that sediment-buffered diagenesis was occurring in foreslope areas while fluid-buffered diagenesis prevailed along lower foreslope. Fluid-buffered diagenetic processes usually generate positive covariation in $\delta^{13}\text{C}$ and $\delta^{18}\text{O}$ isotope compositions of marine carbonates (Kaufman and Knoll,

1995) and can be assessed using Mn/Sr ratios and isotopic values of $\delta^{18}\text{O}$ (Chang et al., 2020). If $\text{Mn/Sr} < 3$ and $\delta^{18}\text{O} > -10\text{‰}$, then it is suggestive of the preservation of primary signatures. A positive correlation between $\delta^{13}\text{C}$ and $\delta^{18}\text{O}$ is observed in the Red Lake carbonate samples (Figure 5.8A). However, the $\delta^{18}\text{O}$ values of Red Lake dolostone samples are consistently $< -10\text{‰}$, and not all of them have Mn/Sr ratios < 3 (data not shown). Due to the intense hydrothermal inputs, Archean seawater was more Mn-rich than modern seawater. Therefore, using Mn/Sr ratio as an alteration index for Archean carbonates may not be appropriate. Satkoski et al (2017) reported that Red Lake limestones have pristine Sr isotopic composition typical of seawater at that time, whereas the dolostone Sr isotope compositions show evidence of resetting. These data indicate that Sr isotope resetting occurred during dolomitization.

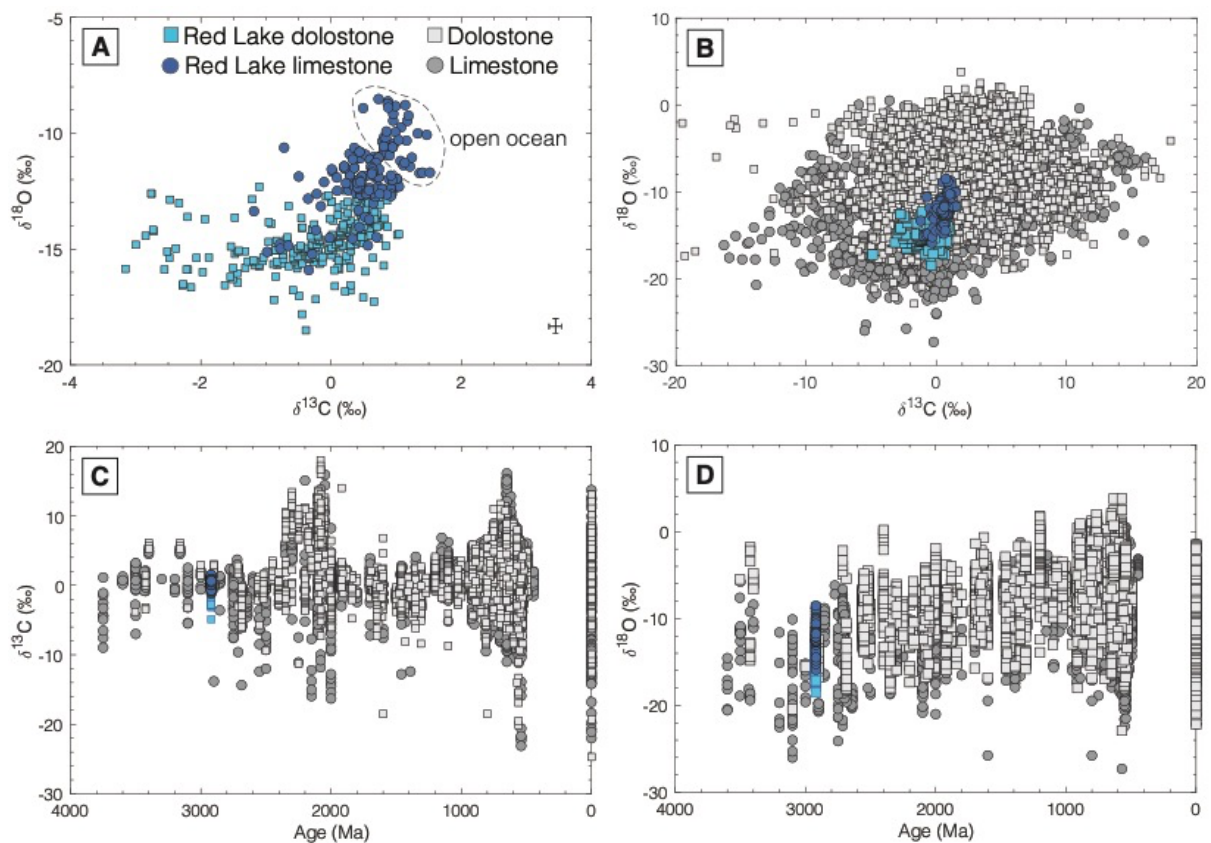


Figure 5.8. (A) $\delta^{13}\text{C}$ vs. $\delta^{18}\text{O}$ plot of Red Lake carbonates Error bars show 3σ values of $\delta^{13}\text{C}$ and $\delta^{18}\text{O}$. (B) Red Lake carbonates data with the global carbonate dataset (C) Geologic age vs. $\delta^{13}\text{C}$ plot. (D) Geologic age vs. $\delta^{18}\text{O}$ plot.

While it remains unclear exactly when diagenesis/dolomitization happened at Red Lake and by what diagenetic pathway, the interbedding of dolomite and calcite in the PB12-35 hole indicates that dolomitization was not regionalized, but rather restricted to individual units, suggesting that at least initial dolomitization processes occurred during early sediment diagenesis. Massive dolostones may occur at higher temperatures due to deep burial or hydrothermal dolomitization of calcite or aragonite precursors by Mg-rich fluids, and the formation of saddle dolomite is diagnostic of high temperature alteration processes (Gregg et al., 2015; Ryb and Eiler, 2018; Shuster et al., 2018). The presence of saddle dolomites and the sweeping extinction of Red Lake dolostone samples suggest high temperature secondary dolomitization to some degree, which is not unexpected given the upper greenschist / lower amphibolite facies metamorphism experienced by the carbonates. However, such processes cannot explain the dolomite and limestone interbedding in the PB12-35 core, which necessitates early diagenetic processes that affected one bed prior to deposition of the next bed. The ensemble of available evidence indicates that dolomite was formed during early diagenesis, but experienced recrystallization at high temperatures, generating saddle dolomite from pre-existing dolomite while the limestone remained undolomitized. It is likely that near-shore dolomitic carbonates underwent fluid-buffered diagenesis during sea level fall, while the deeper water calcic carbonates experienced only sediment-buffered diagenesis as they remained subaqueous. While future paragenetic sequence studies may better resolve this issue, the secular changes in isotopic values between the limestone and dolostone facies in the stratigraphic sequence, and their clear correlation with REE indicators for connectivity to the open ocean, indicates that water depth (i.e., periodic sea level oscillation) was an important control on isotopic compositions, and that the carbonates thus preserve some primary signatures that have not been erased by later overprinting.

5.5.2 Potential paleoenvironmental signals preserved in the Red Lake carbonate platform

Correlation between $\delta^{13}\text{C}$ and $\delta^{18}\text{O}$ in Red Lake carbonate samples shows a somewhat covariant relationship exists in the dataset for some of the samples (Figure 5.8A). In coastal environments, meteoric ground waters mix with marine pore fluids and sediments lithify rapidly (Land et al., 1987) which eventually results in a rough covariation between $\delta^{13}\text{C}$ and $\delta^{18}\text{O}$, i.e., $\delta^{13}\text{C}$ increases as $\delta^{18}\text{O}$ increases (Gross and Tracey Jr, 1966; Melim et al., 2001; Quinn and Matthews, 1990). Therefore, this type of relationship indicates that samples were formed in a meteoric and marine pore fluid mixing environment. In Figure 5.8A, the uppermost cluster (dotted circle) of samples is likely a representation of marine DIC-dominated pore fluid via open marine deposition of carbonates, and samples that are plotted towards the left denote those influenced by post-depositional alteration caused by late-stage deep burial diagenesis or metamorphism. The isotopic composition of $\delta^{18}\text{O}$ in dolostone samples differs from the isotopic composition of limestone samples, which is likely an indication of diagenetic alteration of the composition of $\delta^{18}\text{O}$ in dolostone. As discussed above, limestone and dolostone occur together in the Red Lake carbonate platform, they must have been metamorphosed simultaneously, and thus, resetting of the oxygen isotopic signature during metamorphism in the case of dolostone is ruled out. Overall, the isotopic composition of $\delta^{13}\text{C}$ and $\delta^{18}\text{O}$ is comparable with carbonates of different ages across geological times (Figures 5.8B, 5.8C, and 5.8D).

A comparison of the $\delta^{13}\text{C}$ and $\delta^{18}\text{O}$ values of Red Lake carbonates analyzed here with data from other Archean carbonates reveals that they are typical for the Archean. The $\delta^{13}\text{C}$ values of carbonate samples from the Mesoarchean Chobeni formation (2.96 Ga, Pongola Supergroup in South Africa) range from -2.4 to 2.5 ‰, where the 2.5 ‰ value of $\delta^{13}\text{C}$ obtained from the least altered carbonate samples has been suggested to represent DIC in coeval seawater

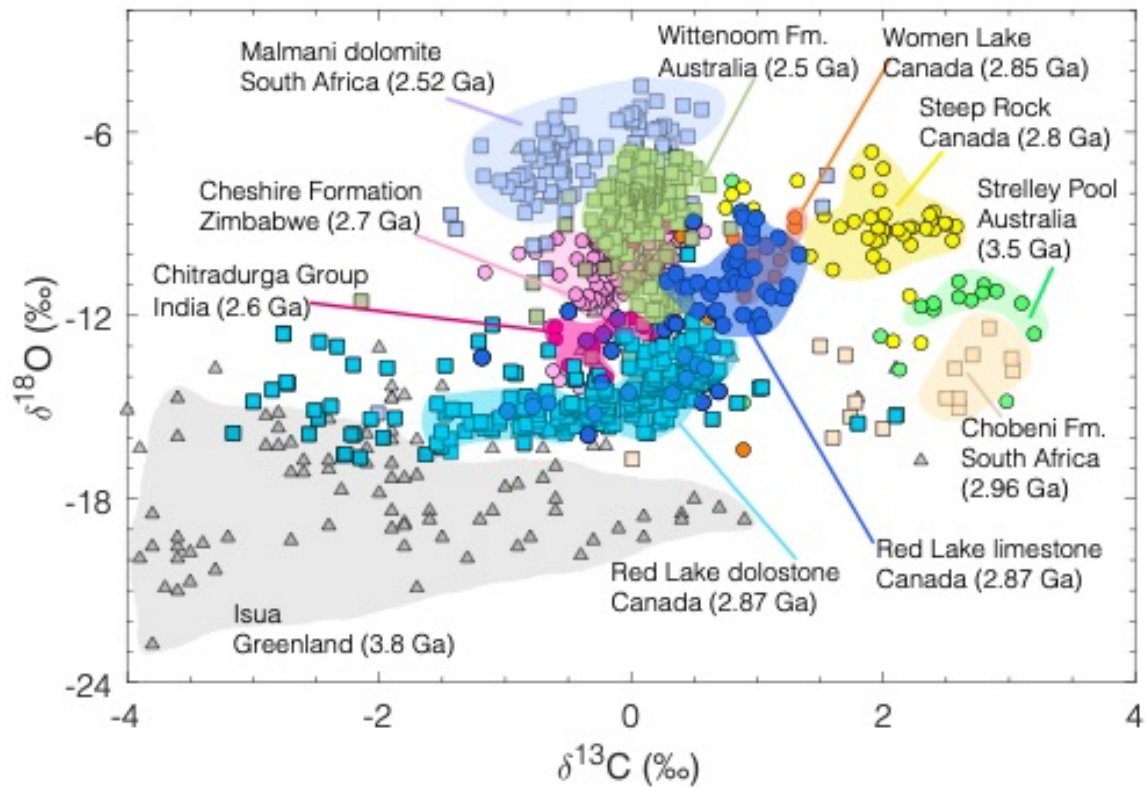


Figure 5.9. $\delta^{13}\text{C}$ vs. $\delta^{18}\text{O}$ plot for Archean (3.6 to 2.5 Ga) carbonates from different localities.

(Siahi et al., 2018). The $\delta^{18}\text{O}$ values of Chobeni carbonates range from -19.6 to -12.0 ‰, and the low $\delta^{18}\text{O}$ values have been interpreted as alteration of carbonates during greenschist facies metamorphism and isotopic exchange during meteoric/burial diagenesis (Siahi et al., 2018). The Woman Lake (2.86 Ga, Superior Craton in Canada) carbonates have $\delta^{13}\text{C}$ isotopic values ranging from -3.83 to 1.30 ‰, the light and heavy carbon isotopes being interpreted as derived from subtidal to upper intertidal flat and lower intertidal flat, respectively, while the $\delta^{18}\text{O}$ values range from -17.96 to -8.82 ‰, with depleted oxygen isotopes interpreted to represent alteration through burial diagenesis (Ramsay, 2020). The Mosher platform carbonates (2.80 Ga, Steep Rock Lake, Canada) have $\delta^{13}\text{C}$ values ranging from 0.1 to 2.7 ‰ (Fralick and Riding, 2015). The $\delta^{13}\text{C}$ and $\delta^{18}\text{O}$ values of the 2.62-2.55 Ga old shallow-marine Campbellrand-Malmani carbonate platform (South Africa) vary from -1.6 to 0.4 ‰ and -13.2 to -5.4 ‰,

respectively, for lagoonal and intertidal carbonates (Eroglu et al., 2017). The $\delta^{13}\text{C}$ and $\delta^{18}\text{O}$ isotopic compositions of limestone and dolostone samples in the Red Lake carbonate platform are thus comparable with the isotopic values of carbonates in these other Archean carbonate platforms (Figure 5.9). It is interesting to note that Mesoarchean carbonates display a slightly heavier carbon isotopic composition relative to Neoarchean carbonates. The most positive $\delta^{13}\text{C}$ values in Mesoarchean carbonates that are most likely to represent the mean ocean DIC pool vary between 0.5 to 2.5 ‰, but in Neoarchean, $\delta^{13}\text{C}$ values shifted towards zero (Figure 5.9). Such an isotopic compositional shift between the Mesoarchean and Neoarchean would typically be interpreted as relating to differences in the burial of organic carbon and/or the productivity of the marine environment; this is explored below through an isotopic mass balance model for the pre-platform Archean carbon cycle.

There are different opinions regarding the interpretation of oxygen isotope values in chemical sediments preserved in the ancient rock record (Galili et al., 2019; Kasting et al., 2006; Muehlenbachs and Clayton, 1976). It has been reported that Archean chemical sedimentary rocks usually have lower (by ~6 to 10 ‰) $\delta^{18}\text{O}$ values relative to modern carbonates (Knauth, 2005; Knauth and Lowe, 2003; Shields and Veizer, 2002; Veizer and Hoefs, 1976). The controlling factors of the oxygen isotope composition of global seawater are surface and seafloor weathering and hydrothermal alteration resulting in isotope exchange with near-zero silicate reservoirs (Alt et al., 1986). Hydrothermal alteration of the oceanic crust occurs largely at elevated temperatures (up to ~300–350 °C) (Bowers and Taylor Jr, 1985), and if hydrothermal alteration of oceanic crust alone dominated the oxygen isotope budget of the oceans, the $\delta^{18}\text{O}_{\text{VSMOW}}$ of seawater would be ~6 ‰ (Ryb and Eiler, 2018).

Kasting et al. (2006) affirm that significant secular trends remain in the oxygen isotope of chemical sedimentary rocks even after considering potential diagenetic and metamorphic effects, and thus that the residual $\delta^{18}\text{O}$ isotope trend towards heavier values in chemical

sedimentary rocks over time must be related to the properties of ancient seawater. There is a significant debate, however, as to whether this trend is a reflection of seawater temperature and its control over the equilibrium isotope fractionation between seawater and chemical sediments, or whether it was driven by important secular evolution in the oxygen isotope composition of seawater. Minerals precipitating at low temperatures characteristic of modern seawater show temperature-dependent isotope equilibrium enrichment in $\delta^{18}\text{O}$, while minerals forming at higher temperatures show muted enrichment (Muehlenbachs and Clayton, 1976). As mentioned above, the isotopic composition of oxygen in seawater is controlled over long timescales by the exchange between oxygen in water and in silicate rocks, where the $\delta^{18}\text{O}$ of unaltered silicate rocks is 5.7 ‰ heavier compared to modern seawater (Muehlenbachs, 1998; Muehlenbachs and Clayton, 1976; Walker and Lohmann, 1989; Wallmann, 2001). During seawater-rock interaction, the isotopic composition of seawater moves towards increasing $\delta^{18}\text{O}$ during high-temperature hydrothermal circulation whereas the isotopic composition of seawater moves towards decreasing $\delta^{18}\text{O}$ if isotope exchange during seawater-rock interaction is less efficient (Kasting et al., 2006). The isotopic trend towards lower sedimentary $\delta^{18}\text{O}$ values in deep time should be considered a primary signal as it is global and not related to mineralogy, metamorphism, or depositional settings (Jaffrés et al., 2007). Galili et al. (2019) explored two hypotheses that might explain secular rise of $\delta^{18}\text{O}$ since Archean. First, a change in seawater $\delta^{18}\text{O}$ through time may have occurred (Jaffrés et al., 2007; Veizer et al., 1999; Walker and Lohmann, 1989), and second, higher seawater temperatures in the early ocean may have muted isotopic fractionation between water and chemical carbonates and silicates, driving $\delta^{18}\text{O}$ towards lower values (Knauth and Epstein, 1976; Knauth and Lowe, 2003; Robert and Chaussidon, 2006). The first suggests that the temperature at Earth's surface was relatively constant throughout Earth's history, while the second implies significantly higher seawater in the deep past and buffering of seawater by seawater-rock interaction with modern-like

efficiency, maintaining seawater $\delta^{18}\text{O}$ to 0 ± 1 ‰ (Vienna standard mean ocean water (VSMOW)) through time.

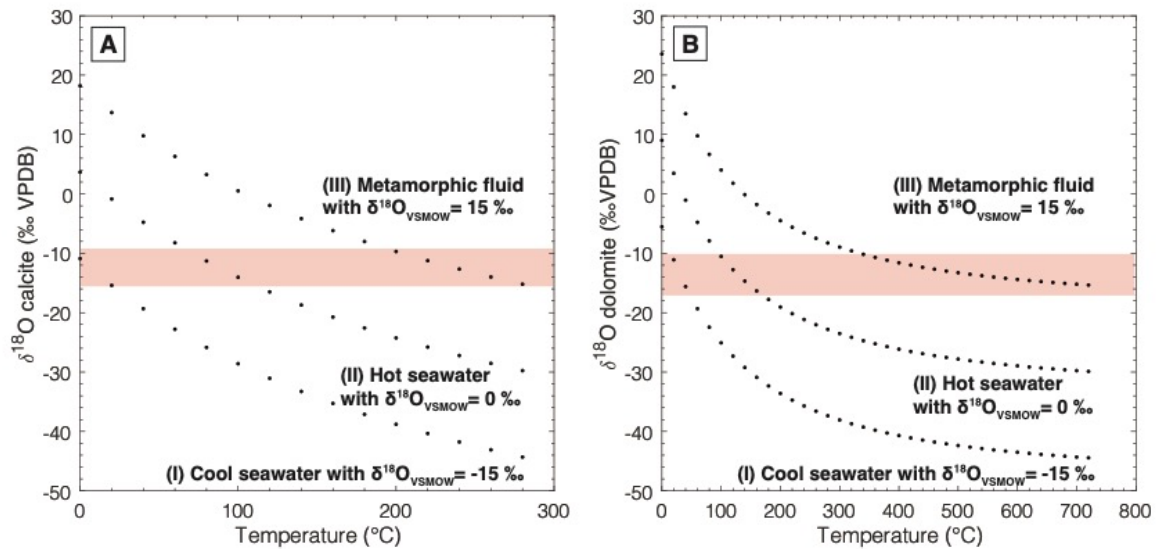


Figure 5.10. (A) and (B) Plots of $\delta^{18}\text{O}_{\text{calcite}}$ and $\delta^{18}\text{O}_{\text{dolomite}}$ values against temperature. These data were calculated using Horita, 2014 equation assuming modeled $\delta^{18}\text{O}_{\text{calcite}}$ and $\delta^{18}\text{O}_{\text{dolomite}}$ compositions are at equilibrium with -15 ‰ to +15 ‰ water of $\delta^{18}\text{O}_{\text{VSMOW}}$.

Assuming a primary $\delta^{18}\text{O}$ signature in calcium carbonate, the temperature of precipitation and/or early diagenesis temperature can be calculated with simple assumptions, namely adopting the temperature-dependence of equilibrium isotope exchange between calcite and water and assigning a value for the original seawater $\delta^{18}\text{O}$ composition (relative to VSMOW). The $^{18}\text{O}/^{16}\text{O}$ fractionation factors of (proto)dolomite–water, $10^3 \ln \alpha_{\text{dolomite-water}} = 3.140(\pm 0.022) \cdot 10^6/T^2 - 3.14(\pm 0.11)$, are here used to calculate the temperature–source water driven $\delta^{18}\text{O}$ variations expected for dolostone samples (Horita, 2014). In combination with the calcite–water equation (Friedman and O’Neil, 1977; O’Neil et al., 1969), the $^{18}\text{O}/^{16}\text{O}$ fractionation factors of (proto)dolomite–calcite, $10^3 \ln \alpha_{\text{dolomite-calcite}} = 0.351(\pm 0.028) \cdot 10^6/T^2 - 0.25(\pm 0.13)$ are also calculated (Horita, 2014). These equations together provide a wide range of temperature and $\delta^{18}\text{O}_{\text{VSMOW}}$ values of sources that might explain the observed $^{18}\text{O}/^{16}\text{O}$

fractionation. Calculated dolomite and calcite formation temperatures are inversely correlated with $\delta^{18}\text{O}$ values (Figure 5.10). In this figure, plots of precipitation/recrystallization temperatures vs. $\delta^{18}\text{O}_{\text{calcite}}$ and $\delta^{18}\text{O}_{\text{dolomite}}$ present three likely scenarios that can account for the $\delta^{18}\text{O}$ compositions of both the calcites and the dolomites analyzed in this study.

For calcites, the three scenarios are: (I) if the original $\delta^{18}\text{O}_{\text{VSMOW}}$ of seawater is assumed to be significantly lighter in deep time as per the findings of Galili et al. (2019), in this case, set at -15 ‰, the calcite crystallization temperature would be $< 40^\circ\text{C}$, indicating a cooler ocean; (II) if seawater is fixed at $\delta^{18}\text{O}_{\text{VSMOW}} = 0$ ‰, the calcite crystallization temperature would be around 70°C , and thus represent a significantly warmer ocean in deep geological time; and finally, (III) to achieve carbonates in equilibrium with metamorphic fluids at around $\delta^{18}\text{O}_{\text{VSMOW}} = 15$ ‰, the crystallization temperature would be ca. 200°C . The same scenarios for dolomite indicate either (I) $< 40^\circ\text{C}$ crystallization temperatures from seawater with $\delta^{18}\text{O}_{\text{VSMOW}}$ values around -15 ‰; (II) crystallization of dolomite at ca. 120°C for seawater buffered to $\delta^{18}\text{O}_{\text{VSMOW}}$ ca. 0 ‰, and (III) dolomite formation at $> 300^\circ\text{C}$ from metamorphic fluids with $\delta^{18}\text{O}_{\text{VSMOW}}$ ca. 15 ‰. As explained above, scenario (III) is counter indicated, and the covariation of $\delta^{18}\text{O}$ carbonate values with REE indicators of the different carbonate depositional environments argue against scenario (II), it remains difficult at present to confidently distinguish between the different scenarios, a long-standing problem in the interpretation of the $\delta^{18}\text{O}$ composition of ancient chemical sediments for which this new data cannot resolve alone.

5.5.3 Isotope mass balance in the Mesoarchean carbon cycle: the carbon lever model revisited

The simple observation that thick carbonate platforms only begin to be preserved in the rock record from ca. 2.9 Ga onwards, starting with Red Lake, means that the Mesoarchean carbon cycle was necessarily different than today simply by the fact that sedimentary

Chapter 5: Carbon and Oxygen Isotope Chemostratigraphy

carbonates were apparently rare, whereas today they represent the most important long term geological sink for carbon at Earth's surface. Here, a simple carbon isotope mass balance model is explored in order to attempt to understand how the carbon cycle might have operated in the Mesoarchean prior to the onset of significant carbonate sedimentation on Earth. For this, we revisit the carbon lever model (Holland, 1984), which has long been utilized to interpret excursions in the carbon stable isotope composition of carbonates in sedimentary records. In this model, the carbon isotope composition of inputs is equal to the carbon isotope composition of carbon sinks. This model traditionally considers only two sinks: organic carbon burial (expressed as a fraction of the total carbon exiting Earth's surface as subducted organic matter, F_{org}) and carbonate or inorganic carbon burial (calculated as $1 - F_{\text{org}}$). The model is thus defined as:

$$\delta^{13}\text{C}_{\text{inputs}} = \delta^{13}\text{C}_{\text{org}} F_{\text{org}} + \delta^{13}\text{C}_{\text{carb}} (1 - F_{\text{org}})$$

Organic carbon with an isotopically light stable isotope composition ($\delta^{13}\text{C}_{\text{org}}$, generally ca. -22 to -25 throughout most of Earth's history) is sequestered from the surface environment during burial of organic matter, pushing the isotope composition of the residual surface reservoir to values above the input flux, which is dominated by mantellic inputs with $\delta^{13}\text{C}$ values around -5 ‰. Carbonate precipitation occurs with only minor carbon isotope fractionation, thus recording the composition of the residual surface reservoir. Calculated for today, with a $\delta^{13}\text{C}_{\text{org}}$ value of ~-25‰ for sedimentary organic matter and with a mean global sedimentary carbonate $\delta^{13}\text{C}_{\text{carb}}$ value of around 0 ‰, the carbon lever model indicates that approximately 20% of surface carbon exits Earth's surface as organic matter ($F_{\text{org}} = 0.2$) while the remaining 80% exists as sedimentary carbonates ($F_{\text{carb}} = 1 - F_{\text{org}} = 0.8$). In this framework, positive $\delta^{13}\text{C}$ excursions in carbonates are interpreted to represent significant organic carbon burial events, while negative $\delta^{13}\text{C}$ excursions represent re-mineralization and re-injection of

large amounts of organic carbon into the surface CO₂ reservoir. This leads to the longstanding conundrum that organic vs. inorganic carbon burial fluxes throughout geological time must be remained in a relatively constant proportion in order to maintain $\delta^{13}\text{C}_{\text{carb}}$ values near zero for billions of years, as observed in the rock record. This conclusion appears untenable in the face of a carbonate-poor Paleo- to Meso-archean Earth. Furthermore, this model, by attributing the entire carbon exit flux to sedimentary carbonates and organic matter, fails to consider other potential sinks that may have been particularly important in deep time, such as carbonization of the seafloor.

The oceanic crust has long been considered a potential sink for carbon, and all available evidence indicates that it acts as an important sink in the global carbon budget (Alt and Teagle, 1999; Brady and Gíslason, 1997; Caldeira, 1995; Staudigel et al., 1989), yet it is ignored in the carbon isotope lever model. Basalt in the oceanic crust participates in the surface carbon cycle by the uptake of CO₂ during seafloor weathering and precipitation of carbonates in the upper crust (Brady and Gíslason, 1997; Francois and Walker, 1992). Uptake of CO₂ by the oceanic crust occurs within the upper few hundred meters of the crust, predominately, at low temperatures (0 - 60°C), and the carbonate content decreases with depth but increases with the aging of crust, i.e., older oceanic ocean crust and has a higher carbon content than the younger oceanic crust (Alt and Teagle, 1999). Decarbonation during the subduction of altered ocean crust is an important mantellic source of CO₂ to the atmosphere (Caldeira, 1995; Kerrick and Connolly, 1998), completing the cycle. There are three potential ways by which carbonates can be incorporated into the upper crust: (I) seawater Ca reacts with bicarbonate (HCO₃⁻) and adds CaCO₃ from seawater to the crust; (II) exchange between basaltic Ca and seawater Mg and then Ca reacts with seawater bicarbonate; (III) dissolution of Ca-silicates from basalt due to intake of CO₂ during submarine weathering and consequent precipitation of CaCO₃ (Alt and Teagle, 1999). There exists relatively few data at present regarding the importance of this sink

in the modern carbon cycle. Alt and Teagle (1999) examined four different IODP drill sites in the Pacific ocean spanning in age from 6 to 165 Ma, and measured carbon content and carbonate vein distribution in seafloor basalts, demonstrating enrichments of up to 4.5 wt. % CO₂ and an increase of carbonate veining with age. Only limited $\delta^{13}\text{C}$ data has been reported for the carbon isotope composition of calcite veins in seafloor basalts. The $\delta^{13}\text{C}$ values of carbonates in the Macquarie Island ophiolite reveal that the isotopic composition of calcite varies from -9.7 to 3.2 ‰, with an average of ca. -5 ‰ (Cocker et al., 1982). This means that seafloor carbonization represents an exit flux that is close in isotopic composition to the mantle input flux, and its role in carbon isotope mass balance may be muted or otherwise cryptic. However, recent estimates for the carbonization exit flux surprisingly indicate that rather than constituting a minor component of Earth's surface carbon cycle, it may in fact be the most important exit flux today; Dasgupta and Hirschmann (2010) estimate that basalt-hosted calcite veins found in modern subduction zones capture approximately 80% of surface carbon entering into subduction, whereas the sedimentary carbonate exit flux (the sum of sedimentary carbonate and organic matter) accounts for only 20% of the total carbon flux exiting Earth's surface. Such an important potential revision to the modern carbon cycle is particularly attractive for application to the Paleo- to Meso-archean carbon cycle when the sedimentary carbonate exit flux was significantly depressed or non-existent at times due to the dearth of sedimentary carbonates.

We, therefore, revisit the carbon lever hypothesis by considering seafloor carbonatization as an additional term that may have affected the carbon cycle and contributed to stabilizing the carbon isotope composition of carbonates back into deep geological time. We can rewrite the carbon lever equation considering seafloor basalt as an additional potential sink for carbon as follows:

Chapter 5: Carbon and Oxygen Isotope Chemostratigraphy

$$\delta^{13}\text{C}_{\text{inputs}} = \delta^{13}\text{C}_{\text{org}} F_{\text{org}} + \delta^{13}\text{C}_{\text{carb}} F_{\text{carb}} + \delta^{13}\text{C}_{\text{seafloor}} F_{\text{seafloor}}$$

$$\text{or } \delta^{13}\text{C}_{\text{carb}} = (\delta^{13}\text{C}_{\text{inputs}} - \delta^{13}\text{C}_{\text{org}} F_{\text{org}} - \delta^{13}\text{C}_{\text{seafloor}} F_{\text{seafloor}}) / F_{\text{carb}}$$

and

$$F_{\text{org}} + F_{\text{carb}} + F_{\text{seafloor}} = 1$$

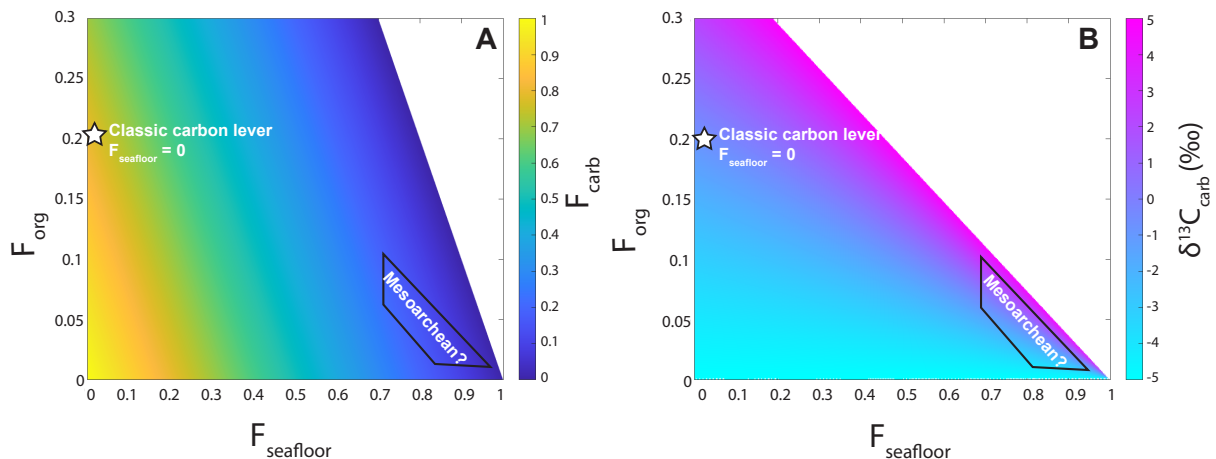


Figure 5.11. Interdependence of carbon exit fluxes (A) and the resulting expected $\delta^{13}\text{C}_{\text{carb}}$ values (B) for a revised carbon lever isotope mass balance model with seafloor carbonatization included as a potentially important carbon exit flux.

A simple model was constructed by assuming the following stable isotope compositions, which appear relatively invariant in $\delta^{13}\text{C}$ within a few per mille for most of the geological time, for the various sources and sinks: $\delta^{13}\text{C}_{\text{inputs}} = -5 \text{ ‰}$, $\delta^{13}\text{C}_{\text{seafloor}} = -5 \text{ ‰}$, $\delta^{13}\text{C}_{\text{org}} = -22 \text{ ‰}$, and $\delta^{13}\text{C}_{\text{carb}} = 0 \text{ ‰}$. The results of this model are presented in Figure 5.11, where the expected $\delta^{13}\text{C}_{\text{carb}}$ values can be calculated for any combination of F_{org} , F_{carb} , and F_{seafloor} that always sum to 1. It's important to note that F_{org} and F_{carb} are not directly comparable to values calculated using the classic carbon lever model, as the introduction of the seafloor sink diminishes the relative importance of organic carbon and sedimentary carbonate burial in the total budget as the seafloor burial flux grows. In this model, at the low F_{carb} values expected of the

Mesoarchean (and Paleoarchean for that matter) before the rise of carbonate platforms on Earth, near-zero $\delta^{13}\text{C}_{\text{carb}}$ values are readily maintained at across a range of realistic (near-modern or below) F_{org} values, as long as the seafloor weathering exit flux remains an important part of the geological carbon cycle. Without this additional sink, carbon isotope mass balance depends solely on the relative importance of organic and sedimentary carbonate burial, and thus the size of the biosphere must scale down with decreasing sedimentary carbonate sinks in deep geological time. This model is attractive as it permits the establishment of an important biosphere on the Archean Earth despite decreased sedimentary carbonate abundances, but perhaps more importantly, it might explain why sedimentary carbonates are relatively static in their carbon stable isotope compositions over geological time, despite dramatic swings in the importance of carbon sinks on Earth (e.g., the rise of carbonate platforms as examined here). Seafloor carbonatization is thus an attractive and perhaps significantly underestimated sink for carbon over geological timescales that would explain how the surface carbon cycle remained relatively unperturbed from a carbon isotope point of view despite the rise of thick carbonate platforms, beginning in the Mesoarchean with the Red Lake carbonate platform.

5.6 Conclusions

The detailed carbon and oxygen stable isotope chemostratigraphy of the > 200 m thick carbonate package constituting the entire thickness of the Mesoarchean Red Lake carbonate platform unveils critical information regarding post-depositional alteration as well as the Mesoarchean carbon cycle. The stromatolitic dolostones of shallow-water origin and the deeper-water limestone samples show a strong mineralogical control on stable isotopic compositions of $\delta^{13}\text{C}$ and $\delta^{18}\text{O}$, which could be related to the sea-level change and the accompanying meteoric water infiltration that may have driven dolomitization on the shallow parts of the platform. Combined with rare earth element systematics, the $\delta^{13}\text{C}$ and $\delta^{18}\text{O}$ isotopic compositions of limestone imply that their relatively heavier $\delta^{13}\text{C}$ (> 0.5 ‰) and $\delta^{18}\text{O}$ (> -10

Chapter 5: Carbon and Oxygen Isotope Chemostratigraphy

‰) values may reflect that they captured the open ocean DIC pool. The lighter $\delta^{13}\text{C}$ signatures in dolostone samples and some limestones show a correlation with TOC content that in some cases may be attributed to enhanced contributions from organic matter in productive shallow waters. The consistently lighter $\delta^{18}\text{O}$ values in dolostone samples indicate meteoric water interaction during dolomitization and but are unlikely to be related to metamorphism or hydrothermal alteration. Finally, a revised version of the carbon lever hypothesis is presented and reveals that seafloor carbonization is an attractive solution to explain the stability in $\delta^{13}\text{C}$ in carbonates in deep geological time prior to the rise of carbonate platforms in the Mesoproterozoic.

5.7 References

- Abell, P.I., McClory, J., Martin, A., Nisbet, E.G., 1985a. Archaean stromatolites from the Ngesi Group, Belingwe greenstone belt, Zimbabwe; preservation and stable isotopes—preliminary results. *Precambrian Res.* 27, 357–383.
- Abell, P.I., McClory, J., Martin, A., Nisbet, E.G., Kyser, T.K., 1985b. Petrography and stable isotope ratios from Archaean stromatolites, Mushandike Formation, Zimbabwe. *Precambrian Res.* 27, 385–398.
- Afroz, M., Fralick, P.W., Lalonde, S. V, 2023. Sedimentology and geochemistry of basinal lithofacies in the Mesoarchean (2.93 Ga) Red Lake carbonate platform, northwest Ontario, Canada. *Precambrian Res.* 388, 106996.
<https://doi.org/https://doi.org/10.1016/j.precamres.2023.106996>
- Alt, J.C., Muehlenbachs, K., Honnorez, J., 1986. An oxygen isotopic profile through the upper kilometer of the oceanic crust, DSDP Hole 504B. *Earth Planet. Sci. Lett.* 80, 217–229.
- Alt, J.C., Teagle, D.A.H., 1999. The uptake of carbon during alteration of ocean crust. *Geochim. Cosmochim. Acta* 63, 1527–1535.
- Banner, J.L., Hanson, G.N., 1990. Calculation of simultaneous isotopic and trace element variations during water-rock interaction with applications to carbonate diagenesis. *Geochim. Cosmochim. Acta* 54, 3123–3137.
- Becker, R.H., Clayton, R.N., 1972. Carbon isotopic evidence for the origin of a banded iron-formation in Western Australia. *Geochim. Cosmochim. Acta* 36, 577–595.
[https://doi.org/https://doi.org/10.1016/0016-7037\(72\)90077-4](https://doi.org/https://doi.org/10.1016/0016-7037(72)90077-4)
- Berner, R.A., 2006. GEOCARBSULF: a combined model for Phanerozoic atmospheric O₂ and CO₂. *Geochim. Cosmochim. Acta* 70, 5653–5664.
- Beukes, N.J., Klein, C., Kaufman, A.J., Hayes, J.M., 1990. Carbonate petrography, kerogen distribution, and carbon and oxygen isotope variations in an early Proterozoic transition from limestone to iron-formation deposition, Transvaal Supergroup, South Africa. *Econ. Geol.* 85, 663–690. <https://doi.org/10.2113/gsecongeo.85.4.663>
- Bowers, T.S., Taylor Jr, H.P., 1985. An integrated chemical and stable-isotope model of the origin of midocean ridge hot spring systems. *J. Geophys. Res. Solid Earth* 90, 12583–12606.
- Brady, P. V, Gíslason, S.R., 1997. Seafloor weathering controls on atmospheric CO₂ and global climate. *Geochim. Cosmochim. Acta* 61, 965–973.
- Bristow, T.F., Kennedy, M.J., 2008. Carbon isotope excursions and the oxidant budget of the Ediacaran atmosphere and ocean. *Geology* 36, 863–866.
- Broecker, W.S., 1970. A boundary condition on the evolution of atmospheric oxygen. *J. Geophys. Res.* 75, 3553–3557.
- Broecker, W.S., Peng, T.-H., 1982. Tracers in the Sea. *Lamont-Doherty Geological*

Observatory, Columbia University Palisades, New York.

- Caldeira, K., 1995. Long-term control of atmospheric carbon dioxide; low-temperature seafloor alteration or terrestrial silicate-rock weathering? *Am. J. Sci.* 295, 1077–1114.
- Chang, B., Li, C., Liu, D., Foster, I., Tripathi, A., Lloyd, M.K., Maradiaga, I., Luo, G., An, Z., She, Z., 2020. Massive formation of early diagenetic dolomite in the Ediacaran ocean: Constraints on the “dolomite problem.” *Proc. Natl. Acad. Sci.* 117, 14005–14014.
- Choquette, P., James, N., 1987. Diagenesis# 12. Diagenesis in Limestones-3. The deep burial environment. *Geosci. Canada* 14, 3–35.
- Cocker, J.D., Griffin, B.J., Muehlenbachs, K., 1982. Oxygen and carbon isotope evidence for seawater-hydrothermal alteration of the Macquarie Island ophiolite. *Earth Planet. Sci. Lett.* 61, 112–122.
- Corfu, F., Wallace, H., 1986. U–Pb zircon ages for magmatism in the Red Lake greenstone belt, northwestern Ontario. *Can. J. Earth Sci.* 23, 27–42. <https://doi.org/10.1139/e86-004>
- Dasgupta, R., Hirschmann, M.M., 2010. The deep carbon cycle and melting in Earth’s interior. *Earth Planet. Sci. Lett.* 298, 1–13.
- Epstein, S., Buchsbaum, R., Lowenstam, H., Urey, H.C., 1951. Carbonate-water isotopic temperature scale. *Geol. Soc. Am. Bull.* 62, 417–426.
- Eroglu, S., van Zuilen, M.A., Taubald, H., Drost, K., Wille, M., Swanner, E.D., Beukes, N.J., Schoenberg, R., 2017. Depth-dependent $\delta^{13}\text{C}$ trends in platform and slope settings of the Campbellrand-Malmani carbonate platform and possible implications for Early Earth oxygenation. *Precambrian Res.* 302, 122–139.
- Fairchild, I.J., Kennedy, M.J., 2007. Neoproterozoic glaciation in the Earth System. *J. Geol. Soc. London.* 164, 895–921.
- Fantle, M.S., Maher, K.M., DePaolo, D.J., 2010. Isotopic approaches for quantifying the rates of marine burial diagenesis. *Rev. Geophys.* 48.
- Ferrill, D.A., Morris, A.P., Evans, M.A., Burkhard, M., Groshong Jr, R.H., Onasch, C.M., 2004. Calcite twin morphology: a low-temperature deformation geothermometer. *J. Struct. Geol.* 26, 1521–1529.
- Fischer, W.W., Schroeder, S., Lacassie, J.P., Beukes, N.J., Goldberg, T., Strauss, H., Horstmann, U.E., Schrag, D.P., Knoll, A.H., 2009. Isotopic constraints on the Late Archean carbon cycle from the Transvaal Supergroup along the western margin of the Kaapvaal Craton, South Africa. *Precambrian Res.* 169, 15–27.
- Fralick, P., Riding, R., 2015. Steep Rock Lake: Sedimentology and geochemistry of an Archean carbonate platform. *Earth-Science Rev.* 151, 132–175. <https://doi.org/10.1016/j.earscirev.2015.10.006>
- Francois, L.M., Walker, J.C.G., 1992. Modelling the Phanerozoic carbon cycle and climate; constraints from the $^{87}\text{Sr}/^{86}\text{Sr}$ isotopic ratio of seawater. *Am. J. Sci.* 292, 81–135.

- Friedman, G.M., 1980. Dolomite is an evaporite mineral: Evidence from the rock record and from sea marginal ponds of the red sea. *Soc. Econ. Paleontol. Mineral. SEPM Spec.*, 69–80.
- Friedman, I., O’Neil, J.R., 1977. *Data of Geochemistry: Compilation of stable isotope fractionation factors of geochemical interest*. Chapter KK. US Government Printing Office.
- Galili, N., Shemesh, A., Yam, R., Brailovsky, I., Sela-Adler, M., Schuster, E.M., Collom, C., Bekker, A., Planavsky, N., Macdonald, F.A., 2019. The geologic history of seawater oxygen isotopes from marine iron oxides. *Science* (80-). 365, 469–473.
- Gregg, J.M., Bish, D.L., Kaczmarek, S.E., Machel, H.G., 2015. Mineralogy, nucleation and growth of dolomite in the laboratory and sedimentary environment: a review. *Sedimentology* 62, 1749–1769.
- Gross, M.G., Tracey Jr, J.I., 1966. Oxygen and carbon isotopic composition of limestones and dolomites, Bikini and Eniwetok Atolls. *Science* (80-). 151, 1082–1084.
- Heimann, A., Johnson, C.M., Beard, B.L., Valley, J.W., Roden, E.E., Spicuzza, M.J., Beukes, N.J., 2010. Fe, C, and O isotope compositions of banded iron formation carbonates demonstrate a major role for dissimilatory iron reduction in ~2.5Ga marine environments. *Earth Planet. Sci. Lett.* 294, 8–18.
<https://doi.org/https://doi.org/10.1016/j.epsl.2010.02.015>
- Henderson, G.M., Slowey, N.C., Haddad, G.A., 1999. Fluid flow through carbonate platforms: Constraints from ²³⁴U/²³⁸U and Cl⁻ in Bahamas pore-waters. *Earth Planet. Sci. Lett.* 169, 99–111.
- Higgins, J.A., Blättler, C.L., Lundstrom, E.A., Santiago-Ramos, D.P., Akhtar, A.A., Ahm, A.S.C., Bialik, O., Holmden, C., Bradbury, H., Murray, S.T., 2018. Mineralogy, early marine diagenesis, and the chemistry of shallow-water carbonate sediments. *Geochim. Cosmochim. Acta* 220, 512–534.
- Hoffman, P.F., Lamothe, K.G., 2019. Seawater-buffered diagenesis, destruction of carbon isotope excursions, and the composition of DIC in Neoproterozoic oceans. *Proc. Natl. Acad. Sci.* 116, 18874–18879.
- Hofmann, H.J., Thurston, P.C., Wallace, H., 1985. Archean stromatolites from Uchi greenstone belt, northwestern Ontario, in: *Evolution of Archean Supracrustal Sequences*. *Geol. Assoc. Can. Spec. Pap.*, pp. 125–132.
- Holland, H.D., 1984. *The Chemical Evolution of the Oceans and Atmosphere*. Princet. Univ. Press. Princet. Farquhar J, Zerkle A, Bekker A *Geol. geochemical constraints Earth’s early Atmos. Treat Geochem* 6, 91–138.
- Holland, H.D., 1978. *The chemistry of the atmosphere and oceans*.
- Horita, J., 2014. Oxygen and carbon isotope fractionation in the system dolomite–water–CO₂ to elevated temperatures. *Geochim. Cosmochim. Acta* 129, 111–124.
- Jaffrés, J.B.D., Shields, G.A., Wallmann, K., 2007. The oxygen isotope evolution of

- seawater: A critical review of a long-standing controversy and an improved geological water cycle model for the past 3.4 billion years. *Earth-Science Rev.* 83, 83–122. <https://doi.org/10.1016/j.earscirev.2007.04.002>
- Kasting, J.F., Howard, M.T., Wallmann, K., Veizer, J., Shields, G., Jaffrés, J., 2006. Paleoclimates, ocean depth, and the oxygen isotopic composition of seawater. *Earth Planet. Sci. Lett.* 252, 82–93.
- Kaufman, A.J., Hayes, J.M., Klein, C., 1990. Primary and diagenetic controls of isotopic compositions of iron-formation carbonates. *Geochim. Cosmochim. Acta* 54, 3461–3473. [https://doi.org/https://doi.org/10.1016/0016-7037\(90\)90298-Y](https://doi.org/https://doi.org/10.1016/0016-7037(90)90298-Y)
- Kaufman, A.J., Knoll, A.H., 1995. Neoproterozoic variations in the C-isotopic composition of seawater: stratigraphic and biogeochemical implications. *Precambrian Res.* 73, 27–49. [https://doi.org/https://doi.org/10.1016/0301-9268\(94\)00070-8](https://doi.org/https://doi.org/10.1016/0301-9268(94)00070-8)
- Kerrick, D.M., Connolly, J.A.D., 1998. Subduction of ophiicarbonates and recycling of CO₂ and H₂O. *Geology* 26, 375–378.
- Knauth, L.P., 2005. Temperature and salinity history of the Precambrian ocean: implications for the course of microbial evolution, in: *Geobiology: Objectives, Concepts, Perspectives*. Elsevier, pp. 53–69.
- Knauth, L.P., Epstein, S., 1976. Hydrogen and oxygen isotope ratios in nodular and bedded cherts. *Geochim. Cosmochim. Acta* 40, 1095–1108.
- Knauth, L.P., Kennedy, M.J., 2009. The late Precambrian greening of the Earth. *Nature* 460, 728–732.
- Knauth, L.P., Lowe, D.R., 2003. High Archean climatic temperature inferred from oxygen isotope geochemistry of cherts in the 3.5 Ga Swaziland Supergroup, South Africa. *Geol. Soc. Am. Bull.* 115, 566–580.
- Knoll, A.H., Hayes, J.M., Kaufman, A.J., Swett, K., Lambert, I.B., 1986. Secular variation in carbon isotope ratios from Upper Proterozoic successions of Svalbard and East Greenland. *Nature* 321, 832–838.
- Kohout, F.A., 1965. A hypothesis concerning cyclic flow of salt water related to geothermal heating in the Floridan aquifer. *Trans. N. Y. Acad. Sci.* 28, 249–271.
- Kump, L.R., Arthur, M.A., 1999. Interpreting carbon-isotope excursions: carbonates and organic matter. *Chem. Geol.* 161, 181–198.
- Land, L.S., Milliken, K. Lou, McBride, E.F., 1987. Diagenetic evolution of Cenozoic sandstones, Gulf of Mexico sedimentary basin. *Sediment. Geol.* 50, 195–225.
- Masters, T., Benestad, R., 2013. Comment on “The phase relation between atmospheric carbon dioxide and global temperature.” *Glob. Planet. Change* 106, 141–142.
- McIntyre, T., Fralick, P., 2017. Sedimentology and Geochemistry of the 2930 Ma Red Lake-Wallace Lake Carbonate Platform, Western Superior Province, Canada. *Depos. Rec.* 3, 258–287. <https://doi.org/10.1002/dep2.36>

- Melezhik, V.A., Fallick, A.E., Smirnov, Y.P., Yakovlev, Y.N., 2003. Fractionation of carbon and oxygen isotopes in ^{13}C -rich Palaeoproterozoic dolostones in the transition from medium-grade to high-grade greenschist facies: a case study from the Kola Superdeep Drillhole. *J. Geol. Soc. London*. 160, 71 LP – 82. <https://doi.org/10.1144/0016-764902-008>
- Melim, L.A., Swart, P.K., Maliva, R.G., 2001. Meteoric and marine-burial diagenesis in the subsurface of Great Bahama Bank.
- Muehlenbachs, K., 1998. The oxygen isotopic composition of the oceans, sediments and the seafloor. *Chem. Geol.* 145, 263–273.
- Muehlenbachs, K., Clayton, R.N., 1976. Oxygen isotope composition of the oceanic crust and its bearing on seawater. *J. Geophys. Res.* 81, 4365–4369.
- O’Neil, J.R., Clayton, R.N., Mayeda, T.K., 1969. Oxygen isotope fractionation in divalent metal carbonates. *J. Chem. Phys.* 51, 5547–5558.
- Patry, L. A., Bonnard, P., Boyet, M., Afroz, M., Wilmeth, D. T., Ramsay, B., Nonnotte, P., Homann, M., Sansjofre, P., Fralick, P. W., & Lalonde, S. V. Archean origins of oxygenic photosynthesis confirmed by La-Ce geochronology. *Nature*, in review (Submission 2023-04-05860)
- Perry Jr, E.C., Tan, F.C., 1972. Significance of oxygen and carbon isotope variations in early Precambrian cherts and carbonate rocks of southern Africa. *Geol. Soc. Am. Bull.* 83, 647–664.
- Quinn, T.M., Matthews, R.K., 1990. Post-Miocene diagenetic and eustatic history of Enewetak Atoll: Model and data comparison. *Geology* 18, 942–945.
- Ramsay, B., 2020. Environmental control of seawater geochemistry in a Mesoarchean Peritidal System, Woman Lake, Superior Province. MSc Thesis. Lakehead University, Canada.
- Reinhold, C., 1998. Multiple episodes of dolomitization and dolomite recrystallization during shallow burial in Upper Jurassic shelf carbonates: eastern Swabian Alb, southern Germany. *Sediment. Geol.* 121, 71–95.
- Robert, F., Chaussidon, M., 2006. A palaeotemperature curve for the Precambrian oceans based on silicon isotopes in cherts. *Nature* 443, 969–972.
- Ryb, U., Eiler, J.M., 2018. Oxygen isotope composition of the Phanerozoic ocean and a possible solution to the dolomite problem. *Proc. Natl. Acad. Sci.* 115, 6602–6607.
- Sanborn-Barrie, M., Skulski, T., Parker, J., Dubé, B., 2000. Integrated regional analysis of the Red Lake greenstone belt and its mineral deposits, western Superior Province, Ontario. *Geol. Surv. Canada Current Re.* 14.
- Sanborn-Barrie, M., Skulski, T., Parker, J.R., 2004. Geology, Red Lake greenstone belt, western Superior province, Ontario: Geological Survey of Canada Open File 4594, 1:50,000 scale color map. <https://doi.org/10.4095/215464>

- Sanborn-Barrie, M., Skulski, T., Parker, J.R., 2001. Three hundred million years of tectonic history recorded by the Red Lake greenstone belt, Ontario. *Geol. Surv. Canada Current Re.* 14. <https://doi.org/10.4095/212109>
- Satkoski, A.M., Fralick, P., Beard, B.L., Johnson, C.M., 2017. Initiation of modern-style plate tectonics recorded in Mesoarchean marine chemical sediments. *Geochim. Cosmochim. Acta* 209, 216–232.
- Schidlowski, M., Eichmann, R., Junge, C.E., 1975. Precambrian sedimentary carbonates: carbon and oxygen isotope geochemistry and implications for the terrestrial oxygen budget. *Precambrian Res.* 2, 1–69.
- Schidlowski, M., Hayes, J.M., Kaplan, I.R., 1983. Isotopic inferences of ancient biochemistries-Carbon, sulfur, hydrogen, and nitrogen.
- Schneiderhan, E.A., Gutzmer, J., Strauss, H., Mezger, K., Beukes, N.J., 2006. The chemostratigraphy of a Paleoproterozoic MnF- BIF succession –the Voëlwater Subgroup of the Transvaal Supergroup in Griqualand West, South Africa. *South African J. Geol.* 109, 63–80.
- Searl, A., 1989. Saddle dolomite: a new view of its nature and origin. *Mineral. Mag.* 53, 547–555.
- Shields, G., Veizer, J., 2002. The Precambrian marine carbonate isotope database: version 1.1. *Geochemistry Geophys. Geosystems* 3, 1–12. <https://doi.org/10.1029/2001GC000266>
- Shuster, A.M., Wallace, M.W., van Smeerdijk Hood, A., Jiang, G., 2018. The Tonian Beck Spring Dolomite: Marine dolomitization in a shallow, anoxic sea. *Sediment. Geol.* 368, 83–104.
- Siahi, M., Hofmann, A., Master, S., Wilson, A., Mayr, C., 2018. Trace element and stable (C, O) and radiogenic (Sr) isotope geochemistry of stromatolitic carbonate rocks of the Mesoarchean Pongola Supergroup: Implications for seawater composition. *Chem. Geol.* 476, 389–406.
- Singh, S.K., Trivedi, J.R., Pande, K., Ramesh, R., Krishnaswami, S., 1998. Chemical and Strontium, Oxygen, and Carbon Isotopic Compositions of Carbonates from the Lesser Himalaya: Implications to the Strontium Isotope Composition of the Source Waters of the Ganga, Ghaghara, and the Indus Rivers. *Geochim. Cosmochim. Acta* 62, 743–755. [https://doi.org/https://doi.org/10.1016/S0016-7037\(97\)00381-5](https://doi.org/https://doi.org/10.1016/S0016-7037(97)00381-5)
- Staudigel, H., Hart, S.R., Schmincke, H.-U., Smith, B.M., 1989. Cretaceous ocean crust at DSDP Sites 417 and 418: Carbon uptake from weathering versus loss by magmatic outgassing. *Geochim. Cosmochim. Acta* 53, 3091–3094.
- Thurston, P.C., Breaks, F.W., 1978. Metamorphic and tectonic evolution of the Uchi-English River Subprovince, in: *Metamorphism in the Canadian Shield.* pp. 49–62.
- Veizer, J., Ala, D., Azmy, K., Bruckschen, P., Buhl, D., Bruhn, F., Carden, G.A.F., Diener, A., Ebner, S., Godderis, Y., 1999. $^{87}\text{Sr}/^{86}\text{Sr}$, $\delta^{13}\text{C}$ and $\delta^{18}\text{O}$ evolution of Phanerozoic seawater. *Chem. Geol.* 161, 59–88.

Chapter 5: Carbon and Oxygen Isotope Chemostratigraphy

- Veizer, J., Clayton, R.N., Hinton, R.W., Von Brunn, V., Mason, T.R., Buck, S.G., Hoefs, J., 1990. Geochemistry of Precambrian carbonates: 3-shelf seas and non-marine environments of the Archean. *Geochim. Cosmochim. Acta* 54, 2717–2729. [https://doi.org/https://doi.org/10.1016/0016-7037\(90\)90007-8](https://doi.org/https://doi.org/10.1016/0016-7037(90)90007-8)
- Veizer, J., Hoefs, J., 1976. The nature of O¹⁸/O¹⁶ and C¹³/C¹² secular trends in sedimentary carbonate rocks. *Geochim. Cosmochim. Acta* 40, 1387–1395.
- Walker, J.C.G., Hays, P.B., Kasting, J.F., 1981. A negative feedback mechanism for the long-term stabilization of Earth's surface temperature. *J. Geophys. Res. Ocean.* 86, 9776–9782.
- Walker, J.C.G., Lohmann, K.C., 1989. Why the oxygen isotopic composition of sea water changes with time. *Geophys. Res. Lett.* 16, 323–326.
- Wallmann, K., 2001. The geological water cycle and the evolution of marine $\delta^{18}\text{O}$ values. *Geochim. Cosmochim. Acta* 65, 2469–2485.
- Wright, V.P., Tucker, M.E., 1990. *Carbonate sedimentology*. Blackwell scientific publications.

Chapter 6

In-situ multiple sulfur isotope analyses of shale-hosted sulfides of the Red Lake carbonate platform

Abstract

The earliest known thick occurrence on Earth of sulfidic black shale is preserved in the 2.87 Ga Ball Assemblage of Red Lake Greenstone Belt in northwest Ontario, Canada. The pyrite and pyrrhotite minerals appear as thin laminae, nodules, and disseminated grains. Five epoxy-mounted disks containing nine samples of Red Lake sulfidic shales were analyzed using high-resolution secondary ion mass spectrometry (SIMS). A total of 150 points were obtained using the SwissSIMS Cameca IMS1280HR by simultaneous measurements of ^{32}S , ^{33}S , ^{34}S , and ^{36}S in multi-collection mode with three Faraday cups. The $\delta^{34}\text{S}$, $\Delta^{33}\text{S}$, and $\Delta^{36}\text{S}$ values range from -17.94 to 11.32 ‰, -0.99 to 1.41 ‰, and - 3.85 to 2.95 ‰, respectively (all values relative to VCDT). Most of the samples show a typical Archean slope value of -1.15 for $\Delta^{36}\text{S}/\Delta^{33}\text{S}$ and the range of $\Delta^{33}\text{S}$ values is comparable to the mass-independent fractionation (MIF) reported from other Mesoarchean sites. The $\Delta^{33}\text{S}$ values of most of the samples reflect an atmospheric contribution of elemental sulfur ($\Delta^{33}\text{S} > 0$ ‰), while a smaller number of samples have $\Delta^{33}\text{S} < 0$ ‰ which is interpreted to reflect atmospheric sulfate. Some disseminated pyrites show negative $\delta^{34}\text{S}$ isotopic compositions together with negative $\Delta^{33}\text{S}$ values, implying microbial sulfate reduction of a surface sulfate reservoir that experienced atmospheric processing. The $\Delta^{33}\text{S}$ values of some samples indicate mass-dependent fractionation (MDF) processes which may be attributed to secondary generation of pyrite and pyrrhotite. This dataset reveals that the Red Lake sulfidic shales preserve typical Mesoarchean MIF signals, and multiple sources, including juvenile sulfur ($\Delta^{33}\text{S} = 0 \pm 0.3$ ‰) as well as atmospherically processed elemental sulfur and sulfate, all likely contributed to the formation of Earth's most ancient sulfidic black shales.

6.1 Introduction

The sulfur isotope geochemistry of ancient sedimentary rocks is a powerful tool for exploring the fundamental features of the evolution of the early Earth, including tracing the rise of free oxygen in Earth's atmosphere and the evolution and operation of sulfur metabolisms (Berner and Petsch, 1998; Canfield and Raiswell, 1999; Farquhar et al., 2000; Monster et al., 1979; Pavlov and Kasting, 2002; Schidlowski et al., 1983; Shen et al., 2009). Sulfur has four naturally occurring stable isotopes (^{32}S , ^{33}S , ^{34}S , and ^{36}S). Isotopic fractionations of sulfur are driven by a variety of processes at Earth's surface, including thermodynamic, kinetic, and biological processes affecting speciation and redox changes, and the magnitude of these fractionations between different isotopes of sulfur generally depend on their relative mass differences, so-called mass dependent fractionation (MDF). However, sulfur stable isotopes are among a small subset of stable isotope systems that show important mass-independent fractionation (MIF) at Earth's surface, where the magnitude of isotopic fractionation processes are at times independent of their masses.

The discovery of mass-independent fractionation (MIF) of sulfur isotopes in Archean sedimentary sulfides and sulfates, and the knowledge on their generation as the result of photochemical reactions as revealed by experimental photochemical and atmospheric model studies, has significantly improved our knowledge regarding the Archean sulfur cycle (Farquhar et al., 2000; Ono et al., 2003; Pavlov and Kasting, 2002). Most remarkably, the disappearance of important sulfur MIF signatures in ancient rock records reveals the onset of atmospheric oxygenation on Earth (Farquhar et al., 2000; Pavlov and Kasting, 2002). Before the Great Oxidation Event (GOE) ca. ~2.45 to 2.32 Ga, sulfur isotope MIF signatures are highly remarkable; however, after 2.32 Ga, significant sulfur MIF (specifically non-zero $\Delta^{33}\text{S}$ values) are largely absent from the rock record (Bekker et al., 2004; Farquhar et al., 2000; Farquhar and Wing, 2003; Mojzsis et al., 2003; Ono et al., 2003; Pavlov and Kasting, 2002). This

fundamental change in sulfur isotope systematics are Earth's surface is widely considered as the “smoking gun” for the oxygenation of Earth's atmosphere in the Paleoproterozoic. The sulfur isotope systematics of ancient sedimentary rocks have also been widely used to trace ancient microbial metabolisms involving sulfur, as elaborated below.

The isotopic composition of sulfur has been studied in ancient rock records via the analysis of both sulfide and sulfate minerals. Sulfur in Paleoproterozoic metasediments (3.8 - 3.2 Ga) mainly occurs as sulfate minerals (barite, BaSO_4), and is reported in the Warrawoona Group (3.45 Ga) and Sulfur Springs Group (3.24 Ga) of the Pilbara Craton, Western Australia (Mojzsis et al., 2003; Roerdink et al., 2012; Shen et al., 2009; Ueno et al., 2008), in the Fig Tree Group (3.25 Ga) and Onverwacht Group (3.45 Ga) in the Barberton Greenstone Belt of the Kaapvaal Craton, South Africa (Bao et al., 2007; Heinrichs and Reimer, 1977; Muller et al., 2016; Roerdink et al., 2016, 2012), as well as in the Sargur Group (3.23 Ga) of the Dharwar Craton, India (Hoering, 1989; Muller et al., 2017). The multiple sulfur isotope analyses of these Paleoproterozoic barites demonstrate that sulfate of photolysis origin was an important source to the early Archean ocean, and that microbial sulfate reduction (MSR) was also operating in the Paleoproterozoic (Bao et al., 2007; Muller et al., 2017, 2016; Roerdink et al., 2016, 2012; Shen et al., 2009; Ueno et al., 2008). Interestingly, however, barite, and indeed sulfur-rich minerals in general, are generally rare in the Mesoproterozoic (3.2 - 2.8 Ga) Era. There is a reported occurrence of sulfur-rich 3.2-Ga black shales preserved in the Cleaverville Group of the Pilbara Supergroup, Australia, where two of three drill cores show pyrite lamina, pyrite nodules, and pyrite veining, although little information exists beyond their basic description in a conference presentation (Yamaguchi et al., 2009). Early diagenetic pyrite is reported in the 2.96 Ga Chobeni formation (Eickmann et al., 2018) and in the 2.83 Ga Mozaan Group (Ono et al., 2006) of the Pongola Supergroup. The negative $\Delta^{33}\text{S}$ values and large $\delta^{34}\text{S}$ isotope variations in pyrite samples in the Chobeni formation suggest photochemical reactions under anoxic atmospheric

conditions, with active MSR occurring in the water column (Eickmann et al., 2018). Detrital, early diagenetic, and epigenetic pyrite are also reported for the 2.98 Ga Witwatersrand Supergroup of the Kaapvaal Craton, South Africa, where the diagenetic pyrites show $\delta^{34}\text{S}$ signatures suggesting MSR while $\Delta^{33}\text{S}$ values for epigenetic pyrite suggests that the sulfur was derived from a mass-dependent or isotopically homogenous metamorphic/hydrothermal fluid (Guy et al., 2014, 2012). Sedimentary units of Neoproterozoic age (2.8 - 2.5 Ga) preserve pyritic shales in 2.6 to 2.5 Ga sediments (Boomplaspas, Vryburg, and Klein Naute Formations) of the Transvaal Supergroup, South Africa (Ono et al., 2009), and the Ngezi Group (ca. 2.7 Ga) of Belingwe Greenstone Belt, Zimbabwe (Grassineau et al., 2006, 2005, 2001; Thomazo et al., 2013), as well as in the Bubi Greenstone Belt (ca. 2.7 Ga), Zimbabwe (Marin-Carbonne et al., 2014). Multiple sulfur isotope analysis of 2.6-2.5 Ga early diagenetic pyrites in the Transvaal Supergroup shows that nodular and layered pyrites contain mostly negative $\Delta^{33}\text{S}$ values representing seawater sulfate trapped through MSR, whereas the disseminated pyrites display positive $\Delta^{33}\text{S}$ values reflecting aqueous H_2S and S^0 reservoirs (Ono et al., 2009). The wide range of negative $\delta^{34}\text{S}$ values with negative $\Delta^{33}\text{S}$ anomalies indicates active MSR in the ~2.7 Ga Manjeri formation in the Ngezi Group of Belingwe Greenstone Belt, Zimbabwe (Grassineau et al., 2006; Thomazo et al., 2013). The analysis of pyrite nodules in 2.7 Ga shales from the Bubi Greenstone Belt, Zimbabwe reveals evidence of MSR (Archer and Vance, 2006) and reflects contributions of different sulfur sources during a complex diagenetic history (Marin-Carbonne et al., 2014).

Prior to Neoproterozoic, the preservation of significant pyritic shale is uncommon in rock records. The few studies that exist have largely focused on nodular pyrite occurrences preserved in metasediments of Neoproterozoic age (Bekker et al., 2004; Kakegawa et al., 1998; Ono et al., 2009, 2003; Rouxel et al., 2005). However, with the exception of the ca. 3.2 Ga Cleaverville Formation sulfides mentioned above (and for which no data are currently

available), one of the oldest known substantial depositions of sulfidic black shale) is preserved in the Mesoarchean Red Lake carbonate platform (Afroz et al., 2023). Here, sulfides are present as both pyrite (FeS_2) and pyrrhotite (Fe_{1-x}S). The sulfidic black shale assemblages were subjected to greenschist to lower amphibolite facies ($300^\circ\text{-}550^\circ\text{ C}$) metamorphism, and apparently, no primary depositional features are preserved (Corfu and Wallace, 1986; Thurston and Breaks, 1978). These assemblages are preserved in numerous industry drill hole cores from the Red Lake area but are rarely preserved in outcrops (Afroz et al., 2023). Together or separately, the black shale and sulfidic shale occur in the drill core in bed thicknesses ranging from 0.5 to 30 m. Such thick deposits of sulfidic carbonaceous shale are uncommon in the Archean rock record and remain understudied despite their potential importance for understanding sulfur biogeochemistry using the ancient rock record. This chapter investigates the in-situ multiple sulfur isotopic composition of a selection of samples from this unique occurrence in order to better understand sulfur sources, including potential atmospheric sulfur sources to the Mesoarchean ocean, as well as to better understand microbial processing of this sulfur and operation of the Mesoarchean sulfur cycle more generally.

6.2 Samples and Methods

In the core samples, pyrites are interlayered with black shale as thin (a few mm) to thick (~1cm) laminae, or disseminated as small particles or larger recrystallized grains, while pyrrhotites occur as patches or layered laminae (Afroz et al., 2023). Sub-rounded to rounded-shaped pyrite nodules (>1 cm in diameter) of fractured and coalescent appearance are often scattered in the sulfidic shale-black shale units. Early diagenetic pyrite is also preserved as disseminated smaller grains in carbonates and sulfur-poor carbonaceous rocks.

Eight slabbed samples of sulfidic shale containing pyrite and pyrrhotite from an approximately 10 m interval of the NGI10-31 hole and one sample from the PB12-32 hole were selected for this study. Five epoxy-mounted 25 mm disks containing nine samples were

analyzed using secondary ion mass spectrometry (SIMS) at the SwissSIMS Facility at the Institut des Sciences de la Terre, Université de Lausanne. A total of 150 points were analyzed to obtain quadruple sulfur isotope compositions using the SwissSIMS Cameca IMS1280HR by simultaneous measurements of ^{32}S , ^{33}S , ^{34}S , and ^{36}S in multi-collection mode with three Faraday cups. A primary Cs^+ beam of 5 nA intensity was focused to a spot of about 15–20 μm in diameter and generated pits less than 1 μm in depth. Various pyrite standards, including Maine ($\delta^{34}\text{S} = -20.61\text{‰}$, $\delta^{33}\text{S} = -10.63\text{‰}$, $\delta^{36}\text{S} = -39.50\text{‰}$), Balmat ($\delta^{34}\text{S} = 15.84\text{‰}$ and $\delta^{33}\text{S} = 8.12\text{‰}$, $\delta^{36}\text{S} = 30.40\text{‰}$), Ruttan ($\delta^{34}\text{S} = 1.2\text{‰}$, $\delta^{33}\text{S} = -0.61\text{‰}$, $\delta^{36}\text{S} = 2.28\text{‰}$), Son ($\delta^{34}\text{S} = 1.61\text{‰}$, $\delta^{33}\text{S} = 0.83\text{‰}$, $\delta^{36}\text{S} = 3.25\text{‰}$), Pyr 123 ($\delta^{34}\text{S} = 1.4\text{‰}$, $\delta^{33}\text{S} = 0.8\text{‰}$), Spain ($\delta^{34}\text{S} = -1.57\text{‰}$ and $\delta^{33}\text{S} = -0.78\text{‰}$) (Muller et al., 2017), and the pyrrhotite standard Anderson ($\delta^{34}\text{S} = 1.4\text{‰}$) were used to determine the instrumental mass fractionation, with standard analyses bracketing every 5 to 10 spots. The internal precision, based on the average of internal precisions measured for all standard repeats, was $\pm 0.03\text{‰}$ for $\delta^{34}\text{S}$ (2σ), $\pm 0.04\text{‰}$ for $\Delta^{33}\text{S}$ (2σ), and $\pm 0.74\text{‰}$ for $\Delta^{36}\text{S}$. The external precision, averaged across each group of standard repeated was $\pm 0.02\text{‰}$ (2σ) for $\delta^{34}\text{S}$ and $\pm 0.02\text{‰}$ (2σ) for $\Delta^{33}\text{S}$, and $\pm 0.15\text{‰}$ for $\Delta^{36}\text{S}$.

The isotopic compositions were calculated in large and small delta notation according to the following equations:

$$\delta^{3a}\text{S} = \left[\left(\frac{{}^{3a}\text{S}}{{}^{32}\text{S}} \right)_{\text{sample}} / \left(\frac{{}^{3a}\text{S}}{{}^{32}\text{S}} \right)_{\text{VCDT}} \right] - 1 * 1000$$

$$\Delta^{33}\text{S} = \delta^{33}\text{S} - \left[\left(1 + \delta^{34}\text{S}/1000 \right)^{0.515} - 1 \right] * 1000$$

$$\Delta^{36}\text{S} = \delta^{36}\text{S} - \left[\left(1 + \delta^{34}\text{S}/1000 \right)^{1.9} - 1 \right] * 1000$$

6.3 Results

The $\delta^{34}\text{S}$, $\Delta^{33}\text{S}$, and $\Delta^{36}\text{S}$ values of shale-hosted sulfide samples are reported relative to VCDT. The nodular pyrite sample (AC-210.7) yielded $\delta^{34}\text{S} = -9.5$ to 11.32‰ , $\Delta^{33}\text{S} = -0.24$ to 1.02‰ , and $\Delta^{36}\text{S} = -2.08$ to 1.28‰ . The disseminated pyrite grains in sample AC-210.7 show $\delta^{34}\text{S} = -17.94$ to -10.54‰ , $\Delta^{33}\text{S} = -0.85$ to 0.52‰ , and $\Delta^{36}\text{S} = -2.18$ to 0.47‰ . The laminated

sulfide sample (AC - 210.7) containing pyrite and pyrrhotite shows values of $\delta^{34}\text{S} = -6.76$ to -1.31 ‰, $\Delta^{33}\text{S} = -0.28$ to 0.45 ‰, and $\Delta^{36}\text{S} = -2.85$ to 0.59 ‰. The pyrite laminae sample (AC-212) yielded $\delta^{34}\text{S} = -0.56$ to 11.32 ‰, $\Delta^{33}\text{S} = -0.13$ to 0.77 ‰, and $\Delta^{36}\text{S} = -1.08$ to 1.02 ‰. The nodular pyrite of AC-214 sample shows $\delta^{34}\text{S} = -0.33$ to -9.55 ‰, $\Delta^{33}\text{S} = -0.64$ to 0.58 ‰, and $\Delta^{36}\text{S} = -1.60$ to 0.95 ‰ while the pyritic laminae of AC-214 sample shows $\delta^{34}\text{S} = -8.84$ to -3.68 ‰, $\Delta^{33}\text{S} = -0.78$ to -0.28 ‰, and $\Delta^{36}\text{S} = -0.67$ to 0.47 ‰. The pyritic sample AC-214.7 show values of $\delta^{34}\text{S} = -2.72$ to 5.96 ‰, $\Delta^{33}\text{S} = -0.36$ to 0.52 ‰, and $\Delta^{36}\text{S} = -0.86$ to 0.76 ‰. The pyrite and pyrrhotite rich sample PB32-282 yield $\delta^{34}\text{S} = -4.89$ to 11.05 ‰, $\Delta^{33}\text{S} = -0.25$ to 1.06 ‰, and $\Delta^{36}\text{S} = -3.85$ to 0.40 ‰. The two exclusively pyrrhotite samples (AC-216 and AC-227.1) together yield $\delta^{34}\text{S} = -4.51$ to -1.89 ‰, $\Delta^{33}\text{S} = 0.09$ to 1.41 ‰, and $\Delta^{36}\text{S} = -2.12$ to 0.23 ‰. The only carbonate-associated sulfide sample (NGI-43.6) shows two clusters of sulfur isotope compositions. One cluster displays negative $\delta^{34}\text{S}$ values while the other cluster displays positive values of $\delta^{34}\text{S}$, while their $\Delta^{33}\text{S}$ values are negative in both cases. Cluster one shows values of $\delta^{34}\text{S} = -6.45$ to -2.28 ‰, $\Delta^{33}\text{S} = -0.97$ to -0.8 ‰, and $\Delta^{36}\text{S} = 0.52$ to 2.95 ‰ whereas cluster two shows values of $\delta^{34}\text{S} = 0.13$ to 3.69 ‰, $\Delta^{33}\text{S} = -0.99$ to -0.85 ‰, and $\Delta^{36}\text{S} = -1.81$ to -0.70 ‰.

6.4 Discussion

Before discussing the sulfur isotope data, some attention is warranted to the fact that two different sulfide minerals are observed in the Red Lake sulfidic black shales. Scanning electron microscope (SEM) micrographs show large euhedral pyrite associated with anhedral pyrrhotite. This type of co-occurrence indicates an epigenetic origin of sulfides linked to regional metamorphism and local hydrothermal events (Hallbauer and Von Gehlen, 1983). The presence of pyrrhotite in carbonaceous shale and pyritic shale samples (Figure 6.1) from Red Lake suggests that earlier pyrite broke down during regional metamorphism and was subject to metamorphic desulfidation reactions (Stock, 2012). Desulfidation reactions during the

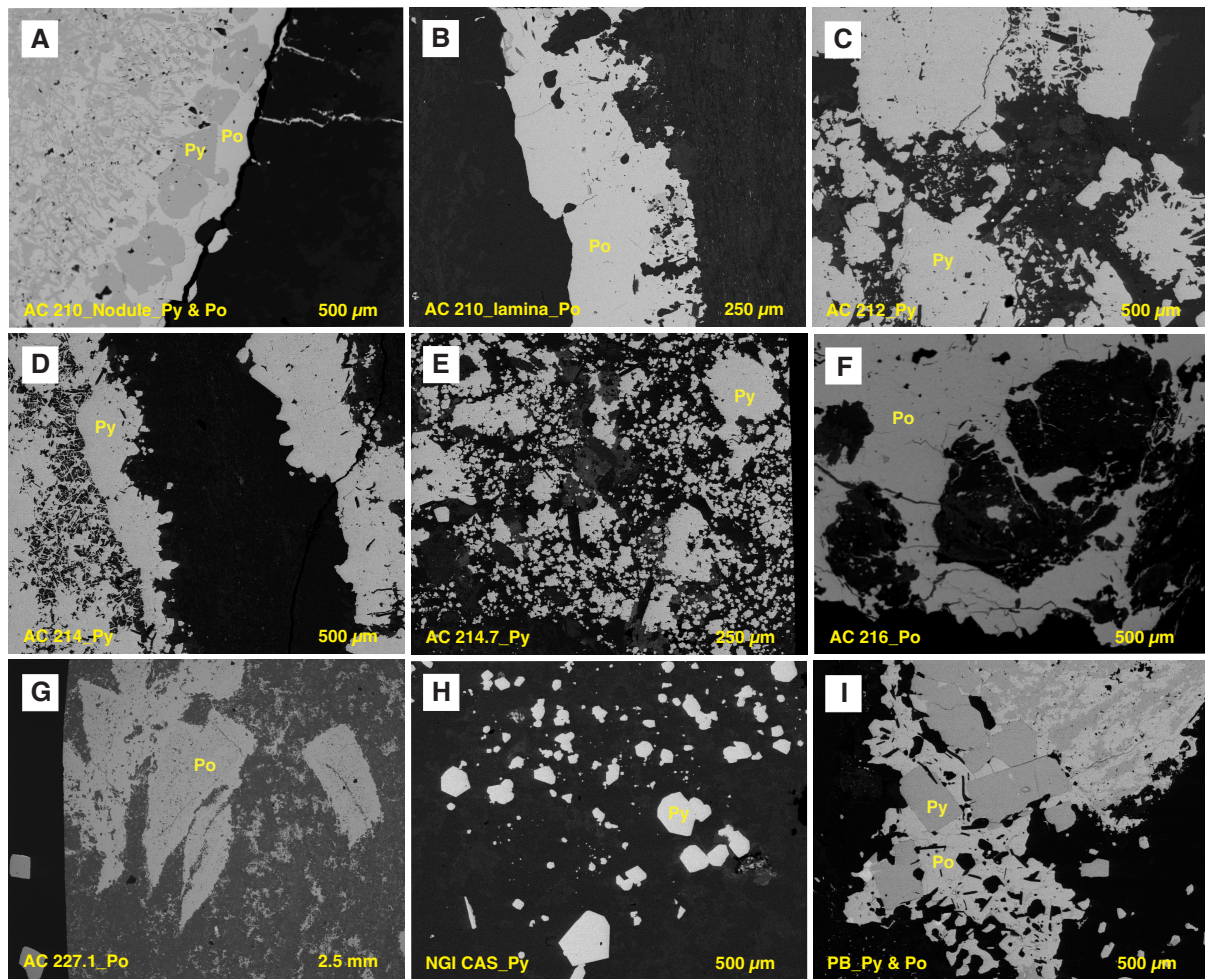


Figure 6.1: SEM-BSE images of sulfide samples containing pyrite and pyrrhotite. (A) Nodular pyrite containing pyrite and pyrrhotite. (B) Pyrrhotite laminae. (C) and (D) Pyrite laminae. (E) Scattered pyrite grains. (F) Patchy appearance of pyrrhotite. (G) Replacement by pyrrhotite. (H) Carbonate-associated pyrite grains. (I) Fractured nodules containing pyrite and pyrrhotite.

metamorphic breakdown of pre-existing pyrite generally produces pyrrhotite and excess sulfur (Tomkins, 2010). This additional sulfur is transported as H_2S dissolved in the metamorphic fluid (Ohmoto, 1997; Rye and Rye, 1974) and is thought to have similar but slightly enriched $\delta^{34}S$ values compared to the initial pyrite (Ohmoto, 1997; Ohmoto et al., 1979). Experimental desulfidation experiments reveal that the fractionation of $\Delta^{33}S$ and $\Delta^{36}S$ between initial pyrite and resultant pyrrhotite is negligible, though the isotopic values of $\delta^{34}S$ may vary to some degree during the chemical and mineralogical conversion of pyrite to pyrrhotite (Liu et al., 2020). These high temperature ($675^\circ C$) experiment data indicate that both the $\Delta^{33}S$ and $\Delta^{36}S$

isotopic values of initial pyrite and secondary pyrrhotite can be effective in tracing sulfur sources in Archean, and that the isotopic composition of pyrrhotite can thus be useful in tracking sulfur MIF signatures in metamorphosed Archean rocks (Liu et al., 2020). Two Red Lake samples analyzed here contain both pyrite and pyrrhotite in the same analyzed chip (AC-210.7 and PB-282). If the pyrite to pyrrhotite transformation was caused by metamorphism under closed system conditions, then pyrite and pyrrhotite are expected to have a similar $\delta^{34}\text{S}$, $\Delta^{33}\text{S}$, and $\Delta^{36}\text{S}$ isotopic compositions and should thus indicate comparable sulfur sources and similar evidence for microbial sulfur processing, if present. In contrast, if pyrrhotite was formed by hydrothermal or magmatic sulfidation, then its isotopic composition would be expected to differ from co-existing pyrite. Two samples composed exclusively of pyrrhotite (AC-216 and AC-227.1) have different (AC-216 sample has $\delta^{34}\text{S} = -2.74$ to -1.89 ‰, $\Delta^{33}\text{S} = 1.28$ to 1.41 ‰, and $\Delta^{36}\text{S} = -2.12$ to -0.91 ‰ while AC-227 sample has $\delta^{34}\text{S} = -4.51$ to 3.18 ‰, $\Delta^{33}\text{S} = 0.09$ to 0.19 ‰, and $\Delta^{36}\text{S} = -1.4$ to 0.23 ‰) isotopic compositions compared to the rest of the samples (Figure 6.2), suggesting an origin by later hydrothermal replacement or magmatic addition (Barnicoat et al., 1997; Myers et al., 1993). Even though epigenetically formed pyrites and pyrrhotites are abundant in Red Lake samples, there is no remarkable differences in their $\Delta^{33}\text{S}$ and $\Delta^{36}\text{S}$ isotopic compositions, which can be best explained by the presence of a somewhat closed sulfur system during post-depositional modification and/or isotopically homogeneous fluid during metamorphism (Guy et al., 2014, 2012).

6.4.1 Sources of sulfur in sedimentary sulfides at Red Lake

Sulfur MIF is generated largely due to photochemical reactions of volcanically derived sulfur dioxide above Earth's modern ozone layer or under the ancient Earth's ozone-poor anoxic atmosphere. These reactions generate anomalous enrichment or depletion in ^{33}S and ^{36}S relative to the expectation calculated for mass dependent fractionation given an associated

$^{34}\text{S}/^{32}\text{S}$ ratio (Bekker et al., 2004; Farquhar et al., 2000; Farquhar and Wing, 2003; Mojzsis et al., 2003; Ono et al., 2003; Pavlov and Kasting, 2002). Photochemical dissociation of volcanic SO_2 in an anoxic Archean atmosphere is expected to produce elemental sulfur (S^0) with positive $\Delta^{33}\text{S}$ values and sulfate (SO_4^{2-}) aerosols with negative $\Delta^{33}\text{S}$ values (Farquhar et al., 2000). The volcanogenic SO_2 is not thought to exhibit a sulfur MIF signature (Farquhar et al., 2010). Thus, with respect to the Mesoarchean during which contributions of sulfur from oxidative continental weathering are expected to have been minimal, sulfur in sedimentary pyrite is thought to be largely obtained from either an elemental sulfur-derived pool of polysulfides that may further react with iron sulfide precursors, or from a sulfate-derived sulfide pool (e.g., following microbial sulfate reduction) where sulfate is supplied largely by rainout of atmospheric sulfate (Farquhar et al., 2013). After the Neoproterozoic, dramatic shifts in the multiple isotope composition of sulfur in the rock record reveals a significant change in sulfur isotope fractionation processes after the Archean driven by the permanent oxygenation of Earth's atmosphere (Farquhar et al., 2000).

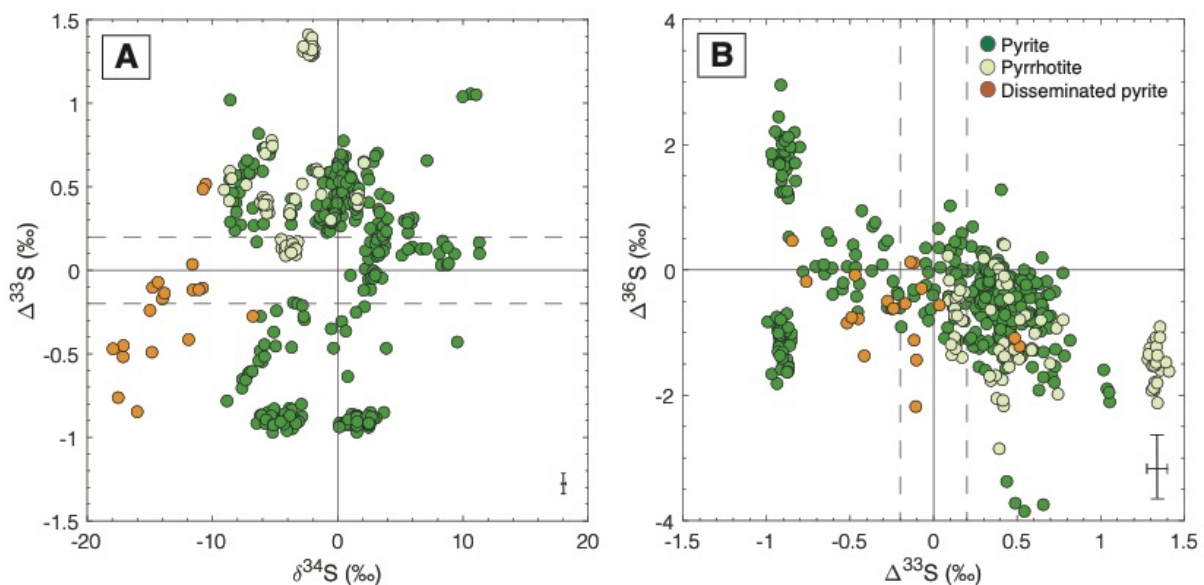


Figure 6.2: (A) $\delta^{34}\text{S}$ vs. $\Delta^{33}\text{S}$ plot for Red Lake sulfidic shale samples show different clustering but their $\Delta^{33}\text{S}$ values are within the range of Mesoarchean samples. (B) $\Delta^{36}\text{S}$ vs. $\Delta^{33}\text{S}$ plot for Red Lake sulfidic shale samples show an average slope value of -1.15 but the slope of individual samples varies between -1.5 and -0.9 which is within the range of the Archean reference array. Error bars represent 4σ values of $\delta^{34}\text{S}$, $\Delta^{33}\text{S}$ and $\Delta^{36}\text{S}$.

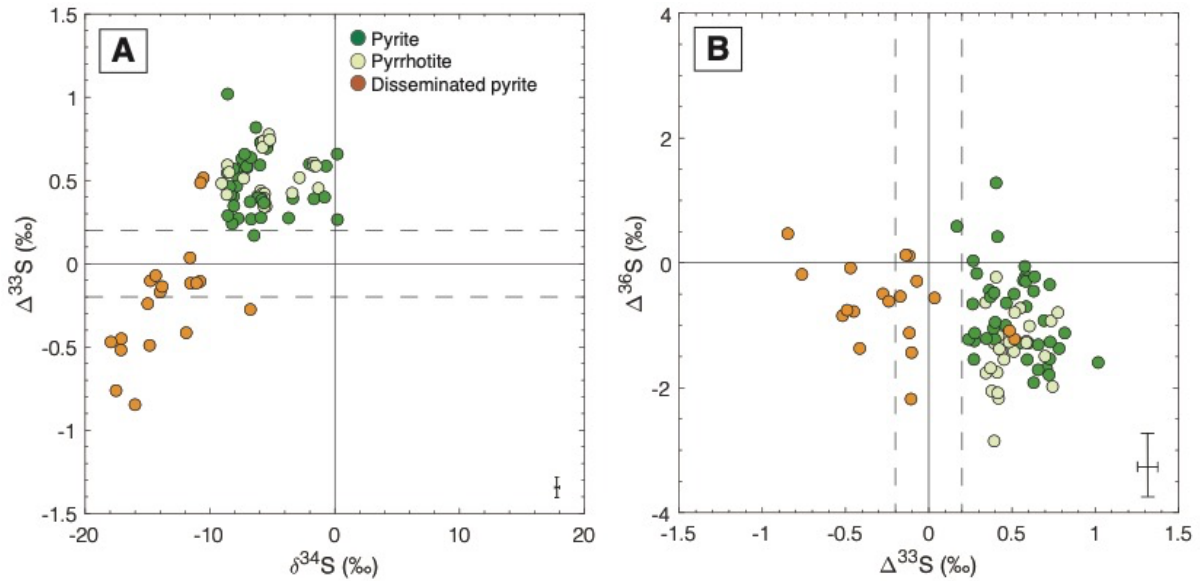


Figure 6.3: $\delta^{34}\text{S}$ vs. $\Delta^{33}\text{S}$ plot (A) and $\Delta^{33}\text{S}$ vs. $\Delta^{36}\text{S}$ plot (B) of nodular and disseminated pyrite sample show isotopic compositional variation. Disseminated pyrite grains show large negative $\delta^{34}\text{S}$ values with accompanying negative $\Delta^{33}\text{S}$ values suggesting microbial sulfate reduction (A). Nodular samples containing pyrite and pyrrhotite show a similar isotopic composition of $\delta^{34}\text{S}$, $\Delta^{33}\text{S}$, and $\Delta^{36}\text{S}$. Error bars represent 4σ values of $\delta^{34}\text{S}$, $\Delta^{33}\text{S}$ and $\Delta^{36}\text{S}$.

Syngenetic and early diagenetic sulfide minerals formed before the GOE generally preserve important MIF signatures in their $\Delta^{33}\text{S}$ compositions ($\Delta^{33}\text{S}$: -1.29 to 2.04 ‰; Farquhar et al., 2000). The presence of positive $\Delta^{33}\text{S}$ values in pyritic shales suggests that pyrite precipitated from elemental sulfur, which is unlikely to be processed in the water column, and but rather is preferentially transported to the sediments as insoluble and unreactive particles (Rickard, 2012). The $\Delta^{33}\text{S}$ values measured for shale-hosted and carbonate-hosted pyrite samples of Red Lake range between -0.99 and 1.05 ‰ (Figure 6.2), and these values are within the range of most other Archean $\Delta^{33}\text{S}$ values (Farquhar et al., 2002; Ohmoto et al., 2006). The $\Delta^{33}\text{S}$ values of individual samples demonstrate a range of isotopic compositions indicating a mixture of sulfur sources at the scale of individual chips, including juvenile sulfur signatures ($\Delta^{33}\text{S}=0\pm 0.2\%$; Farquhar et al., 2010) and sulfur MIF signatures indicating contributions from both atmospheric S^0 and SO_4^{2-} exit pathways (Farquhar et al., 2000).

Chapter 6: In-situ multiple sulfur isotope analysis

A plot of $\delta^{34}\text{S}$ vs. $\Delta^{33}\text{S}$ (Figure 6.2-A) for all samples shows several distinctive populations. Most of the samples show values for $\Delta^{33}\text{S} > 0$ ‰, a lesser number show $\Delta^{33}\text{S} < 0$ ‰, and the remaining data plot at values between -0.2 and 0.2 ‰. Two of the pyrrhotite-dominated samples have contrasting isotopic compositions: one sample (AC-227.1) is characterized by $\Delta^{33}\text{S}$ values between 0.09 and 0.2 ‰, whereas the other sample (AC-216) shows $\Delta^{33}\text{S}$ values between 1.3 and 1.4 ‰. However, pyrrhotite associated with pyrite in the nodule samples AC-210.7 and PB-282 shows similarity with the $\Delta^{33}\text{S}$ values of co-existing pyrite and ranges from -0.25 to 1.06 ‰. Some disseminated pyrites from the nodule sample AC-210.7 exhibit negative $\Delta^{33}\text{S}$ values and significantly negative $\delta^{34}\text{S}$ isotopic compositions (down to -17.94 ‰; Figure 6.3). The only carbonate-associated sulfide sample (NGI-43.6) presents two clusters with distinct isotopic compositions; one group shows positive while the other group shows negative $\delta^{34}\text{S}$ values, but their $\Delta^{33}\text{S}$ values are similar. The overall distribution of multiple sulfur isotope signatures from Red Lake samples suggests an atmospheric source of sulfur, and one that was composed mainly elemental sulfur but also contained a smaller atmospheric sulfate component. That said, the MDF signature preserved in some samples also indicates late-stage pyrite formation, while $\Delta^{33}\text{S}$ values close to zero suggest the incorporation of sulfur from magmatic fluid.

In addition, a plot of $\Delta^{36}\text{S}$ vs. $\Delta^{33}\text{S}$ for Red Lake samples shows a linear array with negative correlation (Figure 6.2-B), which is characteristic of Archean sulfide and sulfate samples. The $\Delta^{36}\text{S}/\Delta^{33}\text{S}$ values from all Red Lake samples combined show an average slope of 1.15, which is typical for sulfide and sulfate in sedimentary rocks deposited between 3.2 and 2.73 Ga (Farquhar et al., 2007, 2002; Thomazo et al., 2009). The slope in $\Delta^{36}\text{S}/\Delta^{33}\text{S}$ defined by individual samples from Red Lake is within the range of the Archean reference array (-1.5 to -0.9), except for the two pyrrhotite samples which show contrasting slopes (AC-216 = 0.14 and AC-227.2 = -2.03).

The $\Delta^{36}\text{S}/\Delta^{33}\text{S}$ ratio can show different slope values in natural samples, and variations in the $\Delta^{36}\text{S}/\Delta^{33}\text{S}$ slope are indicative of different sulfur MIF source reactions (Ono et al., 2009; Whitehill and Ono, 2012). Experimental studies show that photolysis of atmospheric SO_2 produces a $\Delta^{36}\text{S}/\Delta^{33}\text{S}$ slope value of around -1 (Farquhar et al., 2001), while additional photochemical reactions involving elemental sulfur (i.e., $\text{S} + \text{S}_2 \rightarrow \text{S}_3$) would result in a $\Delta^{36}\text{S}/\Delta^{33}\text{S}$ slope value of around -1.6 (Francisco et al., 2005; Ono et al., 2009). The photolysis of SO_2 exposed to different wavelengths of UV light (190 to 220 nm vs. 250 to 330 nm) has also been shown to generate sulfur MIF with different $\Delta^{36}\text{S}/\Delta^{33}\text{S}$ slopes (Whitehill and Ono, 2012). Available broadband UV photolysis experiment results using SO_2 result in more negative values of around -1 in $\Delta^{36}\text{S}/\Delta^{33}\text{S}$ (Masterson et al., 2011). The slope values determined experimentally from these reactions are within the range observed in Archean sedimentary rocks. In the specific case of the Red Lake sulfides, the non-uniform slope values of different Red Lake samples of diagenetic and epigenetic origin may indicate different source reactions supplying sulfur bearing S-MIF, or alternatively, might represent an attenuated S-MIF signal due to the post-depositional isotopic exchange (Penniston-Dorland et al., 2008). In all cases, the sources of sulfur for the sulfidic black shales at Red Lake clearly experienced atmospheric processing by multiple photochemical pathways and cannot be simply attributed to later sulfidation of pre-existing S-poor sediments by juvenile sulfur, consistent with the sedimentary distribution and concentration of disseminated pyrite in specific beds at the cm-scale in certain samples that strongly indicates a near-synsedimentary origin.

Similar to the $\Delta^{33}\text{S}$ isotope compositions, the $\delta^{34}\text{S}$ compositions are not homogeneous in the Red Lake sulfides, and likely represent the isotopic signature of a mixture of sources and processes. These include the isotopic signature of sulfur that has experienced minimal microbial redox processing (0 to 4 ‰; Seal, 2006), that derived from Archean seawater sulfate (6 to 16 ‰; Ono et al., 2003), and sulfate that underwent partial bacterial sulfate reduction in

sediments that led to more negative $\delta^{34}\text{S}$ isotope compositions (Canfield, 2001; Seal, 2006). In an ocean that is limited in sulfate due to a largely anoxic ocean-atmosphere system, bacterial sulfate reduction would be expected to be near-complete, and thus produce sulfides with isotopic compositions close to the seawater value (Canfield, 1998; Poulton, 2011). Sediment-hosted sulfides from the Red Lake gold mine (Stock, 2012) reveal that early diagenetic or syngenetic sulfides display $\delta^{34}\text{S}$ values of -6.9 to 5.6 ‰, where the negative $\delta^{34}\text{S}$ values were interpreted to be formed in anoxic environments by sulfide-reducing bacteria (Crocket and Lavigne, 1984; Lavigne, 1982), while the positive $\delta^{34}\text{S}$ values were thought to be related to magmatic sources (Marini et al., 2011). The large negative $\delta^{34}\text{S}$ isotopic composition and accompanying negative $\Delta^{33}\text{S}$ values observed in this study for the disseminated pyrites of the nodule-dominated sample AC-210.7 suggest that MSR was operating, but perhaps in a limited manner, or alternatively, acting on a small dissolved sulfate reservoir and thus not generating large $\delta^{34}\text{S}$ in variations as the result of muted fractionation at low sulfate concentrations during MSR.

A combined diagram (Figure 6.4) of the multiple sulfur isotopic compositions of bulk rock and in-situ analyses of Red Lake sulfide-rich samples plotted along with data from other Mesoarchean sites, namely the Chobeni Formation of Pongola Supergroup, South Africa (Eickmann et al., 2018), the Mozaan Group, South Africa (Ono et al., 2006), and the Witwatersrand Supergroup, South Africa (Farquhar et al., 2007; Guy et al., 2012), reveal that their $\Delta^{33}\text{S}$ values all generally fall within the range of -1.5 to 1.5 ‰, but that the $\delta^{34}\text{S}$ values vary between the Red Lake and Chobeni Formation samples. The negative correlation of $\Delta^{36}\text{S}$ and $\Delta^{33}\text{S}$ in Red Lake samples is comparable with these Mesoarchean samples, and the slope values are within the range of the Archean reference array. The Chobeni nodular pyrite samples show $\delta^{34}\text{S}$ values that are more negative (down to -22.4 ‰) relative to the Red lake samples, and have been interpreted as reflecting MSR (Eickmann et al., 2018). The $\delta^{34}\text{S}$ isotope

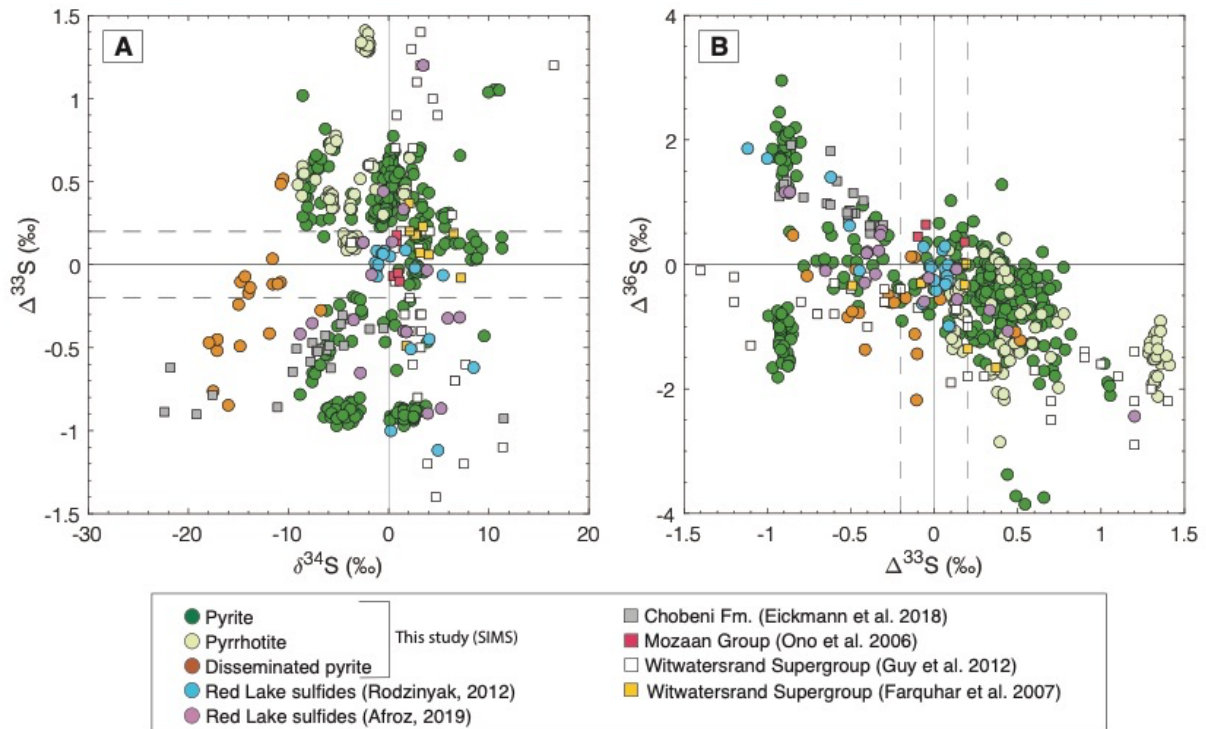


Figure 6.4: $\delta^{34}\text{S}$ vs. $\Delta^{33}\text{S}$ plot (A) and $\Delta^{33}\text{S}$ vs. $\Delta^{36}\text{S}$ plot (B) for Red Lake samples compared with other Mesoarchean samples.

compositions recorded in the Red Lake samples are similar to most Mesoarchean pyrites, including those from the Pongola and Witwatersrand Supergroup, and appear to reflect sulfide formation in sulfate-limited environments, with the exception of the more negative range in $\delta^{34}\text{S}$ values of the Chobeni Formation. The negative $\delta^{34}\text{S}$ and $\Delta^{33}\text{S}$ values in the disseminated pyrite likely indicate a small and soluble sulfate pool in the depositional environment. Archean marine sulfate concentrations started to rise around 2.7 - 2.8 Ga ago, likely as the result of increasing contributions of sulfate from terrestrial weathering and incipient oxidation of pyrite (Stüeken et al., 2012). Signals of MSR are prominent for the Chobeni Formation already at 2.96 Ga, which were proposed to relate to elevated sulfate concentrations as the result of the presence of an oxygenated near-shore shallow-marine environment (Eickmann et al., 2018), whereas the Red Lake samples show in contrast a dominance of elemental sulfur signatures indicating a lack of sulfate in the basin. The mostly positive $\Delta^{33}\text{S}$ values of pyrite suggest that

the oxidation of magmatic pyrite via incipient terrestrial weathering under slightly oxidized atmospheric conditions were not the primary sulfate source for MSR. Incipient continental weathering involving the oxidation of magmatic pyrite are not obvious in the Red Lake basin, despite the fact that an ephemeral presence of oxygen has been reported (Afroz et al., 2023; Patry et al, in review). The dominance of positive $\Delta^{33}\text{S}$ signals in most of the pyrite samples analyzed here points instead to an elemental source of sulfur carrying a clear sulfur MIF signal produced by photochemical reactions in the oxygen-depleted Mesoarchean atmosphere.

6.5 Conclusion

In-situ multiple sulfur isotope compositions were measured for shale-hosted sulfides containing pyrite and pyrrhotite of early diagenetic and epigenetic origin in the Red Lake carbonate platform. These ancient sulfidic shales represent a relatively unique occurrence of for such ancient sediments and represents a significant potential source of information for understanding sulfur sources and cycling on the Mesoarchean Earth. Most of the samples preserve typical Archean slope values of ca. -1.15 for $\Delta^{36}\text{S}/\Delta^{33}\text{S}$ and contain MIF values analogous to other Mesoarchean sites worldwide. Microbial sulfate reduction is not prevalent, but some evidence of its operation is evident from the non-negligible negative $\delta^{34}\text{S}$ isotopic compositions combined with negative $\Delta^{33}\text{S}$ values in the disseminated pyrite grains. A sulfur MDF signature is apparent in pyrite samples of secondary origin. The multiple sulfur isotopic composition of Red Lake sulfidic shales suggests that sulfur was derived predominantly from atmospherically processed sulfur, mainly from an elemental atmospheric sulfur ($\Delta^{33}\text{S}>0\text{ ‰}$) source, and to a lesser extent from atmospheric sulfate ($\Delta^{33}\text{S}<0\text{ ‰}$), with insignificant addition of sulfur from juvenile source ($\Delta^{33}\text{S}=0\pm 0.3\text{ ‰}$). These new isotopic data reveal that the Red Lake sulfidic shales represent a variety of sources and processes that are comparable to those identified for other ancient marine sediments of Mesoarchean age.

6.6 References

- Afroz, M., Fralick, P.W., Lalonde, S. V, 2023. Sedimentology and geochemistry of basinal lithofacies in the Mesoarchean (2.93 Ga) Red Lake carbonate platform, northwest Ontario, Canada. *Precambrian Res.* 388, 106996. <https://doi.org/https://doi.org/10.1016/j.precamres.2023.106996>
- Archer, C., Vance, D., 2006. Coupled Fe and S isotope evidence for Archean microbial Fe(III) and sulfate reduction. *Geology* 34, 153–156. <https://doi.org/10.1130/G22067.1>
- Bao, H., Rumble III, D., Lowe, D.R., 2007. The five stable isotope compositions of Fig Tree barites: Implications on sulfur cycle in ca. 3.2 Ga oceans. *Geochim. Cosmochim. Acta* 71, 4868–4879.
- Barnicoat, A.C., Henderson, I.H.C., Knipe, R.J., Yardley, B.W.D., Napier, R.W., Fox, N.P.C., Kenyon, A.K., Muntingh, D.J., Strydom, D., Winkler, K.S., 1997. Hydrothermal gold mineralization in the Witwatersrand basin. *Nature* 386, 820–824.
- Bekker, A., Holland, H.D., Wang, P.-L., Rumble III, D., Stein, H.J., Hannah, J.L., Coetzee, L.L., Beukes, N.J., 2004. Dating the rise of atmospheric oxygen. *Nature* 427, 117.
- Berner, R.A., Petsch, S.T., 1998. The sulfur cycle and atmospheric oxygen. *Science* (80-.). 282, 1426–1427.
- Canfield, D.E., 2001. Biogeochemistry of sulfur isotopes. *Rev. Mineral. Geochemistry* 43, 607–636.
- Canfield, D.E., 1998. A new model for Proterozoic ocean chemistry. *Nature* 396, 450–453. <https://doi.org/10.1038/24839>
- Canfield, D.E., Raiswell, R., 1999. The evolution of the sulfur cycle. *Am. J. Sci.* 299, 697–723.
- Corfu, F., Wallace, H., 1986. U–Pb zircon ages for magmatism in the Red Lake greenstone belt, northwestern Ontario. *Can. J. Earth Sci.* 23, 27–42. <https://doi.org/10.1139/e86-004>

Chapter 6: In-situ multiple sulfur isotope analysis

- Crocket, J.H., Lavigne, M.J., 1984. Sulphur sources in the Dickenson gold mine as suggested by sulphur isotopes, in: *Gold'82: The Geology, Geochemistry and Genesis of Gold Deposits. Symposium.* pp. 417–433.
- Eickmann, B., Hofmann, A., Wille, M., Bui, T.H., Wing, B.A., Schoenberg, R., 2018. Isotopic evidence for oxygenated Mesoarchaeon shallow oceans. *Nat. Geosci.* 11, 133–138. <https://doi.org/10.1038/s41561-017-0036-x>
- Farquhar, J., Bao, H., Thiemens, M., 2000. Atmospheric Influence of Earth's Earliest Sulfur Cycle. *Science* (80-.). 289, 756 LP – 758. <https://doi.org/10.1126/science.289.5480.756>
- Farquhar, J., Cliff, J., Zerkle, A.L., Kamyshny, A., Poulton, S.W., Claire, M., Adams, D., Harms, B., 2013. Pathways for Neoproterozoic pyrite formation constrained by mass-independent sulfur isotopes. *Proc. Natl. Acad. Sci.* 110, 17638–17643.
- Farquhar, J., Peters, M., Johnston, D.T., Strauss, H., Masterson, A., Wiechert, U., Kaufman, A.J., 2007. Isotopic evidence for Mesoarchaeon anoxia and changing atmospheric sulphur chemistry. *Nature* 449, 706.
- Farquhar, J., Savarino, J., Airieau, S., Thiemens, M.H., 2001. Observation of wavelength-sensitive mass-independent sulfur isotope effects during SO₂ photolysis: Implications for the early atmosphere. *J. Geophys. Res. Planets* 106, 32829–32839. <https://doi.org/10.1029/2000JE001437>
- Farquhar, J., Wing, B.A., 2003. Multiple sulfur isotopes and the evolution of the atmosphere. *Earth Planet. Sci. Lett.* 213, 1–13. [https://doi.org/https://doi.org/10.1016/S0012-821X\(03\)00296-6](https://doi.org/10.1016/S0012-821X(03)00296-6)
- Farquhar, J., Wing, B.A., McKeegan, K.D., Harris, J.W., Cartigny, P., Thiemens, M.H., 2002. Mass-independent sulfur of inclusions in diamond and sulfur recycling on early Earth. *Science* (80-.). 298, 2369–2372.

- Farquhar, J., Wu, N., Canfield, D.E., Oduro, H., 2010. Connections between sulfur cycle evolution, sulfur isotopes, sediments, and base metal sulfide deposits. *Econ. Geol.* 105, 509–533.
- Francisco, J.S., Lyons, J.R., Williams, I.H., 2005. High-level ab initio studies of the structure, vibrational spectra, and energetics of S₃. *J. Chem. Phys.* 123, 54302.
- Grassineau, N. V, Abell, P., Appel, P.W.U., Lowry, D., Nisbet, E.G., 2006. Early life signatures in sulfur and carbon isotopes from Isua, Barberton, Wabigoon (Steep Rock), and Belingwe Greenstone Belts (3.8 to 2.7 Ga). *Mem. Soc. Am.* 198, 33.
- Grassineau, N. V, Appel, P.W.U., Fowler, C.M.R., Nisbet, E.G., 2005. Distinguishing biological from hydrothermal signatures via sulphur and carbon isotopes in Archaean mineralizations at 3.8 and 2.7 Ga. *Geol. Soc. London, Spec. Publ.* 248, 195–212.
- Grassineau, N. V, Nisbet, E.G., Bickle, M.J., Fowler, C.M.R., Lowry, D., Matthey, D.P., Abell, P., Martin, A., 2001. Antiquity of the biological sulphur cycle: evidence from sulphur and carbon isotopes in 2700 million-year-old rocks of the Belingwe Belt, Zimbabwe. *Proc. R. Soc. London. Ser. B Biol. Sci.* 268, 113–119.
- Guy, B.M., Ono, S., Gutzmer, J., Kaufman, A.J., Lin, Y., Fogel, M.L., Beukes, N.J., 2012. A multiple sulfur and organic carbon isotope record from non-conglomeratic sedimentary rocks of the Mesoarchean Witwatersrand Supergroup, South Africa. *Precambrian Res.* 216, 208–231.
- Guy, B.M., Ono, S., Gutzmer, J., Lin, Y., Beukes, N.J., 2014. Sulfur sources of sedimentary “buckshot” pyrite in the auriferous conglomerates of the Mesoarchean Witwatersrand and Ventersdorp Supergroups, Kaapvaal Craton, South Africa. *Miner. Depos.* 49, 751–775.
- Hallbauer, D.K., Von Gehlen, K., 1983. The Witwatersrand pyrites and metamorphism. *Mineral. Mag.* 47, 473–479.
- Heinrichs, T.K., Reimer, T., 1977. A sedimentary barite deposit from the Archean Fig Tree

Chapter 6: In-situ multiple sulfur isotope analysis

- Group of the Barberton Mountain Land (South Africa). *Econ. Geol.* 72, 1426–1441.
- Hoering, T.C., 1989. Development of the sulfur hexafluoride method for sulfur isotope analysis. *Annu. Rep. Dir. Geophys. Lab. Carnegie Institution, Rep. 2200*, 128–131.
- Kakegawa, T., Kawai, H., Ohmoto, H., 1998. Origins of pyrites in the ~ 2.5 Ga Mt. McRae shale, the Hamersley District, western Australia. *Geochim. Cosmochim. Acta* 62, 3205–3220.
- Lavigne, M.J., 1982. A comparative study of sulphur isotope distribution of sulphide facies banded iron formations and the east south c ore zone, Dickenson gold mine, Red Lake district; a preliminary report.
- Liu, L., Mavrogenes, J., Holden, P., Ireland, T., 2020. Quadruple sulfur isotopic fractionation during pyrite desulfidation to pyrrhotite. *Geochim. Cosmochim. Acta* 273, 354–366.
- Marin-Carbonne, J., Rollion-Bard, C., Bekker, A., Rouxel, O., Agangi, A., Cavalazzi, B., Wohlgemuth-Ueberwasser, C.C., Hofmann, A., McKeegan, K.D., 2014. Coupled Fe and S isotope variations in pyrite nodules from Archean shale. *Earth Planet. Sci. Lett.* 392, 67–79.
- Marini, L., Moretti, R., Accornero, M., 2011. Sulfur isotopes in magmatic-hydrothermal systems, melts, and magmas. *Rev. Mineral. Geochemistry* 73, 423–492.
- Masterson, A.L., Farquhar, J., Wing, B.A., 2011. Sulfur mass-independent fractionation patterns in the broadband UV photolysis of sulfur dioxide: Pressure and third body effects. *Earth Planet. Sci. Lett.* 306, 253–260.
- Mojzsis, S.J., Coath, C.D., Greenwood, J.P., McKeegan, K.D., Harrison, T.M., 2003. Mass-independent isotope effects in Archean (2.5 to 3.8 Ga) sedimentary sulfides determined by ion microprobe analysis. *Geochim. Cosmochim. Acta* 67, 1635–1658.
[https://doi.org/10.1016/S0016-7037\(03\)00059-0](https://doi.org/10.1016/S0016-7037(03)00059-0)
- Monster, J., Appel, P.W.U., Thode, H.G., Schidlowski, M., Carmichael, C.M., Bridgwater, D.,

1979. Sulfur isotope studies in early Archaean sediments from Isua, West Greenland: implications for the antiquity of bacterial sulfate reduction. *Geochim. Cosmochim. Acta* 43, 405–413.
- Muller, É., Philippot, P., Rollion-Bard, C., Cartigny, P., 2016. Multiple sulfur-isotope signatures in Archean sulfates and their implications for the chemistry and dynamics of the early atmosphere. *Proc. Natl. Acad. Sci.* 113, 7432–7437.
- Muller, É., Philippot, P., Rollion-Bard, C., Cartigny, P., Assayag, N., Marin-Carbonne, J., Mohan, M.R., Sarma, D.S., 2017. Primary sulfur isotope signatures preserved in high-grade Archean barite deposits of the Sargur Group, Dharwar Craton, India. *Precambrian Res.* 295, 38–47.
- Myers, R.E., Zhou, T., Phillips, G.N., 1993. Sulphidation in the Witwatersrand Goldfields: evidence from the Middelvlei Reef. *Mineral. Mag.* 57, 395–405.
- Ohmoto, H., 1997. Sulfur and carbon isotopes. *Geochemistry hydrothermal ore Depos.* 517–611.
- Ohmoto, H., Rye, R.O., Barnes, H.L., 1979. *Geochemistry of hydrothermal ore deposits.*
- Ohmoto, H., Watanabe, Y., Ikemi, H., Poulson, S.R., Taylor, B.E., 2006. Sulphur isotope evidence for an oxic Archaean atmosphere. *Nature* 442, 908–911.
- Ono, S., Beukes, N.J., Rumble, D., 2009. Origin of two distinct multiple-sulfur isotope compositions of pyrite in the 2.5 Ga Klein Naute Formation, Griqualand West Basin, South Africa. *Precambrian Res.* 169, 48–57.
- Ono, S., Beukes, N.J., Rumble, D., Fogel, M.L., 2006. Early evolution of atmospheric oxygen from multiple-sulfur and carbon isotope records of the 2.9 Ga Mozaan Group of the Pongola Supergroup, Southern Africa. *South African J. Geol.* 109, 97–108.
- Ono, S., Eigenbrode, J.L., Pavlov, A.A., Kharecha, P., Rumble, D., Kasting, J.F., Freeman, K.H., 2003. New insights into Archean sulfur cycle from mass-independent sulfur isotope

- records from the Hamersley Basin, Australia. *Earth Planet. Sci. Lett.* 213, 15–30.
[https://doi.org/https://doi.org/10.1016/S0012-821X\(03\)00295-4](https://doi.org/https://doi.org/10.1016/S0012-821X(03)00295-4)
- Patry, L. A., Bonnard, P., Boyet, M., Afroz, M., Wilmeth, D. T., Ramsay, B., Nonnotte, P., Homann, M., Sansjofre, P., Fralick, P. W., & Lalonde, S. V. Archean origins of oxygenic photosynthesis confirmed by La-Ce geochronology. *Nature*, in review.
- Pavlov, A.A., Kasting, J.F., 2002. Mass-Independent Fractionation of Sulfur Isotopes in Archean Sediments: Strong Evidence for an Anoxic Archean Atmosphere. *Astrobiology* 2, 27–41. <https://doi.org/10.1089/153110702753621321>
- Penniston-Dorland, S.C., Wing, B.A., Nex, P.A.M., Kinnaird, J.A., Farquhar, J., Brown, M., Sharman, E.R., 2008. Multiple sulfur isotopes reveal a magmatic origin for the Platreef platinum group element deposit, Bushveld Complex, South Africa. *Geology* 36, 979–982.
- Poulton, S.W., 2011. Ferruginous Conditions: A Dominant Feature of the Ocean through Earth's History.
- Rickard, D., 2012. Sedimentary sulfur isotope biogeochemistry, in: *Developments in Sedimentology*. Elsevier, pp. 419–473.
- Roerdink, D.L., Mason, P.R.D., Farquhar, J., Reimer, T., 2012. Multiple sulfur isotopes in Paleoproterozoic barites identify an important role for microbial sulfate reduction in the early marine environment. *Earth Planet. Sci. Lett.* 331, 177–186.
- Roerdink, D.L., Mason, P.R.D., Whitehouse, M.J., Brouwer, F.M., 2016. Reworking of atmospheric sulfur in a Paleoproterozoic hydrothermal system at Londozi, Barberton Greenstone Belt, Swaziland. *Precambrian Res.* 280, 195–204.
- Rouxel, O.J., Bekker, A., Edwards, K.J., 2005. Iron isotope constraints on the Archean and Paleoproterozoic ocean redox state. *Science* (80-.). 307, 1088–1091.
- Rye, D.M., Rye, R.O., 1974. Homestake gold mine, South Dakota; I, Stable isotope studies. *Econ. Geol.* 69, 293–317.

- Schidlowski, M., Hayes, J.M., Kaplan, I.R., 1983. Isotopic inferences of ancient biochemistries-Carbon, sulfur, hydrogen, and nitrogen.
- Seal, R.R., 2006. Sulfur Isotope Geochemistry of Sulfide Minerals. *Rev. Mineral. Geochemistry* 61, 633–677. <https://doi.org/10.2138/rmg.2006.61.12>
- Shen, Y., Farquhar, J., Masterson, A., Kaufman, A.J., Buick, R., 2009. Evaluating the role of microbial sulfate reduction in the early Archean using quadruple isotope systematics. *Earth Planet. Sci. Lett.* 279, 383–391.
- Stock, E.D., 2012. The mineralogical, geochemical and isotope characteristics of alteration, mineralization and metamorphism of the Red Lake Gold Mines, Ontario. Doctoral thesis. University of British Columbia, Canada.
- Stüeken, E.E., Catling, D.C., Buick, R., 2012. Contributions to late Archean sulphur cycling by life on land. *Nat. Geosci.* 5, 722–725.
- Thomazo, C., Ader, M., Farquhar, J., Philippot, P., 2009. Methanotrophs regulated atmospheric sulfur isotope anomalies during the Mesoarchean (Tumbiana Formation, Western Australia). *Earth Planet. Sci. Lett.* 279, 65–75.
- Thomazo, C., Nisbet, E.G., Grassineau, N. V, Peters, M., Strauss, H., 2013. Multiple sulfur and carbon isotope composition of sediments from the Belingwe Greenstone Belt (Zimbabwe): A biogenic methane regulation on mass independent fractionation of sulfur during the Neoproterozoic? *Geochim. Cosmochim. Acta* 121, 120–138.
- Thurston, P.C., Breaks, F.W., 1978. Metamorphic and tectonic evolution of the Uchi-English River Subprovince, in: *Metamorphism in the Canadian Shield*. pp. 49–62.
- Tomkins, A.G., 2010. Windows of metamorphic sulfur liberation in the crust: Implications for gold deposit genesis. *Geochim. Cosmochim. Acta* 74, 3246–3259.
- Ueno, Y., Ono, S., Rumble, D., Maruyama, S., 2008. Quadruple sulfur isotope analysis of ca. 3.5 Ga Dresser Formation: New evidence for microbial sulfate reduction in the early

Chapter 6: In-situ multiple sulfur isotope analysis

Archean. Geochim. Cosmochim. Acta 72, 5675–5691.

<https://doi.org/10.1016/j.gca.2008.08.026>

Whitehill, A.R., Ono, S., 2012. Excitation band dependence of sulfur isotope mass-independent fractionation during photochemistry of sulfur dioxide using broadband light sources. Geochim. Cosmochim. Acta 94, 238–253.

Yamaguchi, K.E., Kiyokawa, S., Ito, T., Ikehara, M., Kitajima, F., Suganuma, Y., 2009. Clues of Early Life: Dixon Island–Cleaverville Drilling Project (DXCL-DP) in the Pilbara Craton of Western Australia. Sci. Drill. 7, 34–37.

Chapter 7

Conclusion and Perspectives

7.1. Summary of the principal findings

The Mesoarchean Red Lake carbonate platform preserved, in the Red Lake Greenstone Belt of the Superior Craton, Canada, provided a unique opportunity to fill important knowledge gaps regarding the deposition of Earth's first large carbonate platform and evolution of Earth's carbonate factory during the Mesoarchean. In this thesis, I focused on the elemental and isotopic signatures (carbon and oxygen isotopes, multiple sulfur isotopes) preserved in the carbonates and associated chemical and siliciclastic sedimentary rocks deposited 2.87 Ga ago to better understand marine biogeochemistry at the dawn of carbonate deposition on the early Earth (Figure 7.1). In this final chapter, I review the principal findings of the thesis and explore the perspectives of this work going forwards for several specific subthemes relating to Mesoarchean biogeochemistry.

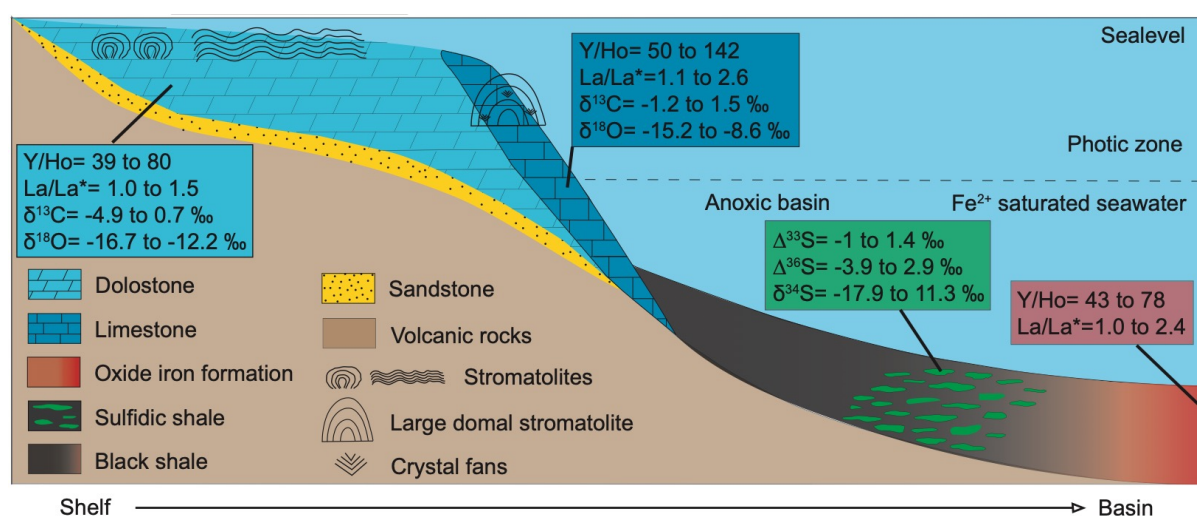


Figure 7.1: A synthetic diagram of the Red Lake carbonate platform showing shallow-to-deep settings containing various assemblages of chemical and siliciclastic sedimentary rocks along with their important geochemical and isotopic values.

The introductory Chapter 1 describes the global occurrence of carbonate rocks of Archean age and places the current study site into the broader context of prior knowledge of the Mesoarchean Earth system. Chapter 2 then described the detailed geological setting of the

Chapter 7: Conclusion and Perspectives

Red Lake greenstone belt of the Red Lake carbonate platform and other Ball Assemblage sediments associated with this platform. The full sample preparation and analytical methodologies used to obtain the elemental and isotopic data for the diverse lithofacies are provided in Chapter 3.

Chapter 4 is the first of three article-style chapters that constitute the core of the geochemical and sedimentological investigations of this thesis. Here, I address the major element, redox-sensitive trace element, and REE chemostratigraphy of the entire 490 m-thick succession, spanning the Red Lake carbonate platform comprised of more than 200 m of stromatolitic carbonate and minor massive carbonate, along with various other chemical sedimentary rocks such as chert and oxide iron formation, as well as siliciclastic sedimentary rocks such as black shale, sulfidic shale, siltstone, and sandstone. Five cored drill holes were selected for chemostratigraphic geochemical studies out of a total of nine available cored drill holes, all of which were logged in order to establish a stratigraphic correlation framework, and ultimately, to better understand the generalized stratigraphy of this unique 2.87 Ga carbonate platform.

The major element, redox-sensitive trace element, and REE data together paint a detailed and coherent picture of sediment weathering, transport, and marine biogeochemical cycling spanning shallow-to-deep settings across the Mesoarchean carbonate-producing margin. The carbonates and other chemical sedimentary rocks show characteristic PAAS-normalized REE+Y patterns typical of seawater, with suprachondritic Y/Ho ratios, positive La and Gd anomalies, and LREE depletion relative to HREE. A general lack of pronounced Ce anomalies and strong positive Eu anomalies suggest anoxic and hydrothermally influenced Archean ocean conditions. Siliciclastic sediments also show mild Eu anomalies, likely suggesting the basin waters were highly influenced by high temperature hydrothermalism, and

that some of the finer siliciclastic sediments also preserved signatures of the seawater composition of the Mesoarchean ocean. The positive Ce anomalies associated with Mn and Cr enrichment in some oxide iron formation and deeper water limestone samples and mild negative Ce anomalies in some limestone samples suggest intermittent oxygenation in the water column by photosynthetic activity, at least locally. Complementary work based on these same samples confirmed by La-Ce geochronology that La/Ce fractionation occurred during the Mesoarchean (Patry et al., in review), anchoring this site as the oldest proposed oxygen oasis that currently enjoys direct geochronological support. Carbonates and oxide iron formations show mild but significant authigenic enrichment of redox-sensitive trace elements (i.e., Mo, V, U, and Cr). These mild enrichments in redox-sensitive trace elements are best attributed to terrestrial weathering and marine hydrothermal inputs, and some oxidative processing may have been implicated in the former, however the low concentration of these elements in nearby chemical sediments appear to reflect an absence of effective oxidative cycling of these elements.

Clastic sediments associated with the Red Lake carbonates revealed important information on surface weathering intensity and sediment provenance. CIA values of ~ 70 for the fine-grained siliciclastic sediments suggest that moderate degrees of chemical weathering were operating in the terrestrial environment, and trace element discrimination diagrams indicate that siliciclastic sediments were supplied from both felsic and mafic sources. Coarse-grained sediments were most likely derived from tonalite, whereas fine-grained sediments were derived from mafic and ultramafic volcanic rocks. Finally, based on the stratigraphic and geochemical observations, a depositional model for the platform was proposed. Carbonate platform building was initiated with a transgressive flooding event that allowed carbonate sedimentation and stromatolites to grow in the warm waters of the photic zone with increasing relative sea level, with carbonate sedimentation initiated on clastic sediments forming the base

of the sedimentary sequence. The platform was exposed subaerially during sea level fall, and massive sand deposition occurred in the shallower areas of the platform. A basin-wide major flooding event is indicated by the accumulation of chert-oxide iron formation along with sulfidic shale-black shale assemblages on the eastern side of the platform, with a thinner accumulation of chert-oxide iron formation on the central and western sides of the platform. Throughout platform-building, a low-energy environment prevailed, and a non-rimmed platform margin is suggested for Red Lake considering the lateral and vertical variations of lithofacies, stromatolites, and associated structures.

Chapter 5 presented a stable carbon and oxygen isotope chemostratigraphic study of the shallow water stromatolitic dolostones and deeper water massive limestones. Carbon stable isotope data revealed a dynamic carbon cycle spanning this shallow to deep paleoenvironmental transect, with $\delta^{13}\text{C}$ values of dolostone and limestone ranging from -4.89 to 1.04 ‰ and -3.27 to 1.33 ‰, respectively. The oxygen isotope compositions vary widely, with $\delta^{18}\text{O}$ values ranging from -17.75 to -12.21 ‰ and -15.12 to -8.62 ‰, for dolostone and limestone samples, respectively. For both isotope systems, isotopically lighter values are prevalent in the dolostone samples while relatively heavier isotopic values are common for the limestone samples. Limestone samples that exhibit the heaviest stable isotope compositions, specifically with $\delta^{13}\text{C} > 0.5$ ‰ and $\delta^{18}\text{O} > -10$ ‰, are interpreted in this work as a possible reflection of the isotope composition of open ocean DIC pool. The lighter isotopic composition of $\delta^{13}\text{C}$ in limestone samples shows a weak correlation with TOC, whereas the dolostones $\delta^{13}\text{C}$ values show a stronger correlation with TOC, and in both cases, lighter $\delta^{13}\text{C}$ values are interpreted to represent the incorporation of carbon derived from organic matter remineralization, which was more important in the more shallow environments where dolostone was ultimately produced. The stromatolitic dolostone shows evidence for meteoric water interaction during dolomitization, and based on REE data, the alteration of $\delta^{18}\text{O}$ isotope

compositions by metamorphic processes is ruled out as the primary driver of the light oxygen isotope compositions. Overall, the $\delta^{18}\text{O}$ -depleted isotopic compositions of the Red Lake carbonates are similar to those reported for other Archean carbonate samples. Given the variety of carbonate mineralogies, textures, and paleoenvironmental settings observed for the Red Lake carbonates, it is inferred that the Red Lake carbonates experienced a variety of diagenetic processes, both early and late. This ultimately cumulated with late-stage burial metamorphism that induced sweeping extinction in both calcite and dolomite and involved dolomitization that continued into high temperature and pressure regimes, as testified by the occurrence of saddle dolomite. The $\delta^{13}\text{C}$ data, while typical of Archean carbonates, are difficult to explain using the classic “carbon isotope lever” model that is traditionally to interpret variations in the carbon isotope compositions of sedimentary carbonates through geological time. A revised version of this lever, with the addition of seafloor carbonatization as an additional carbon sink to compensate for the dearth of sedimentary carbonates prior to the rise of Mesoarchean carbonate platforms, is highly revealing, indicating that the carbon cycle may have operated quite differently than today in deep geological time, and that seafloor carbonatization may be an unappreciated isotopic buffer acting to stabilize Earth’s carbon cycle in over geological timescales.

Chapter 6 presented an in-situ multiple sulfur isotope study of sulfide minerals in Red Lake’s black shale occurrences, which are highly remarkable as some of the most ancient sediments on Earth show evidence for syn-sedimentary sulfide mineral formation. Sulfidic shale samples containing pyrite and pyrrhotite were analyzed by SIMS, yielding $\delta^{34}\text{S}$, $\Delta^{33}\text{S}$, and $\Delta^{36}\text{S}$ values ranging from -17.94 to 11.32 ‰, -0.99 to 1.41 ‰, and - 3.85 to 2.95 ‰, respectively, across all samples. The $\Delta^{36}\text{S}/\Delta^{33}\text{S}$ ratio shows a typical Archean slope value of -1.15 for most of the samples, except for the two pyrrhotite samples. Most of the samples show $\Delta^{33}\text{S}>0$ ‰, and the rest of the samples show $\Delta^{33}\text{S}<0$ ‰, with a small proportion of samples

falling in an unfractionated 0 ± 0.3 ‰ range. These data confirm that the sources of sulfur to the Red Lake platform were atmospherically processed, with sulfur mainly supplied from elemental atmospheric sulfur ($\Delta^{33}\text{S} > 0$ ‰), with some atmospheric sulfate ($\Delta^{33}\text{S} < 0$ ‰), and only minor juvenile sulfur ($\Delta^{33}\text{S} = 0 \pm 0.3$ ‰). Evidence for microbial sulfate reduction is suggested from the important range in negative $\delta^{34}\text{S}$ values that are accompanied by negative $\Delta^{33}\text{S}$ values in disseminated pyrite samples. Finally, the secondary growth of pyrite and their multiple sulfur isotope compositions suggest late-stage MDF processes overprinting the original isotopic signals of sulfur processing in Mesoarchean surface environments.

7.2. Implications for trace element cycling and paleo-redox reconstruction at the dawn of oxygenic photosynthesis

As detailed in Chapter 4, trace element chemostratigraphy of the 490 m succession of the Red Lake carbonate platform shows clear evidence of authigenic enrichment of certain redox-sensitive trace elements, as well as clear evidence for Ce redox cycling. As discussed in Chapter 4, the presence of positive and mild negative Ce anomalies indicate redox cycling of Ce, although in most settings at Red Lake, REE residence times appear to have been too short for Ce(III) oxidation to have generated significant negative water column Ce anomalies, as described by Patry et al. (in review). Nonetheless, mild enrichment of redox-sensitive elements, clear evidence for Ce redox cycling, the occurrence of sulfide-rich reducing sediments, the hints of sulfate reduction indicated by isotopically light $\delta^{34}\text{S}$ in sulfides, and the preservation of positive $\Delta^{33}\text{S}$ signatures over negative $\Delta^{33}\text{S}$ signatures, all indicate that oxidizing marine environments were at times established at Red Lake, at least locally. A predominance of weak positive Ce anomalies in chemical sediments, and restricted occurrence of negative Ce anomalies, indicate that the Red Lake platform captures the establishment of only weakly oxidizing conditions. A crucial question arising out of this work that cannot be avoided when

dealing with the earliest environments on Earth showing weakly oxidizing conditions is: at what levels of early O₂ production by oxygenic photosynthesis are the cycles of different redox-sensitive trace elements affected in the terrestrial or marine realms? In other words, are very mild enrichments in redox-sensitive trace elements, as observed here in a variety of chemical sediments across the platform, necessarily indicative of the presence of free oxygen?

The redox-sensitive trace element data produced in this thesis reveals clear mild but non-negligible enrichments in Mo, V, U, and Cr. Analyses were made on highly pure carbonate samples (ultra-low amounts of Al and Ti) prepared with ultra-clean acids under class 1000 clean laboratory conditions using an HR-ICP-MS instrument with detection limits that are 10 times more sensitive (or more) than conventional quadrupole ICP-MS analyses. The enrichments observed in Mo, V, U, and Cr are by no means large; indeed, considering absolute ppm abundances, they are unremarkable compared to most literature data available for Mesoarchean sediments. However, when normalized to Ti, it is readily apparent that these elements are significantly enriched relative to potential detrital sources. This thus represents a conundrum of sorts: the sediments do not show trace element concentrations that could be considered important, and on this basis, it might be difficult to argue that oxidative enrichment of these trace elements was occurring. However, the trace elements that they do contain, even when present at ultra-low levels, must have been derived partly from seawater sources. Conventional thinking about redox-sensitive trace element enrichment in chemical sediment involves (1) oxidative solubilization of a trace element during chemical weathering, (2) enhanced delivery of that trace element to marine basins, (3) establishment of a larger trace element reservoir in contemporaneous seawater, and (4) preservation of the enrichment during chemical sedimentation as the result of adsorption or co-precipitation. In the case of the enrichments reported here, the evidence we present relates largely to (4). Whether or not the seawater trace element reservoirs were actually enhanced by oxidative processes (1) and (2) is

less certain. Indeed, considering the ultra-low concentrations of the trace elements in question, it is possible that soluble trace elements were captured from ancient seawater that was not necessarily enriched in these elements due to oxidative processes, but simply that some standing reservoir of these trace elements was captured, possibly in reduced form. In other words, for mild enrichments in highly pure chemical sediments analyzed using the most sensitive instruments, when can we say that an authigenic enrichment represents an oxidative enrichment, especially when the marine reservoir of that trace element may have been non-negligible even under fully reducing conditions?

The most promising avenue going forwards lies in the stable isotope study of such trace element enrichments. Indeed, there are already cautionary lessons published in the literature that speak directly to the problem of recognizing oxidation-related vs. non-oxidative trace element enrichments in ancient sedimentary records. For example, Konhauser et al. (2011), based on a combined compilation of Cr sedimentary abundances, enrichments relative to detrital indicators (specifically in this case, Ti), and Cr stable isotope compositions, reported that >2.48 Ga ago, solubilization and sedimentary enrichment of Cr throughout the Archean and early Paleoproterozoic occurred predominantly in reduced Cr(III) form, as the Cr isotope fractionations that would indicate oxidative cycling are muted at that time. Such a scenario can be readily applied to Red Lake, where the Cr enrichments observed in the chemical sedimentary lithologies may actually represent weathering of Cr exclusively as Cr(III), and a similar scenario can be applied to Mo, V, and U. Indeed, a recent Mo stable isotope study of Red Lake samples found that the $\delta^{98/95}\text{Mo}$ isotopic composition across diverse lithofacies of Red Lake, while showing important variations in stable isotope composition, can all be explained by the different fractionating processes associated with uptake to the various lithologies investigated, all starting from on a common dissolved Mo source (presumably seawater) that was near 0 ‰; in other words, the dissolved Mo reservoir responsible for Mo authigenic enrichments at Red

Lake does not indicate an important role for oxic cycling (Migeon, 2022). Furthermore, in Chapter 4, it was seen that pronounced Eu anomalies are pervasive in the chemical sediments at Red Lake and are interpreted to indicate the presence of high-temperature hydrothermal input mixed into ambient seawater. This complicates the trace element enrichment interpretations even further, as hydrothermal fluids represent an additional potential source of solubilized trace elements, especially for Cr and Mo, that are disconnected from oxidative weathering. Future studies aiming to understand low-level trace element enrichments in chemical sedimentary rocks at the dawn of oxic seawater metal cycling will clearly benefit from a stable isotope approach that permits specific redox signatures to be extracted from Archean sediments that are more diagnostic of oxidative processes than studies of trace element enrichment alone.

7.3. Perspectives for global carbon cycling at the dawn of carbonate precipitation on Earth

As discussed in Chapter 5, the deeper water limestone facies show relatively heavier isotopic compositions ($\delta^{13}\text{C} > 0.5 \text{ ‰}$ and $\delta^{18}\text{O} > -10 \text{ ‰}$) relative to the shallow water dolostones. This division in the isotopic composition of carbon and oxygen in the Red Lake carbonates represents a mineralogical and water depth control between the dolostone and limestone facies, possibly related to periodic sea-level variations. Interestingly, for the first time to this author's awareness, the C and O stable isotope compositions of these carbonates were shown to vary with REE indicators that themselves are highly unlikely to be affected by the upper greenalite to lower amphibolite facies metamorphism experienced by the Red Lake carbonate platform. The coupling of robust REE-based paleoenvironmental indicators with C and O stable isotopic proxies that are prone to resetting offers an interesting avenue forwards for re-examining other Precambrian chert and carbonate records where it is uncertain whether

primary signatures are preserved or whether their stable isotope compositions, especially with respect to $\delta^{18}\text{O}$, represent a primary signal of the paleoenvironment, or were generated much later by resetting with high temperature fluids at depth during burial.

The heavier $\delta^{13}\text{C}$ isotopic compositions, considered in light of their correlation with REE indicators for a strong open ocean connection (namely high Y/Ho ratios and important La anomalies) in limestone samples suggests that they may be capturing the DIC of the coeval open ocean, and this reservoir appears to be the most isotopically heavy pool sampled by the dataset. Intriguingly, the $\delta^{13}\text{C}$ values of Mesoarchean samples from different localities show a slight but consistently heavier isotopic composition relative to the Neoproterozoic samples. This observation may represent a previously unrecognized signature of an ancient shift in the Archean carbon cycle. The trend is the opposite that might be expected if it was simply a question of enhanced productivity in the Neoproterozoic, which would have driven the seawater $\delta^{13}\text{C}$ isotopic composition towards more positive $\delta^{13}\text{C}$ values. It may rather indicate that respiration was more effective in the Neoproterozoic as the result of an expanding pool of oxidants fueling carbon remineralization. Or it may reflect changes that need to be interpreted using models more sophisticated than the simple carbon lever hypothesis. Indeed, in the carbon isotope mass balance model developed in Chapter 6 where seafloor carbonatization is an potential sink for carbon prior to the rise of carbonate platforms in the Mesoarchean, the entire sedimentary exit flux may constitute a much smaller relative proportion of the global carbon exit flux than previously considered. Incredibly, this model is built off of re-estimates of the modern partitioning of carbon between sediments and altered crust based on studies of Phanerozoic ophiolites. If true, it means If we consider seafloor basalt sequesters carbon from seawater that can drive the seawater composition.

7.4. A multiple isotope perspective on the deposition of one of Earth's most ancient sulfidic black shales

As described in Chapter 6, the sulfidic shale-black shale assemblages that occur in the Red Lake stratigraphy are highly significant as they constitute one of the earliest known thick occurrences on Earth of sulfidic black shales rich in pyrite and pyrrhotite. The only other Mesoarchean occurrence of such sulfide-rich sediments where the sulfides appear syn-sedimentary to early diagenetic has been reported in the 3.3 Ga Cleaverville Formation (Yamaguchi et al., 2009). The characteristic Archean slope value and the conservation of positive and negative $\Delta^{33}\text{S}$ signatures confirm the preservation of MIF signals, and thus the source of this sulfur saw atmospheric processing by photochemical reactions in the oxygen-depleted Mesoarchean atmosphere. As mentioned in Chapter, MSR is indicated by the range in $\delta^{34}\text{S}$ isotopic compositions of disseminated pyrite grains in Red Lake samples, although these are admittedly muted, and the sulfate reservoir was unlikely to have been large. While Chapter 6 presents only a preliminary study and confirms rather simply that the Red Lake sulfidic black shales are generally comparable to most younger Archean equivalents, it does not address why such sulfide-rich sediments are concentrated at Red Lake but otherwise rare in the Mesoarchean rock record. And despite the typical nature of the range in multiple sulfur isotope compositions, it leads to reflections nonetheless on how exactly sulfur was supplied to the basin. One unanswered question arising from this chapter is whether the direct deposition of atmospherically derived sulfur dominated the dissolved marine sulfur pools. Another intriguing possibility is that much of these signals are simply inherited from the weathering of sedimentary sulfides on land, and the supply of sulfur from the weathering of pyrites that were already bearing MIF signatures of atmospheric processing. Such a mechanism could be an attractive model for explaining at the same time the juxtaposition of such sulfide-rich sediments (reaching 10% FeS_2) with somewhat muted atmospheric sulfur MIF signatures. What would

an important riverine supply of sulfur from the continents, perhaps driven by incipient oxidative weathering on land, actually look like hundreds of millions of years before the GOE? Future workers aiming to explore this question might be able to couple radiogenic isotope source tracers such as Nd isotopes with multiple sulfur isotope systematics to see whether any influence of sediment sources can be discerned on the multiple sulfur isotope record; a marine sulfur pool dominated by atmospheric deposition would presumably not show any such correlation.

7.5. Concluding remarks

Extensive carbonate platform build-up is first observed on Earth in Mesoarchean greenstone belts of the Superior Craton, namely the Red Lake carbonate platform, followed by the Woman Lake, and Steep Rock carbonate platforms. The earliest occurrence of carbonates in Red Lake is not associated with strong signatures of oxygen in the water column, in contrast to these other Superior Craton carbonate platforms (Patry, 2022; Patry et al., in review). Only ephemeral photosynthetic activity is inferred for the Red Lake site juxtaposed with evidence for more intense hydrothermalism affecting the basin, whereas the Woman Lake and Steep Rock carbonates indicate a relatively important and longer-lived presence of oxygen in the water column and less pronounced hydrothermal activity. At Red Lake, the preservation of the MIF signatures, the minor but notable authigenic enrichment of redox-sensitive elements, and the muted nature of any observed Ce anomalies (both positive and negative) all suggest an oxygen-limited environment, even if oxygen was contributed through occasional photosynthetic activity (Patry, 2022; Patry et al., in review). These characteristics, along with the diverse assemblage of lithofacies preserving shallow-to-deep water sediments, makes the Red Lake carbonate platform a rather unique place in Mesoarchean going forwards for understanding the co-evolution of ocean chemistry, photosynthesis, carbon cycling, and the

Chapter 7: Conclusion and Perspectives

incipient production of free oxygen on Earth during the Mesoarchean dawn of Earth's carbonate factory.

References

- Migeon, A., 2022. Stable isotopes of molybdenum as redox tracers at ultra-low O₂ contents: chemo-stratigraphic analysis of the Mesoarchean carbonate platform of Red Lake (Ontario, Canada). MSc Thesis. University of Western Brittany, France.
- Patry, L., 2022. Constraining the Early Evolution of Earth's Photosynthetic Pathways: An Isotopic Approach. Doctoral thesis. Université de Bretagne Occidentale, France.
- Patry, L. A., Bonnand, P., Boyet, M., Afroz, M., Wilmeth, D. T., Ramsay, B., Nonnotte, P., Homann, M., Sansjofre, P., Fralick, P. W., & Lalonde, S. V. Archean origins of oxygenic photosynthesis confirmed by La-Ce geochronology. *Nature*, in review.
- Yamaguchi, K.E., Kiyokawa, S., Ito, T., Ikehara, M., Kitajima, F., Suganuma, Y., 2009. Clues of Early Life: Dixon Island–Cleaverville Drilling Project (DXCL-DP) in the Pilbara Craton of Western Australia. *Sci. Drill.* 7, 34–37.

Chapter 7: Conclusion and Perspectives

Appendix A

Appendix to Chapter 4

Appendix A.1. Whole rock major element concentrations (wt.%) for the Red Lake samples. The relative standard deviation was $\leq 2\%$ for the major elements and $\leq 1\%$ for SiO₂.

Sample	Lithology	Strat-depth (m)	SiO ₂	TiO ₂	Al ₂ O ₃	Fe ₂ O ₃	MnO	MgO	CaO	Na ₂ O	K ₂ O	P ₂ O ₅	S
EBl28-270.63	Sandstone	121.5	81.22	0.09	10.42	1.03	0.03	1.96	2.35	0.99	<BD	0.01	0.19
EBl28-281.65	Sandstone	126.5	74.63	0.32	18.23	0.11	0.00	0.16	0.91	1.00	2.34	0.05	0.03
EBl28-283.32	Sandstone	127.2	79.27	0.17	12.96	2.09	0.02	2.10	1.82	0.49	0.29	0.02	0.60
EBl28-291.73	Chert	131.0	98.19	0.05	0.20	0.26	0.01	0.13	0.10	<BD	<BD	0.02	0.11
EBl28-295.09	Cherty dolomite	132.5	57.32	<BD	<BD	2.65	0.36	8.12	13.39	<BD	<BD	0.01	0.13
EBl28-297.73	Dolostone	133.7	13.05	<BD	<BD	3.12	0.75	18.30	26.73	<BD	<BD	0.02	0.05
EBl28-304	Chert	136.5	75.64	<BD	<BD	1.49	0.24	4.72	7.89	<BD	<BD	0.01	0.09
EBl28-305.9	Chert	137.4	96.64	<BD	0.01	0.32	0.03	0.50	0.78	<BD	<BD	0.01	0.05
EBl28-308.89	Dolostone	138.7	38.29	<BD	<BD	2.39	0.67	13.14	19.64	<BD	<BD	0.01	0.05
EBl28-311.35	Dolostone	139.8	18.21	<BD	<BD	1.99	0.73	17.58	25.67	<BD	<BD	0.01	0.04
EBl28-315.64	Dolostone	141.7	44.15	0.01	0.15	4.45	0.56	9.91	17.02	<BD	<BD	0.02	0.42
EBl28-321.64	Dolostone	144.4	16.13	<BD	<BD	2.60	0.72	18.00	26.29	<BD	<BD	0.01	0.05
EBl28-326.38	Dolostone	146.6	24.29	<BD	<BD	2.03	0.75	16.04	23.48	<BD	<BD	0.01	0.04
EBl28-330	Dolostone	148.2	22.96	<BD	<BD	5.38	1.05	13.27	23.23	<BD	<BD	0.02	0.05
EBl28-332.5	Dolostone	149.3	8.78	<BD	<BD	2.35	0.81	18.80	28.71	<BD	<BD	0.01	0.07
EBl28-338.29	Siltstone	151.9	62.10	0.76	15.55	6.08	0.15	3.15	4.85	0.41	3.26	0.29	0.26
EBl28-340.10	Siltstone	152.7	61.75	0.75	16.20	5.93	0.16	4.08	6.14	0.43	3.74	0.29	0.47
EBl28-344.15	Dolostone	154.5	26.94	<BD	<BD	2.58	0.76	14.15	22.03	<BD	<BD	0.01	0.05
EBl28-347.38	Dolostone	156.0	8.76	<BD	<BD	1.67	0.71	19.08	27.64	<BD	<BD	0.01	0.05
EBl28-350	Dolostone	157.2	38.69	<BD	<BD	1.86	0.64	12.19	19.09	<BD	<BD	0.01	0.04
EBl28-356	Dolostone	159.9	10.39	<BD	<BD	2.20	0.78	18.18	27.10	<BD	<BD	0.01	0.04
EBl28-360.4	Dolostone	161.8	14.46	<BD	<BD	2.49	0.79	17.45	26.50	<BD	<BD	0.01	0.04
EBl28-365.22	Dolostone	164.0	16.36	<BD	<BD	6.35	0.84	14.15	24.99	<BD	<BD	0.02	0.08
EBl28-368.09	Dolostone	165.3	17.33	<BD	<BD	2.11	0.79	16.62	25.09	<BD	<BD	0.01	0.04
EBl28-373.40	Dolostone	167.7	13.84	<BD	<BD	2.38	0.73	17.20	25.71	<BD	<BD	0.01	0.06
EBl28-378.10	Dolostone	169.8	6.63	<BD	<BD	3.28	0.81	18.23	27.95	<BD	<BD	0.02	0.10
EBl28-382.76	Dolostone	171.9	7.43	<BD	<BD	4.54	0.80	17.21	27.10	<BD	<BD	0.01	0.07
EBl28-387	Dolostone	173.8	3.86	<BD	<BD	3.92	0.77	19.27	29.09	<BD	<BD	0.02	0.07
EBl28-389.46	Dolostone	174.9	3.81	<BD	<BD	4.89	0.98	18.31	29.59	<BD	<BD	0.02	0.07
EBl28-395.56	Dolostone	177.6	33.56	<BD	<BD	2.14	0.70	12.99	19.06	<BD	<BD	0.01	0.29
EBl28-400.3	Dolostone	179.7	3.58	<BD	<BD	3.22	0.85	19.71	28.51	<BD	<BD	0.01	0.18
EBl28-402.89	Dolostone	180.9	8.83	<BD	<BD	3.15	0.87	18.82	28.86	<BD	<BD	0.01	0.11
EBl28-407.06	Siltstone	182.8	75.55	0.17	14.52	1.23	0.05	1.24	1.40	0.26	3.82	0.06	0.05
EBl28-411.24	Dolostone	184.7	18.13	<BD	<BD	2.38	0.83	16.28	25.07	<BD	<BD	0.01	0.12
EBl28-416.30	Dolostone	186.9	31.84	<BD	<BD	1.95	0.59	13.46	20.69	<BD	<BD	0.01	0.20
EBl28-421.44	Dolostone	189.2	20.84	<BD	<BD	1.94	0.62	15.98	24.21	<BD	<BD	0.01	0.08
EBl28-426.25	Dolostone	191.4	28.24	<BD	<BD	2.27	0.68	14.10	22.03	<BD	<BD	0.01	0.06
EBl28-429.76	Dolostone	193.0	13.69	<BD	<BD	2.21	0.80	17.99	26.93	<BD	<BD	0.01	0.18
EBl28-433.56	Dolostone	194.7	16.35	<BD	<BD	2.68	0.76	16.72	25.70	<BD	<BD	0.01	0.11
EBl28-436.44	Dolostone	196.0	33.08	<BD	<BD	2.46	0.59	12.97	20.64	<BD	<BD	0.01	0.07
EBl28-443.28	Dolostone	199.0	13.72	<BD	0.01	4.27	0.50	16.71	26.50	<BD	<BD	0.02	0.09
EBl28-446.76	Dolostone	200.6	19.71	<BD	<BD	4.22	0.58	15.42	24.88	<BD	<BD	0.02	0.15
EBl28-451.93	Dolostone	202.9	6.44	<BD	0.02	4.55	0.66	18.47	28.75	<BD	<BD	0.02	0.08

Appendix to Chapter 4

Sample	Lithology	Strat-depth (m)	SiO ₂	TiO ₂	Al ₂ O ₃	Fe ₂ O ₃	MnO	MgO	CaO	Na ₂ O	K ₂ O	P ₂ O ₅	S
PB32-148.92	Dolostone	134.53	36.45	0.03	0.03	3.86	0.66	11.50	19.46	<BD	<BD	0.02	0.14
PB32-152.02	Iron Formation	137.33	36.25	0.01	0.05	44.83	1.46	7.51	2.85	<BD	<BD	0.10	0.89
PB32-152.51	Iron Formation	137.77	72.73	0.01	0.03	17.29	0.45	3.35	2.67	<BD	<BD	0.04	0.25
PB32-154.51	Iron Formation	139.58	68.66	0.01	0.03	19.84	0.48	4.07	4.28	<BD	<BD	0.04	0.66
PB32-155.7	Iron Formation	140.65	13.36	0.02	0.16	39.41	1.74	9.82	13.01	<BD	<BD	0.08	0.14
PB32-156.96	Iron Formation	141.79	20.47	0.03	1.30	43.19	1.88	7.98	8.64	<BD	0.01	0.07	0.87
PB32-160.15	Dolostone	144.67	44.57	0.01	0.02	7.10	0.34	8.14	16.94	<BD	<BD	0.03	0.07
PB32-161.21	Ferroan dolostone	145.63	31.75	0.01	0.03	17.32	1.01	7.97	16.38	<BD	<BD	0.04	2.90
PB32-165	Dolostone	149.05	22.05	0.01	0.02	3.02	0.44	14.81	23.61	<BD	<BD	0.02	0.05
PB32-168.13	Dolostone	151.88	54.05	0.02	0.03	6.39	0.45	6.07	13.19	<BD	0.01	0.02	0.29
PB32-169.57	Dolostone	153.18	54.73	0.01	0.03	9.87	0.51	5.56	11.41	<BD	<BD	0.03	1.22
PB32-172.93	Dolostone	156.21	29.44	0.01	0.03	6.07	0.45	11.98	21.42	<BD	<BD	0.02	0.08
PB32-174.94	Silty Dolostone	158.03	46.00	0.77	11.99	7.75	0.12	9.05	7.65	2.97	3.38	0.60	0.40
PB32-178.29	Dolostone	161.06	32.94	0.01	0.03	3.46	0.51	12.55	19.96	<BD	<BD	0.02	0.08
PB32-179.54	Dolostone	162.19	10.30	0.01	0.05	6.33	0.61	15.84	26.76	<BD	<BD	0.02	0.06
PB32-183.38	Dolostone	165.65	53.89	0.01	0.03	12.70	0.41	7.26	10.81	<BD	<BD	0.04	0.46
PB32-185.22	Dolostone	167.32	25.99	0.01	0.05	26.46	1.14	10.67	15.40	<BD	<BD	0.05	0.18
PB32-189.02	Iron Formation	170.75	39.58	0.02	0.07	4.38	0.53	10.01	18.04	<BD	0.02	0.02	0.07
PB32-190.25	Dolostone	171.86	4.96	0.01	0.05	2.34	0.77	19.32	28.98	<BD	<BD	0.02	0.07
PB32-194.05	Dolostone	175.29	3.38	0.01	0.03	3.79	1.00	18.54	29.24	<BD	<BD	0.02	0.12
PB32-195.5	Dolostone	176.60	6.07	0.01	0.03	3.47	1.04	18.43	28.38	<BD	0.01	0.02	0.06
PB32-197.35	Dolostone	178.27	10.30	0.01	0.05	4.46	0.95	16.64	27.29	<BD	<BD	0.02	0.11
PB32-199.28	Dolostone	180.02	8.38	0.01	0.09	3.79	0.91	16.41	27.79	<BD	0.02	0.02	0.30
PB32-201.92	Dolostone	182.40	9.31	0.01	0.11	3.20	0.90	16.15	27.49	<BD	0.01	0.02	0.11
PB32-205.25	Dolostone	185.41	20.52	0.01	0.09	3.75	0.76	15.38	24.37	<BD	0.01	0.02	0.11
PB32-208.58	Dolostone	188.42	16.28	0.01	0.03	3.67	0.86	16.53	26.59	<BD	<BD	0.02	0.11
PB32-212.08	Dolostone	191.58	1.99	0.01	0.03	4.11	1.11	18.82	29.78	<BD	<BD	0.02	0.12
PB32-215.56	Dolostone	194.72	61.01	0.01	0.06	4.96	0.37	4.82	11.34	<BD	<BD	0.02	0.21
PB32-219.7	Sandstone	198.46	72.01	0.19	14.80	2.08	0.06	1.61	1.50	0.75	3.16	0.07	0.33
PB32-222.13	Sandstone	200.66	70.41	0.21	14.88	1.84	0.06	2.11	2.86	0.93	2.82	0.06	0.20
PB32-225.73	Sandstone	203.91	54.12	0.77	16.35	8.63	0.13	3.26	5.10	3.30	2.71	0.39	0.77
PB32-228.2	Sandstone	206.14	72.45	0.21	15.28	1.45	0.05	1.81	1.90	0.94	3.31	0.06	0.00
PB32-231.88	Siltstone	209.47	72.63	0.21	15.68	1.72	0.06	1.37	1.70	1.18	2.70	0.06	0.06
PB32-233.3	Black slate	210.75	60.02	0.53	15.15	6.30	0.17	1.99	1.78	1.16	2.61	0.05	2.19
PB32-234.35	Siltstone	211.70	64.27	0.42	17.14	3.72	0.15	1.57	4.33	2.44	1.49	0.13	0.54
PB32-237.3	Siltstone	214.36	62.93	0.40	16.68	3.45	0.06	1.28	4.72	3.36	1.44	0.13	0.49
PB32-240.26	Siltstone	217.04	63.71	0.45	16.30	4.55	0.08	2.82	4.45	2.06	1.96	0.12	0.74
PB32-241.5	Siltstone	218.16	64.10	0.46	16.34	4.38	0.05	2.73	2.50	1.77	2.80	0.11	0.50
PB32-242.3	Siltstone	218.88	64.69	0.42	16.13	3.89	0.06	2.22	3.42	1.77	2.61	0.11	0.10
PB32-248.91	Chert	224.85	78.45	0.01	0.17	8.44	0.35	1.74	3.37	<BD	<BD	0.03	0.09
PB32-252.78	Iron Formation	228.35	49.19	0.01	0.35	25.41	1.30	5.75	6.97	<BD	<BD	0.16	0.85
PB32-255.08	Chert	230.42	81.96	<BD	0.16	5.89	0.27	1.51	3.66	<BD	<BD	0.02	0.18
PB32-257.5	Sulfidic slate	232.61	55.02	0.27	7.33	24.70	0.04	1.25	1.03	0.39	1.13	0.10	10.17

Appendix to Chapter 4

Sample	Lithology	Strat-depth (m)	SiO ₂	TiO ₂	Al ₂ O ₃	Fe ₂ O ₃	MnO	MgO	CaO	Na ₂ O	K ₂ O	P ₂ O ₅	S
PB32-260.23	Black slate	235.08	50.24	0.37	15.44	13.57	0.19	1.90	0.32	0.35	3.84	0.05	5.58
PB32-270.71	Black slate	244.54	40.94	0.56	35.71	4.74	0.05	0.57	3.47	1.79	3.58	0.18	2.26
PB32-279.73	Black slate	252.69	55.22	0.48	16.70	9.26	0.23	1.59	2.62	1.50	2.22	0.11	4.30
PB32-291.40	Black slate	258.99	60.98	0.40	10.04	14.18	0.19	1.81	2.69	0.72	1.00	0.11	6.00
PB32-292.37	Dolostone	264.11	12.74	0.01	0.18	3.96	0.80	16.03	26.60	<BD	<BD	0.01	0.19
PB32-295.80	Dolostone	267.21	4.64	<BD	0.03	2.38	0.85	19.20	29.13	<BD	<BD	0.01	0.05

Sample	Lithology	Strat-depth (m)	SiO ₂	TiO ₂	Al ₂ O ₃	Fe ₂ O ₃	MnO	MgO	CaO	Na ₂ O	K ₂ O	P ₂ O ₅	S
PB33-108.27	Dolostone	59.62	13.11	<BD	<BD	2.87	0.71	17.08	26.39	<BD	<BD	0.02	0.05
PB33-112	Dolostone	61.67	21.49	<BD	<BD	1.88	0.62	15.74	23.94	<BD	<BD	0.01	0.04
PB33-116.73	Dolostone	64.28	41.65	<BD	<BD	2.09	0.50	10.63	17.09	<BD	<BD	0.01	0.08
PB33-123.58	Dolostone	68.05	3.67	<BD	<BD	3.61	0.99	18.14	28.90	<BD	<BD	0.02	0.05
PB33-129.05	Dolostone	71.06	3.30	<BD	<BD	2.62	0.81	19.36	29.42	<BD	<BD	0.02	0.05
PB33-134.82	Dolostone	74.24	5.12	<BD	<BD	3.16	0.79	19.54	30.95	<BD	<BD	0.02	0.05
PB33-138.35	Dolostone	76.18	3.14	<BD	0.01	4.10	0.83	19.12	30.91	<BD	<BD	0.02	0.05
PB33-145.63	Dolostone	80.19	11.39	<BD	0.07	4.98	0.94	16.52	27.93	<BD	<BD	0.02	0.12
PB33-157.17	Dolostone	86.55	12.44	<BD	0.02	4.34	0.81	16.13	26.95	<BD	<BD	0.02	0.12
PB33-163.13	Dolostone	89.83	3.10	<BD	0.02	3.78	0.77	19.69	30.81	<BD	<BD	0.02	0.13
PB33-167.40	Black slate	92.18	63.89	0.44	17.15	3.43	0.18	1.90	3.49	1.61	1.66	0.03	1.16
PB33-169.24	Black slate	93.19	61.47	0.53	17.64	4.54	0.17	2.29	2.10	0.98	2.97	0.05	1.93
PB33-170.16	Black slate	93.70	60.87	0.52	17.64	5.25	0.33	2.76	3.96	1.16	2.34	0.04	2.02
PB33-175.08	Black slate	96.41	57.10	0.56	16.20	15.23	0.09	1.77	1.88	0.56	1.27	0.15	6.57
PB33-180.97	Black slate	99.65	51.85	0.51	15.01	10.35	0.26	6.24	10.18	0.38	1.09	0.32	3.19
PB33-185.23	Chert	102.00	94.74	<BD	0.04	0.62	0.05	0.44	0.84	<BD	<BD	0.01	0.07
PB33-191.45	Black slate	105.42	55.89	0.63	16.19	17.03	0.18	1.07	0.80	0.21	1.32	0.09	7.27
PB33-198.19	Black slate	109.14	61.88	0.47	18.24	6.21	0.09	1.80	1.98	0.94	3.11	0.08	2.62
PB33-200.10	Black slate	110.19	67.11	0.45	14.23	4.29	0.24	2.27	2.14	0.63	2.60	0.03	1.76
PB33-201.53	Black slate	110.97	59.16	0.58	16.13	9.70	0.19	2.66	3.32	0.92	2.35	0.05	4.01
PB33-203.73	Black slate	112.19	64.33	0.51	16.48	4.37	0.38	3.07	4.17	1.50	1.55	0.03	1.47
PB33-206.73	Black slate	113.84	64.24	0.50	15.53	3.87	0.51	3.21	4.21	1.28	1.53	0.04	1.02
PB33-208.63	Black slate	114.88	66.35	0.54	16.30	4.26	0.38	2.50	2.98	0.97	1.59	0.05	1.35
PB33-209.80	Black slate	115.53	70.90	0.46	14.61	3.52	0.19	1.65	2.35	0.76	0.91	0.03	1.11
PB33-211.16	Black slate	116.28	65.95	0.45	15.77	9.01	1.18	1.64	1.29	0.52	1.02	0.05	2.91
PB33-215.68	Dolostone	118.77	0.82	0.01	0.26	5.60	0.71	19.28	31.02	<BD	<BD	0.02	0.37
PB33-224.52	Dolostone	123.63	1.90	<BD	<BD	3.53	0.56	20.55	32.00	<BD	<BD	0.02	0.05
PB33-232.46	Dolostone	128.01	5.40	<BD	0.05	3.19	0.81	19.46	29.78	<BD	<BD	0.02	0.05
PB33-235.73	Dolostone	129.81	2.16	<BD	<BD	4.69	0.65	19.75	31.18	<BD	<BD	0.02	0.04
PB33-238.8	Dolostone	131.50	<BD	<BD	0.01	5.31	0.65	19.03	30.76	<BD	<BD	0.02	0.06

Appendix to Chapter 4

Sample	Lithology	Strat-depth (m)	SiO ₂	TiO ₂	Al ₂ O ₃	Fe ₂ O ₃	MnO	MgO	CaO	Na ₂ O	K ₂ O	P ₂ O ₅	S
PB35-22.48	Limestone	19.3	1.30	0.01	0.02	0.31	0.38	0.53	54.97	<BD	<BD	0.01	0.11
PB35-24.22	Limestone	20.8	19.93	0.01	0.08	0.64	0.39	0.53	43.75	0.01	<BD	0.01	0.19
PB35-26.43	Limestone	22.7	3.23	0.01	0.04	1.86	0.91	0.34	51.77	<BD	<BD	0.01	0.67
PB35-29.37	Limestone	25.3	1.36	0.01	0.06	3.14	1.18	0.41	51.70	<BD	0.01	0.01	0.12
PB35-31.20	Limestone	26.8	26.84	0.01	0.04	2.03	0.74	0.72	37.92	<BD	<BD	0.01	0.16
PB35-34.20	Limestone	29.4	4.41	0.01	0.03	1.71	0.76	0.30	51.73	<BD	<BD	0.01	0.10
PB35-36.84	Limestone	31.7	14.01	0.01	0.02	1.57	0.68	0.68	45.72	<BD	<BD	0.01	0.10
PB35-39.70	Limestone	34.1	3.16	0.01	0.02	0.40	0.75	0.29	53.00	<BD	<BD	0.01	0.15
PB35-41.30	Black slate	35.5	63.48	0.46	11.02	4.72	0.07	1.58	2.96	3.50	2.58	0.18	0.29
PB35-43.65	Dolostone	37.5	7.00	0.01	0.07	4.79	0.70	17.54	26.79	<BD	<BD	0.01	0.09
PB35-47.10	Dolostone	40.5	5.84	0.01	0.03	3.22	0.89	17.24	27.82	<BD	<BD	0.01	0.05
PB35-49.43	Limestone	42.5	23.37	0.04	0.99	2.39	0.72	0.55	37.73	0.23	0.19	0.01	0.18
PB35-52.87	Limestone	45.5	10.97	0.02	0.21	2.91	0.70	1.85	45.68	0.03	0.04	0.01	0.51
PB35-54.38	Limestone	46.8	12.42	0.01	0.07	1.29	0.79	0.50	47.55	0.03	<BD	0.01	0.14
PB35-56.57	Dolostone	48.7	4.14	0.02	0.43	7.38	1.14	15.78	27.71	0.02	0.12	0.02	0.37
PB35-58.02	Dolostone	49.9	11.67	0.01	0.03	6.55	1.10	15.24	26.35	<BD	<BD	0.01	0.12
PB35-59.80	Dolostone	51.4	14.22	0.01	0.03	3.67	0.76	16.09	25.70	<BD	<BD	0.01	0.05
PB35-61.20	Dolostone	52.6	5.79	0.01	0.10	6.52	1.04	15.56	27.96	0.01	0.02	0.02	0.17
PB35-65	Black slate	55.9	55.55	0.65	10.16	4.56	0.23	3.48	7.76	1.40	2.91	0.16	0.05
PB35-68.65	Limestone	59.0	4.83	0.01	0.12	0.89	0.74	0.27	52.65	0.04	0.01	0.01	0.19
PB35-69.68	Limestone	59.9	3.04	0.01	0.02	1.51	0.64	0.90	52.43	<BD	<BD	0.01	0.13
PB35-70.63	Limestone	60.8	2.86	0.01	0.02	1.01	0.78	0.27	54.00	<BD	<BD	0.01	0.14
PB35-73.51	Limestone	63.2	2.89	0.01	0.08	0.26	0.84	0.31	54.41	0.01	<BD	0.01	0.12
PB35-76	Black slate	65.4	54.99	0.47	11.88	10.80	0.26	2.44	1.69	0.48	3.59	0.05	4.48
PB35-77.86	Limestone	67.0	10.00	0.01	0.06	<BD	0.21	0.06	50.68	0.01	<BD	0.01	0.14
PB35-79.6	Limestone	68.5	3.79	0.01	0.07	3.72	1.11	8.77	39.72	0.01	<BD	0.02	0.14
PB35-81.15	Limestone	69.8	30.86	0.32	5.39	4.62	0.32	3.73	24.03	3.10	0.72	0.15	0.34
PB35-84.52	Sandstone	72.7	61.62	0.39	8.64	3.92	0.13	2.47	4.43	5.28	1.35	0.09	0.37
PB35-85.7	Black slate	73.7	60.78	0.45	10.62	4.53	0.10	2.91	4.49	1.58	3.95	0.12	0.28
PB35-87.93	Dolostone	75.6	1.04	0.01	0.07	4.72	0.78	17.55	29.21	<BD	<BD	0.01	0.19
PB35-89.76	Dolostone	77.2	7.20	0.01	0.06	2.74	0.69	17.99	27.69	<BD	<BD	0.02	0.05
PB35-91.8	Dolostone	79.0	2.35	0.01	0.03	2.71	0.74	18.92	29.12	<BD	<BD	0.01	0.05
PB35-92.8	Dolostone	79.8	7.76	0.03	0.37	4.90	0.78	16.44	26.58	<BD	0.26	0.02	0.57
PB35-93.80	Dolostone	80.7	6.33	0.03	1.05	4.48	0.93	15.07	26.68	0.50	0.19	0.02	0.12
PB35-96.3	Black slate	82.8	58.62	0.60	18.48	3.38	0.02	1.69	0.46	1.85	5.64	0.05	0.96
PB35-98.94	Dolostone	85.1	12.48	0.02	0.72	5.65	0.82	15.33	25.26	0.29	0.17	0.01	0.39
PB35-102.02	Dolostone	87.7	6.43	0.01	0.19	4.21	0.84	17.34	27.50	0.06	0.04	0.02	0.26
PB35-104.00	Black slate	89.5	57.47	0.52	10.65	5.90	0.17	2.35	4.34	5.39	1.32	0.13	1.39
PB35-105.81	Black slate	91.0	60.61	0.51	11.78	5.39	0.11	2.56	4.03	3.43	2.71	0.13	1.77
PB35-109.08	Black slate	93.8	56.33	0.65	19.37	5.79	0.05	1.10	1.14	1.48	6.22	0.06	2.94
PB35-110.90	Black slate	95.4	59.00	0.59	21.05	3.20	0.05	0.89	0.27	0.71	6.95	0.04	1.20
PB35-112.96	Black slate	97.2	55.59	0.54	19.48	4.78	0.25	1.11	1.67	2.19	5.44	0.05	1.99
PB35-114.34	Black slate	98.3	61.43	0.83	18.72	3.59	0.09	1.15	0.59	0.88	5.92	0.06	1.31

Appendix to Chapter 4

Sample	Lithology	Strat-depth (m)	SiO ₂	TiO ₂	Al ₂ O ₃	Fe ₂ O ₃	MnO	MgO	CaO	Na ₂ O	K ₂ O	P ₂ O ₅	S
PB35-115.9	Black slate	99.7	53.62	0.58	20.56	4.62	0.20	1.78	1.78	1.66	5.19	0.05	2.08
PB35-118.22	Black slate	101.7	60.04	0.58	12.31	5.79	0.24	2.45	5.22	2.73	2.30	0.16	1.31
PB35-120.1	Black slate	103.3	54.15	0.55	19.19	7.41	0.81	2.49	4.34	2.24	3.09	0.06	3.10
PB35-122.14	Black slate	105.1	51.27	0.67	10.31	7.67	0.20	4.59	9.78	0.68	2.71	0.33	2.28
PB35-124.95	Black slate	107.5	50.02	0.60	20.20	11.20	0.04	0.68	0.57	0.73	6.44	0.04	4.53
PB35-126.63	Black slate	108.9	56.80	0.49	16.82	8.74	0.07	1.89	2.57	1.78	3.45	0.04	3.22
PB35-130.43	Black slate	112.2	60.61	0.58	18.22	3.80	0.06	1.50	1.46	1.69	4.73	0.06	1.22
PB35-133.24	Black slate	114.6	54.87	0.60	21.40	4.74	0.21	1.18	1.20	1.50	5.40	0.04	1.87
PB35-136.52	Black slate	117.4	61.06	0.57	12.12	5.21	0.14	2.40	5.27	2.73	2.32	0.21	1.41
PB35-138.74	Black slate	119.3	66.25	0.56	17.05	3.53	0.02	0.51	0.94	1.22	4.31	0.05	1.38
PB35-141.60	Black slate	121.8	56.53	0.62	19.65	6.24	0.06	1.50	1.98	1.96	4.03	0.06	2.23
PB35-144.40	Limestone	124.2	2.20	0.01	0.03	0.17	0.77	0.24	54.43	<BD	<BD	0.01	0.10
PB35-147.00	Limestone	126.4	7.76	0.01	0.02	0.48	0.73	0.41	50.72	<BD	<BD	0.01	0.09
PB35-149.76	Limestone	128.8	6.81	0.01	0.02	0.58	0.80	0.31	51.59	<BD	<BD	0.01	0.09
PB35-151.12	Limestone	130.0	3.47	0.01	0.02	0.74	0.82	0.30	53.53	0.01	<BD	0.01	0.10
PB35-153.50	Limestone	132.0	2.16	0.01	0.02	1.08	0.45	0.48	54.52	<BD	<BD	0.01	0.10
PB35-156.20	Limestone	134.4	8.32	0.01	0.02	0.60	0.64	0.36	51.22	<BD	<BD	0.01	0.11
PB35-157.75	Limestone	135.7	6.39	0.01	0.02	0.45	0.65	0.30	52.56	<BD	<BD	0.01	0.19
PB35-160.96	Limestone	138.4	2.38	0.01	0.02	0.50	0.65	0.32	55.31	<BD	<BD	0.01	0.17
PB35-162.4	Limestone	139.7	12.20	0.01	0.04	0.46	0.65	0.43	50.08	<BD	0.01	0.01	0.23
PB35-163.7	Limestone	140.8	10.42	0.01	0.04	0.78	0.55	0.39	50.55	<BD	0.01	0.01	0.22
PB35-166	Black slate	142.8	61.07	0.61	14.96	5.68	0.08	2.56	4.24	4.14	2.35	0.22	0.29
PB35-168.42	Limestone	144.9	1.42	0.01	0.05	0.23	0.40	0.47	55.86	<BD	0.01	0.01	0.13
PB35-171.13	Limestone	147.2	14.44	0.01	0.05	0.93	1.44	0.66	46.49	<BD	0.01	0.02	0.09
PB35-173.1	Limestone	148.9	8.78	0.01	0.41	0.58	0.88	0.48	50.28	0.21	0.01	0.02	0.13
PB35-176	Limestone	151.4	15.56	0.01	0.06	0.21	0.89	0.37	46.68	<BD	0.01	0.01	0.10
PB35-177.5	Limestone	152.7	14.43	0.01	0.06	0.95	1.28	0.48	45.98	<BD	0.02	0.02	0.13
PB35-178.8	Limestone	153.8	8.29	0.01	0.08	0.87	1.25	0.34	49.89	<BD	0.01	0.02	0.15
PB35-180.8	Limestone	155.5	1.68	0.02	0.06	0.49	0.78	0.54	54.10	<BD	0.01	0.01	0.17
PB35-184.26	Limestone	158.5	8.02	0.01	0.21	0.59	0.67	1.13	49.72	0.01	0.04	0.01	0.10
PB35-187.29	Dolostone	161.1	11.97	0.01	0.26	2.93	1.05	13.40	27.15	<BD	0.06	0.02	0.11
PB35-190.30	Dolostone	163.7	3.77	0.01	0.06	3.58	1.01	16.19	28.88	<BD	0.02	0.02	0.05
PB35-193.40	Dolostone	166.3	53.16	0.01	0.10	2.28	0.59	7.18	15.99	0.01	0.02	0.02	0.05
PB35-195.3	Dolostone	168.0	23.60	0.01	0.24	2.61	0.86	11.61	24.01	<BD	0.09	0.02	0.06
PB35-198.5	Dolostone	170.7	42.97	0.02	0.08	2.09	0.67	9.50	19.11	<BD	0.02	0.02	0.08
PB35-200.6	Dolostone	172.5	3.13	0.01	0.08	2.32	1.03	16.29	29.45	<BD	0.02	0.02	0.07
PB35-202.3	Dolostone	174.0	15.56	0.01	0.08	2.36	0.91	13.09	27.23	<BD	0.02	0.03	0.10
PB35-205	Dolostone	176.3	5.55	0.01	0.12	2.32	0.98	11.90	27.33	<BD	0.03	0.02	0.39
PB35-206.7	Dolostone	177.8	13.04	0.03	0.75	3.35	0.96	11.48	28.36	<BD	0.14	0.02	0.17
PB35-209	Dolostone	179.8	8.07	0.01	0.18	3.27	1.01	13.38	28.39	<BD	0.03	0.02	0.24
PB35-211.5	Dolostone	181.9	17.70	0.02	0.53	4.33	1.10	11.17	28.48	0.02	0.13	0.04	0.27
PB35-213.2	Iron Formation	183.4	43.63	0.37	9.62	19.47	0.54	3.28	8.62	1.27	1.25	0.09	7.11
PB35-215.04	Iron Formation	185.0	49.28	0.16	3.22	23.96	1.20	3.01	6.67	0.43	0.34	0.09	9.21

Appendix to Chapter 4

Sample	Lithology	Strat-depth (m)	SiO ₂	TiO ₂	Al ₂ O ₃	Fe ₂ O ₃	MnO	MgO	CaO	Na ₂ O	K ₂ O	P ₂ O ₅	S
PB35-217.8	Limestone	187.3	7.21	0.01	0.06	0.61	0.56	0.52	52.46	<BD	0.01	0.02	0.12
PB35-219.6	Black slate	188.9	74.11	0.34	14.71	0.76	0.03	1.27	1.46	0.57	3.74	0.01	0.06
PB35-221.3	Limestone	190.3	17.76	0.01	0.05	0.44	0.51	0.64	46.32	<BD	0.01	0.01	0.15
PB35-223.3	Limestone	192.1	30.77	0.01	0.04	0.42	0.57	0.44	39.02	<BD	0.01	0.02	0.21
PB35-225.1	Limestone	193.6	45.61	0.01	0.05	0.19	0.42	0.52	30.55	<BD	0.01	0.01	0.07
PB35-227.8	Limestone	195.9	20.37	0.01	0.11	1.61	0.69	1.04	43.22	<BD	0.02	0.01	0.34
PB35-230.02	Limestone	197.8	8.14	0.02	0.07	0.78	0.78	0.77	48.93	<BD	<BD	0.02	0.22
PB35-231.96	Dolostone	199.5	3.74	0.01	0.01	2.79	0.98	17.78	29.89	<BD	<BD	0.02	0.56
PB35-235.2	Limestone	202.3	6.72	0.02	0.08	0.34	0.35	0.72	52.34	<BD	<BD	0.02	0.14
PB35-237.4	Limestone	204.2	4.49	0.01	0.03	1.16	0.90	0.46	53.70	<BD	<BD	0.02	0.51
PB35-239.3	Limestone	205.8	8.95	0.01	0.03	0.57	0.40	0.58	51.69	<BD	<BD	0.02	0.18
PB35-241.5	Limestone	207.7	6.06	0.01	0.01	0.62	0.26	0.41	52.32	<BD	<BD	0.02	0.23
PB35-243.4	Limestone	209.4	34.19	0.02	<BD	0.54	0.48	0.59	37.49	<BD	<BD	0.02	0.11
PB35-245.5	Limestone	211.2	9.70	0.01	<BD	1.28	0.54	0.39	50.35	<BD	<BD	0.02	0.13
PB35-247.8	Limestone	213.1	10.97	0.01	0.04	1.22	0.57	0.38	46.47	<BD	<BD	0.02	0.49
PB35-250.8	Limestone	215.7	9.37	0.01	0.01	0.38	0.81	0.34	51.64	<BD	<BD	0.02	0.15
PB35-251.11	Limestone	216.0	0.63	0.02	0.03	0.69	1.14	0.30	54.51	<BD	<BD	0.02	0.20
PB35-254.4	Cherty dolomite	218.5	61.75	0.67	14.34	6.33	0.14	2.71	4.79	1.27	3.66	0.16	2.03
PB35-256.2	Chert	219.1	76.14	0.24	14.12	0.81	0.00	0.54	0.19	5.14	1.79	0.07	0.02

Appendix A.2. Whole rock minor and Trace element concentrations (ppm) for the Red Lake samples. Precision for most elements is better than 5% (1 relative standard deviation, RSD).

Sample	Lithology	Strat-depth (m)	Cr	Mo	V	U	Th	Sr	Li	Ba	Hf	Sc	Co	Ni	Cu	Zn	Zr
EBL28-270.63	Sandstone	121.5	140.36	0.60	12.57	0.67	2.65	129.28	138.66	11.64	1.40	2.46	5.10	54.98	10.50	9.24	59.03
EBL28-281.65	Sandstone	126.5	753.16	2.22	123.12	1.89	7.03	147.59	22.97	243.14	3.52	10.41	55.90	438.80	3.82	2.97	136.31
EBL28-283.32	Sandstone	127.2	889.44	0.69	29.46	0.88	6.09	106.40	240.20	34.69	2.03	6.45	27.63	138.82	39.69	21.40	83.57
EBL28-291.73	Chert	131.0	70.09	8.90	2.38	0.14	0.04	1.58	1.45	6.01	0.22	LD	3.68	59.88	2.14	0.97	2.86
EBL28-295.09	Cherty dolomite	132.5	41.19	0.98	3.36	0.12	0.02	22.20	1.41	0.74	0.22	2.04	1.41	32.24	1.74	14.48	2.03
EBL28-297.73	Dolostone	133.7	9.42	0.80	1.84	0.11	0.03	51.02	2.22	0.47	0.22	1.51	0.98	26.34	0.46	28.98	2.84
EBL28-304	Chert	136.5	59.14	0.96	2.64	0.08	0.03	10.06	1.48	2.02	0.23	1.19	1.35	21.53	1.89	9.45	1.25
EBL28-305.9	Chert	137.4	90.44	1.69	0.61	0.09	0.03	2.59	1.47	2.38	0.23	0.22	1.09	18.99	1.90	3.86	1.52
EBL28-308.89	Dolostone	138.7	15.72	0.29	0.62	0.05	0.03	35.02	1.44	0.57	0.22	LD	0.48	8.32	0.44	13.91	2.31
EBL28-311.35	Dolostone	139.8	9.69	0.26	0.89	0.13	0.03	47.91	2.24	0.42	0.22	0.55	0.65	9.80	0.51	24.64	2.56
EBL28-315.64	Dolostone	141.7	34.02	0.96	15.21	0.27	0.02	37.04	1.95	4.26	0.22	2.33	8.13	35.40	5.02	13.29	3.38
EBL28-321.64	Dolostone	144.4	10.64	0.29	2.10	0.09	0.03	43.03	2.25	0.72	0.22	1.13	0.87	8.75	0.41	17.47	2.44
EBL28-326.38	Dolostone	146.6	11.49	0.23	0.36	0.05	0.03	21.37	1.43	0.52	0.22	LD	0.56	6.43	0.37	16.66	1.47
EBL28-330	Dolostone	148.2	14.23	0.30	0.82	0.30	0.03	16.75	2.05	0.79	0.28	LD	0.38	5.45	0.27	9.20	2.74
EBL28-332.5	Dolostone	149.3	7.37	0.22	1.03	0.08	0.03	22.31	2.49	0.97	0.21	0.38	1.59	13.49	0.23	26.22	1.76
EBL28-338.29	Siltstone	151.9	304.21	1.09	192.37	2.46	7.94	112.16	61.47	587.48	4.07	24.48	88.53	314.42	113.14	51.48	162.62
EBL28-340.10	Siltstone	152.7	121.01	0.99	192.86	2.25	8.13	102.98	60.78	497.37	4.04	20.16	23.26	48.82	81.19	51.84	168.93
EBL28-344.15	Dolostone	154.5	16.30	0.24	0.46	0.16	0.03	18.52	1.46	0.66	0.23	LD	0.20	3.42	0.44	10.38	1.41
EBL28-347.38	Dolostone	156.0	6.07	0.16	0.23	0.03	0.03	22.53	1.59	0.42	0.23	LD	0.20	3.42	0.44	10.38	1.41
EBL28-350	Dolostone	157.2	13.68	0.29	1.00	0.42	0.03	16.61	1.39	0.68	0.21	0.21	0.36	8.80	0.51	10.83	1.60
EBL28-356	Dolostone	159.9	6.26	0.09	0.92	0.12	0.03	30.75	1.63	0.52	0.22	0.32	0.35	9.62	0.17	13.72	1.48
EBL28-360.4	Dolostone	161.8	7.13	0.17	0.93	0.15	0.03	29.80	1.58	0.51	0.21	0.47	0.37	10.30	0.23	14.29	1.55
EBL28-365.22	Dolostone	164.0	19.47	0.88	3.09	1.00	0.03	43.86	2.90	1.43	0.22	1.75	5.09	38.75	1.17	21.92	3.81
EBL28-368.09	Dolostone	165.3	13.81	0.36	1.04	0.21	0.03	39.80	2.05	0.71	0.20	0.52	0.44	6.76	0.46	38.63	2.44
EBL28-373.40	Dolostone	167.7	6.21	0.21	0.93	0.04	0.03	29.17	1.43	0.49	0.21	0.46	0.96	18.73	0.25	17.67	1.61
EBL28-378.10	Dolostone	169.8	14.28	0.20	1.34	0.07	0.03	43.55	1.92	0.51	0.22	0.37	1.55	23.59	0.22	24.99	2.00
EBL28-382.76	Dolostone	171.9	6.04	0.29	2.74	0.09	0.03	44.35	1.92	1.01	0.23	1.25	0.67	20.65	0.19	27.52	5.12
EBL28-387	Dolostone	173.8	3.56	0.18	1.50	0.05	0.03	42.61	1.80	0.63	0.22	0.51	0.46	9.75	0.14	18.43	2.01
EBL28-389.46	Dolostone	174.9	4.05	0.24	2.18	0.10	0.02	43.57	2.01	0.60	0.22	0.93	1.10	23.31	0.26	16.99	2.16
EBL28-395.56	Dolostone	177.6	22.91	0.43	0.22	0.09	0.03	11.13	1.40	0.47	0.22	LD	1.22	14.14	0.57	6.42	1.35
EBL28-400.3	Dolostone	179.7	2.95	0.20	0.25	0.09	0.03	28.41	1.39	0.51	0.21	LD	0.83	20.04	0.30	15.62	1.71
EBL28-402.89	Dolostone	180.9	7.49	1.40	0.76	0.08	0.03	33.45	1.42	0.52	0.22	0.27	0.77	11.35	0.55	15.69	1.66
EBL28-407.06	Siltstone	182.8	26.07	1.18	18.52	3.16	10.26	51.56	28.41	278.31	3.97	3.31	1.84	13.23	2.03	16.18	152.32
EBL28-411.24	Dolostone	184.7	10.13	0.29	0.96	0.11	0.03	17.80	1.39	0.47	0.21	0.31	0.36	6.95	0.36	6.69	2.03
EBL28-416.30	Dolostone	186.9	16.27	0.26	0.48	0.06	0.03	18.94	1.40	0.41	0.22	LD	0.69	20.59	0.27	13.91	1.42
EBL28-421.44	Dolostone	189.2	17.51	0.31	0.54	0.10	0.03	24.20	1.44	0.37	0.22	LD	0.28	11.62	0.33	10.66	1.83
EBL28-426.25	Dolostone	191.4	12.63	0.21	1.56	0.13	0.03	20.15	1.44	0.36	0.22	LD	0.19	6.50	0.31	11.83	1.78
EBL28-429.76	Dolostone	193.0	6.41	0.17	4.13	0.21	0.03	26.84	1.67	3.51	0.21	1.18	0.51	7.31	0.69	6.75	2.22
EBL28-433.56	Dolostone	194.7	6.57	0.14	1.16	0.08	0.03	26.50	1.38	0.55	0.21	0.31	0.44	6.40	0.31	8.50	1.62
EBL28-436.44	Dolostone	196.0	11.08	0.13	1.06	0.04	0.03	22.12	1.40	0.27	0.21	0.31	0.21	5.02	0.28	7.57	1.40
EBL28-443.28	Dolostone	199.0	9.34	0.18	0.73	0.12	0.03	33.11	1.57	0.77	0.21	LD	0.68	6.85	0.26	8.32	3.26
EBL28-446.76	Dolostone	200.6	10.97	0.26	1.00	0.15	0.02	34.56	1.91	1.06	0.23	LD	0.89	7.38	0.30	8.82	2.77
EBL28-451.93	Dolostone	202.9	4.59	0.16	0.84	0.10	0.03	32.96	2.43	0.96	0.21	LD	0.45	6.23	0.18	10.98	2.59

Appendix to Chapter 4

Sample	Lithology	Strat-depth (m)	Cr	Mn	V	U	Th	Sr	Li	Ba	Hf	Sc	Co	Ni	Cu	Zn	Zr
PB32-9.66	Sandstone	8.73	1326.80	1.08	57.18	0.53	1.62	95.02	62.73	299.26	2.35	10.54	35.44	308.45	61.89	31.85	102.44
PB32-14.87	Sandstone	13.43	270.65	1.38	33.06	0.37	1.53	87.58	77.46	95.63	1.42	5.20	14.23	124.19	21.53	24.60	58.17
PB32-17.3	Sandstone	15.63	154.53	0.65	18.87	0.88	4.25	129.53	195.77	56.42	1.93	4.17	5.48	72.66	3.15	43.60	83.79
PB32-21.50	Dolostone	19.42	6.51	1.76	3.36	0.60	0.06	66.87	2.46	7.54	0.22	0.51	6.70	294.51	36.72	25.10	2.87
PB32-24.25	Dolostone	21.91	5.72	0.51	0.80	0.12	0.03	39.98	1.78	2.14	0.23	0.20	0.90	14.83	0.97	28.35	1.47
PB32-27.50	Dolostone	24.84	14.93	0.38	2.09	0.41	0.06	33.16	2.44	6.83	0.28	0.27	0.89	11.54	0.97	30.54	3.04
PB32-31.56	Dolostone	28.51	7.81	0.22	0.64	0.18	0.03	29.16	1.84	1.99	0.21	LD	0.32	7.69	0.91	23.69	1.60
PB32-34.62	Dolostone	31.27	11.57	0.27	0.91	0.29	0.04	25.60	2.05	4.70	0.21	0.17	0.28	6.88	1.01	21.76	2.94
PB32-39.11	Dolostone	35.33	5.49	0.25	0.66	0.17	0.03	31.12	2.28	1.50	0.22	LD	1.09	8.23	0.93	24.00	1.93
PB32-43.70	Dolostone	39.48	3.91	0.17	0.68	0.08	0.03	39.87	1.59	1.19	0.21	LD	0.18	3.06	0.89	27.44	1.91
PB32-44.81	Dolostone	40.48	12.32	0.19	0.80	0.09	0.03	44.02	2.00	2.83	0.22	LD	0.42	6.20	0.94	72.73	1.72
PB32-48.88	Dolostone	44.16	2.79	0.28	0.66	0.08	0.03	52.50	1.97	3.98	0.22	LD	0.41	5.08	0.92	28.08	1.71
PB32-50.31	Dolostone	45.45	13.85	0.70	2.79	0.17	0.05	84.89	3.45	13.06	0.21	0.28	0.55	11.81	0.93	149.09	2.00
PB32-56.08	Dolostone	50.66	8.65	0.26	1.21	0.21	0.03	55.72	3.61	3.39	0.23	LD	0.65	7.74	0.98	29.56	1.76
PB32-60.70	Dolostone	54.83	2.53	0.71	2.93	0.11	0.05	75.82	4.00	11.48	0.22	0.45	0.24	7.96	0.94	37.78	1.75
PB32-62.29	Dolostone	56.27	11.37	0.47	5.04	0.53	0.14	66.78	4.50	11.03	0.32	0.88	0.68	15.93	15.85	30.67	3.84
PB32-65.66	Dolostone	59.31	10.98	0.47	3.43	0.10	0.06	72.66	10.30	1.53	0.21	1.88	1.14	7.35	0.90	34.47	2.05
PB32-70.38	Dolostone	63.58	5.24	0.28	0.48	0.10	0.03	32.61	1.58	1.29	0.23	LD	0.18	4.80	0.96	26.92	1.61
PB32-72.89	Dolostone	65.84	4.31	0.26	0.83	0.12	0.04	41.57	1.93	1.57	0.21	LD	0.21	3.53	0.90	28.08	1.63
PB32-75.53	Siltstone	68.23	22.28	0.57	53.95	1.10	4.04	136.21	70.38	933.18	3.22	5.38	11.03	7.77	23.03	51.62	134.19
PB32-78.91	Siltstone	71.28	23.31	0.34	50.63	1.08	4.01	126.19	53.99	753.56	3.20	4.95	8.67	6.90	36.94	59.07	136.94
PB32-83.95	Siltstone	75.84	27.50	0.44	54.69	1.13	4.31	148.34	59.17	832.89	3.33	5.49	10.30	8.59	30.41	56.99	144.12
PB32-85.73	Dolostone	77.44	3.04	2.89	3.35	0.09	0.04	45.74	1.97	4.07	0.21	0.52	0.88	10.58	1.16	109.67	1.80
PB32-88.23	Dolostone	79.70	5.33	0.28	2.51	0.35	0.03	49.55	2.03	5.14	0.22	0.29	0.81	8.56	1.23	86.94	1.50
PB32-90.70	Dolostone	81.93	4.20	0.80	2.21	0.21	0.04	49.89	2.50	2.88	0.21	0.29	3.78	50.56	121.18	36.40	2.33
PB32-93.88	Dolostone	84.81	7.41	0.83	1.52	0.08	0.03	35.42	3.18	3.03	0.22	0.22	0.74	6.19	0.33	20.36	2.25
PB32-96.88	Dolostone	87.52	2.63	0.12	1.72	0.13	0.04	39.66	2.86	2.60	0.22	0.39	0.45	4.45	0.26	19.00	2.52
PB32-98.57	Dolostone	89.04	3.14	0.23	3.55	0.23	0.05	44.39	3.10	4.99	0.22	0.83	0.27	4.95	0.23	19.29	2.54
PB32-102.13	Dolostone	92.26	4.80	0.23	2.14	0.16	0.04	43.69	2.83	4.92	0.22	0.22	0.46	5.88	0.26	19.48	1.71
PB32-104.85	Dolostone	94.72	4.24	0.13	1.09	0.24	0.03	39.50	1.93	2.81	0.21	0.17	0.42	4.92	0.36	19.72	1.41
PB32-108.35	Dolostone	97.88	8.60	0.16	5.33	0.35	0.04	42.05	3.80	5.42	0.22	0.47	0.87	7.33	2.86	32.37	2.16
PB32-112.63	Dolostone	101.74	6.68	0.14	4.81	0.36	0.03	37.86	2.16	4.28	0.22	0.68	0.16	3.54	0.32	24.58	1.67
PB32-116.89	Dolostone	105.59	10.75	0.19	0.99	0.17	0.03	31.39	1.90	2.70	0.22	LD	0.27	5.4	0.21	10.43	1.39
PB32-121.10	Dolostone	109.39	15.48	6.89	2.47	0.15	0.09	49.91	1.61	11.37	0.21	0.32	1.78	9.75	4.44	10.06	3.27
PB32-124.93	Dolostone	112.85	10.77	0.24	0.82	0.11	0.03	38.38	1.41	4.56	0.21	LD	0.76	6.21	0.30	18.91	1.94
PB32-128.48	Dolostone	116.06	14.08	0.17	3.81	0.51	0.04	32.69	1.38	2.19	0.21	LD	0.59	6.68	1.33	4.60	1.42
PB32-131.03	Dolostone	118.36	14.08	0.17	3.81	0.51	0.04	32.69	1.41	3.70	0.22	0.28	0.57	6.63	2.86	7.22	2.64
PB32-133.27	Cherty dolostone	120.39	38.14	0.22	0.84	0.06	0.03	15.68	1.42	0.51	0.22	LD	0.40	5.78	2.97	4.93	1.61
PB32-135.77	Dolostone	122.65	8.57	0.13	1.49	0.12	0.02	49.24	1.70	2.45	0.22	0.30	0.32	3.43	0.81	15.16	3.54
PB32-137.28	Dolostone	124.01	26.40	0.26	2.29	0.20	0.07	32.12	1.45	5.95	0.22	0.61	0.64	6.46	0.52	6.21	2.96
PB32-139.87	Dolostone	126.35	6.59	0.39	3.69	0.20	0.17	27.32	3.53	14.03	0.22	1.11	2.39	14.43	3.67	6.76	5.15
PB32-143.3	Dolostone	129.45	22.58	0.25	3.22	0.14	0.03	44.93	1.69	4.52	0.22	1.25	0.22	7.98	0.95	26.70	3.00
PB32-146.16	Dolostone	132.03	11.52	0.41	0.75	0.18	0.03	40.52	1.31	3.30	0.21	LD	6.64	18.10	0.91	20.50	1.63

Appendix to Chapter 4

Sample	Lithology	Strat-depth (m)	Cr	Mo	V	U	Th	Sr	Li	Ba	Hf	Sc	Co	Ni	Cu	Zn	Zr
PB32-148.92	Dolostone	134.53	18.54	0.23	3.13	0.31	0.03	28.90	1.71	4.65	0.22	0.38	0.33	7.19	0.95	11.47	2.26
PB32-152.02	Iron Formation	137.33	12.29	0.33	1.34	0.22	0.03	6.31	2.11	4.68	0.22	0.22	0.63	9.24	11.67	34.33	8.89
PB32-152.51	Iron Formation	137.77	38.33	0.47	1.64	0.02	0.03	4.88	1.38	2.15	0.23	LD	0.34	7.94	12.05	12.05	3.08
PB32-154.51	Iron Formation	139.58	33.12	0.31	0.40	0.03	0.03	10.25	1.14	2.77	0.23	LD	0.27	4.33	10.92	108.79	3.20
PB32-155.7	Iron Formation	140.65	4.82	0.24	5.03	0.11	0.06	25.85	1.51	3.92	0.21	0.57	0.90	9.42	3.04	19.57	7.01
PB32-156.96	Iron Formation	141.79	6.30	0.24	6.57	0.07	0.62	22.81	4.41	8.72	0.30	1.43	0.91	7.65	6.19	26.85	13.75
PB32-160.15	Dolostone	144.67	15.06	0.18	0.63	0.03	0.03	23.77	1.31	1.24	0.22	LD	0.30	2.15	0.92	105.82	1.44
PB32-161.21	Ferrous dolostone	145.63	9.86	0.18	3.81	0.11	0.03	31.45	1.71	1.25	0.22	0.18	6.19	61.35	69.83	19.92	2.87
PB32-165	Dolostone	149.05	19.34	0.26	0.50	0.08	0.03	45.38	1.52	1.44	0.22	LD	0.18	2.56	0.94	19.06	1.21
PB32-168.13	Dolostone	151.88	16.84	0.23	2.56	0.20	0.03	14.12	1.17	2.52	0.22	0.22	0.28	3.45	4.96	12.34	1.48
PB32-169.57	Dolostone	153.18	16.33	0.29	0.86	0.03	0.03	15.63	1.08	2.21	0.22	LD	0.85	8.04	11.29	15.68	2.07
PB32-172.93	Dolostone	156.21	13.04	0.22	0.47	0.05	0.03	22.18	1.39	2.53	0.22	LD	0.27	3.10	0.92	188.60	1.42
PB32-174.94	Silty Dolostone	158.03	502.27	0.26	158.76	3.63	16.92	1961.50	99.82	1557.13	6.70	18.98	42.42	277.87	34.64	87.35	254.21
PB32-178.29	Dolostone	161.06	15.25	0.26	0.26	0.08	0.03	22.56	1.51	2.22	0.22	LD	0.23	3.54	0.94	55.12	1.33
PB32-179.54	Dolostone	162.19	6.25	0.17	0.36	0.03	0.02	24.05	2.10	2.38	0.22	LD	0.18	1.95	0.92	9.43	2.18
PB32-183.38	Dolostone	165.65	19.70	0.26	1.50	0.11	0.03	17.39	3.42	2.52	0.21	0.19	0.55	3.77	2.46	9.07	2.99
PB32-185.22	Iron Formation	167.32	7.66	0.68	0.65	0.10	0.03	19.09	1.91	3.17	0.21	LD	0.41	8.81	0.91	21.74	4.65
PB32-189.02	Dolostone	170.75	17.59	0.28	0.85	0.05	0.03	19.26	1.28	5.98	0.23	LD	0.33	4.25	0.96	13.65	1.86
PB32-190.25	Dolostone	171.86	3.50	0.28	0.96	0.43	0.03	48.53	2.49	2.17	0.22	LD	0.36	6.22	0.94	18.05	1.92
PB32-194.05	Dolostone	175.29	3.09	0.35	0.86	0.20	0.03	48.01	1.80	1.66	0.22	0.15	0.40	6.73	0.92	140.26	1.51
PB32-195.5	Dolostone	176.60	3.02	0.19	0.60	0.13	0.03	44.64	1.66	2.13	0.22	LD	0.28	5.39	0.95	68.79	1.82
PB32-197.35	Dolostone	178.27	6.32	0.24	1.37	0.39	0.04	40.88	2.14	1.34	0.22	0.21	0.34	6.10	1.29	17.05	2.29
PB32-199.28	Dolostone	180.02	5.00	0.30	1.94	0.26	0.04	40.62	2.82	6.59	0.22	0.27	0.87	6.80	0.92	60.99	2.35
PB32-201.92	Dolostone	182.40	3.19	0.19	0.76	0.11	0.04	35.69	2.59	4.41	0.23	LD	0.27	4.59	0.96	61.01	1.99
PB32-205.25	Dolostone	185.41	8.64	0.20	0.76	0.08	0.03	24.62	2.43	7.74	0.23	LD	0.29	4.30	0.97	60.14	2.11
PB32-208.58	Dolostone	188.42	6.13	0.19	0.46	0.08	0.03	26.26	1.51	1.69	0.22	LD	0.21	3.31	0.95	59.49	1.65
PB32-212.08	Dolostone	191.58	4.60	0.23	1.09	0.22	0.03	27.77	1.52	2.40	0.23	0.26	0.33	3.82	0.97	62.92	2.59
PB32-215.56	Dolostone	194.72	22.86	0.26	0.67	0.04	0.03	28.19	1.67	6.52	0.23	LD	0.48	6.28	0.96	57.53	1.96
PB32-219.7	Sandstone	198.46	14.26	4.33	18.77	2.27	6.95	53.52	70.78	370.66	3.50	2.98	2.81	5.14	22.85	72.73	132.99
PB32-222.13	Sandstone	200.66	21.80	0.40	20.22	2.23	7.00	64.42	70.57	354.04	3.52	3.08	3.24	6.87	2.37	87.34	136.29
PB32-225.73	Sandstone	203.91	12.18	0.22	172.83	1.16	4.17	674.63	122.41	617.98	3.84	16.43	24.17	10.07	9.23	157.09	166.51
PB32-228.2	Sandstone	206.14	17.84	0.42	20.89	2.26	7.20	63.59	60.70	370.93	3.54	3.21	2.28	7.21	0.97	83.81	141.19
PB32-231.88	Siltstone	209.47	26.38	30.39	26.43	2.43	7.62	150.72	91.79	344.34	5.17	4.01	3.63	8.34	13.00	44.16	170.14
PB32-233.3	Black slate	210.75	272.14	5.64	218.53	2.28	8.00	222.40	100.42	287.91	4.13	27.44	102.79	292.56	76.36	225.17	170.63
PB32-234.35	Siltstone	211.70	33.43	0.42	71.00	1.20	4.57	509.41	94.85	425.63	3.66	7.32	15.12	17.64	32.64	96.32	168.63
PB32-237.3	Siltstone	214.36	43.39	0.49	65.37	1.20	4.76	579.95	94.57	497.72	3.69	6.55	11.55	10.11	20.60	76.18	172.37
PB32-240.26	Siltstone	217.04	63.76	0.97	110.63	1.38	4.12	281.89	105.36	377.27	3.12	11.88	16.15	31.10	30.36	76.60	135.38
PB32-241.5	Siltstone	218.16	57.11	1.85	103.77	1.37	4.11	200.01	126.22	511.77	3.09	11.04	16.72	27.88	23.64	63.71	132.12
PB32-242.3	Siltstone	218.88	53.19	1.54	99.73	1.22	3.85	218.02	98.74	591.63	2.83	10.54	13.77	28.35	36.28	65.39	121.95
PB32-248.91	Chert	224.85	86.44	0.85	3.51	0.04	0.07	31.82	8.23	17.16	0.22	0.40	1.95	11.61	4.96	32.89	6.42
PB32-252.78	Iron Formation	228.35	39.46	1.08	7.66	0.13	0.17	39.12	11.60	7.14	0.22	0.86	3.96	12.85	18.14	97.83	10.76
PB32-255.08	Chert	230.42	58.00	0.87	3.12	0.02	0.06	22.80	6.04	1.99	0.22	0.32	1.93	9.97	4.76	22.47	3.55
PB32-257.5	Sulfidic slate	232.61	108.08	3.57	93.26	0.96	3.58	50.85	54.48	45.88	2.02	14.10	98.67	383.79	217.28	863.94	78.56

Appendix to Chapter 4

Sample	Lithology	Strat-depth (m)	Cr	Mo	V	U	Th	Sr	Li	Ba	Hf	Sc	Co	Ni	Cu	Zn	Zr
PB332-260.23	Black slate	235.08	2543.41	4.95	277.55	1.23	3.82	39.04	96.06	85.76	2.50	46.83	63.11	312.90	457.92	2959.29	111.34
PB332-270.71	Black slate	244.54	78.26	1.63	144.90	2.87	12.05	360.81	181.17	915.88	9.58	28.60	6.79	41.99	58.03	135.39	419.16
PB332-279.73	Black slate	252.69	170.26	5.29	153.35	3.06	9.59	183.90	183.53	147.41	4.86	18.08	38.83	150.96	375.03	159.68	228.19
PB332-291.40	Black slate	258.99	131.72	3.88	124.73	1.17	3.83	87.77	67.79	89.32	2.24	18.69	32.42	185.70	390.19	872.52	102.82
PB332-292.37	Dolostone	264.11	11.05	0.94	2.67	0.18	0.15	74.88	9.59	30.27	0.21	0.47	1.01	10.81	1.97	20.10	5.66
PB332-295.80	Dolostone	267.21	5.63	0.50	0.90	0.16	0.03	58.74	2.96	2.36	0.22	LD	0.35	5.60	0.79	25.18	1.70

Sample	Lithology	Strat-depth (m)	Cr	Mo	V	U	Th	Sr	Li	Ba	Hf	Sc	Co	Ni	Cu	Zn	Zr
PB333-108.27	Dolostone	59.6	13.12	0.42	1.71	0.17	0.03	57.60	3.34	2.03	0.23	0.20	0.24	9.02	0.90	13.37	1.51
PB333-112	Dolostone	61.7	32.02	0.47	0.69	0.03	0.03	48.98	2.69	1.10	0.21	LD	0.38	7.93	0.81	12.31	1.80
PB333-116.73	Dolostone	64.3	41.22	0.49	0.58	0.09	0.03	24.47	1.74	0.90	0.22	LD	0.54	10.65	1.53	7.52	1.50
PB333-123.58	Dolostone	68.1	3.04	0.32	0.37	0.10	0.03	28.19	2.37	1.33	0.37	LD	0.19	5.07	0.68	22.96	2.17
PB333-129.05	Dolostone	71.1	8.74	0.33	0.48	0.09	0.03	29.64	2.59	0.83	0.22	LD	0.17	6.06	0.75	35.70	1.92
PB333-134.82	Dolostone	74.2	3.34	0.28	1.21	0.24	0.03	31.50	3.06	1.11	0.22	LD	0.25	5.92	0.64	15.25	1.96
PB333-138.95	Dolostone	76.2	5.75	0.17	3.30	0.09	0.03	38.61	2.57	1.81	0.22	0.26	1.01	10.27	0.67	21.71	1.77
PB333-145.63	Dolostone	80.2	6.07	0.29	1.90	0.13	0.03	57.67	5.52	2.90	0.22	LD	1.45	23.03	0.75	16.09	2.03
PB333-157.17	Dolostone	86.5	8.34	0.23	1.72	0.14	0.03	26.79	2.88	5.66	0.22	0.29	0.77	9.64	1.83	11.44	2.06
PB333-163.13	Dolostone	89.8	4.28	0.17	1.95	0.09	0.03	115.19	4.44	8.64	0.21	0.21	0.43	9.79	3.79	18.25	5.39
PB333-167.40	Black slate	92.2	194.13	3.12	147.43	1.45	5.34	221.67	152.68	348.96	2.92	19.73	26.57	193.86	44.25	58.53	121.30
PB333-169.24	Black slate	93.2	224.53	3.42	167.38	1.81	6.58	193.16	153.04	275.39	3.55	21.89	27.51	171.96	62.33	48.22	147.49
PB333-170.16	Black slate	93.7	210.16	4.82	175.38	1.58	5.72	209.65	112.25	194.12	3.12	21.32	30.58	210.37	54.94	151.08	133.26
PB333-175.08	Black slate	96.4	129.71	4.45	134.00	2.13	7.87	185.79	73.14	111.21	4.16	23.13	84.20	146.64	103.76	1393.24	164.64
PB333-180.97	Black slate	99.7	197.00	1.47	248.80	2.22	13.49	238.55	90.05	325.83	2.99	38.96	45.94	89.05	70.44	114.71	128.57
PB333-185.23	Chert	102.0	55.34	0.65	0.94	0.03	0.03	5.67	10.02	6.55	0.23	LD	0.71	10.08	3.93	3.46	0.62
PB333-191.45	Black slate	105.4	239.17	5.59	205.77	2.05	7.26	175.43	73.15	100.20	4.04	33.10	44.30	194.80	273.42	2657.92	169.08
PB333-198.19	Black slate	109.1	131.96	2.58	132.37	1.94	7.51	191.90	115.10	256.83	4.37	17.96	19.18	136.61	31.34	30.45	189.67
PB333-200.10	Black slate	110.2	213.02	3.67	157.88	1.42	4.93	137.50	128.53	280.92	2.81	18.46	21.40	170.51	42.52	82.24	127.10
PB333-201.53	Black slate	111.0	165.15	4.46	152.17	1.81	6.49	191.06	143.13	136.96	3.27	20.19	251.94	504.41	120.87	118.44	134.01
PB333-203.73	Black slate	112.2	257.97	3.66	175.07	1.64	6.02	261.93	161.95	176.73	3.12	21.84	27.70	184.52	68.86	98.65	134.26
PB333-206.73	Black slate	113.8	227.83	3.10	151.36	1.59	5.43	214.14	205.39	203.00	3.00	19.72	16.10	129.08	44.07	82.05	130.86
PB333-208.63	Black slate	114.9	234.16	3.75	153.24	1.61	5.91	189.98	157.66	237.81	3.22	19.47	22.17	162.57	49.76	59.14	141.65
PB333-209.80	Black slate	115.5	230.77	3.13	137.49	1.47	4.77	149.20	116.30	172.89	2.96	17.04	18.73	144.31	45.84	37.90	120.51
PB333-211.16	Black slate	116.3	216.36	2.76	118.95	1.86	8.00	42.31	109.65	105.07	3.15	17.23	24.87	126.28	32.17	36.44	129.96
PB333-215.68	Dolostone	118.8	8.25	0.54	4.99	0.26	0.12	40.21	6.97	9.04	0.23	0.62	3.80	26.79	2.51	18.12	4.09
PB333-224.52	Dolostone	123.6	2.50	0.20	0.98	0.05	0.03	44.62	3.16	1.08	0.22	0.19	0.47	5.58	0.24	18.12	1.82
PB333-232.46	Dolostone	128.0	7.28	0.20	5.24	0.24	0.02	47.80	3.02	2.35	0.23	1.07	0.80	11.59	0.30	20.12	2.81
PB333-235.73	Dolostone	129.8	3.19	0.33	1.28	0.09	0.03	44.78	2.90	1.08	0.21	0.19	0.53	13.26	0.27	16.59	2.04
PB333-238.8	Dolostone	131.5	2.20	0.15	3.68	0.08	0.03	49.49	3.12	2.03	0.22	LD	1.50	17.89	0.37	20.07	2.06

Appendix to Chapter 4

Sample	Lithology	Strat-depth (m)	Cr	Mn	V	U	Th	Sr	Li	Ba	Hf	Sc	Co	Ni	Cu	Zn	Zr
PB35-22.48	Limestone	19.3	3.00	0.24	0.28	0.05	0.02	1209.64	0.70	21.58	0.18	0.12	0.16	1.53	10.21	60.26	0.91
PB35-24.22	Limestone	20.8	24.69	0.53	4.66	0.15	0.07	496.29	5.14	20.23	0.14	0.36	1.90	7.88	2.13	61.90	3.15
PB35-26.43	Limestone	22.7	5.84	0.42	2.39	0.69	0.06	120.85	3.65	5.53	0.14	0.47	3.23	13.55	1.00	279.43	2.17
PB35-29.37	Limestone	25.3	2.85	0.26	2.30	0.55	0.08	103.49	1.82	16.10	0.14	0.43	0.37	3.41	1.00	174.20	2.28
PB35-31.20	Limestone	26.8	27.08	0.30	1.40	0.23	0.03	220.97	1.97	20.90	0.14	0.11	0.49	6.15	1.00	173.72	1.65
PB35-34.20	Limestone	29.4	5.92	0.23	1.34	0.77	0.04	145.54	2.66	4.15	0.14	0.16	0.18	1.55	1.01	181.99	1.63
PB35-36.84	Limestone	31.7	13.74	0.25	2.28	0.15	0.02	273.34	1.49	3.66	0.14	2.76	3.24	3.24	1.00	138.07	1.71
PB35-39.70	Limestone	34.1	3.12	0.21	0.45	0.33	LD	184.96	0.69	8.21	0.14	0.12	0.14	1.85	1.01	114.79	1.09
PB35-41.30	Black slate	35.5	92.34	8.92	184.51	4.22	18.88	605.40	100.97	1311.94	6.27	18.59	34.15	51.08	45.41	667.66	298.28
PB35-43.65	Dolostone	37.5	8.42	0.28	2.99	0.23	0.05	92.29	6.94	7.65	0.14	0.55	3.35	33.41	1.95	374.31	2.60
PB35-47.10	Dolostone	40.5	7.00	0.47	2.10	0.28	0.04	66.80	2.74	3.90	0.14	0.49	0.79	8.66	1.01	281.64	4.53
PB35-49.43	Limestone	42.5	30.53	2.09	16.85	0.99	0.71	749.56	3.38	134.72	0.34	2.47	1.94	16.11	3.28	93.17	14.18
PB35-52.87	Limestone	45.5	8.23	0.45	3.24	0.41	0.22	234.92	3.87	56.35	0.14	0.63	16.35	13.36	4.37	120.67	8.04
PB35-54.38	Limestone	46.8	6.05	0.27	1.89	0.16	0.02	266.02	0.86	9.85	0.14	0.12	3.84	4.20	1.01	58.46	2.54
PB35-56.57	Dolostone	48.7	15.48	0.70	19.99	0.30	0.22	262.47	9.33	46.44	0.15	1.31	5.04	15.82	5.02	246.48	8.29
PB35-58.02	Dolostone	49.9	15.33	0.73	5.51	0.11	LD	178.73	1.91	5.12	0.14	0.11	0.70	6.57	2.39	97.65	1.79
PB35-59.80	Dolostone	51.4	9.57	0.21	7.41	0.10	0.02	195.37	2.24	4.13	0.14	0.11	0.86	4.53	1.00	106.84	1.84
PB35-61.20	Dolostone	52.6	5.56	0.32	8.79	0.11	0.04	180.80	4.46	5.70	0.14	0.18	1.56	5.70	2.06	98.23	2.39
PB35-65	Black slate	55.9	192.95	2.44	226.61	1.44	5.80	361.36	82.98	545.30	4.59	26.10	23.34	56.03	5.69	111.11	206.75
PB35-68.65	Limestone	59.0	2.91	0.22	1.57	0.14	0.04	400.40	1.14	15.54	0.14	0.11	0.72	3.07	1.30	116.32	1.35
PB35-69.68	Limestone	59.9	1.50	0.22	0.39	0.08	0.02	197.42	0.77	6.09	0.18	0.11	0.49	1.27	1.00	76.01	1.34
PB35-70.63	Limestone	60.8	1.92	0.19	0.51	0.15	LD	228.01	0.69	5.90	0.14	0.12	0.88	1.05	1.01	95.77	1.04
PB35-73.51	Limestone	63.2	2.20	0.16	1.33	0.17	0.06	176.57	1.70	25.65	0.14	0.11	0.37	5.64	1.12	129.78	1.84
PB35-76	Black slate	65.4	281.79	5.05	229.46	1.95	7.36	142.76	156.66	155.76	3.72	28.54	111.82	786.55	274.23	175.98	162.78
PB35-77.86	Limestone	67.0	4.13	0.55	1.32	0.34	0.02	48.78	2.48	3.90	0.14	0.15	0.32	2.05	1.00	162.76	0.90
PB35-79.6	Limestone	68.5	4.64	0.20	2.30	2.94	0.05	85.25	1.49	6.17	0.14	0.76	1.19	6.25	1.07	71.24	2.34
PB35-81.15	Limestone	69.8	396.33	1.36	101.20	1.85	6.66	338.67	8.09	238.61	1.99	25.83	27.09	78.86	6.25	186.41	85.53
PB35-84.52	Sandstone	72.7	188.92	0.98	92.45	1.37	5.50	181.56	36.37	284.45	3.65	16.47	22.68	86.28	10.95	205.83	164.65
PB35-85.7	Black slate	73.7	203.67	0.69	162.61	1.42	6.29	279.15	139.72	1105.59	4.09	19.12	23.51	85.92	34.45	429.22	185.60
PB35-87.93	Dolostone	75.6	16.65	0.23	12.26	0.07	0.10	263.29	6.79	4.76	0.14	0.74	7.61	7.91	1.28	225.29	1.54
PB35-89.76	Dolostone	77.2	6.77	0.38	6.83	0.09	0.05	219.63	5.40	3.96	0.25	0.24	0.57	4.58	1.00	102.67	2.08
PB35-91.7	Dolostone	78.9	2.98	0.19	4.26	0.09	0.04	156.95	1.87	2.65	0.14	0.19	0.61	3.39	1.01	88.07	1.58
PB35-92.8	Dolostone	79.8	7.67	1.74	9.66	0.19	0.11	227.34	12.72	8.06	0.14	1.05	12.35	46.34	7.66	123.41	3.69
PB35-93.80	Dolostone	80.7	14.82	0.41	17.46	0.38	0.31	327.27	4.83	13.97	0.20	2.02	5.34	27.14	1.81	148.16	8.58
PB35-96.3	Black slate	82.8	282.73	4.15	233.08	2.25	9.77	285.29	112.11	1416.40	5.01	31.75	56.88	270.69	54.46	112.02	215.19
PB35-98.94	Dolostone	85.1	19.07	0.76	19.17	0.27	0.18	307.37	10.76	11.19	0.14	0.76	5.50	36.60	5.64	116.01	6.29
PB35-102.02	Dolostone	87.7	10.24	0.50	9.62	0.09	0.07	268.19	4.41	6.49	0.14	0.76	5.00	24.67	6.32	98.08	1.56
PB35-104.00	Black slate	89.5	165.27	0.88	166.42	1.21	5.38	369.16	27.63	354.51	3.90	21.66	27.25	69.80	53.85	184.17	175.55
PB35-105.81	Black slate	91.0	161.93	1.56	167.66	1.53	7.23	372.35	49.43	677.60	4.09	19.59	28.16	106.90	54.68	156.62	184.23
PB35-109.08	Black slate	93.8	281.73	6.23	266.94	2.31	8.98	468.07	77.83	390.66	4.79	36.71	87.43	403.36	116.69	152.61	205.79
PB35-110.90	Black slate	95.4	316.13	5.37	268.37	2.15	8.36	234.95	91.63	1147.24	4.54	36.38	34.74	229.92	91.47	148.39	193.12
PB35-112.96	Black slate	97.2	287.50	6.18	228.54	2.28	8.66	380.08	62.76	795.94	4.50	29.99	53.02	504.32	93.56	384.46	196.75
PB35-114.34	Black slate	98.3	323.90	4.69	333.87	1.96	7.45	277.09	95.03	854.28	4.97	46.69	62.19	302.04	95.35	281.29	215.80

Appendix to Chapter 4

Sample	Lithology	Strat-depth (m)	Cr	Mn	V	U	Th	Sr	Li	Ba	Hf	Sc	Co	Ni	Cu	Zn	Zr
PB35-115.9	Black slate	99.7	178.56	3.78	154.82	1.45	5.31	297.95	73.47	491.99	3.92	21.33	35.97	182.87	47.62	103.25	136.42
PB35-118.22	Black slate	101.7	177.19	1.45	209.99	1.38	5.84	413.02	66.74	478.99	4.29	25.40	36.08	77.62	62.97	172.55	202.84
PB35-120.1	Black slate	103.3	177.22	3.09	156.04	1.28	4.66	406.19	60.30	165.95	2.82	20.32	35.83	314.98	93.63	357.42	117.45
PB35-122.14	Black slate	105.1	510.49	0.94	340.10	3.46	11.96	424.36	99.64	939.88	3.51	44.35	43.33	103.01	109.32	341.27	158.04
PB35-124.95	Black slate	107.5	370.97	10.56	263.27	2.11	8.16	440.09	106.10	137.85	3.88	35.53	113.81	640.61	120.07	390.95	178.27
PB35-126.63	Black slate	108.9	401.34	8.27	222.69	1.69	6.84	523.09	87.41	646.64	3.21	30.90	83.23	529.69	96.65	205.66	151.13
PB35-130.43	Black slate	112.2	262.20	3.98	219.73	2.13	8.07	614.15	86.16	1074.43	4.27	29.13	36.60	262.44	47.57	175.04	190.07
PB35-133.24	Black slate	114.6	307.63	5.16	260.65	2.39	8.75	784.25	96.16	890.30	4.42	35.70	41.97	317.19	84.16	170.08	197.32
PB35-136.52	Black slate	117.4	108.70	0.53	207.34	4.37	16.07	376.16	77.25	712.88	4.22	21.58	29.55	50.64	63.41	191.98	196.78
PB35-138.74	Black slate	119.3	263.08	5.25	209.01	1.64	6.08	458.38	54.66	976.00	3.57	28.20	83.78	303.78	56.63	148.44	158.80
PB35-141.60	Black slate	121.8	316.90	5.23	275.02	2.46	9.41	631.38	91.91	544.61	4.86	34.31	54.57	340.66	91.37	169.22	215.79
PB35-144.40	Limestone	124.2	1.81	0.16	0.36	0.20	LD	80.99	0.68	7.30	0.14	0.20	0.30	1.95	1.00	62.56	0.76
PB35-147.00	Limestone	126.4	3.28	0.22	0.35	0.18	LD	82.99	0.86	8.79	0.14	0.12	0.38	2.25	1.01	66.58	0.65
PB35-149.76	Limestone	128.8	3.71	0.20	0.29	0.13	0.01	137.14	1.17	5.47	0.14	0.11	0.11	1.15	1.00	52.42	0.75
PB35-151.12	Limestone	130.0	1.79	0.25	0.38	0.14	0.02	400.15	1.27	5.20	0.14	0.11	1.70	0.93	1.00	69.33	0.73
PB35-153.50	Limestone	132.0	2.80	0.13	0.27	0.09	LD	636.97	1.50	25.33	0.14	0.12	0.11	1.02	1.01	99.49	0.80
PB35-156.20	Limestone	134.4	2.72	0.11	0.32	0.08	LD	117.34	1.46	11.57	0.14	0.11	0.37	0.83	1.01	54.03	0.74
PB35-157.75	Limestone	135.7	3.12	0.18	0.14	0.09	LD	138.06	1.31	16.00	0.14	0.11	0.39	2.69	1.00	65.70	0.69
PB35-160.95	Limestone	138.4	1.75	0.19	0.38	0.15	LD	158.74	1.31	10.06	0.14	0.11	0.38	1.46	1.00	213.56	0.70
PB35-162.4	Limestone	139.7	7.74	0.41	0.18	0.10	0.02	146.12	1.11	13.24	0.21	0.11	0.36	2.76	1.00	57.64	0.79
PB35-163.7	Limestone	140.8	4.29	0.29	0.32	0.15	0.02	337.30	1.03	14.17	0.14	0.12	0.71	2.54	1.15	73.21	0.85
PB35-166	Black slate	142.8	98.58	0.73	209.78	4.68	17.72	931.56	29.79	2090.80	4.59	21.18	30.97	52.94	3.41	161.39	196.37
PB35-168.41	Limestone	144.9	7.55	0.30	0.67	0.07	0.03	476.58	0.69	28.82	0.14	0.15	0.36	3.62	1.03	102.48	0.75
PB35-171.13	Limestone	147.2	7.02	0.24	0.60	0.18	0.02	125.82	0.95	9.37	0.14	0.12	0.36	2.43	1.01	56.71	1.08
PB35-173.1	Limestone	148.9	8.07	0.21	4.30	0.28	0.26	482.30	0.91	24.09	0.14	0.48	1.22	4.40	1.69	68.33	4.37
PB35-175	Limestone	150.5	3.39	0.17	0.30	0.06	LD	39.61	1.18	5.04	0.14	0.12	0.26	1.09	1.01	88.26	0.46
PB35-177.5	Limestone	152.7	4.49	0.20	1.04	0.14	0.03	133.67	0.87	12.10	0.14	0.16	0.28	2.08	1.00	64.18	1.30
PB35-178.8	Limestone	153.8	3.24	0.16	1.69	0.32	0.03	89.43	1.57	6.80	0.14	0.26	0.85	3.61	1.50	62.29	1.39
PB35-180.8	Limestone	155.5	4.08	0.20	0.72	0.09	0.04	123.99	1.36	12.43	0.14	0.13	0.40	2.09	1.58	138.93	1.02
PB35-184.26	Limestone	158.5	8.86	0.59	5.97	0.14	0.14	430.16	1.55	90.76	0.27	0.53	0.73	7.04	1.01	68.97	3.76
PB35-187.29	Dolostone	161.1	4.26	0.59	10.48	0.26	0.08	169.03	7.32	39.64	0.14	0.34	1.45	14.95	1.24	150.87	2.94
PB35-190.30	Dolostone	163.7	2.49	0.23	2.30	0.28	0.03	113.99	2.49	7.44	0.14	0.16	0.93	13.40	1.00	151.36	1.90
PB35-193.40	Dolostone	166.3	15.96	0.31	4.00	0.13	0.04	60.41	2.65	7.90	0.14	0.39	0.88	11.96	1.00	247.00	2.08
PB35-195.3	Dolostone	168.0	7.00	0.22	5.43	0.10	0.07	93.94	4.29	16.63	0.14	0.85	1.12	9.76	1.01	263.43	1.42
PB35-198.5	Dolostone	170.7	19.46	0.32	1.82	0.15	0.03	67.42	1.90	6.62	0.14	0.30	0.94	10.31	2.34	91.93	1.41
PB35-200.6	Dolostone	172.5	3.20	0.24	1.46	0.10	0.05	130.47	2.40	7.42	0.14	0.30	0.59	6.77	1.01	108.58	1.72
PB35-202.3	Dolostone	174.0	3.40	0.24	1.16	0.20	0.05	142.67	2.53	9.50	0.14	0.12	0.73	7.76	1.19	236.86	1.92
PB35-205	Dolostone	176.3	2.44	0.44	4.40	0.12	0.02	100.42	3.33	15.02	0.14	0.25	3.60	12.88	0.98	95.52	1.61
PB35-206.7	Dolostone	177.8	13.27	0.44	9.06	0.42	0.32	134.45	9.37	90.01	0.18	1.28	2.58	15.15	1.92	88.02	8.83
PB35-209	Dolostone	179.8	3.61	0.50	4.01	0.15	0.07	133.10	3.55	27.69	0.14	0.25	1.29	13.32	2.56	89.16	2.27
PB35-211.41	Dolostone	181.8	4.52	0.26	16.11	0.28	0.15	109.74	5.92	26.24	0.14	1.46	3.11	15.96	7.17	116.39	3.54
PB35-213.2	Iron Formation	183.4	103.66	3.47	120.07	1.97	6.28	186.61	74.75	292.94	3.39	14.22	20.19	138.39	85.40	268.82	139.48
PB35-215.04	Iron Formation	185.0	101.76	2.38	62.57	0.93	2.58	91.37	22.22	143.77	1.40	8.94	57.33	170.96	160.54	252.53	63.84

Appendix to Chapter 4

Sample	Lithology	Strat-depth (m)	Cr	Mo	V	U	Th	Sr	Li	Ba	Hf	Sc	Co	Ni	Cu	Zn	Zr
PB35-217.8	Limestone	187.3	4.39	0.23	1.23	0.15	0.05	567.86	0.91	21.61	0.14	0.15	0.37	1.84	1.01	127.27	1.38
PB35-219.6	Black slate	188.9	1519.37	1.74	54.87	2.76	11.06	176.65	52.22	637.46	5.32	7.01	28.79	240.67	22.84	94.31	232.01
PB35-221.3	Limestone	190.3	4.16	0.24	0.44	0.11	0.02	244.39	0.75	22.20	0.14	0.12	0.63	3.21	5.23	100.09	0.85
PB35-223.3	Limestone	192.1	7.13	0.19	0.32	0.04	LD	136.00	0.69	13.18	0.14	0.11	0.44	3.09	1.80	54.32	0.53
PB35-225.1	Limestone	193.6	13.62	0.30	0.63	0.08	0.03	328.08	0.74	16.21	0.14	0.11	0.46	3.00	14.21	270.00	1.08
PB35-227.8	Limestone	195.9	11.23	0.35	2.06	0.21	0.07	301.10	0.72	20.40	0.14	0.24	1.13	8.06	3.72	86.99	1.92
PB35-230.02	Limestone	197.8	2.80	0.24	0.95	0.08	0.05	262.79	0.80	22.80	0.22	0.29	0.40	2.71	0.96	6.95	1.78
PB35-231.96	Dolostone	199.5	1.44	0.98	0.79	0.08	0.03	74.46	1.47	2.50	0.23	0.15	5.72	10.60	5.19	35.11	1.28
PB35-235.2	Limestone	202.3	2.83	0.23	0.72	0.08	0.06	147.28	0.38	9.64	0.23	0.20	0.24	1.80	0.97	4.63	2.13
PB35-237.4	Limestone	204.2	1.98	0.30	0.66	0.15	0.03	92.93	0.44	12.95	0.22	0.15	1.70	3.71	4.95	8.70	1.16
PB35-239.3	Limestone	205.8	2.37	0.21	0.72	0.06	0.03	236.57	0.34	42.84	0.23	0.18	0.74	2.16	1.09	4.63	0.91
PB35-241.5	Limestone	207.7	1.13	0.21	0.12	0.06	0.03	452.62	0.32	16.58	0.23	LD	0.06	0.47	0.98	4.72	0.54
PB35-243.4	Limestone	209.4	5.59	0.21	0.15	0.03	0.03	78.65	0.30	1.82	0.21	LD	0.19	1.15	0.91	4.37	0.33
PB35-245.5	Limestone	211.2	2.33	0.21	0.20	0.05	0.03	107.09	0.29	7.92	0.21	LD	0.15	0.78	0.91	4.37	0.60
PB35-247.8	Limestone	213.1	2.13	0.36	0.57	0.12	0.06	272.70	0.57	41.17	0.52	0.19	0.49	2.49	0.94	13.59	1.46
PB35-250.7	Limestone	215.6	1.31	0.21	0.28	0.08	0.03	58.76	0.29	5.37	0.21	0.13	0.12	1.19	0.90	13.54	0.75
PB35-251.11	Limestone	216.0	0.80	0.21	0.34	0.13	0.04	61.74	0.30	18.92	0.21	LD	0.19	1.13	0.90	13.80	1.07
PB35-254.4	Cherty dolomite	218.5	108.30	1.18	131.39	0.94	4.09	171.63	60.40	135.00	3.21	15.42	24.84	48.25	170.92	172.46	136.73
PB35-256.2	Chert	219.1	14.31	0.78	34.67	0.93	3.14	78.02	15.70	769.43	3.04	3.48	5.22	8.83	12.09	21.71	122.04

Appendix A.3. Whole rock REE concentrations (ppm) for the Red Lake samples. Precision is better than 2% RSD for REE.

Sample	Lithology	Strat-depth (m)	La	Ce	Pr	Nd	Sm	Eu	Gd	Tb	Dy	Y	Ho	Er	Tm	Yb	Lu
FBL28-270.63	Sandstone	121.5	10.59	18.18	1.79	5.53	0.89	0.44	0.89	0.10	0.43	2.26	0.07	0.16	0.02	0.12	0.02
FBL28-281.65	Sandstone	126.5	29.59	48.41	4.69	14.93	2.30	0.72	1.87	0.17	0.58	3.04	0.10	0.27	0.04	0.26	0.04
FBL28-283.32	Sandstone	127.2	17.03	29.78	2.88	8.99	1.37	0.48	1.33	0.15	0.69	4.18	0.13	0.31	0.04	0.23	0.04
FBL28-291.73	Chert	131.0	1.71	2.34	0.24	0.83	0.13	0.03	0.13	0.01	0.04	0.22	0.01	0.01	0.00	0.01	0.00
FBL28-295.09	Cherty dolomite	132.5	0.22	0.34	0.04	0.28	0.06	0.05	0.11	0.02	0.19	2.00	0.03	0.13	0.02	0.10	0.02
FBL28-297.73	Dolostone	133.7	0.47	0.66	0.07	0.28	0.06	0.09	0.09	0.02	0.12	1.37	0.04	0.08	0.01	0.06	0.01
FBL28-304	Chert	136.5	0.26	0.38	0.04	0.18	0.05	0.03	0.07	0.02	0.11	1.13	0.03	0.07	0.01	0.06	0.01
FBL28-305.9	Chert	137.4	0.06	0.11	0.01	0.05	0.01	0.01	0.02	0.03	0.02	0.23	0.01	0.02	0.00	0.02	0.00
FBL28-308.89	Dolostone	138.7	1.11	1.66	0.18	0.71	0.14	0.10	0.19	0.03	0.21	2.76	0.05	0.16	0.02	0.12	0.02
FBL28-311.35	Dolostone	139.8	0.71	1.02	0.11	0.44	0.08	0.06	0.11	0.02	0.09	2.03	0.02	0.08	0.01	0.06	0.01
FBL28-315.64	Dolostone	141.7	1.04	1.68	0.20	0.81	0.19	0.11	0.25	0.04	0.26	2.97	0.06	0.18	0.03	0.16	0.03
FBL28-321.64	Dolostone	144.4	0.80	1.10	0.12	0.44	0.08	0.08	0.10	0.02	0.10	1.58	0.03	0.07	0.01	0.06	0.01
FBL28-326.38	Dolostone	146.6	0.36	0.42	0.04	0.16	0.03	0.03	0.04	0.01	0.04	0.86	0.01	0.03	0.00	0.02	0.00
FBL28-330	Dolostone	148.2	1.55	2.30	0.26	1.06	0.22	0.16	0.31	0.05	0.31	3.83	0.08	0.23	0.03	0.17	0.03
FBL28-332.5	Dolostone	149.3	1.17	1.75	0.20	0.77	0.15	0.10	0.16	0.02	0.13	1.50	0.03	0.07	0.01	0.06	0.01
FBL28-338.29	Siltstone	151.9	33.94	66.74	7.82	29.29	5.27	1.43	4.70	0.60	2.88	15.54	0.55	1.47	0.21	1.28	0.21
FBL28-340.10	Siltstone	152.7	33.79	64.80	7.50	28.00	4.98	1.36	4.45	0.58	2.81	15.45	0.55	1.48	0.21	1.30	0.21
FBL28-344.15	Dolostone	154.5	0.71	1.19	0.14	0.58	0.12	0.10	0.15	0.02	0.14	1.68	0.10	0.10	0.02	0.09	0.02
FBL28-347.38	Dolostone	156.0	0.18	0.21	0.02	0.08	0.01	0.02	0.02	0.03	0.02	0.44	0.00	0.01	0.00	0.01	0.00
FBL28-350	Dolostone	157.2	0.70	1.29	0.16	0.71	0.17	0.10	0.23	0.04	0.27	2.90	0.07	0.20	0.03	0.19	0.03
FBL28-356	Dolostone	159.9	0.75	1.05	0.12	0.44	0.08	0.09	0.11	0.02	0.10	1.40	0.02	0.07	0.01	0.06	0.01
FBL28-360.4	Dolostone	161.8	0.77	0.94	0.10	0.38	0.07	0.08	0.10	0.02	0.10	1.48	0.03	0.17	0.02	0.13	0.02
FBL28-365.22	Dolostone	164.0	0.91	1.26	0.14	0.57	0.12	0.12	0.19	0.03	0.22	3.23	0.06	0.17	0.02	0.13	0.02
FBL28-368.09	Dolostone	165.3	0.62	0.77	0.09	0.34	0.08	0.07	0.11	0.02	0.13	1.71	0.03	0.09	0.01	0.08	0.01
FBL28-373.40	Dolostone	167.7	0.36	0.41	0.04	0.15	0.03	0.05	0.05	0.01	0.06	1.13	0.02	0.05	0.01	0.03	0.01
FBL28-378.10	Dolostone	169.8	0.84	1.19	0.13	0.51	0.10	0.10	0.12	0.02	0.11	1.81	0.03	0.08	0.01	0.06	0.01
FBL28-382.76	Dolostone	171.9	1.21	1.48	0.15	0.55	0.09	0.10	0.13	0.02	0.15	2.10	0.04	0.11	0.02	0.09	0.02
FBL28-387	Dolostone	173.8	0.92	1.32	0.15	0.57	0.11	0.11	0.14	0.02	0.16	2.16	0.04	0.11	0.02	0.09	0.02
FBL28-389.46	Dolostone	174.9	0.87	1.25	0.15	0.63	0.13	0.09	0.18	0.03	0.18	2.81	0.04	0.13	0.02	0.10	0.02
FBL28-395.56	Dolostone	177.6	0.33	0.37	0.04	0.14	0.02	0.01	0.03	0.01	0.04	1.09	0.01	0.04	0.01	0.03	0.01
FBL28-400.3	Dolostone	179.7	0.29	0.40	0.04	0.17	0.04	0.03	0.05	0.01	0.05	0.97	0.01	0.04	0.01	0.03	0.01
FBL28-402.89	Dolostone	180.9	1.05	1.51	0.14	0.48	0.08	0.07	0.09	0.01	0.07	1.02	0.01	0.04	0.01	0.03	0.01
FBL28-407.06	Siltstone	182.8	27.59	44.86	4.30	13.49	2.03	0.58	1.94	0.21	0.87	5.55	0.16	0.43	0.06	0.41	0.07
FBL28-411.24	Dolostone	184.7	0.30	0.35	0.04	0.16	0.03	0.03	0.06	0.01	0.08	1.52	0.02	0.06	0.01	0.05	0.01
FBL28-416.30	Dolostone	186.9	0.35	0.43	0.05	0.19	0.04	0.03	0.06	0.01	0.06	1.30	0.02	0.05	0.01	0.04	0.01
FBL28-421.44	Dolostone	189.2	0.51	0.74	0.09	0.36	0.08	0.06	0.11	0.02	0.11	1.73	0.03	0.08	0.01	0.06	0.01
FBL28-426.25	Dolostone	191.4	0.41	0.56	0.06	0.26	0.06	0.05	0.09	0.02	0.11	1.48	0.03	0.08	0.01	0.06	0.01
FBL28-429.76	Dolostone	193.0	0.40	0.45	0.05	0.19	0.05	0.05	0.09	0.02	0.15	1.94	0.04	0.11	0.01	0.08	0.01
FBL28-433.56	Dolostone	194.7	0.54	0.76	0.08	0.31	0.07	0.07	0.10	0.02	0.11	1.77	0.03	0.08	0.01	0.07	0.01
FBL28-436.44	Dolostone	196.0	0.48	0.76	0.08	0.32	0.06	0.06	0.08	0.01	0.09	1.28	0.02	0.06	0.01	0.05	0.01
FBL28-443.28	Dolostone	199.0	1.38	1.96	0.24	0.91	0.18	0.11	0.24	0.04	0.24	4.31	0.06	0.19	0.03	0.15	0.03
FBL28-446.76	Dolostone	200.6	1.70	2.55	0.30	1.17	0.23	0.12	0.31	0.05	0.30	5.45	0.08	0.24	0.03	0.19	0.03
FBL28-451.93	Dolostone	202.9	1.08	1.38	0.16	0.64	0.12	0.08	0.18	0.03	0.16	3.51	0.04	0.13	0.02	0.10	0.02

Appendix to Chapter 4

Sample	Lithology	Strat-depth (m)	La	Ce	Pr	Nd	Sm	Eu	Gd	Tb	Dy	Y	Ho	Er	Tm	Yb	Lu
PB32-9.66	Sandstone	8.73	8.19	16.74	1.73	5.76	0.94	0.33	0.73	0.12	0.66	4.11	0.14	0.42	0.07	0.44	0.08
PB32-14.87	Sandstone	13.43	7.75	14.37	1.46	4.92	0.80	0.28	0.75	0.09	0.44	2.44	0.09	0.24	0.04	0.23	0.04
PB32-17.3	Sandstone	15.63	15.60	28.08	2.64	8.22	1.18	0.42	1.11	0.11	0.40	1.79	0.06	0.15	0.02	0.12	0.02
PB32-21.50	Dolostone	19.42	1.56	2.65	0.30	1.24	0.25	0.16	0.36	0.06	0.39	5.34	0.10	0.33	0.05	0.29	0.06
PB32-24.25	Dolostone	21.91	0.83	1.10	0.11	0.41	0.07	0.06	0.09	0.01	0.08	1.37	0.02	0.06	0.01	0.05	0.01
PB32-27.50	Dolostone	24.84	1.81	3.25	0.38	1.56	0.35	0.21	0.45	0.07	0.46	5.87	0.11	0.35	0.05	0.29	0.05
PB32-31.56	Dolostone	28.51	1.11	2.09	0.25	1.04	0.22	0.15	0.30	0.05	0.29	3.87	0.07	0.21	0.03	0.17	0.03
PB32-34.62	Dolostone	31.27	0.97	1.78	0.22	0.96	0.24	0.17	0.34	0.06	0.40	5.36	0.10	0.31	0.04	0.25	0.05
PB32-39.11	Dolostone	35.33	1.43	2.15	0.24	1.00	0.22	0.17	0.30	0.05	0.29	4.25	0.07	0.21	0.03	0.16	0.03
PB32-43.70	Dolostone	39.48	1.14	1.84	0.22	0.88	0.19	0.18	0.27	0.04	0.27	3.55	0.06	0.18	0.02	0.14	0.02
PB32-44.81	Dolostone	40.48	1.25	1.97	0.21	0.88	0.16	0.11	0.21	0.03	0.19	2.91	0.05	0.15	0.02	0.12	0.02
PB32-48.88	Dolostone	44.16	0.97	1.58	0.17	0.70	0.14	0.09	0.17	0.02	0.13	2.15	0.03	0.09	0.01	0.07	0.01
PB32-50.31	Dolostone	45.45	1.57	3.00	0.36	1.37	0.28	0.19	0.34	0.05	0.34	4.10	0.08	0.24	0.02	0.20	0.04
PB32-56.08	Dolostone	50.66	1.74	3.17	0.35	1.42	0.27	0.16	0.32	0.04	0.25	3.48	0.06	0.16	0.02	0.12	0.02
PB32-60.70	Dolostone	54.83	2.31	3.98	0.44	1.68	0.30	0.16	0.34	0.05	0.27	3.63	0.06	0.19	0.03	0.16	0.03
PB32-62.29	Dolostone	56.27	2.62	4.75	0.55	2.20	0.44	0.24	0.55	0.09	0.53	8.28	0.14	0.43	0.06	0.37	0.07
PB32-65.66	Dolostone	59.31	2.06	3.49	0.40	1.58	0.31	0.17	0.36	0.06	0.32	3.80	0.06	0.22	0.03	0.19	0.03
PB32-70.38	Dolostone	63.58	0.90	1.29	0.15	0.63	0.14	0.10	0.19	0.03	0.17	2.43	0.04	0.11	0.02	0.08	0.01
PB32-72.89	Dolostone	65.84	1.12	1.74	0.20	0.81	0.17	0.12	0.22	0.03	0.19	2.54	0.05	0.13	0.02	0.10	0.02
PB32-75.53	Siltstone	68.23	22.59	43.52	4.72	17.14	2.67	0.78	2.42	0.28	1.22	6.77	0.23	0.61	0.09	0.55	0.09
PB32-78.91	Siltstone	71.28	22.77	44.29	4.78	17.06	2.62	0.86	2.38	0.27	1.12	6.21	0.21	0.56	0.08	0.51	0.09
PB32-83.95	Siltstone	75.84	23.88	46.24	5.05	17.87	2.74	0.91	2.45	0.27	1.15	6.32	0.22	0.58	0.08	0.52	0.09
PB32-85.73	Dolostone	77.44	1.05	1.65	0.19	0.74	0.15	0.09	0.19	0.03	0.19	2.10	0.04	0.12	0.02	0.10	0.02
PB32-88.23	Dolostone	79.70	1.61	2.71	0.32	1.33	0.30	0.16	0.38	0.06	0.41	4.44	0.10	0.32	0.05	0.29	0.05
PB32-90.70	Dolostone	81.93	1.03	1.79	0.22	0.86	0.17	0.10	0.23	0.03	0.20	2.63	0.05	0.15	0.02	0.12	0.02
PB32-93.88	Dolostone	84.81	1.08	1.66	0.19	0.76	0.15	0.08	0.19	0.03	0.17	2.40	0.04	0.12	0.02	0.10	0.02
PB32-96.88	Dolostone	87.52	1.02	1.71	0.20	0.79	0.16	0.08	0.19	0.03	0.16	1.96	0.04	0.09	0.02	0.09	0.03
PB32-98.57	Dolostone	89.04	1.61	2.73	0.32	1.32	0.29	0.15	0.37	0.06	0.36	4.04	0.09	0.25	0.04	0.21	0.03
PB32-102.13	Dolostone	92.26	1.24	2.10	0.24	0.95	0.19	0.13	0.25	0.04	0.23	2.77	0.05	0.16	0.02	0.13	0.02
PB32-104.85	Dolostone	94.72	1.00	1.74	0.20	0.84	0.18	0.10	0.25	0.04	0.28	3.50	0.07	0.21	0.03	0.19	0.04
PB32-108.35	Dolostone	97.88	1.64	2.97	0.36	1.44	0.33	0.18	0.46	0.08	0.52	5.84	0.13	0.38	0.05	0.33	0.06
PB32-112.63	Dolostone	101.74	1.87	3.28	0.38	1.51	0.32	0.19	0.43	0.07	0.44	4.87	0.11	0.32	0.05	0.28	0.05
PB32-116.89	Dolostone	105.59	0.84	1.39	0.16	0.67	0.13	0.09	0.19	0.03	0.18	2.63	0.04	0.14	0.02	0.11	0.02
PB32-121.10	Dolostone	109.39	1.33	2.38	0.28	1.08	0.21	0.12	0.27	0.04	0.25	3.19	0.06	0.18	0.02	0.14	0.02
PB32-124.93	Dolostone	112.85	0.89	1.28	0.15	0.58	0.11	0.07	0.15	0.02	0.12	2.02	0.03	0.08	0.01	0.06	0.01
PB32-128.48	Dolostone	116.06	0.59	1.08	0.13	0.49	0.10	0.05	0.13	0.02	0.12	1.57	0.03	0.09	0.01	0.07	0.01
PB32-131.03	Dolostone	118.36	2.99	4.61	0.53	2.08	0.40	0.26	0.50	0.08	0.51	5.29	0.13	0.40	0.06	0.39	0.07
PB32-133.27	Chertydolostone	120.39	0.29	0.48	0.06	0.24	0.05	0.05	0.08	0.01	0.08	1.12	0.02	0.06	0.01	0.06	0.01
PB32-135.77	Dolostone	122.65	0.85	1.41	0.16	0.61	0.13	0.07	0.16	0.03	0.15	1.74	0.04	0.11	0.02	0.09	0.02
PB32-137.28	Dolostone	124.01	0.56	1.03	0.12	0.49	0.11	0.06	0.16	0.03	0.18	2.21	0.04	0.14	0.02	0.12	0.02
PB32-139.87	Dolostone	126.35	4.28	8.08	0.87	3.11	0.51	0.20	0.62	0.09	0.53	5.62	0.13	0.40	0.06	0.39	0.07
PB32-143.3	Dolostone	129.45	0.73	1.23	0.13	0.52	0.10	0.06	0.13	0.02	0.12	1.36	0.03	0.08	0.01	0.07	0.01
PB32-146.16	Dolostone	132.03	0.95	1.23	0.13	0.52	0.10	0.08	0.14	0.02	0.16	3.07	0.04	0.13	0.02	0.11	0.02

Appendix to Chapter 4

Sample	Lithology	Strat-depth (m)	La	Ce	Pr	Nd	Sm	Eu	Gd	Tb	Dy	Y	Ho	Er	Tm	Yb	Lu
PB32-148.92	Dolostone	134.53	2.25	3.47	0.38	1.58	0.32	0.21	0.46	0.08	0.51	7.19	0.14	0.44	0.06	0.39	0.07
PB32-152.02	Iron Formation	137.33	1.32	1.58	0.17	0.72	0.13	0.05	0.18	0.03	0.18	2.47	0.05	0.17	0.03	0.20	0.04
PB32-152.51	Iron Formation	137.77	1.04	1.08	0.09	0.34	0.05	0.03	0.07	0.01	0.05	0.87	0.01	0.04	0.01	0.04	0.01
PB32-154.51	Iron Formation	139.58	0.96	1.00	0.09	0.32	0.04	0.02	0.06	0.03	0.03	0.75	0.01	0.03	0.00	0.03	0.01
PB32-155.7	Iron Formation	140.65	3.10	3.21	0.29	1.08	0.16	0.08	0.23	0.03	0.19	3.51	0.05	0.17	0.02	0.14	0.03
PB32-156.96	Iron Formation	141.79	3.42	4.00	0.38	1.40	0.25	0.08	0.31	0.05	0.29	3.03	0.07	0.22	0.04	0.23	0.04
PB32-160.15	Dolostone	144.67	0.28	0.30	0.03	0.11	0.02	0.01	0.03	0.03	0.03	0.68	0.01	0.02	0.00	0.02	0.00
PB32-161.21	Ferrous dolostone	145.63	2.46	3.49	0.34	1.32	0.21	0.11	0.25	0.03	0.17	2.73	0.04	0.13	0.02	0.12	0.00
PB32-165	Dolostone	149.05	0.27	0.36	0.04	0.15	0.03	0.04	0.04	0.03	0.03	0.64	0.01	0.02	0.00	0.00	0.00
PB32-168.13	Dolostone	151.88	1.03	1.69	0.19	0.77	0.16	0.10	0.21	0.04	0.24	2.85	0.06	0.20	0.03	0.20	0.04
PB32-169.57	Dolostone	153.18	0.81	1.25	0.13	0.53	0.09	0.06	0.11	0.01	0.09	1.35	0.02	0.06	0.01	0.05	0.01
PB32-172.93	Dolostone	156.21	0.58	0.87	0.10	0.39	0.07	0.03	0.08	0.01	0.06	1.18	0.02	0.05	0.01	0.04	0.01
PB32-174.94	Silty Dolostone	158.03	116.96	269.34	33.94	138.70	27.44	6.05	23.74	3.03	12.59	60.32	2.02	4.47	0.54	2.90	0.44
PB32-178.29	Dolostone	161.06	0.46	0.68	0.07	0.29	0.05	0.03	0.07	0.01	0.05	1.05	0.01	0.04	0.01	0.03	0.01
PB32-179.54	Dolostone	162.19	0.57	1.00	0.11	0.44	0.08	0.03	0.09	0.01	0.06	1.03	0.02	0.04	0.01	0.03	0.01
PB32-183.38	Dolostone	165.65	3.32	3.96	0.37	1.27	0.18	0.07	0.23	0.03	0.17	2.06	0.04	0.13	0.02	0.12	0.02
PB32-185.22	Iron Formation	167.32	0.73	0.73	0.07	0.27	0.05	0.03	0.08	0.01	0.08	1.66	0.02	0.07	0.01	0.05	0.01
PB32-189.02	Dolostone	170.75	0.35	0.56	0.06	0.24	0.05	0.02	0.06	0.01	0.05	0.88	0.01	0.03	0.01	0.03	0.01
PB32-190.25	Dolostone	171.86	0.78	1.14	0.13	0.53	0.11	0.06	0.15	0.02	0.16	2.98	0.04	0.14	0.02	0.12	0.02
PB32-194.05	Dolostone	175.29	1.29	2.12	0.25	1.05	0.22	0.15	0.31	0.05	0.33	4.49	0.08	0.26	0.04	0.23	0.04
PB32-195.5	Dolostone	176.60	0.93	1.36	0.15	0.62	0.12	0.09	0.16	0.02	0.15	2.28	0.04	0.11	0.02	0.08	0.02
PB32-197.35	Dolostone	178.27	1.59	2.71	0.33	1.39	0.31	0.19	0.43	0.07	0.47	6.27	0.12	0.38	0.06	0.34	0.07
PB32-199.28	Dolostone	180.02	1.00	1.40	0.15	0.63	0.13	0.08	0.18	0.03	0.16	2.47	0.04	0.12	0.02	0.10	0.02
PB32-201.92	Dolostone	182.40	0.98	1.59	0.18	0.71	0.14	0.08	0.19	0.03	0.17	2.48	0.04	0.13	0.02	0.11	0.02
PB32-205.25	Dolostone	185.41	0.72	1.09	0.13	0.52	0.10	0.07	0.14	0.02	0.12	1.93	0.03	0.08	0.01	0.06	0.01
PB32-208.58	Dolostone	188.42	0.56	0.80	0.09	0.37	0.07	0.06	0.11	0.02	0.10	1.61	0.02	0.07	0.01	0.05	0.01
PB32-212.08	Dolostone	191.58	1.23	1.87	0.21	0.87	0.18	0.13	0.24	0.04	0.23	3.27	0.05	0.17	0.02	0.13	0.02
PB32-215.56	Dolostone	194.72	0.61	0.90	0.09	0.37	0.06	0.03	0.08	0.01	0.07	1.18	0.02	0.06	0.01	0.05	0.01
PB32-219.7	Sandstone	198.46	16.99	29.66	2.86	9.19	1.44	0.57	1.39	0.16	0.65	3.47	0.11	0.28	0.04	0.25	0.04
PB32-222.13	Sandstone	200.66	20.00	33.33	3.18	10.19	1.55	0.48	1.49	0.16	0.65	3.37	0.11	0.28	0.04	0.26	0.05
PB32-225.73	Sandstone	203.91	31.26	67.81	7.89	30.67	5.34	1.57	4.77	0.62	2.96	16.03	0.58	1.58	0.23	1.41	0.24
PB32-228.2	Sandstone	206.14	19.51	33.53	3.16	10.11	1.53	0.49	1.45	0.16	0.63	3.41	0.11	0.29	0.04	0.26	0.05
PB32-231.88	Siltstone	209.47	21.13	35.56	3.55	11.32	1.79	0.68	1.66	0.18	0.74	4.10	0.13	0.33	0.05	0.30	0.05
PB32-233.3	Black slate	210.75	23.08	47.40	5.49	20.11	4.15	1.35	4.08	0.66	3.85	25.70	0.83	2.45	0.38	2.39	0.41
PB32-234.35	Siltstone	211.70	27.07	52.00	5.85	20.57	3.17	1.08	2.76	0.31	1.35	7.79	0.25	0.67	0.10	0.61	0.10
PB32-237.3	Siltstone	214.36	30.02	57.26	6.39	22.09	3.30	1.12	2.87	0.31	1.30	7.42	0.24	0.63	0.09	0.58	0.09
PB32-240.26	Siltstone	217.04	19.92	39.77	4.63	16.76	2.90	1.03	2.55	0.32	1.48	8.46	0.28	0.76	0.11	0.68	0.11
PB32-241.5	Siltstone	218.16	15.52	32.70	3.82	13.83	2.46	0.92	2.16	0.28	1.34	7.87	0.26	0.72	0.11	0.66	0.11
PB32-242.3	Siltstone	218.88	15.46	32.15	3.75	13.55	2.33	0.93	2.03	0.26	1.22	7.32	0.24	0.66	0.10	0.61	0.10
PB32-248.91	Chert	224.85	0.83	1.52	0.18	0.76	0.18	0.12	0.23	0.04	0.24	2.46	0.06	0.16	0.02	0.15	0.03
PB32-252.78	Iron Formation	228.35	2.70	4.88	0.61	2.58	0.60	0.39	0.85	0.13	0.81	8.80	0.19	0.54	0.08	0.45	0.08
PB32-255.08	Chert	230.42	1.39	2.49	0.29	1.17	0.25	0.14	0.30	0.05	0.27	2.25	0.06	0.18	0.03	0.17	0.03
PB32-257.5	Sulfidic slate	232.61	13.87	29.54	3.50	13.01	2.55	0.77	2.27	0.28	1.22	6.25	0.22	0.60	0.09	0.65	0.12

Appendix to Chapter 4

Sample	Lithology	Strat-depth (m)	La	Ce	Pr	Nd	Sm	Eu	Gd	Tb	Dy	Y	Ho	Er	Tm	Yb	Lu
PB32-260.23	Black slate	235.08	12.80	27.32	3.20	11.87	2.44	0.62	2.16	0.27	1.15	5.72	0.21	0.58	0.10	0.70	0.13
PB32-270.71	Black slate	244.54	18.21	38.59	4.51	16.81	3.56	1.66	3.49	0.53	2.76	15.51	0.55	1.60	0.25	1.71	0.28
PB32-279.73	Black slate	252.69	35.86	71.88	8.10	28.85	5.35	1.56	4.79	0.57	2.40	12.82	0.44	1.19	0.19	1.31	0.23
PB32-291.40	Black slate	258.99	17.70	35.49	4.22	15.94	3.25	1.00	2.88	0.35	1.47	7.85	0.26	0.74	0.12	0.88	0.16
PB32-292.37	Dolostone	264.11	0.70	1.00	0.11	0.41	0.08	0.04	0.10	0.01	0.09	0.82	0.02	0.07	0.01	0.06	0.01
PB32-295.80	Dolostone	267.21	0.37	0.47	0.05	0.21	0.05	0.04	0.07	0.01	0.08	1.81	0.02	0.07	0.01	0.05	0.01

Sample	Lithology	Strat-depth (m)	La	Ce	Pr	Nd	Sm	Eu	Gd	Tb	Dy	Y	Ho	Er	Tm	Yb	Lu
PB33-108.27	Dolostone	59.6	1.83	2.92	0.34	1.35	0.26	0.14	0.31	0.04	0.25	3.78	0.06	0.18	0.03	0.14	0.03
PB33-112	Dolostone	61.7	1.13	1.41	0.14	0.51	0.08	0.06	0.10	0.01	0.07	1.46	0.02	0.05	0.01	0.04	0.01
PB33-116.73	Dolostone	64.3	0.54	0.74	0.08	0.34	0.06	0.04	0.09	0.01	0.08	1.38	0.02	0.06	0.01	0.04	0.01
PB33-123.58	Dolostone	68.1	1.28	1.61	0.17	0.68	0.12	0.09	0.18	0.02	0.14	2.46	0.03	0.10	0.01	0.07	0.01
PB33-129.05	Dolostone	71.1	0.99	1.28	0.14	0.52	0.09	0.08	0.13	0.02	0.10	1.65	0.02	0.07	0.01	0.05	0.01
PB33-134.82	Dolostone	74.2	1.37	2.08	0.25	0.99	0.20	0.13	0.26	0.04	0.26	3.76	0.06	0.18	0.03	0.14	0.03
PB33-138.35	Dolostone	76.2	1.12	1.58	0.17	0.66	0.13	0.09	0.17	0.03	0.17	2.69	0.04	0.13	0.02	0.10	0.02
PB33-145.63	Dolostone	80.2	1.67	2.57	0.29	1.10	0.21	0.12	0.25	0.04	0.23	3.41	0.06	0.17	0.02	0.14	0.02
PB33-157.17	Dolostone	86.5	1.13	1.80	0.21	0.85	0.16	0.09	0.20	0.03	0.16	2.54	0.04	0.11	0.01	0.08	0.01
PB33-163.13	Dolostone	89.8	0.82	1.41	0.17	0.67	0.13	0.07	0.15	0.02	0.13	1.90	0.03	0.09	0.01	0.07	0.01
PB33-167.40	Black slate	92.2	21.74	42.89	4.88	17.72	3.53	1.08	3.39	0.49	2.49	14.29	0.49	1.38	0.21	1.33	0.23
PB33-169.24	Black slate	93.2	25.21	48.86	5.53	20.18	3.91	1.11	3.64	0.48	2.36	13.67	0.47	1.32	0.21	1.34	0.23
PB33-170.16	Black slate	93.7	22.19	43.30	4.90	17.90	3.60	1.15	3.52	0.50	2.57	15.56	0.51	1.46	0.22	1.43	0.24
PB33-175.08	Black slate	96.4	29.92	62.06	7.39	27.83	5.29	1.31	4.41	0.51	2.19	11.58	0.41	1.19	0.20	1.39	0.25
PB33-180.97	Black slate	99.7	77.00	162.12	19.91	73.75	10.86	2.52	8.39	0.85	3.19	16.43	0.57	1.48	0.21	1.28	0.21
PB33-185.23	Chert	102.0	0.18	0.28	0.03	0.12	0.03	0.02	0.03	0.01	0.04	0.31	0.01	0.02	0.00	0.02	0.00
PB33-191.45	Black slate	105.4	26.44	51.24	5.93	22.22	4.20	1.05	3.64	0.42	1.82	9.59	0.34	0.99	0.16	1.13	0.20
PB33-198.19	Black slate	109.1	19.11	37.93	4.28	15.62	3.03	0.95	2.80	0.37	1.83	10.50	0.36	1.02	0.17	1.10	0.19
PB33-200.10	Black slate	110.2	18.35	35.33	3.99	14.53	2.81	0.82	2.78	0.41	2.24	14.27	0.47	1.39	0.22	1.39	0.24
PB33-201.53	Black slate	111.0	27.54	53.79	6.10	21.82	4.36	1.05	4.00	0.52	2.40	13.18	0.45	1.25	0.19	1.24	0.21
PB33-203.73	Black slate	112.2	23.65	45.94	5.22	19.08	3.88	1.21	3.96	0.60	3.32	20.75	0.68	1.93	0.29	1.82	0.30
PB33-206.73	Black slate	113.8	19.20	37.86	4.31	15.61	3.15	1.02	3.25	0.51	2.86	17.98	0.59	1.68	0.25	1.56	0.26
PB33-208.63	Black slate	114.9	25.53	49.02	5.55	20.16	3.91	1.07	3.82	0.55	2.93	17.85	0.60	1.68	0.25	1.55	0.26
PB33-209.80	Black slate	115.5	19.16	36.94	4.12	14.90	2.93	0.86	2.89	0.43	2.26	13.89	0.46	1.32	0.20	1.26	0.21
PB33-211.16	Black slate	116.3	17.83	34.89	3.83	13.49	2.61	0.69	2.67	0.41	2.26	14.49	0.47	1.37	0.21	1.28	0.21
PB33-215.68	Dolostone	118.8	2.16	4.31	0.55	2.17	0.43	0.23	0.49	0.07	0.42	6.09	0.10	0.30	0.04	0.24	0.05
PB33-224.52	Dolostone	123.6	1.16	1.96	0.24	0.96	0.18	0.09	0.21	0.03	0.15	2.49	0.04	0.10	0.01	0.07	0.01
PB33-232.46	Dolostone	128.0	0.64	1.01	0.12	0.45	0.09	0.06	0.12	0.02	0.12	2.13	0.03	0.09	0.01	0.07	0.01
PB33-235.73	Dolostone	129.8	0.59	0.80	0.09	0.36	0.09	0.07	0.13	0.02	0.15	2.12	0.04	0.11	0.02	0.09	0.02
PB33-238.8	Dolostone	131.5	1.17	2.00	0.23	0.94	0.21	0.14	0.28	0.05	0.27	2.95	0.06	0.17	0.02	0.13	0.02

Appendix to Chapter 4

Sample	Lithology	Strat-depth (m)	La	Ce	Pr	Nd	Sm	Eu	Gd	Tb	Dy	Y	Ho	Er	Tm	Yb	Lu
PB35-22.48	Limestone	19.3	0.21	0.15	0.02	0.06	0.02	0.01	0.02	0.03	0.02	0.07	0.01	0.02	0.00	0.02	0.03
PB35-24.22	Limestone	20.8	2.75	2.47	0.30	1.24	0.21	0.13	0.32	0.04	0.29	10.18	0.09	0.29	0.04	0.23	0.05
PB35-26.43	Limestone	22.7	2.80	3.87	0.41	1.59	0.32	0.23	0.41	0.07	0.46	7.38	0.12	0.37	0.05	0.33	0.06
PB35-29.37	Limestone	25.3	3.43	5.88	0.71	2.98	0.61	0.49	0.68	0.10	0.55	7.69	0.12	0.33	0.04	0.23	0.04
PB35-31.20	Limestone	26.8	3.68	4.92	0.50	1.88	0.32	0.38	0.35	0.05	0.26	4.43	0.06	0.16	0.02	0.12	0.02
PB35-34.20	Limestone	29.4	2.08	2.65	0.27	1.00	0.18	0.15	0.25	0.04	0.28	5.50	0.08	0.26	0.04	0.22	0.04
PB35-36.84	Limestone	31.7	1.14	1.40	0.03	0.41	0.06	0.15	0.08	0.01	0.06	1.44	0.02	0.05	0.01	0.04	0.01
PB35-39.70	Limestone	34.1	0.39	0.43	0.15	0.21	0.05	0.03	0.07	0.01	0.07	1.84	0.02	0.04	0.01	0.04	0.01
PB35-41.30	Black slate	35.5	76.95	150.91	15.82	54.70	7.96	2.28	6.57	0.71	2.94	16.94	0.54	1.46	0.21	1.33	0.31
PB35-43.65	Dolostone	37.5	1.63	2.51	0.27	1.09	0.21	0.14	0.29	0.05	0.29	4.34	0.07	0.23	0.03	0.20	0.05
PB35-47.10	Dolostone	40.5	1.28	1.93	0.21	0.82	0.16	0.09	0.22	0.04	0.23	3.49	0.06	0.19	0.03	0.18	0.04
PB35-49.43	Limestone	42.5	6.49	4.92	0.70	2.76	0.56	0.35	0.75	0.12	0.81	12.22	0.21	0.66	0.10	0.58	0.11
PB35-52.87	Limestone	45.5	1.22	1.61	0.17	0.63	0.13	0.08	0.16	0.03	0.17	2.93	0.04	0.13	0.02	0.12	0.07
PB35-54.38	Limestone	46.8	1.77	1.15	0.21	0.77	0.12	0.13	0.15	0.02	0.10	1.65	0.02	0.07	0.01	0.05	0.01
PB35-56.57	Dolostone	48.7	3.92	7.56	0.87	3.47	0.67	0.33	0.69	0.10	0.54	5.05	0.11	0.32	0.04	0.26	0.05
PB35-58.02	Dolostone	49.9	1.07	1.58	0.17	0.64	0.11	0.08	0.14	0.02	0.10	1.60	0.02	0.06	0.01	0.04	0.01
PB35-59.80	Dolostone	51.4	0.71	0.96	0.09	0.33	0.06	0.05	0.08	0.01	0.06	1.09	0.01	0.04	0.01	0.03	0.01
PB35-61.20	Dolostone	52.6	1.96	3.07	0.31	1.12	0.20	0.13	0.23	0.03	0.17	2.61	0.04	0.11	0.01	0.08	0.02
PB35-65	Black slate	55.9	30.14	58.28	6.28	22.77	3.84	1.14	3.53	0.47	2.37	14.26	0.48	1.31	0.19	1.20	0.21
PB35-68.65	Limestone	59.0	0.38	0.57	0.06	0.26	0.05	0.03	0.06	0.01	0.05	1.05	0.01	0.04	0.01	0.03	0.01
PB35-69.68	Limestone	59.9	0.48	0.49	0.05	0.18	0.03	0.02	0.05	0.01	0.04	1.16	0.01	0.03	0.01	0.03	0.01
PB35-70.63	Limestone	60.8	0.15	0.15	0.02	0.07	0.02	0.01	0.02	0.03	0.02	0.89	0.01	0.02	0.00	0.02	0.01
PB35-73.51	Limestone	63.2	2.96	5.01	0.50	1.69	0.28	0.09	0.30	0.03	0.15	1.61	0.03	0.07	0.01	0.05	0.01
PB35-76	Black slate	65.4	32.84	66.88	7.29	26.56	5.08	1.20	4.65	0.64	3.07	17.84	0.59	1.66	0.25	1.64	0.29
PB35-77.86	Limestone	67.0	28.92	56.26	6.21	25.82	4.21	1.00	3.57	0.35	1.23	7.75	0.22	0.52	0.08	0.50	0.10
PB35-79.6	Limestone	68.5	25.95	49.01	5.06	20.09	3.22	0.96	3.38	0.39	1.72	15.49	0.34	0.85	0.10	0.57	0.10
PB35-81.15	Limestone	69.8	25.10	50.02	5.59	21.15	3.68	1.07	3.15	0.40	1.86	10.60	0.36	0.99	0.15	0.92	0.16
PB35-85.7	Sandstone	72.7	15.80	33.87	3.73	13.57	2.45	0.77	2.24	0.30	1.53	9.12	0.30	0.81	0.12	0.70	0.12
PB35-87.93	Black slate	73.7	24.15	49.63	5.39	19.23	3.26	1.17	2.92	0.36	1.71	9.70	0.32	0.86	0.12	0.75	0.14
PB35-89.76	Dolostone	75.6	4.34	4.34	0.49	1.84	0.35	0.23	0.38	0.06	0.30	3.45	0.07	0.19	0.03	0.16	0.04
PB35-91.7	Dolostone	77.2	1.02	1.76	0.19	0.69	0.12	0.09	0.13	0.02	0.09	1.45	0.02	0.05	0.01	0.05	0.02
PB35-92.8	Dolostone	78.9	1.41	2.56	0.28	0.99	0.17	0.10	0.17	0.02	0.10	0.97	0.02	0.04	0.01	0.03	0.01
PB35-93.80	Dolostone	79.8	2.40	4.73	0.52	1.92	0.35	0.19	0.38	0.05	0.30	3.24	0.07	0.19	0.03	0.17	0.03
PB35-96.3	Dolostone	80.7	4.73	9.51	1.08	4.16	0.79	0.37	0.82	0.12	0.65	6.11	0.14	0.38	0.05	0.32	0.06
PB35-98.94	Black slate	82.8	20.07	42.37	4.65	17.27	3.76	1.08	3.58	0.53	2.71	15.56	0.53	1.53	0.25	1.62	0.30
PB35-102.02	Dolostone	85.1	2.85	5.33	0.59	2.22	0.40	0.26	0.43	0.06	0.34	3.62	0.08	0.22	0.03	0.20	0.05
PB35-104.00	Dolostone	87.7	3.01	5.80	0.65	2.42	0.47	0.28	0.48	0.07	0.36	3.11	0.07	0.19	0.03	0.14	0.03
PB35-105.81	Black slate	89.5	26.96	53.98	5.90	21.44	3.70	1.06	3.47	0.47	2.30	13.04	0.44	1.20	0.17	1.07	0.18
PB35-109.08	Black slate	91.0	29.94	58.90	6.45	23.14	3.77	1.36	3.44	0.44	2.08	12.00	0.40	1.08	0.16	0.96	0.17
PB35-110.90	Black slate	93.8	27.54	54.68	6.00	22.15	4.23	1.08	3.86	0.52	2.49	15.23	0.48	1.40	0.23	1.50	0.28
PB35-112.96	Black slate	95.4	34.52	67.13	7.35	27.08	5.07	1.25	4.52	0.57	2.63	15.03	0.50	1.43	0.23	1.54	0.29
PB35-114.34	Black slate	97.2	32.68	63.54	6.86	24.84	4.66	1.16	4.44	0.62	3.21	20.52	0.64	1.79	0.27	1.69	0.30
PB35-115.9	Black slate	98.3	29.33	59.68	6.71	25.65	5.36	1.32	4.95	0.67	3.34	20.23	0.67	1.91	0.30	1.98	0.36
PB35-118.22	Black slate	99.7	21.17	41.96	4.62	17.17	3.50	0.97	3.63	0.55	3.03	20.46	0.63	1.80	0.27	1.64	0.28
PB35-120.1	Black slate	101.7	31.71	63.14	6.89	24.79	4.20	1.27	3.91	0.51	2.45	14.32	0.48	1.29	0.19	1.17	0.20
PB35-122.14	Black slate	103.3	17.02	33.67	3.75	13.86	2.83	0.84	2.90	0.45	2.45	16.71	0.50	1.39	0.21	1.30	0.22
PB35-122.14	Black slate	105.1	46.24	89.27	10.23	38.67	6.78	1.70	6.07	0.77	3.67	21.11	0.71	1.93	0.28	1.74	0.30

Appendix to Chapter 4

Sample	Lithology	Strat-depth (m)	La	Ce	Pr	Nd	Sm	Eu	Gd	Tb	Dy	Y	Ho	Er	Tm	Yb	Lu
PB35-124.95	Black slate	107.5	33.75	65.70	7.15	26.09	4.90	1.08	4.37	0.54	2.42	13.96	0.45	1.26	0.20	1.34	0.25
PB35-126.63	Black slate	108.9	28.09	53.83	5.85	21.28	3.93	1.07	3.55	0.43	1.89	10.98	0.35	0.98	0.15	1.03	0.19
PB35-130.43	Black slate	112.2	27.30	53.20	5.79	21.36	4.16	1.21	3.88	0.51	2.44	14.31	0.47	1.33	0.21	1.38	0.26
PB35-133.24	Black slate	114.6	35.11	68.41	7.53	27.62	5.27	1.45	5.22	0.77	4.19	28.06	0.87	2.41	0.35	2.16	0.37
PB35-136.52	Black slate	117.4	54.10	100.06	10.66	38.15	5.84	1.69	5.25	0.60	2.63	15.32	0.50	1.34	0.20	1.22	0.22
PB35-138.74	Black slate	119.3	28.59	56.67	6.24	22.65	3.99	1.04	3.64	0.44	2.01	11.54	0.39	1.10	0.18	1.18	0.22
PB35-141.60	Black slate	121.8	29.75	59.22	6.48	23.73	4.52	1.27	4.21	0.53	2.40	13.55	0.45	1.28	0.21	1.43	0.27
PB35-144.40	Limestone	124.2	0.08	0.11	0.05	0.01	0.01	0.01	0.02	0.03	0.02	0.36	0.00	0.01	0.00	0.01	0.01
PB35-147.00	Limestone	126.4	0.13	0.12	0.01	0.06	0.01	0.01	0.02	0.03	0.02	0.62	0.01	0.02	0.00	0.02	0.01
PB35-149.76	Limestone	128.8	2.01	2.70	0.21	0.55	0.05	0.04	0.07	0.03	0.02	0.59	0.01	0.02	0.00	0.02	0.01
PB35-151.12	Limestone	130.0	1.32	2.14	0.23	0.82	0.14	0.20	0.16	0.02	0.13	1.27	0.03	0.06	0.01	0.04	0.01
PB35-153.50	Limestone	132.0	0.25	0.24	0.02	0.08	0.01	0.01	0.02	0.03	0.02	0.73	0.01	0.02	0.00	0.02	0.01
PB35-156.20	Limestone	134.4	0.21	0.25	0.03	0.11	0.02	0.02	0.03	0.03	0.03	0.73	0.01	0.03	0.00	0.02	0.01
PB35-157.75	Limestone	135.7	0.15	0.17	0.02	0.08	0.02	0.01	0.03	0.03	0.03	0.78	0.01	0.03	0.00	0.02	0.01
PB35-160.95	Limestone	138.4	0.24	0.24	0.03	0.10	0.02	0.01	0.03	0.03	0.03	1.17	0.01	0.03	0.00	0.03	0.01
PB35-162.4	Limestone	139.7	0.17	0.21	0.02	0.09	0.02	0.02	0.03	0.03	0.03	0.91	0.01	0.03	0.01	0.03	0.01
PB35-163.7	Limestone	140.8	0.34	0.33	0.03	0.13	0.02	0.01	0.03	0.03	0.03	1.23	0.01	0.03	0.01	0.03	0.01
PB35-166	Black slate	142.8	55.34	102.94	11.09	39.46	6.10	1.94	5.58	0.64	2.85	15.87	0.54	1.46	0.21	1.33	0.25
PB35-168.41	Limestone	144.9	0.25	0.27	0.03	0.12	0.02	0.02	0.04	0.03	0.05	0.74	0.01	0.03	0.01	0.03	0.02
PB35-171.13	Limestone	147.2	0.70	0.81	0.08	0.27	0.04	0.04	0.07	0.01	0.05	1.28	0.01	0.04	0.01	0.03	0.02
PB35-173.1	Limestone	148.9	2.05	3.21	0.34	1.26	0.22	0.27	0.24	0.03	0.16	2.36	0.04	0.11	0.02	0.09	0.02
PB35-175	Limestone	150.5	0.17	0.24	0.03	0.10	0.02	0.01	0.03	0.03	0.03	0.59	0.01	0.02	0.00	0.02	0.01
PB35-177.5	Limestone	152.7	1.19	1.55	0.15	0.55	0.09	0.09	0.12	0.02	0.08	1.21	0.02	0.05	0.01	0.05	0.01
PB35-178.8	Limestone	153.8	1.08	1.61	0.19	0.79	0.18	0.11	0.26	0.04	0.29	4.38	0.07	0.04	0.04	0.21	0.04
PB35-180.8	Limestone	155.5	0.34	0.40	0.04	0.16	0.03	0.01	0.05	0.03	0.05	1.32	0.01	0.05	0.01	0.04	0.01
PB35-184.26	Limestone	158.5	1.67	1.13	0.18	0.76	0.17	0.09	0.32	0.05	0.41	18.57	0.13	0.47	0.07	0.41	0.09
PB35-187.29	Dolostone	161.1	1.25	2.07	0.23	0.90	0.19	0.09	0.24	0.04	0.22	3.01	0.05	0.15	0.02	0.11	0.03
PB35-190.30	Dolostone	163.7	1.32	2.08	0.22	0.81	0.14	0.09	0.16	0.02	0.13	2.07	0.03	0.08	0.01	0.07	0.02
PB35-193.40	Dolostone	166.3	1.71	3.02	0.34	1.28	0.24	0.09	0.28	0.04	0.23	2.41	0.05	0.14	0.02	0.11	0.02
PB35-195.3	Dolostone	168.0	4.67	8.24	0.91	3.41	0.60	0.21	0.64	0.09	0.45	3.48	0.09	0.23	0.03	0.17	0.03
PB35-198.5	Dolostone	170.7	2.06	3.51	0.39	1.49	0.28	0.10	0.32	0.05	0.26	2.61	0.06	0.16	0.02	0.14	0.03
PB35-200.6	Dolostone	172.5	3.35	5.78	0.63	2.37	0.43	0.14	0.46	0.06	0.32	3.13	0.07	0.18	0.02	0.13	0.02
PB35-202.3	Dolostone	174.0	1.95	2.88	0.30	1.11	0.20	0.09	0.23	0.03	0.17	2.13	0.04	0.11	0.01	0.08	0.02
PB35-205	Dolostone	176.3	2.35	3.93	0.43	1.64	0.29	0.14	0.32	0.04	0.24	2.70	0.05	0.15	0.02	0.12	0.02
PB35-206.7	Dolostone	177.8	3.12	5.05	0.54	1.99	0.33	0.17	0.41	0.06	0.32	3.96	0.08	0.24	0.03	0.21	0.04
PB35-209	Dolostone	179.8	1.68	2.50	0.26	0.96	0.16	0.09	0.19	0.03	0.15	1.96	0.03	0.10	0.02	0.09	0.02
PB35-211.41	Dolostone	181.8	2.84	4.77	0.54	2.18	0.47	0.24	0.57	0.09	0.51	5.41	0.11	0.32	0.04	0.25	0.05
PB35-213.2	Iron Formation	183.4	21.53	42.40	4.61	16.31	2.86	0.86	2.96	0.41	2.17	12.83	0.44	1.25	0.19	1.22	0.22
PB35-215.04	Iron Formation	185.0	11.29	21.88	2.43	8.96	1.68	0.63	1.89	0.29	1.57	10.45	0.33	0.95	0.15	0.91	0.17
PB35-217.8	Limestone	187.3	0.38	0.52	0.06	0.22	0.05	0.02	0.06	0.01	0.06	1.06	0.01	0.04	0.01	0.04	0.01
PB35-219.6	Black slate	188.9	44.69	77.05	7.23	22.62	3.26	0.98	3.13	0.30	1.06	4.53	0.17	0.39	0.05	0.33	0.06
PB35-221.3	Limestone	190.3	0.43	0.37	0.04	0.14	0.03	0.03	0.04	0.03	0.05	1.61	0.01	0.05	0.01	0.04	0.02
PB35-223.3	Limestone	192.1	0.06	0.11	0.03	0.06	0.03	0.01	0.01	0.03	0.01	0.20	0.00	0.01	0.00	0.01	0.01
PB35-225.1	Limestone	193.6	2.09	3.33	0.33	1.08	0.10	0.03	0.11	0.01	0.03	0.62	0.01	0.02	0.00	0.02	0.01
PB35-227.8	Limestone	195.9	1.38	2.01	0.22	0.85	0.17	0.11	0.23	0.04	0.24	3.14	0.06	0.16	0.02	0.14	0.03
PB35-230.02	Limestone	197.8	0.37	0.55	0.06	0.23	0.04	0.03	0.06	0.01	0.05	0.67	0.01	0.04	0.01	0.03	0.01
PB35-231.96	Limestone	199.5	0.47	0.76	0.08	0.31	0.06	0.04	0.08	0.01	0.07	0.94	0.02	0.05	0.01	0.04	0.01
PB35-235.2	Dolostone	202.3	0.73	0.83	0.09	0.33	0.06	0.03	0.08	0.01	0.07	1.74	0.02	0.06	0.01	0.05	0.01

Appendix to Chapter 4

Sample	Lithology	Strat-depth (m)	La	Ce	Pr	Nd	Sm	Eu	Gd	Tb	Dy	Y	Ho	Er	Tm	Yb	Lu
PB35-237.4	Limestone	204.2	0.73	0.97	0.10	0.38	0.07	0.04	0.09	0.01	0.08	1.40	0.02	0.06	0.01	0.05	0.01
PB35-239.3	Limestone	205.8	0.26	0.37	0.04	0.17	0.03	0.03	0.05	0.03	0.05	0.74	0.01	0.03	0.01	0.03	0.01
PB35-241.5	Limestone	207.7	0.11	0.12	0.01	0.05	0.01	0.02	0.02	0.03	0.02	0.63	0.01	0.02	0.00	0.02	0.00
PB35-243.4	Limestone	209.4	0.22	0.28	0.02	0.11	0.02	0.07	0.02	0.03	0.01	0.39	0.00	0.01	0.00	0.01	0.00
PB35-245.5	Limestone	211.2	0.27	0.25	0.02	0.08	0.01	0.04	0.02	0.03	0.02	0.48	0.00	0.02	0.00	0.01	0.00
PB35-247.8	Limestone	213.1	0.27	0.38	0.04	0.17	0.04	0.03	0.05	0.01	0.04	0.77	0.01	0.03	0.01	0.03	0.01
PB35-250.7	Limestone	215.6	0.37	0.56	0.06	0.23	0.04	0.03	0.06	0.01	0.06	0.80	0.01	0.04	0.01	0.03	0.01
PB35-251.11	Limestone	216.0	0.20	0.31	0.03	0.14	0.03	0.02	0.03	0.03	0.03	0.38	0.01	0.02	0.00	0.02	0.00
PB35-254.4	Cherty dolomite	218.5	21.61	43.47	4.83	17.66	3.02	0.91	2.88	0.38	1.82	10.12	0.36	0.97	0.14	0.89	0.15
PB35-256.2	Chert	219.1	16.99	30.71	3.10	10.59	1.70	0.51	1.56	0.16	0.60	2.99	0.10	0.24	0.04	0.23	0.04

Sample	Lithology	Strat-depth (m)	La	Ce	Pr	Nd	Sm	Eu	Gd	Tb	Dy	Y	Ho	Er	Tm	Yb	Lu
I7GA1-36	Limestone	0.01	1.52	2.16	0.24	1.01	0.22	0.15	0.31	0.05	0.27	2.96	0.06	0.15	0.02	0.10	0.02
I7GA1-35	Limestone	0.11	0.81	1.55	0.19	0.81	0.21	0.18	0.31	0.06	0.45	4.54	0.12	0.39	0.06	0.36	0.07
I7GA1-34	Limestone	0.22	0.99	1.59	0.18	0.83	0.18	0.23	0.24	0.04	0.23	2.83	0.05	0.15	0.02	0.11	0.02
I7GA1-33	Limestone	0.3	0.98	1.56	0.18	0.73	0.14	0.16	0.18	0.03	0.18	2.67	0.04	0.14	0.02	0.11	0.02
I7GA1-32	Limestone	0.36	1.41	1.78	0.19	0.80	0.17	0.10	0.25	0.04	0.31	4.44	0.08	0.27	0.04	0.25	0.04
I7GA1-31	Limestone	0.53	0.96	0.70	0.05	0.14	0.01	0.06	0.03	0.00	0.02	1.01	0.01	0.02	0.00	0.02	0.00
I7GA1-30	Limestone	0.58	0.59	0.82	0.11	0.53	0.14	0.10	0.22	0.04	0.24	3.47	0.06	0.18	0.02	0.13	0.02
I7GA1-29	Limestone	0.69	0.88	1.08	0.11	0.40	0.04	0.14	0.05	0.01	0.02	0.90	0.01	0.02	0.00	0.02	0.00
I7GA1-28	Limestone	0.73	1.12	1.53	0.19	0.87	0.19	0.23	0.24	0.03	0.18	3.15	0.04	0.09	0.01	0.06	0.01
I7GA1-27	Limestone	0.82	1.00	1.12	0.14	0.59	0.12	0.07	0.18	0.03	0.19	3.34	0.05	0.14	0.02	0.11	0.02
I7GA1-26	Limestone	0.85	2.85	2.92	0.37	1.58	0.35	0.17	0.56	0.09	0.64	13.57	0.16	0.53	0.07	0.43	0.07
I7GA1-25	Limestone	0.89	2.55	2.51	0.32	1.42	0.32	0.17	0.51	0.08	0.59	13.69	0.16	0.53	0.07	0.44	0.08
I7GA1-24	Limestone	0.93	1.30	1.29	0.17	0.73	0.15	0.10	0.24	0.04	0.27	6.11	0.07	0.25	0.04	0.23	0.04
I7GA1-23	Limestone	1.03	1.92	1.92	0.26	1.08	0.22	0.13	0.32	0.05	0.31	6.69	0.08	0.30	0.04	0.30	0.06
I7GA1-22	Limestone	1.06	2.80	2.20	0.30	1.34	0.31	0.18	0.61	0.10	0.77	26.60	0.23	0.83	0.12	0.72	0.15
I7GA1-21	Limestone	1.09	0.90	0.85	0.14	0.64	0.13	0.18	0.19	0.03	0.17	4.59	0.04	0.12	0.02	0.08	0.01
I7GA1-20	Limestone	1.14	0.76	0.66	0.12	0.57	0.14	0.15	0.23	0.04	0.25	8.07	0.07	0.21	0.03	0.13	0.02
I7GA1-19	Limestone	1.21	2.32	1.34	0.23	1.10	0.29	0.17	0.61	0.10	0.79	30.95	0.24	1.03	0.14	0.78	0.16
I7-GA1-18	Limestone	1.28	3.38	2.13	0.36	1.65	0.38	0.20	0.76	0.13	0.94	33.18	0.29	1.03	0.14	0.92	0.19
I7-GA1-17	Limestone	1.34	5.44	3.74	0.60	2.58	0.51	0.22	0.84	0.13	0.88	27.14	0.25	0.92	0.13	0.90	0.19
I7-GA1-16	Limestone	1.4	4.72	3.52	0.57	2.51	0.52	0.24	0.84	0.13	0.87	26.04	0.25	0.90	0.13	0.89	0.19
I7-GA1-15	Limestone	1.44	0.01	0.01	0.01	0.01	0.01	0.00	0.01	0.01	0.01	0.00	0.01	0.01	0.01	0.01	0.01
I7GA1-15	Limestone	1.44	4.52	3.34	0.53	2.36	0.49	0.26	0.78	0.11	0.80	25.48	0.23	0.83	0.12	0.82	0.18
I7-GA1-14	Limestone	1.46	2.51	2.12	0.32	1.43	0.33	0.22	0.55	0.09	0.65	19.27	0.19	0.66	0.09	0.57	0.11
I7-GA1-13	Limestone	1.54	2.97	2.76	0.38	1.66	0.35	0.19	0.56	0.09	0.62	16.43	0.17	0.60	0.08	0.51	0.10
I7-GA1-12	Limestone	1.6	3.99	3.85	0.53	2.25	0.47	0.23	0.72	0.11	0.74	19.83	0.20	0.73	0.11	0.68	0.14
I7-GA1-11	Limestone	1.65	3.03	3.04	0.43	1.84	0.41	0.19	0.62	0.10	0.67	18.03	0.19	0.67	0.10	0.66	0.13
I7-GA1-10	Limestone	1.73	0.75	0.91	0.13	0.65	0.18	0.13	0.29	0.05	0.37	7.34	0.09	0.31	0.04	0.26	0.04
I7-GA1-09	Limestone	1.78	0.68	0.85	0.11	0.49	0.11	0.12	0.15	0.02	0.13	2.27	0.03	0.08	0.01	0.06	0.01
I7-GA1-08	Limestone	1.81	0.88	0.97	0.11	0.42	0.08	0.09	0.11	0.01	0.09	1.93	0.02	0.07	0.01	0.05	0.01
I7-GA1-07	Limestone	1.87	0.75	0.98	0.12	0.52	0.12	0.07	0.18	0.03	0.19	2.82	0.05	0.15	0.02	0.12	0.02
I7-GA1-06	Limestone	1.9	0.01	0.01	0.01	0.01	0.01	0.01	0.01	0.01	0.01	0.01	0.01	0.01	0.01	0.01	0.01
I7-GA1-05	Limestone	1.94	0.95	1.43	0.18	0.80	0.20	0.15	0.27	0.04	0.28	3.60	0.06	0.19	0.03	0.15	0.02
I7-GA1-04	Limestone	1.98	0.61	0.87	0.10	0.44	0.10	0.05	0.14	0.02	0.15	1.90	0.03	0.11	0.02	0.09	0.02
I7-GA1-03	Limestone	2.04	1.19	1.69	0.19	0.78	0.16	0.10	0.21	0.03	0.20	2.78	0.05	0.15	0.02	0.13	0.02
I7-GA1-02	Limestone	2.07	1.19	1.72	0.19	0.76	0.15	0.10	0.21	0.03	0.21	2.89	0.05	0.16	0.02	0.13	0.02
I7-GA1-01	Limestone	2.1	1.06	1.67	0.20	0.87	0.19	0.10	0.26	0.04	0.28	3.42	0.07	0.21	0.03	0.17	0.03

Appendix to Chapter 4

Appendix A.4. Carbonate leach minor and Trace element concentrations (ppm) for the Red Lake samples

Sample name	Lithology	Strat-depth (m)	Cr	Mn	V	U	Th	Sr	Li	Ba	Hf	Sc	Co	Ni	Cu	Zn	Zr
EBL28-297.73	Dolostone	133.7	1.06	0.05	0.45	0.02	0.05	13.96	0.30	0.13	0.06	3.51	0.16	5.18	0.03	10.20	0.06
EBL28-304	Dolostone	136.5	4.11	0.03	0.62	0.02	0.03	5.90	0.15	0.11	0.04	5.95	0.14	2.22	0.04	6.15	0.04
EBL28-305.9	Dolostone	137.4	4.23	0.05	0.05	0.01	4.23	1.49	0.10	0.10	0.06	0.85	0.07	1.25	0.17	1.57	0.06
EBL28-308.89	Dolostone	138.7	1.29	0.04	0.18	0.02	0.04	12.74	0.24	0.15	0.05	0.45	0.09	1.99	0.17	5.89	0.05
EBL28-311.35	Dolostone	139.8	0.82	0.04	0.04	0.01	0.04	9.55	0.24	0.09	0.04	0.89	0.09	1.39	0.05	5.71	0.04
EBL28-315.64	Dolostone	141.7	1.84	0.04	1.49	0.04	0.04	13.47	0.26	0.29	0.05	7.41	0.16	1.76	0.02	5.84	0.05
EBL28-318.36	Dolostone	143.0	1.59	0.03	0.24	0.02	0.03	10.23	0.28	0.18	0.04	1.15	0.15	2.38	0.05	7.23	0.04
EBL28-321.64	Dolostone	144.4	0.73	0.03	0.36	0.02	0.03	8.94	0.23	0.15	0.04	2.03	0.12	1.05	0.05	4.22	0.04
EBL28-322.95	Dolostone	145.0	1.24	0.04	0.28	0.03	0.04	14.11	0.25	0.17	0.05	0.85	0.15	2.01	0.06	5.35	0.05
EBL28-326.38	Dolostone	146.6	0.94	0.03	0.08	0.01	0.03	6.67	0.22	0.11	0.04	0.20	0.11	1.54	0.05	5.91	0.04
EBL28-330	Dolostone	148.2	1.10	0.03	0.20	0.06	0.03	5.54	0.32	0.17	0.04	0.33	0.05	0.33	0.03	3.46	0.04
EBL28-332.5	Dolostone	149.3	0.67	0.04	0.25	0.02	0.04	8.16	0.39	0.21	0.05	1.18	0.30	3.91	0.02	10.64	0.05
EBL28-344.15	Dolostone	154.5	1.29	0.03	0.10	0.04	0.03	6.83	0.22	0.24	0.04	0.23	0.06	0.84	0.04	3.91	0.04
EBL28-347.38	Dolostone	156.0	0.35	0.04	0.05	0.01	0.04	7.34	0.22	0.13	0.05	0.24	0.03	0.78	0.03	4.42	0.05
EBL28-351	Dolostone	157.6	1.40	0.03	0.29	0.08	0.04	6.05	0.20	0.09	0.04	6.03	0.04	1.72	0.06	5.47	0.04
EBL28-351.93	Dolostone	158.0	2.97	0.05	0.22	0.04	0.03	4.91	0.19	0.12	0.04	0.63	0.04	0.98	0.04	3.74	0.04
EBL28-357	Dolostone	160.3	0.65	0.04	0.25	0.04	0.04	9.85	0.26	0.13	0.05	0.90	0.09	2.67	0.04	5.35	0.05
EBL28-360.4	Dolostone	161.8	0.73	0.03	0.25	0.06	0.03	10.00	0.26	0.15	0.04	1.33	0.10	2.76	0.06	5.70	0.04
EBL28-362.40	Dolostone	162.7	2.35	0.05	0.18	0.05	0.04	8.12	0.29	0.19	0.05	0.32	0.07	1.25	0.06	4.30	0.05
EBL28-365.22	Dolostone	164.0	0.84	0.03	0.54	0.17	0.03	10.65	0.40	0.28	0.04	3.70	0.71	4.50	0.02	6.55	0.04
EBL28-368.09	Dolostone	165.3	0.86	0.04	0.22	0.06	0.04	10.24	0.25	0.15	0.05	1.16	0.09	1.05	0.06	4.58	0.05
EBL28-369.52	Dolostone	165.9	1.11	0.03	0.07	0.02	0.03	5.84	0.18	0.13	0.04	0.20	0.10	3.38	0.09	5.04	0.04
EBL28-373.40	Dolostone	167.7	0.81	0.04	0.27	0.01	0.04	10.60	0.26	0.22	0.04	1.31	0.11	5.43	0.04	7.65	0.04
EBL28-376.8	Dolostone	169.2	1.06	0.04	0.26	0.01	0.04	10.35	0.27	0.15	0.05	0.88	0.16	2.54	0.03	7.88	0.05
EBL28-378.10	Dolostone	169.8	0.33	0.03	0.21	0.02	0.03	9.33	0.22	0.15	0.04	0.74	0.16	4.34	0.05	6.66	0.04
EBL28-382.76	Dolostone	171.9	0.49	0.04	0.61	0.01	0.04	14.08	0.35	0.38	0.05	3.62	0.15	5.27	0.02	10.21	0.05
EBL28-387	Dolostone	173.8	0.37	0.04	0.36	0.01	0.04	13.65	0.29	0.21	0.04	1.56	0.12	2.52	0.03	7.07	0.04
EBL28-389.46	Dolostone	174.9	0.52	0.03	0.52	0.02	0.03	13.16	0.29	0.23	0.04	2.71	0.24	4.02	0.05	6.16	0.04
EBL28-395.56	Dolostone	177.6	2.16	0.03	0.05	0.03	0.03	4.50	0.19	0.22	0.04	0.20	0.06	0.75	0.01	3.04	0.04
EBL28-397.02	Dolostone	178.3	4.93	0.08	0.06	0.03	0.05	6.74	0.23	0.26	0.06	0.29	0.10	2.16	0.15	3.18	0.06
EBL28-400.3	Dolostone	179.7	0.32	0.03	0.07	0.03	0.03	9.97	0.26	0.19	0.04	0.22	0.13	2.96	0.01	6.71	0.04
EBL28-402.89	Dolostone	180.9	0.64	0.03	0.17	0.02	0.03	9.68	0.22	0.10	0.04	0.68	0.08	2.02	0.04	5.84	0.04
EBL28-408.29	Dolostone	183.3	1.06	0.03	0.21	0.02	0.03	6.69	0.15	0.19	0.04	1.26	0.04	1.64	0.05	3.37	0.04
EBL28-411.24	Dolostone	184.7	0.83	0.03	0.23	0.03	0.03	5.19	0.19	0.10	0.04	0.70	0.02	1.07	0.06	2.55	0.04
EBL28-416.30	Dolostone	186.9	1.47	0.04	0.16	0.03	0.04	7.92	0.22	0.14	0.05	0.28	0.03	4.71	0.03	7.42	0.05
EBL28-421.44	Dolostone	189.2	0.95	0.03	0.13	0.03	0.03	7.66	0.22	0.12	0.04	0.30	0.03	2.01	0.07	4.52	0.04
EBL28-426.25	Dolostone	191.4	1.21	0.03	0.36	0.03	0.04	8.75	0.24	0.13	0.05	0.60	0.04	1.69	0.10	6.45	0.05
EBL28-429.76	Dolostone	193.0	0.77	0.03	1.08	0.05	0.03	12.27	0.28	0.17	0.04	4.31	0.01	1.28	0.08	3.74	0.04
EBL28-433.56	Dolostone	194.7	0.51	0.03	0.32	0.02	0.03	8.76	0.21	0.14	0.04	0.93	0.03	1.43	0.10	3.95	0.04
EBL28-436.44	Dolostone	196.0	1.08	0.04	0.31	0.01	0.04	8.23	0.14	0.13	0.05	1.01	0.03	1.13	0.08	3.92	0.05
EBL28-443.28	Dolostone	199.0	0.85	0.03	0.13	0.02	0.03	11.06	0.25	0.28	0.04	0.27	0.07	1.15	0.03	3.89	0.04
EBL28-446.76	Dolostone	200.6	0.81	0.03	0.20	0.03	0.03	10.70	0.24	0.25	0.04	0.39	0.04	1.28	0.03	3.78	0.04
EBL28-451.93	Dolostone	202.9	0.57	0.03	0.13	0.02	0.03	9.13	0.23	0.30	0.04	0.31	0.09	1.14	0.03	4.02	0.04

Appendix to Chapter 4

Sample name	Lithology	Strat-depth (m)	Cr	Mo	V	U	Th	Sr	Li	Ba	Hf	Sc	Co	Ni	Cu	Zn	Zr
P832-21.50	Dolomite	19.42	0.42	0.05	0.52	0.17	0.04	13.94	0.26	2.17	0.05	1.15	0.07	9.11	0.13	6.66	0.05
P832-24.25	Dolomite	21.91	0.33	0.03	0.15	0.04	0.03	9.81	0.22	0.58	0.04	0.25	0.09	2.50	0.01	6.22	0.04
P832-27.50	Dolomite	24.84	0.99	0.04	0.25	0.09	0.04	10.50	0.22	0.68	0.05	0.43	0.09	1.65	0.02	6.12	0.05
P832-29.24	Dolomite	26.41	3.76	0.04	0.26	0.07	0.04	8.82	0.18	0.23	0.05	1.03	0.07	1.17	0.04	6.22	0.05
P832-31.56	Dolomite	28.51	0.85	0.04	0.09	0.05	0.04	8.21	0.24	0.14	0.05	0.25	0.06	1.43	0.04	6.89	0.05
P832-34.62	Dolomite	31.27	1.26	0.04	0.10	0.06	0.04	7.14	0.24	0.20	0.05	0.33	0.20	0.84	0.03	6.10	0.05
P832-37.56	Dolomite	33.93	1.71	0.03	0.10	0.02	0.03	7.58	0.20	0.15	0.04	0.20	0.03	0.87	0.05	4.27	0.04
P832-39.11	Dolomite	35.33	0.63	0.04	0.13	0.04	0.04	8.15	0.31	0.27	0.05	0.25	0.03	0.82	0.01	5.99	0.05
P832-40.85	Dolomite	36.90	0.98	0.03	0.08	0.02	0.03	7.23	0.27	0.14	0.04	0.19	0.02	0.80	0.02	4.72	0.04
P832-43.70	Dolomite	39.48	0.47	0.03	0.13	0.02	0.03	9.07	0.22	0.19	0.04	0.21	0.02	0.46	0.02	6.17	0.04
P832-44.81	Dolomite	40.48	0.56	0.03	0.11	0.02	0.03	10.88	0.22	0.40	0.04	0.19	0.03	1.07	0.02	5.51	0.04
P832-48.88	Dolomite	44.16	0.29	0.03	0.10	0.02	0.03	12.65	0.27	0.22	0.04	0.21	0.03	1.07	0.02	6.89	0.04
P832-50.31	Dolomite	45.45	0.94	0.04	0.28	0.03	0.04	26.23	0.31	0.28	0.05	0.74	0.06	2.53	0.03	11.11	0.05
P832-56.08	Dolomite	50.66	0.49	0.03	0.15	0.05	0.03	15.51	0.34	0.50	0.04	0.19	0.08	1.61	0.04	7.04	0.04
P832-60.70	Dolomite	54.83	0.19	0.03	0.30	0.02	0.03	17.31	0.35	0.39	0.04	0.92	0.04	1.61	0.02	8.52	0.04
P832-62.29	Dolomite	56.27	0.63	0.03	0.38	0.08	0.03	17.20	0.28	2.16	0.04	2.00	0.07	2.58	0.37	6.85	0.04
P832-65.66	Dolomite	59.31	1.08	0.03	0.70	0.02	0.03	21.31	0.42	0.19	0.04	5.04	0.04	1.02	0.01	9.63	0.04
P832-67.93	Dolomite	61.36	1.57	0.03	0.32	0.05	0.03	12.61	0.22	0.20	0.04	0.59	0.02	0.57	0.06	7.20	0.04
P832-70.38	Dolomite	63.56	0.42	0.03	0.09	0.03	0.03	8.06	0.19	0.10	0.04	0.21	0.03	0.88	0.03	6.46	0.04
P832-71.89	Dolomite	64.94	1.36	0.03	0.17	0.01	0.03	10.82	0.23	0.15	0.04	0.21	0.04	1.18	0.02	6.16	0.04
P832-85.73	Dolomite	71.44	0.41	0.03	0.48	0.01	0.03	13.53	0.25	0.90	0.04	1.33	0.08	1.30	0.01	8.30	0.04
P832-88.23	Dolomite	79.70	0.45	0.04	0.41	0.10	0.04	19.07	0.31	1.68	0.05	1.04	0.14	1.64	0.01	11.05	0.05
P832-90.70	Dolomite	81.93	0.34	0.03	0.24	0.04	0.03	12.49	0.22	0.47	0.04	0.69	0.22	8.26	2.26	6.64	0.04
P832-92.2	Dolomite	83.29	0.82	0.03	0.13	0.05	0.03	12.96	0.22	0.61	0.04	0.32	0.10	1.99	0.01	6.34	0.04
P832-94.1	Dolomite	85.00	0.57	0.03	0.29	0.01	0.03	11.34	0.30	0.61	0.04	0.64	0.05	1.05	0.01	5.45	0.04
P832-96.88	Dolomite	87.52	0.31	0.03	0.33	0.03	0.03	11.21	0.30	0.41	0.04	1.03	0.03	0.92	0.02	5.65	0.04
P832-98.57	Dolomite	89.04	0.40	0.04	0.48	0.06	0.04	15.24	0.32	0.96	0.05	2.73	0.04	1.16	0.02	6.92	0.05
P832-100.4	Dolomite	90.70	0.59	0.03	0.27	0.04	0.03	11.00	0.16	0.62	0.04	1.25	0.04	1.12	0.01	5.34	0.04
P832-102.13	Dolomite	92.26	0.52	0.03	0.27	0.03	0.03	13.44	0.28	0.55	0.04	0.75	0.10	1.45	0.03	6.23	0.04
P832-104.85	Dolomite	94.72	0.58	0.04	0.21	0.06	0.04	12.51	0.26	0.18	0.04	0.49	0.10	1.25	0.03	6.75	0.04
P832-108.35	Dolomite	97.88	0.46	0.03	0.37	0.06	0.03	10.77	0.21	1.35	0.04	1.24	0.03	0.58	0.01	6.99	0.04
P832-112.63	Dolomite	101.74	0.52	0.04	0.71	0.09	0.04	14.50	0.31	1.29	0.05	2.54	0.03	0.93	0.02	11.93	0.05
P832-114.1	Dolomite	103.07	0.93	0.03	0.34	0.04	0.03	11.95	0.25	0.99	0.04	0.89	0.05	2.17	0.03	5.04	0.04
P832-116.89	Dolomite	105.59	1.20	0.04	0.25	0.04	0.03	10.83	0.26	0.22	0.04	0.34	0.06	1.29	0.04	4.67	0.04
P832-118.9	Dolomite	107.41	1.51	0.06	0.31	0.04	0.03	8.23	0.18	1.73	0.04	1.28	0.12	0.62	0.01	3.12	0.04
P832-121.10	Dolomite	109.39	1.10	0.03	0.24	0.02	0.03	17.59	0.16	0.41	0.04	1.07	0.16	0.87	0.01	3.73	0.04
P832-123.2	Dolomite	111.29	6.44	0.04	0.16	0.01	0.04	5.93	0.08	0.16	0.05	0.73	0.14	1.21	0.05	2.18	0.05
P832-124.93	Dolomite	112.85	1.02	0.03	0.16	0.02	0.03	12.18	0.17	0.19	0.04	0.33	0.15	0.90	0.05	2.72	0.04
P832-128.48	Dolomite	116.06	2.49	0.03	0.21	0.02	0.03	8.76	0.11	0.20	0.04	0.71	0.11	0.87	0.01	2.61	0.04
P832-138.7	Dolomite	125.29	2.29	0.03	0.13	0.01	0.03	12.85	0.17	0.23	0.04	0.78	0.05	0.58	0.01	2.89	0.04
P832-139.87	Dolomite	126.35	0.37	0.03	0.27	0.08	0.03	9.29	0.15	1.28	0.04	3.41	0.07	0.37	0.01	2.17	0.04
P832-143.3	Dolomite	129.45	1.06	0.03	0.73	0.01	0.03	16.95	0.28	0.34	0.04	5.02	0.03	2.43	0.05	10.09	0.04

Appendix to Chapter 4

Sample name	Lithology	Strat-depth (m)	Cr	Mo	V	U	Th	Sr	Li	Ba	Hf	Sc	Co	Ni	Cu	Zn	Zr
PB32-146.16	Dolostone	132.03	1.03	0.04	0.12	0.06	0.04	13.02	0.17	0.82	0.05	0.26	0.20	3.05	0.01	6.32	0.05
PB32-148.92	Dolostone	134.53	1.44	0.04	0.56	0.06	0.04	11.60	0.32	0.30	0.04	1.43	0.02	1.52	0.03	4.27	0.04
PB32-150.8	Dolostone	136.22	0.45	0.03	0.34	0.01	0.03	13.93	0.29	0.31	0.04	1.31	0.09	1.65	0.01	5.55	0.04
PB32-159.13	Dolostone	143.75	1.26	0.03	0.28	0.03	0.03	6.08	0.20	0.80	0.04	0.26	0.10	0.56	0.02	2.58	0.04
PB32-165	Dolostone	149.05	1.27	0.03	0.12	0.02	0.03	13.42	0.18	0.17	0.04	0.20	0.04	0.42	0.05	4.59	0.04
PB32-167.5	Dolostone	151.31	0.90	0.03	0.12	0.02	0.03	11.98	0.19	0.18	0.04	0.21	0.03	0.49	0.02	4.80	0.04
PB32-171.2	Dolostone	154.65	1.86	0.03	0.93	0.02	0.03	8.31	0.28	0.23	0.04	0.21	0.04	0.91	0.04	4.16	0.04
PB32-172.93	Dolostone	156.21	1.19	0.03	0.12	0.01	0.03	7.94	0.22	0.32	0.04	0.22	0.04	0.50	0.01	3.56	0.04
PB32-183.38	Dolostone	165.65	2.47	0.04	0.14	0.02	0.04	11.34	0.23	0.51	0.05	0.26	0.06	0.33	0.02	4.05	0.05
PB32-189.02	Dolostone	170.75	1.41	0.03	0.79	0.01	0.03	7.09	0.13	1.62	0.04	0.47	0.05	0.47	0.01	4.94	0.04
PB32-190.25	Dolostone	171.86	0.43	0.04	0.22	0.11	0.04	16.29	0.31	0.35	0.05	0.36	0.08	0.90	0.01	7.93	0.05
PB32-194.05	Dolostone	175.29	0.35	0.04	0.19	0.08	0.04	14.54	0.30	0.46	0.04	0.39	0.04	1.24	0.01	8.27	0.05
PB32-195.5	Dolostone	176.60	0.38	0.04	0.14	0.03	0.04	14.76	0.30	0.38	0.06	0.27	0.07	1.66	0.04	8.09	0.06
PB32-197.35	Dolostone	178.27	0.73	0.03	0.21	0.09	0.03	10.76	0.21	0.37	0.04	0.50	0.04	0.80	0.01	6.02	0.04
PB32-199.28	Dolostone	180.02	0.37	0.03	0.17	0.06	0.03	9.97	0.20	1.09	0.04	0.55	0.02	0.88	0.01	5.84	0.04
PB32-201.92	Dolostone	182.40	0.38	0.03	0.09	0.02	0.03	8.84	0.22	0.42	0.04	0.22	0.06	0.91	0.02	5.42	0.04
PB32-203.5	Dolostone	183.83	0.85	0.03	0.06	0.06	0.03	7.59	0.21	0.19	0.04	0.20	0.05	0.68	0.02	5.13	0.04
PB32-205.25	Dolostone	185.41	0.85	0.03	0.12	0.01	0.03	9.02	0.25	1.00	0.04	0.35	0.04	0.49	0.01	2.66	0.04
PB32-208.58	Dolostone	188.42	0.58	0.04	0.13	0.04	0.04	9.22	0.24	0.30	0.04	0.23	0.05	0.93	0.05	3.57	0.04
PB32-210.2	Dolostone	189.88	1.92	0.03	0.30	0.09	0.03	7.79	0.23	1.13	0.04	0.77	0.03	0.72	0.03	3.43	0.04
PB32-212.08	Dolostone	191.58	0.38	0.03	0.29	0.05	0.03	8.75	0.24	0.35	0.04	0.75	0.05	0.47	0.01	3.73	0.04
PB32-292.37	Dolostone	264.11	0.47	0.04	0.23	0.02	0.04	18.03	0.27	1.33	0.05	0.79	0.06	0.43	0.01	5.20	0.05
PB32-295.80	Dolostone	267.21	0.19	0.04	0.14	0.04	0.04	14.46	0.27	0.32	0.05	0.24	0.05	0.81	0.04	6.93	0.05

Sample name	Lithology	Strat-depth (m)	Cr	Mo	V	U	Th	Sr	Li	Ba	Hf	Sc	Co	Ni	Cu	Zn	Zr
PB33-108.27	Dolostone	59.6	0.86	0.03	0.37	0.05	0.03	17.81	0.39	0.62	0.04	0.43	0.04	1.75	0.02	4.63	0.04
PB33-112	Dolostone	61.7	1.61	0.04	0.15	0.01	0.04	16.29	0.35	0.39	0.05	0.27	0.05	1.50	0.04	4.49	0.05
PB33-116.73	Dolostone	64.3	2.62	0.03	0.11	0.01	0.03	7.44	0.15	0.15	0.04	0.22	0.04	1.27	0.29	2.62	0.04
PB33-123.58	Dolostone	68.1	0.24	0.03	0.06	0.04	0.03	6.44	0.25	0.19	0.04	0.22	0.02	0.92	0.02	6.14	0.04
PB33-129.05	Dolostone	71.1	0.35	0.03	0.07	0.03	0.03	5.93	0.24	0.13	0.04	0.19	0.02	0.82	0.01	8.61	0.04
PB33-134.82	Dolostone	74.2	0.28	0.04	0.28	0.07	0.04	9.61	0.37	0.03	0.06	0.29	0.06	1.46	0.02	5.46	0.06
PB33-138.35	Dolostone	76.2	0.65	0.04	0.67	0.03	0.04	11.48	0.30	0.19	0.05	0.65	0.16	2.13	0.05	7.50	0.05
PB33-145.63	Dolostone	80.2	0.46	0.04	0.31	0.03	0.04	13.75	0.35	0.47	0.05	0.27	0.13	4.53	0.01	4.72	0.05
PB33-157.17	Dolostone	86.5	0.43	0.03	0.27	0.03	0.03	7.81	0.30	0.33	0.04	0.69	0.05	1.22	0.02	3.54	0.04
PB33-163.13	Dolostone	89.8	0.30	0.04	0.24	0.01	0.04	28.61	0.38	0.83	0.05	0.46	0.02	1.61	0.01	4.75	0.05
PB33-215.68	Dolostone	118.8	0.38	0.04	0.44	0.03	0.04	10.23	0.36	0.24	0.04	1.37	0.19	1.68	0.01	5.13	0.04
PB33-224.52	Dolostone	123.6	0.19	0.04	0.23	0.02	0.04	13.37	0.31	0.31	0.05	0.39	0.09	1.34	0.02	6.13	0.05
PB33-232.46	Dolostone	128.0	0.71	0.03	0.85	0.05	0.03	9.85	0.23	0.19	0.04	1.80	0.11	2.09	0.02	4.68	0.04
PB33-235.73	Dolostone	129.8	0.30	0.04	0.22	0.03	0.04	9.42	0.22	0.24	0.05	0.33	0.10	2.62	0.03	4.57	0.05
PB33-238.8	Dolostone	131.5	0.15	0.03	0.47	0.02	0.03	9.45	0.26	0.26	0.04	0.22	0.16	2.48	0.02	4.63	0.04

Appendix to Chapter 4

Sample name	Lithology	Strat-depth (m)	Cr	Mn	V	U	Th	Sr	Li	Ba	Hf	Sc	Co	Ni	Cu	Zn	Zr
PB35-22.48	Limestone	19.3	0.14	0.09	0.09	0.02	0.05	774.32	0.18	12.84	0.04	0.64	0.01	0.16	0.21	0.59	0.06
PB35-24.22	Limestone	20.8	0.45	0.09	0.41	0.02	0.05	211.89	0.14	1.85	0.02	0.88	0.02	0.18	0.02	0.51	0.03
PB35-26.06	Limestone	22.4	0.23	0.10	0.36	0.07	0.06	44.45	0.10	0.86	0.02	0.91	0.01	0.19	0.01	0.77	0.04
PB35-26.43	Limestone	22.7	0.24	0.07	0.39	0.06	0.04	33.96	0.07	0.53	0.02	1.21	0.01	0.09	0.01	0.53	0.02
PB35-27.57	Limestone	23.7	0.12	0.06	0.14	0.07	0.04	31.52	0.08	0.84	0.01	1.06	0.01	0.14	0.01	0.56	0.02
PB35-29.37	Limestone	25.3	0.10	0.10	0.08	0.10	0.05	38.31	0.10	0.44	0.02	1.40	0.02	0.33	0.02	0.33	0.03
PB35-31.20	Limestone	26.8	0.49	0.09	0.15	0.05	0.05	95.33	0.19	2.87	0.02	0.67	0.02	0.16	0.01	0.99	0.03
PB35-34.20	Limestone	29.4	0.19	0.09	0.20	0.10	0.05	44.33	0.18	0.54	0.02	0.63	0.01	0.08	0.04	1.28	0.03
PB35-36.84	Limestone	31.7	0.42	0.09	0.57	0.03	0.05	102.36	0.13	0.52	0.02	0.63	0.03	0.06	0.01	1.02	0.03
PB35-38.4	Limestone	33.1	0.14	0.07	0.09	0.03	0.04	91.33	0.09	1.07	0.02	0.53	0.01	0.13	0.02	1.02	0.02
PB35-39.70	Limestone	34.2	0.16	0.08	0.12	0.03	0.04	61.35	0.08	1.86	0.02	0.55	0.01	0.13	0.01	1.40	0.02
PB35-43.9	Dolostone	37.8	0.32	0.10	0.23	0.04	0.04	11.53	0.50	0.70	0.02	0.64	0.17	2.51	0.01	5.41	0.02
PB35-45.10	Dolostone	38.8	1.04	0.07	1.04	0.12	0.06	13.88	0.66	1.51	0.02	0.91	0.14	3.25	0.01	6.87	0.03
PB35-47.11	Dolostone	40.5	0.41	0.07	0.24	0.05	0.04	8.56	0.26	1.02	0.01	0.57	0.09	1.24	0.02	4.05	0.02
PB35-48.3	Limestone	41.5	0.61	0.10	0.34	0.03	0.05	195.18	0.10	1.02	0.02	0.70	0.09	0.11	0.02	2.79	0.03
PB35-49.44	Limestone	42.5	0.58	0.08	0.18	0.16	0.09	337.22	0.08	1.96	0.02	0.83	0.08	0.28	0.01	2.87	0.05
PB35-50.49	Limestone	43.4	2.27	0.07	0.71	0.11	0.56	15.75	0.67	16.59	0.01	1.81	0.41	0.89	0.16	1.63	0.03
PB35-52.88	Limestone	45.5	0.18	0.08	0.10	0.08	0.06	121.55	0.16	4.95	0.02	2.61	0.30	0.25	0.01	1.15	0.03
PB35-54.38	Limestone	46.8	0.31	0.10	0.74	0.05	0.05	157.99	0.11	3.58	0.02	0.71	0.04	0.09	0.02	2.27	0.03
PB35-55.57	Limestone	47.8	1.13	0.07	1.04	0.04	0.28	9.66	1.16	8.50	0.01	2.58	0.41	0.45	0.01	6.09	0.03
PB35-56.57	Dolostone	48.7	0.39	0.07	1.07	0.03	0.04	41.61	0.40	0.66	0.02	1.80	0.20	0.56	0.00	12.09	0.05
PB35-58.02	Dolostone	49.9	0.54	0.09	1.09	0.04	0.05	42.58	0.32	0.32	0.02	0.68	0.07	0.42	0.03	9.38	0.02
PB35-59.80	Dolostone	51.4	0.34	0.07	1.37	0.03	0.04	40.73	0.34	0.24	0.02	0.54	0.09	0.55	0.05	9.29	0.02
PB35-61.20	Dolostone	52.6	0.28	0.09	1.43	0.03	0.05	37.40	0.36	0.96	0.02	0.67	0.11	0.46	0.02	9.90	0.03
PB35-66.65	Limestone	59.1	0.17	0.07	0.33	0.02	0.04	150.60	0.07	1.82	0.02	0.54	0.02	0.02	0.03	1.05	0.02
PB35-69.68	Limestone	59.9	0.03	0.07	0.03	0.01	0.04	75.90	0.10	1.50	0.02	0.51	0.01	0.02	0.02	1.11	0.02
PB35-70.63	Limestone	60.8	0.09	0.07	0.12	0.02	0.04	85.17	0.07	1.46	0.02	0.52	0.02	0.03	0.03	1.28	0.02
PB35-73.52	Limestone	63.2	0.07	0.09	0.14	0.04	0.05	94.57	0.09	2.70	0.02	0.67	0.02	0.35	0.05	1.09	0.03
PB35-77.86	Limestone	67.0	0.11	0.09	0.26	0.16	0.05	22.90	0.09	0.33	0.02	0.62	0.02	0.08	0.06	0.12	0.02
PB35-79.6	Limestone	68.6	0.10	0.08	0.29	1.11	0.04	32.97	0.08	0.94	0.02	1.97	0.08	0.26	0.13	0.51	0.08
PB35-81.15	Limestone	68.8	3.01	0.09	1.11	0.05	0.25	85.85	0.22	3.36	0.02	19.65	0.91	2.49	0.01	8.67	0.07
PB35-83.7	Limestone	72.0	4.64	0.08	1.33	0.04	0.32	30.82	0.53	18.52	0.02	10.69	0.95	3.93	0.01	8.23	0.05
PB35-87.94	Dolostone	75.6	0.40	0.07	1.95	0.02	0.04	47.77	0.38	0.34	0.01	1.27	0.14	0.68	0.02	9.37	0.02
PB35-89.77	Dolostone	77.2	0.25	0.06	1.19	0.03	0.04	44.25	0.32	0.39	0.01	0.46	0.10	0.69	0.02	8.52	0.02
PB35-91.8	Dolostone	79.0	0.20	0.07	0.89	0.02	0.04	34.65	0.27	0.34	0.02	0.52	0.11	0.65	0.04	6.86	0.02
PB35-92.9	Dolostone	79.9	0.58	0.09	1.71	0.04	0.05	57.28	0.56	0.95	0.02	2.60	0.32	1.08	0.01	9.59	0.03
PB35-93.80	Dolostone	80.7	1.58	0.07	2.08	0.04	0.04	65.66	0.40	0.45	0.02	3.91	0.28	2.20	0.01	11.55	0.02
PB35-98.95	Dolostone	85.1	1.39	0.07	2.70	0.03	0.04	65.57	0.56	0.40	0.01	1.50	0.22	1.49	0.01	13.52	0.04
PB35-102.03	Dolostone	87.8	0.68	0.08	1.61	0.02	0.04	57.17	0.37	0.46	0.02	1.50	0.16	1.39	0.01	11.52	0.03
PB35-144.40	Limestone	124.2	0.11	0.07	0.07	0.03	0.04	28.86	0.07	1.49	0.01	0.47	0.03	0.06	0.04	0.94	0.02
PB35-146.2	Limestone	125.7	0.13	0.10	0.11	0.03	0.06	37.58	0.10	2.39	0.02	0.75	0.04	0.08	0.04	1.02	0.03
PB35-147.01	Limestone	126.4	0.14	0.09	0.09	0.04	0.05	37.57	0.09	3.24	0.02	0.64	0.04	0.14	0.03	0.94	0.03
PB35-149.77	Limestone	128.8	0.20	0.10	0.08	0.02	0.05	64.81	0.10	1.04	0.02	0.70	0.02	0.36	0.03	2.05	0.03
PB35-151.12	Limestone	130.0	0.04	0.07	0.04	0.02	0.04	153.02	0.07	1.20	0.02	0.52	0.21	0.08	0.07	1.72	0.02
PB35-153.50	Limestone	132.0	0.14	0.09	0.03	0.03	0.05	270.23	0.09	9.99	0.02	0.64	0.01	0.05	0.03	0.91	0.03
PB35-156.21	Limestone	134.4	0.19	0.08	0.10	0.01	0.05	57.17	0.08	4.52	0.02	0.61	0.01	0.05	0.02	0.67	0.03
PB35-157.76	Limestone	135.7	0.19	0.09	0.05	0.02	0.05	68.67	0.09	7.05	0.02	0.62	0.01	0.09	0.02	0.83	0.03
PB35-160.96	Limestone	138.4	0.09	0.09	0.11	0.03	0.05	76.91	0.09	3.90	0.02	0.62	0.01	0.11	0.03	0.71	0.03
PB35-162.4	Limestone	139.8	0.47	0.09	0.05	0.03	0.05	85.82	0.09	7.05	0.02	0.62	0.01	0.25	0.01	0.59	0.03
PB35-163.8	Limestone	140.9	0.27	0.09	0.09	0.03	0.05	176.88	0.09	5.85	0.02	0.63	0.02	0.10	0.05	1.49	0.03

Appendix to Chapter 4

Sample name	Lithology	Strat-depth (m)	Cr	Mo	V	U	Th	Sr	Li	Ba	Hf	Sc	Co	Ni	Cu	Zn	Zr
P835-168.42	Limestone	144.9	0.16	0.10	0.16	0.01	0.05	204.86	0.10	6.63	0.02	0.70	0.01	0.05	0.06	0.97	0.03
P835-171.14	Limestone	147.2	0.37	0.09	0.12	0.04	0.05	59.34	0.09	2.71	0.02	0.65	0.02	0.13	0.13	1.15	0.03
P835-173.2	Limestone	149.0	0.92	0.08	1.41	0.04	0.04	224.10	0.07	10.43	0.02	1.90	0.06	0.14	0.07	1.79	0.02
P835-176	Limestone	151.4	0.31	0.07	0.21	0.04	0.04	52.97	0.08	2.27	0.02	0.50	0.01	0.08	0.05	0.87	0.02
P835-177.6	Limestone	152.8	0.31	0.08	0.26	0.02	0.05	62.41	0.08	2.86	0.02	0.61	0.03	0.07	0.03	1.29	0.03
P835-178.9	Limestone	153.9	0.24	0.09	0.50	0.06	0.05	50.14	0.09	1.66	0.02	1.37	0.04	0.13	0.05	2.11	0.03
P835-180.9	Limestone	155.6	0.20	0.09	0.16	0.01	0.05	58.11	0.09	2.60	0.02	0.65	0.02	0.08	0.02	0.97	0.03
P835-182.05	Limestone	156.6	0.29	0.08	0.17	0.04	0.04	66.35	0.08	2.34	0.02	0.56	0.01	0.16	0.01	0.82	0.03
P835-184.14	Limestone	158.4	0.54	0.08	0.21	0.03	0.05	52.77	0.08	2.08	0.03	0.83	0.03	0.17	0.02	1.57	0.04
P835-184.26	Limestone	158.5	0.20	0.08	0.23	0.04	0.04	196.03	0.07	1.88	0.02	1.88	0.03	0.33	0.04	0.99	0.04
P835-185.16	Limestone	159.3	0.17	0.07	0.14	0.03	0.04	274.21	0.07	17.16	0.02	0.49	0.02	0.09	0.03	1.02	0.02
P835-185.88	Limestone	159.9	0.12	0.09	0.11	0.01	0.04	451.92	0.07	20.56	0.02	0.51	0.01	0.83	0.02	0.85	0.02
P835-187.30	Dolomite	161.1	0.36	0.07	0.36	0.05	0.05	45.84	0.13	6.79	0.02	0.72	0.13	0.03	0.01	11.28	0.03
P835-188.57	Dolomite	162.2	0.46	0.07	0.21	0.04	0.04	29.42	0.22	1.40	0.02	0.51	0.13	1.64	0.01	18.07	0.02
P835-189.2	Dolomite	162.7	0.75	0.07	0.18	0.04	0.04	29.62	0.20	1.63	0.01	0.48	0.15	2.43	0.01	20.43	0.02
P835-190.31	Dolomite	163.7	0.38	0.07	0.31	0.03	0.04	24.77	0.32	1.72	0.02	0.52	0.17	2.27	0.01	19.79	0.02
P835-191.8	Dolomite	165.0	0.32	0.08	0.16	0.03	0.04	34.03	0.20	1.26	0.02	0.58	0.12	1.89	0.03	16.71	0.03
P835-193.41	Dolomite	166.4	1.19	0.07	0.36	0.02	0.04	22.42	0.22	2.31	0.02	0.69	0.13	1.84	0.02	12.77	0.02
P835-195.4	Dolomite	168.1	0.81	0.08	0.37	0.02	0.04	29.11	0.22	2.75	0.03	1.33	0.17	1.64	0.02	9.52	0.04
P835-196.4	Dolomite	168.9	0.39	0.09	0.94	0.04	0.05	37.00	0.34	3.04	0.02	2.01	0.21	1.72	0.01	11.98	0.03
P835-198.6	Dolomite	170.8	1.52	0.07	0.19	0.04	0.04	27.14	0.23	1.42	0.01	0.56	0.12	1.16	0.01	8.01	0.02
P835-200.7	Dolomite	172.6	0.27	0.07	0.17	0.02	0.04	25.61	0.29	0.96	0.02	0.52	0.08	1.12	0.02	10.81	0.02
P835-202.4	Dolomite	174.1	0.42	0.07	0.08	0.02	0.04	32.88	0.19	1.50	0.01	0.48	0.06	0.66	0.01	6.96	0.02
P835-206	Dolomite	177.2	0.19	0.07	0.26	0.04	0.04	21.17	0.26	1.38	0.02	0.49	0.07	0.84	0.01	8.78	0.02
P835-206.8	Dolomite	177.9	0.44	0.08	0.25	0.05	0.04	32.77	0.28	1.01	0.02	2.62	0.07	0.54	0.02	6.80	0.03
P835-210	Dolomite	180.6	0.30	0.07	0.28	0.03	0.04	23.41	0.23	0.39	0.02	1.51	0.10	0.54	0.03	150.42	0.02
P835-211.5	Dolomite	181.9	0.15	0.08	0.26	0.05	0.04	42.30	0.18	3.92	0.02	1.13	0.11	0.80	0.02	107.30	0.03
P835-217.9	Limestone	187.4	0.30	0.08	0.35	0.03	0.04	238.90	0.11	4.68	0.02	0.58	0.06	1.11	0.02	106.22	0.02
P835-221.4	Limestone	190.4	0.44	0.08	0.10	0.03	0.05	116.37	0.09	9.66	0.02	0.60	0.06	0.32	0.14	100.69	0.03
P835-223.4	Limestone	192.2	0.18	0.07	0.09	0.01	0.04	69.98	0.07	5.47	0.02	0.51	0.04	0.10	0.10	88.85	0.02
P835-225.2	Limestone	193.7	1.23	0.06	0.13	0.01	0.04	175.82	0.06	3.85	0.01	0.47	0.07	0.31	0.23	81.00	0.02
P835-227.9	Limestone	196.0	0.56	0.07	0.16	0.03	0.04	131.40	0.07	3.04	0.01	0.82	0.04	0.10	0.01	85.52	0.02
P835-230.03	Limestone	197.9	0.39	0.06	0.19	0.02	0.04	162.17	0.06	4.53	0.01	0.75	0.05	0.09	0.02	100.44	0.02
P835-231.97	Dolomite	199.5	0.20	0.06	0.14	0.03	0.04	15.48	0.17	0.39	0.01	0.47	0.19	0.40	0.03	442.04	0.02
P835-235.3	Limestone	202.4	0.33	0.07	0.21	0.03	0.04	106.69	0.07	1.16	0.02	0.64	0.03	0.16	0.07	23.82	0.02
P835-237.5	Limestone	204.3	0.21	0.06	0.13	0.04	0.04	56.68	0.06	2.18	0.01	0.46	0.04	0.08	0.04	22.16	0.02
P835-239.4	Limestone	205.9	0.37	0.07	0.22	0.02	0.04	178.03	0.07	5.84	0.02	0.73	0.02	0.09	0.03	25.22	0.02
P835-241.6	Limestone	207.8	0.19	0.08	0.05	0.02	0.05	333.80	0.08	11.52	0.02	0.59	0.03	0.04	0.04	26.66	0.03
P835-243.5	Limestone	209.4	0.53	0.07	0.05	0.01	0.04	54.39	0.07	1.11	0.01	0.48	0.01	0.10	0.04	17.11	0.02
P835-245.6	Limestone	211.2	0.17	0.08	0.09	0.01	0.04	70.75	0.08	3.54	0.02	0.58	0.04	0.04	0.07	24.03	0.03
P835-246.1	Limestone	211.7	0.08	0.07	0.04	0.01	0.04	41.60	0.07	1.81	0.01	0.49	0.01	0.04	0.02	19.06	0.02
P835-246.7	Limestone	212.2	0.07	0.08	0.07	0.03	0.04	33.62	0.08	2.28	0.02	0.58	0.02	0.04	0.01	20.09	0.03
P835-247.9	Limestone	213.2	0.11	0.09	0.10	0.02	0.05	145.08	0.09	4.64	0.02	0.61	0.01	0.03	0.01	20.06	0.03
P835-248.4	Limestone	213.7	0.04	0.07	0.04	0.02	0.04	58.42	0.07	2.15	0.01	0.48	0.01	0.02	0.01	14.94	0.02
P835-250.8	Limestone	215.7	0.07	0.08	0.12	0.02	0.05	30.01	0.08	2.39	0.02	0.59	0.02	0.02	0.03	19.30	0.03
P835-251	Limestone	215.9	0.27	0.09	0.45	0.03	0.05	207.21	0.09	18.87	0.02	0.82	0.04	0.04	0.01	28.35	0.03
P835-251.12	Limestone	216.0	0.06	0.07	0.07	0.02	0.04	27.29	0.07	2.78	0.02	0.50	0.02	0.02	0.03	17.44	0.02
P835-252.30	Limestone	217.0	0.16	0.07	0.15	0.02	0.04	48.92	0.07	5.39	0.02	0.50	0.01	0.16	0.06	17.63	0.02
P835-253.38	Limestone	217.9	0.17	0.07	0.23	0.04	0.04	32.97	0.07	0.67	0.02	1.55	0.03	0.07	0.01	16.80	0.02
P835-254.38	Limestone	218.5	1.56	0.08	0.76	0.02	0.42	5.60	0.70	6.70	0.02	1.48	0.23	0.66	1.67	22.70	0.02

Appendix to Chapter 4

Sample name	Lithology	Strat-depth (m)	Cr	Mo	V	U	Th	Sr	Li	Ba	Hf	Sc	Co	Ni	Cu	Zn	Zr
17-GA1-01	Limestone	2.1	0.71	0.07	0.19	0.03	0.03	165.78	0.09	1.39	0.07	0.57	0.03	0.19	0.53	1.91	0.03
17-GA1-02	Limestone	2.07	0.94	0.09	0.22	0.03	0.04	188.30	0.11	1.10	0.09	0.76	0.02	0.45	0.30	1.40	0.03
17-GA1-03	Limestone	2.04	0.85	0.08	0.13	0.04	0.07	151.05	0.10	0.69	0.08	0.68	0.02	0.23	0.15	0.75	0.03
17-GA1-04	Limestone	1.98	2.48	0.10	0.18	0.03	0.02	90.94	0.12	0.68	0.10	0.77	0.08	0.45	0.69	1.65	0.03
17-GA1-05	Limestone	1.94	0.82	0.10	0.30	0.03	0.02	188.08	0.12	0.67	0.10	0.82	0.02	0.43	0.57	1.43	0.03
17-GA1-06	Limestone	1.9	0.03	0.09	0.15	0.02	0.02	0.12	0.11	0.12	0.09	0.72	0.01	0.02	0.01	0.18	0.03
17-GA1-07	Limestone	1.87	2.11	0.10	0.25	0.04	0.02	131.24	0.12	0.56	0.10	0.80	0.12	0.39	1.25	1.36	0.03
17-GA1-08	Limestone	1.81	0.67	0.09	0.19	0.03	0.02	208.00	0.12	1.00	0.09	0.77	0.02	0.20	0.27	1.18	0.03
17-GA1-09	Limestone	1.78	0.89	0.08	0.22	0.03	0.02	178.85	0.10	0.87	0.08	0.63	0.02	0.32	0.17	1.27	0.03
17-GA1-10	Limestone	1.73	0.46	0.08	0.41	0.04	0.01	155.83	0.10	0.78	0.08	0.66	0.02	0.27	0.31	1.47	0.05
17-GA1-11	Limestone	1.65	0.24	0.09	0.52	0.11	0.06	187.59	0.11	1.25	0.09	0.70	0.03	0.38	1.26	1.71	0.06
17-GA1-12	Limestone	1.6	0.17	0.10	0.69	0.11	0.04	237.90	0.12	1.71	0.10	0.81	0.05	0.26	2.71	2.22	0.04
17-GA1-13	Limestone	1.54	0.27	0.10	1.00	0.19	0.03	187.32	0.14	1.02	0.10	0.84	0.06	0.46	1.94	2.37	0.03
17-GA1-14	Limestone	1.46	0.09	0.08	0.58	0.12	0.02	228.82	0.10	150.01	0.08	0.69	0.05	0.22	0.84	1.46	0.03
17-GA1-15	Limestone	1.44	0.04	0.11	0.19	0.03	0.03	0.15	0.14	0.15	0.11	0.91	0.01	0.03	0.01	0.23	0.04
17-GA1-16	Limestone	1.4	0.10	0.11	0.91	0.14	0.02	216.46	0.13	4.94	0.11	0.89	0.03	0.32	1.16	1.15	0.04
17-GA1-17	Limestone	1.34	0.08	0.10	0.71	0.14	0.01	227.86	0.12	3.78	0.10	0.82	0.02	0.22	1.10	1.16	0.03
17-GA1-18	Limestone	1.28	0.20	0.10	1.12	0.13	0.02	162.12	0.13	1.54	0.10	0.83	0.05	0.17	2.00	0.89	0.03
17-GA1-15	Limestone	1.44	0.18	0.08	0.88	0.15	0.06	269.65	0.24	2.36	0.29	0.89	0.11	0.35	0.22	2.14	0.09
17-GA1-19	Limestone	1.21	0.21	0.08	0.95	0.11	0.06	189.06	0.25	1.73	0.30	1.12	0.03	0.29	1.77	1.49	0.09
17-GA1-20	Limestone	1.14	0.48	0.06	0.41	0.03	0.05	178.25	0.20	1.84	0.24	0.53	0.04	0.21	1.29	1.49	0.07
17-GA1-21	Limestone	1.09	0.29	0.07	0.23	0.04	0.06	188.05	0.23	1.60	0.28	0.63	0.05	0.17	1.59	3.98	0.08
17-GA1-22	Limestone	1.06	0.14	0.08	0.55	0.10	0.06	162.29	0.24	1.30	0.28	0.65	0.02	0.26	1.00	1.32	0.09
17-GA1-23	Limestone	1.03	0.53	0.09	1.89	0.10	0.07	57.14	0.57	1.94	0.33	0.75	0.24	1.12	0.30	5.92	0.10
17-GA1-24	Limestone	0.93	0.50	0.06	1.10	0.09	0.05	56.74	0.52	1.85	0.32	0.54	0.16	0.76	0.75	7.18	0.10
17-GA1-25	Limestone	0.89	0.34	0.09	0.58	0.13	0.07	124.33	0.29	1.38	0.34	0.78	0.09	0.54	0.69	2.67	0.10
17-GA1-26	Limestone	0.85	0.42	0.08	0.37	0.14	0.06	132.60	0.24	1.27	0.29	0.67	0.11	0.40	1.45	1.60	0.09
17-GA1-27	Limestone	0.82	2.43	0.07	0.62	0.05	0.05	50.13	0.37	1.98	0.25	0.57	0.34	1.67	7.73	7.35	0.07
17-GA1-28	Limestone	0.73	0.25	0.09	0.09	0.04	0.07	491.23	0.28	2.58	0.33	0.75	0.06	0.35	1.08	1.27	0.10
17-GA1-29	Limestone	0.69	0.33	0.06	0.04	0.03	0.05	436.03	0.20	2.46	0.55	1.62	0.02	0.19	1.00	1.22	0.09
17-GA1-30	Limestone	0.58	1.63	0.06	0.09	0.07	0.04	319.32	0.18	1.66	0.21	0.49	0.16	0.49	3.90	1.52	0.06
17-GA1-31	Limestone	0.53	0.14	0.09	0.05	0.04	0.07	712.27	0.43	4.34	0.34	0.76	0.03	0.44	1.45	1.90	0.10
17-GA1-32	Limestone	0.36	2.31	0.08	0.42	0.09	0.06	221.90	0.24	1.56	0.29	0.65	0.11	0.30	0.29	3.21	0.09
17-GA1-33	Limestone	0.3	0.45	0.07	0.21	0.08	0.05	314.03	0.23	7.27	0.28	0.63	0.03	0.31	0.38	1.35	0.08
17-GA1-34	Limestone	0.22	0.70	0.07	0.12	0.08	0.70	235.64	0.23	2.01	0.27	0.61	0.06	0.55	0.66	5.83	0.08
17-GA1-35	Limestone	0.11	1.31	0.08	1.38	0.11	0.17	105.64	0.68	4.38	0.51	1.98	1.40	1.98	0.07	17.74	0.09
17-GA1-36	Limestone	0.01	0.71	0.06	0.11	0.06	0.04	123.65	0.18	3.17	0.21	0.49	0.13	0.44	3.80	2.64	0.06

Appendix to Chapter 4

Appendix A.5. Carbonate leach REE concentrations (ppm) for the Red Lake samples

Sample name	Lithology	Strat-depth (m)	La	Ce	Pr	Nd	Sm	Eu	Gd	Tb	Dy	Y	Ho	Er	Tm	Yb	Lu
EBL28-397.73	Dolomite	133.7	0.15	0.20	0.02	0.08	0.01	0.02	0.02	0.00	0.03	0.32	0.01	0.02	0.00	0.01	0.00
EBL28-304	Dolomite	136.5	0.12	0.18	0.02	0.08	0.02	0.01	0.04	0.01	0.05	0.55	0.01	0.03	0.00	0.03	0.00
EBL28-305.9	Dolomite	137.4	0.05	0.06	0.01	0.02	0.00	0.00	0.01	0.01	0.01	0.09	0.00	0.01	0.01	0.00	0.01
EBL28-308.89	Dolomite	138.7	0.29	0.46	0.05	0.20	0.04	0.03	0.06	0.01	0.07	0.88	0.02	0.05	0.01	0.04	0.01
EBL28-311.35	Dolomite	139.8	0.21	0.32	0.03	0.13	0.02	0.01	0.02	0.00	0.02	0.35	0.00	0.01	0.00	0.01	0.00
EBL28-315.64	Dolomite	141.7	0.24	0.40	0.05	0.20	0.05	0.03	0.08	0.01	0.08	0.96	0.02	0.06	0.01	0.04	0.01
EBL28-318.36	Dolomite	143.0	0.34	0.51	0.05	0.20	0.03	0.02	0.04	0.01	0.02	0.38	0.01	0.02	0.00	0.01	0.00
EBL28-321.64	Dolomite	144.4	0.24	0.35	0.04	0.13	0.02	0.01	0.02	0.00	0.02	0.29	0.00	0.01	0.00	0.01	0.00
EBL28-322.95	Dolomite	145.0	0.37	0.56	0.06	0.21	0.03	0.03	0.04	0.01	0.03	0.43	0.01	0.02	0.00	0.01	0.00
EBL28-326.38	Dolomite	146.6	0.17	0.20	0.02	0.07	0.01	0.01	0.01	0.00	0.01	0.24	0.00	0.01	0.00	0.01	0.00
EBL28-330	Dolomite	148.2	0.50	0.75	0.08	0.33	0.07	0.05	0.10	0.03	0.10	1.17	0.02	0.07	0.01	0.05	0.01
EBL28-332.5	Dolomite	149.3	0.60	0.86	0.09	0.33	0.06	0.03	0.07	0.01	0.05	0.54	0.01	0.03	0.00	0.02	0.00
EBL28-344.15	Dolomite	154.5	0.33	0.53	0.06	0.22	0.04	0.03	0.05	0.01	0.05	0.57	0.01	0.03	0.00	0.03	0.00
EBL28-347.38	Dolomite	156.0	0.07	0.07	0.01	0.02	0.00	0.01	0.01	0.01	0.00	0.13	0.00	0.01	0.01	0.00	0.01
EBL28-351	Dolomite	157.6	0.30	0.51	0.06	0.24	0.05	0.03	0.07	0.01	0.08	0.92	0.02	0.06	0.01	0.05	0.01
EBL28-351.93	Dolomite	158.0	0.48	0.70	0.07	0.29	0.06	0.04	0.08	0.01	0.08	0.95	0.02	0.06	0.01	0.05	0.01
EBL28-357	Dolomite	160.3	0.27	0.38	0.04	0.14	0.03	0.02	0.03	0.01	0.03	0.41	0.01	0.02	0.00	0.02	0.00
EBL28-360.4	Dolomite	161.8	0.31	0.35	0.03	0.12	0.02	0.03	0.03	0.00	0.03	0.48	0.01	0.02	0.00	0.02	0.00
EBL28-362.40	Dolomite	162.7	0.31	0.47	0.05	0.20	0.04	0.03	0.05	0.01	0.05	0.74	0.01	0.03	0.00	0.03	0.00
EBL28-365.22	Dolomite	164.0	0.29	0.39	0.04	0.15	0.03	0.03	0.05	0.01	0.05	0.74	0.01	0.04	0.01	0.03	0.01
EBL28-368.09	Dolomite	165.3	0.20	0.24	0.02	0.09	0.02	0.02	0.03	0.00	0.03	0.40	0.01	0.02	0.00	0.02	0.00
EBL28-369.52	Dolomite	165.9	0.10	0.10	0.01	0.03	0.01	0.01	0.01	0.00	0.01	0.19	0.00	0.01	0.00	0.01	0.00
EBL28-373.40	Dolomite	167.7	0.14	0.15	0.01	0.05	0.01	0.01	0.02	0.00	0.02	0.35	0.00	0.01	0.00	0.01	0.00
EBL28-376.8	Dolomite	169.2	0.15	0.17	0.02	0.06	0.01	0.01	0.02	0.00	0.02	0.35	0.00	0.01	0.00	0.01	0.00
EBL28-378.10	Dolomite	169.8	0.21	0.29	0.03	0.11	0.02	0.02	0.02	0.00	0.02	0.36	0.01	0.02	0.00	0.01	0.00
EBL28-382.76	Dolomite	171.9	0.19	0.26	0.03	0.11	0.02	0.02	0.04	0.01	0.04	0.60	0.01	0.03	0.00	0.02	0.00
EBL28-387	Dolomite	173.8	0.35	0.47	0.05	0.18	0.03	0.03	0.04	0.01	0.04	0.62	0.01	0.03	0.00	0.02	0.00
EBL28-389.46	Dolomite	174.9	0.34	0.50	0.06	0.22	0.04	0.03	0.05	0.01	0.05	0.78	0.01	0.03	0.00	0.03	0.00
EBL28-395.56	Dolomite	177.6	0.16	0.19	0.02	0.06	0.01	0.00	0.01	0.00	0.01	0.36	0.00	0.01	0.00	0.01	0.00
EBL28-397.02	Dolomite	178.3	0.13	0.13	0.01	0.05	0.01	0.01	0.01	0.00	0.01	0.36	0.00	0.01	0.00	0.01	0.00
EBL28-400.3	Dolomite	179.7	0.10	0.13	0.01	0.05	0.01	0.01	0.02	0.00	0.02	0.30	0.00	0.01	0.00	0.01	0.00
EBL28-402.89	Dolomite	180.9	0.40	0.58	0.05	0.16	0.02	0.02	0.03	0.00	0.02	0.28	0.00	0.01	0.00	0.01	0.00
EBL28-408.29	Dolomite	183.3	0.12	0.14	0.01	0.05	0.01	0.01	0.02	0.00	0.02	0.24	0.00	0.01	0.00	0.01	0.00
EBL28-411.24	Dolomite	184.7	0.09	0.11	0.01	0.04	0.01	0.01	0.02	0.00	0.02	0.38	0.01	0.02	0.00	0.01	0.00
EBL28-416.30	Dolomite	186.9	0.16	0.19	0.02	0.07	0.01	0.01	0.02	0.00	0.02	0.47	0.01	0.02	0.00	0.01	0.00
EBL28-421.44	Dolomite	189.2	0.16	0.23	0.02	0.10	0.02	0.02	0.03	0.00	0.03	0.46	0.01	0.02	0.00	0.01	0.00
EBL28-426.25	Dolomite	191.4	0.18	0.24	0.02	0.10	0.02	0.02	0.04	0.01	0.04	0.59	0.01	0.03	0.00	0.02	0.00
EBL28-429.76	Dolomite	193.0	0.19	0.21	0.02	0.08	0.02	0.02	0.04	0.01	0.05	0.76	0.01	0.04	0.01	0.03	0.01
EBL28-433.56	Dolomite	194.7	0.19	0.25	0.03	0.10	0.02	0.02	0.03	0.01	0.03	0.53	0.01	0.02	0.00	0.02	0.00
EBL28-436.44	Dolomite	196.0	0.19	0.29	0.03	0.11	0.02	0.02	0.03	0.00	0.03	0.42	0.01	0.02	0.00	0.01	0.00
EBL28-443.28	Dolomite	199.0	0.46	0.72	0.08	0.30	0.05	0.03	0.08	0.01	0.07	1.30	0.02	0.05	0.01	0.04	0.01
EBL28-446.76	Dolomite	200.6	0.49	0.83	0.09	0.35	0.07	0.03	0.09	0.01	0.09	1.55	0.02	0.06	0.01	0.05	0.01
EBL28-451.93	Dolomite	202.9	0.41	0.53	0.05	0.21	0.03	0.02	0.05	0.01	0.04	0.89	0.01	0.03	0.00	0.02	0.00

Appendix to Chapter 4

Sample name	Lithology	Strat-depth (m)	La	Ce	Pr	Nd	Sm	Eu	Gd	Tb	Dy	Y	Ho	Er	Tm	Yb	Lu
P832-21.50	Dolomite	19.42	0.62	1.03	0.11	0.42	0.08	0.05	0.11	0.02	0.11	1.45	0.03	0.09	0.01	0.08	0.01
P832-24.25	Dolomite	21.91	0.27	0.38	0.04	0.13	0.02	0.02	0.03	0.00	0.02	0.34	0.00	0.01	0.00	0.01	0.00
P832-27.50	Dolomite	24.84	0.60	1.06	0.12	0.48	0.10	0.06	0.14	0.02	0.14	1.76	0.03	0.10	0.01	0.08	0.01
P832-29.24	Dolomite	26.41	0.56	1.03	0.12	0.49	0.11	0.06	0.15	0.03	0.15	1.70	0.04	0.11	0.02	0.09	0.02
P832-31.56	Dolomite	28.51	0.32	0.60	0.07	0.29	0.06	0.04	0.09	0.01	0.08	1.05	0.01	0.06	0.01	0.04	0.01
P832-34.62	Dolomite	31.27	0.33	0.61	0.07	0.31	0.07	0.05	0.11	0.02	0.11	1.50	0.03	0.08	0.01	0.07	0.01
P832-37.56	Dolomite	33.93	0.30	0.44	0.05	0.20	0.04	0.03	0.05	0.01	0.04	1.04	0.01	0.03	0.00	0.02	0.01
P832-39.11	Dolomite	35.33	0.33	0.52	0.06	0.25	0.05	0.04	0.08	0.01	0.07	1.04	0.02	0.05	0.01	0.04	0.01
P832-40.85	Dolomite	36.90	0.23	0.35	0.04	0.14	0.03	0.02	0.04	0.01	0.03	0.51	0.01	0.02	0.00	0.02	0.00
P832-43.70	Dolomite	39.48	0.32	0.52	0.06	0.23	0.05	0.04	0.07	0.01	0.06	0.82	0.01	0.04	0.01	0.03	0.00
P832-44.81	Dolomite	40.48	0.36	0.60	0.06	0.25	0.04	0.03	0.06	0.01	0.05	0.69	0.01	0.03	0.00	0.03	0.00
P832-48.88	Dolomite	44.16	0.29	0.49	0.05	0.21	0.04	0.02	0.04	0.01	0.03	0.50	0.01	0.02	0.00	0.01	0.00
P832-50.31	Dolomite	45.45	0.39	0.82	0.10	0.39	0.08	0.05	0.10	0.02	0.10	1.24	0.02	0.07	0.01	0.06	0.01
P832-56.08	Dolomite	50.66	0.57	1.05	0.11	0.44	0.08	0.04	0.10	0.01	0.07	0.94	0.01	0.04	0.01	0.03	0.00
P832-60.70	Dolomite	54.83	0.37	0.71	0.08	0.31	0.06	0.03	0.07	0.01	0.06	0.81	0.01	0.04	0.01	0.03	0.01
P832-62.29	Dolomite	56.27	0.60	1.19	0.14	0.54	0.11	0.06	0.14	0.02	0.14	2.08	0.03	0.10	0.01	0.08	0.02
P832-65.66	Dolomite	59.31	0.34	0.67	0.08	0.32	0.07	0.04	0.09	0.01	0.08	0.99	0.02	0.06	0.01	0.05	0.01
P832-67.93	Dolomite	61.36	0.25	0.47	0.06	0.24	0.06	0.04	0.09	0.01	0.09	1.22	0.02	0.07	0.01	0.06	0.01
P832-70.38	Dolomite	63.56	0.28	0.42	0.05	0.20	0.05	0.03	0.06	0.01	0.05	0.65	0.01	0.03	0.00	0.02	0.00
P832-71.89	Dolomite	64.94	0.24	0.39	0.04	0.17	0.04	0.02	0.04	0.01	0.04	0.56	0.01	0.03	0.00	0.02	0.00
P832-85.73	Dolomite	71.44	0.29	0.46	0.05	0.19	0.04	0.02	0.05	0.01	0.05	0.57	0.01	0.03	0.00	0.02	0.00
P832-88.23	Dolomite	79.70	0.36	0.63	0.07	0.31	0.07	0.05	0.11	0.02	0.13	1.55	0.03	0.10	0.02	0.09	0.02
P832-90.70	Dolomite	81.93	0.31	0.56	0.06	0.25	0.05	0.02	0.05	0.01	0.05	0.61	0.01	0.03	0.00	0.03	0.00
P832-92.2	Dolomite	83.29	0.30	0.44	0.05	0.17	0.03	0.02	0.04	0.01	0.03	0.48	0.01	0.02	0.00	0.02	0.00
P832-94.1	Dolomite	85.00	0.40	0.62	0.07	0.26	0.05	0.02	0.06	0.01	0.05	0.72	0.01	0.03	0.00	0.03	0.00
P832-96.88	Dolomite	87.52	0.34	0.58	0.06	0.25	0.05	0.02	0.06	0.01	0.04	0.54	0.01	0.03	0.00	0.02	0.00
P832-98.57	Dolomite	89.04	0.45	0.80	0.09	0.41	0.09	0.05	0.12	0.02	0.11	1.30	0.03	0.07	0.01	0.06	0.01
P832-100.4	Dolomite	90.70	0.30	0.59	0.07	0.29	0.07	0.03	0.08	0.01	0.07	0.85	0.02	0.05	0.01	0.04	0.01
P832-102.13	Dolomite	92.26	0.35	0.64	0.07	0.29	0.06	0.04	0.07	0.01	0.06	0.82	0.01	0.04	0.01	0.03	0.01
P832-104.85	Dolomite	94.72	0.32	0.57	0.07	0.27	0.05	0.03	0.07	0.01	0.07	0.98	0.02	0.05	0.01	0.05	0.01
P832-108.35	Dolomite	97.88	0.38	0.70	0.08	0.34	0.08	0.04	0.11	0.02	0.13	1.45	0.03	0.09	0.01	0.07	0.01
P832-112.63	Dolomite	101.74	0.45	0.87	0.10	0.42	0.10	0.06	0.14	0.02	0.14	1.69	0.03	0.10	0.01	0.09	0.02
P832-114.1	Dolomite	103.07	0.36	0.72	0.08	0.35	0.08	0.04	0.10	0.02	0.10	1.09	0.02	0.07	0.01	0.05	0.01
P832-116.89	Dolomite	105.59	0.31	0.54	0.06	0.24	0.05	0.03	0.06	0.01	0.06	0.83	0.01	0.04	0.01	0.03	0.01
P832-118.9	Dolomite	107.41	0.48	0.87	0.10	0.41	0.09	0.05	0.12	0.02	0.13	2.32	0.03	0.11	0.02	0.09	0.02
P832-121.10	Dolomite	109.39	0.53	0.99	0.11	0.42	0.08	0.04	0.10	0.01	0.08	1.12	0.02	0.05	0.01	0.04	0.01
P832-123.2	Dolomite	111.29	0.07	0.13	0.02	0.06	0.02	0.01	0.02	0.00	0.03	0.35	0.01	0.02	0.00	0.02	0.00
P832-124.93	Dolomite	112.85	0.35	0.54	0.06	0.23	0.04	0.02	0.05	0.01	0.04	0.67	0.01	0.03	0.00	0.02	0.00
P832-128.48	Dolomite	116.06	0.30	0.57	0.06	0.24	0.05	0.02	0.06	0.01	0.06	0.76	0.01	0.04	0.01	0.03	0.01
P832-138.7	Dolomite	125.29	0.35	0.63	0.07	0.26	0.05	0.02	0.06	0.01	0.05	0.71	0.01	0.04	0.01	0.03	0.01
P832-139.87	Dolomite	126.35	1.32	2.50	0.26	0.92	0.15	0.06	0.17	0.02	0.15	1.60	0.03	0.11	0.02	0.10	0.02
P832-143.3	Dolomite	129.45	0.30	0.51	0.05	0.20	0.04	0.02	0.04	0.01	0.04	0.45	0.01	0.03	0.00	0.02	0.00

Appendix to Chapter 4

Sample name	Lithology	Strat-depth (m)	La	Ce	Pr	Nd	Sm	Eu	Gd	Tb	Dy	Y	Ho	Er	Tm	Yb	Lu
PB32-146.16	Dolomite	132.03	0.32	0.44	0.05	0.18	0.03	0.02	0.04	0.01	0.04	0.86	0.01	0.04	0.01	0.03	0.01
PB32-148.92	Dolomite	134.53	0.50	0.85	0.10	0.41	0.09	0.06	0.15	0.03	0.17	2.48	0.05	0.14	0.02	0.12	0.02
PB32-150.8	Dolomite	136.22	0.24	0.43	0.05	0.19	0.04	0.03	0.06	0.01	0.05	0.61	0.01	0.03	0.00	0.02	0.00
PB32-153.13	Dolomite	143.75	0.19	0.22	0.02	0.09	0.01	0.01	0.02	0.00	0.02	0.45	0.01	0.02	0.00	0.01	0.00
PB32-165	Dolomite	149.05	0.10	0.15	0.02	0.06	0.01	0.01	0.01	0.00	0.01	0.18	0.00	0.01	0.01	0.00	0.01
PB32-167.5	Dolomite	151.31	0.19	0.27	0.03	0.11	0.02	0.01	0.02	0.00	0.02	0.39	0.00	0.02	0.00	0.01	0.00
PB32-171.2	Dolomite	154.65	0.32	0.56	0.06	0.26	0.05	0.03	0.07	0.01	0.07	0.90	0.00	0.06	0.01	0.05	0.01
PB32-172.93	Dolomite	156.21	0.21	0.32	0.03	0.12	0.02	0.01	0.03	0.00	0.02	0.38	0.01	0.00	0.00	0.01	0.00
PB32-183.38	Dolomite	165.65	1.91	2.28	0.20	0.70	0.10	0.04	0.13	0.02	0.09	1.14	0.02	0.07	0.01	0.06	0.01
PB32-189.02	Dolomite	170.75	0.14	0.23	0.02	0.09	0.02	0.01	0.02	0.00	0.02	0.26	0.00	0.01	0.00	0.01	0.00
PB32-190.25	Dolomite	171.86	0.28	0.42	0.05	0.18	0.03	0.02	0.04	0.01	0.04	0.85	0.01	0.04	0.01	0.03	0.01
PB32-194.05	Dolomite	175.29	0.41	0.66	0.07	0.30	0.06	0.04	0.08	0.01	0.09	1.19	0.02	0.07	0.01	0.06	0.01
PB32-195.5	Dolomite	176.60	0.32	0.49	0.05	0.20	0.04	0.02	0.05	0.01	0.04	0.68	0.01	0.03	0.00	0.02	0.00
PB32-197.35	Dolomite	178.27	0.40	0.69	0.08	0.33	0.07	0.04	0.10	0.02	0.10	1.42	0.03	0.08	0.01	0.07	0.01
PB32-199.28	Dolomite	180.02	0.27	0.39	0.04	0.16	0.03	0.02	0.04	0.01	0.03	0.54	0.01	0.02	0.00	0.02	0.00
PB32-201.92	Dolomite	182.40	0.27	0.43	0.05	0.18	0.03	0.02	0.04	0.01	0.04	0.53	0.00	0.03	0.00	0.02	0.00
PB32-203.5	Dolomite	183.83	0.18	0.25	0.03	0.10	0.02	0.01	0.02	0.00	0.02	0.33	0.00	0.01	0.00	0.01	0.00
PB32-205.25	Dolomite	185.41	0.29	0.45	0.05	0.19	0.04	0.02	0.05	0.01	0.04	0.62	0.01	0.03	0.00	0.02	0.00
PB32-208.58	Dolomite	188.42	0.22	0.32	0.03	0.14	0.02	0.02	0.04	0.01	0.03	0.52	0.01	0.02	0.00	0.02	0.00
PB32-210.2	Dolomite	189.88	0.56	0.82	0.11	0.45	0.10	0.06	0.15	0.03	0.17	2.38	0.04	0.14	0.02	0.12	0.02
PB32-212.08	Dolomite	191.58	0.42	0.65	0.07	0.28	0.05	0.04	0.07	0.01	0.06	0.93	0.02	0.05	0.01	0.03	0.01
PB32-292.37	Dolomite	264.11	0.24	0.30	0.03	0.11	0.02	0.01	0.02	0.00	0.02	0.41	0.01	0.02	0.00	0.01	0.00
PB32-295.80	Dolomite	267.21	0.11	0.13	0.01	0.05	0.01	0.01	0.02	0.00	0.02	0.42	0.01	0.02	0.00	0.01	0.00

Sample name	Lithology	Strat-depth (m)	La	Ce	Pr	Nd	Sm	Eu	Gd	Tb	Dy	Y	Ho	Er	Tm	Yb	Lu
PB33-108.27	Dolomite	59.6	0.66	1.06	0.12	0.47	0.08	0.04	0.10	0.01	0.08	1.14	0.02	0.05	0.01	0.04	0.01
PB33-112	Dolomite	61.7	0.41	0.49	0.05	0.16	0.03	0.02	0.03	0.00	0.02	0.46	0.01	0.02	0.00	0.01	0.00
PB33-116.73	Dolomite	64.3	0.20	0.27	0.03	0.11	0.02	0.01	0.03	0.00	0.02	0.39	0.01	0.02	0.00	0.01	0.00
PB33-123.58	Dolomite	68.1	0.49	0.58	0.06	0.21	0.03	0.02	0.05	0.01	0.03	0.59	0.01	0.02	0.00	0.02	0.00
PB33-129.05	Dolomite	71.1	0.31	0.38	0.04	0.14	0.02	0.02	0.03	0.00	0.02	0.35	0.01	0.02	0.00	0.01	0.00
PB33-134.62	Dolomite	74.2	0.62	0.90	0.10	0.38	0.07	0.04	0.09	0.01	0.08	1.12	0.02	0.06	0.01	0.04	0.01
PB33-138.35	Dolomite	76.2	0.39	0.51	0.05	0.19	0.03	0.03	0.05	0.01	0.05	0.74	0.01	0.04	0.00	0.03	0.00
PB33-145.63	Dolomite	80.2	0.58	0.85	0.09	0.31	0.05	0.03	0.07	0.01	0.05	0.80	0.01	0.04	0.01	0.03	0.01
PB33-157.17	Dolomite	86.5	0.40	0.66	0.07	0.28	0.05	0.02	0.06	0.01	0.05	0.67	0.01	0.03	0.00	0.02	0.00
PB33-163.13	Dolomite	89.8	0.27	0.48	0.05	0.20	0.04	0.02	0.04	0.01	0.03	0.44	0.01	0.02	0.00	0.02	0.00
PB33-215.68	Dolomite	118.8	0.68	1.37	0.16	0.63	0.11	0.05	0.13	0.02	0.10	1.51	0.02	0.07	0.01	0.06	0.01
PB33-224.52	Dolomite	123.6	0.42	0.76	0.09	0.35	0.06	0.03	0.07	0.01	0.04	0.70	0.01	0.03	0.00	0.02	0.00
PB33-232.46	Dolomite	138.0	0.19	0.32	0.03	0.13	0.02	0.01	0.03	0.00	0.02	0.38	0.01	0.02	0.00	0.01	0.00
PB33-235.73	Dolomite	129.8	0.16	0.20	0.02	0.08	0.02	0.01	0.03	0.00	0.03	0.40	0.01	0.02	0.00	0.01	0.00
PB33-238.8	Dolomite	131.5	0.23	0.41	0.05	0.18	0.04	0.02	0.05	0.01	0.05	0.52	0.01	0.03	0.00	0.02	0.00

Appendix to Chapter 4

Sample name	Lithology	Strat depth (m)	La	Ce	Pr	Nd	Sm	Eu	Gd	Tb	Dy	Y	Ho	Er	Tm	Yb	Lu
PB35-22.48	Limestone	19.3	0.13	0.08	0.01	0.03	0.01	0.01	0.01	0.00	0.01	0.50	0.00	0.01	0.00	0.01	0.00
PB35-24.22	Limestone	20.8	1.17	1.03	0.13	0.52	0.09	0.06	0.14	0.02	0.12	4.17	0.04	0.12	0.02	0.02	0.02
PB35-26.06	Limestone	22.4	1.00	1.27	0.14	0.55	0.10	0.08	0.15	0.03	0.16	3.06	0.04	0.13	0.02	0.11	0.02
PB35-26.43	Limestone	22.7	0.94	1.25	0.13	0.51	0.10	0.08	0.15	0.03	0.16	2.96	0.04	0.13	0.02	0.11	0.02
PB35-27.57	Limestone	23.7	1.07	1.61	0.18	0.68	0.14	0.12	0.19	0.03	0.17	3.21	0.04	0.12	0.02	0.10	0.02
PB35-29.37	Limestone	25.3	1.40	2.40	0.29	1.23	0.25	0.20	0.31	0.04	0.24	3.27	0.05	0.14	0.02	0.09	0.02
PB35-31.20	Limestone	26.8	1.69	2.22	0.23	0.84	0.14	0.18	0.17	0.02	0.12	2.02	0.03	0.07	0.01	0.05	0.01
PB35-34.20	Limestone	29.4	0.73	0.89	0.09	0.34	0.06	0.05	0.09	0.02	0.10	1.99	0.03	0.09	0.01	0.08	0.01
PB35-36.84	Limestone	31.7	0.45	0.52	0.05	0.15	0.02	0.06	0.03	0.00	0.02	0.58	0.01	0.02	0.00	0.02	0.00
PB35-38.4	Limestone	33.1	0.29	0.24	0.02	0.06	0.01	0.01	0.02	0.00	0.02	0.71	0.01	0.03	0.00	0.02	0.00
PB35-39.70	Limestone	34.2	0.13	0.14	0.02	0.07	0.01	0.01	0.03	0.00	0.03	0.68	0.01	0.02	0.00	0.02	0.00
PB35-43.9	Dolomite	37.8	0.28	0.41	0.04	0.17	0.03	0.02	0.05	0.01	0.05	0.69	0.01	0.04	0.01	0.03	0.01
PB35-45.10	Dolomite	38.8	0.59	0.79	0.08	0.32	0.06	0.04	0.09	0.01	0.09	1.27	0.02	0.07	0.01	0.06	0.01
PB35-47.11	Dolomite	40.5	0.24	0.32	0.03	0.13	0.02	0.02	0.04	0.01	0.05	0.61	0.01	0.03	0.00	0.03	0.01
PB35-48.3	Limestone	41.5	0.77	0.74	0.07	0.23	0.04	0.07	0.05	0.01	0.04	1.59	0.01	0.05	0.01	0.04	0.01
PB35-49.44	Limestone	42.5	2.21	3.18	0.35	1.36	0.16	0.16	0.40	0.06	0.41	6.51	0.10	0.33	0.05	0.28	0.05
PB35-50.49	Limestone	43.4	10.02	18.24	1.92	6.49	0.77	1.19	2.70	0.70	0.20	1.28	0.04	0.10	0.01	0.09	0.01
PB35-52.88	Limestone	45.5	0.61	0.81	0.08	0.32	0.06	0.04	0.09	0.01	0.08	1.47	0.02	0.06	0.01	0.06	0.01
PB35-54.38	Limestone	46.8	1.11	1.33	0.13	0.46	0.07	0.08	0.10	0.01	0.07	1.06	0.01	0.04	0.01	0.03	0.01
PB35-55.57	Limestone	47.8	3.45	6.45	0.72	2.63	0.41	0.08	0.43	0.06	0.27	1.75	0.05	0.14	0.02	0.11	0.02
PB35-56.57	Dolomite	48.7	0.80	1.50	0.17	0.67	0.12	0.05	0.14	0.02	0.10	0.93	0.02	0.06	0.01	0.04	0.01
PB35-58.02	Dolomite	49.9	0.31	0.45	0.05	0.18	0.03	0.02	0.04	0.01	0.03	0.48	0.01	0.02	0.00	0.01	0.00
PB35-59.80	Dolomite	51.4	0.18	0.24	0.02	0.08	0.01	0.01	0.02	0.00	0.01	0.27	0.00	0.01	0.00	0.01	0.00
PB35-61.20	Dolomite	52.6	0.50	0.77	0.08	0.28	0.04	0.03	0.06	0.01	0.04	0.67	0.01	0.03	0.00	0.02	0.00
PB35-68.65	Limestone	59.1	0.14	0.19	0.02	0.09	0.02	0.01	0.02	0.00	0.02	0.42	0.00	0.01	0.00	0.01	0.00
PB35-69.68	Limestone	59.9	0.18	0.17	0.02	0.06	0.01	0.01	0.02	0.00	0.01	0.45	0.00	0.01	0.00	0.01	0.00
PB35-70.63	Limestone	60.8	0.05	0.05	0.00	0.02	0.00	0.00	0.01	0.00	0.01	0.37	0.00	0.01	0.00	0.01	0.00
PB35-73.52	Limestone	63.2	1.87	3.14	0.32	1.04	0.17	0.05	0.20	0.02	0.09	1.00	0.02	0.04	0.00	0.02	0.00
PB35-77.86	Limestone	67.0	16.09	30.70	3.34	13.74	2.22	0.53	2.09	0.20	0.67	4.34	0.12	0.28	0.04	0.26	0.05
PB35-79.6	Limestone	68.6	12.74	23.26	2.35	8.95	1.39	0.41	1.62	0.18	0.74	6.82	0.15	0.36	0.04	0.23	0.04
PB35-81.15	Limestone	69.8	1.99	3.78	0.45	1.73	0.33	0.14	0.35	0.05	0.23	1.55	0.04	0.11	0.01	0.08	0.01
PB35-83.7	Limestone	72.0	3.50	7.35	0.82	2.76	0.36	0.09	0.36	0.04	0.19	1.20	0.04	0.04	0.01	0.09	0.01
PB35-87.94	Dolomite	75.6	0.51	0.98	0.11	0.42	0.08	0.04	0.09	0.01	0.06	0.70	0.01	0.04	0.01	0.03	0.01
PB35-89.77	Dolomite	77.2	0.26	0.45	0.05	0.17	0.03	0.02	0.03	0.00	0.02	0.33	0.00	0.01	0.00	0.01	0.00
PB35-91.8	Dolomite	79.0	0.36	0.67	0.07	0.26	0.04	0.02	0.05	0.01	0.02	0.25	0.00	0.01	0.00	0.01	0.00
PB35-92.9	Dolomite	79.9	0.77	1.49	0.16	0.59	0.10	0.05	0.12	0.02	0.09	1.00	0.02	0.06	0.01	0.05	0.01
PB35-93.80	Dolomite	80.7	0.75	1.66	0.21	0.82	0.17	0.08	0.19	0.03	0.14	1.39	0.03	0.08	0.01	0.06	0.01
PB35-98.95	Dolomite	85.1	0.70	1.33	0.15	0.57	0.10	0.06	0.11	0.01	0.08	0.83	0.02	0.05	0.01	0.04	0.01
PB35-102.03	Dolomite	87.8	0.76	1.46	0.17	0.61	0.11	0.06	0.12	0.02	0.08	0.74	0.02	0.04	0.01	0.03	0.00
PB35-144.40	Limestone	124.2	0.03	0.03	0.00	0.02	0.00	0.00	0.01	0.00	0.01	0.14	0.00	0.00	0.00	0.00	0.00
PB35-146.2	Limestone	125.7	0.12	0.14	0.01	0.05	0.01	0.01	0.01	0.00	0.01	0.33	0.00	0.01	0.00	0.01	0.00
PB35-147.01	Limestone	126.4	0.06	0.05	0.01	0.02	0.00	0.00	0.01	0.00	0.01	0.30	0.00	0.01	0.00	0.01	0.00
PB35-149.77	Limestone	128.8	1.01	1.33	0.10	0.26	0.02	0.02	0.03	0.00	0.01	0.29	0.00	0.01	0.00	0.01	0.00
PB35-151.12	Limestone	130.0	0.59	0.92	0.10	0.34	0.05	0.08	0.07	0.01	0.05	0.50	0.01	0.02	0.00	0.01	0.00
PB35-153.50	Limestone	132.0	0.10	0.07	0.01	0.02	0.00	0.01	0.01	0.00	0.01	0.32	0.00	0.01	0.00	0.01	0.00
PB35-156.21	Limestone	134.4	0.10	0.12	0.01	0.05	0.01	0.01	0.02	0.00	0.01	0.36	0.00	0.01	0.00	0.01	0.00
PB35-157.76	Limestone	135.7	0.08	0.08	0.01	0.04	0.01	0.01	0.01	0.00	0.01	0.40	0.00	0.01	0.00	0.01	0.00
PB35-160.96	Limestone	138.4	0.11	0.08	0.01	0.03	0.01	0.00	0.01	0.00	0.01	0.62	0.00	0.02	0.00	0.01	0.00
PB35-162.4	Limestone	139.8	0.10	0.12	0.01	0.06	0.01	0.01	0.02	0.00	0.01	0.59	0.01	0.02	0.00	0.02	0.00
PB35-163.8	Limestone	140.9	0.18	0.16	0.02	0.06	0.01	0.01	0.02	0.00	0.02	0.67	0.01	0.02	0.00	0.01	0.00

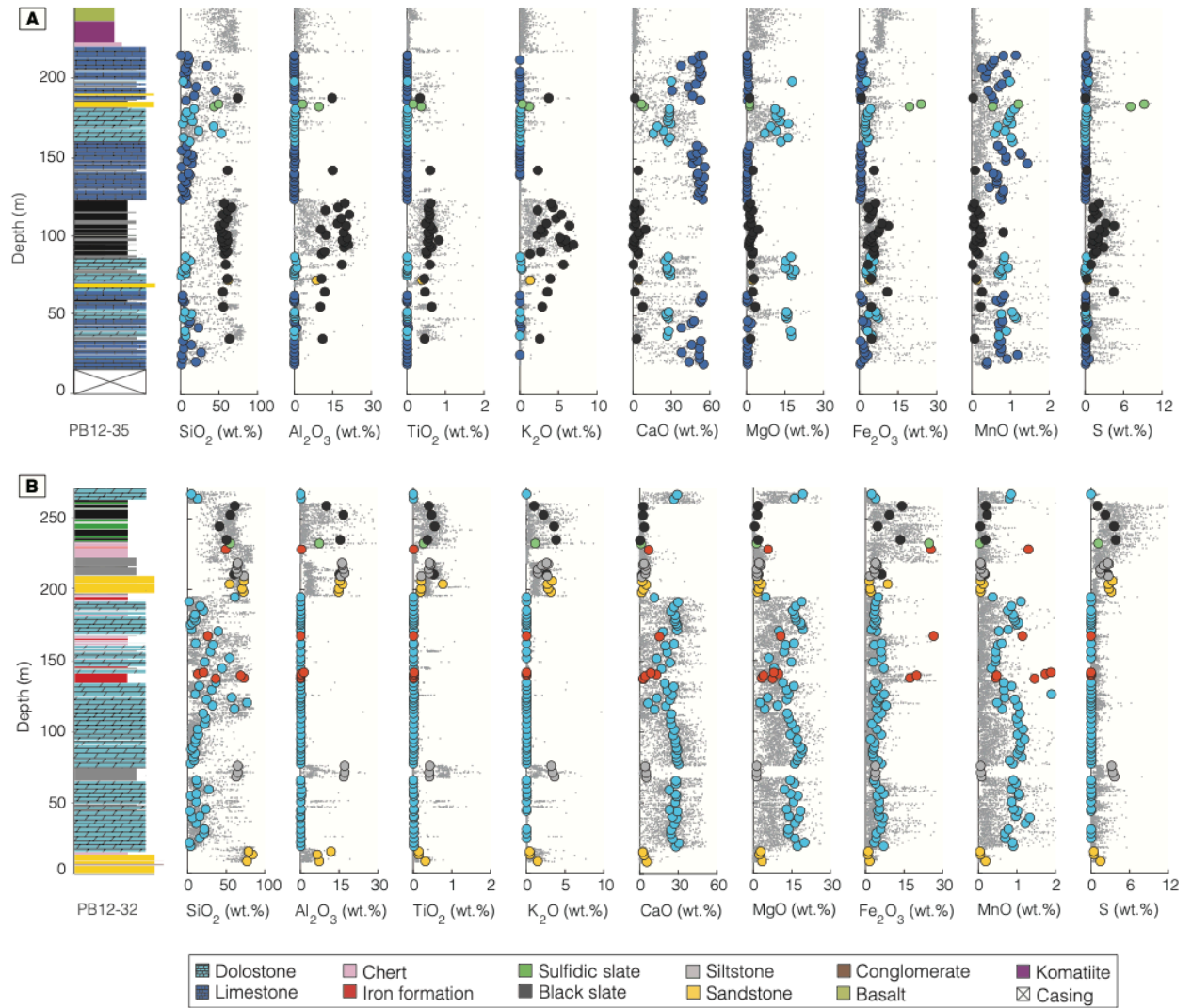
Appendix to Chapter 4

Sample name	Lithology	Strat-depth (m)	La	Ca	Pr	Nd	Sm	Eu	Gd	Tb	Dy	Y	Ho	Er	Tm	Yb	Lu
PB85-168.42	Limestone	144.9	0.10	0.09	0.01	0.04	0.01	0.00	0.01	0.00	0.01	0.31	0.00	0.01	0.00	0.01	0.00
PB85-171.14	Limestone	147.2	0.36	0.40	0.04	0.13	0.02	0.02	0.03	0.00	0.02	0.65	0.01	0.02	0.00	0.01	0.00
PB85-173.2	Limestone	149.0	1.07	1.64	0.18	0.64	1.07	0.14	0.12	0.02	0.08	1.15	0.02	0.05	0.01	0.04	0.01
PB85-176	Limestone	151.4	0.23	0.29	0.03	0.12	0.03	0.01	0.04	0.01	0.04	0.90	0.01	0.04	0.01	0.03	0.01
PB85-177.6	Limestone	152.8	0.69	0.62	0.08	0.28	0.05	0.07	0.06	0.01	0.04	0.61	0.01	0.03	0.00	0.02	0.00
PB85-178.9	Limestone	153.9	0.07	1.01	0.12	0.49	0.11	0.05	0.06	0.03	0.19	2.65	0.05	0.15	0.02	0.13	0.00
PB85-180.9	Limestone	155.6	0.15	0.15	0.01	0.06	0.01	0.01	0.02	0.00	0.02	0.67	0.01	0.02	0.00	0.02	0.00
PB85-182.05	Limestone	156.6	0.57	0.71	0.07	0.29	0.05	0.03	0.08	0.01	0.07	1.26	0.02	0.06	0.01	0.05	0.01
PB85-184.14	Limestone	158.4	0.38	0.45	0.05	0.18	0.03	0.02	0.05	0.01	0.06	1.19	0.02	0.05	0.01	0.05	0.01
PB85-184.26	Limestone	158.5	0.85	0.56	0.09	0.39	0.08	0.04	0.16	0.03	0.21	9.02	0.07	0.24	0.03	0.20	0.04
PB85-185.16	Limestone	159.3	0.10	0.11	0.01	0.04	0.01	0.01	0.01	0.00	0.01	0.25	0.00	0.01	0.00	0.01	0.00
PB85-185.88	Limestone	159.9	0.07	0.05	0.01	0.02	0.00	0.01	0.01	0.00	0.01	0.35	0.00	0.01	0.00	0.01	0.00
PB85-187.30	Dolomite	161.1	0.51	0.76	0.08	0.32	0.06	0.03	0.08	0.01	0.07	0.93	0.02	0.05	0.01	0.04	0.01
PB85-188.57	Dolomite	162.2	0.59	0.92	0.10	0.36	0.06	0.03	0.08	0.01	0.06	0.75	0.01	0.04	0.01	0.03	0.01
PB85-189.2	Dolomite	162.7	0.26	0.31	0.03	0.12	0.02	0.02	0.03	0.01	0.03	0.54	0.01	0.02	0.00	0.02	0.00
PB85-190.31	Dolomite	163.7	0.40	0.57	0.06	0.21	0.04	0.02	0.04	0.01	0.03	0.52	0.01	0.02	0.00	0.02	0.00
PB85-191.8	Dolomite	165.0	0.45	0.55	0.05	0.18	0.03	0.02	0.04	0.00	0.03	0.63	0.01	0.02	0.00	0.02	0.00
PB85-195.41	Dolomite	166.4	0.82	1.40	0.15	0.57	0.10	0.04	0.12	0.02	0.10	1.09	0.02	0.06	0.01	0.05	0.01
PB85-195.4	Dolomite	168.1	2.69	4.44	0.48	1.72	0.27	0.08	0.28	0.04	0.18	1.44	0.04	0.10	0.01	0.07	0.01
PB85-196.4	Dolomite	168.9	2.36	4.31	0.47	1.69	0.25	0.03	0.25	0.03	0.15	1.29	0.03	0.08	0.01	0.06	0.01
PB85-198.6	Dolomite	170.8	1.15	1.86	0.20	0.73	0.13	0.04	0.15	0.02	0.12	1.28	0.03	0.08	0.01	0.07	0.01
PB85-200.7	Dolomite	172.6	1.12	1.79	0.19	0.69	0.12	0.03	0.12	0.02	0.08	0.78	0.02	0.04	0.01	0.03	0.01
PB85-202.4	Dolomite	174.1	0.93	1.21	0.12	0.42	0.07	0.03	0.08	0.01	0.06	0.80	0.01	0.04	0.01	0.03	0.01
PB85-206	Dolomite	177.2	1.09	1.69	0.18	0.63	0.09	0.04	0.10	0.01	0.06	0.73	0.01	0.04	0.01	0.03	0.01
PB85-206.8	Dolomite	177.9	1.69	2.50	0.26	0.90	0.12	0.06	0.15	0.02	0.11	1.49	0.03	0.09	0.01	0.08	0.02
PB85-210	Dolomite	180.6	0.85	1.12	0.11	0.38	0.05	0.02	0.06	0.01	0.04	0.63	0.01	0.03	0.01	0.03	0.01
PB85-211.5	Dolomite	181.9	1.56	2.42	0.27	1.02	0.20	0.10	0.26	0.04	0.23	2.67	0.05	0.15	0.02	0.12	0.02
PB85-217.9	Limestone	187.4	0.15	0.18	0.02	0.08	0.02	0.01	0.02	0.00	0.02	0.46	0.01	0.02	0.00	0.01	0.00
PB85-221.4	Limestone	190.4	0.20	0.15	0.01	0.06	0.01	0.01	0.02	0.00	0.02	0.81	0.01	0.02	0.00	0.02	0.00
PB85-223.4	Limestone	192.4	0.03	0.02	0.00	0.01	0.00	0.00	0.00	0.00	0.00	0.11	0.00	0.00	0.00	0.01	0.00
PB85-225.2	Limestone	193.7	1.34	2.07	0.21	0.66	0.06	0.01	0.06	0.00	0.01	0.34	0.00	0.01	0.00	0.01	0.00
PB85-227.9	Limestone	196.0	0.68	0.97	0.10	0.40	0.08	0.05	0.11	0.02	0.11	1.46	0.03	0.08	0.01	0.06	0.01
PB85-230.03	Limestone	197.9	0.21	0.31	0.03	0.13	0.02	0.01	0.03	0.00	0.03	0.36	0.01	0.02	0.00	0.01	0.00
PB85-231.97	Dolomite	199.5	0.16	0.24	0.02	0.09	0.02	0.01	0.02	0.00	0.02	0.24	0.01	0.02	0.00	0.02	0.00
PB85-235.3	Limestone	202.4	0.55	0.61	0.06	0.24	0.04	0.02	0.06	0.01	0.05	1.19	0.01	0.05	0.01	0.04	0.01
PB85-237.5	Limestone	204.3	0.48	0.63	0.06	0.24	0.04	0.02	0.06	0.01	0.05	0.80	0.01	0.04	0.01	0.03	0.01
PB85-239.4	Limestone	205.9	0.21	0.28	0.03	0.12	0.02	0.01	0.04	0.01	0.04	0.55	0.01	0.03	0.00	0.02	0.00
PB85-241.6	Limestone	207.8	0.08	0.08	0.01	0.03	0.01	0.01	0.01	0.00	0.01	0.44	0.00	0.01	0.00	0.01	0.00
PB85-243.5	Limestone	209.4	0.15	0.19	0.02	0.07	0.01	0.05	0.02	0.00	0.01	0.26	0.00	0.01	0.00	0.00	0.00
PB85-245.6	Limestone	211.2	0.19	0.17	0.01	0.05	0.01	0.03	0.01	0.00	0.01	0.32	0.00	0.01	0.00	0.01	0.00
PB85-245.6	Limestone	211.7	0.06	0.06	0.01	0.03	0.00	0.00	0.01	0.00	0.01	0.22	0.00	0.01	0.00	0.01	0.00
PB85-246.1	Limestone	211.7	0.21	0.29	0.03	0.13	0.03	0.01	0.04	0.01	0.04	0.60	0.01	0.04	0.01	0.03	0.01
PB85-246.7	Limestone	213.2	0.15	0.21	0.02	0.09	0.02	0.01	0.02	0.00	0.03	0.40	0.01	0.02	0.00	0.02	0.00
PB85-247.9	Limestone	213.7	0.77	1.08	0.11	0.38	0.06	0.02	0.06	0.01	0.03	0.45	0.01	0.02	0.00	0.02	0.00
PB85-248.4	Limestone	215.7	0.19	0.29	0.03	0.12	0.02	0.01	0.03	0.00	0.03	0.39	0.01	0.02	0.00	0.02	0.00
PB85-250.8	Limestone	215.9	0.37	0.58	0.06	0.24	0.05	0.03	0.06	0.01	0.05	0.57	0.01	0.03	0.01	0.03	0.01
PB85-251	Limestone	216.0	0.09	0.14	0.02	0.06	0.01	0.01	0.01	0.00	0.01	0.16	0.00	0.01	0.00	0.01	0.00
PB85-251.12	Limestone	216.0	0.15	0.19	0.02	0.09	0.02	0.01	0.03	0.00	0.04	0.55	0.01	0.03	0.00	0.03	0.01
PB85-252.30	Limestone	217.0	0.65	1.05	0.11	0.42	0.07	0.03	0.09	0.01	0.08	1.26	0.02	0.07	0.01	0.06	0.01
PB85-253.38	Limestone	217.9	3.35	6.58	0.75	2.72	0.43	0.09	0.41	0.05	0.20	0.88	0.03	0.08	0.01	0.07	0.01
PB85-254.38	Limestone	218.5	3.35	6.58	0.75	2.72	0.43	0.09	0.41	0.05	0.20	0.88	0.03	0.08	0.01	0.07	0.01

Appendix to Chapter 4

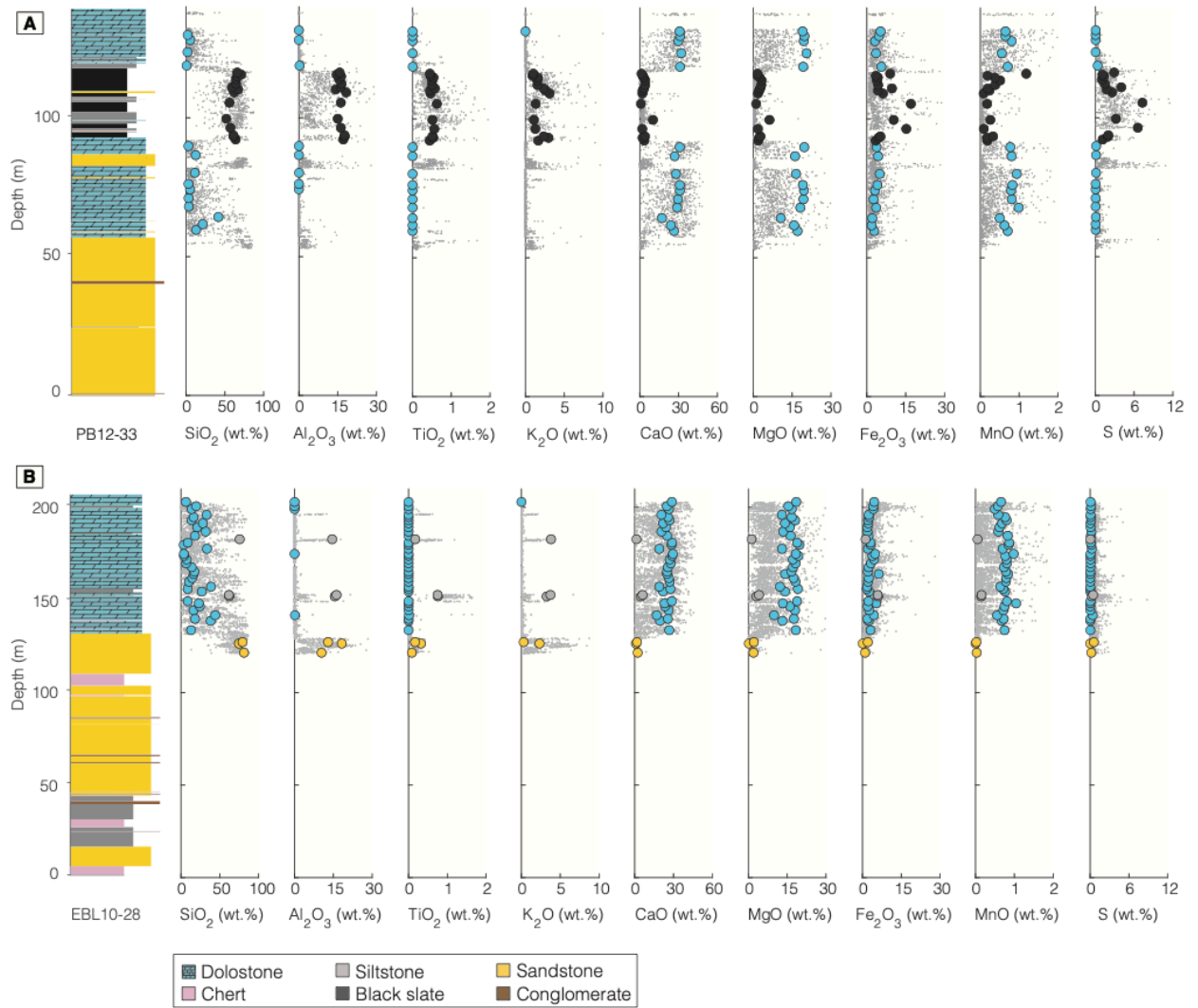
Sample name	Lithology	Strat-depth (m)	La	Ce	Pr	Nd	Sm	Eu	Gd	Tb	Dy	Y	Ho	Er	Tm	Yb	Lu
17-GA1-01	Limestone	2.1	1.05	1.67	0.20	0.87	0.19	0.10	0.26	0.04	0.28	3.42	0.07	0.21	0.03	0.17	0.03
17-GA1-02	Limestone	2.07	1.19	1.72	0.19	0.76	0.15	0.10	0.21	0.03	0.21	2.89	0.05	0.16	0.02	0.13	0.02
17-GA1-03	Limestone	2.04	1.19	1.69	0.19	0.78	0.16	0.10	0.21	0.03	0.20	2.78	0.05	0.15	0.02	0.13	0.02
17-GA1-04	Limestone	1.98	0.61	0.87	0.10	0.44	0.10	0.05	0.14	0.02	0.15	1.90	0.03	0.11	0.02	0.09	0.02
17-GA1-05	Limestone	1.94	0.95	1.43	0.18	0.80	0.20	0.08	0.27	0.04	0.28	3.60	0.06	0.19	0.03	0.15	0.02
17-GA1-06	Limestone	1.9	0.01	0.01	0.01	0.01	0.01	0.01	0.01	0.01	0.01	0.01	0.01	0.01	0.01	0.01	0.01
17-GA1-07	Limestone	1.87	0.75	0.98	0.12	0.52	0.12	0.08	0.18	0.03	0.19	2.82	0.05	0.15	0.02	0.12	0.02
17-GA1-08	Limestone	1.81	0.88	0.97	0.11	0.42	0.08	0.09	0.11	0.01	0.09	1.93	0.02	0.07	0.01	0.05	0.01
17-GA1-09	Limestone	1.78	0.68	0.85	0.11	0.49	0.11	0.12	0.15	0.02	0.13	2.27	0.03	0.08	0.01	0.06	0.01
17-GA1-10	Limestone	1.73	0.75	0.91	0.13	0.65	0.18	0.13	0.29	0.05	0.37	7.34	0.09	0.31	0.04	0.26	0.04
17-GA1-11	Limestone	1.65	3.03	3.04	0.43	1.84	0.41	0.19	0.62	0.10	0.67	18.03	0.19	0.67	0.10	0.66	0.13
17-GA1-12	Limestone	1.6	3.99	3.85	0.53	2.25	0.47	0.23	0.72	0.11	0.74	19.83	0.20	0.73	0.11	0.68	0.14
17-GA1-13	Limestone	1.54	2.97	2.76	0.38	1.66	0.35	0.19	0.56	0.09	0.62	16.43	0.17	0.60	0.08	0.51	0.10
17-GA1-14	Limestone	1.46	2.51	2.12	0.32	1.43	0.33	0.22	0.55	0.09	0.65	19.27	0.19	0.66	0.09	0.57	0.11
17-GA1-15	Limestone	1.44	0.01	0.01	0.01	0.01	0.01	0.00	0.01	0.01	0.01	0.00	0.01	0.01	0.01	0.01	0.01
17-GA1-16	Limestone	1.4	4.72	3.52	0.57	2.51	0.52	0.24	0.84	0.13	0.87	26.04	0.25	0.90	0.13	0.89	0.19
17-GA1-17	Limestone	1.34	5.44	3.74	0.60	2.58	0.51	0.22	0.84	0.13	0.88	27.14	0.25	0.92	0.13	0.90	0.19
17-GA1-18	Limestone	1.28	3.38	2.13	0.36	1.65	0.38	0.20	0.78	0.13	0.94	33.18	0.29	1.03	0.14	0.92	0.19
17-GA1-15	Limestone	1.44	4.52	3.34	0.53	2.36	0.49	0.26	0.78	0.11	0.80	25.48	0.23	0.83	0.12	0.82	0.18
17-GA1-19	Limestone	1.21	2.32	1.34	0.23	1.10	0.29	0.17	0.61	0.10	0.79	30.95	0.24	0.89	0.12	0.78	0.16
17-GA1-20	Limestone	1.14	0.76	0.66	0.12	0.57	0.14	0.15	0.23	0.04	0.25	8.07	0.07	0.21	0.03	0.13	0.02
17-GA1-21	Limestone	1.09	0.90	0.85	0.14	0.64	0.13	0.18	0.19	0.03	0.17	4.59	0.04	0.12	0.02	0.08	0.01
17-GA1-22	Limestone	1.06	2.80	2.20	0.30	1.34	0.31	0.18	0.61	0.10	0.77	26.60	0.23	0.83	0.12	0.72	0.15
17-GA1-23	Limestone	1.03	1.92	1.92	0.26	1.08	0.22	0.13	0.32	0.05	0.31	6.69	0.08	0.30	0.04	0.30	0.06
17-GA1-24	Limestone	0.93	1.30	1.29	0.17	0.73	0.15	0.10	0.24	0.04	0.27	6.11	0.07	0.25	0.04	0.23	0.04
17-GA1-25	Limestone	0.89	2.55	2.51	0.32	1.42	0.32	0.17	0.51	0.08	0.59	13.69	0.16	0.53	0.07	0.44	0.08
17-GA1-26	Limestone	0.85	2.85	2.92	0.37	1.58	0.35	0.17	0.56	0.09	0.64	13.57	0.16	0.53	0.07	0.43	0.07
17-GA1-27	Limestone	0.82	1.00	1.12	0.14	0.59	0.12	0.23	0.18	0.03	0.19	3.34	0.05	0.14	0.02	0.11	0.02
17-GA1-28	Limestone	0.73	1.12	1.53	0.19	0.87	0.19	0.23	0.24	0.03	0.18	3.15	0.04	0.09	0.01	0.06	0.01
17-GA1-29	Limestone	0.69	0.88	1.08	0.11	0.40	0.04	0.14	0.05	0.01	0.02	0.90	0.01	0.02	0.00	0.02	0.00
17-GA1-30	Limestone	0.58	0.59	0.82	0.11	0.53	0.14	0.10	0.22	0.04	0.24	3.47	0.06	0.18	0.02	0.13	0.02
17-GA1-31	Limestone	0.53	0.96	0.70	0.05	0.14	0.01	0.06	0.03	0.00	0.02	1.01	0.01	0.02	0.00	0.02	0.00
17-GA1-32	Limestone	0.36	1.41	1.78	0.19	0.80	0.17	0.10	0.25	0.04	0.31	4.44	0.08	0.27	0.04	0.25	0.04
17-GA1-33	Limestone	0.3	0.98	1.56	0.18	0.73	0.14	0.16	0.18	0.03	0.18	2.67	0.04	0.14	0.02	0.11	0.02
17-GA1-34	Limestone	0.22	0.99	1.59	0.19	0.83	0.18	0.23	0.24	0.04	0.23	2.83	0.05	0.15	0.02	0.11	0.02
17-GA1-35	Limestone	0.11	0.81	1.55	0.19	0.81	0.21	0.18	0.31	0.06	0.45	4.54	0.12	0.39	0.06	0.36	0.07
17-GA1-36	Limestone	0.01	1.52	2.16	0.24	1.01	0.22	0.15	0.31	0.05	0.27	2.96	0.06	0.15	0.02	0.10	0.02

Appendix A.6. Supplementary figures



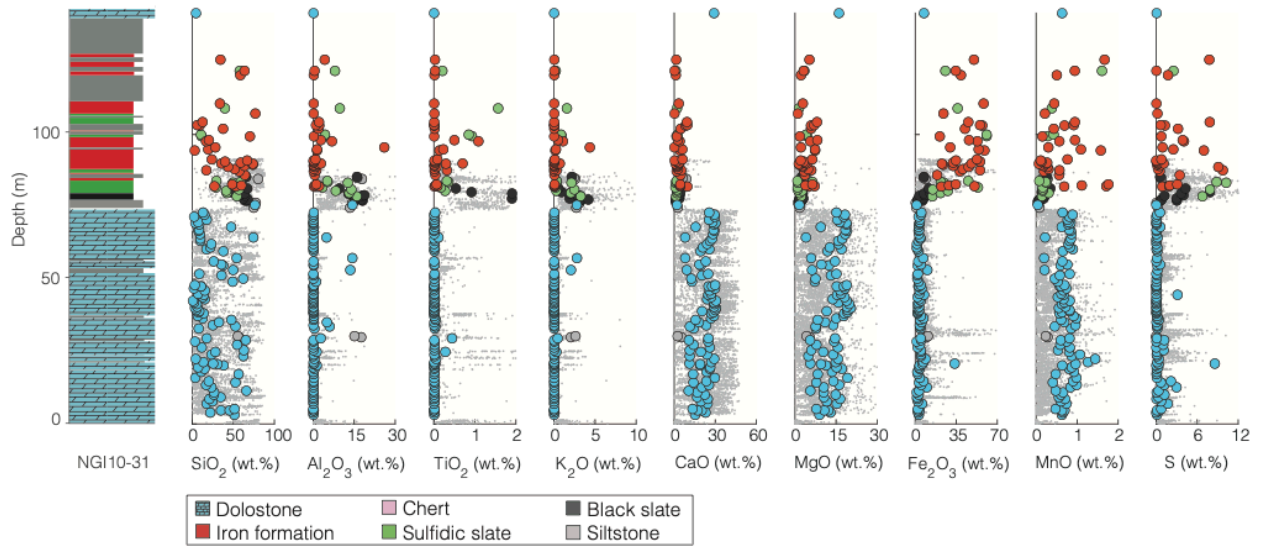
Supplementary Figure 4.1. (A) Depth profiles of the PB12-35 drill hole showing calibrated XRF data superimposed with high precision major element concentrations determined by ICP-AES. (B) PB12-32 drill hole showing calibrated XRF data superimposed depth profiles with high precision major element concentrations determined by ICP-AES.

Appendix to Chapter 4

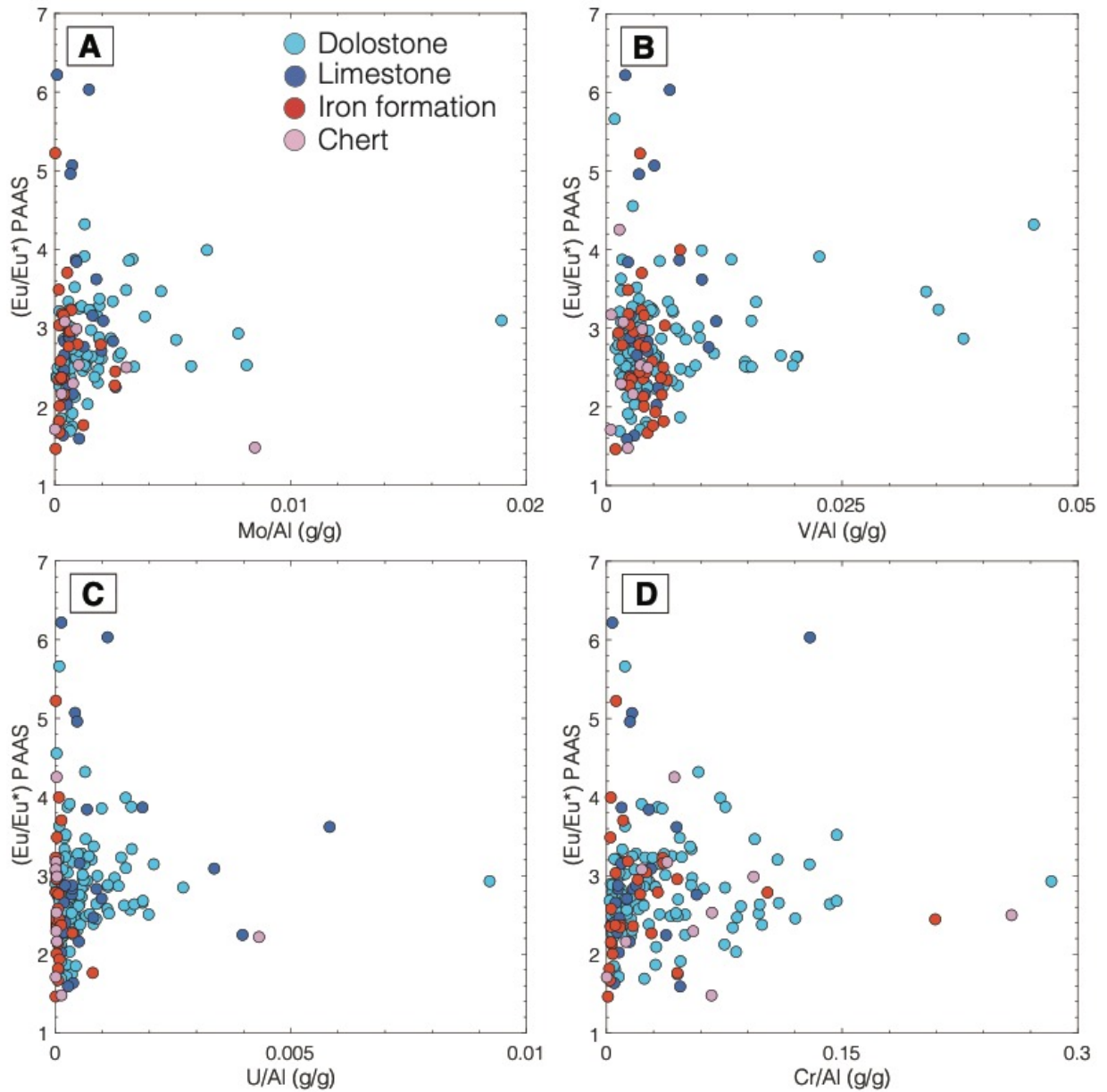


Supplementary Figure 4.2. (A) Depth profiles of the PB12-33 drill hole showing calibrated XRF data superimposed with high-precision major element concentrations determined by ICP-AES. (B) Depth profiles of the EBL10-28 drill hole showing calibrated XRF data superimposed with high-precision major element concentrations determined by ICP-AES.

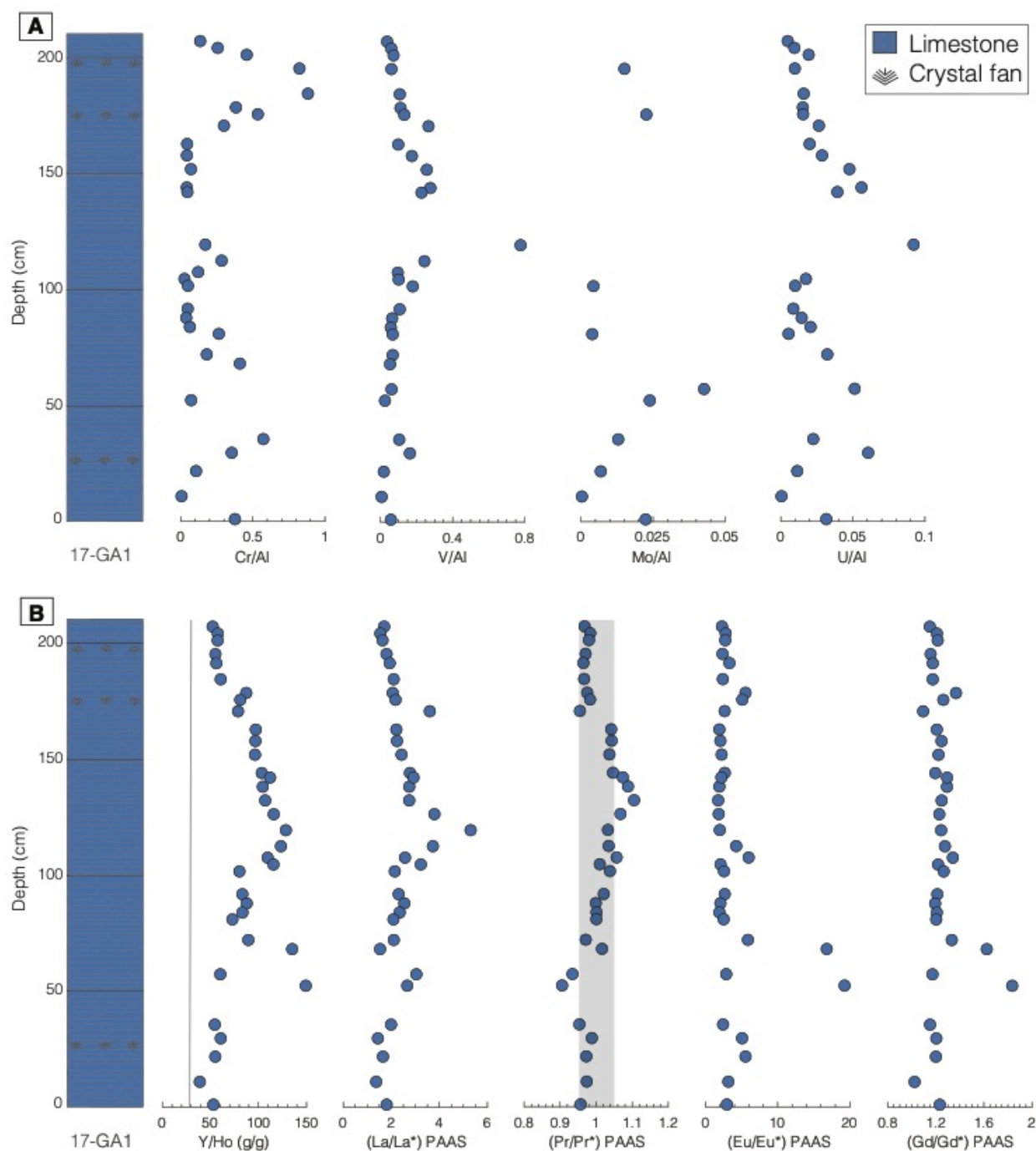
Appendix to Chapter 4



Supplementary Figure 4.3. Depth profiles of the NGI10-31 drill hole showing calibrated XRF data superimposed with high-precision major element concentrations determined by ICP-AES.



Supplementary Figure 4.4. Al-normalized redox-sensitive trace elements plotted against Eu/Eu* anomalies. Some carbonates, iron formation, and chert samples show enrichment of Mo, V, U, and Cr correlate with Eu anomalies, suggesting that these enrichments were related to hydrothermal input to seawater.



Supplementary Figure 4.5. (A) Al-normalized redox-sensitive element profiles of the 17-GA1 drill hole. The limestone samples near the base and at the top of the hole show remarkable Cr enrichment. There is minimal enrichment of V. Mo and U show noticeable enrichment. (B) PAAS-normalized rare earth element profiles of the 17-GA1 drill hole. Y/Ho ratios and La/La*, Pr/Pr* anomalies increase upward to the interval with negative Ce (Pr/Pr*) anomalies then decrease upward from there. Two of the samples show positive Pr/Pr* anomalies (true negative Ce anomalies) and four of the samples show negative Pr/Pr* anomalies (true positive Ce anomalies).

Appendix B

Appendix to Chapter 5

Appendix B.1. $\delta^{13}\text{C}$ and $\delta^{18}\text{O}$ isotope data for the Red Lake carbonate samples. Values are reported in per mille (‰) units relative to the VPDB standard. Precision of $\delta^{13}\text{C}$ and $\delta^{18}\text{O}$ was 0.1 ‰ (2σ) and 0.2 ‰ (2σ), respectively.

Sample	Lithology	Strat-depth (m)	TOC (%)	$\delta^{13}\text{C}$ carb	$\delta^{18}\text{O}$ carb
EBL28-318.36	Dolostone	143.0		-0.19	-15.06
EBL28-365.22	Dolostone	164.0	0.01	-0.04	-15.05
EBL28-378.10	Dolostone	169.8	0.01	0.01	-14.91
EBL28-357	Dolostone	160.3		0.02	-15.07
EBL28-322.95	Dolostone	145.0		0.14	-14.49
EBL28-400.3	Dolostone	179.7	0.01	0.19	-14.07
EBL28-311.35	Dolostone	139.8	0.02	0.22	-15.51
EBL28-297.73	Dolostone	133.7	0.02	0.24	-15.31
EBL28-326.38	Dolostone	146.6		0.26	-13.44
EBL28-382.76	Dolostone	171.9	0.01	0.29	-14.88
EBL28-344.15	Dolostone	154.5	0.01	0.31	-15.08
EBL28-446.76	Dolostone	200.6		0.34	-14.30
EBL28-416.30	Dolostone	186.9	0.01	0.37	-14.80
EBL28-436.44	Dolostone	196.0	0.01	0.37	-14.59
EBL28-373.40	Dolostone	167.7	0.01	0.39	-14.68
EBL28-389.46	Dolostone	174.9	0.02	0.40	-13.98
EBL28-397.02	Dolostone	178.3		0.42	-14.19
EBL28-351.93	Dolostone	158.0		0.42	-13.42
EBL28-421.44	Dolostone	189.2	0.01	0.47	-14.75
EBL28-429.76	Dolostone	193.0		0.57	-14.22
EBL28-332.5	Dolostone	149.3	0.02	0.59	-13.69
EBL28-443.28	Dolostone	199.0	0.01	0.64	-14.00
EBL28-408.29	Dolostone	183.3		0.67	-13.88
EBL28-451.93	Dolostone	202.9	0.03	0.75	-13.07

Sample	Lithology	Strat-depth (m)	TOC (%)	$\delta^{13}\text{C}$ carb	$\delta^{18}\text{O}$ carb
PB33-108.27	Dolostone	59.6	0.02	-0.32	-15.38
PB33-112	Dolostone	61.7		0.12	-14.73
PB33-116.73	Dolostone	64.3		0.84	-14.86
PB33-123.58	Dolostone	68.1	0.01	-0.18	-15.32
PB33-129.05	Dolostone	71.1		0.09	-15.39
PB33-134.82	Dolostone	74.2		-0.03	-15.04
PB33-138.35	Dolostone	76.2	0.01	-0.58	-15.38
PB33-145.63	Dolostone	80.2	0.01	-1.10	-15.75
PB33-157.17	Dolostone	86.5	0.01	-0.20	-14.48
PB33-163.13	Dolostone	89.8		-0.02	-13.69
PB33-215.68	Dolostone	118.8	0.03	-0.92	-13.90
PB33-224.52	Dolostone	123.6	0.03	-0.28	-14.18
PB33-232.46	Dolostone	128.0	0.01	-0.51	-15.31
PB33-235.73	Dolostone	129.8		-0.56	-15.45
PB33-238.8	Dolostone	131.5	0.02	-0.47	-15.08

Appendix to Chapter 5

Sample	Lithology	Strat-depth (m)	TOC (%)	$\delta^{13}\text{C carb}$	$\delta^{18}\text{O carb}$
PB32-21.50	Dolostone	19.42		-1.20	-15.49
PB32-24.25	Dolostone	21.91	0.02	-0.82	-15.68
PB32-27.50	Dolostone	24.84		-1.05	-15.52
PB32-31.56	Dolostone	28.51		-0.73	-15.44
PB32-34.62	Dolostone	31.27	0.02	-0.31	-14.45
PB32-39.11	Dolostone	35.33		0.01	-14.96
PB32-43.70	Dolostone	39.48		-0.51	-15.02
PB32-48.88	Dolostone	44.16		-0.49	-15.33
PB32-56.08	Dolostone	50.66	0.01	-1.47	-15.21
PB32-62.29	Dolostone	56.27		-1.27	-15.53
PB32-65.66	Dolostone	59.31		-1.97	-15.99
PB32-70.38	Dolostone	63.58		-0.83	-15.56
PB32-72.89	Dolostone	65.84		-0.55	-15.52
PB32-85.73	Dolostone	77.44		-0.75	-15.07
PB32-88.23	Dolostone	79.70		-1.11	-15.68
PB32-94.1	Dolostone	85.00	0.01	-0.03	-14.69
PB32-98.57	Dolostone	89.04		-0.18	-15.65
PB32-100.4	Dolostone	90.70		-0.82	-15.03
PB32-102.13	Dolostone	92.26		-0.41	-14.95
PB32-104.85	Dolostone	94.72	0.01	-0.13	-15.55
PB32-108.35	Dolostone	97.88		-0.89	-15.65
PB32-112.63	Dolostone	101.74	0.02	-0.65	-15.73
PB32-116.89	Dolostone	105.59		-0.33	-15.44
PB32-118.9	Dolostone	107.41		-0.29	-14.84
PB32-121.10	Dolostone	109.39	0.05	-0.65	-13.15
PB32-124.93	Dolostone	112.85		0.00	-12.95
PB32-128.48	Dolostone	116.06		-0.08	-12.73
PB32-131.03	Dolostone	118.36	0.01	-0.44	-15.00
PB32-133.27	Cherty dolostone	120.39		-1.19	-15.53
PB32-137.28	Dolostone	124.01		-0.26	-13.94
PB32-139.87	Dolostone	126.35		0.45	-10.00
PB32-143.3	Dolostone	129.45	0.01	0.29	-15.42
PB32-146.16	Dolostone	132.03		-0.50	-15.67
PB32-148.92	Dolostone	134.53		-0.25	-15.35
PB32-160.15	Dolostone	144.67		-0.67	-14.50
PB32-165	Dolostone	149.05		0.10	-15.82
PB32-168.13	Dolostone	151.88		-0.47	-14.87
PB32-172.93	Dolostone	156.21	0.02	-0.30	-14.85
PB32-174.94	Silty Dolostone	158.03		-4.89	-17.26
PB32-178.29	Dolostone	161.06		0.47	-14.34
PB32-183.38	Dolostone	165.65		-0.91	-8.75

Appendix to Chapter 5

Sample	Lithology	Strat-depth (m)	TOC (%)	$\delta^{13}\text{C carb}$	$\delta^{18}\text{O carb}$
PB32-189.02	Dolostone	170.75		-0.29	-14.56
PB32-194.05	Dolostone	175.29		-0.35	-15.40
PB32-197.35	Dolostone	178.27		-0.33	-15.30
PB32-199.28	Dolostone	180.02	0.01	-0.30	-14.82
PB32-205.25	Dolostone	185.41	0.01	0.01	-12.95
PB32-210.2	Dolostone	189.88		0.00	-14.47
PB32-212.08	Dolostone	191.58		0.18	-13.95
PB32-215.56	Dolostone	194.72	0.02	-0.04	-12.68
PB32-292.37	Dolostone	264.11		-0.83	-14.64
PB32-295.80	Dolostone	267.21		-1.32	-15.09

Sample	Lithology	Strat-depth (m)	TOC (%)	$\delta^{13}\text{C carb}$	$\delta^{18}\text{O carb}$
PB35-22.48	Limestone	19.3	0.04	1.21	-11.43
PB35-24.22	Limestone	20.8	0.08	0.96	-9.46
PB35-26.06	Limestone	22.4	0.02	0.99	-8.83
PB35-26.43	Limestone	22.7	0.10	0.89	-8.79
PB35-27.57	Limestone	23.7	0.01	0.87	-8.62
PB35-29.37	Limestone	25.3	0.93	0.49	-8.91
PB35-31.20	Limestone	26.8	0.25	0.36	-10.63
PB35-34.20	Limestone	29.4	0.20	0.96	-9.16
PB35-36.84	Limestone	31.7	0.06	0.85	-9.92
PB35-38.4	Limestone	33.1	0.04	1.33	-10.01
PB35-39.70	Limestone	34.1		1.17	-9.47
PB35-43.9	Dolostone	37.8	0.88	-1.32	-15.80
PB35-45.10	Dolostone	38.8		-0.76	-15.62
PB35-47.10	Dolostone	40.5	1.02	-0.19	-15.03
PB35-48.3	Limestone	41.5		-0.11	-12.11
PB35-49.43	Limestone	42.5	0.15	-1.18	-13.37
PB35-52.87	Limestone	45.5	0.25	-0.50	-11.87
PB35-54.38	Limestone	46.8	0.23	-0.35	-12.82
PB35-56.57	Dolostone	48.7	0.98	-1.48	-13.64
PB35-58.02	Dolostone	49.9	0.71	-0.96	-13.84
PB35-59.80	Dolostone	51.4	1.28	-1.21	-12.85
PB35-61.20	Dolostone	52.6	0.77	-1.10	-12.31
PB35-68.65	Limestone	59.1	0.18	0.53	-10.92
PB35-70.63	Limestone	60.8	0.04	0.68	-11.84
PB35-73.51	Limestone	63.2	0.20	-0.22	-12.62
PB35-77.86	Limestone	67.0	0.19	-3.27	-6.55
PB35-79.6	Limestone	68.5	0.92	-8.43	-5.99
PB35-87.93	Dolostone	75.6	0.93	-2.38	-14.97
PB35-89.76	Dolostone	77.2	0.97	-2.51	-15.11

Appendix to Chapter 5

Sample	Lithology	Strat-depth (m)	TOC (%)	$\delta^{13}\text{C carb}$	$\delta^{18}\text{O carb}$
PB35-91.8	Dolostone	79.0		-2.07	-15.38
PB35-92.8	Dolostone	79.8	1.70	-2.76	-12.61
PB35-93.80	Dolostone	80.7	1.02	-2.48	-15.38
PB35-102.02	Dolostone	87.7	1.06	-2.56	-15.88
PB35-144.40	Limestone	124.2	0.08	0.81	-10.74
PB35-146.2	Limestone	125.7	0.07	0.63	-11.25
PB35-147.00	Limestone	126.4	0.12	0.33	-12.21
PB35-149.76	Limestone	128.8	0.02	0.43	-13.32
PB35-151.12	Limestone	130.0	0.07	0.44	-14.05
PB35-153.50	Limestone	132.0	0.07	0.97	-10.43
PB35-156.20	Limestone	134.4	0.04	0.76	-10.98
PB35-157.75	Limestone	135.7	0.06	1.07	-11.19
PB35-160.96	Limestone	138.4		1.08	-9.74
PB35-162.4	Limestone	139.7	0.02	1.24	-11.05
PB35-163.7	Limestone	140.8	0.01	1.04	-12.30
PB35-168.42	Limestone	144.9		0.92	-10.51
PB35-171.13	Limestone	147.2	0.11	0.41	-11.08
PB35-173.1	Limestone	148.9	0.03	-0.23	-14.18
PB35-175	Limestone	150.5	0.12	0.73	-12.32
PB35-177.5	Limestone	152.7	0.07	0.52	-13.61
PB35-178.8	Limestone	153.8	0.02	0.89	-11.98
PB35-180.8	Limestone	155.5	0.17	1.02	-12.02
PB35-182.05	Limestone	156.6		-0.16	-13.15
PB35-184.14	Limestone	158.4		0.59	-13.72
PB35-184.26	Limestone	158.5	0.15	-0.98	-15.12
PB35-185.16	Limestone	159.3		0.33	-14.55
PB35-185.88	Limestone	159.9		0.57	-14.84
PB35-187.29	Dolostone	161.1		-1.15	-15.53
PB35-188.57	Dolostone	162.2		-0.96	-15.13
PB35-189.2	Dolostone	162.7	0.02	-0.46	-14.91
PB35-190.30	Dolostone	163.7		0.13	-15.86
PB35-191.8	Dolostone	165.0		-1.54	-14.89
PB35-195.3	Dolostone	168.0		-1.51	-16.29
PB35-196.4	Dolostone	168.9		-1.44	-16.04
PB35-198.5	Dolostone	170.7	0.02	-1.54	-16.20
PB35-200.6	Dolostone	172.5		-0.85	-16.19
PB35-202.3	Dolostone	174.0	0.03	-1.16	-15.71
PB35-205	Dolostone	176.3		-0.52	-15.84
PB35-206.7	Dolostone	177.8	0.03	-0.58	-15.15
PB35-209	Dolostone	179.8	0.47	-0.20	-15.23
PB35-211.41	Dolostone	181.8	0.03	-3.00	-14.82

Appendix to Chapter 5

Sample	Lithology	Strat-depth (m)	TOC (%)	$\delta^{13}\text{C carb}$	$\delta^{18}\text{O carb}$
PB35-217.8	Limestone	187.3		-0.29	-15.22
PB35-221.3	Limestone	190.3	0.02	-0.34	-15.90
PB35-223.3	Limestone	192.1		-0.02	-14.51
PB35-225.1	Limestone	193.6		-0.78	-14.78
PB35-227.8	Limestone	195.9	0.02	-0.78	-14.98
PB35-230.02	Limestone	197.8		0.70	-14.48
PB35-231.96	Dolostone	199.5		-1.51	-15.81
PB35-235.2	Limestone	202.3		0.99	-12.35
PB35-237.4	Limestone	204.2		0.65	-13.02
PB35-239.3	Limestone	205.8		0.90	-10.95
PB35-241.5	Limestone	207.7	0.02	1.11	-11.38
PB35-243.4	Limestone	209.4		0.28	-10.89
PB35-245.5	Limestone	211.2		0.84	-10.93
PB35-246.1	Limestone	211.7		0.84	-10.20
PB35-246.7	Limestone	212.2		0.66	-11.03
PB35-247.8	Limestone	213.1		0.81	-10.18
PB35-248.4	Limestone	213.7		0.79	-10.36
PB35-250	Limestone	215.0		-0.66	-14.86
PB35-250.7	Limestone	215.6		0.53	-11.85
PB35-251.11	Limestone	216.0		0.27	-12.45
PB35-252.30	Limestone	217.0		0.45	-11.07
PB35-253.38	Limestone	217.9		0.67	-11.89

Appendix to Chapter 5

Sample	Lithology	Strat-depth (m)	TOC (%)	$\delta^{13}\text{C carb}$	$\delta^{18}\text{O carb}$
17-GA1-01	Limestone	2.1	0.01	0.68	-12.74
17-GA1-02	Limestone	2.07	0.03	0.63	-12.61
17-GA1-03	Limestone	2.04	0.05	0.67	-12.39
17-GA1-04	Limestone	1.98	0.01	0.41	-12.57
17-GA1-05	Limestone	1.94	0.02	0.38	-12.58
17-GA1-06	Limestone	1.9	0.02	0.10	-12.48
17-GA1-07	Limestone	1.87	0.23	0.47	-12.45
17-GA1-08	Limestone	1.81	0.09	0.92	-12.38
17-GA1-09	Limestone	1.78	0.05	0.79	-12.40
17-GA1-10	Limestone	1.73	0.68	0.73	-11.90
17-GA1-11	Limestone	1.65	0.65	0.29	-11.79
17-GA1-12	Limestone	1.6	0.10	0.47	-11.87
17-GA1-13	Limestone	1.54	0.62	0.67	-11.66
17-GA1-14	Limestone	1.46	0.54	0.42	-12.01
17-GA1-15	Limestone	1.44	2.17	0.21	-11.52
17-GA1-16	Limestone	1.4	0.33	0.20	-11.43
17-GA1-17	Limestone	1.34	0.78	0.36	-11.49
17-GA1-18	Limestone	1.28	0.32	0.60	-11.13
17GA1-19	Limestone	1.21	0.91	0.67	-11.32
17GA1-20	Limestone	1.14	0.08	1.01	-11.97
17GA1-21	Limestone	1.09	0.08	0.94	-12.02
17GA1-22	Limestone	1.06	0.23	0.44	-10.80
17GA1-23	Limestone	1.03	0.53	0.81	-10.57
17GA1-24	Limestone	0.93	0.13	0.95	-10.60
17GA1-25	Limestone	0.89	0.13	0.73	-11.05
17GA1-26	Limestone	0.85	0.16	0.69	-11.27
17GA1-27	Limestone	0.82	0.02	0.33	-11.12
17GA1-28	Limestone	0.73	0.12	1.13	-11.28
17GA1-29	Limestone	0.69		1.40	-11.70
17GA1-30	Limestone	0.58	0.01	0.74	-11.56
17GA1-31	Limestone	0.53		1.52	-11.70
17GA1-32	Limestone	0.36	0.01	0.61	-11.45
17GA1-33	Limestone	0.3	0.04	0.92	-11.83
17GA1-34	Limestone	0.22	0.03	0.64	-11.54
17GA1-35	Limestone	0.11	0.09	-0.72	-10.62
17GA1-36	Limestone	0.01	0.01	0.02	-11.67

Appendix to Chapter 5

Sample	Lithology	Strat-depth (m)	TOC (%)	$\delta^{13}\text{C carb}$	$\delta^{18}\text{O carb}$
17-GA2-14	Limestone	1.75	0.24	0.64	-11.67
17-GA2-14	Limestone	1.75		0.63	-11.75
17-GA2-13	Limestone	1.77	0.36	0.41	-12.14
17-GA2-13	Limestone	1.77		0.45	-12.10
17-GA2-12	Limestone	1.78	0.02	0.09	-11.91
17-GA2-11	Limestone	1.79	0.02	0.23	-12.16
17-GA2-10	Limestone	1.8	0.01	0.58	-12.46
17-GA2-9	Limestone	1.81	0.02	0.59	-12.37
17-GA2-08	Limestone	1.83	0.02	0.45	-12.27
17-GA2-8	Limestone	1.83		0.41	-12.34
17-GA2-07	Limestone	1.85	0.04	0.44	-12.42
17-GA2-7	Limestone	1.85	0.01	0.42	-12.38
17-GA2-06	Limestone	1.87	0.05	0.54	-12.58
17-GA2-6	Limestone	1.87	0.01	0.54	-12.62
17-GA2-05	Limestone	1.89	0.04	0.45	-12.57
17-GA2-5	Limestone	1.89		0.46	-12.66
17-GA2-04	Limestone	1.91	0.01	0.46	-12.67
17-GA2-4	Limestone	1.91	0.04	0.46	-12.58
17-GA2-3	Limestone	1.92	0.03	0.75	-12.62
17-GA2-2	Limestone	1.93	0.04	0.86	-12.64
17-GA2-01	Limestone	1.95	0.01	0.93	-12.63
17-GA2-1	Limestone	1.95		0.92	-12.71

Appendix to Chapter 5

Sample	Lithology	Strat-depth (m)	TOC (%)	$\delta^{13}\text{C carb}$	$\delta^{18}\text{O carb}$
17-NG-1	Dolostone	1.77	0.17	0.66	-13.97
17-NG-3	Dolostone	1.72	0.05	0.73	-12.76
17-NG-5	Dolostone	1.67	0.21	0.86	-12.91
17-NG-7	Dolostone	1.62	0.05	0.72	-13.49
17-NG-9	Dolostone	1.57	0.09	0.61	-13.60
17-NG-11	Dolostone	1.52		0.64	-13.49
17-NG-13	Dolostone	1.47	0.02	0.65	-13.29
17-NG-15	Dolostone	1.42		0.67	-13.42
17-NG-17	Dolostone	1.37	0.08	0.58	-12.99
17-NG-19	Dolostone	1.32	0.07	0.50	-13.82
17-NG-21	Dolostone	1.27	0.10	0.70	-11.89
17-NG-25	Dolostone	1.22	0.05	0.62	-13.76
17-NG-27	Dolostone	1.17	0.04	0.59	-13.73
17-NG-29	Dolostone	1.12	0.07	0.77	-13.83
17-NG-31	Dolostone	1.07	0.04	0.65	-14.03
17-NG-33	Dolostone	1.02		0.67	-13.97
17-NG-35	Dolostone	0.97	0.06	0.58	-14.16
17-NG-37	Dolostone	0.92	0.07	0.50	-14.49
17-NG-39	Dolostone	0.87	0.04	0.69	-13.82
17-NG-41	Dolostone	0.82	0.07	0.76	-13.94
17-NG-43	Dolostone	0.77	0.04	0.34	-14.23
17-NG-45	Dolostone	0.72	0.14	0.60	-14.24
17-NG-47	Dolostone	0.67	0.03	0.62	-14.42
17-NG-49	Dolostone	0.62		0.47	-14.47
17-NG-51	Dolostone	0.57	0.18	0.73	-13.99
17-NG-53	Dolostone	0.52		0.82	-13.68
17-NG-55	Dolostone	0.47	0.08	0.87	-14.04
17-NG-57	Dolostone	0.42	0.16	0.55	-13.85
17-NG-59	Dolostone	0.37	0.10	0.58	-13.79
17-NG-61	Dolostone	0.32	0.03	0.59	-13.76
17-NG-63	Dolostone	0.27	0.04	0.37	-14.13
17-NG-65	Dolostone	0.22	0.11	0.49	-13.85
17-NG-67	Dolostone	0.17	0.03	0.38	-14.01
17-NG-69	Dolostone	0.12	0.06	0.51	-14.01
17-NG-71	Dolostone	0.07	0.02	0.41	-13.91
17-NG-73	Dolostone	0.02	0.03	0.49	-13.78

Appendix to Chapter 5

Appendix C

Appendix to Chapter 6

Appendix C.1. Multiple sulfur ($\delta^{34}\text{S}$, $\Delta^{33}\text{S}$, and $\Delta^{36}\text{S}$) isotope data for the Red Lake sulfidic shale samples. Values are reported in per mille (‰) units relative to the VCDT standard. The internal precision, based on the average of internal precisions measured for all standard repeats, was ± 0.03 ‰ for $\delta^{34}\text{S}$ (2σ), ± 0.04 ‰ for $\Delta^{33}\text{S}$ (2σ), and ± 0.74 ‰ for $\Delta^{36}\text{S}$ (2σ). The external precision, averaged across each group of standard repeated was ± 0.02 ‰ (2σ) for $\delta^{34}\text{S}$ and ± 0.02 ‰ (2σ) for $\Delta^{33}\text{S}$, and ± 0.15 ‰ for $\Delta^{36}\text{S}$ (2σ).

Sample name	Lithology	Strat-depth (m)	$\delta^{34}\text{S}$	$\Delta^{33}\text{S}$	$\Delta^{36}\text{S}$
Mount-1_AC-227-1@02	Pyrrhotite	85.07	-3.43	0.12	-1.12
Mount-1_AC-227-1@03	Pyrrhotite	85.07	-3.82	0.17	-1.40
Mount-1_AC-227-1@04	Pyrrhotite	85.07	-3.29	0.15	-0.44
Mount-1_AC-227-1@05	Pyrrhotite	85.07	-3.34	0.09	-0.17
Mount-1_AC-227-1@06	Pyrrhotite	85.07	-4.47	0.13	-0.57
Mount-1_AC-227-1@07	Pyrrhotite	85.07	-3.59	0.11	-1.35
Mount-1_AC-227-1@08	Pyrrhotite	85.07	-4.19	0.13	-0.62
Mount-1_AC-227-1@09	Pyrrhotite	85.07	-4.51	0.19	-0.35
Mount-1_AC-227-1@1	Pyrrhotite	85.07	-4.01	0.09	-0.49
Mount-1_AC-227-1@10	Pyrrhotite	85.07	-3.18	0.17	-0.80
Mount-1_AC-227-1@11	Pyrrhotite	85.07	-3.63	0.13	-0.44
Mount-1_AC-227-1@12	Pyrrhotite	85.07	-3.51	0.12	-0.73
Mount-1_AC-227-1@13	Pyrrhotite	85.07	-3.78	0.14	-0.73
Mount-1_AC-227-1@14	Pyrrhotite	85.07	-4.15	0.09	0.23
Mount-1_AC-227-1@15	Pyrrhotite	85.07	-4.12	0.15	-0.41
Mount-1_AC-227-1@16	Pyrrhotite	85.07	-3.70	0.13	-1.12
Mount-1_AC-227-1@17	Pyrrhotite	85.07	-3.59	0.16	-0.32
Mount-1_AC-227-1@18	Pyrrhotite	85.07	-3.41	0.13	-1.25
Mount-1_AC-227-1@19	Pyrrhotite	85.07	-3.31	0.13	-1.07
Mount-1_AC-227-1@20	Pyrrhotite	85.07	-3.70	0.11	-1.19

Appendix to Chapter 6

Sample name	Lithology	Strat-depth (m)	$\delta^{34}\text{S}$	$\Delta^{33}\text{S}$	$\Delta^{36}\text{S}$
Mount-2_NGI@02	Pyrite	16.35	-6.17	-0.87	0.52
Mount-2_NGI@03	Pyrite	16.35	-6.45	-0.92	1.24
Mount-2_NGI@04	Pyrite	16.35	-4.81	-0.89	1.65
Mount-2_NGI@05	Pyrite	16.35	-5.91	-0.87	1.15
Mount-2_NGI@06	Pyrite	16.35	-5.72	-0.90	1.25
Mount-2_NGI@07	Pyrite	16.35	-5.76	-0.88	1.26
Mount-2_NGI@08	Pyrite	16.35	-5.18	-0.87	1.93
Mount-2_NGI@09	Pyrite	16.35	-5.55	-0.88	1.66
Mount-2_NGI@1	Pyrite	16.35	-5.86	-0.87	1.20
Mount-2_NGI@10	Pyrite	16.35	-5.56	-0.85	1.94
Mount-2_NGI@11	Pyrite	16.35	-5.85	-0.88	1.59
Mount-2_NGI@12	Pyrite	16.35	-6.05	-0.87	1.81
Mount-2_NGI@13	Pyrite	16.35	-5.31	-0.89	1.78
Mount-2_NGI@14	Pyrite	16.35	-4.70	-0.91	2.12
Mount-2_NGI@15	Pyrite	16.35	-5.07	-0.83	1.71
Mount-2_NGI@16	Pyrite	16.35	-5.13	-0.89	2.03
Mount-2_NGI@17	Pyrite	16.35	-5.14	-0.92	1.85
Mount-2_NGI@18	Pyrite	16.35	-5.34	-0.89	1.89
Mount-2_NGI@19	Pyrite	16.35	-5.30	-0.87	2.11
Mount-2_NGI@20	Pyrite	16.35	-5.76	-0.92	2.13
Mount-2_NGI@21	Pyrite	16.35	-5.71	-0.89	1.66
Mount-2_NGI@22	Pyrite	16.35	-5.16	-0.92	1.72
Mount-2_NGI@23	Pyrite	16.35	-3.85	-0.83	1.42
Mount-2_NGI@24	Pyrite	16.35	-3.65	-0.83	2.20
Mount-2_NGI@25	Pyrite	16.35	-2.28		
Mount-2_NGI@26	Pyrite	16.35	-2.90	-0.80	1.96
Mount-2_NGI@27	Pyrite	16.35	-2.86	-0.88	1.99
Mount-2_NGI@28	Pyrite	16.35	-3.38	-0.89	2.07
Mount-2_NGI@29	Pyrite	16.35	-4.20	-0.91	1.43
Mount-2_NGI@30	Pyrite	16.35	-3.61	-0.95	2.21
Mount-2_NGI@31	Pyrite	16.35	-3.12	-0.91	2.01
Mount-2_NGI@32	Pyrite	16.35	-4.05	-0.93	2.44
Mount-2_NGI@33	Pyrite	16.35	-4.21	-0.86	1.97
Mount-2_NGI@34	Pyrite	16.35	-4.01	-0.89	2.06
Mount-2_NGI@35	Pyrite	16.35	-4.05	-0.96	1.73
Mount-2_NGI@36	Pyrite	16.35	-2.65		
Mount-2_NGI@37	Pyrite	16.35	-5.19	-0.97	1.85
Mount-2_NGI@38	Pyrite	16.35	-5.15	-0.93	1.70
Mount-2_NGI@39	Pyrite	16.35	-4.31	-0.92	1.69
Mount-2_NGI@40	Pyrite	16.35	-3.34	-0.92	2.95
Mount-2_NGI@41	Pyrite	16.35	-3.81	-0.87	2.12

Appendix to Chapter 6

Sample name	Lithology	Strat-depth (m)	$\delta^{34}\text{S}$	$\Delta^{33}\text{S}$	$\Delta^{36}\text{S}$
Mount-2_NGI@42	Pyrite	16.35	-4.56	-0.91	1.51
Mount-2_NGI@43	Pyrite	16.35	1.52	-0.87	-1.52
Mount-2_NGI@44	Pyrite	16.35	1.72	-0.89	-1.15
Mount-2_NGI@45	Pyrite	16.35	1.49	-0.89	-1.44
Mount-2_NGI@46	Pyrite	16.35	1.48	-0.94	-1.81
Mount-2_NGI@47	Pyrite	16.35	2.47	-0.94	-0.88
Mount-2_NGI@48	Pyrite	16.35	2.62	-0.85	-1.12
Mount-2_NGI@49	Pyrite	16.35	2.39	-0.92	-1.06
Mount-2_NGI@50	Pyrite	16.35	1.53	-0.97	-1.66
Mount-2_NGI@51	Pyrite	16.35	0.92	-0.91	-0.83
Mount-2_NGI@52	Pyrite	16.35	1.65	-0.89	-1.22
Mount-2_NGI@54	Pyrite	16.35	2.40	-0.92	-1.09
Mount-2_NGI@55	Pyrite	16.35	3.69	-0.85	-1.02
Mount-2_NGI@56	Pyrite	16.35	3.07	-0.88	-0.98
Mount-2_NGI@57	Pyrite	16.35	2.88	-0.89	-1.21
Mount-2_NGI@58	Pyrite	16.35	1.66	-0.88	-1.42
Mount-2_NGI@59	Pyrite	16.35	1.47	-0.90	-1.48
Mount-2_NGI@60	Pyrite	16.35	0.16	-0.91	-0.83
Mount-2_NGI@61	Pyrite	16.35	1.30	-0.92	-1.15
Mount-2_NGI@62	Pyrite	16.35	0.44	-0.92	-0.95
Mount-2_NGI@63	Pyrite	16.35	0.54	-0.92	-0.77
Mount-2_NGI@64	Pyrite	16.35	1.51	-0.91	-1.59
Mount-2_NGI@65	Pyrite	16.35	0.87	-0.92	-1.20
Mount-2_NGI@66	Pyrite	16.35	1.14	-0.86	-1.20
Mount-2_NGI@67	Pyrite	16.35	0.62	-0.92	-1.04
Mount-2_NGI@68	Pyrite	16.35	1.50	-0.93	-1.23
Mount-2_NGI@69	Pyrite	16.35	1.51	-0.93	-1.30
Mount-2_NGI@70	Pyrite	16.35	1.66	-0.90	-1.31
Mount-2_NGI@71	Pyrite	16.35	-0.02	-0.99	-0.83
Mount-2_NGI@72	Pyrite	16.35	0.13	-0.94	-0.75
Mount-2_NGI@73	Pyrite	16.35	1.50	-0.87	-1.56
Mount-2_NGI@74	Pyrite	16.35	1.54	-0.93	-0.98
Mount-2_NGI@75	Pyrite	16.35	1.52	-0.87	-1.62
Mount-2_NGI@76	Pyrite	16.35	0.86	-0.89	-0.91
Mount-2_NGI@77	Pyrite	16.35	1.51	-0.88	-0.70
Mount-2_NGI@78	Pyrite	16.35	2.39	-0.87	-0.92
Mount-2_NGI@79	Pyrite	16.35	1.56	-0.91	-1.41
Mount-2_NGI@80	Pyrite	16.35	2.68	-0.88	-1.63
Mount-2_NGI@81	Pyrite	16.35	2.52	-0.93	-1.01
Mount-2_NGI@82	Pyrite	16.35	2.56	-0.92	-1.37
Mount-2_NGI@83	Pyrite	16.35	2.49	-0.92	-0.79

Appendix to Chapter 6

Sample name	Lithology	Strat-depth (m)	$\delta^{34}\text{S}$	$\Delta^{33}\text{S}$	$\Delta^{36}\text{S}$
Mount-2_PB@02	Pyrite	254.74	7.13	0.66	-3.75
Mount-2_PB@03	Pyrite	254.74	1.70	0.49	-3.72
Mount-2_PB@04	Pyrite	254.74	1.66	0.44	-3.37
Mount-2_PB@05c	Pyrite	254.74	4.02	0.43	-1.57
Mount-2_PB@06	Pyrite	254.74	-3.54	-0.19	-0.91
Mount-2_PB@07	Pyrite	254.74	-4.89	-0.24	-0.18
Mount-2_PB@08	Pyrite	254.74	-3.21	-0.20	-0.60
Mount-2_PB@09	Pyrite	254.74	-2.82	-0.21	-0.39
Mount-2_PB@1	Pyrite	254.74	2.49	0.54	-3.85
Mount-2_PB@10	Pyrite	254.74	2.08	-0.12	-0.32
Mount-2_PB@11	Pyrite	254.74	1.47	-0.25	-0.62
Mount-2_PB@12	Pyrite	254.74	1.44	0.44	-0.23
Mount-2_PB@13	Pyrite	254.74	1.51	0.39	-0.26
Mount-2_PB@17	Pyrite	254.74	-0.19	0.32	-0.04
Mount-2_PB@18	Pyrite	254.74	1.57	0.41	-0.51
Mount-2_PB@19	Pyrite	254.74	1.57	0.42	0.04
Mount-2_PB@20	Pyrite	254.74	10.62	1.06	-2.11
Mount-2_PB@21	Pyrite	254.74	1.68	0.45	-0.45
Mount-2_PB@22	Pyrite	254.74	2.84	0.65	-0.70
Mount-2_PB@23	Pyrite	254.74	3.18	0.70	-0.73
Mount-2_PB@24	Pyrite	254.74	3.01	0.68	-0.74
Mount-2_PB@25	Pyrite	254.74	0.68	0.52	-0.59
Mount-2_PB@26	Pyrite	254.74	-0.45	0.30	-0.53
Mount-2_PB@28	Pyrite	254.74	-3.80	0.36	0.09
Mount-2_PB@30	Pyrite	254.74	1.61	0.39	0.02
Mount-2_PB@32	Pyrite	254.74	-1.38	0.32	0.00
Mount-2_PB@33	Pyrite	254.74	-1.03	0.33	-0.23
Mount-2_PB@34	Pyrite	254.74	-3.86	0.34	-0.43
Mount-2_PB@36	Pyrite	254.74	1.56	0.34	-0.19
Mount-2_PB@38	Pyrite	254.74	-0.55	0.30	0.18
Mount-2_PB@39	Pyrite	254.74	1.43	0.37	-0.47
Mount-2_PB@40	Pyrite	254.74	1.58	0.39	0.16
Mount-2_PB@41	Pyrite	254.74	1.56	0.39	-0.37
Mount-2_PB@44	Pyrite	254.74	-3.69	0.43	-0.72
Mount-2_PB@45	Pyrite	254.74	-0.47	0.29	0.23
Mount-2_PB@47	Pyrite	254.74	1.50	0.42	-0.39
Mount-2_PB@48	Pyrite	254.74	1.72	0.42	-0.10
Mount-2_PB@49	Pyrite	254.74	1.04	0.55	-0.24
Mount-2_PB@50	Pyrite	254.74	-3.81	0.34	-1.69
Mount-2_PB@51	Pyrite	254.74	-3.75	0.34	-0.11
Mount-2_PB@52	Pyrite	254.74	-3.74	0.33	-0.18
Mount-2_PB@54	Pyrite	254.74	9.99	1.04	-1.90
Mount-2_PB@56	Pyrite	254.74	11.05	1.05	-1.95
Mount-2_PB@59	Pyrite	254.74	2.10	0.64	-0.80
Mount-2_PB@61	Pyrite	254.74	1.52	0.43	0.40
Mount-2_PB@62	Pyrite	254.74	1.60	0.40	-0.49
Mount-2_PB@63	Pyrite	254.74	-0.24	0.34	-0.02
Mount-2_PB@64	Pyrite	254.74	1.54	0.39	0.10
Mount-2_PB@65	Pyrite	254.74	-0.21	0.31	-0.44
Mount-2_PB@66	Pyrite	254.74	1.29	0.41	0.03

Appendix to Chapter 6

Sample name	Lithology	Strat-depth (m)	$\delta^{34}\text{S}$	$\Delta^{33}\text{S}$	$\Delta^{36}\text{S}$
Mount-3_AC-210.7@02	Pyrrhotite	78.93	-1.70	0.61	-1.01
Mount-3_AC-210.7@03	Pyrite	78.93	-5.44	0.69	-0.92
Mount-3_AC-210.7@04	Pyrrhotite	78.93	-1.66	0.59	-1.25
Mount-3_AC-210.7@05	Pyrrhotite	78.93	-1.50	0.59	-1.28
Mount-3_AC-210.7@06	Pyrite	78.93	0.06		
Mount-3_AC-210.7@07	Pyrite	78.93	-0.32		
Mount-3_AC-210.7@08	Pyrrhotite	78.93	-5.72	0.74	-0.93
Mount-3_AC-210.7@09	Pyrite	78.93	-5.62	0.72	-1.79
Mount-3_AC-210.7@1	Pyrite	78.93	-5.40	0.71	-1.69
Mount-3_AC-210.7@10	Pyrite	78.93		0.78	-1.37
Mount-3_AC-210.7@11	Pyrite	78.93	0.21	0.26	-0.66
Mount-3_AC-210.7@12	Pyrite	78.93	-5.96	0.73	-1.54
Mount-3_AC-210.7@13	Pyrite	78.93	-5.91	0.73	-1.27
Mount-3_AC-210.7@14	Pyrite	78.93	-0.69	0.59	-0.70
Mount-3_AC-210.7@15	Pyrrhotite	78.93	-5.79	0.70	-1.49
Mount-3_AC-210.7@16	Pyrrhotite	78.93	-8.60	0.59	0.01
Mount-3_AC-210.7@17	Pyrite	78.93	-5.46	0.73	-0.35
Mount-3_AC-210.7@18	Pyrite	78.93	-8.62	0.55	-1.29
Mount-3_AC-210.7@19	Pyrite	78.93	-7.75	0.51	-0.50
Mount-3_AC-210.7@20	Pyrite	78.93	-6.32	0.82	-1.12
Mount-3_AC-210.7@21	Pyrite	78.93	-7.39	0.58	-0.21
Mount-3_AC-210.7@22	Pyrrhotite	78.93	-8.65	0.42	-2.08
Mount-3_AC-210.7@23	Pyrite	78.93	-7.02	0.58	-0.06
Mount-3_AC-210.7@24	Pyrrhotite	78.93	-8.47	0.55	-0.73
Mount-3_AC-210.7@25	Pyrite	78.93	-7.85	0.47	-0.64
Mount-3_AC-210.7@26	Pyrite	78.93	-8.11	0.57	-0.28
Mount-3_AC-210.7@27	Pyrite	78.93	-7.36	0.63	-1.92
Mount-3_AC-210.7@28	Pyrite	78.93	-7.44	0.63	-0.45
Mount-3_AC-210.7@29	Pyrrhotite	78.93	-5.27	0.78	-0.80
Mount-3_AC-210.7@30	Pyrrhotite	78.93	-5.21	0.74	-1.98
Mount-3_AC-210.7@31	Pyrite	78.93	-3.36	0.39	-0.48
Mount-3_AC-210.7@32	Pyrite	78.93	-8.41	0.46	-1.00
Mount-3_AC-210.7@33	Pyrrhotite	78.93	-3.41	0.42	-1.38
Mount-3_AC-210.7@34	Pyrrhotite	78.93	-7.31	0.51	-1.42
Mount-3_AC-210.7@35	Pyrrhotite	78.93	-2.83	0.52	-0.79
Mount-3_AC-210.7@36	Pyrite	78.93	-7.06	0.58	-0.30
Mount-3_AC-210.7@37	Pyrite	78.93	-2.03	0.60	-1.28
Mount-3_AC-210.7@38	Pyrite	78.93	-6.73	0.64	-0.22
Mount-3_AC-210.7@39	Pyrite	78.93	-7.23	0.66	-1.71
Mount-3_AC-210.7@40	Pyrrhotite	78.93	-9.06	0.48	-1.27
Mount-3_AC-210.7@41	Pyrite-disseminated	78.93	-14.99	-0.24	-0.61
Mount-3_AC-210.7@42	Pyrite-disseminated	78.93	-13.83	-0.14	0.12
Mount-3_AC-210.7@43	Pyrite-disseminated	78.93	-14.78	-0.10	-1.44
Mount-3_AC-210.7@44	Pyrite-disseminated	78.93	-14.35	-0.07	-0.29
Mount-3_AC-210.7@45	Pyrite-disseminated	78.93	-10.54	0.52	-1.22
Mount-3_AC-210.7@46	Pyrite-disseminated	78.93	-10.76	0.49	-1.09
Mount-3_AC-210.7@47	Pyrite-disseminated	78.93	-17.11	-0.45	-0.78
Mount-3_AC-210.7@48	Pyrite-disseminated	78.93	-17.94	-0.47	-0.08
Mount-3_AC-210.7@49	Pyrite-disseminated	78.93	-14.84	-0.49	-0.76
Mount-3_AC-210.7@50	Pyrite	78.93	-5.22	0.04	-0.50
Mount-3_AC-210.7@51	Pyrite	78.93	-0.81	0.40	-0.95
Mount-3_AC-210.7@52	Pyrite	78.93	0.20	0.66	-1.31

Appendix to Chapter 6

Sample name	Lithology	Strat-depth (m)	$\delta^{34}\text{S}$	$\Delta^{33}\text{S}$	$\Delta^{36}\text{S}$
Mount-4_AC-216@02	Pyrrhotite	80.92	-1.91	1.30	-1.40
Mount-4_AC-216@03	Pyrrhotite	80.92	-1.98	1.32	-1.14
Mount-4_AC-216@04	Pyrrhotite	80.92	-2.17	1.31	-1.92
Mount-4_AC-216@05	Pyrrhotite	80.92	-2.16	1.36	-1.60
Mount-4_AC-216@06	Pyrrhotite	80.92	-1.89	1.33	-1.52
Mount-4_AC-216@07	Pyrrhotite	80.92	-2.15	1.34	-2.12
Mount-4_AC-216@08	Pyrrhotite	80.92	-2.09	1.28	-1.42
Mount-4_AC-216@09	Pyrrhotite	80.92	-2.74	1.31	-1.53
Mount-4_AC-216@1	Pyrrhotite	80.92	-2.01	1.32	-1.92
Mount-4_AC-216@10	Pyrrhotite	80.92	-2.41	1.32	-1.52
Mount-4_AC-216@11	Pyrrhotite	80.92	-2.14	1.33	-1.48
Mount-4_AC-216@12	Pyrrhotite	80.92	-2.11	1.30	-1.25
Mount-4_AC-216@13	Pyrrhotite	80.92	-2.30	1.29	-1.35
Mount-4_AC-216@14	Pyrrhotite	80.92	-2.14	1.33	-1.08
Mount-4_AC-216@15	Pyrrhotite	80.92	-2.34	1.41	-1.62
Mount-4_AC-216@16	Pyrrhotite	80.92	-2.56	1.33	-1.23
Mount-4_AC-216@17	Pyrrhotite	80.92	-2.12	1.36	-0.91
Mount-4_AC-216@18	Pyrrhotite	80.92	-2.33	1.32	-1.80
Mount-4_AC-216@19	Pyrrhotite	80.92	-2.13	1.36	-1.07
Mount-4_AC-216@20	Pyrrhotite	80.92	-2.04	1.39	-1.47
Mount-4_AC-216@21	Pyrrhotite	80.92	-2.03	1.34	-1.36
Mount-4_AC-216@22	Pyrrhotite	80.92	-2.05	1.32	-1.88
Mount-4_AC-216@23	Pyrrhotite	80.92	-2.74	1.34	-1.80

Sample name	Lithology	Strat-depth (m)	$\delta^{34}\text{S}$	$\Delta^{33}\text{S}$	$\Delta^{36}\text{S}$
Mount-4_AC-212@02	Pyrite	79.42	5.88	0.28	-0.48
Mount-4_AC-212@03	Pyrite	79.42	6.11	0.01	0.19
Mount-4_AC-212@04	Pyrite	79.42	0.37	0.64	-0.98
Mount-4_AC-212@05	Pyrite	79.42	1.61		
Mount-4_AC-212@06	Pyrite	79.42	3.90	0.23	-0.35
Mount-4_AC-212@07	Pyrite	79.42	4.22	-0.01	-0.16
Mount-4_AC-212@08	Pyrite	79.42	3.36	0.35	-0.02
Mount-4_AC-212@09	Pyrite	79.42	-0.02	0.61	-0.97
Mount-4_AC-212@1	Pyrite	79.42	1.04	0.56	-0.81
Mount-4_AC-212@10	Pyrite	79.42	9.97	-0.04	0.02
Mount-4_AC-212@11	Pyrite	79.42	-0.35	0.59	-0.73
Mount-4_AC-212@12	Pyrite	79.42	5.80	0.08	0.60
Mount-4_AC-212@13	Pyrite	79.42	0.33	0.66	-0.61
Mount-4_AC-212@14	Pyrite	79.42	0.29	0.58	-0.45
Mount-4_AC-212@15	Pyrite	79.42	10.05	0.03	0.60
Mount-4_AC-212@16	Pyrite	79.42	8.44	-0.07	0.37
Mount-4_AC-212@17	Pyrite	79.42	6.03	0.31	0.28
Mount-4_AC-212@18	Pyrite	79.42	5.62	0.22	-1.08
Mount-4_AC-212@19	Pyrite	79.42	2.34	0.57	-0.16
Mount-4_AC-212@20	Pyrite	79.42	2.08	0.65	0.20
Mount-4_AC-212@21	Pyrite	79.42	0.39	0.62	-0.85
Mount-4_AC-212@22	Pyrite	79.42	-0.56	0.59	-0.81
Mount-4_AC-212@23	Pyrite	79.42	5.64	0.31	0.03
Mount-4_AC-212@24	Pyrite	79.42	-0.04	0.45	-0.31
Mount-4_AC-212@25	Pyrite	79.42	0.34	0.50	-0.42
Mount-4_AC-212@26	Pyrite	79.42	0.27	0.54	0.00
Mount-4_AC-212@27	Pyrite	79.42	0.61	0.68	-0.40

Appendix to Chapter 6

Sample name	Lithology	Strat-depth (m)	$\delta^{34}\text{S}$	$\Delta^{33}\text{S}$	$\Delta^{36}\text{S}$
Mount-4_AC-212@28	Pyrite	79.42	-0.07	0.42	-0.80
Mount-4_AC-212@29	Pyrite	79.42	0.35	0.47	-0.82
Mount-4_AC-212@30	Pyrite	79.42	0.50	0.55	-0.30
Mount-4_AC-212@31	Pyrite	79.42	0.00	0.64	-0.72
Mount-4_AC-212@32	Pyrite	79.42	-0.17	0.57	-0.68
Mount-4_AC-212@33	Pyrite	79.42	0.36	0.68	-0.18
Mount-4_AC-212@34	Pyrite	79.42	0.11	0.65	-0.55
Mount-4_AC-212@35	Pyrite	79.42	7.23	-0.13	0.20
Mount-4_AC-212@36	Pyrite	79.42	7.91	-0.10	0.51
Mount-4_AC-212@37	Pyrite	79.42	2.47	0.40	-0.54
Mount-4_AC-212@38	Pyrite	79.42	0.24	0.69	-0.39
Mount-4_AC-212@39	Pyrite	79.42	-0.03	0.62	-0.21
Mount-4_AC-212@40	Pyrite	79.42	-0.04	0.40	-0.95
Mount-4_AC-212@41	Pyrite	79.42	0.31	0.56	-0.72
Mount-4_AC-212@42	Pyrite	79.42	0.45	0.77	-0.05
Mount-4_AC-212@43	Pyrite	79.42	8.38	0.18	0.00
Mount-4_AC-212@44	Pyrite	79.42	9.33	0.10	0.32
Mount-4_AC-212@45	Pyrite	79.42	8.27	0.03	0.66
Mount-4_AC-212@46	Pyrite	79.42	8.75	0.03	0.35
Mount-4_AC-212@47	Pyrite	79.42	8.85	0.04	0.04
Mount-4_AC-212@48	Pyrite	79.42	11.30	0.17	0.43
Mount-4_AC-212@49	Pyrite	79.42	11.32	0.10	0.32
Mount-4_AC-212@50	Pyrite	79.42	6.68	0.13	0.15
Mount-4_AC-212@51	Pyrite	79.42	8.10	0.10	1.02
Mount-4_AC-212@52	Pyrite	79.42	7.08	0.13	0.45
Mount-4_AC-212@53	Pyrite	79.42	0.13	0.53	-0.17
Mount-4_AC-212@54	Pyrite	79.42	8.75	0.14	-0.06
Mount-4_AC-212@55	Pyrite	79.42	5.57	0.28	-0.22

Appendix to Chapter 6

Sample name	Lithology	Strat-depth (m)	$\delta^{34}\text{S}$	$\Delta^{33}\text{S}$	$\Delta^{36}\text{S}$
Mount-5_AC-214-7@02	Pyrite	80.43	0.64	-0.36	0.70
Mount-5_AC-214-7@04	Pyrite	80.43	-0.51	-0.35	0.76
Mount-5_AC-214-7@05	Pyrite	80.43	-2.66	-0.30	0.40
Mount-5_AC-214-7@06	Pyrite	80.43	-0.37	0.37	0.03
Mount-5_AC-214-7@08	Pyrite	80.43	-2.72	-0.28	0.47
Mount-5_AC-214-7@1	Pyrite	80.43	-0.54	0.29	0.29
Mount-5_AC-214-7@11	Pyrite	80.43	-0.87	0.23	0.38
Mount-5_AC-214-7@12	Pyrite	80.43	-0.43	0.33	-0.67
Mount-5_AC-214-7@13	Pyrite	80.43	-0.42	0.30	-0.49
Mount-5_AC-214-7@14	Pyrite	80.43	-0.54	0.28	-0.73
Mount-5_AC-214-7@17	Pyrite	80.43	-0.67	0.29	-0.58
Mount-5_AC-214-7@18	Pyrite	80.43	-0.74	0.31	-0.08
Mount-5_AC-214-7@20	Pyrite	80.43	-0.40	0.34	0.04
Mount-5_AC-214-7@21	Pyrite	80.43	-0.85	0.25	-0.59
Mount-5_AC-214-7@23	Pyrite	80.43	-1.15	0.52	-0.33
Mount-5_AC-214-7@24	Pyrite	80.43	-0.40	0.34	-0.58
Mount-5_AC-214-7@27	Pyrite	80.43	-0.42	0.32	-0.86
Mount-5_AC-214-7@28	Pyrite	80.43	-0.12	0.35	-0.55
Mount-5_AC-214-7@30	Pyrite	80.43	-0.26	0.45	-0.11
Mount-5_AC-214-7@32	Pyrite	80.43	-1.72	0.29	-0.23
Mount-5_AC-214-7@33	Pyrite	80.43	-1.45	0.28	-0.53
Mount-5_AC-214-7@34	Pyrite	80.43	-0.71	0.27	-0.37
Mount-5_AC-214-7@35	Pyrite	80.43	-0.62	0.23	0.69
Mount-5_AC-214-7@36	Pyrite	80.43	-0.29	0.31	-0.23
Mount-5_AC-214-7@38	Pyrite	80.43	-0.39	0.33	0.12
Mount-5_AC-214-7@41	Pyrite	80.43	-0.33	0.30	-0.46
Mount-5_AC-214-7@43	Pyrite	80.43	-0.60	0.29	-0.32
Mount-5_AC-214-7@44	Pyrite	80.43	-0.47	0.28	-0.13
Mount-5_AC-214-7@45	Pyrite	80.43	-1.29	0.30	-0.29
Mount-5_AC-214-7@46	Pyrite	80.43	4.51	-0.18	0.69
Mount-5_AC-214-7@50	Pyrite	80.43	5.13	0.09	-0.42
Mount-5_AC-214-7@53	Pyrite	80.43	5.96	0.14	0.31
Mount-5_AC-214-7@54	Pyrite	80.43	3.29	0.36	-0.72
Mount-5_AC-214-7@55	Pyrite	80.43	5.32	0.30	-0.44
Mount-5_AC-214-7@56	Pyrite	80.43	5.63	0.13	-0.78
Mount-5_AC-214-7@64	Pyrite	80.43	-0.20	0.35	-0.37
Mount-5_AC-214-7@65	Pyrite	80.43	2.91		
Mount-5_AC-214-7@68	Pyrite	80.43	-0.49	0.52	-0.15

Appendix to Chapter 6

Sample name	Lithology	Strat-depth (m)	$\delta^{34}\text{S}$	$\Delta^{33}\text{S}$	$\Delta^{36}\text{S}$
Mount-5_AC-214@002	Pyrite	80.17	-5.11	-0.37	-0.01
Mount-5_AC-214@003	Pyrite	80.17	-7.60	-0.65	-0.06
Mount-5_AC-214@006	Pyrite	80.17	-6.20	-0.48	0.40
Mount-5_AC-214@008	Pyrite	80.17	-6.04	-0.55	-0.31
Mount-5_AC-214@009	Pyrite	80.17	-7.12	-0.62	0.47
Mount-5_AC-214@011	Pyrite	80.17	-6.30	-0.54	-0.21
Mount-5_AC-214@012	Pyrite	80.17	-7.01	-0.61	0.03
Mount-5_AC-214@015	Pyrite	80.17	-3.68	-0.46	-0.42
Mount-5_AC-214@017	Pyrite	80.17	-7.64	-0.71	0.06
Mount-5_AC-214@018	Pyrite	80.17	-6.17	-0.28	-0.60
Mount-5_AC-214@020	Pyrite	80.17	-5.84	-0.52	0.05
Mount-5_AC-214@021	Pyrite	80.17	-7.35	-0.66	0.08
Mount-5_AC-214@023	Pyrite	80.17	-6.82	-0.60	-0.39
Mount-5_AC-214@025	Pyrite	80.17	-8.84	-0.78	-0.03
Mount-5_AC-214@027	Pyrite	80.17	-5.85	-0.44	-0.22
Mount-5_AC-214@028	Pyrite	80.17	-4.96	-0.45	-0.67
Mount-5_AC-214@030	Pyrite	80.17	0.13	0.36	-1.26
Mount-5_AC-214@032	Pyrite	80.17	3.16	0.20	-0.37
Mount-5_AC-214@033	Pyrite	80.17	0.66	0.42	-1.41
Mount-5_AC-214@035	Pyrite	80.17	3.77	0.15	-1.13
Mount-5_AC-214@036	Pyrite	80.17	2.19	0.01	-0.32
Mount-5_AC-214@037	Pyrite	80.17	2.49	0.07	-1.09
Mount-5_AC-214@038	Pyrite	80.17	0.31	0.48	-0.77
Mount-5_AC-214@040	Pyrite	80.17	2.86	0.00	-0.40
Mount-5_AC-214@041	Pyrite	80.17	3.29	0.21	-1.11
Mount-5_AC-214@043	Pyrite	80.17	3.11	0.08	-0.92
Mount-5_AC-214@044	Pyrite	80.17	2.22	0.12	-0.60
Mount-5_AC-214@046	Pyrite	80.17	2.14	-0.22	-0.35
Mount-5_AC-214@047	Pyrite	80.17	0.35	0.33	-1.14
Mount-5_AC-214@049	Pyrite	80.17	2.44	-0.05	-0.69
Mount-5_AC-214@050	Pyrite	80.17	2.65	-0.05	0.10
Mount-5_AC-214@051	Pyrite	80.17	3.06	-0.02	-0.63
Mount-5_AC-214@053	Pyrite	80.17	3.21	0.28	-0.46
Mount-5_AC-214@054	Pyrite	80.17	1.53	0.50	-1.23
Mount-5_AC-214@055	Pyrite	80.17	2.63	0.17	-0.03
Mount-5_AC-214@056	Pyrite	80.17	3.61	0.26	-0.26

Appendix to Chapter 6

Sample name	Lithology	Strat-depth (m)	$\delta^{34}\text{S}$	$\Delta^{33}\text{S}$	$\Delta^{36}\text{S}$
Mount-5_AC-214@059	Pyrite	80.17	0.09	0.40	-0.63
Mount-5_AC-214@060	Pyrite	80.17	0.29	0.44	-1.12
Mount-5_AC-214@061	Pyrite	80.17	3.97	0.31	-1.60
Mount-5_AC-214@062	Pyrite	80.17	3.02	0.16	-0.22
Mount-5_AC-214@064	Pyrite	80.17	1.21	0.53	-1.38
Mount-5_AC-214@065	Pyrite	80.17	3.54	-0.05	0.35
Mount-5_AC-214@066	Pyrite	80.17	0.45	0.45	-0.97
Mount-5_AC-214@067	Pyrite	80.17	0.43	0.40	-0.89
Mount-5_AC-214@069	Pyrite	80.17	2.86	-0.05	-0.25
Mount-5_AC-214@070	Pyrite	80.17	2.99	-0.03	-0.04
Mount-5_AC-214@071	Pyrite	80.17	3.29	0.09	-0.42
Mount-5_AC-214@072	Pyrite	80.17	0.38	0.48	-0.85
Mount-5_AC-214@073	Pyrite	80.17	2.62	0.25	-0.99
Mount-5_AC-214@074	Pyrite	80.17	3.64	0.11	-0.46
Mount-5_AC-214@076	Pyrite	80.17	0.67	0.53	-0.87
Mount-5_AC-214@078	Pyrite	80.17	3.15	0.18	-0.82
Mount-5_AC-214@079	Pyrite	80.17	3.43	0.46	-0.82
Mount-5_AC-214@080	Pyrite	80.17	3.70	0.19	-0.54
Mount-5_AC-214@081	Pyrite	80.17	0.60	0.42	-0.64
Mount-5_AC-214@082	Pyrite	80.17	3.29	0.11	-0.03
Mount-5_AC-214@083	Pyrite	80.17	3.79	0.21	-0.41
Mount-5_AC-214@085	Pyrite	80.17	0.43	0.46	-0.11
Mount-5_AC-214@086	Pyrite	80.17	0.85	0.50	-1.34
Mount-5_AC-214@087	Pyrite	80.17	1.39	0.30	-1.20
Mount-5_AC-214@089	Pyrite	80.17	3.59	0.21	-0.01
Mount-5_AC-214@090	Pyrite	80.17	0.52	0.45	-0.26
Mount-5_AC-214@091	Pyrite	80.17	0.24	0.43	-0.75
Mount-5_AC-214@092	Pyrite	80.17	0.91	0.40	-1.08
Mount-5_AC-214@093	Pyrite	80.17	0.32	-0.31	0.09
Mount-5_AC-214@094	Pyrite	80.17	-0.33	-0.47	0.04
Mount-5_AC-214@095	Pyrite	80.17	2.63	-0.12	-0.41
Mount-5_AC-214@096	Pyrite	80.17	0.20	0.37	-0.78
Mount-5_AC-214@097	Pyrite	80.17	0.66	0.58	-0.35
Mount-5_AC-214@098	Pyrite	80.17	9.55	-0.43	0.95
Mount-5_AC-214@101	Pyrite	80.17	1.01	-0.03	-0.81
Mount-5_AC-214@102	Pyrite	80.17	3.88	-0.47	0.24
Mount-5_AC-214@106	Pyrite	80.17	0.80	-0.64	0.59

Appendix to Chapter 6

Titre : Biogéochimie à l'aube de la déposition des carbonates sur Terre: chimiostatigraphie élémentaire et isotopique de la plateforme carbonatée Mésoarchéenne de Red Lake, Canada

Mots clés : Craton Supérieur, Mésoarchéen, Plateforme carbonatée, Chimiostatigraphie

Résumé : L'assemblage de Ball de Red Lake, préservé au Canada et daté de 2,87 Ga, représente la plus ancienne plate-forme carbonatée connue sur Terre. Cette étude présente des analyses sédimentologiques, élémentaires et isotopiques (carbone, oxygène et multiples isotopes du soufre) de cinq forages englobant une variété de roches chimiques et silicoclastiques déposées dans des eaux de grande à faible profondeur. Les spectres de terres rares des divers lithofaciès révèlent des caractéristiques à la fois archéens et modernes. La présence occasionnelle du dioxygène est déduite à partir d'anomalies positives et négatives en Ce, et des enrichissements en Mn et Cr dans certaines formations ferrifères et carbonatées suggèrent également une oxygénation périodique de la

colonne d'eau, au moins localement. Des enrichissements authigènes légers mais significatifs en Mo, V, U et Cr dans les carbonates et les formations ferrifères suggèrent un cycle d'oxydoréduction sous conditions légèrement oxique. La composition isotopique du carbone et de l'oxygène dans les carbonates est contrôlée par la minéralogie et la profondeur d'eau. La dolomie montre elle des signes d'interaction avec l'eau météorique, tandis que la calcite capture la signature isotopique du DIC de l'océan ouvert. Les données multi-isotopiques du soufre indiquent que les schistes sulfurés de Red Lake ont enregistré une variété de sources et de processus affectant le soufre comparable à d'autres roches sulfurées mésoarchéennes.

Title : Biogeochemistry at the dawn of carbonate deposition on Earth: elemental and isotopic chemostratigraphy of the Mesoarchean Red Lake carbonate platform, Canada

Keywords : Superior Craton, Mesoarchean, Carbonate platform, Chemostratigraphy

Abstract : The 2.87 Ga Ball Assemblage of the Red Lake Greenstone Belt, Canada preserves Earth's oldest known thick carbonate platform. This study presents sedimentological, elemental, and isotopic (carbon, oxygen, and multiple sulfur isotope) analyses of five cored drill holes capturing a variety of chemical and siliciclastic rocks deposited in shallow-to-deep water settings. The rare earth element systematics of the diverse lithofacies reveal features similar to both Archean and modern oceans. The occasional presence of oxygen is inferred from both positive and negative Ce anomalies, and associated Mn and Cr enrichments in some iron formation and limestone samples, suggesting periodic

oxygenation of the water column, at least locally. The mild but significant authigenic enrichment of Mo, V, U, and Cr in carbonates and iron formations suggest redox cycling under mildly oxic water column conditions. The isotopic composition of carbon and oxygen in carbonates are mineralogically and water-depth-controlled; dolostone shows evidence of meteoric water interaction during dolomitization, while limestone captured the isotopic signature of the open ocean DIC pool. Multiple sulfur isotope data indicate that the Red Lake sulfidic shales preserve a variety of sulfur sources and processing similar to other Mesoarchean rocks.